Simone Napolitano *Editor*

Non-equilibrium Phenomena in Confined Soft Matter

Irreversible Adsorption, Physical Aging and Glass Transition at the Nanoscale

Springer

Soft and Biological Matter

"Soft and Biological Matter" is a series of authoritative books covering established and emergent areas in the realm of soft matter science, including biological systems spanning from the molecular to the mesoscale. It aims to serve a broad interdisciplinary community of students and researchers in physics, chemistry, biophysics and materials science.

Pure research monographs in the series as well as those of more pedagogical nature, will emphasize topics in fundamental physics, synthesis and design, characterization and new prospective applications of soft and biological matter systems. The series will encompass experimental, theoretical and computational approaches.

Both authored and edited volumes will be considered.

Simone Napolitano

Editor

Non-equilibrium Phenomena in Confined Soft Matter

Irreversible Adsorption, Physical Aging and Glass Transition at the Nanoscale

Springer

Editor
Simone Napolitano
Polymer and Soft Matter Dynamics,
    Faculté des Science
Université Libre de Bruxelles (ULB)
Brussels
Belgium

Preface

Confined at the nanoscale level, soft matter reveals a fascinating behavior, strongly deviating from what is observed in macroscopic samples. Shifts in phase transition temperatures by almost 100 K, impressive increases in elastic moduli, tremendously longer lifetimes of amorphous compounds—these are just a few examples of the *confinement effects* which, for more than 20 years have been fascinating a broad community of researchers.

The classical view of the deviation from bulk behavior focuses on the balance of finite size effects and interfacial interactions in systems at thermodynamic equilibrium. For example, thin films (thickness typically below 100 nm) are treated as slabs where the bulk molecular dynamics is locally perturbed by the presence of free surfaces (~ 2 nm layer at the interface with air, other gases, or vacuum) and adsorbing interfaces (proximity of non-repulsive wall). A reduction in the glass transition temperature is commonly imputed to the faster dynamics of free surfaces, while the presence of an adsorbing interface is considered as a source of slower molecular modes.

Such a picture, although very intuitive, cannot describe the peculiar features of soft matter under confinement, including exotic phenomena like the increase in glass transition temperature, T_g, at the free surface of star-shaped polymers and the reduction in T_g of capped films (no free surfaces), in several nanocomposites and in adsorbed layers. It is obvious that one or more key parameters are still missing in our understanding of confined systems.

A solution to this problem could come from the large and growing experimental evidence remarking the presence of ultraslow relaxation processes manifesting at timescales exceeding by several orders of magnitude the bulk equilibration time. These observations aliment the idea that the commonly used preparation protocols (deposition of a solid phase upon rapid solvent evaporation) lock molecular conformations into non-equilibrium states. The deviation from bulk behavior should thus be treated as the manifestation of non-equilibrium phenomena.

In this book, collecting the results of experiments and simulations, we provide the first comprehensive coverage of the impact of non-equilibrium structure and dynamics on the properties of soft matter confined at the nanoscale level.

The 12 chapters of this volume are grouped into three main parts, providing a broad overview of the state of the art in the field. *Equilibration and Physical Aging*: treating non-equilibrium phenomena via the formal methodology of statistical physics in bulk, the analysis of the kinetics of equilibration permits shedding light on the physical origin of the non-equilibrium character of thin polymer films. Both the impact of sample preparation and that of interfacial interactions are analyzed using a very large set of experiments, including dewetting and spinodal decomposition. A historical overview of the investigation of the non-equilibrium character of thin polymer films is also presented. Furthermore, the discussion focuses on how interfaces and geometrical confinement perturb the pathways and kinetics of equilibrations of soft glasses (a process of tremendous technological interest, commonly known as *physical aging*). *Irreversible Adsorption*: the formation of stable adsorbed layers occurs at timescales much larger than the time necessary to equilibrate soft matter in bulk. It is questioned whether this process could be considered as the driving force of equilibration. Recent work showed, in fact, a strong correlation between the behavior of polymers under confinement and the presence of a layer irreversibly adsorbed onto the supporting substrate. This correlation furthermore hints at the possibility to tailor the properties of ultrathin films by controlling the adsorption kinetics. In this section, the investigation of the physics of irreversible chain adsorption is accompanied by a detailed analysis of the molecular dynamics, structure, morphology, and crystallization of adsorbed layers. *Glass Transition and Material Properties*: the discussion covers a broad range of non-equilibrium phenomena affecting different family of soft materials—polymers, low molecular glass formers, liquid crystals. In these systems, geometrical confinement induces the formation of non-equilibrium phases, otherwise not achievable via processing of bulk samples. For example, ferroelectricity is unexpectedly observed in thin films and nanotubes of a polymer being paraelectric in bulk, while the interfacial phases of OH-bonded liquids and of discotic liquid crystals present a remarkable increase in structural order, not achievable via processing of macroscopic samples; an efficient example of chemical engineer at the nanoscale level, where nanopores are employed to obtain stress-free products, is also introduced. These examples show how non-equilibrium phenomena could be exploited as innovative processing parameters to fabricate novel nanomaterials with improved performance.

Finally, the differences between experiments performed under equilibrium conditions (e.g., a frequency sweep at constant temperature) and temperature scan from equilibrium to non-equilibrium states (e.g., differential scanning calorimetry or ellipsometry) at the nanoscale are discussed here.

I sincerely hope that this book can contribute to the progress of understanding soft matter and stimulate the discussion on non-equilibrium phenomena at the nanoscale level.

Bruxelles   Simone Napolitano
May 2015

Contents

Part I
Equilibration and Physical Aging

Chapter 1
History Dependent Temporal Changes of Properties of Thin Polymer Films

Günter Reiter

Abstract Despite an extensive number of investigations, it is becoming increasingly obvious that a clear understanding of thin polymer film properties has not yet been reached. The origin of (some of) the puzzling behavior of thin polymer films is still not satisfactorily unveiled. At present, we are still missing a consistent understanding of how film preparation and confinement affect film properties, in particular on approaching the glass transition temperature. While it may be disputable if the change from the initial solution to a dry glassy film introduces a "conformational state" with its "own" properties, we will present various findings, mainly observed in dewetting experiments, which demonstrate the influence of sample preparation and of the thermal history these films have undergone. We conclude that thickness is not the only parameter defining the properties of thin polymer films, i.e., they depend in addition on what happened to a film before a particular measurement was performed.

1.1 Introduction and General Aspects

Polymers represent one of the most important, versatile and strongest growing classes of materials for constructing functional systems. Polymers are thus included in a wide range of applications, e.g., as structural elements (deformable parts, lightweight matrix for composite materials, fiber materials, …) or as functional units (organic electronics, photovoltaics, optical and mechanical meta-materials, …).

Two key aspects are performance and processability. To meet future challenges in energy production and storage, medical technology, information technology and sustainable development we therefore require significant advancements in improving

G. Reiter (✉)
Institute of Physics and Freiburg Materials Research Center,
University of Freiburg, 79104 Freiburg, Germany
e-mail: guenter.reiter@physik.uni-freiburg.de

3

the performance of polymeric materials. At the same time, fast and efficient processing conditions are required for the production of such innovative and advanced polymeric materials. These conditions can, especially when the intrinsic molecular relaxation times are longer than the processing time, i.e., Weissenberg numbers larger than 1, determine the final properties of these materials and thus their suitability for various applications (a few examples are given in: [1–6]). Accordingly, influencing material properties by processing conditions allows to widen the range of applications as these properties may become adaptable to the needs of the application. Thus, it is essential that concepts for polymer processing change from empirically optimizing processing parameters to a rational and predictive strategy in designing the desired properties. In the here presented experimental studies on varying properties of polymers of thin films, we aim to develop some preliminary concepts for tuning properties of polymers via processing steps.

Polymers are entropy-dominated systems. During processing, these systems can evolve through different sequences of states, corresponding to different topological pathways of similar energy [3]. These pathways may involve structure formation by self-assembly, phase separation, phase transitions, etc. Small free-energy differences between these states offer the possibility to select pathways to desired morphologies that may not correspond to equilibrium. Fast processing of polymers unavoidably introduces out-of-equilibrium chain conformations because polymers cannot fully relax during the limited time allowed by processing conditions [1–6]. A multitude of possible non-equilibrium states can be established, mainly due to the chain-like structure of polymers, which allows for a vast number of possible arrangements of the monomers without risking to loose connectivity between these segments. Here, in the context of thin polymer films, we mainly concentrate on non-equilibrium states introduced by different ways of thin film preparation from rather dilute solutions and show how properties of such thin polymer films can be affected by such states.

Processing of polymers often involves a sequence of physical operations such as evaporation, temperature change or shear which will generate forces acting on the polymer chains. Under the influence of such forces, polymer chains can change their conformations, i.e., the arrangements of the connected monomers, and are thus able to exist in different states of order. Polymer conformations sensitively affect mechanical, rheological, optical, electronic properties. Taking advantage of this molecular flexibility and adaptability, even a single component polymer system may become functional and adaptable.

Recently, several research groups have begun to investigate how polymer conformations and structures topologically evolve and how this evolution could be guided during typical processing situations [1–6]. However, we still need to undertake significant efforts to identify fundamental steps during polymer processing to finally be able to actively guide structural evolution of appropriate designed materials to realize the desired functions and properties.

We may hope to improve material performance by strategically exploiting non-equilibrium preparation pathways for the formation of these complex

macromolecular systems, which includes possibilities to reduce processing time through ultra-fast processes and high throughput approaches. In addition, the long-term stability (slow aging behavior) may be enhanced through the identification and implementation of long-lived metastable non-equilibrium structures.

Thin films are often prepared from a dilute solution. Spin-casting is one of the most frequently applied techniques [7–9], yielding extremely smooth and apparently homogenous films with a thickness down to ca. 2 nm within seconds [10–14]. By varying the concentration of the solution, the process of spin-casting allows to vary easily and controllably the film thickness. In the course of spin-casting, the solvent evaporates rapidly. Due to evaporation, the concentration of the polymer within the solution increases and eventually the film vitrifies. Often, vitrification occurs already at a point when there is still a significant amount of solvent within the film. Due to the short processing time and the increasing polymer relaxation time, it is questionable if the initially swollen and significantly separated polymers are able to sufficiently interpenetrate and equilibrate in the course of film preparation.

During such processing, often significant forces are acting on a polymer chain which may respond via changes of its conformation. For a given length of a polymer, the magnitude of these changes will depend on the value of the acting force and the time scale on which this force is acting. Often the time scale of processing is much shorter than the relaxation time scales of macromolecules, which can be quite long due to the large size and a correspondingly low mobility of macromolecules. Thus, one has to expect a large spectrum of non-equilibrium states.

Presently we do not have detailed and systematic studies on how acting forces change polymer conformations and we are consequently lacking fundamental understanding for a rational design of processing steps in terms of modifying/adjusting macromolecular conformations or controlling of macromolecular conformations of non-equilibrium states. We do not possess a theoretical framework for describing non-equilibrium states of macromolecules.

A large number of studies on thin polymer films revealed that various physical properties exhibited characteristics strongly deviating from their bulk behavior [10–47], with major implications for most technological applications based on such nanoscopic films. Diverse measurements have shown anomalous irreversible and reversible density changes after annealing below the bulk glass transition temperature, unexpected instabilities of these films, unusual aging, deviations in mobility, deformed chain conformations, dewetting processes independent of molecular weight and much faster than suggested by bulk visco-elasticity, clear indications for residual stresses within these spin-coated thin polymer films, a thickness but also history dependent glass transition temperature, and fast relaxation processes. The cause of these deviations is a matter of ongoing debate.

1.2   "Historical" Remarks on Thin Polymer Films

As mentioned above, the consequences of non-equilibrium chain conformations of the polymers on film properties are not yet well understood. But we may speculate that sample preparation represents a possible cause for the anomalous behavior in glassy thin polymer films. Film preparation may have an influence on measurements of visco-elastic properties, film stability, glass transition temperature, diffusion coefficient, etc. In particular, we have to examine if fast evaporation of the solvent during the widely used process of spin-casting [7–9] can potentially affect the properties of polymer thin films.

In this context, it is instructive to have a look at some previous studies on spin-cast thin polymer films [10–13, 15–18, 47]. Being able to prepare smooth thin polymer films of variable thickness allowed to study questions related to the chain-like nature of macromolecules. In particular, it has been speculated that polymer properties like viscosity, chain orientation, interdiffusion rates, or mechanical properties and the glass transition temperature may change once the thickness of the film decreased below the diameter which Gaussian polymer coils have in bulk samples.

In Fig. 1.1 we show observations on changes in film thickness published already in 1993 [10]. There, annealing freshly spin-cast thin polymer films well below the glass transition temperature of the bulk system ($T_{g,bulk}$) for one hour under vacuum, followed by a quench to room temperature, showed significant increase in film thickness, i.e. a decrease in film density by X-ray reflectometry. It has to be emphasized that at these low temperatures well below $T_{g,bulk}$, no dewetting was observed. It also has to be noted that such films, when annealed (or aged) at temperatures well below $T_{g,bulk}$, showed a reversible behavior in the change of film
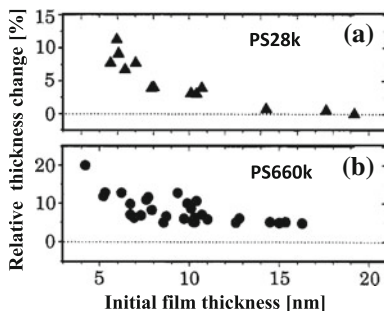
Fig. 1.1 Maximum relative change in thickness normalized by the initial thickness h_0 of the film as a function of h_0 for **a** polystyrene of M_w = 28 kg/mol (PS28 k) and **b** polystyrene of M_w = 660 kg/mol (PS660 k). The density of these films was lower than in the bulk and decreased with decreasing h_0. This change in density caused an increase of the mobility of the molecules with decreasing h_0. It was suggested that these effects resulted from an enlargement of the number of inaccessible sites caused by segregation of the molecules as h_0 decreased. The figure is adapted from Ref. [10]

thickness with temperature. The observed values of the relative change in film thickness decreased as h_0 increased. In addition, the observed thickness changes showed an influence of molecular weight.

From these observations, published in 1993 [10], it has been concluded that *"sufficiently thin films show, compared to the bulk, a lower density and an increased mobility. The latter corresponds to a reduction of the glass transition temperature which, in turn, can be related to the lower density."* As a tentative answer for the question "Why is the density of polymers confined in a thin film lower than that in the bulk?" it was speculated that *"chains do not significantly interpenetrate each other due to high entropy losses* [48], *the density of these swollen chains has to be lower than in the bulk. One might call the empty sites within the chains the <inaccessible volume>".*

Reflectometry studies of spin-cast thin polymer films [10–13, 20, 21, 23, 24] provided rather detailed information on changes in film thickness and interfacial roughness of the film/air interface. In particular, it was found that thin polymer films "shrink" by large amounts when annealed in the glassy state at temperatures even well below $T_{g,bulk}$. Changes in film thickness by more than 10 % have been observed at temperature well below $T_{g,bulk}$, even at room temperature when storing these films for days or months. This is not compatible with the assumption that polymer films are incompressible. Consequently, one has to anticipate that right after the film has been prepared by spin-casting, i.e. by rapid evaporation of the solvent, polymer films contained a large amount of unoccupied volume. Tentatively, one may assume that this then unoccupied volume was previously taken up by the solvent molecules which have evaporated from an already vitrified film. These observations of anomalously large thickness changes in ultra thin films of glassy polystyrene polymers have been summarized in [18] through a cascade of metastable states. There, also some (tentative) interpretations of these states, schematically shown in Fig. 1.2, have been suggested.

Unexpectedly, in several cases these films were not stable, i.e., dewetted and transformed into droplets, when annealed above $T_{g,bulk}$. Even more surprisingly, the thinnest films were unstable even below $T_{g,bulk}$ [10]. Stability, however, is a precondition for investigating specific properties as a function of film thickness.
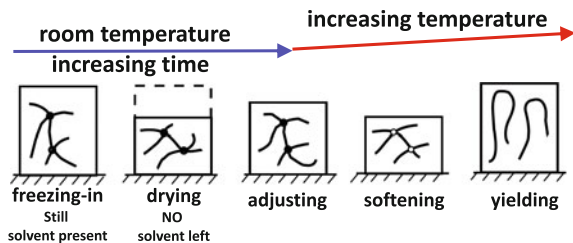
Fig. 1.2 Schematic presentation of some typical states of a spin-cast polymer film. While some initial processes may take place within seconds, subsequent relaxation and aging processes, in particular at temperatures below the glass transition temperature, may involve significantly longer times. The figure is adapted from Ref. [18]

For somewhat thicker films annealed at higher temperatures, but still well below $T_{g,bulk}$, simple inspection of these thin films by optical microscopy made it clear that the instability of the film was related to a retraction of the film from the substrate, i.e. the film dewetted the substrate [49]. The dewetting process provides profound insight into rheological properties of thin polymer films [32]. Polymers have negligible vapor pressure (polymers are non-volatile) which ensures mass conservation in the course of dewetting. Their typically rather high viscosity assures that dewetting is slow enough to allow for simple, time resolved measurements. Moreover, the possibility to tune the film thickness in the nanometer range allowes for testing the influence of short and long range intermolecular forces on film stability and dewetting dynamics [50–52]. Dewetting allows to investigate kinetic effects like friction (energy dissipation) at an interface. Dewetting experiments are attractive because of their simplicity, sensitivity and rapidity.

We conclude by stating that dewetting allows to link static and kinetic molecular and interfacial properties with macroscopically easily observable parameters like dewetting velocity and shape of the rim [47]. Despite its simplicity with respect to experimental observation, dewetting turned out to be extremely sensitive to even tiniest changes in the system under investigation. Thus, dewetting has proven to be a highly successful and time-efficient tool for obtaining time-resolved information on a molecular scale, allowing to determine interfacial properties and their changes in real time and in situ. Finally, dewetting experiments can provide information about relaxation and aging processes of polymers in the film.

1.3 Dewetting: Some Basic Features and Theoretical Considerations

In general, if a substrate has a lower surface tension than a fluid, this fluid will not form a stable film when deposited onto such a substrate. Consequently, such an unstable fluid film will retract from this substrate by a dewetting process [49, 53–57]. Capillary forces resulting from intermolecular interactions are responsible for this retraction of the fluid film [53]. The process can be described by the balance of driving forces, which try to remove the fluid, and dissipative processes, which reflect the resistance of the fluid to its removal. In particular, the temporal evolution of the dewetting process is controlled by this balance of forces.

In this context, it is an advantage that we are investigating thin films. Under such conditions, we can neglect gravity (because the mass of the film is extremely small) and inertia (because we investigate cases where the dewetting velocity is comparatively small). While many geometries and interfacial conditions can be considered, we concentrate on the simple case of a visco-elastic fluid on a smooth substrate. Accordingly, we assume that the fluid is completely characterized by its viscosity and elastic component. Moreover, we assume that the substrate is inert and does not generate hysteretic behavior, i.e., we exclude contact line pinning and chemical reactions at the substrate.

In Fig. 1.3, we define the central parameters, which have to be measured systematically in a dewetting experiment. The changes of the dewetted distance (this is either the radius $R(t)$ of a hole, when dewetting is initiated by a point, or the distance $L(t)$ to an initiating straight contact line) are controlled by the balance of acting forces, for example related to frictional properties at the film-substrate interface. The parameters $W(t)$ and $H(t)$, which characterize the rim, reflect information on the rheological properties of the fluid film.

As mentioned above, on non-wettable substrates, capillary forces are responsible for the retraction of a fluid film. These forces will also act if the film is vitrified or highly viscous, characterized by an elastic or visco-elastic behavior. Thus, one may expect that dewetting of visco-elastic films is following similar laws [58, 59]. Dewetting, however, may be slow or quasi-stopped on experimentally accessible time-scales if the acting forces are weak. In the following, we will discuss how visco-elastic properties of a film, and in particular stresses within the film, affect the dewetting process. For thin PS films the time-scale of such dewetting experiments is expected to be extremely long, especially at temperatures not too far above $T_{g,bulk}$ [19, 56, 57]. Furthermore, it may be questioned if capillary forces of the order of 10 mN/m are strong enough to provoke dewetting. In order to be able to observe dewetting within acceptable times, and to emphasize the consequences of driving forces, we have reduced interfacial friction by using low friction surfaces like silicon substrates coated with polydimethylsiloxane (PDMS). This allowed us to follow the process of hole growth in polystyrene (PS) films in detail across many length- and time-scales.

As one may have guessed, elasticity of the film is affecting characteristic features of the dewetting morphology. The dynamics of dewetting, i.e., the temporal
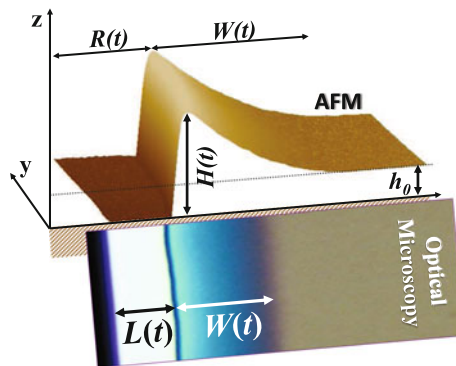
Fig. 1.3 Typical 3D view (measured by atomic force microscopy), compared with the observation by optical microscopy, of a section of a typical rim around a dewetting hole obtained in a PS film on a PDMS-coated substrate at temperatures close to the glass transition of PS. $H(t)$ is the maximum height of the rim which depends on dewetting time t. h_0 is the initial height of the film, $L(t)$ and $R(t)$ represent the dewetted distance for dewetting from a straight line or for the opening of a hole, respectively. $W(t)$ is the width of the rim. While h_0 and $H(t)$ are in the nanometer range, all other lengths are of the order of micrometers
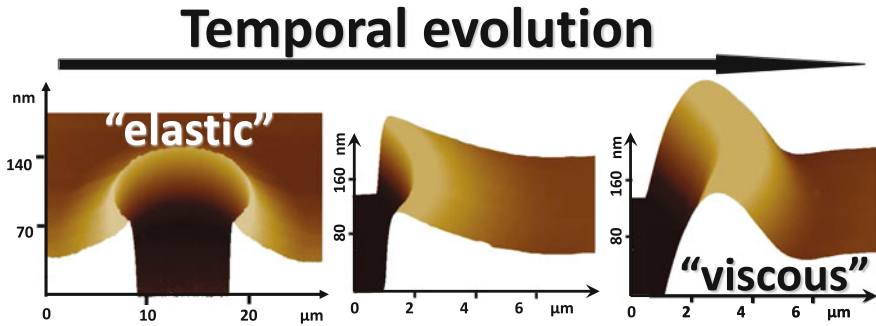
Fig. 1.4 3D-view (measured by atomic force microscopy) of a typical hole obtained by dewetting a polystyrene film on a PDMS-coated substrate at temperatures close to the glass transition of PS. The focus is on the evolution of the cross-section of the rim, which changes from an asymmetric shape at early stages to a more symmetric shape at late stages

evolution of the shape of the rim or the hole diameter is differing from purely Newtonian liquid films [58, 59]. For long dewetting times, however, even polystyrene films switch from an initially highly elastic behavior to a purely viscous fluid [60]. Visco-elastic fluids behave elastically at short time-scales and show viscous flow at long times. This change in rheological behavior becomes clearly evident in the dewetting features, e.g., represented by the shape of the rim, as can be seen in Fig. 1.4. Of course, the time of this transition depends on the characteristic relaxation time of the visco-elastic fluid, which typically decreases with increasing temperature.

1.4 Dewetting Experiments with Polystyrene Films at Temperatures Slightly Above the Glass Transition

A surprise and thus representing a significant result concerns dewetting of ca. 10–20 nm thin PS films of widely different molecular weight at temperatures around $T_{g,bulk}$ [19]. Like for dewetting at high temperatures, these films ruptured upon annealing. Here, we concentrate on the probability of hole formation and how these holes evolve with time at temperatures above ca. 103 °C. Complementary experiments indicated, however, that hole formation was possible at even lower temperatures [27].

In Fig. 1.5, we present typical atomic force microscopy (AFM) results for early stages of dewetting in very thin films. Many holes of similar size were formed within the small area detected by AFM [19]. Most holes were formed within a narrow time interval at the very beginning of annealing at 105 °C. At such early stages, the material displaced from the dewetted areas was not collected in visible rims around these areas but it was distributed evenly within the whole film in
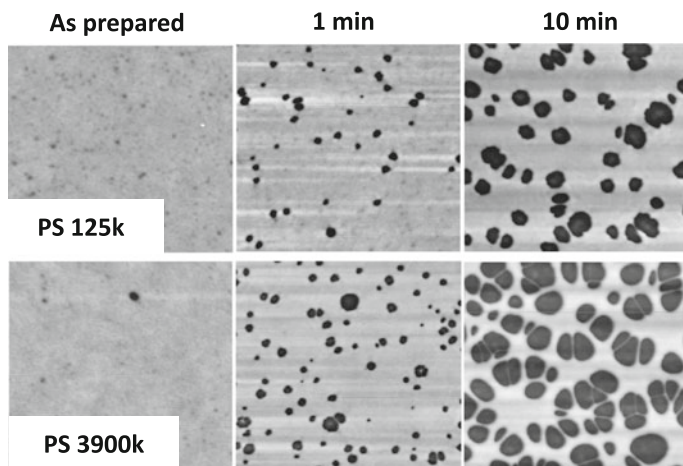
Fig. 1.5 Typical atomic force micrographs showing the consequences of annealing thin PS films on PDMS coated Si-wafers at a temperature close to the glass transition of PS. Rimless holes of some 100 nm in diameter were formed within minutes. Two different molecular weights are compared as indicated in the figure. First row: 16 nm polystyrene of $M_w = 125$ kg/mol (PS125 k); second row: 13 nm polystyrene of $M_w = 3900$ kg/mol (PS3900 k). First column: the as-prepared samples; second and third column: measured after annealing for 1 and 10 min at 105 °C, respectively. The size of the images is 3×3 μm^2. The figure is adapted from Ref. [19]

between the holes. Thus, imposing mass conservation, the film thickness between the holes had to increase, as was verified by AFM by measuring the depth of the holes.

The surprising aspects are twofold: First, independent of how long the polymers were, the rate of hole opening was almost identical. This implies that the viscosity of the polymer, which increases significantly with molecular weight and differed by many orders of magnitude for the two polymers investigated, was not the key rheological parameter characterizing the rate of hole opening. This result rather indicated that the plateau shear modulus of PS, which does not depend significantly on chain length, was the essential control parameter for the growth rate. Second, the initial opening velocity of the holes was of the order of 100 nm/min. For temperatures close to the glass transition with reptation times of the order of years, we cannot interpret the observed dewetting by viscous flow of the polymer. In addition, as could be deduced from the asymmetric shape of the rim observed for larger holes obtained in thicker PS films, the film behaved mainly like an elastic sheet. However, assuming a purely elastic material, the acting capillary forces, derived from known values of interfacial and surface tensions, would not be sufficient to lead to such an unexpectedly high dewetting velocity. Thus, it became obvious that an additional driving force was required.

Based on these experiments of 2001, it was concluded that a thin film does not need to be purely liquid in order to allow for dewetting. Also, thin solid films of low elastic modulus and large deformability can be dewetted, given that intermolecular

Dewetting time [125°C]
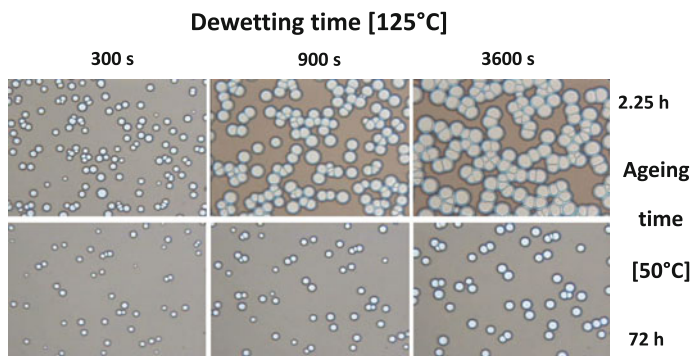
Fig. 1.6 A typical example showing the influence of aging at 50 °C on the probability of film rupture. The consequences of aging well below T_g were visualized by subsequent dewetting at 125 °C. Clearly, the number of holes and the diameter at a given time of dewetting decreased with aging time. The size of the images is $310 \times 210 \ \mu m^2$. The figure is adapted from Ref. [47]

forces are strong enough. Furthermore, it was stated in [19] that "phenomena like changes in film morphology or apparent thickening may also occur below the glass transition temperature (T_g) and can therefore not be taken as a criterion for determining T_g."

Some time later [28], the required additional driving force was identified through aging experiments (see Fig. 1.6): holes formed less rapidly and less frequently in films which were stored for some time (days up to years) at room temperature. Thus, it was speculated that polymers within a thin spin-cast film experience internal tensions (residual stresses) which relaxed during aging. It was assumed that these residual stresses were induced during sample preparation and attributed to the fact that the polymers were confined to thin films, which sometimes were even thinner than the size of the unperturbed coil.

Intriguingly, as e.g. clearly shown by the diameter of the holes after one hour of dewetting, aging for only a few hours at temperatures well below T_g caused dramatic changes in the dewetting behavior. Thus, even in the glassy state the induced stresses were able to relax, at least partially. This reduction of stresses occurred at an unexpectedly fast rate, given that no long range movements of the polymers are possible in the glassy state.

1.5 Consequences of Transient Residual Stresses in Thin Polymer Films

The relaxation process of residual stresses can also be followed indirectly by studying dewetting of spin-cast thin viscoelastic polymer films on soft elastic substrates [33]. There, the transient contribution of residual stresses leads to a nonmonotonic, two-stage dewetting behavior (see Fig. 1.7). The magnitude of the
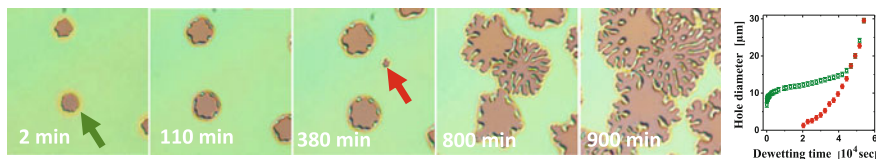
Fig. 1.7 Optical micrographs showing dewetting of a 40 nm PS film (M_w = 1.0 Mg/mol) on a 200 nm PDMS layer at 180 °C for increasing time. The size of the images is 58 × 58 μm^2. The graph at the end represents the hole diameter (for uneven holes, a mean diameter of the enveloping perimeter of the hole was taken for a hole starting to grow immediately (labeled by a *gray arrow*) and a hole (labeled by a *dark arrow*) starting to grow with a delay of several times the reptation time. The figure is adapted from Ref. [33]

residual stresses, introduced by out-of-equilibrium molecular conformations, can amount up to several times the capillary force [31, 61, 62]. In these dewetting experiments, part of the corresponding energy of the residual stresses is temporarily stored in the form of deformation energy of an elastic substrate. The size of this deformation is thus making the magnitude of these stresses visible.

Due to the formation of an elastic deformation of the substrate (the trench), achieved after only few minutes of annealing at 140 °C (see Fig. 1.8), hole opening came to an apparent standstill. The forces resisting dewetting due to the elastic trench remained until polymer diffusion and viscous flow were able to equilibrate the trench. This equilibration needed times of the order of the reptation time and led to the formation of a much shallower "viscous trench" caused by the normal component of the capillary force. At that point, most resistance due to deformation of the rubbery PDMS film was removed and the PS film slipped on the PDMS substrate.

The substrate depression (*D*), measured inside the hole (see Fig. 1.8f), was considered as a direct indicator of the local strain in the PDMS layer, from which the total dewetting force exerted on the film was estimated [28, 32, 58, 59]. *D* reached a maximum value within relatively short time and slowly started to decrease afterward (see Fig. 1.8g). The maximum value of *D*, but also the size of the maximum (quasistatic) hole diameter, which also was reached rapidly in times much shorter than the reptation time (τ_{rep}), were found to be largely independent of molecular weight for the high molecular weight samples studied.

In conclusion, at times shorter than the relaxation time of the polymer (i.e., $t < \tau_{rep}$), dewetting generated deep trenches in the soft rubbery substrate which, in turn, almost stopped dewetting. At later stages ($t > \tau_{rep}$), dewetting accelerated, accompanied by an unstable rim. However, when holes were nucleated only after the relaxation of residual stresses, they never caused large deformations of the soft substrate. There, no significant elastic trench was formed and equilibration of the trench was fast. The transition to a viscous dewetting behavior occurred soon after hole nucleation. Thus, the observation of two stages in the dewetting process is
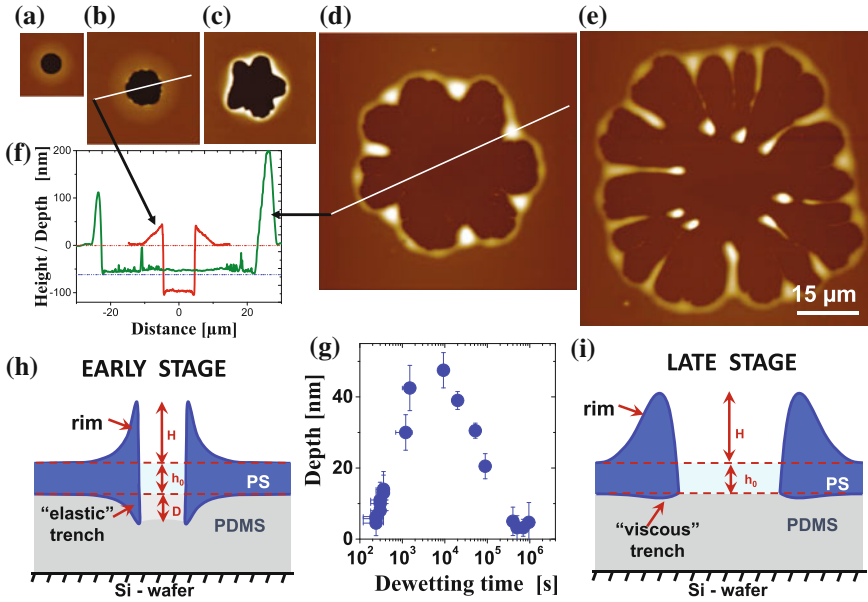
Fig. 1.8 Atomic force microscopy dewetted holes in a 55 nm PS film (M_w = 1.0 Mg/mol) on a 360 nm PDMS layer, dewetting at 140 °C (τ_{rep} = 160000 s) for **a** 300, **b** 1500, **c** 20 000, **d** 800 000, and **e** 950 000 s, respectively. **f** Cross sections indicated by white lines through holes (**b**) and (**d**). The surface of the unperturbed PS film has been set to zero depth level. Accordingly, the level of the unperturbed PDMS surfaces is at 55 nm below the unperturbed PS surface. The trace through the hole (**b**) represents the transient depression of depth D in the soft substrate. **g** Depth of the depression within the hole versus dewetting time for the sample shown in **a–e**. **h** and **i**: Schematic representation of the shape of the rim and the trench of a dewetting hole in a PS film deforming the soft rubbery PDMS layer underneath. Because of elastic deformation of the PS film at early stages the corresponding elastic trench is digging into the soft PDMS under-layer quite deeply. At late stages, after the relaxation time τ_{rep}, only a small deformation (viscous trench) due to the normal component of the capillary force at the three phase contact line is left in the PDMS layer. The figure is adapted from Ref. [33]

attributed to large elastic deformations in the substrate which are caused by transient residual stresses within the film.

If stresses would not relax and the elastic deformation of the substrate could be maintained indefinitely, holes would never grow beyond a maximum diameter determined by the balance of forces driving dewetting and the counteracting elastic force resulting from the induced elastic deformation of the rubbery substrate. Thus, the slow disappearance of such elastic behavior in the course of time demonstrates the existence of long-lasting, but nonetheless transient metastable states within spin-cast thin polymer films.

1.6 Aging and Relaxation Processes of Residual Stresses in Thin Polymer Films

The non-equilibrium properties of spin-cast polymer films manifest themselves also in the hole-opening kinetics [38, 45]. Because the effects introduced by film preparation may change with time, special care must be taken when conducting hole-opening experiments: Since PS films are known to change their properties when stored at room temperature (aging), the time elapsed between film preparation and the beginning of the dewetting experiment must be taken into account. When brought to the dewetting temperature (above T_g), holes nucleate at various times during annealing. Dewetting of holes nucleated after some incubation time are thus reflecting the behavior of an already (partially) annealed film with no or with reduced residual stresses. As can be seen in Fig. 1.9a, we can follow simultaneously the temporal evolution of several holes, nucleated after different incubation times. While all holes show qualitatively a similar behavior (see Fig. 1.9b), the super-position of these curves as a function of the time for which they actually grew (see Fig. 1.9c) shows significant slowing down of growth with incubation time,
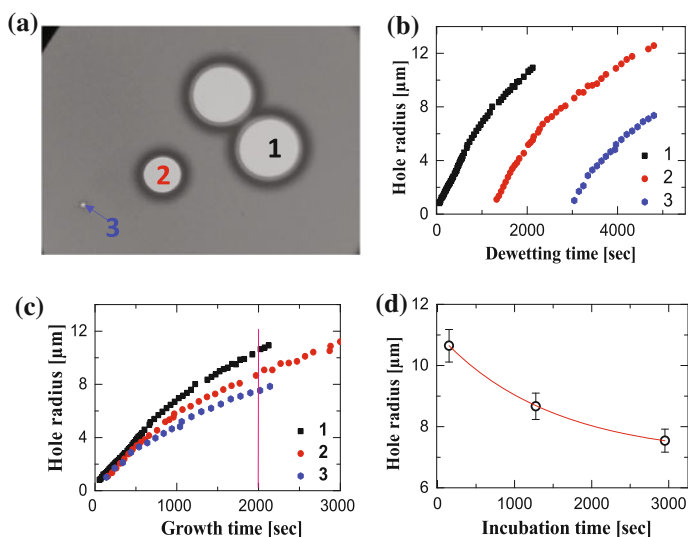
Fig. 1.9 **a** Optical micrograph (size: $143 \times 106 \ \mu m^2$) of a PS film ($M_w = 16800$ kg/mol, thickness is ca. 40 nm) cast from toluene at 23 °C, after heating for 53 min at 125 °C. Smaller holes were nucleated after longer incubation times compared to the bigger holes nucleated at earlier times. **b** Growth of the three holes marked 1, 2, and 3 in **a**, which were nucleated 90, 1275, and 2950 s after the film was brought to 125 °C. **c** Growth of the same holes where the ordinate is the time that each hole has grown since it was nucleated, rather than the time elapsed since the film reached T = 125 °C. **d** Plot of the hole radii of the three holes after a growth time of 2000 s (*vertical line* in (**c**)), showing an exponential decay with a time constant of 1000 ± 500 s. The figure is adapted from the doctoral thesis of Mithun Chowdhury (2012)

following approximately an exponential decay (see Fig. 1.9d, yielding a characteristic decay time of 1000 ± 500 s). This clearly demonstrates that in the course of annealing the contribution of residual stresses to the driving force has decayed, indicating that the out-of-equilibrium chains in the films (partially) relaxed during annealing in the course of the dewetting process. Note that the decay time deduced in Fig. 1.9d is much smaller than the bulk reptation time at the dewetting temperature ($\tau_{rep} \approx 2 \cdot 10^8$ s [32] for the high molecular weight PS used here).

Obviously, non-equilibrated films will evolve towards equilibrium causing a change in film properties with time. However, when films are kept at temperatures below the glass transition, it is not clear whether significant and detectable changes can occur on experimentally accessible time scales. Under such conditions of aging, relaxations on the level of entire chains are not expected. Rather, local motion at the level of chain segments are possible, characterized, e.g., by the β-relaxation [63, 64]. This raises the question, whether such segmental relaxations have an impact on static and dynamic properties of polymers observed at a macroscopic level, for example, through changes in film thickness or the dynamics of dewetting.

Furthermore, it is not clear whether the presence of residual stresses, caused by strong deviations of chain conformations from equilibrium, accelerate or slow down relaxations at the segmental level. Thus, we have investigated the consequences of physical aging in thin spin-cast polystyrene films through detailed dewetting studies [38, 45], focusing on the relaxation dynamics during aging of the glassy film. We detected changes induced by aging below $T_{g,bulk}$ through systematic variations of the duration and the temperature of aging. A simultaneous study of different observables (diameter of the dewetting hole, and shape and size of the rim formed during dewetting) enabled us to exclude purely interfacial phenomena and to relate the relaxations to changes occurring within the entire film. From these observations, we were able to deduce the relaxation dynamics, i.e., the decay time of residual stresses inside the film as a function of aging temperature.

The temporal evolution at the early stages of hole formation was followed in real time by optical microscopy and, after quenching the dewetted films to room temperature, height profiles of the rim were measured by atomic force microscopy (AFM). We note that only holes detectable immediately after initiating dewetting were investigated. Thus, the opening of all holes was subject to the same residual stress. Figure 1.10a displays typical images characteristic for the influence of aging on the dewetting dynamics. For a fixed dewetting time for each sample, the hole radius R, the width W, and the height H of the rim decreased upon physical aging at 80 °C with increasing aging times. As shown for aging at 25 °C in more detail in Fig. 1.10b, R increased more slowly the longer the film was aged. This effect was more pronounced, i.e., less time was needed to achieve the same amount of changes, at high aging temperatures. From such aging experiments we thus can deduce a temperature dependent decay time τ_A, simultaneously for the evolution of R, W, and H. The values of τ_A, deduced from the exponential decay of the dewetting velocity, the width, and the height of the rim with aging time were found to be rather equal. Independent of aging-temperature, the determined values of τ_A,
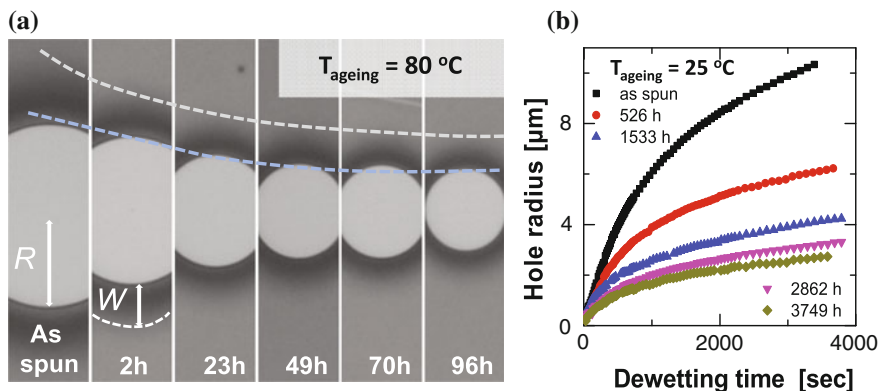
Fig. 1.10 **a** Section of dewetting holes in nominally identical PS films (thickness 40 ± 2 nm, $M_w = 4060$ kg/mol) that have been aged at 80 °C for varying periods ranging from 2 to 96 h, taken after dewetting at 125 °C for ca. 1 h. The size of the optical micrographs is ca. 14 × 60 μm^2 each. **b** Temporal evolution of the radius of dewetting holes, nucleated immediately upon heating to 125 °C in PS films (40 ± 2 nm, 4060 kg/mol) that have been aged at 25 °C. At any fixed dewetting time (for example at 1000 s), both the hole radius and its growth velocity (derivative of the radius with respect to dewetting time) exhibited a decrease with aging time. The figure is adapted from Ref. [45]

characterizing the relaxation of residual stresses inside the film caused by out-of-equilibrium chain conformations induced by the spin-casting process [28, 32], were smaller than τ_{rep}.

In an analogous series of experiments, we measured the characteristic decay time with aging time at room temperature for thin films cast from solutions of strongly differing quality of the solvent. We used trans-decalin as solvent which has a Θ-temperature of ≈ 21°C. In Fig. 1.11a, we schematically indicate how the coil diameter in solution varied with the temperature of the solution from which the films were cast. As can be seen from Fig. 1.11b, varying the temperature of the spin-casting solution has a substantial effect on the room temperature relaxation times of these films. Comparing both, the variation of the relaxation time and the coil diameter as a function of spin-casting temperature, clearly shows that both follow the same trend.

While the coil diameter changes only little as the solution is becoming more concentrated in the course of solvent evaporation, the coil volume is increasingly interpenetrated by other chains. The segmental mobility is, however, simultaneously reduced and is arrested when the solution reaches the glass transition temperature. With a lack of segmental mobility, further solvent evaporation leads to a collapse of the chains onto themselves. In a thin film, this collapse is restricted to one dimension, resulting in oblate coil structures. The deformation of the coil structure gives rise to an in-plane stress, while the reduction in entanglements lower the elastic modulus and the melt viscosity [37].
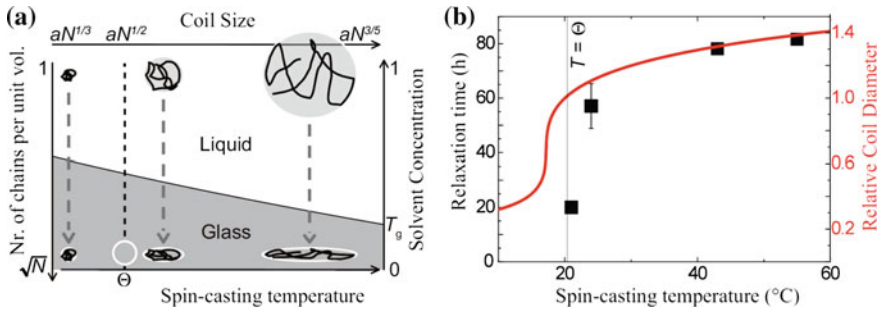
Fig. 1.11 a Schematic of polymer coil conformations upon spin-coating for temperatures above and below Θ-temperature. The *open circle* indicates a fully entangled chain in equilibrium. **b** Relaxation times τ_A as a function of the temperature of the solution from which the films were spun. The curve represents the result of the calculation of the coil diameter (end-to-end distance of the polymer coil) as a function of temperature with respect to Θ of PS in trans-decalin (indicated by the *vertical dotted line*), with the concentration as a fitting parameter. The variation of the solution temperature thereby provides control over the swelling of PS chains in the solution over a considerable range, given by [65]. The figure is adapted from Ref. [38]

Figure 1.11b shows that the quality of the solvent from which polymer films are cast plays a significant role in determining the aging behavior of the non-equilibrium conformations of the chains in the film. Interestingly, the aging time increases with improving solvent quality, with the strongest effect observed for the athermal solvent. Faster stress relaxation does, however, not necessarily imply a faster overall equilibration of the chains. Full equilibration is likely to be of the same order of magnitude as the bulk (equilibrium) reptation time.

In Fig. 1.12a we show the temperature dependence of the characteristic relaxation times (τ_A) upon aging as extracted from the dynamics of R, W, and H, demonstrating that all three observables yielded quantitatively similar behavior. These results clearly indicate that the dynamics of all dewetting observables is governed by the same physical parameters. As changes in interfacial properties (friction with the substrate) are not expected to cause a change in H, the similar decay of all three quantities strongly points to a relaxation process occurring within the entire film.

The only dewetting parameter which affects all three quantities in a similar way is the ratio of the total stress acting at the contact line over the elastic modulus of the film. Thus, the relative decay of H during aging can either be due to a decay of residual stress (assuming that the capillary stress is constant and interfacial tensions do not significantly change with aging), or be caused by an increase in the elastic modulus [32, 58, 59]. The latter requires, however, the formation of a significant number of new entanglements during the course of aging. Below the glass transition temperature, chain reptation is suppressed and entanglement formation is extremely unlikely. Intrachain segmental motions are however still possible. Thus, the simultaneous and equally fast decay of all three observables can only be attributed to a decay of residual stress, and consequently, to relaxations at a segmental level.
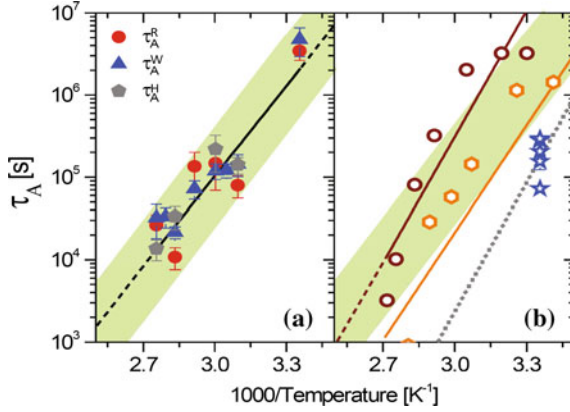
Fig. 1.12 **a** Relaxation times (τ_A) deduced from the evolution of the hole radius, the maximal rim width, and the rim height, respectively, vs. inverse aging temperature, of nominally identical PS films (M_w = 4060 and 4840 kg/mol) prepared by spin-casting from toluene. The *solid line* is an Arrhenius fit of all relaxation times, yielding an activation energy E_a = 70 ± 6 kJ/mol. The highlighted area encompassing all data points and their *error bars* gives rise to a range in E_a values between 50 and 107 kJ/mol. **b** Comparison of the results of **a** (*shaded area*) with reported relaxation times derived from the surface relaxations of (i) nano deformations (*open hexagons*) [34] and (ii) nano bumps (*open circles*) [46], including Arrhenius fits to these data (*solid lines*). The *dotted line* represents results from dye probe reorientation measurements [44] and *the stars* show relaxation times for PS films spun from trans-decalin [38]. The figure is adapted from Ref. [45]

The results of Fig. 1.12a suggest an Arrhenius behavior for the relaxation time

$$\tau_A = A_0 \exp\left(\frac{E_a}{k_B T}\right),\tag{1.1}$$

where A_0 is a constant, k_B is the Boltzmann constant and E_a is the activation energy of the underlying relaxation process. From a fitting to our results we obtain E_a = 70 ± 6 kJ/mol.

It is instructive to compare this value derived from a macroscopic dewetting study to the β-relaxation process, which is believed to involve non-cooperative motions at the segmental level of the polymer chain [63, 64]. In the literature, values of 150 ± 80 kJ/mol for the β-relaxation in thin film and bulk PS can be found [14, 63, 64, 66]. Similar values were also found when measuring the kinetics of irreversible chain adsorption [67].

Several studies on thin polymer films also indicated a sub-T_g Arrhenius-type relaxation process, which was related to the motion within a distinct surface layer of higher mobility or to increased heterogeneity [35, 44, 63, 64], yielding $E_a \approx$ 100 kJ/mol [44] and E_a = 185 ± 3 kJ/mol [14]. Lateral force microscopy measurements on thin PS films [63] found a thickness dependent surface β-relaxation process, with E_a = 55 kJ/mol for a 65 nm thick film. Fast sub-T_g-relaxations at surfaces of thin polymer films were measured by AFM, including the relaxation of

surface dimples ($E_a = 83 \pm 16$ kJ/mol) [34] and the reduction in the height of surface bumps in water ($E_a = 98 \pm 17$ kJ/mol) [46]. Interestingly, within the scatter of the data, our results exhibit the same order of magnitude in relaxation time as these surface relaxation processes, cf., Fig. 1.12b.

Dewetting is not a surface sensitive technique. In particular, the height of the rim is not controlled by a possible high mobility surface layer. Dewetting involves the displacement of whole polymer chains and takes place across the entire film thickness. Moreover, at the used dewetting temperature, the film behaved like an elastic body, as demonstrated by the asymmetric shape of the rim. Stress relaxation could therefore, only occur by motion on the level of chain segments.

Furthermore, it is illuminating to compare room temperature relaxation times shown in Fig. 1.11b for aging films spun from different solvents (see stars in Fig. 1.12b. A reduction in solvent quality gave rise to a decrease in relaxation times, indicating that the state of polymer chain entanglement in solution was transferred to the dried film [38]. The change from a good solvent (toluene) to a near-θ solvent (transdecalin) corresponds to a decrease in chain swelling (radius of gyration) in solution, leading to reduced chain overlap and thus to a decrease in observed relaxation times. These results indicate that segmental relaxation depends on the local chain environment, which is strongly affected by preparation conditions such as solvent quality and film deposition technique.

In conclusion, the experiments presented here suggest that motion on the level of chain segments is sufficient to partially relax frozen-in out-of-equilibrium local chain conformations, which are the cause of residual stresses in thin polymer films. These relaxations are not expected to fully equilibrate the polymer film, which would require reptation of entire chains. It is also unlikely that segmental rearrangements lead to a homogeneous system on a nanometer length-scale. It is interesting and surprising to discover that changes in PS surface topography and the here studied influence of aging on dewetting exhibit similar relaxation times and rather similar activation energies. This might indicate that segmental relaxations are responsible for both observations. However, further studies are needed to answer the question whether local changes at the level of chain segments are responsible for changes in the surface topography on length-scales which are several orders of magnitude larger than the size of the relaxing segments. In film dewetting, however, such local rearrangements have a dramatic influence, revealing the effect of sub-molecular (segmental) processes on macroscopic length-scales. Our results further suggest that rearrangements at the level of chain segments are sufficient to partially relax frozen-in out-of-equilibrium local chain conformations, i.e., the cause of residual stresses, and they might also be responsible for macroscopic relaxations at polymer surfaces.

Finally, the strong dependence of the aging behavior of thin films far below T_g on film preparation conditions sheds a new light on the low temperature softening of thin polymer films (that is their lowered glass transition temperature). While the deformation of polymer coils as a whole should not modify the solidification temperature of the film, which is dominated by the segmental dynamics, our aging experiments indicate that spin-coating perturbs the polymer coils down to the

segmental length scale. While this needs further experimental verification, our experiments point towards an explanation for the "abnormal" glass transition temperature in thin films in terms of non-equilibrium chain conformations caused by film preparation.

1.7 Concluding Remarks

For achieving functional macromolecular systems with adaptable properties engineered via processing, we need to establish fundamental understanding of generic processes of polymer (re-)organization and rearrangements during the various processing steps, all causing potentially chain conformations (far **beyond** thermodynamic equilibrium, characterized e.g. by a Gaussian chain statistics representing the minimum of free energy. Based on such insight, a rational design of the processing steps will be possible and so macromolecular systems can be achieved which have unprecedented and adaptable (improved) mechanical, optical, surface, … properties.

Non-equilibrium states are often anisotropic and consist of preferentially oriented/aligned polymer chains. Thus, under appropriate processing conditions, these non-equilibrium states represent, or evolve into, ordered structures and metastable states, which exhibit properties not achievable under equilibrium condition. For example, changes at the conformational level of polymers may lead to macroscopic changes in behaviour, e.g. represented by changes in the glass transition temperature.

The difference in energy of various non-equilibrium states is often extremely small which enables large deformability of polymers at rather low energetic costs. For example, by changing their conformation from a coiled state to a largely extended state, macromolecules are highly suitable to flow under extreme conditions (high shear rates, large deformations) without leading to macroscopic disintegration. Corresponding low molecular weight systems would often not be homogeneously processable under such extreme conditions. The dynamics of the resulting non-equilibrium states can deviate strongly (by many orders of magnitude!) from the behavior of the same polymers in the equilibrium state.

An equilibrated system, which is "dead" in the sense that, after a small perturbation, it will always try to return to a stable and well defined equilibrium state of lowest free energy. By contrast, non-equilibrated systems can explore a large variety of energetically similar non-equilibrated states: Switching between such states provides a possibility for adaption. For example, a semi-crystalline polymer material may respond to a mechanical deformation not only be relaxing back to the initial state but may alternatively form crystalline nuclei facilitated by a shear-induced reduction of the nucleation barrier. In such a case, the growth of crystalline domains (lamellae) will be in the direction orthogonal to the direction of the applied force. Thus, as an attempt to avoid e.g. damage through the applied force, such materials may potentially exhibit a self-enforcing capability of their

mechanical properties, in some sense similar to biological (plant) systems. Crystallization is also a well suited example for how changes at the level of the monomer (e.g. through variations in side-groups) can affect order and the thereof derived properties. Taking advantage of the high degree of polymerization, changes at the level of a monomer are "multiplied" by the number of monomers connected in the polymer chain. Thus, by synthesizing/designing appropriate monomers one may achieve a massive amplification and control of the above-mentioned structure formation processes during processing.

References

1. Keller, A., Odell, J.A.: Colloid Polym. Sci. **263**, 181 (1985)
2. Bernardin III, F.E., Rutledge, G.C.: Polymer **48**, 7211–7220 (2007)
3. Müller, de Pablo, J.J.: Annu. Rev. Mater. Res. **43**, 134 (2013)
4. Sprakel, J., Padding, J.T., Briels, W.J.: EPL **93**, 58003 (2011)
5. Huang, C.C., Winkler, R.G., Sutmann, G., Gompper, G.: Macromolecules **43**, 10107 (2010)
6. Mizunoa, H., Yamamoto, R.: Eur. Phys. J. E **35**, 29 (2012)
7. Croll, S.G.: J. Appl. Polym. Sci. **23**, 847858 (1979)
8. Bornside, D., Macosko, C., Scriven, L.J.: Imag. Technol. **13**, 122128 (1987)
9. Karpitschka, S., Weber, C.M., Riegler, H.: http://arxiv.org/abs/1205.3295
10. Reiter, G.: Europhys. Lett. **23**, 579–584 (1993) (Macromolecules **27**, 3046–3052 (1994))
11. Orts, W.J., van Zanten, J.H., Wu, W.L., Satija, S.K.: Phys. Rev. Lett. **71**, 867–870 (1993)
12. Sanyal, M.K., Basu, J.K., Datta, A., Banerjee, S.: Europhys. Lett. **36**, 265–270 (1996)
13. Bollinne, C., Cuenot, S., Nysten, B., Jonas, A.M.: Eur. Phys. J. E **12**, 389–395 (2003)
14. Yang, Z., Fujii, Y., Lee, F.K., Lam, C.H., Tsui, O.K.C.: Science **328**, 1676 (2010)
15. Keddie, J., Jones, R.A.L., Cory, R.: Europhys. Lett. **27**, 59 (1994)
16. Dalnoki-Veress, K., Nickel, B., Roth, C., Dutcher, J.: Phys. Rev. E **59**, 21532156 (1999)
17. Brulet, A., Boue, F., Menelle, A., Cotton, J.P.: Macromolecules **33**, 9971001 (2000)
18. Reiter, G., de Gennes, P.G.: Eur. Phys. J. E **6**, 2528 (2001)
19. Reiter, G.: Phys. Rev. Lett. **87**, 186101 (2001)
20. Mukherjee, M., Bhattacharya, M., Sanyal, M.K., Geue, T., Grenzer, J., Pietsch, U.: Phys. Rev. E **66**, 061801 (2002)
21. Kanaya, T., Miyazaki, T., Watanabe, H., Nishida, K., Yamana, H., Tasaki, S., Bucknall, D.B.: Polymer **44**, 3769–3773 (2003)
22. Efremov, M., et al.: Phys. Rev. Lett. **91**, 085703 (2003)
23. Miyazaki, T., Nishida, K., Kanaya, T.: Phys. Rev. E **69**, 022801 (2004)
24. Bhattacharya, M., Sanyal, M.K., Geue, T., Pietsch, U.: Phys. Rev. E **71**, 041801 (2005)
25. Si, L., Massa, M.V., Dalnoki-Veress, K., Brown, H.R., Jones, R.A.L.: Phys. Rev. Lett. **94**, 127801 (2005)
26. O'Connell, P.A., McKenna, G.B.: Science **307**, 1760 (2005)
27. Roth, C.B., Deh, B., Nickel, B.G., Dutcher, J.R.: Phys. Rev. E **72**, 021802 (2005)

28. Reiter, G., Hamieh, M., Damman, P., Sclavons, S., Gabriele, S., Vilmin, T., Raphaël, E.: Nat. Mater. **4**, 754 (2005)
29. Bodiguel, H., Fretigny, C.: Eur. Phys. J. E **19**, 185 (2006)
30. Peter, S., Meyer, H., Baschnagel, J.: J. Polym. Sci. B Polym. Phys. **44**, 2951–2967 (2006)
31. Yang, M.H., Hou, S.Y., Chang, Y.L., Yang, A.C.M.: Phys. Rev. Lett. **96**, 066105 (2006)
32. Damman, P., Gabriele, S., Sclavons, S., Desprez, S., Villers, D., Vilmin, T., Raphaël, E., Hamieh, M., Al Akhrass, S., Reiter, G.: Phys. Rev. Lett. **99**, 036101 (2007)
33. Al Akhrass, S., Reiter, G., Hou, S.Y., Yang, M.H., Chang, Y.L., Chang, F.C., Wang C.F., Yang, A.C.M.: PRL **100**, 178301 (2008)
34. Fakhraai, Z., Forrest, J.: Science **319**, 600 (2008)
35. Fukao, K., Koizumi, H.: Phys. Rev. E **77**, 021503 (2008)
36. Serghei, A., Kremer, F.: Macrom. Chem. Phys. **209**, 810–817 (2008)
37. Barbero, D.R., Steiner, U.: Phys. Rev. Lett. **102**, 248303 (2009)
38. Raegen, A., Chowdhury, M., Calers, C., Schmatulla, A., Steiner, U., Reiter, G.: Phys. Rev. Lett. **105**, 227801 (2010)
39. Roth, C.B.: J. Polym. Sci. B: Polym. Phys. **48**, 25582560 (2010)
40. Tress, M., Erber, M., Mapesa, E.U., Huth, H., Müller, J., Serghei, A., Schick, C., Eichhorn, K.-J., Voit, B., Kremer, F.: Macromolecules **43**, 99379944 (2010)
41. Napolitano, S., Pilleri, A., Rolla, P., Wübbenhorst, M.: ACS Nano **4**, 841–848 (2010)
42. Reiter, G., Napolitano, S.: J. Polym. Sci. B: Polym. Phys. **48**, 2544 (2010)
43. Napolitano, S., Wübbenhorst, M.: Nat. Commun. **2**, 260 (2011)
44. Paeng, K., Swallen, S.F., Ediger, M.D.: J Am Chem Soc **133**, 84448447 (2011) (Paeng K, Richert R, Ediger MD: Soft Matter **8**, 819 (2012))
45. Chowdhury, M., Freyberg, P., Ziebert, F., Yang, A.C.M., Steiner, U., Reiter, G.: PRL **109**, 136102 (2012)
46. Siretanu, I., Chapel, J.P., Drummond, C.: Macromolecules **45**, 10011005 (2012)
47. Reiter, G.: Glass transition, dynamics and heterogeneity of polymer thin films. In: Kanaya T (ed) Adv. Polym. Sci. **252**, 29 (2013)
48. Carmesin, I., Kremer, K.: J Phys (Paris) **51**, 915 (1990)
49. Reiter, G.: Phys. Rev. Lett. **68**, 75 (1992) (Langmuir **9**, 1344 (1993))
50. Brochard-Wyart, F., Daillant, J.: Can. J. Phys. **68**, 1084 (1990)
51. Herminghaus, S.: Phys. Rev. Lett. **83**, 2359 (1999)
52. Reiter, G., Khanna, R., Sharma, A.: Phys. Rev. Lett. **85**, 1432 (2000)
53. de Gennes, P.G., Brochard-Wyart, F., Quéré, D.: Gouttes bulles perles et ondes, Belin, Paris OR: Capillarity and Wetting Phenomena: Drops Bubbles Pearls Waves, Springer, Heidelberg (2002)
54. Redon, C., Brochard-Wyart, F., Rondelez, F.: Phys. Rev. Lett. **66**, 715 (1991)
55. Brochard-Wyart, F., Martin, P., Redon, C.: Langmuir **9**, 3682 (1993)
56. Krausch, G.: J. Phys.: Condens. Matter **9**, 7741 (1997)
57. Seemann, R., Herminghaus, S., Jacobs, K.: Phys. Rev. Lett. **87**, 196101 (2001)
58. Vilmin, T., Raphaël, E.: Eur. Phys. J. E. **21**, 161 (2006)
59. Ziebert, F., Raphaël, E.: Phys. Rev. E **79**, 031605 (2009)
60. Gabriele, S., Sclavons, S., Reiter, G., Damman, P.: Phys. Rev. Lett. **96**, 156105 (2006)
61. Thomas, K.R., Steiner, U.: Soft Matter **7**, 7839 (2011)
62. McGraw, J.D., Fowler, P.D., Ferrari, M.L., Dalnoki-Veress, K.: Eur. Phys. J. E **36**, 7 (2013)
63. Akabori, K.I., Tanaka, K., Kajiyama, T., Takahara, A.: Macromolecules **36**, 4937 (2003)
64. Lupaşçu, V., Picken, S.J., Wübbenhorst, M.: J. Non-Cryst. Solids **352**, 5594 (2006)
65. Sun, S., et al.: J. Chem. Phys. **73**, 5971 (1980)
66. Dhinojwala, A., Wong, G., Torkelson, J.: J. Chem. Phys. **100**, 6046 (1994)
67. Housmans, C., Sferrazza, M., Napolitano, S.: Macromolecules **47**, 3390 (2014)

Chapter 2
Equilibrium Pathway of Ultrathin Polymer Films as Revealed by Their Surface Dynamics

Kun Geng, Fei Chen, Zhaohui Yang and Ophelia K.C. Tsui

Abstract The majority of thin polymer films are prepared by spin-coating. In spin-coating, a drop of polymer solution is spread into a film which then dries into a solid in less than a minute. Abruptness of this process is believed to leave the polymer chains insufficient time to equilibrate, causing them to be kinetically trapped in an intermediate, transitory state. Indeed, several out-of-equilibrium attributes have been unequivocally identified, including residual stress, reduced chain entanglement and on-going polymer adsorption to the substrate surface. Upon annealing above the glass transition temperature, T_g, these attributes evolve toward equilibrium. Another important, though less discussed out-of-equilibrium attribute is the smoother-than-equilibrium surface structure of as-cast spin-coated polymer films. Because of this, these films usually roughen upon heating. Importantly, the roughening process, especially for nanometer films, often results in the formation of deep holes and thereby ultimate rupture of the films. A question then naturally arises as to whether evolutions in the residual stress, chain entanglement and polymer adsorption may interfere with the roughening process, whereby modify the film stability. In recent years, our group has developed methods to monitor and analyze the surface roughening process. By applying these methods, important physical properties such as the effective viscosity and shear modulus of the films have been deduced. In this chapter, we shall briefly review these methods and the

K. Geng · F. Chen · O.K.C. Tsui (✉)
Department of Physics, Boston University, Boston, MA 02215, USA
e-mail: okctsui@bu.edu

O.K.C. Tsui
Division of Materials Science and Engineering, Boston University, Boston, MA 02215, USA

Z. Yang
Center for Soft Condensed Matter Physics and Interdisciplinary Research, Soochow University, Suzhou 215006, People's Republic of China

Z. Yang
College of Physics, Optoelectronics and Energy, Soochow University, Suzhou, China

respectively model analyses. On the basis of these discussions, we then deliberate whether or not evolutions in the chain entanglement density, residual stress and adsorption phenomenon in the films may have influenced the roughening process measured, and thereby project their impacts on the film stability.

2.1 Introduction

Polymers are large molecules made of repetition of the monomer unit. The resultant large molecular mass renders polymers unique properties such as toughness and viscoelasticity. These, together with their relatively low-cost and abundance in variety, have made polymer the material of choice in a myriad of applications. As new technologies are introduced to enable the manufacturing of ever smaller devices, the past two decades have witnessed a rapid growth in the use of polymer nanometer films.

Spin-coating is a prevalent method for making polymer nanometer films. During spin-coating, a drop of polymer solution is deposited on a substrate surface, which is then spun at ~ 500 to ~ 4000 rpm. The rapid spinning causes the solution to spread and dry into a solid film. Such a process, typically completes in less than a minute, is believed to be too rapid for the polymer chains to equilibrate before the film vitrifies. As a result, polymers in spin-coated films are frequently cited to be out-of-equilibrium [1]. Supposition as such has been exploited to explain some of the more bizarre results, such as negative thermal expansivity [2–5] and existence of a large residual stress comparable to the rubbery elastic modulus of the bulk polymer [6–8]. More recent experiments also found that polymer chains are prone to adsorb irreversibly onto solid substrates. Moreover, the slow process by which it takes place can cause certain dynamic responses to take a prohibitively long time to attain equilibrium [9–13]. A number of effective methods have been developed to diagnose and understand the out-of-equilibrium properties of spin-coated polymer films, as one may readily see by browsing through this book. In this chapter, we shall focus on the equilibrium pathway of the films as revealed by the evolution of their surface. As noticed early on, the surface profile of as-cast spin-coated polymer films is usually smoother than equilibrium [2]. As a result, these films roughen when they are heated above the T_g [14]. An illustration is given in Fig. 2.1, which compares the power spectral densities (PSDs) of a spin-coated polystyrene (PS) film before and after annealing at ~ 20 °C above the bulk T_g for ~ 2 h. Evidently, the PSD grew notably upon annealing, which signifies roughening. By examining how the common out-of-equilibrium attributes of spin-coated films, such as residual stress, reduced chain entanglement and chain adsorption to the substrate surface, correlate with the roughening process, one may gain insight about whether or not the out-of-equilibrium attributes modify the film stability.

This chapter is organized as follows. In the next section (Sect. 2.2), we describe how PSDs like the ones shown in Fig. 2.1 are measured. In Sect. 2.3, we discuss the
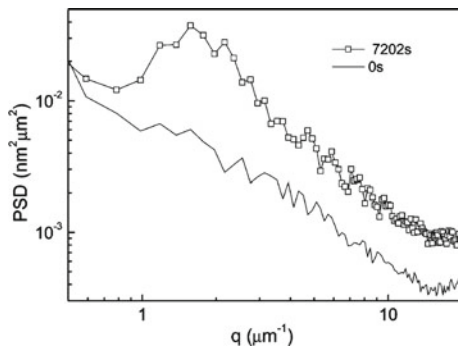
Fig. 2.1 Power spectral density of an $h_0 = 18$ nm and $M_w = 2.3$ kg/mol spin-cast polystyrene film, freshly prepared (*plain solid line*) and after annealing for 7202 s (open squares) at 85 °C (Reproduced with permission from Ref. [13])

theoretical models we developed to analyze the time-varying PSDs whereby the effective viscosity and effective shear modulus of the films can be determined. In addition, we also discuss how the information hence obtained may be used to infer the density of chain entanglement and other properties of the films that may affect the transport processes. In Sect. 2.4, we discuss how by exploiting any temporal variation in the effective viscosity and shear modulus or lack thereof in our measurements, one may infer information about the out-of-equilibrium state of the films. Finally, we conclude this chapter with a summary of the major observations.

2.2 Experimental Method

Experimentally, we determine the dynamics a film by studying how its power spectral density (PSD) evolves with time upon annealing at a given measurement temperature. To determine the PSD, we first measure the surface topography of the films by using tapping-mode atomic force microscopy (AFM). Then we convert each topographic data (a 2-dimensional image) to its PSD (a 1-dimensional array) [15–18] by first multiplying it by a Welch function then Fourier-transforming it [15–18]. The resulting two-dimensional Fourier spectrum is then radial averaged to produce the one-dimensional PSD.

It is important to clarify that the present AFM measurement is fundamentally different from most other AFM measurements used for materials characterization [19–23]. In typical AFM measurements [19, 23], the AFM probe tip actively perturbs the specimen surface and thereafter monitors the dynamic response *local* to the film surface. Because the size of the probe tip is often quite small (typically $< \sim 10$ nm), even a small probing force can translate into a large stress (e.g. for a force of 0.1 nN, the stress is ~ 1 MPa) that can result in non-linear response for

soft materials like polymer. But in our method, the AFM probe tip acts as a *passive*, benign monitor (through the use of light and high-frequency tapping) of the surface topography of the film as the film surface roughens spontaneously by thermal activation. Although our method measures the surface dynamics of the film (namely the dynamics by which the film surface evolves), it will become apparent in Sect. 2.3 that the measured dynamics arises from flow transport of *all* the materials in the film and so should reflect an overall dynamics. That being said, one may still be able to infer information about the local dynamics at the free surface by applying a layer model to the measurement as discussed in the next Section.

It should also be clarified that the dynamics we measure can differ from that inferred from experiments involving capillary action of a solid substrate or wall, such as dewetting (more specifically, holes opening) or wicking of the polymer liquid into an empty capillary [24–28]. In contrast, our measurement is based on thermally activated dynamics, where the driving stress, σ, (neglecting the conjoining pressure due to the interfacial potential) is due to gradient in the Laplace pressure, $\Delta P \sim 2\gamma/R$, arising from undulations in the film surface. (Here, $\gamma \approx 30$ mN/m is the surface tension and R is the local radius of curvature of the undulating film surface.) For undulations with amplitude δh and wavevector q, $R \sim 1/(q^2 \delta h)$. Adopting the experimental condition, $\delta h < 0.1 h_0$ (see below) and for $h_0 = 10$ nm, $\sigma \sim \gamma \delta h q^2 < \sim 30$ Pa. But in the experiments involving capillary action, the stress is provided by the polymer-substrate surface tension and given by $\sigma = \gamma/h_0$. As pointed out by Reiter [26], $\gamma \sim 20$ to 30 mN/m and so for $h_0 \sim 10$ nm, the stress is ~ 2 to 3 MPa and large enough to cause plastic deformation of thin films of common polymers such as polystyrene. Indeed, spectacular phenomena had been observed in these experiments, including molecular layering of the precursor film of a polymer liquid spreading on a solid substrate [29] and formation of a highly asymmetric rim on the periphery of an enlarging hole in a viscoelastic (entangled) polymer film [26]. The latter should be contrasted with the relatively symmetric holes rims found in situations where there is no capillary action—a condition realized when the holes only appear as indentations, and have not yet grown deep enough to touch the substrate surface (see Fig. 2.11).

As we shall discuss in the next section, the dynamics we measure can be succinctly characterized by the effective viscosity of the film, η_{eff} [30]. In general, the value of η_{eff} varies with measurement time and does not reach the steady-state value until a sufficiently long time [15–18]. In any given measurement, a priori we do not know how long it will take η_{eff} to reach the steady-state value. To ensure that the steady-state value is reached, we continue the measurement until the measured η_{eff} no longer change when the annealing time is lengthened four times or more. Because our analysis is based on linear approximations [31], measurements are only taken in the initial stage of roughening where the root-mean-square roughness is less than $0.1 h_0$, where h_0 is the average film thickness.

2.3   Model Analysis for the Temporal Evolution of Power Spectral Density

2.3.1   Analysis for the Surface Dynamics of Newtonian Liquid Films

In this subsection, we shall discuss the model we developed to describe the surface dynamics of unentangled polymer films, which we treat as Newtonian liquids.

For a film possessing small undulations on its surface, the height profile can be written as $h(r) = h_0 + \delta h(r)$, where h_0 is the average film height, r denotes positions in the plane of the film and $<\delta h(r)>_r = 0$. The presence of $\delta h(r)$, whether spontaneously [32–34] or artificially created [35–37], produces a spatially inhomogeneous excess pressure according to $\Delta P(r) = -\gamma \nabla^2 \delta h(r) + dG(h_0)/dh$ [17, 38], where γ is the surface tension and $G(h)$ the van der Waals potential of the film. Given this, the pressure gradient, ∇P, is generally nonzero, causing the film fluid to flow, which in turn produces temporal variations in $\delta h(r)$ and $P(r)$ (Here, $P(r) = P_{atm} + \Delta P(r)$, where P_{atm} is the atmospheric pressure.) In the lubrication approximation, where the in-plane length scale of the undulations is much bigger than h_0, the unit-width, in-plane current is given by $j(r, t) = -M_{tot} \nabla P(r, t) + \xi(r, t)$ [31], where M_{tot} denotes the mobility and $\xi(r, t)$ conserved thermal noise. It should be remarked that inclusion of thermal noise in the treatment is essential for yielding good agreement with experiment [39].

By applying linear analysis, the following expression for the time-varying PSD, $A_q^2(t)$, was derived [2, 16, 30, 31, 40, 41]:

$$A_{\boldsymbol{q}}^2(t) = A_{\boldsymbol{q}}^2(0) \exp(2\Gamma t) + \left[\frac{k_B T}{d^2 G(h_0)/dh^2 + \gamma q^2}\right](1 - \exp(2\Gamma t)) \qquad (2.1a)$$

where

$$\Gamma(\boldsymbol{q}) = -M_{tot}\left[(d^2 G(h_0)/dh^2)q^2 + \gamma q^4\right]. \qquad (2.1b)$$

In here, $\boldsymbol{q}$ is the wavevector and $q \equiv |\boldsymbol{q}|$, k_B is the Boltzmann constant, T is absolute temperature. Figure 2.2a, b, respectively, shows a sequence of AFM images and corresponding PSDs acquired from a representative low molecular weight (M_w) PS film. The solid lines in Fig. 2.2b represent the best fit to (2.1a). As one can see, the model is able to describe the data well.

If the no-slip boundary condition applies at the substrate surface and the film viscosity is homogeneous and given by η, one may derive that [31]

$$M_{tot} = h_0^3/(3\eta). \qquad (2.2)$$

The mobility M_{tot} defined here is analogous to the proportionality constant, $\pi R_0^4/(8\eta)$ found in the Poiseuille equation (i.e., $dV/dt = [\pi R_0^4/(8\eta)]\nabla P$), which relates
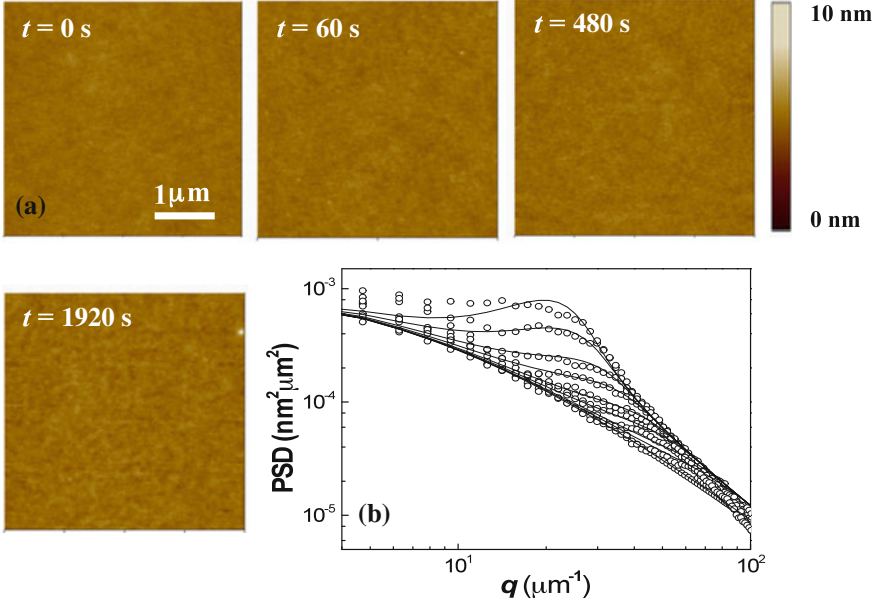
Fig. 2.2 A representative sequence of atomic force microscopic (AFM) topographic images and power spectral density we obtained. The data was taken from a film with initial thickness, $h_0 = 4$ nm and $M_w = 2.4$ kg/mol annealed at 61 °C. **a** A subset of the AFM images. **b** The full set of power spectral, PSD, of the film at times (from *bottom* to *top*): 0, 15, 30, 60, 90, 210, 600, 1080, 2100, 3840 and 7200 s (*open circles*). The *solid lines* are the best fit to (2.1a) (Reproduced with permission from Ref. [43])

the fluid current engendered by applying a pressure gradient across a fluid-filled cylindrical pipe with radius R_0 and non-slipping wall [42]. One may observe that this mobility follows the pipe dimension to the power 4, but $M_{tot} \sim h_0^3$ in (2.2). The different power laws arise from the fact that the current considered in the Poiseuille equation is the volumetric fluid flow rate (dV/dt, m^3/s) through the entire cross-section of the cylindrical conduit, but that considered in thin films ($j(r, t)$, m^2/s) is the fluid flow rate per unit width of the film cross-section. Given the above expression of M_{tot}, it is common to define the effective viscosity as follows [30, 31]:

$$\eta_{eff} \equiv h_0^3/[3M_{tot}]. \tag{2.3}$$

In general, the dynamics and hence local viscosity in the film may not be uniform. In fact, more often than not the region near the polymer-air surface has a lower local viscosity [44] than the rest of the films [30]. Assuming the mobility of the near-air surface to be M_{mobile} and the viscosity of the rest of the film to be bulk-like and given by η_{bulk}, it has been shown that $M_{tot} \approx M_{mobile} + h_0^3/(3\eta_{bulk})$ for polymer films [43, 45, 46]. In the presence of dynamic heterogeneity as such, the value of η_{eff} obtained from (2.3) would be an effective viscosity, which explains the

subscript "eff" attributed to the symbol η_{eff}. Experiments performed on thick ($h_0 \geq \sim 80$ nm) low-M_w polystyrene supported by silica (PS-SiO$_x$) and poly(methyl methacrylate) supported by silica (PMMA-SiO$_x$) had found good agreement between the measured η_{eff} and bulk viscosity [2, 43, 47, 48]. These agreements confirm the present method for viscosity measurement. They also indicate that any effects of enhanced surface mobility [2, 35, 43, 47, 48] or interfacial slippage are insignificant in these films.

2.3.2   Analysis for the Surface Dynamics of Viscoelastic Films

To develop a model for analyzing the surface dynamics of entangled polymer films, which are viscoelastic (and so not Newtonian), we use an adiabatic approximation described as follows [31]. Figure 2.3 depicts a representative sequence of PSDs obtained from an entangled polymer film upon annealing above the T_g from the as-cast state for various times t as indicated in the figure legend (open symbols). After the first annealing time step (namely from $t = 0$–640 s, Fig. 2.3), the PSD shows an abrupt jump. This jump is caused by the glass-to-rubber transition, and not treated in our model. After this jump, there is a lengthy period of time of about 22400 s or 6.2 h where the PSDs show insignificant growth. Even though the PSDs show little growth in this time, frame-to-frame comparison between the PSDs acquired in separate, in situ measurements showed that the surface topography of the film was actually not stationary. This indicates that the film was in a quasi-steady state, undergoing equilibrium vibrations. We attribute the vibrations to the normal modes of the film in the rubbery elastic state. After $t = 22400$ s, the
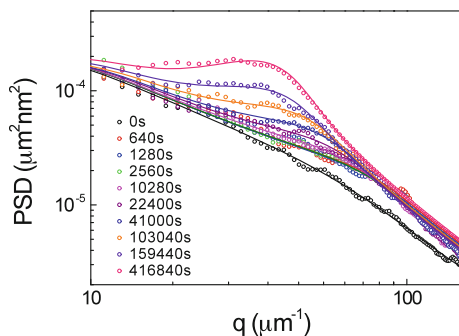
Fig. 2.3 Power spectral density of a $h_0 = 3$ nm, $M_w = 115$ kg/mol PS film upon annealing at 115 ° C for various times as shown in the legend (*open circles*). The *solid lines* are model lines obtained by fitting the data to (2.4a), which gives $\eta_{eff,0} \equiv h_0^3/(3M_{tot}) = 4.2 \times 10^8$ Pas and $\mu_0 = 10$ kPa (Reproduced with permission from Ref. [41])

growth of the PSDs becomes apparent again (Fig. 2.3). Therefore, there are two dynamic processes with different time scales, corresponding to the fast vibrations associated with the initial "stagnant PSD regime" and the slow dynamic process associated with the later stage where the growth of the PSDs becomes visible. Adopting an adiabatic approximation, we analyzed slow evolution of the film surface or PSD in the presence of the ensemble-averaged quasi-equilibrium fast vibrations [31]. We ascribe the slow evolution to the in-plane transport currents $j(r, t)$ caused by the local pressure gradient $\nabla P(r, t)$ as discussed in the last section. For the fast vibrations, we assume the energy of the modes to be $[3\mu_0/(2h_0^3 q^2)]|u_{\mathbf{q}}|^2$, in accord with that of the surface vibrations of an elastic film with wavevector $\mathbf{q}$, amplitude $u_{\mathbf{q}}$, and shear modulus μ_0 [49]. A linear calculation assuming lubrication approximation ($qh_0 \ll 1$) and stable films gives [31]:

$$A_{\boldsymbol{q}}^2(t) = A_{\boldsymbol{q}}^2(0)\exp(2\Gamma't) + \left[\frac{k_B T}{d^2 G(h_0)/dh^2 + \gamma q^2}\right](1 - \exp(2\Gamma't)) \qquad (2.4a)$$

where

$$\Gamma'(\boldsymbol{q}) = -M_{\text{tot}}q^2\left[\left((d^2 G(h_0)/dh^2) + \gamma q^2\right)^{-1} + \left(\frac{3\mu_0}{h_0^3 q^2}\right)^{-1}\right]^{-1}. \qquad (2.4b)$$

The solid lines in Fig. 2.3 are model lines obtained by fitting the data to (2.4a). As one can see, the model lines are able to simultaneously capture the stagnant PSD and subsequent PSD growth regimes, and also provide a good description to the data.

On writing $M_{\text{tot}} = h_0^3/(3\eta_{\text{eff},0})$ as in (2.2), where $\eta_{\text{eff},0}$ denotes the effective viscosity of the film in the slow or growing PSD regime, we observe that the expression of $\Gamma'(\boldsymbol{q})$ in (2.4b) becomes identical to that derived by Safran and Klein [50] for a uniform Maxwell liquid film with no slip. This demonstrates consistency of our model with the Maxwell liquid model. However, we emphasize that in deriving (2.4a) and (2.4b), little assumption had been made about the slow process, and certainly no assumption had been made about whether there is dynamic homogeneity or interfacial slippage in the film. The only attribute we had assumed of the slow process is the generic relation, $j(r, t) = -M_{\text{tot}}\nabla P(r, t)$. As a result, the value of M_{tot} or equivalently the steady-value of η_{eff} we measure (we measure) should be open to interpretation.

As mentioned in Sect. 2.2, in each measurement we do not know beforehand when the slow process is fully established and has reached the steady state. To ensure that the steady state of the slow process has been reached, we continue the measurement until further increase in the measurement time causes no change to the fitted value of M_{tot} and hence η_{eff}. To illustrate this, we fit the PSDs displayed in Fig. 2.3 one-by-one to (2.1a) and (2.1b) and deduce η_{eff} then plot the result as a function of annealing time t in Fig. 2.4 by solid circles. There, one sees that η_{eff} establishes the steady-state value after $t > \sim 20000$ s. The fact that the steady-state
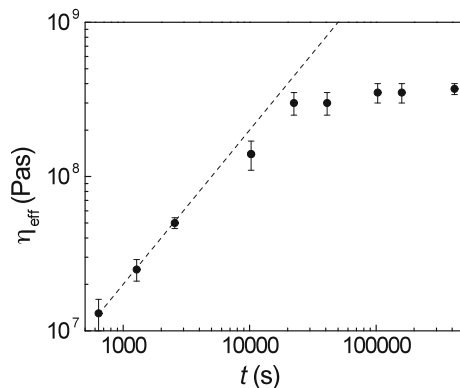
Fig. 2.4 Values of η_{eff} obtained by fitting the PSDs in Fig. 2.3 one-by-one to (2.1a, 2.1b), plotted versus the annealing time, t. The *dashed line* is a plot of $\eta_{\text{eff}} = 2\mu_0 t$ (Reproduced with permission from Ref. [41])

value ($\sim 4 \times 10^8$ Pas, Fig. 2.4) is consistent with the value obtained above by fitting the data directly to (2.4a, 2.4b) (Fig. 2.3) affirms our measurement protocol for determining the steady-state η_{eff}.

We summarize this subsection by recapitulating that we have derived (2.4a, 2.4b), which are able to simultaneously describe the short-time stagnant and long-time PSD growth regimes. In deriving these equations, the short-time (fast) dynamics is assumed to be caused by the normal modes of the films in the rubbery elastic state. For the long-time (slow) dynamic process, the only assumption that has been made is the general relation, $j(\mathbf{r}, t) = -M_{\text{tot}} \nabla P(\mathbf{r}, t)$. With this, a steady-state effective viscosity may be defined as before, namely $\eta_{\text{eff},0} \equiv h_0^3/(3M_{\text{tot}})$. In the case of thick PS-SiO$_x$, a previous experiment [2] showed that the value of $\eta_{\text{eff},0}$ is the same as the bulk viscosity of the polymer, indicating that dynamic inhomogeneity and slippage can be ignored in these films. However, in cases where dynamic inhomogeneity or slippage cannot be ignored, $\eta_{\text{eff},0}$ is an effective viscosity and can depend on the film thickness in general. In such circumstances, further analysis of the $\eta_{\text{eff},0}(h_0)$ dependence would be necessary to pinpoint the origin of the slow process.

2.4 Factors Contributing to the Out-of-Equilibrium State

In this section, we discuss how our measurement may or may not reflect the three factors commonly attributed to the out-of-equilibrium state of thin polymer films, namely reduced entanglement density, residual stress and on-going chain adsorption to the substrate surface.

2.4.1 Reduced Entanglement Density

As discussed above, due to the abruptness of the spin-coating process, some memories of the polymer chain conformation in the original polymer solution may get carried over to the final dry film. One common speculation is that spin-coated films may inherit the lower degree of entanglement the polymer chains have in the solution state just before vitrifying [51, 52]. This proposition gains support from the experiment of Barbero et al. [52], who studied the viscosity of spin-coated PS-SiO$_x$ ($h_0 \geq \sim 100$ nm) before and after thermal annealing. For the unentangled films ($M_w < M_e \approx 18$ kg/mol [53]), they found that the unannealed and annealed films both exhibited the bulk viscosity. But for the entangled films (c.f. $M_w = 113$ and 655 kg/mol), the unannealed films exhibited reduced viscosity as though the entanglement density of the as-cast films was lower than equilibrium. With annealing, the viscosity of the films increased, but the extent to which the bulk value was recovered differed for different M_w's. For $M_w = 113$ kg/mol, the recovery was complete, but for $M_w = 655$ kg/mol it was partial.

As Fig. 2.4 shows, our measurements of the entangled films also exhibit temporal variation in the value of η_{eff}. Specifically, η_{eff} first increases linearly with time then reaches the steady-state value, $\eta_{eff,0}$ after a characteristic time, τ_r. For the films with $h_0 > 4R_g$, we had previously found that the value of $\eta_{eff,0}$ agrees with the bulk viscosity [2]. Moreover, the characteristic time increases with M_w [2]. These observations are in keeping with the observations of Barbero et al. [52]. But as discussed below, interpretation of this data may not be straightforward. Sometimes, if not most times, it is more appropriate to estimate the rubbery-state shear modulus μ_0 from the data and then the density of entanglement, ρ_e, by using the relation, $\mu_0 = \rho_e RT = \rho RT/M_e$ [54], where ρ is mass density. As discussed below, the values of μ_0 we measure show that ρ_e is $\sim 1/10$ times the equilibrium value.

For $t < \tau_r$, the films are in the rubbery elastic state. According to Fredrickson et al., the PSD of an elastic film with shear modulus μ_0 and no slip at the substrate surface is given by [49]:

$$A_{\boldsymbol{q}}^2(t) = \text{Background} + \frac{k_B T}{d^2 G(h_0)/dh^2 + \gamma q^2 + \frac{3\mu_0}{h_0^3 q^2}}, \tag{2.5}$$

where "Background" refers to the low-q segment of the PSD corresponding to the surface modes with relaxation times longer than the measurement time t and so have not been able to evolve yet [2]. Separately, the expression for the liquid-film PSD (2.1a) can be written in the following approximated form [2]

$$A_{\boldsymbol{q}}^2(t) = \text{Background} + \frac{k_B T}{d^2 G(h_0)/dh^2 + \gamma q^2 + \frac{3(\eta_{eff}/2t)}{h_0^3 q^2}}. \tag{2.6}$$

During the rubbery elastic regime, the films are elastic so (2.5) should apply. But on reaching the slow dynamic regime, (2.6) should apply. A comparison between (2.5) and (2.6) indicates that if we fit the data in the elastic regime to (2.1a), we should find that the fitted value of η_{eff} increases linearly with t, with the constant of proportionality equal to $2\mu_0$. Clearly, this prediction is supported by the short-time data of Fig. 2.4. By fitting this data to $\eta_{eff} = 2\mu_0 t$ (dashed line, Fig. 2.4), we obtain $\mu_0 = 10$ kPa. We remark that this value of μ_0 is consistent with the one we obtained by fitting the PSDs directly to (2.4a, 2.4b). We have applied this analysis to the PS-SiO$_x$ films with $M_w = 115$ kg/mol [41] and 212 kg/mol [40] and $h_0 = 2$ to 125 nm, and found that the values of μ_0 agree with 10 kPa within a factor of 2. Since the bulk value of μ_0 is also independent of M_w and ≈ 100 kPa [55], this implies a ~ 10 times reduction in μ_0.

Now we interpret the meaning of the noted reduction in μ_0. First, we discern that the linear t dependence seen in our η_{eff} measurement (Fig. 2.4) should not be interpreted "literally", meaning that the data should not be interpreted as being caused by the as-cast film already in the viscous flow regime with an effective viscosity that increased linearly with t. To this end, we examine the η_{eff} versus t data taken from the $h_0 = 125$ nm PS-SiO$_x$ films with $M_w = 212$ kg/mol at various temperatures, T, between 130 and 160 °C (Fig. 2.5). Since our earlier experiment showed that for thick films as such the steady-state effective viscosity $\eta_{eff,0}$ agrees with the bulk viscosity, η_{bulk} [2], the reptation model should apply to these films. According to the reptation model, the viscosity and reptation time is $\eta \sim M_e^{-2}$ and $\tau_{rep} \sim M_e^{-1}$, respectively [2]. In Fig. 2.5, one observes that the value of η_{eff} acquired at the shortest time accessible to experiment ($t \approx 10$ s) is always about the same ($\sim 2 \times 10^5$ Pas) and independent of T. The steady-state viscosity $\eta_{eff,0}$ ($\equiv \eta_{eff}(t \rightarrow \infty)$), on the other hand, shows a strong T dependence following that of η_{bulk}, as expected [48]. So, a "literal" interpretation of the $\eta_{eff}(t)$ data in Fig. 2.5 would mean that the entanglement molecular weight of the as-cast films, $M_e' = M_e$
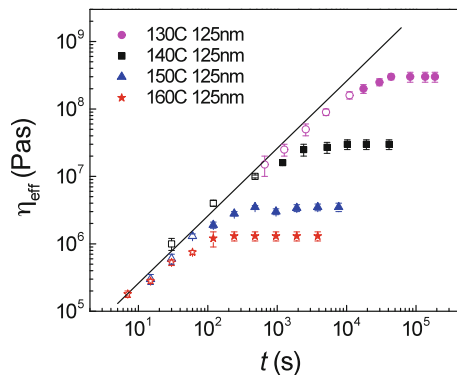
Fig. 2.5 Effective viscosity η_{eff} versus time obtained from PS-SiO$_x$ films with $h_0 = 125$ nm films annealed at various temperatures between 130 and 160 °C. The *solid line* is a plot of $\eta_{eff} = 2 \times (10.5 \text{ kPa}) \times t$ (Data reproduced with permission from Ref. [40])

$[\eta_{eff}(t \rightarrow \infty)/\eta_{eff}(t \approx 10 \text{ s})]^2$ varies between ~ 25 and 2.2×10^6 times the equilibrium M_e. This is clearly not physical since all the films were prepared in the same way. On the other hand, the data of all these films show the same linear t-dependence before reaching the steady-state value. Adopting the interpretation that the linear t dependence is due to the films being in the elastic-state or stagnant PSD regime for which $\eta_{eff} = 2\mu_0 t$, this observation implies that the films exhibit the same shear modulus μ_0 independent of the measurement temperature T. But a constant value of μ_0 is expected in here since $\mu_0 = \rho RT/M_e$ and T varies by less than $\sim 7\%$ in Fig. 2.5. This confirms the latter interpretation for a linear $\eta_{eff}(t)$ dependence, namely it corresponds to the films being in the elastic dynamic regime, with a measured value of μ_0 equal to $\sim 1/10$ times the equilibrium value. It should be underlined that the "literal" interpretation of $\eta_{eff}(t)$ cannot be excluded in general. It is excluded here only because of the data shown in Fig. 2.5 as discussed above. Invalidation (or validation) of the literal interpretation has yet to be examined for polymer films spin-cast from a θ solvent [56].

A simple explanation for the 10 times reduction in μ_0 would be that the entanglement molecular weight is increased to $\sim 10 M_e$ in the as-cast films. In the final stage of spin-coating, the concentration of polymer in the film (while still a solution) increases and the chain dynamics slows down. As the volume fraction of the polymer in the film reaches a large enough value, say ϕ^*, the chain conformation may be kinetically frozen in. One may estimate the value of ϕ^* as follows. Assuming $M_e(\phi^*) = M_e(1)(\phi^*)^{-1.3}$ for polymer in an athermal solvent (see p. 370 of [54]), $\mu_0 = \mu_{0,equilibrium}(M_e(1)/M_e(\phi^*))$ and $\mu_0/\mu_{0,equilibrium} = 1/10$, we may deduce that $\phi^* = 17 \%$. We observe [40] that this is close to the volume fraction where chain overlap begins to occur inside an athermal solvent (n.b. $\phi_e \approx [M_e(1)/M_w]^{0.76} = [17 \text{ k}/212 \text{ k}]^{0.76} = 15 \%$; see p. 369 of [54].), but much smaller than the volume fraction ($\approx 80 \%$ [57]) where a PS/toluene solution (which is the solution used here) vitrifies at room temperature. We find such a result for the estimated value of ϕ^* reasonable. It is because changes in the entanglement density M_e' should be viable only by chain motions with length scales at least on the order of the instantaneous tube size; the motions associated with the glass transition, being on the segmental length level, are too local to be relevant. All being said, we should however caution that the value of μ_0 is derived from (2.5), which assumes the no slip boundary condition. If slippage cannot be ignored, it may also constitute a cause for the measure μ_0 to be smaller than the bulk value.

Next, we ponder the possibility of observing recovery of the entanglement density in this experiment, if it takes place. As discussed above, glass-to-rubber transition occurs in the first time step of heating, causing the PSD to jump to the rubbery elastic PSD. Correspondingly, the PSD upon the first time step should be given by (2.5) with μ_0 being equal to $\mu_0(t = 0)$, i.e., the rubbery elastic modulus of the as-cast film. As evident from (2.5), this PSD has a lower cut-off wavevector, $q_{lc,solid}$ (i.e., a characteristic wavevector below which the PSD has negligible amplitude) that fulfills the relation, $\gamma q_{lc,solid}^2 + \mathrm{d}^2 G(h_0)/h^2 = 3\mu_0/(h_0^3 q_{lc,solid}^2)$.

By applying the same consideration to (2.6), the PSD of the films in the slow dynamic regime should also have a lower cut-off wavevector, q_{lc}, which however is time-varying and fulfills the relation, $\gamma q_{lc}^2 + d^2 G(h_0)/h^2 = 3(\eta_{eff}/2t)/(h_0^3 q_{lc}^2)$. Such a time variation of q_{lc} has been studied in detail in [58]. From Fig. 2.4, a crossover to the steady state or slow dynamic regime should occur when t reaches the relaxation time τ_r, where $\tau_r \equiv \eta_{eff,0}/\mu_0$. Based on (2.1b) and (2.4b), simple algebra leads to the relation, $\Gamma_q' = \Gamma_q/(1 - \Gamma_q \tau_r)$ [41]. This relation allows for another way of predicting where the crossover in dynamic regimes occurs. Specifically, on reaching the steady state the viscoelastic relaxation rate should become the same as the liquid relaxation rate or $\Gamma_q' \approx \Gamma_q$. Clearly, this condition begins when $\Gamma_q \tau_r \approx -1$ (and establishes as this quantity diminishes) [41], which can be shown to be mathematically equivalent to $\gamma q^2 + d^2 G(h_0)/h^2 = 3\mu_0/(h_0^3 q^2)$ [41] or $q = q_{lc,solid}$ as discussed above. Clearly, the viscous regime $q_{lc}(t)$ equals to $q_{lc,solid}$ at the crossover time τ_r. Taken together, these considerations suggest that the crossover between the rubbery elastic regime and the slow dynamic regime occurs when t exceeds $1/\Gamma_q(q = q_{lc,solid})$, which is the relaxation time of the *liquid* capillary wave mode with $q = q_{lc,solid}$.

Now imagine that μ_0 increases with time. Given (2.4b), this should cause the relaxation rate of the modes Γ_q' to decrease (Fig. 2.6). In that case, the instantaneous experimental time would be shorter than the new relaxation times, so the PSD should be kinetically locked into the current one (namely, the PSD corresponds to a rubbery elastic film with $\mu_0 = \mu_0(t = 0)$.) Based on the above discussion, the PSD becomes able to evolve from the locked-in PSD only after the time t where $q_{lc}(t)$ is equal to $q_{lc,solid}$ of the locked-in PSD. It is easy to see that this happens when $t \sim \eta_{eff,0}/\mu_0(0)$. In other words, $\eta_{eff}(t)$ should maintain the same linear dependence, $\eta_{eff}(t) = 2\mu_0(0)t$ until $t \sim \eta_{eff,0}/\mu_0(0)$, which is observed in Fig. 2.4. This deliberation shows that our measurement would not be able to detect any evolution in the entanglement density of the film, even if it does. Physically, this is because the relaxation rate of the surface modes decreases upon growth of the entanglement
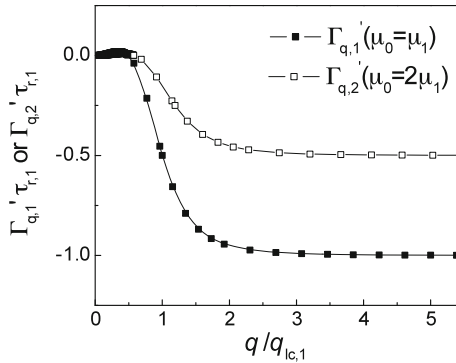
Fig. 2.6 An illustration of the effect of doubling μ_0 on Γ_q'. The *vertical axis* is normalized by $1/\tau_{r,1} \equiv \lim_{q \to \infty} \Gamma_{q,1}'$, the original limiting value before μ_0 is doubled. The *horizontal axis* is normalized by $q_{lc,1}$, the original lower cut-off wavevector of the elastic-state or "rubbery" PSD

density. This causes the rubbery elastic PSD to be locked into the initial one. Only for times exceeding the crossover time for the slow dynamic regime can the PSD grow again.

2.4.2 Residual Stress

In the rapid drying process of spin-coating, it is also speculated that the polymer chains may become compressively deformed [51] besides getting locked into a low entanglement state. Shrinkage of the film upon drying may force the chains into an oblate conformation. This is because the volumetric shrinkage can only take place in the dimension perpendicular to the film, but not the planar dimensions, which are held rigid to the solid substrate [51]. With this, an in-plane residual stress or pre-stress may result [56]. Such a residual stress has been suggested [51] to be responsible for physical aging in as-cast spin-coated polymer films below the T_g [6, 51, 59]. Indeed, large residual stresses ($\sim 10^5$ to $\sim 10^7$ Pa) have been reportedly observed in the dewetting phenomena of PS films supported by a thin liquid layer of polydimethylsilosane (PDMS) [6, 51, 57, 60] or a liquid bath of glycerol [61], surface wrinkling experiments [62, 63] and bending of a polymer-coated micro-cantilever [64].

Vilmin and Raphaël [65], predicted that an in-plane pre-stress in elastic polymer films may cause the occurrence of destabilization analogous to the Asaro-Tiller-Grinfeld instability, well-known in the process of thin film growth by molecular beam epitaxy [66, 67]. In a later publication, Closa, Ziebert and Raphaël discussed in more detail the conditions for this instability [68]. In particular, they showed that, by having surface diffusion in conjunction with a kinematic boundary condition at the free surface, the Asaro-Tiller-Grinfeld instability can occur. But in the absence of surface diffusion, this instability cannot develop, unless if an un-physically large compression (corresponding to an unreasonable stretch ratio λ of >0.03) is applied across the film [68].

In all the systems we studied, including PS-SiO$_x$, PMMA-SiO$_x$ and poly(α-methyl styrene) on silica, we find that the surface dynamics can be fully accounted for without invoking the Asaro-Tiller-Grinfeld instability. For instance, the calculation of Vilmin and Raphaël in [65] predicts that the growth rates of the unstable capillary wave modes should peak at a characteristic wavevector. But the PSDs found in our measurements (Fig. 2.3) clearly do not show such a characteristic wavevector. We observe that this instability may only exist before the pre-stress is fully relaxed [65], which is found by many experiments to occur within the relaxation time of the elastic regime, as expected [51, 57, 60, 62, 64]. If the instability had ever occurred during our measurement, we should observe a qualitative change in the time variation of η_{eff} before and after the pre-stress relaxes. But the only time-variation we had found of η_{eff} occurs during the PSD stagnant regime (where $\eta_{eff} \sim t$). Stagnancy in the PSD growth clearly cannot result from an act of instability. Therefore we conclude that while a large residual stress is probably

present in our films, it does not play any detectable role in the dynamics we observed. Most probably, the condition for the Asaro-Tiller-Grinfeld instability is not fulfilled in our films.

2.4.3 Chain Adsorption

Recently, a slow adsorption process, in which the polymer chains irreversibly bind to the substrate surface [9–12, 56, 69–71], was also found to contribute to the out-of-equilibrium state of the films. In this subsection, we briefly review the basic features observed of this phenomenon and the out-of-equilibrium properties attributed to this process.

In [9], Fujii et al. observed that upon annealing PS-H-Si and PS-SiO$_x$ (where PS-H-Si denotes PS supported by hydrogen-terminated silicon (H-Si)) at 150 °C, a thin layer of PS formed on the surface of both substrates [9], and could not be removed by rigorous rinsing in toluene—a good solvent of PS. To confirm that this residue layer was formed during annealing by the adsorption of the PS chains to the substrate surface, Fujii et al. measured the thickness of the residue layer, $h_{residue}$, as a function of annealing time. The solid symbols of Fig. 2.7 depict a representative result they obtained. As seen, $h_{residue}$ grows relatively quickly in the first ∼20 h, then the growth slows down significantly. Thereafter, $h_{residue}$ continues to grow at the slower rate and reach the steady-state value only after a much later time of ∼100 h. Fujii et al. also explored the M_w dependence of the equilibrium thickness of the residue layer, $h_{residue,\infty}$, and found that it scales linearly with the radius of gyration of the polymer, R_g (Fig. 2.8). On fitting their data to the expression, $h_{residue,\infty} = aR_g$, where a is a constant, they found that $a = 0.81$ and 0.47 for H-Si and SiO$_x$-Si, respectively. This finding illustrates that H-Si is more
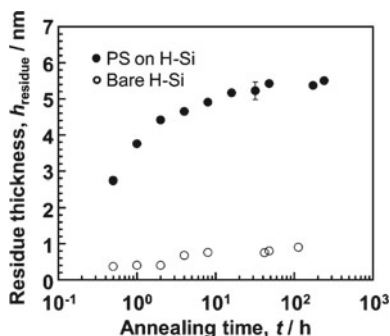
Fig. 2.7 Annealing time dependence of the thickness of the residual film, $h_{residue}$ obtained from PS/H-Si (*solid symbols*) and bare H-Si (*open symbols*). The annealing was carried out at 150 °C in air. The PS has $M_w = 44.1$ kg/mol and initial thickness, $h_0 = 200$ nm (Reproduced with permission from Ref. [33])
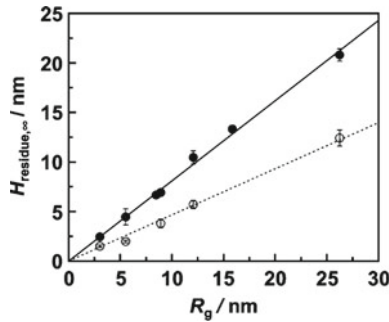
Fig. 2.8 R_g dependence of the equilibrium residue thickness, $h_{residue,\infty}$ for residual films obtained from PS/H-Si (*solid circles*) and PS/SiO$_x$-Si (*open circles*). In this plot, the value of R_g is deduced from the weight average molecular weight of the polymer (Reproduced with permission from Ref. [33])

attractive to PS than SiO$_x$ is, in keeping with observations that PS-H-Si are more stable against dewetting instability than PS-SiO$_x$ are [9].

In a series of elaborate experiments [10, 69, 70], Napolitano and Wübbenhost showed that the growth of the PS residue layer at an interface upon annealing could lead to measurable change in some physical properties of the films. Specifically, they found that the dielectric relaxation of PS capped between Al electrodes depended on the amount of polymer adsorbed onto the Al electrodes surface. Based on this, they determined that the films might not reach the steady state even upon more than one day of annealing at $T_g + 50$ °C and the slow relaxation correlated closely with the growth of the adsorbed layer.

In a different experiment performed by the Koga group, using a combination of x-ray reflectivity and AFM imaging [71], it was uncovered that the adsorbed layer formed in PS-H-Si is composed of a high-density inner flattened nanolayer with a surface coverage of ~ 75 % and a less dense outer layer (Fig. 2.9). In contrast to the thickness of the full adsorbed layer, which, as discussed above, is a fraction of R_g and hence scales with $\sim M_w^{1/2}$ [9], that of the flattened inner layer is independent of M_w and equal to ~ 2 nm [71]. Based on these observations, Koga et al. proposed that the flattened layer was composed of a tight sequence of polymer trains (Fig. 2.9e) and the outer layer much more loosely packed adsorbed chains grown out from the areas of the substrate not occupied by the flattened layer.

Here, we discuss any discernible influence of the adsorbed layer formation process on our dynamic measurement. As noted above, the viscosity of thick PS-SiO$_x$ with $h_0 > 4R_g$ is the same as bulk viscosity [2]. This shows that the polymer chains constituting the adsorbed layer should make insignificant contribution to the total mobility of the films. In that experiment [2], the steady-state effective viscosity $\eta_{eff,0}$ was established within ~ 1 h at 150 °C for $M_w = 44$ to 393 kg/mol. We notice from Fig. 2.7 that this duration is of the same order as the duration of the initial rapid development of the residue film noted above for the same temperature. The fact that the steady-state effective viscosity is established
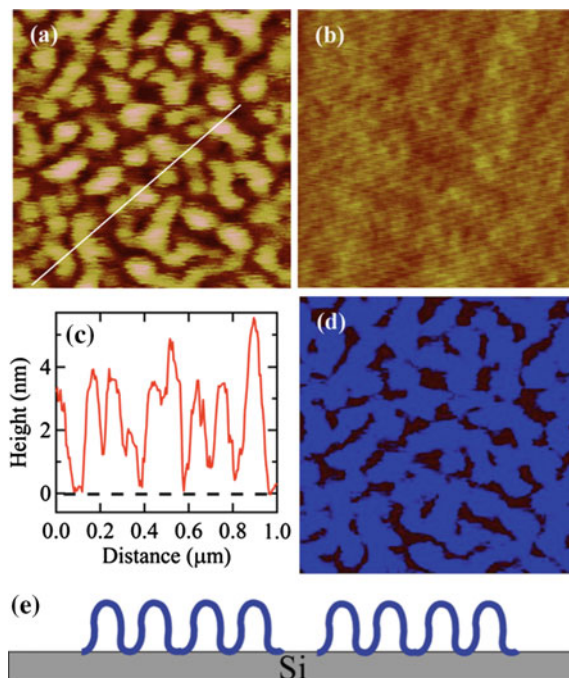
Fig. 2.9 Data and schematic illustrating the structure of the adsorbed layer. **a** AFM topographic image of the flattened inner nanolayer of the PS adsorbed layer left on H-Si after aggressive leaching with chloroform. **b** The full PS adsorbed layer left on H-Si after moderate leaching of ≥5 times with toluene. **c** The cross-sectional profile along the *white line* shown in Panel (**a**). **d** A thresholded image of the image shown in (**a**) with a threshold height value of zero. It shows that the area of the substrate occupied by the flattened layer is ∼75 %. **e** Schematic showing the structure of the flattened nanolayer proposed by Jiang et al. [71] (Reproduced with permission from Ref. [71])

[2, 58] even though $h_{residue}$ is still growing suggests that binding of the PS to the substrate surface in the slow-growth phase has little to no effect on the overall mobility of the films [33]. Perhaps this should not be surprising since the adsorbed layer thickness is only a fraction of R_g and hence much smaller than the thickness of these films (which is $h_0 > 4R_g$). For the thinner films, especially those with thickness $< \sim R_g$, the issue warrants further considerations. To address the issue, we study the growth of the adsorbed layer of PS-SiO$_x$ films with various thicknesses h_0 between 3 and 20 nm at an annealing temperature of 120 °C. In this study, the films were annealed for different annealing times then leached in fresh toluene for four or more times. The thickness of the resulting residue film, $h_{residue}$, was determined by using ellipsometry. The results obtained from the films with $M_w = 212$ and 940 kg/mol are shown in Fig. 2.10a, b, respectively. As one can see, $h_{residue}$ increases with the initial thickness of the films used to create the adsorbed layer, h_0 (which are specified in the figure legend). This should be contrasted with the above finding that $h_{residue}$ is $\sim R_g$ and independent of h_0. Apparently, the different results

(a)

(b)
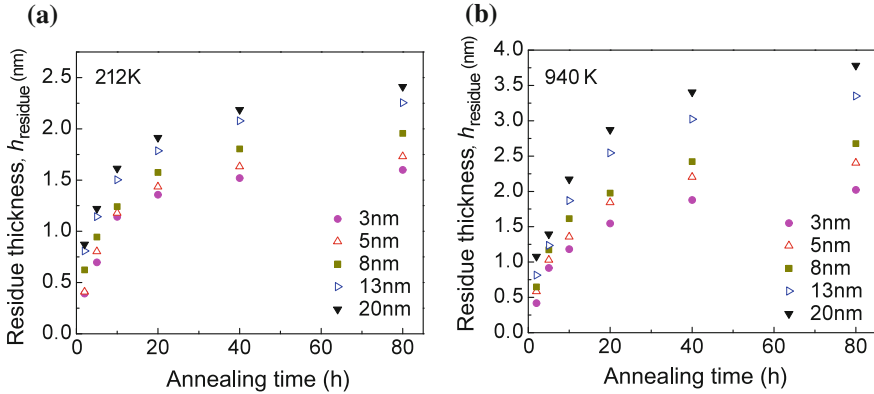
Fig. 2.10 Temporal evolution of h_{residue}, the thickness of the adsorbed layer produced from PS spun-cast on silica with various initial thicknesses. **a** Data taken from films with $M_w = 212$ kg/mol and **b** 940 kg/mol. The annealing temperature was 120 °C. The initial thicknesses are as shown in the legend

are due to the different starting thicknesses h_0 used to create the adsorbed layers. As discussed above for $h_0 > 4R_g$, $h_{\text{residue},\infty} = aR_g$, where $a \sim 0.5$ to 0.8. Therefore, one expects $h_{\text{residue},\infty}$ to depend on h_0 when h_0 is not adequately bigger than R_g [9]. Importantly, Fig. 2.10 shows that the growth of h_{residue} slows down notably after ~ 20 h for the films with $h_0 \leq 8$ nm and ~ 40 h for the thicker films. We observe that these times are comparable to the respective times for the η_{eff} measurement to reach the steady-state value (data not shown). This indicates that much of the development of the adsorbed layer occurs during the stagnant PSD regime. As discussed in Sect. 2.4.1, if any structural change in the films associated with the development of the adsorbed layer should cause the growth rate of the surface modes Γ_q' to decrease, the PSD would be locked into the "rubbery elastic" PSD of the as-cast film and our measurement will not be able to detect these changes. This may explain why the chain adsorption process does not seem to have any impact on our PSD measurement.

In light of the slow recovery (~ 10 d) observed by Napolitano et al. of the dielectric response of the Al-PS-Al films they studied [10], we perform PSD measurements on some of our PS-SiO$_x$ films for an extensive period of time until rupturing takes place. A representative set of data, taken from a PS-SiO$_x$ film with $h_0 = 5$ nm and $M_w = 393$ kg/mol, heated at 120 °C up to 774,000 s or 9 days, is shown in Fig. 2.11. There, one sees that the PSDs fit well to (2.4a) with a single $\eta_{\text{eff},0}$ (= 1.5×10^8 Pas) up to $t = 253,420$ s or 2.9 days. For the PSD taken at a subsequent time of 9 days, (2.4a) clearly underestimates its growth. An examination of the AFM topographic data (Fig. 2.11b) reveals that deep holes were already formed in the film by 9 days of annealing (Fig. 2.11c, d). Since (2.4a) is based on linear analyses, the poor agreement between (2.4a) and the respective PSD is understood to be due to violation of the linear approximation.

Constancy of the measured $\eta_{eff,0}$ up to the time when holes begins to form in the film strongly suggests that our measurement of the steady-state effective viscosity in *thin* films, same as for thick films ($h_0 > 4R_g$), is not visibly affected by the development of the adsorbed layer in the slow dynamic regime. It follows that $\eta_{eff,0}$ can be used as a measure of the film stability. The bigger $\eta_{eff,0}$ is, the more long-lived the film should be. For the 5 nm, 393 kg/mol film considered above (Fig. 2.11), the measured $\eta_{eff,0}$ (i.e., 1.5×10^8 Pas) is $\sim 1/100$ times the bulk value, indicating that this film is much less stable than thick films. A preliminary result shows that when the film is deposited on H-Si, the value of $\eta_{eff,0}$ increases by a factor of 2–3. This implies that by depositing polymer films on a substrate surface that adsorbs the polymer chains more, the lifetime of the films can be improved. Further investigations are warranted to explore to what extent the stability of a film can be improved by using this approached.
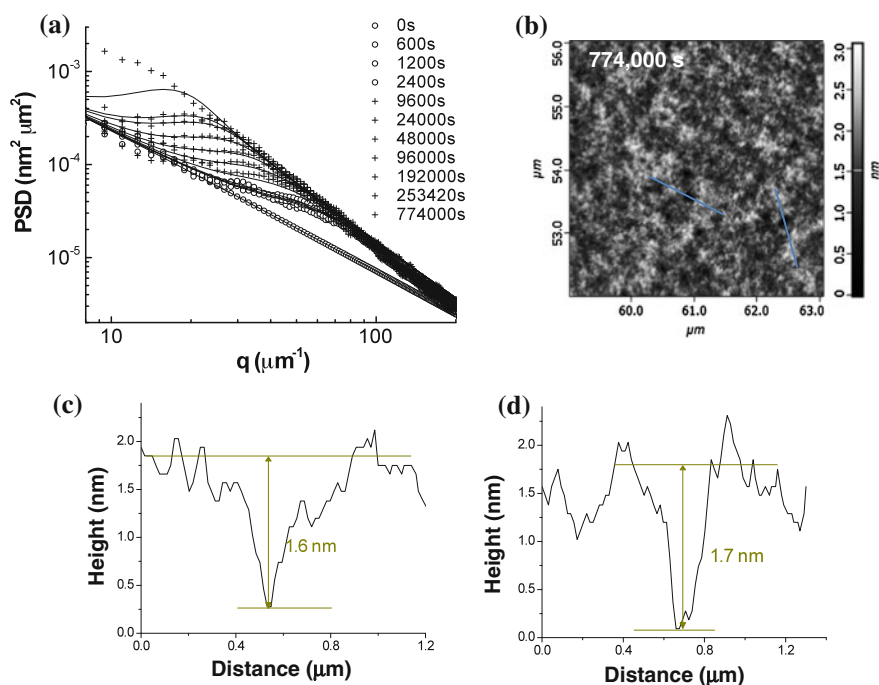
Fig. 2.11 Surface topographic data of a 5 nm, 393 kg/mol PS film upon extensive annealing at 120 °C. **a** The power spectral density found at various times as shown in the legend. The *symbols* denote the experimental data. The *solid lines* are model lines obtained by fitting the $t \leq 253420$ s data to (2.4a). The fitted value of $\eta_{eff,0}$ ($\equiv M_{tot}/3\ h_0^3$) = 1.5×10^8 Pas is $\sim 1/140$ times the bulk value. The film maintains this anomalously low viscosity until after 253,420 s (or 2.9 days), whereupon further annealing brought about deep holes with depth $\approx 0.3\ h_0$ as seen in the AFM topographic image displayed in panel **b** and the cross-sectional profiles in panels **c–d**

2.5 Conclusion

In conclusion, issues concerning the out-of-equilibrium properties of spin-coated polymer films are both academically challenging and of practical importance. An important, but relatively little discussed out-of-equilibrium attribute of spin-coated polymer films is their thickness uniformity. Because the films are smoother than equilibrium, they roughen on heating. Our studies show that the equilibrium pathway of the film surface is governed by the dynamics of the surface capillary wave modes, which in turn can be characterized by the total mobility, or equivalently effective viscosity of the films. For entangled polymer films that are visco-elastic, model analysis of the experimental data allows for additional determination of the shear modulus of the as-cast films. By using the information gathered from PS-SiOx films with a broad range of M_w and h_0 at various temperatures, we addressed several out-of-equilibrium phenomena commonly attributed to as-cast polymer films, including reduced chain entanglement, residual stress and irreversible chain adsorption to the substrate surface. Our measurement shows that the shear modulus of the as-cast films is typically $\sim 1/10$ the equilibrium bulk value. On the other hand, the effective viscosity of the same films (for those with $h_0 > 4R_g$) may reach a steady-state value that agrees with bulk viscosity. A simple interpretation would be that the as-cast films have a reduction in the density of entanglement, but upon heating the density of entanglement regains the equilibrium value. As for residual stress, although numerous experiments support its presence in thin films, we do not notice any influence on our measurement. This observation, however, may not be surprising as existing theory shows that residual stress may not produce instability in a film if there is no surface diffusion. We surmise that surface diffusion may be suppressed in high-M_w films. Various experiments had found that the surface mobile regime is several nanometers thick. So for the films with sufficiently high M_w, the surface chains may be partially embedded in the slower inner region and so have a lessened mobility. Finally for chain adsorption on the substrate surface, we also do not observe any noticeable influence on our measurement. For the thick films with thickness much larger than R_g, effects of the adsorbed layer are expected to be inconsequential due to its relatively insignificant thickness. For the films with thickness comparable to R_g, our residue thickness versus annealing time measurement indicates that the majority of the development of the adsorbed layer occurs before the steady-state effective viscosity is established. Apparently, the subsequent, minor development of the adsorbed layer has negligible effect on the steady-state effective viscosity.

References

1. Reiter, G., de Gennes, P.-G.: Eur. Phys. J. E **6**, 25 (2001)
2. Tsui, O.K.C., Wang, Y.J., Lee, F.K., Lam, C.H., Yang, Z.: Macromolecules **41**, 1465 (2008)
3. Orts, W.J., Vanzanten, J.H., Wu, W.L., Satija, S.K.: Phys. Rev. Lett. **71**, 867 (1993)
4. Mukherjee, M., Bhattacharya, M., Sanyal, M.K., Geue, T., Grenzer, J., Pietsch, U.: Phys. Rev. E **66**, 061801 (2002)
5. Miyazaki, T., Nishida, K., Kanaya, T.: Phys. Rev. E **69**, 022801 (2004)
6. Reiter, G., Hamieh, M., Damman, P., Sclavons, S., Gabriele, S., Vilmin, T., Raphael, E.: Nat. Mater. **4**, 754 (2005)
7. Vilmin, T., Raphael, E.: Europhys. Lett. **72**, 781 (2005)
8. Vilmin, T., Raphael, E.: Eur. Phys. J. E **21**, 161 (2006)
9. Fujii, Y., Yang, Z., Leach, J., Atarashi, H., Tanaka, K., Tsui, O.K.C.: Macromolecules **42**, 7418 (2009)
10. Napolitano, S., Wubbenhorst, M.: Nat. Commun. **2**, 260 (2011)
11. Housmans, C., Sferrazza, M., Napolitano, S.: Macromolecules **47**, 3390 (2014)
12. Koga, T., Jiang, N., Gin, P., Endoh, M.K., Narayanan, S., Lurio, L.B., Sinha, S.K.: Phys. Rev. Lett. **107**, 225901 (2011)
13. Jiang, N.S., Shang, J., Di, X.Y., Endoh, M.K., Koga, T.: Macromolecules **47**, 2682 (2014)
14. Chen, F., Lam, C.-H., Tsui, O.K.C.: Science **343**, 975 (2014)
15. Wang, Y.J., Lam, C.H., Zhang, X., Tsui, O.K.C.: Eur. Phys. J. **141**, 181 (2007). (Special Topics)
16. Wang, Y.J., Tsui, O.K.C.: Langmuir **22**, 1959 (2006)
17. Wang, Y.J., Tsui, O.K.C.: J. Non-Cryst. Solids **352**, 4977 (2006)
18. Yang, Z., Lam, C.-H., DiMasi, E., Bouet, N., Jordan-Sweet, J., Tsui, O.K.C.: Appl. Phys. Lett. **94**, 251906 (2009)
19. Kajiyama, T., Tanaka, K., Takahara, A.: Macromolecules **30**, 280 (1997)
20. Tsui, O.K.C., Wang, X.P., Ho, J.Y.L., Ng, T.K., Xiao, X.D.: Macromolecules **33**, 4198 (2000)
21. Wang, X.P., Xiao, X.D., Tsui, O.K.C.: Macromolecules **34**, 4180 (2001)
22. Du, B.Y., Tsui, O.K.C., Zhang, Q.L., He, T.B.: Langmuir **17**, 3286 (2001)
23. Dubourg, F., Aime, J.P., Marsaudon, S., Couturier, G., Boisgard, R.: J. Phys.: Condens. Matter **15**, 6167 (2003)
24. Valignat, M.P., Oshanin, G., Villette, S., Cazabat, A.M., Moreau, M.: Phys. Rev. Lett. **80**, 5377 (1998)
25. Manias, E., Chen, H., Krishnamoorti, R., Genzer, J., Kramer, E.J., Giannelis, E.P.: Macromolecules **33**, 7955 (2000)
26. Reiter, G.: Phys. Rev. Lett. **87**, 186101 (2001)
27. Damman, P., Gabriele, S., Sclavons, S., Desprez, S., Villers, D., Vilmin, T., Raphael, E., Hamieh, M., Alakhrass, S., Reiter, G.: Phys. Rev. Lett. **99**, 036101 (2007)
28. Shin, K., Obukhov, S., Chen, J.-T., Huh, J., Hwang, Y., Mok, S., Dobriyal, P., Thiyagarajan, P., Russell, T.P.: Nat. Mater. **6**, 961 (2007)
29. Heslot, F., Fraysse, N., Cazabat, A.M.: Nature **338**, 640 (1989)
30. Yang, Z., Fujii, Y., Lee, F.K., Lam, C.-H., Tsui, O.K.C.: Science **328**, 1676 (2010)
31. Lam, C.-H., Tsui, O.K.C., Peng, D.: Langmuir **28**, 10217 (2012)
32. Kim, H., Ruhm, A., Lurio, L.B., Basu, J.K., Lal, J., Lumma, D., Mochrie, S.G.J., Sinha, S.K.: Phys. Rev. Lett. **90**, 068302 (2003)
33. Li, C.H., Koga, T., Jiang, J., Sharma, S., Narayanan, S., Lurio, L.B., Hu, Y., Jiao, X., Sinha, S.K., Billet, S., Sosnowik, D., Kim, H., Sokolov, J.C., Rafailovich, M.H.: Macromolecules **38**, 5144 (2005)
34. Wang, S.-F., Yang, S., Lee, J., Akgun, B., Wu, D.T., Foster, M.D.: Phys. Rev. Lett. **111**, 068303 (2013)
35. Chai, Y., Salez, T., McGraw, J.D., Benzaquen, M., Dalnoki-Veress, K., Raphael, E., Forrest, J. A.: Science **343**, 994 (2014)

36. McGraw, J.D., Salez, T., Baeumchen, O., Raphael, E., Dalnoki-Veress, K.: Phys. Rev. Lett. **109**, 128303 (2012)
37. Zhu, L., Brian, C.W., Swallen, S.F., Straus, P.T., Ediger, M.D., Yu, L.: Phys. Rev. Lett. **106**, 256103 (2011)
38. Vrij, A., Overbeek, J.T.: J. Am. Chem. Soc. **90**, 3074 (1968)
39. Yang, Z., Peng, D., Clough, A., Lam, C.H., Tsui, O.K.C.: Eur. Phys. J. **189**, 155 (2010). (Special Topics)
40. Yang, Z., Clough, A., Lam, C.-H., Tsui, O.K.C.: Macromolecules **44**, 8294 (2011)
41. Peng, D., Yang, Z., Tsui, O.K.C.: Macromolecules **44**, 7460 (2011)
42. Hiemenz, P.C., Lodge, T.P.: Polymer Chemistry, 2nd edn. Marcel Dekker Inc, New York (1984)
43. Yang, Z., Fujii, Y., Lee, F.K., Lam, C.-H., Tsui, O.K.C.: Science **328**, 1676 (2010)
44. Paeng, K., Ediger, M.D.: Macromolecules **44**, 7034 (2011)
45. Peng, D., Li, R.N., Lam, C.-H., Tsui, O.K.C.: Chin. J. Polym. Sci. **31**, 12 (2013)
46. Lam, C.-H., Tsui, O.K.C.: Phys. Rev. E **88**, 042604 (2013)
47. Li, R.N., Chen, F., Lam, C.-H., Tsui, O.K.C.: Macromolecules **46**, 7889 (2013)
48. Yang, Z., Clough, A., Lam, C.-H., Tsui, O.K.C.: Macromolecules **44**, 8294 (2011)
49. Fredrickson, G.H., Ajdari, A., Leibler, L., Carton, J.P.: Macromolecules **25**, 2882 (1992)
50. Safran, S.A., Klein, J.: J. Phys. II Fr. **3**, 749 (1993)
51. Raegen, A., Chowdhury, M., Calers, C., Schmatulla, A., Steiner, U., Reiter, G.: Phys. Rev. Lett. **105**(22), 227801 (2010)
52. Barbero, D.R., Steiner, U.: Phys. Rev. Lett. **102**, 248303 (2009)
53. Fetters, L.J., Lohse, D.J., Milner, S.T.: Macromolecules **32**, 6847 (1999)
54. Rubinstein, M., Colby, R.H.: Polymer Physics, 1st edn. Oxford University Press, New York (2003)
55. Strobl, G.R.: The Physics of Polymers. Springer, Berlin (1996)
56. Li, R.N., Clough, A., Yang, Z., Tsui, O.K.C.: Macromolecules **45**, 1085 (2012)
57. Damman, P., Gabriele, S., Coppee, S., Desprez, S., Villers, D., Vilmin, T., Raphael, E., Hamieh, M., Al Akhrass, S., Reiter, G.: Phys. Rev. Lett. **99**, 036101 (2007)
58. Yang, Z.H., Wang, Y., Todorova, L., Tsui, O.K.C.: Macromolecules **41**, 8785 (2008)
59. Priestley, R.D., Ellison, C.J., Broadbelt, L.J., Torkelson, J.M.: Science **309**, 456 (2005)
60. Chowdhury, M., Freyberg, P., Ziebert, F., Yang, A.C.M., Steiner, U., Reiter, G.: Phys. Rev. Lett. **109**, 136102 (2012)
61. Bodiguel, H., Fretigny, C.: Eur. Phys. J. E **19**, 185 (2006)
62. Chung, J.Y., Chastek, T.Q., Fasolka, M.J., Ro, H.W., Stafford, C.M.: ACS Nano **3**, 844 (2009)
63. Chung, J.Y., Nolte, A.J., Stafford, C.M.: Adv. Mater. **23**, 349 (2011)
64. Thomas, K.R., Steiner, U.: Soft Matter **7**, 7839 (2011)
65. Vilmin, T., Raphael, E.: Phys. Rev. Lett. **97**, 036105 (2006)
66. Asaro, R.J., Tiller, W.A.: Metall. Trans. **3**, 1789 (1972)
67. Grinfeld, M.A.: J. Nonlinear Sci. **3**, 35 (1993)
68. Closa, F., Ziebert, F., Raphael, E.: Phys. Rev. E **83**, 051603 (2011)
69. Napolitano, S., Capponi, S., Vanroy, B.: Eur. Phys. J. E **36**, 61 (2013)
70. Napolitano, S., Rotella, C., Wubbenhorst, M.: ACS Macro Lett. **1**, 1189 (2012)
71. Jiang, N., Shang, J., Di, X., Endoh, M.K., Koga, T.: Macromolecules **27**, 2682 (2014)

Chapter 3
Structural Relaxation of Confined Glassy Polymers

Yunlong Guo and Rodney D. Priestley

Abstract Glasses are non-equilibrium, amorphous materials. They undergo glassy-state structural relaxation towards thermodynamic equilibrium. Consequently, glasses exhibit time-dependent engineering properties in a process termed physical aging. Understanding structural relaxation is important for predicting long-term material properties and useful lifetimes. Here, we highlight the influence of nanoscale confinement and interfaces on the structural relaxation of polymers. Whenever possible, we also discuss correlations or lack thereof between the well-documented influence of confinement on the glass transition temperature (T_g). How confinement might be used to engineer different aging responses in polymer glasses is also mentioned. Finally, we conclude with perspectives and future work.

3.1 Introduction

The advancement in many technologies is the miniaturization of devices to the nanometer length scale or the blending of nano elements within a matrix to make composites. For example, in the area of separations, 100 nm thick polymeric skin layers are used in the production of asymmetric membranes [1]. In microelectronics, future devices will require the development of photoresists with feature

Y. Guo (✉)
University of Michigan-Shanghai Jiao Tong University Joint Institute,
Shanghai Jiao Tong University, Shanghai 200240, People's Republic of China
e-mail: yunlong.guo@sjtu.edu.cn

R.D. Priestley (✉)
Department of Chemical and Biological Engineering, Princeton University,
Princeton, NJ 08544, USA
e-mail: rpriestl@princeton.edu

R.D. Priestley
Princeton Institute for the Science and Technology of Materials,
Princeton University, Princeton, NJ 08544, USA

sizes less than 100 nm [2]. Confined polymers are also critical in the development of new materials [3]. For polymer nanocomposites, in which the nanofiller load level is only several percent by volume, all polymer chains can reside less than 100 nm from a nanofiller interface. Thus, the properties of polymer nanocomposites, which are bulk material, are controlled by confined polymer. Critical to the optimal use of polymers in nanotechnology applications is an understanding of how their properties are impacted by nanoconfinement. As polymers continue to play a major role in material solutions, they will be utilized at length scales approaching the dimensions of the macromolecule. Moreover, with confinement, a larger fraction of molecules are in direct contact with interfaces. Here, the term "confinement" refers to the physical confinement of polymers to the nanometer length scale. With confinement, it is well known that the properties of materials can deviate substantially from the bulk. In particular, for polymeric systems, changes in glass transition temperature (T_g), [4, 5] physical aging, [6] elastic modulus, [7–9] creep compliance, [10] crystallization, [11, 12] and alpha-relaxation time distribution have been observed with confinement [13–16]. It is the deviation in properties of confined polymers relative to the bulk that is commonly referred to as the "confinement effect."

The influence of confinement on T_g, i.e., the T_g-confinement, has been the most extensively investigated phenomenon. From a historical point of view, Keddie et al. [4, 5] were the first to measure a change in T_g of ultrathin polymer films compared to bulk T_g ($T_{g,bulk}$). It was observed that T_g of polystyrene (PS) films supported on silicon decreased with confinement while that of poly(methyl methacrylate) (PMMA) increased with confinement. Conversely, PMMA films supported on gold exhibited a decrease in T_g with confinement. In 1996, Forrest et al. [17] showed that freely standing films of PS and PMMA exhibited reductions in T_g with confinement. The results were generally understood to result from interfacial effects. In those cases in which T_g decreased with confinement, it was hypothesized that the effect was associated with the presence of the free surface enhancing the dynamics associated with T_g. When T_g increased with confinement, it was proposed that the effect was associated with how attractive polymer-substrate interactions reduced the dynamics associated with T_g. The influence of interfaces in modifying the T_g of polymers was revealed by the ability to suppress the T_g-confinement effect of supported PS films by capping the free surface [18, 19] and the discovery that doubly silicon-supported PMMA films exhibited a greater T_g enhancement with confinement than singly supported films do [20]. Torkelson and coworkers [21, 22] employed a fluorescence approach to locally measure T_g at the free surface and substrate of PS and PMMA. For PS and PMMA films supported on a silicon substrate, T_g was reduced at the free surface, while for PMMA T_g at the substrate was enhanced compared to the bulk. These results suggested that the change in T_g of confined polymer films was related to the presence or lack of solid and free interfaces. Other factors that are known to influence T_g in confined systems include geometry, [23, 24] sample preparation and measurement environment, [25] annealing conditions, [26] and chemical structure [27, 28]. The reader is referred to

Refs. [29, 30] for reviews on the T_g-confinement effect, Refs. [31, 32] for articles highlighting the challenges associated with understanding confined polymer behavior, Refs. [33–36] for theoretical contributions, and Refs. [37–40] for studies that challenge the premise of the T_g-confinement effect.

Irrespective of deviations in T_g within confinement, confined glasses undergo structural relaxation (i.e., physical aging). Structural relaxation is the spontaneous relaxation of glasses toward equilibrium, which results in a time dependence of end-use properties [41]. The first study that investigated the effect of confinement on physical aging was from the membrane literature [42]. Pfromm and Koros observed that the physical aging response of polyimide films was accelerated compared to the bulk. Work conducted by Huang and Paul [43] nearly a decade later was in agreement with work of Pfromm and Koros. In recent years, the influence of confinement on the structural relaxation of polymers has received growing attention as technology demands an understanding of the long-term performance of confined glasses. In comparison to the well-studied T_g-confinement effect, fewer studies have characterized the influence of confinement physical aging [44–52].

In this chapter, we highlight key investigations that have examined the influence of size and interfaces on the physical aging response of polymer glasses confined to the thin film, nanoparticle and nanocomposite geometries. When possible, we discuss potential correlations or lack thereof between the size-dependent T_g and physical aging. In Sect. 3.2, we provide a brief introduction to the phenomenology of the glass transition. In Sect. 3.3, we outline the key features of structural relaxation as well as provide an introduction to models of structural relaxation. Section 3.4 is where we review the literature of confined polymer structure relaxation. Finally, Sect. 3.5 concludes the chapter with comments about future work.

3.2 The Glass Transition

As noted by Angell, "a glass in the popular and basically correct conception is a liquid that has lost its ability to flow." [53] From a structural viewpoint, there is virtually no difference between the glass and the supercooled liquid. If the liquid is cooled at a high rate, crystallization can be avoided. Eventually, upon further cooling, molecular motions become progressively slower, and the molecules are unable to sample equilibrium configurations in the experimental time scale, as set by the cooling rate. The temperature at which the liquid falls out of equilibrium is termed the T_g. The glass transition is a kinetic phenomenon [54]. The faster the cooling rate, the less time is available for molecular rearrangement in the liquid state. Consequently, the liquid will abruptly transform into a glass at a higher temperature. The properties of glasses, hence, depend on the path to the glassy state.

Figure 3.1a illustrates volume or enthalpy as a function of temperature for a supercooled polymeric liquid. The intersection of the liquid state and glassy state lines provides one measure of T_g. The behavior depicted in Fig. 3.1a does not
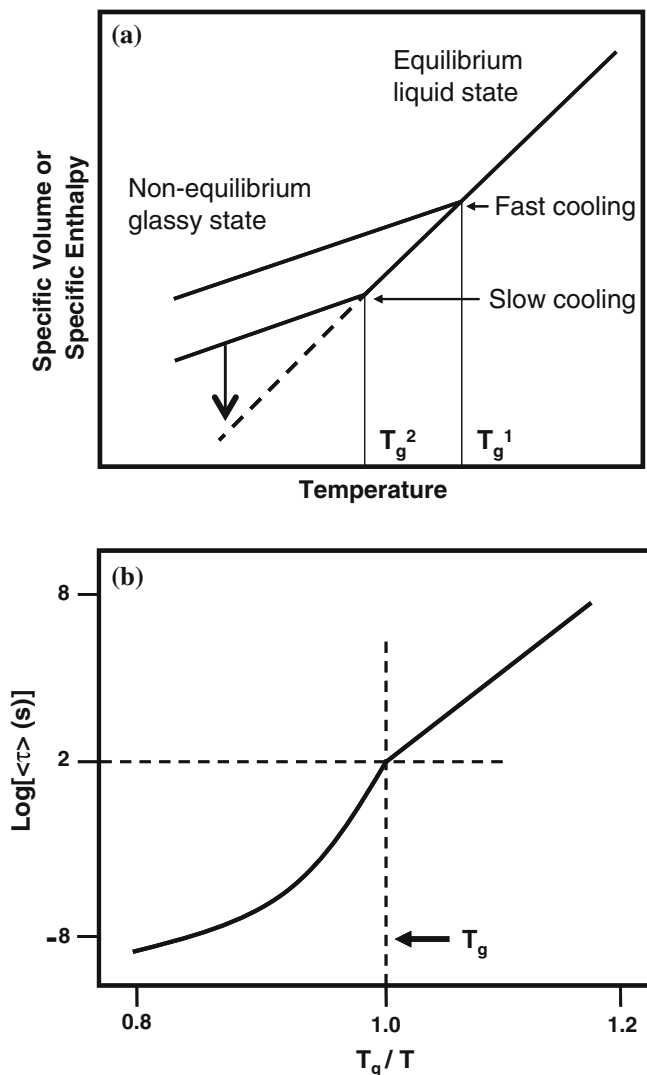
Fig. 3.1 a Temperature dependence of volume or enthalpy for an amorphous polymer. The vertical lines denote T_g determined using fast and slow cooling rates. The vertical arrow denotes glassy-state structural relaxation (physical aging) of the glass formed on slow cooling. **b** Normalized Arrhenius plot of the average alpha-relaxation time for an amorphous polymer. Above T_g, polymer relaxation exhibits a non-Arrhenius temperature dependence while below T_g, polymer relaxation exhibits an Arrhenius temperature dependence

represent a true second-order thermodynamic transition, as there is no discontinuity in volume or enthalpy as a function of temperature [54, 55]. Also illustrated in Fig. 3.1a is the conceptual dependence of the cooling rate on T_g.

The molecular dynamics associated with the glass transition of polymers are cooperative segmental dynamics. The relaxation process of the cooperative segmental motions is known as the α-relaxation process. At the glass transition, the length scale of a cooperative segmental motion is believed to be 1–4 nm, and the average α-relaxation time is ~ 100 s [56]. The α-relaxation process is represented by a distribution of relaxation times. In time-domain measurements, the α-relaxation is non-exponential and can be described by a stretched-exponential function. The most common function used to describe the α-process is that of the Kohlrausch-Williams-Watts (KWW) [57, 58] equation:

$$F(t) = \exp\left[-\left(\frac{t}{\tau}\right)^{\beta}\right] \tag{3.1}$$

where $F(t) = [\sigma(t)-\sigma(\infty)]/[\sigma(0)-\sigma(\infty)]$ and σ is the measured quantity (for example, the capacitance following the removal of a voltage), t is time, τ is the relaxation time, and β is the stretching parameter that describes the width of the distribution. The parameter β can vary between 0 and 1. When the value of β is near 0, the distribution of α-relaxation times is very broad, and when β is near 1, the distribution of α-relaxation times is near a single exponential. Ngai has suggested that β in the KWW function is a measure of the extent of cooperative motion of the α-process [59] (In the "Ngai Coupling Model", β is expressed as 1-n.). As β decreases, the extent of cooperative motion increases. A lower β value represents a broad α-process. The average α-relaxation time, <τ>, can be determined from the fitting parameters of the KWW function by the following equation:

$$<\tau> \; = \int\limits_{0}^{\infty} \exp\left[-\left(\frac{t}{\tau}\right)^{\beta}\right] dt \tag{3.2}$$

Such an approach has been used to determine the average α-relaxation time based on second harmonic generation measurements [60, 61] and fluorescence recovery after pattern photobleaching measurements [62, 63].

The average α-relaxation time of polymers exhibit a dramatic sensitivity to temperature as T_g is approached. Figure 3.1b shows the temperature dependence of the average α-relaxation time as a function of inverse temperature normalized to T_g for an amorphous polymer. The temperature dependence of the average α-relaxation (or viscosity) can be well described by the Vogel-Fulcher-Tammann-Hesse (VFTH) equation: [64–66]

$$\tau = A \cdot \exp\left[\frac{B}{(T - T_0)}\right] \tag{3.3}$$

where A and B are temperature-independent constants. The value of T_o is typically found to be ~ 50 K below the experimentally determined T_g [54]. Although purely empirical, the VFTH equation describes polymer data over ten orders of magnitude

for the average α-relaxation time. The temperature range over which the VFTH equation is valid is approximately $T_g + 10$ K $< T < T_g + 100$ K [54].

Equivalent to VFTH, the Williams, Landel and Ferry (WLF) expression can be applied to explain the temperature dependence of viscosity for polymers above T_g: [67]

$$\log\left(\frac{\eta(T)}{\eta(T_S)}\right) = \frac{-C_1 \cdot (T - T_S)}{C_2 + T - T_S} \tag{3.4}$$

where η is the zero-shear rate viscosity. In the WLF equation, C_1 and C_2 are fitting parameters that are dependent on the polymer, [54, 68] and T_s is a reference temperature and is often taken to be T_g. We note that the WLF expression can be derived from free volume arguments if a linear dependence on the fractional free volume is assumed. The idea of mobility being controlled by volume was first introduced by Doolittle [69]. Doolittle found that the temperature dependence of viscosity could be described by the following equation:

$$\ln(\eta) = \ln(A) + B\left(\frac{(v - v_f)}{v_f}\right) \tag{3.5}$$

where A and B are fitting parameters, v is specific volume, and v_f is free volume. As defined by Doolittle, free volume, v_f, is equal to:

$$v_f = v - v_o \tag{3.6}$$

where v_o is the occupied volume of the liquid.

3.3 Structural Relaxation

The properties of glass continuously evolve toward thermodynamic equilibrium with relaxation rates depending on time and temperature; see Fig. 3.1a. This evolution is referred to as structural relaxation or physical aging [41]. In the past several decades, there has been significant interest in the underlying physics of the structural relaxation of polymeric materials. Better understanding of physical aging can provide both scientific and engineering insight for the vast applications of polymeric materials in modern industries.

The kinetic features of structural relaxation in polymer glasses were first reported by Kovacs in the 1960s [70]. He systematically studied the structural relaxation phenomenon by measuring the volumetric response of polymers subjected to various thermal histories. The findings can be summarized as three ingredients: [71] (1) intrinsic isotherm, (2) asymmetry of approaching equilibrium, and (3) memory effect.

In the isotherm testing, after rejuvenation from the supercooled liquid state, a polymer is quenched and held at a constant temperature below T_g. As a result, the

specific volume of the polymer decreases with time and eventually levels off as equilibrium is approached. As the aging temperature is lowered, longer times are required to reach equilibrium. This intrinsic isotherm behavior shows the temperature and time dependence of structural relaxation, but in practical applications, materials undergo complicated temperature histories instead of isothermal conditions; therefore, nonisothermal conditions should be considered to fully characterize the relaxation behavior.

The asymmetry of approaching equilibrium demonstrates a relaxation process subject to more complex thermal histories. That is, the material is initially equilibrated at temperature T_0 that departs ΔT from the test temperature T_1, i.e., $T_0 = T_1 + \Delta T$ or $T_0 = T_1 - \Delta T$, in cases of down-jump or up-jump, respectively. Subsequently, the temperature is controlled to jump to T_1, where the volumetric evolution is then measured in the relaxation induced from the temperature jump. Although the magnitude of the temperature jump ΔT in both cases of the up-jump and down-jump is the same, the volume recovery towards equilibrium is found to be much faster in the down-jump experiment ($T_1 < T_0$) than in the up-jump experiment ($T_1 > T_0$). This result indicates the inherent nonlinearity of the structural relaxation process and has been widely used to determine that the aging response depends upon the instantaneous state of the material.

Memory effect shows a more complicated relaxation process. The sample is isothermally aged at a lower temperature T_0 for a period until the volume response at an instant is equal or very close to the equilibrium value of a higher temperature ($T_1 > T_0$), then the temperature is immediately jumped to T_1, and the volume recovery process after the up-jump is monitored right away. Although starting from an initial value numerically equal to the equilibrium value, the polymer is not in a steady state; instead, it reveals complex relaxation behavior at T_1: the volumetric response first increases for a period of time, then decreases after reaching a maximum, and finally merges into the isothermal response at T_1. These results have been referred to as "crossover" or "memory effect." The memory effect is evidence of the existence of a non-exponential relaxation process. It arises from the multiplicity of the retardation mechanism. The relaxation behavior cannot be described by a single relaxation time; a stretched exponential function (KWW equation) of relaxation is usually employed [72–76].

The signatures of structural relaxation have attracted a great deal of scientific interest. Investigations on volume/enthalpy recovery and creep/stress-relaxation response of polymer glasses subject to temperature, pressure, and humidity changes are reported in the literature [77–83]. Moreover, the essential ingredients above were also detected in the molecular dynamics of polymers, [84] and others glasses beyond polymers such as colloids [85] and inorganic glasses [86, 87]. It was found in previous studies [88–92] that the relaxation timescale of structural recovery depends on the measured physical properties. As such, the relaxation behavior of one recovery process could not be directly predicted by another. A few reports are available in the literature on physical aging into equilibrium induced by environment changes other than temperature, such as pressure or humidity [93–95].

Concurrently with experimental investigations, structural relaxation has also received a great deal of interest from theoretical studies. Several kinetic or thermodynamic models were developed to capture the three essential ingredients of structural relaxation. Among these models, the most famous two are the Tool-Narayanaswamy-Moynihan (TNM) model [96–98] and the Kovacs-Aklonis-Hutchinson-Ramos (KAHR) model [99].

3.3.1   TNM-KAHR Model

Most theoretical analysis on relaxation behavior of glassy polymers has concentrated on volumetric response or enthalpy recovery, including several theories on specific volume, [99, 100] free volume, [101, 102] fictive temperature, [97, 98, 103] and relaxation time [104–107]. The Kovacs-Aklonis-Hutchinson-Ramos (KAHR) model, the Tool-Narayanaswamy-Moynihan (TNM) model, Ngai-Rendell's coupling model [104–107] and Robertson-Simha-Curro (RSC) theory [101, 102, 108] are able to capture many of the experimental observations associated with glass transition and structural relaxation. The volume and enthalpy responses of polymers are important from a practical view, because the changing thermodynamic state of the non-equilibrium glass impacts the mechanical response of the polymer in physical aging [109]. Therefore, the KAHR model and TNM model are usually utilized in modeling material behavior for the prediction of material response under complicated conditions. Mathematically, the KAHR model and the TNM model are equivalent in essence. Hence, we elect to introduce the KAHR model in this section.

In the KAHR model, the volume recovery behavior can be expressed by the normalized departure from equilibrium δ (= $(V - V_\infty)/V_\infty$), where V_∞ is the equilibrium volume. The volume response is determined as: [99]

$$\delta(z) = -\Delta\alpha \int_0^z R(z - \varsigma)\frac{dT}{d\varsigma}d\varsigma \qquad (3.7)$$

where $\Delta\alpha = \alpha_l - \alpha_g$ is the difference in the coefficient of thermal expansion between the liquid and glassy state, T is temperature, $R(z)$ is a normalized retardation function that ranges between 1 at $z = 0$ and 0 at $z = \infty$, and z is the reduced time defined as:

$$z = \int_0^t \frac{d\xi}{a_T a_\delta} \qquad (3.8)$$

where t is time, a_T is the temperature shift factor, and a_δ is the structural shift factor.

In general, $R(z)$ is chosen as a normalized sum of Kohlrausch modulus functions of the form:

$$R(z) = \left(\sum_{q=1}^{K} R_q\right)^{-1} \left(\sum_{k=1}^{K} R_k e^{-\left(\frac{z}{\tilde{\tau}_k}\right)^{\tilde{\beta}}}\right) \qquad (3.9)$$

where K is the number of elements of $R(z)$ and R_k, τ_k and β_k are the kth coefficients of relaxation time and exponential parameter, respectively. This expression is normalized such that $R(0) = 1$ as required in the KAHR model [99].

The shift factors a_T and a_δ follow the exponential forms suggested by the KAHR model: [99]

$$a_T = \exp(-\Delta\alpha\zeta e^b(T - T_r)); \; a_\delta = \exp(-\zeta\delta) \qquad (3.10)$$

$$e^{-b} = 1 - x; \; \zeta = \frac{(1 - x)\theta}{\Delta\alpha} \qquad (3.11)$$

where T_r is a reference temperature, x is a partition parameter ($0 \le x \le 1$), and θ is a material constant; note that b and ζ are introduced to simplify the solution in the case of $T = T_r$ (i.e., a_T is fixed at unity and a_δ is related to a single parameter ζ) [110].

Recently, the KAHR model has been expanded to characterize and predict the mechanical response of polymeric materials under complicated thermal histories, i.e., the nonisothermal physical aging response. The model in that case is referred to as the KAHR-a_{te} model [110]. The KAHR-a_{te} model combines the KAHR model of volume recovery with a suitable linear relationship between the specific volume and the mechanical aging shift factors [111]. Therefore, it can be utilized to both predict aging response and to determine necessary model parameters from a set of aging shift factor data. Predictions of mechanical response were demonstrated to be in good agreement with the experimental results for several complicated thermal histories, as shown in Fig. 3.2. In addition to short-term nonisothermal aging, long-term creep tests under identical thermal conditions were also analyzed. Effective time theory was unitized to predict long-term response under both isothermal and nonisothermal temperature histories. The long-term compliance after a series of temperature changes was predicted by the KAHR-a_{te} model, and the theoretical predictions match experimental data for complicated thermal histories [73]. Figure 3.3 illustrates long-term mechanical behavior prediction from the KAHR-a_{te} model working together with the effective time theory. The formulation of the KAHR-a_{te} model is described below.

The KAHR model can be extended to predict mechanical response shift factors a_{te} if a relationship between a_{te} and δ (or v) could be ascertained. Based on the findings of Struik [111] and McKenna [89], the logarithmic a_{te} data appear to be well represented by a straight line versus δ (or v) for materials that do not reach

(a)

(b)

(c)
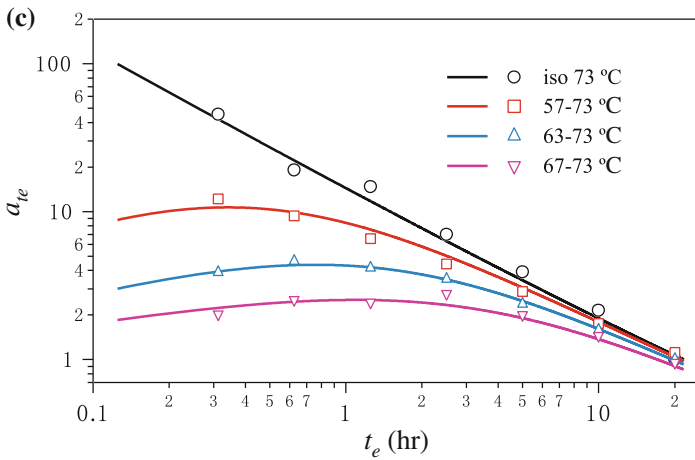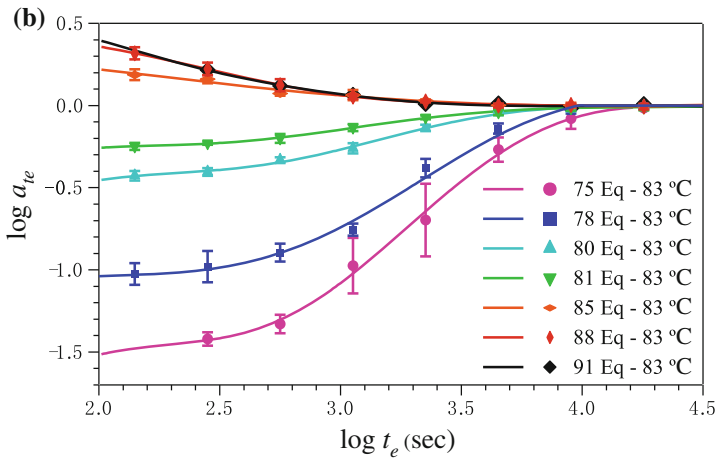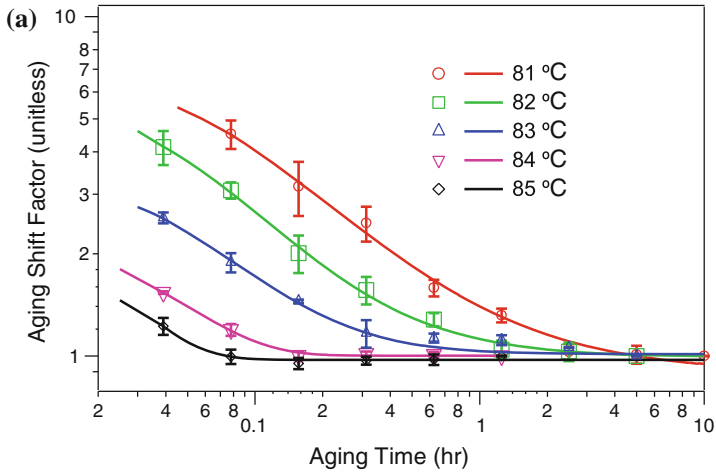
◄ **Fig. 3.2** Prediction of time-dependent mechanical response of poly(phenylene sulfide)(PPS) utilizing the KAHR-a_{te} model: **a** Isothermal relaxation of mechanical aging shift factor for PPS near T_g. **b** Asymmetry of approaching equilibrium of aging shift factor in PPS subject to temperature up-jumps and down-jumps from previous equilibrium state. **c** Evolution of mechanical aging shift factor showing the memory effect. The samples were quenched to the soaking temperatures for 14 h then was heated to 73 °C. Isothermal aging shift factors at 73 °C were plotted for comparison. Error bars represent the standard deviation from separate measurements. Unpublished data from Guo and coworkers
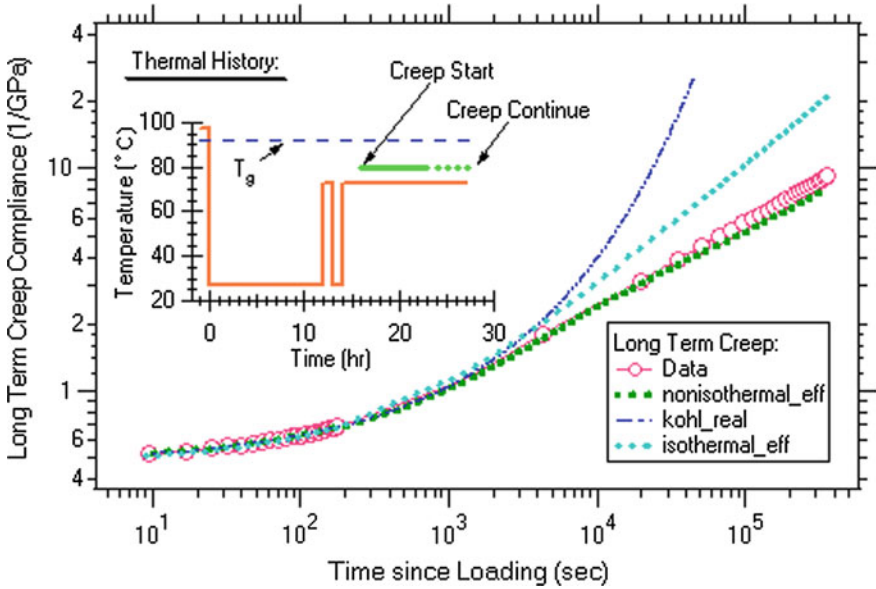
Fig. 3.3 Long-term creep predictions by KAHR-a_{te} model, combined with the isothermal and nonisothermal effective time theory and original Kohlrausch function from short-term response. Thermal histories: 97 °C → 27 °C → 73 °C → 27 °C → 73 °C. Kohlrausch function parameters: $D_0 = 0.460$ GPa^{-1}, $\tau = 1593$ s, $\beta = 0.417$. The inset is the nonisothermal temperature history prior to long-term creep tests. Data reproduced with permission from Ref. [73]

thermodynamic equilibrium. Assuming this behavior, the relationship between a_{te} and δ can be expressed as:

$$a_{te} = e^{r_0(T)+r_1(T)\delta} \tag{3.12}$$

where r_0 describes the equilibrium value of the shift factor a_{te} and r_1 describes how a_{te} changes with a departure from volume equilibrium ($\delta \neq 0$). Recalling the expression for a_δ in Eq. 3.10, this expression was written by Bradshaw [110] as:

$$a_{te}(a_\delta, T) = e^{r_0(T)}\left(\frac{1}{a_\delta}\right)^{r_1(T)/\zeta} \tag{3.13}$$

The dependence of r_0 and r_1 on the temperature T were assumed to take on the form:

$$a_{te}(a_\delta)|_T = \left(\frac{c_0}{a_\delta}\right)^{c_1}; \; c_0, c_1 > 0 \tag{3.14}$$

where constants c_0 and c_1 are specific to the temperature at which the mechanical responses were measured. The equation indicates a temperature-dependent linear relationship between a_{te} and a_δ in log-log plot. At a given temperature, mechanical response (a_{te}) can be evaluated if the thermal history is known. This relationship is assumed based on the experimental findings of Struik [111] and McKenna [89].

There are two basic problems of interest for the KAHR-a_{te} model formation: (1) prediction of mechanical aging shift factor a_{te} for a given set of parameters, and (2) determination of those parameters to fit a known mechanical response data set. Here, we focus on the former.

An essential step is to determine the reduced time z. This derivation follows that presented by Bradshaw [110]. Once z is obtained, volume response and then aging shift factors can be found by using KAHR-a_{te} model parameters. Differentiating Eq. 3.8, we find:

$$\frac{dz}{dt} = \frac{1}{a_T(z)a_\delta(z)} \tag{3.15}$$

Substituting δ from Eq. 3.7, a_T and a_δ from Eq. 3.10 and a_{te} from Eq. 3.14 leads to:

$$\frac{dz}{dt}(z) = e^{\Delta\alpha\zeta e^b(T(z)-T_r)}e^{\left[-\Delta\alpha\zeta\int_0^z R(z-\varsigma)\frac{dT}{d\varsigma}d\varsigma\right]} \tag{3.16}$$

This represents an ordinary differential equation in z that can be solved using suitable numerical methods.

If the temperature history is restricted to a series of temperature jumps, since the material was at $T = T_g$ (i.e., the last moment it was in equilibrium before quenching to $T < T_g$), Eq. 3.16 can be further simplified. Specifically, a temperature history consisting of m temperature jumps can be expressed as a function of the time since the quench from $T_g(t_a)$ as:

$$T(t_a) = T_g + \sum_{m=0}^{M-1} H(t_a - \theta_m)\Delta T_m$$

$$\theta_0 = 0; \quad \Delta T_m = \begin{cases} T_0 - T_g & m = 0 \\ T_m - T_{m-1} & m > 0 \end{cases} \tag{3.17}$$

where ΔT_m and θ_m are the temperature change and time at the mth step, respectively, and $H(t)$ is the Heaviside function. Substituting this into Eq. 3.16 leads to the following simplified differential equation for z:

$$t_a \in \left[\theta_p, \ \theta_{p+1}\right] \to \frac{dz}{dt}(z) = e^{\Delta\alpha\zeta e^b (T_p - T_r)} e^{\left[-\Delta\alpha\zeta \sum_{m=0}^{p} \Delta T_m R(z - \tilde{\theta}_m)\right]} \tag{3.18}$$

where $p \in [0, M{-}1]$, $\tilde{\theta}_m = z(\theta_m)$ and $\theta_m = \infty$.

The expression in Eq. 3.18 is an ordinary differential equation. Since the initial condition at time $t_a = 0$ is known to be $z(0) = 0$, this represents an initial value problem that can be solved using a variety of approaches. In some work, [74, 110] the reduced time z is evaluated using a 5th order Runge-Kutta method with the Cash-Karp parameters as detailed in Ref. [112] further details regarding the solution method are available elsewhere [110]. Once z is obtained, all quantities of interest (δ, a_δ, a_{te}, etc.) can be obtained by algebraic evaluation.

3.3.2 Free Volume Holes Diffusion Model

Physical aging leads to a densification of glasses upon isothermal annealing. The structural (or volume) relaxation can be viewed as a loss of free volume. Indeed, from positron annihilation lifetime spectroscopy [113] and absorbance spectroscopy [114] studies, it has been shown that free volume decreases with increasing physical aging time. Struik has suggested a closed-loop scheme for the reduction in free volume with physical aging time given as:

$$v_f \to M \to \frac{dv_f}{dt} \qquad 19 \tag{3.19}$$

where M is the segmental mobility [41]. In this picture, the rate of relaxation (dv_f/dt) is determined by the segmental mobility, which itself is determined by the free volume. This scheme implies that volume relaxation during physical aging is a non-linear relaxation process (the rate of relaxation depends on the instantaneous state of the system). In the development of the so-called Free Volume Holes Diffusion (FVHD) model, segmental mobility is essentially replaced by the

diffusion equation [108, 115]. In this manner, the central feature of FVHD model is that free volume is localized in the form of vacant sites and that physical aging proceeds by the vacancy diffusion to a boundary, where they are annihilated. In the FVHD model free volume is governed by:

$$\frac{\partial f}{\partial t} = \nabla \cdot (D\nabla f) \qquad (3.20)$$

where f is the free volume fraction and D is the diffusion constant of holes and depends on free volume. The equation suggests that a free volume gradient is the driving force for vacancy diffusion and hence, structural relaxation. Non-linearity is achieved by making the diffusion coefficient be dependent on free volume. Rewriting Eq. 3.5, i.e., the Doolittle expression, for diffusion is given as:

$$D = D_o \exp(\frac{B}{f_{vo}} - \frac{B}{f_v}) \qquad (3.21)$$

where B is the material constant, D_o is the diffusion coefficient prior to relaxation, and f_{vo} is the unrelaxed value of the fractional free volume. Once the appropriate boundary conditions are defined, Eqs. 3.20 and 3.21 can be solved for a specific thermal history to monitor the evolution of free volume during physical aging. Since its inception, the FVHD model has been criticized because early work by Kovacs showed that the physical aging rate did not depend on sample size when performing aging experiments on bulk samples and powders [70]. In addition, quantitative fits of the FVHD model relied on the introduction of internal boundaries whereby free volume was annihilated [115]. However, the FVHD model has recently received renewed interest as a model for describing the physical aging behavior of nanoconfined polymer [116–119].

3.4 Confined Structural Relaxation

In this section, we discuss the influence of confinement on the physical aging response of polymers. The discussion is organized in terms of the type of confinement, i.e., thin films, nanocomposites and nanoparticles. We also briefly discuss contributions from simulations. We conclude with a summary and our thoughts on future studies.

3.4.1 Thin Films

In 2002, the effect of film thickness on the physical aging rate of spin-cast poly (iso-butyl methacrylate) (PiBMA) films supported on silicon substrates was

investigated by fluorescence [120]. The fluorescence of dye molecules either doped or chemical labeled to the polymer can be used to monitor physical aging [121]. Physical aging leads to an increase in the fluorescence intensity of the dye molecules. The increase in intensity is due to a densification of the nanoscale medium surrounding the dye molecule, with a slightly denser environment yielding a higher intensity due to a reduced rate of non-radiative decay, as illustrated in Fig. 3.4a. Here, 4-tricyanovinyl-[N(2-hydroxyethyl)-N-ethyl]aniline (TC1) chemically labeled
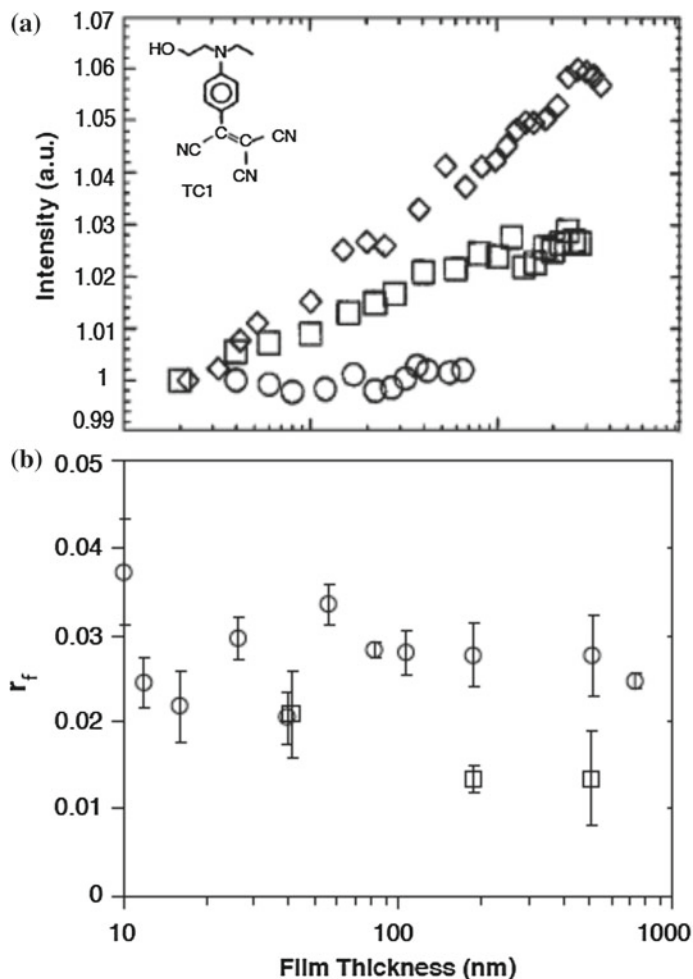
Fig. 3.4 a Time dependence of the normalized fluorescence intensity of the dye molecule TC1 chemically labeled to PiBMA in a thin film geometry (film thickness = 39 nm) when annealed at 343 K (*circles*) and after quenching to 298 K (*diamonds*) and 323 K (*squares*). The inset show the TC1 molecule. **b** Thickness dependence of the fluorescence physical aging rate as determined by eq. 3.21 for TC1-labeled PiBMA. Reproduced with permission from Ref. [120]

to PiBMA was used to monitor physical aging. The increased sensitivity of fluorescence to physical aging makes studies on thin films feasible. When annealed at $T_{g,bulk} - T_a = 39$ K and 14 K, respectively, no change in the physical aging rate was observed with decreasing film thickness from 724 to 10 nm, as illustrated in Fig. 3.4b . The physical aging rate was taken to be the slope of the normalized fluorescence intensity:

$$r_f = F_o^{-1}(dF/d \log t) \qquad (3.22)$$

where F is the fluorescence intensity at time t and F_o is the initial fluorescence intensity. Several years later, Priestley and coworkers reported no influence of film thickness on the T_g of PiBMA [22]. Via a unique fluorescence multilayer approach [21] it was determined that the influence of the free surface and substrate interface, which acted to reduce and increase the local T_g, respectively, were counterbalanced, resulting in a size-independent T_g for PiBMA. Combined, these two studies suggest an intimate correlation between the influence of confinement on T_g and physical aging [6, 51]. The rationale seems straightforward since physical aging can only occurs below T_g and is influenced by the aging depth. In reviewing the literature on the influence of film thickness on physical aging, when possible, we will seek to confirm whether T_g conformed in a similar manner.

Kawana and Jones used ellipsometry to detect the overshoot of the expansivity-temperature curve upon heating for PS thin films supported on silicon substrates aged for 7 days at $T_{g,bulk} - 20$ °C [44]. Figure 3.5 shows representative data from the study. The expansivity versus temperature plots were obtained by numerically differentiating the thickness-temperature curves. With decreasing film thickness there is a reduction in the overshoot curves until the point at which a 10 nm film exhibited no evidence of an overshoot. Interestingly, clear structural relaxation peaks were observed at bulk T_g, i.e., for all films with thickness greater than 10 nm. The reduction in structural relaxation with confinement was attributed to the presence of a liquid-like layer at the free surface approximately 10 nm thick. In other words, the T_g of a10 nm thick film was less than $T_{g,bulk} - 20$ °C. Hence, the local structural relaxation would be depth dependent, reflecting a gradient in T_g.
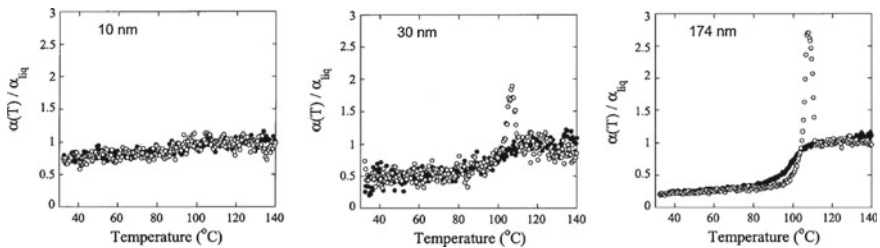
Fig. 3.5 Temperature dependence of the normalized expansivity for PS thin films supported on a silicon substrate. Original data from Ref. [44]. Reproduced with permission from Ref. [6]

In a series of studies, Priestley et al. investigated the physical aging response of poly(methyl methacrylate) (PMMA) and PS films supported on a silica substrate using fluorescence spectroscopy [45, 46]. When annealed above $T_{g,bulk}$, ultrathin PMMA films showed evidence of physical aging while PS films did not. Conversely, when annealed slightly below $T_{g,bulk}$, ultrathin PS films showed no evidence of physical aging, a result consistent with an earlier report [44]. These anomalous aging responses were consistent with the influence of interfacial effects modifying the T_g of the thin films. That is, T_g is enhanced and suppressed with confinement for PMMA and PS films supported on a silica substrate, respectively, thereby modifying the conditions by which aging proceeds.

A unique advantage of fluorescence is that physical aging can be monitored locally within a thin film in a depth-controlled manner. This allows for the direct measurement of interface-induced gradients in the physical aging response of thin films. This was achieved via a multilayer film geometry in which one layer contains fluorescence molecules while the others do not. Figure 3.6 show the effect of interfaces on the physical aging response of PMMA aged at $T_a = T_{g,bulk} - 87$ K. In the center of the film, physical aging was greatest and was consistent with the response of bulk. At the free surface, the aging response was reduced by nearly a factor of two while at the substrate-polymer interface, aging was nearly completely suppressed. When annealed at $T_a = T_{g,bulk} - 5$ K (data not shown), the physical aging response was similar in the film center and at the polymer-substrate interface while at the free surface, aging did not occur over the experimental time scale. These measurements revealed that interfaces could have a significant impact on physical
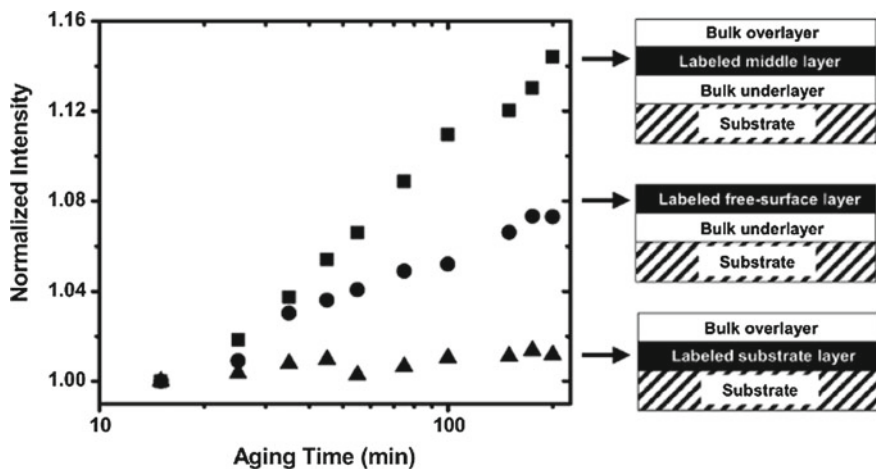
Fig. 3.6 Normalized fluorescence intensity as a function of aging time of TC1-labeled PMMA 12 nm thick layers placed within a multilayer film geometry of neat PMMA layers. The multilayer films where aged at $T_a = T_{g,bulk} - 87$ K. The substrate layer (*triangles*) exhibited near suppression in physical aging while the free surface layer (*circles*) and middle layer (*squares*) exhibited more pronounced physical aging. Original data from Ref. [46]. Reproduced with permission from Ref. [6]

aging, and that the effect was dependent on aging temperature. The suppressed aging at the substrate was due to hydrogen-bonding interactions locally impeding mobility. At the free-surface interface, an absence of aging at temperatures near bulk followed the notion of a liquid-like layer with a reduced T_g at the surface of glassy polymers. Remarkably, it was discovered that the gradient in the physical aging rate propagated into the film at a length scale significantly larger than that observed for T_g.

Koh and Simon employed a stacked multilayer film geometry to investigate the structural relaxation of thin "freely standing" polystyrene films via calorimetry [52]. In prior work, it was illustrated that stacked PS films exhibited a suppression in T_g, albeit to a lesser extent, than freestanding films do [122]. They found that with decreasing film thickness the rate of physical aging as measured by the slope of the aging isotherm curve was decreased compared to the bulk when aging was performed at a constant value of T_a. However, when the comparison was performed at the same distance below T_g, i.e., a constant value of $T_g - T_a$, the aging rate of the thin films was unchanged from the bulk value. The time required to reach equilibrium, i.e., another measure of aging response, increased with decreasing film thickness even when aging was performed at a constant depth below T_g. The results imply that changes in aging rate with confinement were due to shifts in T_g at the nanoscale while the changes in the time required to reach equilibrium were not solely due to shifts in T_g.

Employing a streamlined ellipsometry technique, [123] Roth and coworkers measured the temperature dependence of the physical aging rate in ultrathin PS films supported on a silicon substrate [48]. For PS films with thicknesses <100 nm, the physical aging rate was reduced compared to bulk at all temperature investigated. Figure 3.7 compares the aging response for 2430 and 29 nm thick PS films. The data show that the aging rates in thinner films are not simply just shifted to lower temperatures due to a reduction in T_g of the film. If this were the case, due to the non-monotonic temperature dependence of the aging rate, a thin film would exhibit a lower or higher aging rate compared to the bulk depending on the aging temperature. Consistent with these findings were the measurements of Green and coworkers, who also utilized ellipsometry to probe the aging response of star-shaped PS as a function of film thickness, number of arms, f, and arm length, N [124]. Compared to the linear PS, the star-shaped PS exhibited a reduction in physical aging rate. Nonetheless, in the thin film geometry, both the linear and star-shaped PSs exhibit reduced rates of physical aging compared to the bulk at all temperatures investigated. In agreement with the study of Roth and coworkers, [48] the reduction in aging rate could not be merely accounted for by a shift in T_g. Instead both studies presented similar arguments that the reduction in aging was consistent with a gradient in T_g away from the free interface.

The consensus form the membrane literature is that thin glassy polymeric membranes exhibit an increase in the rate of physical aging with decreasing film thickness. The range of polymeric membranes that have been shown to exhibit this anomalous aging response include polysulfone, [42, 43, 125, 126] polyimides, [42, 43, 50, 125, 126] polynorborene [127] and poly(phenylene oxide)s [43, 125, 126]. Figure 3.8 shows the impact of film thickness on the physical aging of polysulfone
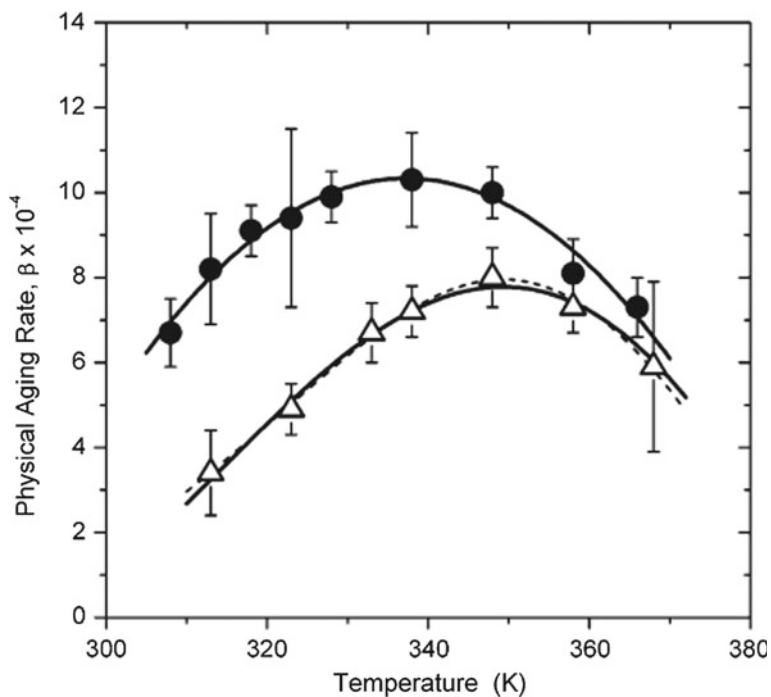
Fig. 3.7 Temperature dependence of the physical aging rate, as determined by ellipsometry measurements, for 2430 nm thick (*filled circles*) and 29 nm thick (*open triangle*) films aged for 360 min. Reproduced with permission from Ref. [48]
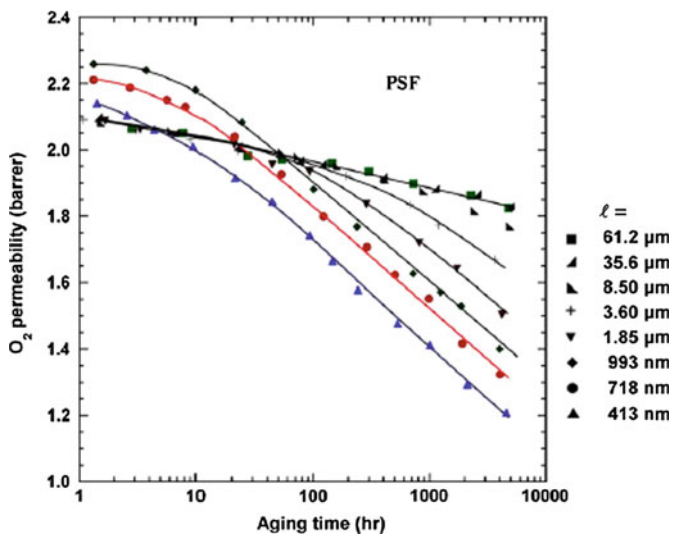
Fig. 3.8 Oxygen permeability as a function of aging time at room temperature for freestanding films of PSF. Reproduced with permission from Ref. [43]

membranes as measured via oxygen permeability at room temperature [43]. As measured by the rate of physical aging, polysulfone membranes begin to exhibit a size-dependent aging rate at ~ 4 microns. The enhanced physical aging rate with decreasing film thickness has also been observed via refractive index studies for polysulfone [126]. The length scales at which size-dependent aging rates are observed in membrane film are remarkably large and often occur at a thickness in which no size-dependence of T_g is observed. However, in recent work, Rowe et al. observed a correlation between accelerated physical aging and T_g in thin membranes of PSF with thicknesses less than 500 nm supported on a polydimethylsiloxane layer; see Fig. 3.9a for physical aging data [128]. Accelerated aging was described via a self-retarding model developed by Struik to describe the variation in specific volume with aging time and is given as:

$$\frac{d\Delta f}{dt} = \frac{\Delta f}{\tau_\infty \exp(-\gamma \Delta f)} \qquad (3.23)$$

where Δf is the excess fractional free volume, τ_∞ is the relaxation time at equilibrium, and γ is a constant characterizing the sensitivity of the relaxation time to the excess fractional free volume. To fit the thickness dependence of physical aging, τ_∞ was allowed to vary with thickness. The model was able to capture the thickness dependence of the physical aging rate. The values of τ_∞ determined from the model fit to experimental observations and the T_g show a similar trend with thickness as illustrated in Fig. 3.9b. This suggests that, at least for this film thickness range, accelerated aging is governed by a decrease in the high temperature characteristic of the relaxation time, which in turn is correlated to the size-dependent T_g.

As noted above, a faster physical aging rate has been observed in micrometer thick films of glassy polymeric membranes [42, 43, 127, 129]. This effect was found in a range of rigid backbone and high free volume polymers. With a few exceptions, [117] in contrast, flexible polymers, including PS and PMMA typically exhibit size-dependent physical aging phenomenon at ~ 100 nm in thickness [45, 48]. This vast difference in length scales at which rigid and flexible polymer physical aging response departs from bulk remains an intriguing puzzle. In recent work, Roth and coworkers have examined this phenomenon in depth [130, 131]. In their work, they focused on the importance of quench conditions on physical aging in thin films, i.e., freestanding versus supported quench conditions. Via ellipsometry, it was shown that films quenched in the freestanding state exhibited a strong thickness-dependent aging rate extending to the micrometer length scale. Films quenched in the supported geometry did not display a thickness-dependent aging rate at micrometer thicknesses. The findings were independent of molecular structure and aging temperature. As a matter of protocol, glassy membrane films were quenched in the freestanding geometry supported on steel wire frames. This approach imposed a thickness-dependent uniaxial tension on the film, which Roth and coworkers argue leads to the observed thickness-dependent aging response at micrometers.

Freestanding glassy membrane films exhibit accelerated physical aging relative to the bulk. Hence, time-dependent permeation and selectivity are accelerated for
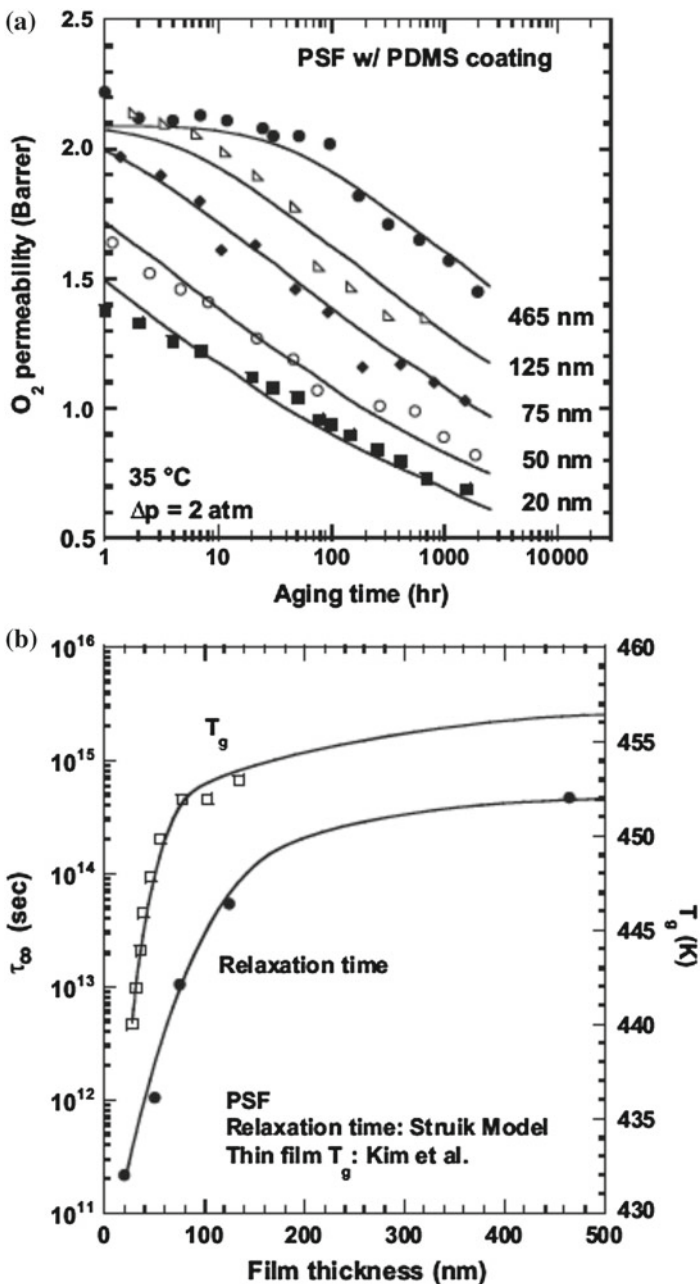
Fig. 3.9 a Oxygen permeability as a function of aging time at room temperature for films of PSF coated with rubbery PDMS layers used to cover defects in the membrane films. **b** Dependence of film thickness on τ_∞ from Eq. 3.22 and T_g of PSF films. The T_g data is from Kim et al. [174] Reproduced with permission from Ref. [128]

thin films. Engineering approaches to suppress or completely eliminate the size-dependent aging response remains a challenge. In one approach, the inclusion of nanofillers into a polymer matrix was shown to strongly suppress physical aging in flexible polymers [47, 132, 133]. Recently, Baer and coworkers [134] investigated the physical aging response of PSF thin films sandwiched between rubbery polyolefin layers, i.e., a multilayer film geometry, as shown in Fig. 3.10a. The multilayer films were made by a co-extrusion method developed by Baer and coworkers. The overall thickness of the multilayer films was >80 microns, while the layer thickness of the PSF ranged from 400 to 185 nm. Due to the difference in T_g of the PSF and polyolefin, i.e., 184 °C and −52 °C, respectively, aging of the PSF should not be convoluted with an aging response from the rubbery layer. Physical aging was tracked by measuring the O_2 and N_2 permeability as a function of time. Prior to all aging studies, the films were annealed in an oven at 195 °C for 15 min to remove all thermal history. Quenching to room temperature was performed in air. Figure 3.10b compares the aging response of bulk PSF and thin films of PSF in the multilayer film geometry. The calculated aging rate, defined as the slope of the aging isotherm curves, was within error, independent of film thickness.

This results are in stark contrast to the studies of Huang and Paul, [43] who observed a significant acceleration in physical aging with decreasing thickness of freestanding films as illustrated by the comparison in Fig. 3.10b. The results stand to highlight the importance of free surfaces in the aging response of glassy membrane films. Freestanding films of PSF have two free interfaces, while the PSF in the multilayer film geometry has capped interfaces. In the former, enhanced surface mobility and free volume hole diffusion could facilitate accelerated aging in the films. In the latter, sandwiching the PSF within a polyolefin layers could suppress or eliminate such a mechanism.

The above-mentioned results of sandwiched PSFs have been supported by structural relaxation studies probed by calorimetry on polyolefin/PSF [135] and PS/polycarbonate (PC) [136] multilayer systems. In the latter, the aging response of thin PS layers confined between PCs was investigated. The T_g and aging rate of the PS layers were found to be unchanged from the bulk. In the calorimetry studies, all samples were quenched into the glassy state from equilibrium within a DSC pan. Hence, unlike in similar studies performed on freestanding films, no size-dependent residual stresses induced during the quench step are expected. The results would appear to be in agreement with the argument presented by Roth and coworkers that proposed a connection between confined accelerated aging and stresses induced during quenching [130]. On the other hand, the multilayer films are not freestanding; hence, there are no free surfaces. This makes a direct comparison to the work of Roth and coworkers not entirely accurate.

Baer and coworkers demonstrated that thin glassy films without free interfaces exhibited bulk physical aging behavior. For instance, PSF, when confined between polyolefin layers, showed no dependence of film thickness on the rate of physical aging. Motivated by these studies, Roth and coworkers devised a set of experiments to directly investigate the influence of an adjacent rubbery layer on T_g and physical aging in thin polymeric films [137]. The sample geometry consisted of a thin PS
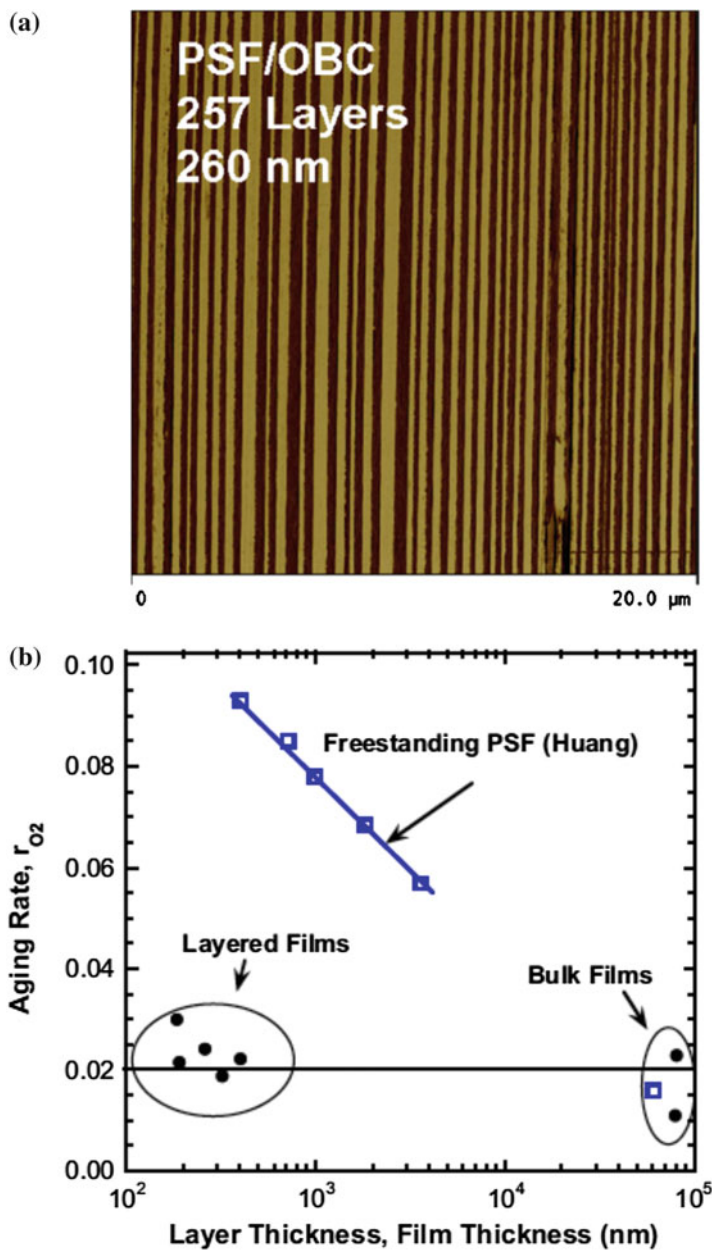
Fig. 3.10 a AFM image of PSF/OBC (olefin block copolymer) multilayer film with 257 layers and an average layer thickness of 260 nm. b Physical aging rate as a function of layer thickness (film thickness) for PSF films in the multilayer film geometry (*filled circles*) and freestanding film geometry (*open squares*). Data on freestanding films from Huang and Paul [43]. Reproduced with permission from Ref. [134]

layer atop a bulk rubbery poly(n-butyl methacrylate) underlayer. The T_g and physical aging of the PS layer as a function of layer thickness were measured via fluorescence and ellipsometry, respectively. We note that the T_g of the PS layer within the bilayer film was selectively measured following a modified fluorescence approach originally developed by Torkelson and coworkers [21]. They demonstrated that the physical aging rate of the PS layer atop the rubbery PnBMA did not exhibit any film thickness response down to ~90 nm. Complementary measurements of the T_g of the PS layer revealed a sharp reduction in T_g below a film thickness of ~200 nm reminiscent of the response of freestanding films, though the film thickness at which T_g begins to deviate from the bulk is greater for the bilayer geometry. Unlike the work of Baer and coworkers, the PS layer is exposed to one free interface, and it is this free interface that is speculated to lead to the observed size-dependence of T_g. Yet, the same film geometry does not result in a size-dependence of the physical aging rate. The results are summarized in Fig. 3.11 (filled symbols). Roth and coworkers put forth a number of plausible explanations for the size-invariant aging rate, including (1) competition of locally different dynamics at the opposite interfaces that cancel each other, leading to, on average, bulk response; and (2) stresses imparted at the glassy-rubbery interface that alter the energy landscape.

3.4.2 Nanocomposites

The effects of confinement on the physical aging of polymers are not unique to the thin film geometry and have also been observed in polymer nanocomposites [47, 132, 133, 138–140]. In fact, thin films could be considered model systems for nanocomposites for which the thickness of a thin film is related to the average interparticle distance of nanoparticles in a polymer matrix [47]. For an epoxy/clay nanocomposite, enthalpy relaxation was reduced by nearly a factor of four with the incorporation of ten parts per hundred clay compared to the neat epoxy [138, 139]. The reduction in aging with the addition of clay was rationalized assuming a layer with reduced mobility at the organic-inorganic interface [138]. Fluorescence studies have shown that the physical aging of PMMA [47, 132, 133] and poly (2-vinylpyridine) [47, 132] deep in the glassy state could be suppressed almost completely using silica nanoparticles that have an attraction with the polymer. When nanoparticles did not possess an attraction with the polymer, such as in the case of PS and silica nanoparticles, aging was not suppressed.

Beyond the above cases, given a larger sample space of polymer nanocomposites, the literature is composed of seemingly contradictory results: the aging process could be either accelerated [118, 141–146] or suppressed [138–140, 147–150]. In a recent review article on the physical aging of polymer nanocomposites, [151] the authors remarked that the apparently different conclusions may originate from the different definitions of physical aging rate. Nevertheless, the diverse physical aging behavior in experimental observations should be related to the interactions between the
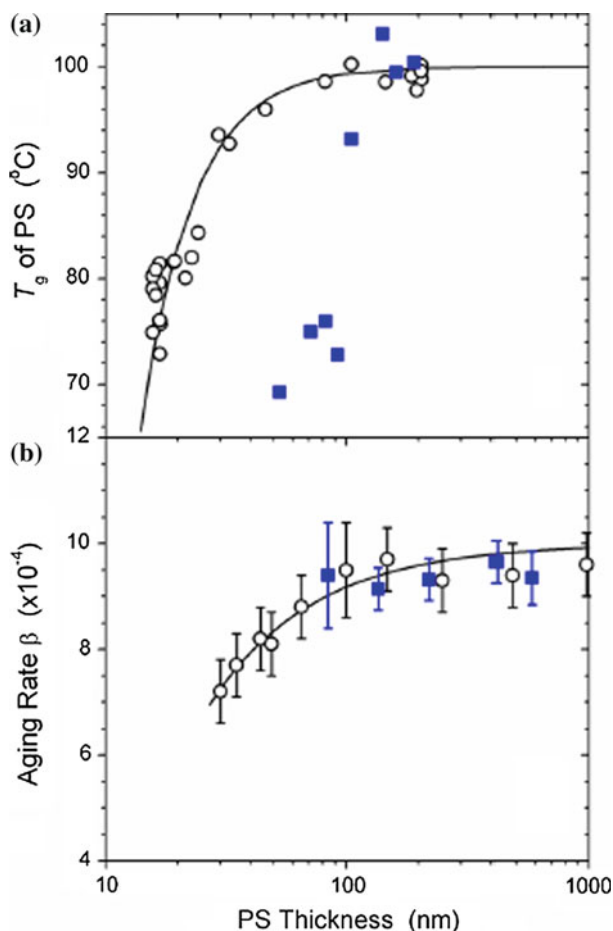
Fig. 3.11 Influence of film thickness on **a** T_g (*closed squares*) and **b** physical aging rate (*closed squares*) of PS films supported on a PiBMA rubbery layer. The open circles represent the T_g (**a**) and physical aging rates (**b**) of PS films supported on a silicon substrate. Reproduced with permission from Ref. [137]

polymer matrix and the nano-fillers in the composites, and thus strongly dependent on the design and processing of the nanocomposites. The ordinary materials of polymer matrix are polystyrene [145, 152], poly(methyl methacrylate), [116, 118, 143, 153] poly(2-vinyl pyridine), [132] polypropylene, [150, 154], nylon [78, 140] etc., while the common fillers include carbon nanotubes (e.g., single-walled carbon nanotubes), [148] inorganic (e.g., silica and metal) [116, 118, 138–140, 142–145, 147, 151, 155] or organic (e.g., carbon black) nanoparticles, [156] nanoplates (e.g., clay), [78, 153, 154, 157] and nanosheets (e.g., graphene) [158].

Closely related to the diverse aging rate of polymer nanocomposites, the time of approaching equilibrium does not show a universal trend. To reduce the aging effect

on material performance, i.e., decrease aging rate and shorten the time for reaching equilibrium, two major aspects need to be carefully investigated in composite design: (1) perturbed segmental dynamics in polymers in the proximity of the interfaces, and (2) interaction between the matrix and fillers [151].

A significant investigation of physical aging in polymer nanocomposites has recently been undertaken by Boucher, Cangialosi and coworkers. On PMMA/silica nanocomposites, [116, 118] one of the most common model systems, they monitored the isothermal aging response by DSC at various silica particle concentrations. Their results showed accelerated aging was correlated to the ratio of area/volume of silica particles in PMMA. Furthermore, they measured the time evolution of dielectric strength of the PMMA secondary relaxation process which dominates dielectric dynamics overall below T_g, for the same PMMA/silica composites used in DSC studies. The striking findings of invariance in PMMA dynamics, together with accelerated aging, posed questions on the role of molecular dynamics in the process of polymer aging. By keeping silica particles as nanofillers, Cangialosi and coworkers changed the hosting polymer matrix to polystyrene (PS) [159] and poly(vinyl acetate) (PVAc); [142] they monitored unvaried segmental dynamics from dielectric measurements, while physical aging still sped up in these two material systems. The results confirmed their observation on PMMA/silica nanocomposites. The conclusion on the decoupling of molecular mobility and out-of-equilibrium dynamics of polymers will certainly be further investigated to attain a better understanding of their mechanism, but these recent results demonstrated an acceleration of the aging process as well as the undisturbed segmental dynamics of the nanocomposite [117, 142, 160]. The results have been rationalized by the FVHD model [115]. That is, aging is driven by the diffusion of free volume and that this diffusion process is unrelated to segmental dynamics. Whether this claim is strictly valid is a matter of debate [161]. We note that the FVHD model has also been utilized to account for the suppression in T_g of PS/silica nanocomposites without invoking a change in segmental dynamics [162]. Via the FVHD model, T_g can be defined as the temperature at which the mean square displacement of free volume holes is equal to half of the equivalent thickness (s) of the sample in the experimental time scale, which is given as the inverse of the cooling rate (q). Thus, T_g can be defined as: [160]

$$(s/2)^2 = 4D(T_g)q^{-1} \tag{3.24}$$

In this regard, FVHD is able to account for the cooling rate- and confinement-dependence of T_g without any modification of segmental dynamics.

3.4.3 Nanoparticles

The exploration on the generality of nanoconfinement effects on glassy dynamics beyond thin films and nanocomposites could help obtain a more complete

understanding of confined polymer properties. From a practical viewpoint, polymers are widely used in a range of confinement geometries. As recently highlighted by Reiter and Napolitano, [163] thin films are inherently meta-stable with respect to polymer chain confirmations. That is, the formation of thin polymer films by typical means (i.e., spin coating) generates systems in which polymer chain conformations are different from the equilibrium melt. While interfaces are known to influence the properties of thin polymer films, how non-equilibrium chain conformations impact thin film properties remains to be elucidated. In addition, questions remain as to whether thin films prepared by spin coating may be equilibrated and residual stresses relaxed by thermal annealing or if other approaches to producing thin films with controlled polymer chain conformations may be developed. In this section, we review recent studies on physical aging and T_g of polymer nanoparticles, in which, the polymeric material is under 3-dimensional confinement. One advantage for studying confined polymer properties using nanoparticles, in addition to thin films, is that the former is processed in a very different manner. Hence, the polymer chain conformations within nanoparticles may be different from those of thin films. Nanoparticles suspended in solution may be annealed above T_g for prolonged periods of time for equilibration. A second advantage for studying polymer nanoparticles is that the surface area-to-volume ratio is much greater for nanoparticles than for thin films. Hence, the influence of interfaces on the properties of nanoparticles may be probed under conditions in which the extent of confinement is not extreme.

Although a few reports on structural relaxation of single-chain polymer nano-globules are available in the literature, [164–166] we have recently reported the first systematic investigation of the structural relaxation of polymer nanoparticles [167]. As the properties of glasses depend on the path to the glassy state, different environmental conditions and thermal histories during vitrification lead to glasses with different properties. Utilizing aqueous-suspended (soft confinement) and silica-capped (hard confinement) PS nanoparticles as model systems, we have been able to investigate the structural relaxation of confined glass formed under isobaric (constant pressure) and isochoric (constant volume) conditions from bare and core-shell nanoparticles, respectively [167].

In order to eliminate the effects of previous thermal histories, PS nanoparticles were first annealed at temperature $T_g + 20$ K for 20 min. Subsequently, samples were quenched to the desired aging temperature at a cooling rate of 40 K/min. Structural relaxation at various aging times (i.e., t_{aging}) was measured by DSC. Figure 3.12 depicts differential thermograms which show thermal peaks related to enthalpy recovery at $T_g - T_a = 8$ K for different aging times in bulk PS, and 200 nm diameter aqueous-suspended and silica-capped PS nanoparticles, where T_a is the aging temperature. The enthalpy peaks represent the recovery of energy relaxed during physical aging. Larger enthalpy peaks signify greater structural relaxation. In comparison to bulk PS, both PS nanoparticles samples exhibited a longer aging process toward equilibrium.

Figure 3.13 show aging isotherms in terms of $T_f - T_a$ for bulk PS and 200 nm diameter PS nanoparticle systems at different temperatures. The quantity $T_f - T_a$ is

Fig. 3.12 Apparent heat capacity curves as a function of physical aging time at $T_g - T_a = 8$ K for **a** bulk PS, **b** 200 nm bare PS nanoparticles and **c** 200 nm PS-silica core-shell (silica-capped) nanoparticles. Data are reproduced with permission from Ref. [167]
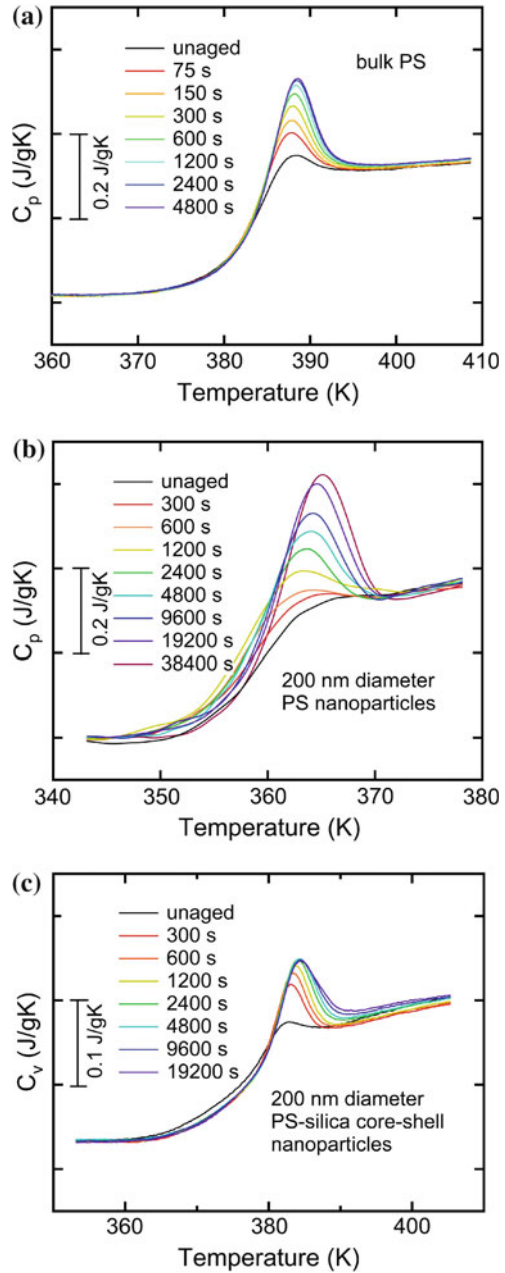
a measure of the departure from equilibrium, decreases with time, and by definition equals zero at equilibrium; where T_f, the fictive temperature, is a measure of the glass structure. For all systems, structural relaxation curves asymptotically

Fig. 3.13 Aging isotherms of **a** bulk PS, **b** 200 nm aqueous-suspended PS nanoparticles, and **c** 200 nm silica-capped PS nanoparticles aged at different quench depths ($T_g - T_a$). *Solid lines* are fits to the TNM model. Data are reproduced with permission from Ref. [167]
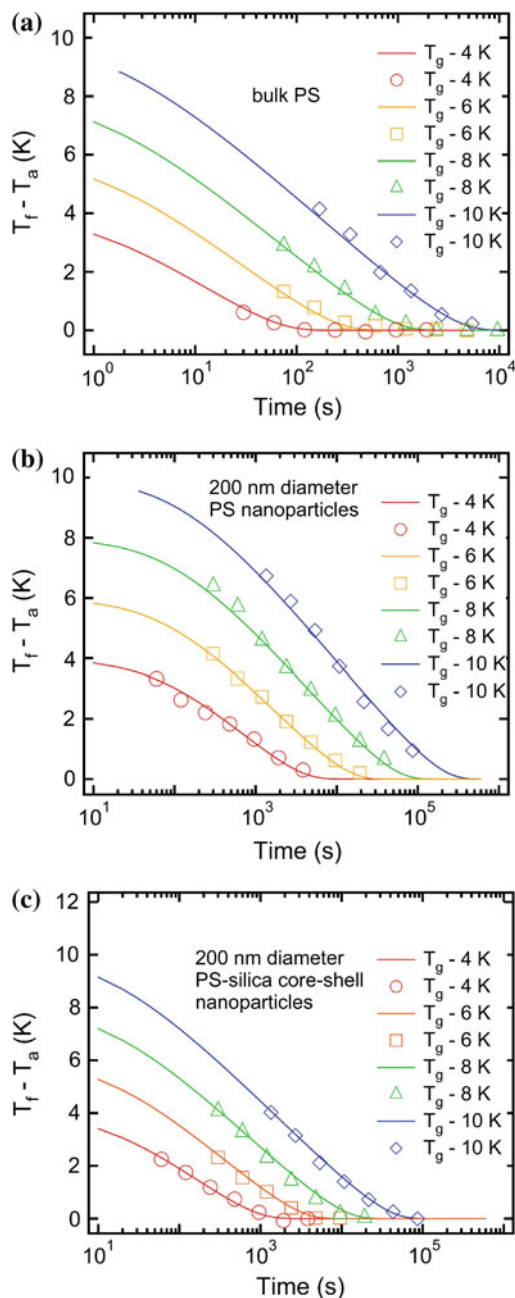
approached $T_f - T_a = 0$, which indicated the attainment or approach to equilibrium. Consistent with results from thin films and bulk behavior, decreasing T_a resulted in longer equilibration times. However, for the same value of $T_f - T_a$, the time

required for the attainment of equilibrium was longest for the bare nanoparticles while shortest for bulk PS.

Solid lines in Fig. 3.13 are fits to the TNM model. To model the structural relaxation behavior of polymer nanoparticles, the we utilized the relationship $T_f - T_a = \delta_h/\Delta C_p$ in the TNM model, where ΔC_p is the change in heat capacity at T_g, δ_h is the departure from equilibrium of enthalpy, analogous to δ in the KAHR model, as presented in the earlier section in this chapter. δ_h for enthalpy relaxation is given by:

$$\delta_h = \Delta H_{a,\infty} - \Delta H_a(t) = \delta_{h0} \exp\left[-\left(\int_0^t \frac{dt}{\tau} \right)^\beta \right] \tag{3.25}$$

where δ_h, is defined as the difference between the equilibrium enthalpy ($\Delta H_{a,\infty}$) and the instantaneous enthalpy of the glass (ΔH_a); as such, δ_{h0} is the initial enthalpy departure from equilibrium at the start of the aging process. The parameter τ is the characteristic relaxation time, and β is the non-exponential parameter related to the width of the relaxation time distribution. The relaxation time, which is dependent on temperature and structure, is approximated by:

$$\ln \tau = \ln A + \frac{x\Delta h}{RT} + \frac{(1-x)\Delta h}{RT_f} \tag{3.26}$$

where the parameter A is a material constant, x partitions the structure and temperature dependence on τ, and $\Delta h/R$ is the relative activation energy.

The model provided a good fit to the experimental data for bulk PS and aqueous-suspended PS nanoparticles. Activation energies for aqueous-suspended PS nanoparticles were slightly lower than those of bulk PS. The partition parameter, x, and stretched exponential parameter, β, were larger with soft confinement when compared to bulk PS at identical values of $T_g - T_a$. At early aging times, the initial plateau was predicted to be longer for aqueous suspended PS nanoparticles compared to bulk PS.

From the data presented in Fig. 3.13, the aging rate, which is determined as the slope of the linear portion of the aging isotherms given as $R = d(T_f - T_a)/d \log t_{aging}$ can be determined. In comparison to the bulk, the aging rate increased with confinement for aqueous-suspended nanoparticles. All things being equal, silica-capped PS nanoparticles exhibited reduced rates compared to the analogous bare nanoparticles. This result demonstrated that the path to the glassy state does have an impact on the physical aging dynamics of confined glass.

As mentioned above, Koh and Simon, [52] measured the structural relaxation of stacked freestanding PS thin films by DSC. Their study provided a good comparison to the results of bare PS nanoparticles, the case of isobaric aging. They found

that the time required to reach equilibrium increased with decreasing film thickness, and the physical aging rate did not show a systematic deviation from bulk. The two studies of bare PS nanoparticles and stacked PS thin films are in reasonable agreement. In both cases, nanoconfined polymers required a longer aging time to reach equilibrium. For comparison, Fig. 3.14 illustrates the time required for the attainment of equilibrium for PS nanoparticles and stacked PS thin films. We have previously argued that the apparent discrepancy of confinement effects on aging rates between nanoparticles and thin films may be resolved when the comparison is made via a characteristic length, i.e., the surface area-to-volume ratio; see Ref. [168] for more discussion. Similar to the T_g-confinement effect, the consistency in size-dependent aging rates of nanoparticles and thin films suggests a common origin of the aging-confinement effect, that is, interfacial effects, irrespective of the confining geometry, i.e., interfacial effects.

Fig. 3.14 The time required for the attainment of equilibrium during aging for **a** PS nanoparticles and bulk PS at different quench depths $(T_g - T_a)$, as reported from Ref. [167] and for **b** stacked PS thin films and the corresponding bulk polymer. Data in panel (**b**) are reproduced from Ref. with permission [52]
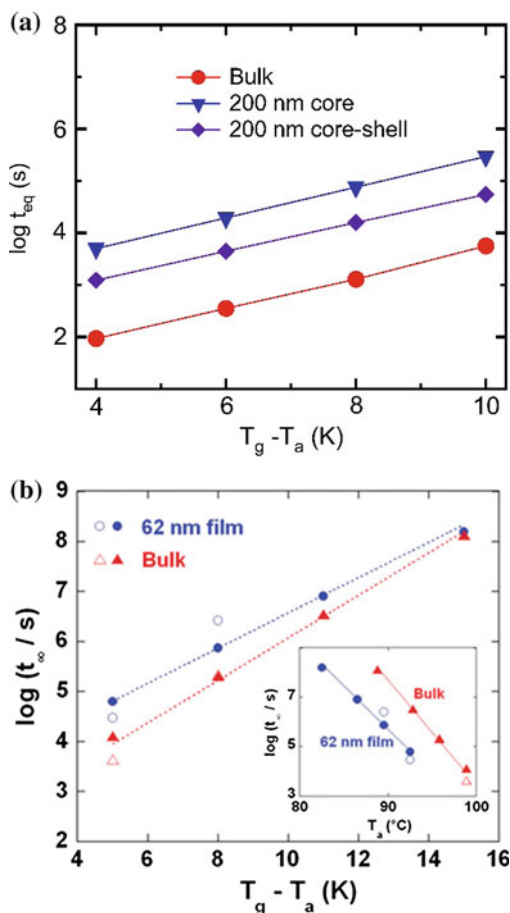
The extended influence of the quenching condition (freestanding geometry vs. substrate-supported geometry) on glassy-state structural relaxation was examined by Roth and coworkers [130]. They observed that thin (in micrometer scale) films quenched in the freestanding geometry exhibited a stronger aging-confinement effect and that these differences could be explained by thickness-dependent stresses introduced into the freestanding film during vitrification. We noted that silica-capped core-shell nanoparticles could be utilized as a model system to investigate the internal stress effects on physical aging. This is because the reaction temperature under which the silica shell is grown atop the nanoparticle sets the stress-free state of the 3-dimensionally confined polymer within the rigid shell. Due to the isochoric confinement condition of polymer nanoparticles encompassed in a rigid inorganic shell, temperature changes away from the reaction temperature will induce a significant internal pressure change. As such, the pressure under which the aging response is observed could be tuned by setting the difference between T_a and the reaction temperature.

3.4.4 Simulations

For better understanding the diverse relaxation behavior of confined polymers, researchers have utilized models or simulation tools to capture the kinetic features of the material at the molecular level, aiming to represent the results observed in experiments. The FVHD model, which has been widely employed in characterizing physical aging in bulk polymers, is reformulated to describe the relaxation behavior of polymers under nanoconfinement. A dual mechanism combines the effect of vacancy diffusion and lattice contraction, and was recently applied with time-dependent internal length scales to characterize the free volume reduction in the aging process [169]. The dual mechanism model (DMM) fits the data of thin film permeability fairly well. The potential predictive capability of the DMM model depends on the accuracy of the relationship between the internal length and time scale on the description of complex material dynamics [161].

The DMM was first proposed by Paul and coworkers [170] in order to predict the gas transport behavior of glassy polymers over their lifetimes, and to provide insight into mechanisms of the aging process. In the physical aging of thin polymer films, lattice contraction, which is independent of film thickness, describes a rapid decrease in free volume following a temperature quench, while the vacancy diffusion, which is thickness dependent, characterizes the free volume out of a membrane due to diffusion, and hence providing a rather accurate simulation of the self-retarding nature of the mode of aging. Together with reasonable assumptions, the DMM matches the experimental data remarkably well, showing its potential for further development [170, 171].

Although the DMM is applicable to describe the aging data of thin films, there are a few simulation studies that have demonstrated directly the validity of DMM from the molecular level. Hu and coworkers introduced the DMM into a Monte

Carlo (MC) simulation [161, 169]. As observed in many experiments, their results showed an accelerated structural relaxation process, occurring in thin polymer films. There are several key contributions from their work. First, the local average density of segments was shown to increase linearly with the logarithm of aging time. Second, the relaxation (aging) rate of ultrathin polymer films was shown to first increase and then decrease after passing through a peak. These two features are consistent with experimental results, and could be attributed to the competition of two mechanisms (segment mobility and accurate initial vacancy concentration) on the molecular level. Additionally, from the diffusion mechanism, their model provided direct evidence of the relationship between the sliding motion of short chain fragments and the structural relaxation of thin polymer films.

Besides the Monte Carlo method, polymer diffusion on surfaces is also simulated by molecular dynamic (MD) analysis [172, 173]. Mukherji and Müser [173] presented a generic model for a polymer adsorbed on a discrete surface. They examined the effect of surface roughness on the film diffusion and found that glassy dynamics is intimately linked to roughness, which is controlled by changing the interaction potential between surface atoms and adsorbed particles. The results qualitatively reproduce many experimental features, such as the power law aging of the diffusion constant with time and logarithmic aging of structure factor. The authors obtained an orientationally averaged and time-dependent static structure factor via an ensemble average over different initial microstructures, and could distinguish rather unambiguously whether a monomer belongs or does not belong to the first layer near substrate in their simulations. Interestingly, the results did not show any time-dependent behavior of the diffusion constant when the surface was smooth, even as adhesion and confinement were increased.

One should note that no chemical structures are involved in the simulation work above. As such, the validation of the simulated scenarios for specific materials need to be examined by further experiments. We briefly introduced several recent simulation works on physical aging of confined polymers. Considering the next chapter of this book will describe simulations on the structural relaxation of ultrathin polymer films, we keep this section concise. For further details, please refer to the next chapter.

3.5 Conclusions and Future Work

Although the physics of glass formation and the glassy state in confinement for polymers has been the subject of intense research for two decades, the research area remains rich in unexplained and unexplored phenomena. In this chapter, we highlighted the influence of confinement on the structural relaxation (physical aging) of polymer glasses. Both observations of acceleration and suppression in physical aging of polymers have been reported. Suppressions in physical aging rate have been attributed to interfacial effects, which perturb glassy dynamics. In the absence of interfacial effects, i.e., strong polymer substrate interactions, physical

aging is either accelerated or remains unchanged in comparison to the bulk. Location-specific measurements of the aging rate in the films support the argument that interfacial effects are important, i.e., perturbing the dynamics associated with physical aging. Of course, the nature of the molecular-scale interpretation of how interfaces influence aging dynamics and what controls the length scale of these effects remain intriguing questions. Other questions that arise from recent work include: What is the influence of process conditions on physical aging in confinement? Are more complex thermal histories, i.e., asymmetry of approach and memory effect, observed in confinement, and if so what can we learn from them? Can physical aging observed in thin films be used to predict the aging response in other confinement geometries? How much of the T_g-confinement effect, if any, can be used to account for the aging-confinement effect? From an engineering perspective, the major question is: How can confined aging be exploited to create materials with new properties?

References

1. Koros, W.J., Fleming, G.K.: Membrane-based gas separation. J. Membr. Sci. **83**, 1 (1993)
2. Mundra, M.K., Donthu, S.K., Dravid, V.P., Torkelson, J.M.: Effect of spatial confinement on the glass transition temperature of patterned polymer nanostructures. Nano Lett. **7**, 713 (2007)
3. Winey, K.I., Vaia, R.A.: Polymer nanocomposites. MRS Bull. **32**, 314 (2007)
4. Keddie, J.L., Jones, R.A.L., Cory, R.A.: Interface and surface effects on the glass transition temperature in thin polymer films. Faraday Discuss. **98**, 219 (1994)
5. Keddie, J.L., Jones, R.A.L., Cory, R.A.: Size-dependent depression of the glass transition temperature in polymer films. Europhysics **27**, 59 (1994)
6. Priestley, R.D.: Physical aging of confined glasses. Soft Matter **5**, 919 (2009)
7. Torres, J.M., Wang, C., Coughlin, E.B., Bishop, J.P., Register, R.A., Riggleman, R.A., Stafford, C.M., Vogt, B.D.: Influence of chain stiffness on thermal and mechanical properties of polymer thin films. Macromolecules **44**, 9040 (2011)
8. Stafford, C., Vogt, B.D., Harrison, C., Julthongpiput, D., Huang, R.: Elastic moduli of ultrathin amorphous polymer films. Macromolecules **39**, 5095 (2006)
9. Stafford, C.M., Roskov, K.E., Epps, I.T.H., Fasolka, M.J.: Generating thickness gradients of thin polymer films via flow coating. Rev. Sci. Instrum. **77**, 023908 (2006)
10. O'Connell, P.A., McKenna, G.B.: Rheological measurements of the thermoviscoelastic response of ulthathin polymer films. Science **307**, 1760 (2005)
11. Vanroy, B., Wubbenhorst, M., Napolitano, S.: Crystallization of thin polymer layers confined between two adsorbing walls. Acs Macro Lett. **2**, 168 (2013)
12. Napolitano, S., Wubbenhorst, M.: Slowing down of the crystallization kinetics in ultrathin polymer films: a size or an interface effect? Macromolecules **39**, 5967 (2006)

13. Elmahdy, M.M., Chrissopoulou, K., Afratis, A., Floudas, G., Anastasiadis, S.H.: Effect of confinement on polymer segmental motion and ion mobility in peo/layered silicate nanocomposites. Macromolecules **39**, 5170 (2006)
14. Fukao, K., Miyamoto, Y.: Glass transitions and dynamics in thin polymer films: dielectric relaxation of thin films of polystyrene. Phys. Rev. E **61**, 1743 (2000)
15. Fukao, K., Miyamoto, Y.: Glass transition temperature and dynamics of alpha-process in thin polymer films. Europhys. Lett. **46**, 649 (1999)
16. Hall, D.B., Hooker, J.C., Torkelson, J.M.: Ultrathin polymer films near the glass transition: effect on the distribution of alpha-relaxation times as measured by second harmonic generation. Macromolecules **30**, 667 (1997)
17. Forrest, J.A., Dalnoki-Veress, K., Stevens, J.R., Dutcher, J.R.: Effect of free surfaces on the glass transition temperature of thin polymer films. Phys. Rev. Lett. **77**, 2002 (1996)
18. Forrest, J.A., Dalnoki-Veress, K., Dutcher, J.R.: Interface and chain confinement effects on the glass transition temperature of thin polymer films. Phys. Rev. E **56**, 5705 (1997)
19. Sharp, J.S., Forrest, J.A.: Free surfaces cause reductions in the glass transition temperature of thin polystyrene films. Phys. Rev. Lett. **91**, 235701 (2003)
20. Rittigstein, P., Priestley, R.D., Broadbelt, L.J., Torkelson, J.M.: Model polymer nanocomposites provide an understanding of confinement effects in real nanocomposites. Nat. Mater. **6**, 278 (2007)
21. Ellison, C.J., Torkelson, J.M.: The distribution of glass transition temperatures in nanoscopically confined glass formers. Nat. Mater. **2**, 695 (2003)
22. Priestley, R.D., Mundra, M.K., Barnett, N., Broadbelt, L.J., Torkelson, J.M.: Effects of nanoscale confinement and interfaces on the glass transition of a series of poly (n-methyacrylate) films. Aust. J. Chem. **60**, 765 (2007)
23. Sasaki, T., Shimizu, A., Mourey, T.H., Thurau, C.T., Ediger, M.D.: Glass transition of small polystyrene spheres in aqueous suspensions. J. Chem. Phys. **119**, 8730 (2003)
24. Chen, R., Huang, D.: Preparation of polymer nanoparticles, and the effect of nanoconfinement on glass transition, structural relaxation and crystallization. Front. Chem. China **6**, 332 (2011)
25. Raegen, A., Massa, M., Forrest, J., Dalnoki-Veress, K.: Effect of atmosphere on reductions in the glass transition of thin polystyrene films. Eur. Phys. J. E **27**, 375 (2008)
26. Napolitano, S., Wubbenhorst, M.: The lifetime of the deviations from bulk behaviour in polymers confined at the nanoscale. Nat. Commun. **2**, 260 (2011)
27. Roth, C.B., Dutcher, J.R.: Glass transition temperature of freely-standing films of atactic poly (methyl methacrylate). Eur. Phys. J. E **12**, S103 (2003)
28. Priestley, R.D., Mundra, M.K., Barnett, N.J., Broadbelt, L.J., Torkelson, J.M.: Effects of nanoscale confinement and interfaces on the glass transition temperatures of a series of poly (n-methacrylate) films. Aust. J. Chem. **60**, 765 (2007)
29. Forrest, J.A., Dalnoki-Veress, K.: The glass transition in thin polymer films. Adv. Colloid Interface Sci. **94**, 167 (2001)
30. Alcoutlabi, M., McKenna, G.B.: Effects of confinement on material behaviour at the nanometre size scale. J. Phys. Condens. Matter **17**, R461 (2005)
31. Serghei, A.: Challenges in glassy dynamics of polymers. Macromol. Chem. Phys. **209**, 1415 (2008)
32. McKenna, G.B.: Ten (or more) years of dynamics in confinement: Perspectives for 2010. Eur. Phys. J. Spec. Top. **189**, 285 (2010)
33. Ngai, K.L., Rizos, A.K., Plazek, D.J.: Reduction of the glass temperature of thin freely standing polymer films caused by the decrease of the coupling parameter in the coupling model. J. Non-Cryst. Solids **235**, 435 (1998)
34. de Gennes, P.G.: Glass transitions in thin polymer films. Eur. Phys. J. E **2**, 201 (2000)
35. Long, D., Lequeux, F.: Heterogeneous dynamics at the glass transition in van der waals liquids, in the bulk and in thin films. Eur. Phys. J. E **4**, 371 (2001)

36. Napolitano, S., Capponi, S., Vanroy, B.: Glassy dynamics of soft matter under 1d confinement: How irreversible adsorption affects molecular packing, mobility gradients and orientational polarization in thin films. Eur. Phys. J. E **36**, 61 (2013)
37. Serghei, A., Huth, H., Schick, C., Kremer, F.: Glassy dynamics in thin polymer layers having a free upper interface. Macromolecules **41**, 3636 (2008)
38. Serghei, A., Tress, M., Kremer, F.: The glass transition of thin polymer films in relation to the interfacial dynamics. J. Chem. Phys. **131**, 154904 (2009)
39. Erber, M., Tress, M., Mapesa, E.U., Serghei, A., Eichhorn, K.J., Voit, B., Kremer, F.: Glassy dynamics and glass transition in thin polymer layers of pmma deposited on different substrates. Macromolecules **43**, 7729 (2010)
40. Tress, M., Erber, M., Mapesa, E.U., Huth, H., Muller, J., Serghei, A., Schick, C., Eichhorn, K.J., Volt, B., Kremer, F.: Glassy dynamics and glass transition in nanometric thin layers of polystyrene. Macromolecules **43**, 9937 (2010)
41. Struik, L.C.E.: Phsyical aging in amorphous polymers and other materials. Elsevier, Amsterdam (1978)
42. Pfromm, P.H., Koros, W.J.: Accelerated physical aging of thin glassy polymer films: Evidence from gas transport measurments. Polymer **36**, 2379 (1995)
43. Huang, Y., Paul, D.R.: Physical aging of thin glassy polymer films monitored by gas permeability. Polymer **45**, 8377 (2004)
44. Kawana, S., Jones, R.A.L.: Effect of physical ageing in thin glassy polymer films. Eur. Phys. J. E **10**, 223 (2003)
45. Priestley, R.D., Broadbelt, L.J., Torkelson, J.M.: Physical aging of ultrathin polymer films above and below the bulk glass transition temperature: effects of attractive vs neutral polymer-substrate interactions measured by fluorescence. Macromolecules **38**, 654 (2005)
46. Priestley, R.D., Ellison, C.J., Broadbelt, L.J., Torkelson, J.M.: Structural relaxation of polymer glasses at surfaces, interfaces, and in between. Science **309**, 456 (2005)
47. Rittigstein, P., Priestley, R.D., Broadbelt, L.J., Torkelson, J.M.: Model polymer nanocomposites provide understanding of confinement effects in real nanocomposites. Nat. Mater. **6**, 278 (2007)
48. Pye, J.E., Rohald, K.A., Baker, E.A., Roth, C.B.: Physical aging in ultrathin polystyrene films: Evidence of a gradient in dynamics at the free surface and its connection to the glass transition temperature reductions. Macromolecules **43**, 8296 (2010)
49. Wu, J., Huang, G., Wang, X., He, X., Lei, H.: Confinement effect of polystyrene on the relaxation behavior of polyisobutylene. J. Polym. Sci. B: Polym. Phys. **48**, 2165 (2010)
50. Zhou, C., Chung, T.-S., Wang, R., Goh, S.H.: A governing equation for physical aging of thick and thin fluoropolyimide films. J. Appl. Polym. Sci. **92**, 1758 (2004)
51. Cangialosi, D., Boucher, V.M., Alegria, A., Colmenero, J.: Physical aging in polymers and polymer nanocomposites: Recent results and open questions. Soft Matter **9**, 8619 (2013)
52. Koh, Y.P., Simon, S.L.: Structural relaxation of stacked ultrathin polystyrene films. J. Polym. Sci. Part B Polym. Phys. **46**, 2714 (2008)
53. Angell, C.A.: Formation of glasses from liquids and biopolymers. Science **267**, 1924 (1995)
54. McKenna, G.B.: Glass formation and glassy behavior. In: Booth, C., Price C. (ed.) Comprehensive Polymer Science. Polymer properties, vol. 2, p. 311. Pergamon, Oxford (1989)
55. Debenedetti, P.G., Stillinger, F.H.: Supercooled liquids and the glass transition. Nature **410**, 259 (2001)
56. Ediger, M.D.: Spatially heterogeneous dynamics in supercooled liquids. Annu. Rev. Phys. Chem. **51**, 99 (2000)
57. Kohlrausch, R.: Theorie des elektrischen ruckstandes in der leidener flasche. Annu. Phys. Chem. **91**, 179 (1874)
58. Williams, G., Watts, D.C.: Non-symmetrical dielectric relaxation behavior arising from a simple empirical decay function. Trans. Faraday Soc. **66**, 80 (1970)
59. Ngai, K.L., Capaccioli, S.: On the relevance of the coupling model to experiments. J. Phys. Condens. Matter **19**, 205114 (2007)

60. Dhinojwala, A., Wong, G.K., Torkelson, J.M.: Rotational reorientation dynamics of nonlinear optical chromophores in rubbery and glassy polymers: A-relaxation dynamics probed by second harmonic generation and dielectric relaxation. Macromolecules **26**, 5943 (1993)

61. Dhinojwala, A., Wong, G.K., Torkelson, J.M.: Rotational reorientation dynamics of disperse red 1 in polystyrene: A-relaxation dynamics probed by second harmonic generation and dielectric relaxation. J. Chem. Phys. **100**, 6046 (1994)

62. Thurau, C.T., Ediger, M.D.: Influence of spatially heterogeneous dynamics on physical aging of polystyrene. J. Chem. Phys. **116**, 9089 (2002)

63. Thurau, C.T., Ediger, M.D.: Spatially heterogeneous dynamics during phsyical aging far below the glass transition temperature. J. Polym. Sci. Part B Polym. Phys. **40**, 2463 (2002)

64. Vogel, H.: Das temperatur-abhangigkeitsgesetz der viskositat von flussigkeiten. Phys. Unserer Zeit **22**, 645 (1921)

65. Tammann, G., Hesse, W.: Die abhangigkeit der viskositat von der temperatur bei unterkuhlten flussigkeiten. Z. Anorg. Allg. Chem. **156**, 245 (1926)

66. Fulcher, G.S.: Analysis of recent measurements of the viscosity of glasses. J. Am. Ceram. Soc. **8**, 339 (1925)

67. Williams, M.L., Landel, R.F., Ferry, J.D.: The temperature dependence of relaxation mechanisms in amorphous polymers and other glass-forming liquids. J. Am. Chem. Soc. **77**, 1471 (1955)

68. Tant, M.R., Wilkes, G.L.: An overview of the nonequilibrium behavior of polymer glasses. Polym. Eng. Sci. **21**, 874 (1981)

69. Doolittle, A.K.: Studies in newtonian flow. Ii. The dependence of the viscosity of liquids on free-space. J. Appl. Phys. **22**, 1471 (1951)

70. Kovacs, A.J.: Transition vitreuse dans les polymeres amorphes. Etude phenomenologique. In Fortschritte der hochpolymeren-forschung, p. 394 (1963)

71. McKenna, G.B.: Glassy states: Concentration glasses and temperature glasses compared. J. Non-Cryst. Solids **353**, 3820 (2007)

72. Guo, Y., Bradshaw, R.D.: Isothermal physical aging characterization of polyether-ether-ketone (peek) and polyphenylene sulfide (pps) films by creep and stress relaxation. Mech. Time-Depend. Mater. **11**, 61 (2007)

73. Guo, Y., Bradshaw, R.D.: Long-term creep of polyphenylene sulfide (pps) subjected to complex thermal histories: The effects of nonisothermal physical aging. Polymer **50**, 4048 (2009)

74. Guo, Y., Wang, N., Bradshaw, R.D., Brinson, L.C.: Modeling mechanical aging shift factors in glassy polymers during nonisothermal physical aging. I. Experiments and kahr-a_{te} model prediction. J. Polym. Sci. Part B Polym. Phys. **47**, 340 (2009)

75. Kohlrausch, F.: Ueber die elastiche nachwirkung bei der torsion. Poogendorff's Annalen der Physik und Chemie **119**, 337 (1863)

76. McKenna G.B., Simon, S.L.: The glass transition: Its measurement and underlying physics. In: Cheng S.Z.D. (ed.) Handbook of thermal analysis and calorimetry. 2002, Elsevier Science

77. Bernazzani, P., Simon, S.L.: Volume recovery of polystyrene: Evolution of the characteristic relaxation time. J. Non-Cryst. Solids **307–310**, 470 (2002)

78. Pramoda, K.P., Liu, T.: Effect of moisture on the dynamic mechanical relaxation of polyamide-6/clay nanocomposites. J. Polym. Sci. Part B Polym. Phys. **42**, 1823 (2004)

79. Putz, K.W., Palmeri, M.J., Cohn, R.B., Andrews, R., Brinson, L.C.: Effect of cross-link density on interphase creation in polymer nanocomposites. Macromolecules **41**, 6752 (2008)

80. Sobieski, J.W., Simon, S.L., Plazek, D.J.: Dilatometric studies of physical aging of polyetherimide. J. Therm. Anal. **49**, 455 (1997)

81. Srebnik, S.: Physical association of polymers with nanotubes. J. Polym. Sci. Part B Polym. Phys. **46**, 2711 (2008)

82. Svoboda, R., Pustkova, P., Malek, J.: Structural relaxation of polyvinyl acetate (pvac). Polymer **49**, 3176 (2008)

83. Zheng, Y., McKenna, G.B.: Structural recovery in a model epoxy: Comparison of responses after temperature and relative humidity jumps. Macromolecules **36**, 2387 (2003)

84. Papakonstantopoulos, G.J., Yoshimoto, K., Doxastakis, M., Nealey, P.F., de Pablo, J.J.: Local mechanical properties of polymeric nanocomposites. Phys. Rev. E **72**, 031801 (2005)

85. Di, X., Win, K.Z., McKenna, G.B., Narita, T., Lequeux, F., Pullela, S.R., Cheng, Z.: Signatures of structural recovery in colloidal glasses. Phys. Rev. Lett. **106**, 095701 (2011)

86. Rendell, R.W., Ngai, K.L.: Evidence for anomalous structural relaxation in SiO_2 films. Appl. Phys. Lett. **57**, 2428 (1990)

87. Svoboda, R., Pustkova, P., Malek, J.: Relaxation behavior of glassy selenium. J. Phys. Chem. Solids **68**, 850 (2007)

88. Badrinarayanan, P., Zheng, W., Li, Q., Simon, S.L.: The glass transition versus the fictive temperature. J. Non-Crystal. Solids **353**, 2603 (2007)

89. McKenna, G.B., Leterrier, Y., Schultheisz, C.R.: The evolution of material properties during physical aging. Polym. Eng. Sci. **35**, 403 (1995)

90. Schultheisz, C.R., McKenna, G.B., Leterrier, Y., Stefanis, E.: A comparison of structure and aging time shift factors from simultaneous volume and mechanical measurements. In: Proceedings of 1995 SEM Spring Conference on Experimental Mechanics (1995)

91. Simon, S.L., Plazek, D.J., Sobieski, J.W., McGregor, E.T.: Physical aging of a polyetherimide: Volume recovery and its comparison to creep and enthalpy measurements. J. Polym. Sci. Part B Polym. Phys. **35**, 929 (1997)

92. Simon, S.L., Sobieski, J.W., Plazek, D.J.: Volume and enthalpy recovery of polystyrene. Polymer **42**, 2555 (2001)

93. Alcoutlabi, M., Briatico-Vangosa, F., McKenna, G.B.: Effect of chemical activity jumps on the viscoelastic behavior of an epoxy resin: Physical aging response in carbon dioxide pressure jumps. J. Polym. Sci. Part B Polym. Phys. **40**, 2050 (2002)

94. Meng, Y., Simon, S.L.: Pressure relaxation of polystyrene and its comparison to the shear response. J. Polym. Sci. Part B Polym. Phys. **45**, 3375 (2007)

95. Zheng, Y., Priestley, R.D., McKenna, G.B.: Physical aging of an epoxy subsequent to relative humidity jumps through the glass concentration. J. Polym. Sci. Part B Polym. Phys. **42**, 2107 (2004)

96. Moynihan, C.T., Macedo, P.B., Montrose, C.J., Gupta, P.K., Debolt, M.A., Dill, J.F., Dom, B.E., Drake, P.W., Easteal, A.J., Elterman, P.B., Moeller, R.P., Sasabe, H., Wilder, J.A.: Structural relaxation in vitreous materials. Ann. N. Y. Acad. Sci. **279**, 15 (1976)

97. Narayanaswamy, O.S.: Model of structural relaxation in glass. J. Am. Ceram. Soc. **54**, 491 (1971)

98. Tool, A.Q.: Relation between inelastic deformability and thermal expansion of glass in its annealing range. J. Am. Ceram. Soc. **29**, 240 (1946)

99. Kovacs, A.J., Aklonis, J.J., Hutchinson, J.M., Ramos, A.R.: Isobaric volume and enthalpy recovery of glasses. 2. A transparent multiparameter theory. J. Polym. Sci. Polym. Phys. Ed. **17**, 1097 (1979)

100. Ramos, A.R., Hutchinson, J.M., Kovacs, A.J.: Isobaric thermal behavior of glasses during uniform cooling and heating. 3. Predictions from the multiparameter kahr model. J. Polym. Sci. Polym. Phys. Ed. **22**, 1655 (1984)

101. Robertson, R.E.: Effect of free volume fluctuations on polymer relaxation in the glass state 2. Calculated results. J. Polym. Sci. Polym. Phys. Ed. **17**, 597 (1979)

102. Robertson, R.E.: Free-volume theory and its application to polymer relaxation in the glass state. In: Bicerano, J. (ed.) Computational modeling of polymers. Marcel Dekker Inc, New York (1992)

103. Moynihan, C.T., Crichton, S.N., Opalka, S.M.: Linear and non-linear structural relaxation. J. Non-Cryst. Solids **131**, 420 (1991)

104. Ngai, K.L.: Short-time and long-time relaxation dynamics of glass-forming substances: A coupling model perspective. J. Phys. Condens. Matter **12**, 6437 (2000)

105. Ngai, K.L.: An extended coupling model description of the evolution of dynamics with time in supercooled liquids and ionic conductors. J. Phys. Condens. Matter **15**, S1107 (2003)

106. Rendell, R.W., Ngai, K.L.: Coupling model interpretation of dielectric relaxation of poly (vinyl acetate) near tg. J. Chem. Phys. **87**, 2359 (1987)
107. Rendell, R.W., Ngai, K.L., Fong, C.R.: Volume recovery near the glass transition temperature in poly(vinyl acetate): predictions of a coupling model. Macromolecules **20**, 1070 (1987)
108. Robertson, R.E., Simha, R., Curro, J.G.: Free-volume and the kinetics of aging of polymer glasses. Macromolecules **17**, 911 (1984)
109. McKenna, G.B., Simon, S.L.: Time dependent volume and enthalpy responses in polymers. In: Sun, R.A.S.A.C.T. (ed.) Time dependent and nonlinear effects in polymers and composites, astm stp 1357, p. 18. American Society for Testing and Materials: West Conshohocken, PA (2000)
110. Bradshaw, R.D.: Characterization and modeling of viscoelastic composite laminates with nonisothermal physical aging, in Mechanical Engineering. Northwestern University, Evanston (1997)
111. Struik, L.C.E.: Dependence of relaxation times of glassy polymers on their specific volume. Polymer **29**, 1347 (1988)
112. Press, W.H., Teukolsky, S.A., Vetterling, W.T., Flannery, B.P.: Numerical recipes in c: the art of scientific computing. Cambridge University Press, Cambridge (1992)
113. Cangialosi, D., Schut, H., Veen, A.V., Picken, S.J.: Positron annihilation lifetime spectroscopy for measuring free volume during physical aging of polycarbonate. Macromolecules **36**, 142 (2003)
114. Victor, J.G., Torkelson, J.M.: Photochromic and fluorescent probe studies in glassy polymer matrices. 3. Effects of physical aging and molar weight on the size distribution of local free volume in polystyrene. Macromolecules **21**, 3490 (1988)
115. Curro, J.G., Lagasse, R.R., Simha, R.: Diffusion model for volume recovery in glasses. Macromolecules **15**, 1621 (1982)
116. Boucher, V.M., Cangialosi, D., Alegria, A., Colmenero, J.: Enthalpy recovery of pmma/silica nanocomposites. Macromolecules **43**, 7594 (2010)
117. Boucher, V.M., Cangialosi, D., Alegria, A., Colmenero, J.: Enthalpy recovery in nanometer to micrometer thin ps films. Macromolecules **45**, 5296 (2012)
118. Boucher, V.M., Cangialosi, D., Alegria, A., Colmenero, J., Gonzalez-Irun, J., Liz-Marzan, L. M.: Accelerated physical aging in pmma/silica nanocomposites. Soft Matter **6**, 3306 (2010)
119. Boucher, V.M., Cangialosi, D., Alegria, A., Colmenero, J.: Accounting for the thickness dependence of the tg in supported ps films via the volume holes diffusion model. Thermochim. Acta **575**, 233 (2014)
120. Ellison, C.J., Kim, S.D., Hall, D.B., Torkelson, J.M.: Confinement and processing effects on glass transition temperature and phsyical aging in ultrathin polymer films: Novel fluorescence measurements. Eur. Phys. J. E **8**, 155 (2002)
121. Royal, J.S., Torkelson, J.M.: Monitoring the molecular scale effects of physical aging in polymer glasses with fluorescence probes. Macromolecules **23**, 3536 (1990)
122. Koh, Y.P., McKenna, G.B., Simon, S.L.: Calorimetric glass transition temperature and absolute heat capacity of polystyrene ultrathin films. J. Polym. Sci. Part B Polym. Phys. **44**, 3518 (2006)
123. Baker, E.A., Rittigstein, P., Torkelson, J.M., Roth, C.B.: Streamlined ellipsometry procedure for characterizing physical aging rates of thin polymer films. J. Polym. Sci. Part B Polym. Phys. **47**, 2509 (2009)
124. Frieberg, B., Glynos, E., Green, P.F.: Structural relaxation of thin polymer films. Phys. Rev. Lett. **108**, 268304 (2012)
125. Huang, Y., Paul, D.R.: Physical aging of thin glassy polymer films monitored by optical properties. Macromolecules **39**, 1554 (2006)
126. Huang, Y., Paul, D.R.: Effect of temperature of physical aging of thin glassy polymer films. Macromolecules **38**, 10148 (2005)

127. Dorkenoo, K.D., Pfromm, P.H.: Experimental evidence and theoretical analysis of physical aging in thin and thick amorphous glassy polymer films. J. Polym. Sci. Part B Polym. Phys. **37**, 2239 (1999)
128. Rowe, B.W., Freeman, B.D., Paul, D.R.: Physical aging of ultrathin glassy polymer films tracked by gas permeability. Polymer **50**, 5565 (2009)
129. Dorkenoo, K., Pfromm, P.H.: Accelerated physical aging of thin poly[1-(trimethylsilyl)-1-propyne] films. Macromolecules **33**, 3747 (2000)
130. Gray, L.A.G., Yoon, S.W., Pahner, W.A., Davidheiser, J.E., Roth, C.B.: Importance of quench conditions on the subsequent physical aging rate of glassy polymer films. Macromolecules **45**, 1701 (2012)
131. Pye, J.E., Roth, C.B.: Physical aging of polymer films quenched and measured free-standing via ellipsometry: Controlling stress imparted by thermal expansion mismatch between film and support. Macromolecules **46**, 9455 (2013)
132. Rittigstein, P., Torkelson, J.M.: Polymer-nanoparticle interfacial interactions in polymer nanocomposites: Confinement effects on the glass transition temperature and suppression of physical aging. J. Polym. Sci. Part B Polym. Phys. **44**, 2935 (2006)
133. Priestley, R.D., Rittigstein, P., Broadbelt, L.J., Fukao, K., Torkelson, J.M.: Evidence for the molecular-scale origin of the suppression of physical ageing in confined polymer: Fluorescence and dielectric spectroscopy studies of polymer-silica nanocomposites. J. Phys. Condens. Matter **19**, 205120 (2007)
134. Murphy, T.M., Langhe, D.S., Ponting, M., Baer, E., Freeman, B.D., Paul, D.R.: Physical aging of layered glassy polymer films via permeability tracking. Polymer **52**, 6117 (2011)
135. Murphy, T.M., Langhe, D.S., Ponting, M., Baer, E., Freeman, B.D., Paul, D.R.: Enthalpy recovery and structural relaxation in layered glassy polymer films. Polymer **53**, 4002 (2012)
136. Langhe, D.S., Murphy, T.M., Shaver, A., LaPorte, C., Freeman, B.D., Paul, D.R., Baer, E.: Structural relaxation of polystyrene in nanolayer confinement. Polymer **52**, 1925 (2012)
137. Rauscher, P.M., Pye, J.E., Baglay, R.R., Roth, C.B.: Effect of adjacent rubbery layers on the physical aging of glassy polymers. Macromolecules **46**, 9806 (2013)
138. Lu, H., Nutt, S.: Restricted relaxation in polymer nanocomposites near the glass transition. Macromolecules **36**, 4010 (2003)
139. Lu, H., Nutt, S.: Enthalpy relaxation of layered silicate-epoxy nanocomposites. Macromol. Chem. Phys. **204**, 1832 (2003)
140. Vlasveld, D.P.N., Bersee, H.E.N., Picken, S.J.: Creep and physical aging behavior of pa6 nanocomposites. Polymer **46**, 12539 (2005)
141. Bian, Y., Pejanovic, S., Kenny, J., Mijovic, J.: Dynamics of multifunctional polyhedral oligomeric silsesquioxane/poly(propylene oxide) nanocomposites as studied by dielectric relaxation spectroscopy and dynamic mechanical spectroscopy. Macromolecules **40** (2007)
142. Boucher, V.M., Cangialosi, D., Alegria, A., Colmenero, J.: Time dependence of the segmental relaxation time of poly(vinyl acetate)-silica nanocomposites. Phys. Rev. E **86**, 041501 (2012)
143. Boucher, V.M., Cangialosi, D., Alegria, A., Colmenero, J., Gonzalez-Irun, J., Liz-Marzan, L.M.: Physical aging in pmma/silica nanocomposites: Enthalpy and dielectric relaxation. J. Non-crystalline Solids **35** (2011)
144. Cangialosi, D., Boucher, V.M., Alegria, A., Colmenero, J.: Enhanced physical aging of polymer nanocomposites: the key role of the area to volume ratio. Polymer **53**, 1362 (2012)
145. Lin, Y., Liu, L., Cheng, J., Shangguan, Y., Yu, W., Qiu, B., Zheng, Q.: Segmental dynamics and physical aging of polystyrene/silver nanocomposites. RSC Adv. **4**, 20086 (2014)
146. Greco, A., Esposito-Corcione, C., Cavallo, A., Maffezzoli, A.: Structural relaxation of amorphous pet matrix nanocomposites. AIP Conf. Proc. **1255**, 395 (2010)
147. Amanuel, S., Gaudette, A.N., Sternstein, S.S.: Enthalpic relaxation of silica-polyvinyl acetate nanocomposites. J. Polym. Sci. B Polym. Phys. **46**, 2733 (2008)
148. Flory, A.L., Ramanathan, T., Brinson, L.C.: Physical aging of single wall carbon nanotube polymer nanocomposites: effect of functionalization of the nanotube on the enthalpy relaxation. Macromolecules **43**, 4247 (2010)

149. Liu, A.Y.H., Rottler, J.: Physical aging and structural relaxation in polymer nanocomposites. J. Polym. Sci. B Polym. Phys. **47**, 1789 (2009)
150. Wang, K., Liang, S., Deng, J., Yang, H., Zhang, Q., Fu, Q., Dong, X., Wang, D., Han, C.C.: The role of clay network on macromolecular chain mobility and relaxation in isotactic polypropylene/organoclay nanocomposites. Polymer **47**, 7131 (2006)
151. Cangialosi, D., Boucher, V.M., Alegria, A., Colmenero, J.: Physical aging in polymers and polymer nanocomposites: recent results and open questions. Soft Matter **9**, 8619 (2013)
152. Sohn, J.-I., Lee, C.H., Lim, S.T., Kim, T.H., Choi, H.J., Jhon, M.S.: Viscoelasticity and relaxation characteristics of polystyrene/clay nanocomposites. J. Mater. Sci. **38**, 1849 (2003)
153. Wang, Y., Chen, W.-C.: Dielectric probing of relaxation behaviors in pmma/organoclay nanocomposites: effect of organic modification, composite interfaces. Compos. Interfaces **17**, 803 (2010)
154. Wang, Y., Huang, S.-W.: Solution intercalation and relaxation properties of maleated polypropylene/organoclay nanocomposites. Polym Plast. Technol. Eng. **46**, 1039 (2007)
155. Cangialosi, D., Wubbenhorst, M., Groenewold, J., Mendes, E., Schut, H., van Veen, A., Picken, S.J.: Physical aging of polycarbonate far below the glass transition temperature: Evidence for the diffusion mechanism. Phys. Rev. B **70**, 224213 (2004)
156. Yurekli, K., Krishnamoorti, R., Tse, M.F., McElrath, K.O., Tsou, A.H., Wang, H.-C.: Structure and dynamics of carbon black-filled elastomers. J. Polym. Sci. B Polym. Phys. **39**, 256 (2001)
157. Chong, S.-H., Aichele, M., Meyer, H., Fuchs, M., Baschnagel, J.: Structural and conformational dynamics of supercooled polymer melts: Insights from first-principles theory and simulations. Phys. Rev. E **76**, 051806 (2007)
158. Ramanathan, T., Abdala, A.A., Stankovich, S., Dikin, D.A., Herrera-Alonso, M., Piner, R.D., Adamson, D.H., Schniepp, H.C., Chen, X., Ruoff, R.S., Nguyen, S.T., Aksay, I.A., Prudhomme, R.K., Brinson, L.C.: Functionalized graphene sheets for polymer nanocomposites. Nat. Mater. **3**, 327 (2008)
159. Cangialosi, D., Boucher, V.M., Alegria, A., Colmenero, J.: Volume recovery of polystyrene/silica nanocomposites. J. Polym. Sci. Part B Polym. Phys. **51**, 847 (2013)
160. Boucher, V.M., Cangialosi, D., Alegria, A., Colmenero, J., Pastoriza-Santos, I., Liz-Marzan, L.M.: Physical aging of polystyrene/gold nanocomposites and its relation to the calorimetric t_g depression. Soft Matter **7**, 3607 (2011)
161. Tang, Q., Hu, W., Napolitano, S.: Slowing down of accelerated structural relaxation in ultrathin polymer films. Phys. Rev. Lett. **112**, 148306 (2014)
162. Boucher, V.M., Cangialosi, D., Yin, H., Schonhals, A., Alegria, A., Colmenero, J.: Tg depression and invariant segmental dynamics in polystyrene thin films. Soft Matter **8**, 5119 (2012)
163. Reiter, G., Napolitano, S.: Possible origin of thickness-dependent deviations from bulk properties of thin polymer films. J. Polym. Sci. B Polym. Phys. **48**, 2544 (2010)
164. Li, L., Li, B., Chen, J., Zhou, D., Xue, G., Liu, X.: Glass transition and structural relaxation of nano-particle aggregates of atactic poly(methyl methacrylate) formed in microemulsions. Polymer **45**, 2813 (2004)
165. Mi, Y., Xue, G., Wang, X.: Glass transition of nano-sized single chain globules. Polymer **43**, 6701 (2002)
166. Sing, C.E., Einert, T.R., Netz, R.R., Alexander-Katz, A.: Probing structural and dynamics transitions in polymer globules by force. Phys. Rev. E **83**, 040801 (2011)
167. Guo, Y., Zhang, C., Lai, C., Priestley, R.D., D'Acunzi, M., Fytas, G.: Structural relaxation of polymer nanospheres under soft and hard confinement: Isobaric versus isochoric conditions. ACS Nano **5**, 5365 (2011)
168. Zhang, C., Guo, Y., Priestley, R.D.: Glass transition temperature of polymer nanoparticles under soft and hard confinement. Macromolecules **44**, 4001 (2011)
169. Tang, Q., Hu, W.: Molecular simulation of structural relaxation in ultrathin polymer films. Phys. Chem. Chem. Phys. **15**, 20679 (2013)

170. McCaig, M.S., Paul, D.R., Barlow, J.W.: Effect of film thickness on the changes in gas permeability of a glassy polyarylate due to physical aging. Polymer **41**, 639 (2000)
171. Thornton, A.W., Hill, A.J.: Vacancy diffusion with time-dependent length scale: an insightful new model for physical aging in polymers. Ind. Eng. Chem. Res. **49**, 12119 (2010)
172. Curgul, S., Van Vliet, K.J., Rutledge, G.C.: Molecular dynamics simulation of size-dependent structural and thermal properties of polymer nanofibers. Macromolecules **40**, 8483 (2007)
173. Mukherji, D., Muser, M.H.: Glassy dynamics, aging in mobility, and structural relaxation of strongly adsorbed polymer films: Corrugation or confinement? Macromolecules **40**, 1754 (2007)
174. Kim, J.H., Jang, J., Zin, W.C.: Estimation of the thickness dependence of the glass transition temperature in various thin polymer films. Langmuir **16**, 4064 (2000)

Chapter 4
Understanding Physical Aging in Ultrathin Polymer Films via Molecular Simulations

Qiyun Tang and Wenbing Hu

Abstract Physical aging in glassy polymer films has attracted much attention in the past two decades due to its strong correlation with the lifetime of polymer-based nano-devices. However, understanding the physical aging from the simulation point of view is still a big challenge due to the huge differences between the simulation and experimental time scales (microseconds vs. hours, days, and even years). Recently, we made a survey on the free volume diffusion and annihilation (FVDA) model as employed in dynamic Monte Carlo simulations to study the volume contraction of ultrathin polymer films. In this chapter, based on our recently developed simulation route, we discuss in what sense the simulation results could be applied to understand the physical aging in experiments. Some new insights, such as the slowing down of accelerated aging at extremely small thickness, and the existence of new confinement length scale in ultrathin polymer films based on the inversed free volume diffusion process, are also discussed.

4.1 Introduction

It has been shown nearly 80 years ago that amorphous solids are not in thermodynamic equilibrium state at temperatures below the glass transition temperature [1]. The specific volume of these glassy materials usually experiences a very slow contraction to approach equilibrium, which is also called "physical aging" [2–6]. By measuring more than 40 materials, Struik et al. systematically investigated the aging behaviors and provided some general features of the aging phenomena [2]. One of the basic features is that the aging is found in all glasses, such as polymers,

Q. Tang (✉) · W. Hu (✉)
State Key Laboratory of Coordination Chemistry, School of Chemistry
and Chemical Engineering, Nanjing University, 210093 Nanjing, China
e-mail: tqy553new@gmail.com

W. Hu
e-mail: wbhu@nju.edu.cn

monomers, organic, or inorganic materials, and the aging behaves in a similar way in all glassy materials. This non-equilibrium aging process results in volume contraction of glassy materials, leading to significant changes of mechanical, optical, and electrical properties at macroscopic time scales [3–5].

The study of physical aging in thin polymer films could date back to early 1990s when experiments demonstrated strongly time-dependent gas-transport properties in thin glassy polymer-ceramic composite films [7–16]. Factors such as collapse of underlying porous scaffold [8] and solvent loss [10] were soon excluded, concluding that the physical aging of glassy films played a vital role. The main methods employed to study the aging behavior of thin films were the gas permeation measurements, which were valid for high free volume polymers, such as polynorbornene [11], polyimide [10, 14, 16], polysulfone (PSF) [10, 14, 15], polyphenylene oxide (PPO) [14, 16], poly-1-trimethylsilyl-1-propyne (PTMSP) [12], and bisphenol-A benzophenone-dicarboxylic acid (BPA-BnzDCA) [13]. However, polymers with low free volume content such as poly(methyl methacrylate) (PMMA) [17], polystyrene (PS) [18], polyetherimide [19], and poly(isobutyl methacrylate) (PiBMA) [20], the gas permeability properties showed minor changes upon aging. For example, Baker et al. [17] used oxygen permeation methods to study the aging behavior of free-standing PMMA films ranging from 800 um to 190 nm but no change of permeability was observed. In this case, other methods such as ellipsometry [17, 21–24] and fluorescence [18, 25–31] measurements were employed to overcome this limitation. These procedures usually require substrates to support the sample, leading to enormous investigations of physical aging in supported polymer films. The main observable obtained in these experiments is the physical aging rate, which is obtained from the specific volume-time curve at particular aging temperatures. As aging temperature decreases further below the glass transition temperature, the aging rate increases first, and then decreases after passing through a maximum. This trend was observed both in bulk polymers [32] and thin films [23]. As film thickness decreases, the physical aging rate of thin polymer films usually increases, indicating a well-known accelerated aging behavior [14, 33]. These diversity aging behaviors emerged in free-standing and supported thin polymer films are of great importance in practical applications due to its strong correlation with the lifetime and performance of polymer-based nano-devices.

Due to the universality in all glasses, physical aging can be theoretically explained in a straightforward way based on the free-volume concept. As proposed by Struik, "This is the basic and rather obvious idea that the transport mobility of particles in a closely packed system is primarily determined by the degree of packing of the system or by its inverse measure, viz. the free volume" [2]. The idea could date back to 1943 when Alfrey et al. proposed that the isothermal aging below T_g can be attributed to the diffusion of free volume holes from the interior of polymers into the surface [34]. This free volume diffusion model (FVDM) was developed by Curro et al. [35] to quantitatively analyze the volume relaxation experiments of poly(vinyl acetate) [36, 37]. The motion of free volume holes can be described by a diffusion equation:

$$\frac{\partial f}{\partial t} = \nabla \cdot (D\nabla f) \tag{4.1}$$

where D is the diffusion coefficient for free volume holes. This model was shown to semiquantitatively match the major phenomena observed for the aging of poly (vinyl acetate) [36]. In 2000, McCaig et al. extended this model by employing the lattice contraction mechanism to explain the observed gas permeation experiments of thin polymer films ranging from 0.25−33 um [13, 38]. Results demonstrated that the lattice contraction dominated the aging for thicker films ($l > 2.5$ um), while for thinner films ($l < 2.5$ um), aging was primarily determined by free volume diffusion process. Cangialosi et al. postulated that the glassy polymers contained low-density regions where free volume holes could diffuse to and annihilate, and the incorporation of this internal annihilation into free volume diffusion model was shown to successfully explain the aging behaviors observed in positron annihilation lifetime spectroscopy [39]. The free volume diffusion model provides an obvious and intuitive way to understand the physical aging. However, modern theory demonstrates that dynamical heterogeneity emerges during the glass transition [40], indicating that the diffusion of free volume holes in glassy state might also show dynamical heterogeneity, that is, some free volumes diffuse faster and others move slower. Recent experiments confirmed the existence of two physical aging processes in bulk glassy polymers at a extremely long time [41]. These new progresses in experiments and theories cannot be explained by conventional free volume diffusion model. This model, in fact, cannot provide the information at the molecular level to understand physical aging. In this case, computer simulation would play a vital role.

In the past two decades, some computer simulations were already performed to investigate physical aging in polymers [42–51]. For example, Andrejew et al. showed the physical aging of a bond-fluctuation model glass occurring on all length scales of a polymer, which could be expressed by a time-temperature superposition principle for the aging time [42]. Molecular dynamics simulations were used to study the effect of physical aging on the mechanical properties of a model polymer glass [45, 46], the impact of nanoparticles on physical aging of polymer nanocomposite [47], the isothermal volume relaxation behavior of atactic polystyrene [49], and the effect of stringlike cooperative motions on the physical aging of coarse-grained polymer glass [51]. Although these simulations showed some interesting aspects of the aging behaviors in polymers, it is still a big challenge to directly apply the simulation results in understanding the real experimental aging behaviors, especially the variation of aging rate to temperatures and film thickness. The main challenge is the huge difference between the simulation and experimental time scales. As is well known, the physical aging in real experiments usually lasts to macroscopic time scales, such as hours, days, and even years. However, the typical simulation time scales are within microseconds (for coarse-grain models) [52], which is far smaller than that in the real experiments. In what sense could the molecular simulation be applied in understanding the physical aging in experiments? Could some new

insights of physical aging be extracted from the molecular simulations to guide the experiments? In this chapter, we try to discuss these issues.

The reminder of the chapter is organized as follows. In the next section, we set up a lattice model of free-standing ultrathin polymer film, and then add a free volume diffusion and annihilation mechanism into Monte Carlo simulation to study the physical aging in ultrathin polymer films. In Sect. 4.3, the feasibility of our model in understanding the physical aging is discussed, followed by the influence of temperature and film thickness on the aging rate of ultrathin films. Especially, some new insights, such as the slowing down of accelerated aging at extremely small thickness, and the existence of new confinement length scale at the nanoscale are extracted and discussed from the simulation results. Finally, we summarize our results in Sect. 4.4 with an outlook for future investigations.

4.2 Model and Simulation Details

4.2.1 Model of Free-Standing Ultrathin Polymer Films

Here we use the lattice model to simulate the coexisting situations of polymer chains and free volumes (represented by vacancy sites) [53], to generate the free-standing ultrathin polymer films. We consider n polymer chains with each polymer consecutively occupying N lattice sites (N is the polymer chain length). The vacancies occupy N_v lattice sites, resulting in the volume of the film: $V = nN + N_v$. Our simulation is performed on a cuboid lattice with its size of $80 \times 80 \times (H + 20)$, where H is the pure thickness (the thickness where all the segments in polymer films are close-packed on the lattice) of the ultrathin films. The motion of polymer chains is generated through a microrelaxation model [53] which allows each segment to change its position with neighboring vacancies or air sites, accompanied by the sliding motions between two "kink" segments along the counter of chain molecules if necessary. This procedure is similar to the theoretical consideration of the jumping and sliding motions proposed by de Gennes to explain the anomalous drop down of glass transition temperature in free-standing polymer films [54, 55]. Conventional Metropolis sampling algorithm was employed in each microrelaxation step with the potential energy change

$$
\begin{aligned}
\frac{\Delta E}{k_B T} &= \frac{a E_{ss} + b B_{sv} + c E_c + d B_{sa}}{k_B T} \\
&= \left(a \frac{E_{ss}}{E_c} + b \frac{B_{sv}}{E_c} + c + d \frac{B_{sa}}{E_c} \right) \frac{E_c}{k_B T}
\end{aligned}
\tag{4.2}
$$

where E_{ss} represents the non-bonded nearest-neighbor segment-segment interaction. B_{sv} and B_{sa} are the mixing energies between *segments*−vacancies and *segments*−air molecules. The factors a, b, and d are the total number of
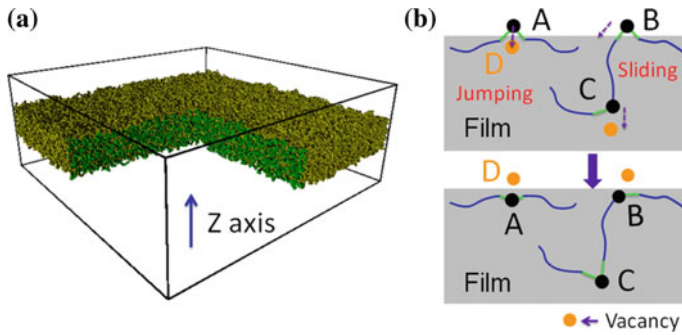
Fig. 4.1 **a** Snapshot of free-standing ultrathin polymer film at thickness $H = 8$. **b** Illustration of free volume annihilation process caused by the jumping and sliding motions of segments. The figures are reprinted from [62]

corresponding contact pairs. E_c is the bending energy for two adjacent bonds connected along the chain and c is the net number of non-collinear-connected bond pairs. The reduced temperature $T' = k_B T / E_c$ is introduced in our simulation, where k_B is the Boltzmann constant and T is the temperature. In the following we use T instead of T' to represent this reduced temperature. The unit of time evolution is defined as one Monte Carlo step (MCS), including the number of trial moves equal to the number of segments in the sample system.

Quenching polymer films to lower temperatures usually generates some "excess" free volumes [2, 3, 5, 56]. In our simulation, these "excess" free volumes are modeled by the vacancy sites. Thus the vacancies can be occupied by segments without changing potential energy, that is $B_{sv}/E_c = 0$. To obtain the free-standing ultrathin films, we apply periodic conditions in the X and Y directions and set the cohesive non-bonded segment-segment interaction $E_{ss}/E_c = -1.0$. The interaction between polymer segments and air sites is set to be $B_{sa}/E_c = 1.0$. This repulsive interaction will separate the segments and air sites from each other and generate two phase separated interfaces to stabilize the ultrathin polymer films, which is similar to previously reported free surfaces in polymer solutions [57]. Figure 4.1a shows the morphology of a free-standing ultrathin polymer film with thickness $H = 8$, where we can clearly find two flat free-standing surfaces located at Z axis.

4.2.2 Free Volume Diffusion and Annihilation (FVDA) Model

As discussed before, the typical aging behavior of glassy materials is the extremely slow volume relaxation process towards equilibrium. In ultrathin polymer films with thickness smaller than 600 nm, it has been previously demonstrated that the free volume diffusion mechanism dominates the aging behavior [13]. Here, we apply the idea of free volume diffusion into Monte Carlo simulation to study the physical aging

in ultrathin polymer films. The basic procedure is shown in Fig. 4.1b. At the interior of ultrathin films, the success trial moves of chain segments are mainly obtained by the interchange of positions between vacancies and segments, this trial move also gives rise to the diffusion of vacancies into new positions. For example, successful jumping move of segment A in Fig. 4.1b interchanges its position with vacancy D, leading to the diffusion of vacancy D into new position. When this process happens inside the films, the vacancies are diffused throughout the whole films. While the process occurs at the free surface, see Fig. 4.1b, the vacancy D diffuses outside the film, and then it will be occupied by the high-mobile air molecules immediately. In our simulation, this process is defined as free volume annihilation [13, 34, 35]. The sliding motion along chain contour direction can also diffuse and annihilate the vacancies, or the free volume holes, see the illustration in Fig. 4.1b. This irreversible free volume annihilation process gradually decreases the volume of the total film, and eventually gives rise to the volume contraction of ultrathin polymer films, which mimics the physical aging in experiments.

Compared to the conventional free volume diffusion theory [13, 34, 35], our simulation route takes the following advantages. First, the diffusion of the vacancies, or the free volume holes, is obtained by the interchange of positions with segments. Thus the diffusion of free volume, and eventually the physical aging, would be directly connected to the motions of segments at the molecular level, which overcomes the limitation of traditional free volume diffusion theory. Second, the direct connection of free volume diffusion and segment motions makes it possible to study the influence of different segmental motion modes on the physical aging in ultrathin polymer films. For example, the sliding motion of chain molecules, which was proposed by de Gennes in 2000 to explain the anomalous dropping down of T_g in free standing polymer films [54], is included in our simulation to investigate its influence on physical aging, and it effectively perturbs the aging rate at extremely small thickness. Third, the outlined simulation route could be easily extended to study the influence of chain architectures on the physical aging in polymer films [23, 24]. In the following section, based on the FVDA model, we discuss the influence of temperature, thickness, and even the sliding motion of chain molecules on the physical aging in ultrathin polymer films, trying to provide an understanding of physical aging from the simulation point of view.

4.3 Results and Discussion

4.3.1 Feasibility of the Model in Understanding Physical Aging

In this section, we provide the volume relaxation results of ultrathin polymer films based on the FVDA model, and discuss the feasibility of simulation results in understanding the physical aging in experiments. The system is constructed by $n = 160$ polymer chains with each chain length of $N = 400$. We initialize the film

at $T = 7.6$ with vacancy concentration $\phi_v = N_v/(nN + N_v) = 0.05$, and then quench the system into $T = 5.0$ and set the volume of the film at this time as $V(0)(= nN + N_v(0))$. As time proceeds, the vacancies gradually annihilate from the two free surfaces of the film due to the motion of segments, resulting in the non-linear decrease of film volume: $V(t) = nN + N_v(t)$ (see Fig. 4.2a). However, in Fig. 4.2a we can identify a linear relaxation region of reduced volume as a function of the logarithm of time. The red line in Fig. 4.2a gives the best fit of this region with a slope of -0.035. During this regime, due to the annihilation of vacancies from the two free surfaces, the film gradually becomes denser. The average density of segments in the middle region and that near the surface layers also increase and decrease linearly with the logarithm of time, see Fig. 4.2b, c, which identifies the shrink and densification of the ultrathin polymer films. This densification behavior can be monitored in experiments by the fluorescence measurements of mobility-sensitive chromophores-labeled films [18, 29] and the intensity measurements of dielectric strength [31]. From the aspect of qualitative comparison between simulation and experiments, we can say that our simulation based on the FVDA model could indeed reproduce the volume evolution of physical aging reported in experiments for glassy polymer thin films [17, 18, 22–24, 29, 31].
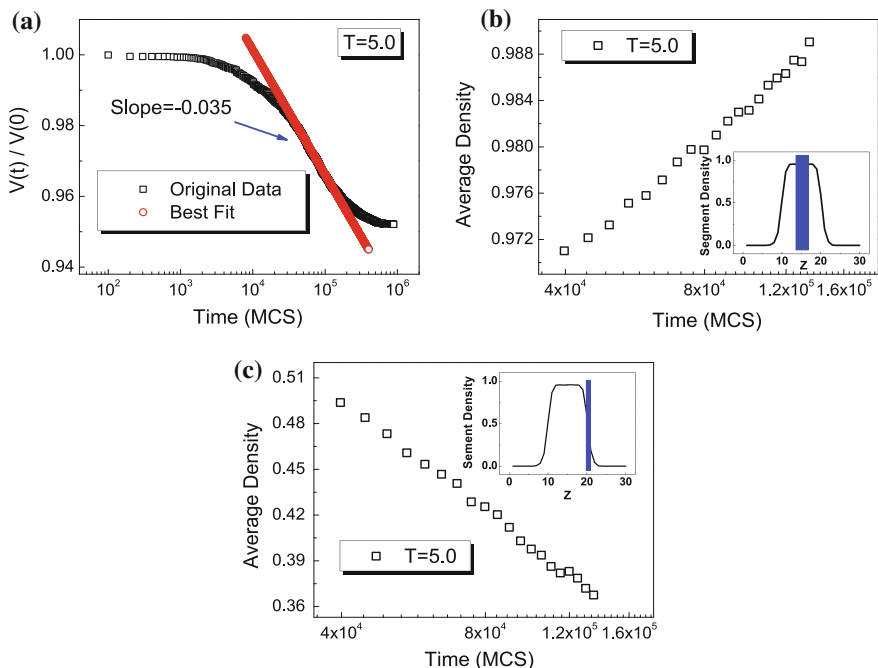
Fig. 4.2 **a** Variation of reduced volume $V(t)/V(0)$ of ultrathin polymer film as a function of time at $T = 5.0$. The *red line* of slope -0.035 is the best fit within the linear aging region. Time-evolution of average density in the middle and surface layers (see indicators in *inset*) are shown in (**b**) and (**c**). The figures are replotted from [61]

However, when we try to understand the physical aging based on our simulation results, we encounter a big challenge due to the existence of the huge timescale differences between the simulations and experiments. For example, the simulation timescales of linear relaxation region shown in Fig. 4.2a are within 10^4–10^5 MCSs. Each MC step in our coarse-grain model is nearly equal to 10^{-11} s [52], thus the linear relaxation time region is within 10^{-7}–10^{-6} s. On the other hand, the typical physical aging phenomena in most experiments are often last to macroscopic time scales, such as hours, days, or even weeks [5]. This long-term aging process could not be directly compared with our simulation results due to the huge differences of the time-scales. In the next, we discuss how to rationalize our simulations in understanding the physical aging in experiments.

As is well known, when polymers are cooled down from the melt to the glassy states, the relaxation time at different temperatures obeys the WLF empirical relationship [58]:

$$\log a_T = -\frac{C_1(T - T_g)}{C_2 + T - T_g} \tag{4.3}$$

where $C_1 = 17.44$, $C_2 = 51.6$, and T_g is the glass transition temperature. In our simulation, the reduced temperature, for example $T' = k_B T/E_c = 5.0$, can be transformed into the real temperature, $T = 5.0 * E_c/k_B$, with E_c the energy difference between the *gauche* and *trans* states along polymer chains. Here we choose polyethylene as an example to provide a rough estimation of the relaxation time at simulation temperature T (other polymers will lead to similar results). For polyethylene, the energy difference E_c takes the value of about 0.5 kJ/mol [59], resulting in the real temperature $T = 5.0 E_c/k_B \simeq 300$ K. The glass transition temperature for polyethylene is $T_g = 193$ K [60]. Thus we have $\log a_T \simeq -11.8$, indicating that the real relaxation time at T_g is about 10^{11} times larger than that at simulation time $T = 5.0$. As discussed before, the linear relaxation region in our simulations (see Fig. 4.2a) is within 10^{-7}–10^{-6} s. Multiplied by a factor of 10^{11}, the simulation time could correspond to the real time-range of 10^4–10^5 s, about 2.8–27.8 h, at glass transition temperature. For the aging temperature T, which is far lower than T_g, the corresponding linear aging time could even last longer. The outlined estimation is rather rough, but qualitatively suggests that the short relaxation timescales in the simulation could be reasonably related to the long timescales of the aging process observed in many experiments.

Strictly speaking, the volume contraction in our simulation actually refers to a structural relaxation process at high temperatures. However, the striking consistency between our simulation and aging experiments (see discussions above and further results in the next sections) indicates that the volume contraction of ultrathin films observed here can be employed to understand the physical aging behaviors described in many experiments. To keep the discussion more smoothly, in the following we also use the term of physical aging when referring to our simulation results.

4.3.2 Temperature Dependence of Aging Rate

In this section, we discuss the variation of aging rate as a function of temperature in our simulation. The physical aging rate can be calculated by [17, 29, 61, 62]:

$$\beta = -\frac{1}{V_0}\frac{dV(t)}{d\log t} = -\frac{d(V(t)/V_0)}{d\log t} \tag{4.4}$$

where V_0 is the volume at the reference time $t = 0$, and the aging rate is directly related to the slope of linear relaxation region in Fig. 4.2a. Figure 4.3a shows the aging rate β when the films are quenched to different temperatures from two distinct initial vacancy concentrations, ϕ_{v0}. As decreasing the temperature, the aging rate increases first and then declines after passing through a maximum, which is consistent with the experimental physical aging rates observed in glassy thin films [17, 22–24]. In Fig. 4.3a, we can also find that the aging rates at high $\phi_{v0} = 0.05$ are larger than that at lower $\phi_{v0} = 0.025$. Interestingly, these two curves could approach one master curve by normalizing the aging rate with the corresponding ϕ_{v0}, see Fig. 4.3b, indicating that the initial vacancy concentration has little effects on the response of aging rate to external stimuli, such as temperature. This conclusion is of great importance in practical applications due to the fact that the experimental preparation of ultrathin polymer films usually generates distinct ϕ_{v0} at different thickness. In this case, experimental aging rate should be normalized by the measured ϕ_{v0} and then can be employed to compare with each other.

The emergence of a peak in the variation of β as a function of T indicates the existence of two competing mechanisms that contribute distinctly to the aging rate of ultrathin films. Experimentally, this peak was attributed to the two intuitive mechanisms: one is the molecular mobility at aging temperature T_a, and the other is the deviation of aging temperature to the glass transition temperature $\Delta T = T_g - T_a$. As the aging temperature T_a decreases, the movement of molecules in polymers becomes slower, giving rise to the decrease of aging rate. However,
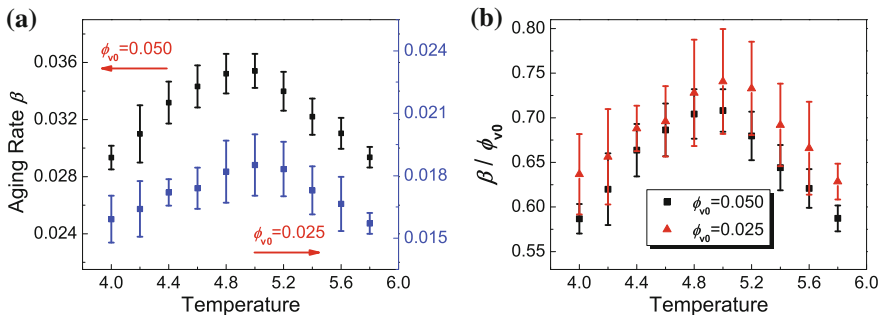
Fig. 4.3 **a** Temperature dependence aging rate β at different initial vacancy concentrations $\phi_{v0} = 0.05$ and $\phi_{v0} = 0.025$. **b** Normalized aging rate β/ϕ_{v0} as a function of temperature. The figures are reprinted from [61]

when the system is quenched to a lower temperature, the vibration of molecules becomes weaker and generates more free volumes in the polymers. This increase of free volume eventually makes the physical aging process faster. These two mechanisms compete with each other, leading to the emergence of the peak of aging rate upon decreasing temperature. Although these understandings are very insightful, the explanations are still qualitative. In the next, based on our simulation results, we provide some quantitative discussion of these two mechanisms at the molecular level.

First we provide a quantitative description of the motion of segments in ultrathin films. The instantaneous segment mobility in our simulation can be defined as [61, 63, 64]:

$$\alpha(t) = 1 - \sum_{i=1}^{n}\sum_{j=1}^{N}\delta[\boldsymbol{r}_{ij}(t) - \boldsymbol{r}_{ij}(t - \Delta t)]/N_{total} \tag{4.5}$$

where $\boldsymbol{r}_{ij}(t)$ represents the position of segment j in the i-th chain at the t-th MC step ($\Delta t = 1$ MC step) and N_{total} is the total number of segments. Figure 4.4a shows the variation of $\alpha(t)$ as a function of time. At the beginning, the vacancy concentration at different T takes the same value of 0.05, leading to nearly the same segment mobilities in ultrathin films. However, as t is larger than 300,000 MC steps, the $\alpha(t)$ approaches a stable value where the contribution of vacancy concentration to the segmental mobility can be ignored. In this case, the segment mobility is mainly determined by the temperature, and we average the instantaneous segment mobility from 400,000 to 500,000 MC steps to label the average segment mobility α at each aging temperature, which was shown in Fig. 4.4b. One can find that the average segment mobility in ultrathin films decreases as lowering the temperature, which slows down the vacancy diffusion and annihilation processes and eventually decreases the physical aging rate in ultrathin films.

The emergency of peak in Fig. 4.3 indicates that another factor similar to the deviation of $\Delta T = T_g - T_a$ should exist in our simulation. To identify this factor, let's go back to the volume reduction curve of Fig. 4.2a, where one can find that the system starts the linear aging process after an initial volume relaxation plateau. The intersection point of the initial plateau and linear aging region defines an accurate vacancy concentration ϕ_{vi} (see inset in Fig. 4.4c). ϕ_{vi}, in fact, determines the aging rate during the linear volume reduction region in ultrathin polymer films. Figure 4.4b depicts ϕ_{vi} as a function of aging temperatures, where ϕ_{vi} increases upon decreasing the temperature. This increase can be attributed to the slower volume contraction process within the initial plateau at lower temperatures. This explanation could be compared with the qualitative description of the deviations of temperatures $\Delta T = T_g - T_a$ in experiments [17, 22–24, 31]. In summary, decreasing temperatures will increase the accurate vacancy concentration ϕ_{vi}, and enhance the aging rate of ultrathin films. Competing with the decrease of aging rate caused by the decline of segment mobility, the aging rate of ultrathin polymer films eventually shows a peak when lowering the aging temperature.
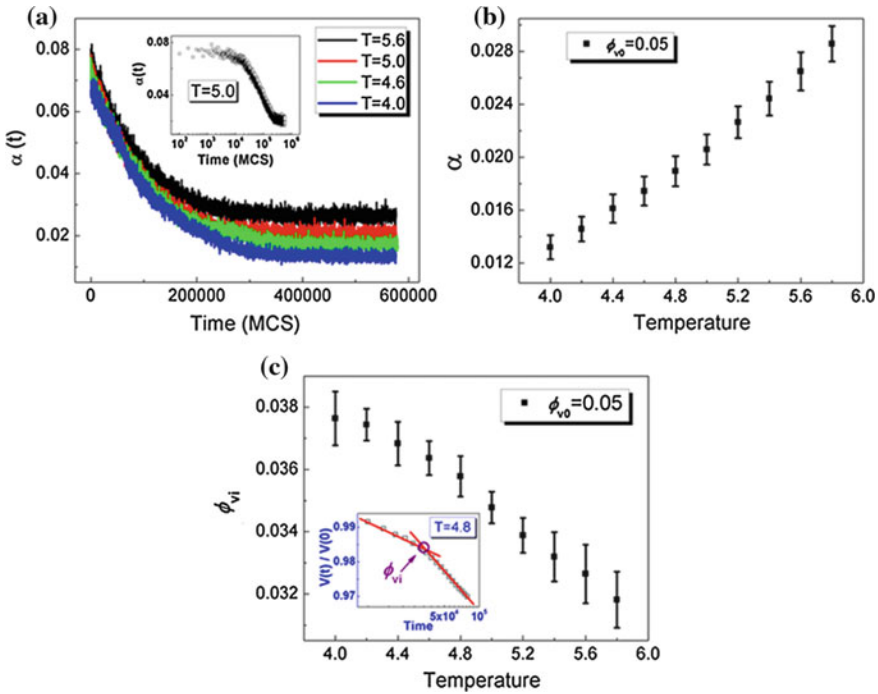
Fig. 4.4 **a** Time evolution of instantaneous segment mobility $\alpha(t)$ in ultrathin films. *Inset* shows the variation of $\alpha(t)$ as a function of time at $T = 5.0$. **b** Temperature dependence average segment mobility α. **c** Variation of the accurate initial vacancy concentration ϕ_{vi} as a function of temperature. *Inset* illustrates the intersection point that defines the ϕ_{vi}. These figures are replotted from [61]

Here we demonstrate that incorporation of FVDA model into Monte Carlo simulation can generate an interesting response of aging rate to temperatures, which is similar to that observed in experiments. Moreover, we provide a quantitative discussion at the molecular level to explain the emergence of a maximum in aging rate upon decreasing temperature. In the next section, we study further the response of physical aging rate to film thickness, and discuss the new insights observed from our simulation route.

4.3.3 Thickness Dependent of Aging Rate: Anomalous Slowing Down of Accelerated Aging

With the development of modern technology, the size of polymer-based devices gradually approaches nanoscale. In this case, the lifetime of the device's functionality and performance is highly related to lifetime of confined polymer layers,

giving rise to the continuous research focus on the physical aging of confined polymer films in the last decades [2, 4–6, 41]. Recently, several experiments demonstrated that, upon reduction of film thickness, the physical aging of polymer films was gradually accelerated [10, 12–14, 29, 33, 39, 65, 66]. For example, Huang et al. performed the gas permeability measurements of the three glassy polymers, polysulfone, polyimide, and poly(2,6-dimethyl-1,4-phenylene oxide), at 35 °C for over 200 days. Results showed that as film thickness decreased from 62 to 400 nm, the decline of gas permeability displayed a pronounced steeper decrease for thinner films, implying a clear accelerated physical aging phenomenon [14]. Recently, differential scanning calorimetry measurements of enthalpy recovery of free-standing polystyrene films showed an acceleration of physical aging process when film thickness lowered from 6 µm towards 29 nm [33]. The occurrence of these phenomena reduces the lifetime of polymer-based nano-devices, and eventually limits its potential applications [6].

In this section, we employ previously described simulation route to investigate in detail the influence of film thickness on the physical aging of ultrathin polymer films [62]. Surprisingly, we find that the acceleration in physical aging of thin polymer films could be strongly reduced at extremely small thicknesses. Especially, the onset thickness of the slowing down of accelerated aging shifts to lower values in the case of low molecular-weight films. We analyze the simulation data in detail and eventually demonstrate that these anomalous phenomena can be attributed to the occurrence of an inversed free volume diffusion process caused by the sliding motion [54, 55, 67] of short chain fragments. More interestingly, the average length of the sliding motion defines a critical film thickness, which confirms the existence of a new confinement length scale in ultrathin polymer films.

4.3.3.1 Slowing Down of Accelerated Aging

Here we provide the simulation results of the thickness-dependent aging rate in free-standing ultrathin polymer films. Figure 4.5a shows the variation of aging rate at reduced temperature $T = 4.8$ in films with chain length of $N = 400$ and the initial free volume concentration $\phi_{v0} = 0.05$. Each point was obtained by averaging the aging rates from six independent simulations. We can find that as the film thickness decreases towards $H = 9$, the aging rate gradually increases, consistently with the acceleration of aging reported in experiments [14, 33]. Remarkably, upon further reduction of the thickness, such as at $H = 6$, the aging rate drops down. At the best of our knowledge, there is no evidence from experiments or simulations showing a slowing down of the acceleration in physical aging in free-standing ultrathin polymer films. To explore the universality of this phenomenon, we evaluated the thickness-dependence of aging rates in ultrathin films with two other chain lengths, $N = 100$ and 5, shown in Fig. 4.5b, c respectively. For $N = 100$, the drop in $\beta(H)$ is still present and onsets at nearly the same thickness $H = 6$, while for $N = 5$, the onset thickness shifts to lower value of $H = 5$. This anomalous slowing down of accelerated aging indicates that the polymer films at extremely
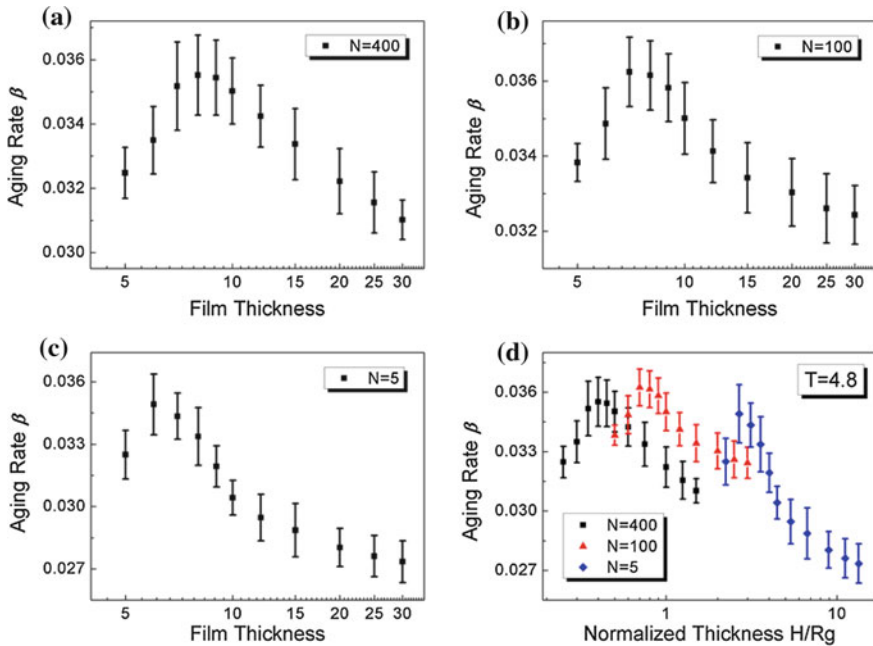
Fig. 4.5 Thickness dependence of aging rate β in ultrathin polymer films with chain length of **a** N = 400, **b** N = 100, and **c** N = 5 and aging temperature of T = 4.8. **d** Variation of aging rate as a function of normalized thickness H/R_g. The figures are reprinted from [62]

small thickness could have an unexpected longer lifetime, which would be of great significance in the design of polymer-based nano-devices.

Exploring the origin of this slowing down would not only be of practical importance, but also be useful for our understanding of new physics in polymer science. The slight shift of onset thickness at distinct chain lengths indicates, in fact, that the anomalous behavior strongly depends on the feature size of chain molecules. As a first attempt, we normalized the film thickness by the radius of gyration (R_g) of random coil. It is shown in Fig. 4.5d that the three curves could not be normalized towards one master curve. This indicates that the size of polymer chain does not represent the critical thickness that could account for the slowing down of accelerated aging. In the next, we provide an analysis of this phenomenon permitting to identify an appropriate molecular length scale to explain the abnormal aging behavior in ultrathin polymer films.

4.3.3.2 Inversed Free Volume Diffusion Mechanism

Before explaining the anomalous phenomena at the molecular level, let's go back to the relationship between the free volume diffusion and annihilation model and the non-equilibrium volume contraction behaviors. Due to the non-reversible free

volume annihilation occurring at the two free surfaces [61, 62], the vacancy holes inside polymer films normally tend to diffuse from the core towards the two surface regions. This diffusion eventually determines the aging rate of polymer films. However, the slowing down of accelerated aging indicates, in fact, that another mechanism that impedes the irreversible free volume diffusion and annihilation process should exist at the extremely small film thickness. To identify this mechanism, we count the number of free volume holes diffused back and forth between the lower and upper surface regions, $N_{IFVD}(t, \Delta t)$ with $\Delta t = 10$ MCS, and calculate the diffusion rate of this inversed motion [62]:

$$\gamma(t) = \frac{N_{IFVD}(t, \Delta t)}{N_f(t)} \tag{4.6}$$

where $N_f(t)$ is the number of free volume holes at time t. Figure 4.6a, b show the time-evolution of $\gamma(t)$ for ultrathin polymer films at distinct thickness. It is depicted in Fig. 4.6a that as time proceeds, $\gamma(t)$ at thickness $H = 6$ shows three stages, similar to the evolutionary behavior of reduced volume illustrated in Fig. 4.1b.
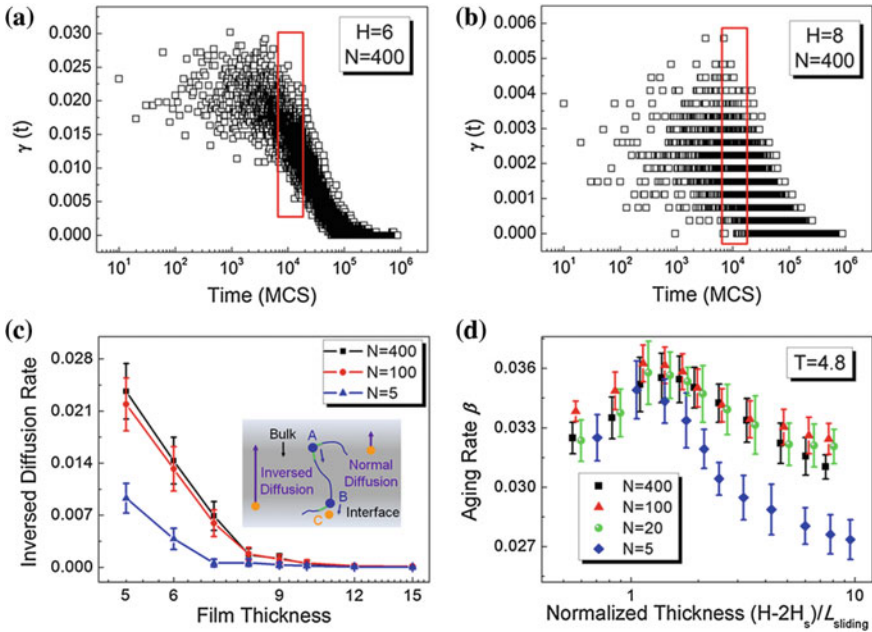
Fig. 4.6 Time evolution of inversed free volume diffusion rate $\gamma(t)$ for ultrathin polymer films at thickness **a** $H = 6$, and **b** $H = 8$. *Red box* depicts the area where Γ is calculated. **c** Thickness dependence of inversed diffusion rate Γ in ultrathin films at distinct chain length. *Inset* illustrates the IFVD process caused by the sliding motion along chain molecules. **d** Variation of aging rate as a function of normalized film thickness $(H - 2H_s)/L_{sliding}$, β for $N = 20$ are calculated for comparison. The figures are reprinted from [62]

Interestingly, $\gamma(t)$ at the early stage of aging fluctuates around different values at distinct thickness. In Fig. 4.6a of $H = 6$, $\gamma(t)$ is nearly 0.02, while for $H = 8$, $\gamma(t)$ stays around 0.002, an order of magnitude smaller than that in Fig. 4.6a. This indicates that as thickness decreases, free volume holes are more favored to move inversely between the upper and lower surface layers in ultrathin films.

To get a deeper impression, we calculate the average inversed diffusion rate within the early stage of aging (see red box depicted in Fig. 4.6a, b), Γ, at different film thickness, and the results are shown in Fig. 4.6c. One can clearly find that at larger thickness, such as $H > 9$, there is nearly no inversed free volume diffusion between the two free surface layers. However, as film thickness decreases further after approaching $H = 9$, the inversed free volume diffusion becomes gradually stronger. In this case, the free volume holes inside the film tend to diffuse inversely between the two free surface layers, and in average hinder the normal diffusion of free volume holes and their consecutive vanishing at the free surfaces. Eventually, the rate of volume contraction of film decreases, resulting in the slowing down of accelerated physical aging at extremely small thickness (see Fig. 4.5).

The above qualitative description looks reasonable in understanding the slowing down of accelerated aging. However, we still do not know what factor determines the inversed free volume diffusion (IFVD), and also have no idea how to explain the shift of the onset thickness of slowing down at distinct chain length (see Fig. 4.5). In our simulation, we included the slithering diffusion terminated by extending the nearest kink conformation along the chain [68] with a combination of kink-jump method and the "slithering snake" ("reptation") algorithms [69]. This procedure provided a direct simulation route to mimic the sliding motion proposed by de Gennes to explain the anomalous drop of glass transition temperature for high molecular weight free-standing polystyrene films [54, 55], and was recognized as a powerful technique in the simulation of polymer systems [53]. Inset in Fig. 4.6c illustrates one possible relationship between the IFVD and the sliding motion of chain molecules. A successful jump of segment B into free volume hole C draws the chain along its contour direction until approaching the position of a kink segment A, which diffuses free volume hole C into the position of segment A. Here, the kink segments A and B are located at the upper and lower surface layers correspondingly, thus they take nearly the same mobilities and energies. In this case, the movements of segments A or B will diffuse the free volume hole C back and forth between the two surfaces without introducing additional energetic cost, giving rise to the IFVD process.

Based on the hypothesis of relationship between the IFVD and the sliding motion of chain molecules, one can expect that the IFVD becomes relevant when the bulk portion of the film is smaller than the average sliding length between the nearest kink segments A and B along one chain [53], $L_{sliding}$ (see the inset in Fig. 4.7a). This condition is achieved when $H - 2H_s < L_{sliding}$, where H_s indicates the thickness of the surface layer. In our simulation, $L_{sliding}$ holds the average values of 3.6 and 3.5 for $N = 400$ and 100, and 2.8 for $N = 5$ (see Fig. 4.7a). At $H = 6$, $H - 2H_s$ takes the same value of 3 regardless of N, which is smaller than $L_{sliding}$ for
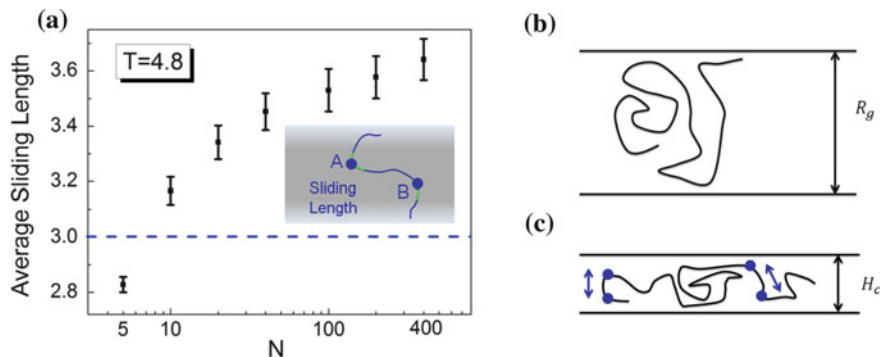
Fig. 4.7 **a** Variation of average sliding length as a function of chain length N. *Inset* depicts the sliding length between segments A and B. This figure is reprinted from [62]. **b** Illustration of confinement of random coil. **c** Illustration of new confinement of aging caused by the sliding motion

$N = 400$ and 100, but larger than that for $N = 5$. Thus, at $H = 6$ the IFVD is predominant for films with $N = 400$ and 100 ($\Gamma \simeq 0.014$), while for $N = 5$ the inversed diffusion is not relevant ($\Gamma \simeq 0.014$). Interestingly, when plotting the three curves of aging rates shown in Fig. 4.5 as a function of the normalized thickness $(H - 2H_s)/L_{sliding}$, these curves are collapsed into one master curve at the same maximum of $(H - 2H_s)/L_{sliding} \simeq 1.0$ (see Fig. 4.6d). Our findings verify the relationship between the IFVD and sliding motions, and demonstrate the significance of the sliding motion of short chain-fragments on the slowing down of accelerated physical aging in ultrathin polymer films. We speculate that such behavior would not exist for simple-molecules ($N = 1$), where no sliding motion occurs, in line with the idea of de Gennes [54].

4.3.3.3 New Confinement Length Scale

The critical thickness defined by $H_c = L_{sliding}(N) + 2H_s$ indicates a new characteristic length scale in polymer thin films. As is well known, when the thickness of polymer films approaches R_g (see Fig. 4.7b), the conformation of chain molecules greatly varies due to the compression of random coils along the confinement direction. This confinement effect results in the change of many physical properties, such as configurational entropy and diffusion coefficient, and has been considered as the molecular origins for anomalous phenomena in ultrathin polymer films [54, 55, 70]. However, our findings demonstrate that as the film thickness approaches another critical length defined by H_c (see Fig. 4.7c), the aging rate of films is perturbed due to the IFVD caused by the sliding motion of short chain fragments. Usually, the radius of gyration for chain molecules of $N = 400$ is $R_g = 20$. However, in Fig. 4.7a, the average sliding length for $N = 400$ takes the value of $L_{sliding} = 3.6$, leading to the $H_c = L_{sliding}(N) + 2H_s = 6.6$, which is far lower than R_g. This

interesting behavior indicates the existence of a new confinement effect at the nanoscale upon decreasing film thickness below R_g, where the physical aging rate is perturbed. This new phenomenon originates from the sliding motion of short chain fragment, and the findings are not only of importance in the practical design of polymer-based nano devices, but also significant in fulfilling our understandings with new insights in ultrathin polymer films.

We can also provide a rough estimation of the real length scale of H_c. Here we choose polystyrene as an example. The persistence length of polystyrene is about $l_{pers} \simeq 10$ nm [71], which is nearly equal to the distance between nearest neighbor segments along chain molecules, and also the same as the lattice spacing of the simulation box in our lattice model. The real length of H_c for $N = 400$ could be roughly estimated as $H_c = L_{sliding}(N) + 2H_s \simeq 3.6 l_{pers} + 3 l_{pers} \simeq 6.6$ nm. We speculate that the perturbation of accelerated aging would not exist in films of simple molecules. Thus we believe that the chain connectivity, which contributes to the sliding motion along the contour of chain molecules, dominates the slowing down of accelerated aging behaviors at the nanoscale. These findings shed light on the possibility of unveiling the molecular origins of the abnormal behavior of ultrastable polymer glasses [72] compared to that of low molecular weight glasses [73, 74] and liquids with enhanced orientational order [75].

4.3.4 Discussion

So far, we have demonstrated that with the inclusion of FVDA model into Monte Carlo simulation, the volume of ultrathin polymer films gradually relaxes to shrink. The responses of volume relaxation rate to temperatures and film thickness are similar to that of physical aging rate in experiments. The striking consistency between the simulation and experiments makes us believe that the outlined simulation procedure would indeed be useful for understanding the diverse aging behaviors in glassy polymer films. In this section, we discuss some further aspects based on simulations to promote our understanding on the non-equilibrium physical aging at the molecular level.

As demonstrated by Struik, the physical aging behaves in a very similar way in all glasses, such as polymers, monomers, organic, or inorganic glassy materials, and is independent of specific chemical architectures of materials [2]. In this chapter, we demonstrate that chain connectivity perturbs the aging rate at extremely small thickness in ultrathin polymer films, and we speculate that this perturbation disappears in simple molecule glassy films. These findings confirm that the chemical details of glassy materials can contribute greatly to the physical aging at extremely conditions (such as extremely small thickness). Our simulations provide a complementary to the basic features of physical aging summarized by Struik [2].

In 2000, de Gennes first proposed that the sliding motions along chain molecules should be considered in glassy polymers to explain the anomalous T_g behavior in free standing thin polymer films. Here in our simulation, we assume the validity of

this proposal and also include the sliding motion in our simulation to investigate its influence on physical aging. Interestingly, results demonstrate that at extremely small thickness, the sliding motion along chain contour could induce an inversed free volume diffusion process between the two free surface layers, and eventually slow down the accelerated aging behaviors. However, so far as we know, there is still no experiment to directly confirm the existence of sliding motion in glassy polymers. Usually, the segments in polymer glasses are modeled as frozen in a cage. However, at extremely large time scales, the segments are expected to escape the cages, thus the sliding motion would probably also exist in polymer glasses. In this sense, the inclusion of sliding motion in computer simulations shows its rationality in understanding the physical aging in polymer glasses, especially in ultrathin films. Definitely, future dedicated experiments are highly expected to verify the existence of sliding motion in polymer glasses.

In the end, we would like to emphasize that although the great significance of the physical aging of glassy polymer films is shown in practical applications, current description of polymer glasses is still in controversial both in theories and simulations [40], which limits the direct descriptions at the molecular levels of the aging behaviors at present. Also, the long aging time in glassy polymer films (usually hours or days) [5] is hard to achieve within the simulation time scales. In these cases, the simulation of volume relaxation in polymer films at temperatures above T_g with the inclusion of free volume diffusion and annihilation mechanism, as well as the investigation of the responses of volume relaxation rate β to environments (temperatures, confinements, and so on), would be very helpful to understand the diverse aging behaviors in glassy polymer films at the molecular level.

4.4   Summary

In summary, we show that the inclusion of irreversible FVDA model into Monte Carlo simulation could indeed generate the volume shrink of ultrathin polymer films, which mimics the non-equilibrium physical aging behaviors observed in experiments. The short simulation timescales can be related to the long-term experimental aging timescales by the time-temperature superposition principle. In this sense, the outlined simulation route could be employed to understand the diverse physical aging behaviors in glassy polymer films. Results confirm that the responses of volume relaxation rate to temperatures and film thickness are strikingly consistent with that of physical aging rate in experiments. Some new insights, such as the slowing down of accelerated aging at extremely small thickness, and the existence of new confinement length scale in ultrathin polymer films, are also discussed. We expect that some more sophisticated experiments could verify these new findings in the near future. The direct connection between the segment motions and physical aging makes it easier to extend the current simulation framework to study the influence of chain architectures on the physical aging [23, 24], and to test the dynamical heterogeneity on the double-step aging in polymer glasses [41].

References

 1. Simon, F.: Z. Anorg. Allgem. Chem. **203** (1931)
 2. Struik, L.C.E.: Physical Aging in Amorphous Polymers and Other Materials. Elsevier, Amsterdam (1978)
 3. Kovacs, A.J.: Adv. Polym. Sci. **3**, 394 (1963)
 4. Hodge, I.M.: Science **267**, 1945 (1995)
 5. Hutchinson, J.M.: Prog. Polym. Sci. **20**, 703 (1995)
 6. Priestley, R.D.: Soft Matter **5**, 919 (2009)
 7. Pfromm, P.H., Pinnau, I., Koros, W.J.: J. Appl. Polym. Sci. **48**, 2161 (1993)
 8. Rezac, M.E., Pfromm, P.H., Costello, L.M., Koros, W.J.: Ind. Eng. Chem. Res. **32**, 1921 (1993)
 9. McKenna, G.B.: Comput. Mater. Sci. **4**, 349 (1995)
10. Pfromm, P.H., Koros, W.J.: Polymer **36**, 2379 (1995)
11. Dorkenoo, K.D., Pfromm, P.H.: J. Polym. Sci. B **37**, 2239 (1999)
12. Dorkenoo, K.D., Pfromm, P.H.: Macromolecules **33**, 3747 (2000)
13. McCaig, M.S., Paul, D.R.: Polymer **41**, 629 (2000)
14. Huang, Y., Paul, D.R.: Polymer **45**, 8377 (2004)
15. Huang, Y., Paul, D.R.: J. Mem. Sci. **244**, 167 (2004)
16. Huang, Y., Paul, D.R.: Ind. Eng. Chem. Res. **46**, 2342 (2007)
17. Baker, E.A., Rittigstein, P., Torkelson, J.M., Roth, C.B.: J. Polym. Sci. B **47**, 2509 (2009)
18. Priestley, R.D., Broadbelt, L.J., Torkelson, J.M.: Macromolecules **38**, 654 (2005)
19. Punsalan, D., Koros, W.J.: Polymer **46**, 10214 (2005)
20. Ellison, C.J., Kim, S.D., Hall, D.B., Torkelson, J.M.: Eur. Phys. J. E **8**, 155 (2002)
21. Kawana, S., Jones, R.A.L.: Eur. Phys. J. E **10**, 223 (2003)
22. Pye, J.E., Rohald, K.A., Baker, E.A., Roth, C.B.: Macromolecules **43**, 8296 (2010)
23. Frieberg, B., Glynos, E., Green, P.F.: Phys. Rev. Lett. **108**, 268304 (2012)
24. Frieberg, B., Glynos, E., Sakellariou, G., Green, P.F.: ACS Macro Lett. **1**, 636 (2012)
25. Meyer, E.F., Jamieson, A.M., Simha, R., Palmen, J.H.M., Booij, H.C., Maurer, F.H.J.: Polymer **31**, 243 (1990)
26. Royal, J.S., Torkelson, J.M.: Macromolecules **23**, 3536 (1990)
27. Royal, J.S., Torkelson, J.M.: Macromolecules **25**, 4792 (1992)
28. Royal, J.S., Torkelson, J.M.: Macromolecules **26**, 5331 (1993)
29. Priestley, R.D., Ellison, C.J., Broadbelt, L.J., Torkelson, J.M.: Science **309**, 456 (2005)
30. Lee, H.-N., Ediger, M.D.: J. Chem. Phys. **133**, 014901 (2010)
31. Napolitano, S., Wubbenhorst, M.: Nat. Commun. **2**, 260 (2011)
32. Greiner, R., Schwarzl, F.R.: Rheol. Acta **23**, 378 (1984)
33. Boucher, V.M., Cangialosi, D., Alegria, A., Colmenero, J.: Macromolecules **45**, 5296 (2012)
34. Alfrey, T., Goldfinger, G., Mark, H.: J. Appl. Phys. **14**, 700 (1943)
35. Curro, J.G., Lagasse, R.R., Simha, R.: Macromolecules **15**, 1621 (1982)
36. Kovacs, A.J., Stratton, R.A., Ferry, J.D.: J. Phys. Chem. **67**, 152 (1963)
37. Kovacs, A.J., Aklonis, J.J., Hutchinson, J.M., Ramos, A.R.: J. Polym. Sci. B **17**, 1097 (1979)
38. McCaig, M.S., Paul, D.R., Barlow, J.W.: Polymer **41**, 639 (2000)
39. Cangialosi, D., Wubbenhorst, M., Groenewold, J., Mendes, E., Schut, H., van Veen, A., Picken, S.J.: Phys. Rev. B **70**, 224213 (2004)
40. Berthier, L., Biroli, G.: Rev. Mod. Phys. **83**, 587 (2011)

41. Cangialosi, D., Boucher, V.M., Alegria, A., Colmenero, J.: Phys. Rev. Lett. **111**, 095701 (2013)
42. Andrejew, E., Baschnagel, J.: Phys. A **233**, 117 (1996)
43. Klompen, E.T.J., Engels, T.A.P., Govaert, L.E., Meijer, H.E.H.: Macromolecules **38**, 6997 (2005)
44. Wang, X.-Y., Willmore, F.T., Raharjo, R.D., Wang, X., Freeman, B.D., Hill, A.J., Sanchez, I. C.: J. Phys. Chem. B **110**, 16685 (2006)
45. Warren, M., Rottler, J.: Phys. Rev. E **76**, 031802 (2007)
46. Rottler, J.: J. Phys.: Condens. Matter **21**, 463101 (2009)
47. Liu, A.Y.H., Rottler, J.: J. Polym. Sci. B **47**, 1789 (2009)
48. Arnoult, M., Saiter, J.M., Pareige, C., Meseguer Duenas, J.M., Gomez Ribelles, J.L., Molina Mateo, J.: J. Chem. Phys. **130**, 214905 (2009)
49. Chen, X., Ye, Y., Hao, L.: J. Chem. Phys. **137**, 044907 (2012)
50. Hou, T., Chen, H.: Polymer **53**, 2509 (2012)
51. Shavit, A., Douglas, J.F., Riggleman, R.A.: J. Chem. Phys. **138**, 12A528 (2013)
52. Binder, K., Baschnagel, J., Paul, W.: Prog. Polym. Sci. **28**, 115 (2003)
53. Hu, W., Frenkel, D.: Adv. Polym. Sci. **191**, 1 (2005)
54. de Gennes, P.G.: Eur. Phys. J. E **2**, 201 (2000)
55. de Gennes, P.G.: C. R. Acad. Sci. Paris, Serie IV Phys. Astrophys. **1**, 1179 (2000)
56. Napolitano, S., Rotella, C., Wubbenhorst, M.: Acs Macro Lett. **1**, 1189 (2012)
57. Milchev, A., Binder, K.: Europhys. Lett. **59**, 81 (2002)
58. Williams, M.L., Landel, R.F., Ferry, J.D.: J. Am. Chem. Soc. **77**, 3701 (1955)
59. Gedde, U.W.: Polymer Physics. Chapman & Hall, London (1995)
60. Brandrup, J., Immergut, E.H., Grulke, E.A.: Polymer Handbook, 4th edn. Wiley, New York (2003)
61. Tang, Q., Hu, W.: Phys. Chem. Chem. Phys. **15**, 20679 (2013)
62. Tang, Q., Hu, W., Napolitano, S.: Phys. Rev. Lett. **112**, 148306 (2014)
63. Bennemann, C., Donati, C., Baschnagel, J., Glotzer, S.C.: Nature **399**, 246 (1999)
64. Baljon, A.R.C., Billen, J., Khare, R.: Phys. Rev. Lett. **93**, 255701 (2004)
65. Zhou, C., Chung, T.S., Wang, R., Goh, S.H.: J. Appl. Polym. Sci. **92**, 1758 (2004)
66. Huang, Y., Paul, D.R.: Macromolecules **38**, 10148 (2005)
67. de Gennes, P.G.: J. Chem. Phys. **55**, 572 (1971)
68. Hu, W.: J. Chem. Phys. **109**, 3686 (1998)
69. Kremer, K., Binder, K.: Comput. Phys. Rep. **7**, 259 (1988)
70. Siretanu, I, Chapel, J.P., Drummond, C.: Macromolecules **45**, 1001 (2012)
71. Wignall, G.D., Schelten, J., Ballard, D.G.H.: J. Appl. Cryst. **7**, 190 (1974)
72. Guo, Y., Morozov, A., Schneider, D., Chung, J., Zhang, C., Waldmann, M., Yao, N., Fytas, G., Arnold, C.B., Priestley, R.D.: Nat. Mater. **11**, 337 (2012)
73. Swallen, S.F., Kearns, K.L., Mapes, M.K., Kim, Y.S., McMahon, R.J., Ediger, M.D., Wu, T., Yu, L., Satija, S.: Science **315**, 353 (2007)
74. Singh, S., Ediger, M.D., de Pablo, J.J.: Nat. Mater. **12**, 139 (2013)
75. Capponi, S., Napolitano, S., Wubbenhorst, M.: Nat. Commun. **3**, 1233 (2012)
76. Lang, M., Sommer, J.U.: Phys. Rev. Lett. **104**, 177801 (2010)

Part II
Irreversible Adsorption

Chapter 5
Kinetics of Irreversible Adsorption of Polymer Melts onto Solid Substrates

Caroline Housmans, Philippe Vandestrick, Michele Sferrazza, Jean-Paul Ryckaert and Simone Napolitano

Abstract Polymer films prepared by spincoating are intrinsically non-equilibrium systems. Differently than in bulk melts, equilibration is not achieved upon relaxation of the chains on the timescale of the reptation time. Prolonged annealing above the glass transition temperature induces, in fact, the formation of interfacial layers irreversibly adsorbed onto the supporting substrate, which affect several properties of the confined system. Although a large experimental evidence demonstrated a strong correlation between the presence of these adsorbed layers and the deviation from bulk behavior, the mechanisms permitting pinning onto a solid substrate are not well known in the case of polymer melts. In this chapter, after reviewing current theoretical models on adsorption of macromolecules, we will present recent experimental results on polystyrene, a flexible polymer, and the outcome of molecular dynamics simulations on a similar model system. In particular we show that at short annealing times the adsorbed amount (experimentally determined as the thickness of the irreversibly adsorbed layer) increases linearly with time. This first order reaction mechanism is inhibited at longer annealing times, where the space available for pinning of new chains is strongly limited by previously adsorbed chains. This condition is achieved at a molecular weight independent crossover time, and at adsorbed amount scaling as $N^{1/2}$, where N is the polymerization degree. In this regime, following models treating adsorption via the formation of loops, we show that the growth of the adsorbed amount becomes logarithmic in time. We developed a series of analytical expressions permitting to follow the kinetics of irreversible adsorption, in line with the outcome of our experiments and simulations.

C. Housmans · P. Vandestrick · J.-P. Ryckaert · S. Napolitano (✉)
Laboratory of Polymer and Soft Matter Dynamics, Faculté Des Sciences,
Université Libre de Bruxelles (ULB), Boulevard Du Triomphe, Brussels 1050, Belgium
e-mail: snapolit@ulb.ac.be

M. Sferrazza
Département de Physique, Faculté Des Sciences, Université Libre de Bruxelles (ULB),
Boulevard Du Triomphe, Brussels 1050, Belgium

5.1   Introduction

The behavior of materials confined at the nanoscale level is determined by the balance between (a) finite size effects, fixed by the surface/volume ratio (i.e. the thickness in the thin films geometry), and (b) interfacial interactions, that is, guest/host interfacial energy [1].

Recent work has, however, shown that these two components are not sufficient to univocally describe the deviation from bulk behavior observed in macromolecular systems [2–4]. As an example, packing density plays a fundamental role for star-shaped polystyrene confined in thin films, whose glass transition temperature (T_g) is influenced also by the arms' number (f), and their length, thus molecular weight (M_w) [2]. In particular, at constant thickness and constant M_w, the shift in T_g with respect to the bulk value (ΔT_g) is negative at small functionalities (for $f = 2$ one recovers the behavior of linear chains), but upon increase of f, it steeply grows reaching positive values (increase in T_g). ΔT_g shows a maximum for $f = 8$ and then smoothly drops to 0 (lack of confinement effects) at larger functionalities. Green and coworkers explained these findings considering the role of chain packing and conformational entropy, verifying that the maximum in T_g for $f = 8$ corresponds to the largest monomer packing density. This trend suggests that the condition $\Delta T_g > 0$ is due to a reduction in free volume content. In a very recent work [3]. Glynos et al. [3], have demonstrated that the value of ΔT_g for films of star shaped polymers of constant thickness is directly proportional to the number of chains adsorbed onto the supporting substrate. Remarkably this linear trend is valid regardless of the functionality of the chains, that is, the adsorption degree overrules the effects imposed by the macromolecular architecture.

The correlation between the deviation from bulk behavior and the presence of a layer irreversibly adsorbed onto the host substrate is not limited to star-shaped polymers, but seems to be a universal feature of confined polymers [4]. In particular, in 2011 Napolitano demonstrated that the T_g of thin films of polystyrene (PS) capped in between aluminum layers (no free surface) is affected by prolonged annealing in the liquid state [5]. Surprisingly the timescale required to achieve a steady state in $\Delta T_g(t)$ is orders of magnitude larger than the reptation time, t_{REP}, which in bulk sets the longest relaxation time, corresponding to the time needed to erase memory of previous conformations and thus to reach an equilibrium state.

The evidence that ΔT_g shows a time dependence in the regime $t \gg t_{REP}$ rather than fluctuating over a mean value, implies that thin films are intrinsically non-equilibrium systems and that their equilibration cannot be achieved via the same molecular mechanisms as in bulk. Remarkably, for PS $|\Delta T_g(t)|$ vanishes to zero following the same kinetics of the thickening of the layers irreversibly adsorbed onto the capping interfaces ($h_{ads}(t)$), implying $|\Delta T_g(t)| \sim h_{ads}(t)$. Consequently, adsorption acts as a driving force pushing the system towards an equilibrium state [6].

Further work has shown that the reduction in T_g with respect to the bulk value increases linearly with the interfacial free volume content, [7, 8] suggesting that the
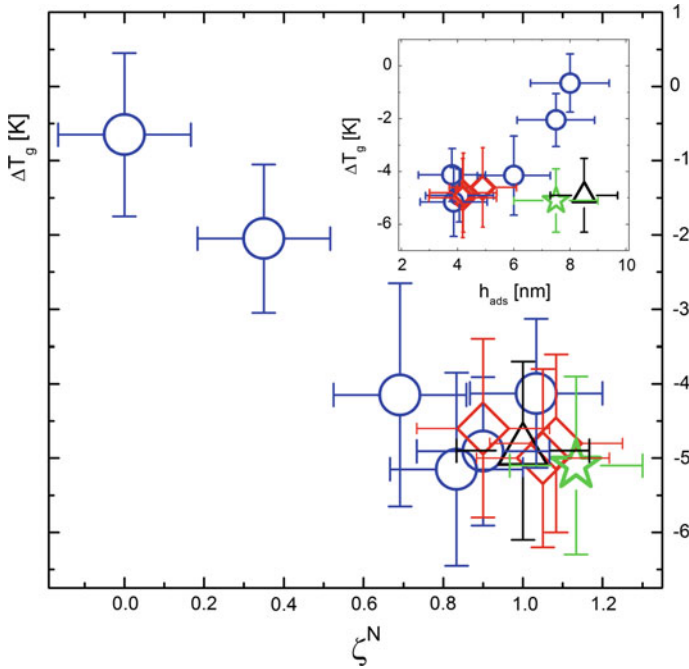
Fig. 5.1 Correlation between the normalized local free volume, ζ_N, and the shift in T_g for 20 nm thin films of polystyrene of different molecular weight (here indicated in kg/mol) 97 (*blue circles*), 160 (*red diamond*), 640 (*green star*), 932 (*black triangle*). In the *panel*, shift in T_g as a function of the thickness of the irreversibly adsorbed layer. Reproduced with permission from Ref. [7]

molecular origin for the reduction in T_g observed in proximity of supporting interfaces is due an excess in the local amount of free volume where molecules can relax, see in Fig. 5.1; a detailed description of the experiment is given in [7]. Noteworthy, the latter quantity can be promptly tuned by controlling the degree of adsorption. In the next paragraphs we will show further examples showing a correlation between confinement effects and adsorption.

The viscosity at the free surface of thin films of PS supported on silicon oxide is usually smaller than that of a bulk melt equilibrated at the same temperature [9–11]. Koga et al. found that the surface viscosity can reach values larger than in bulk in the presence of an irreversibly adsorbed layer of thickness smaller than a macromolecular size, the radius of gyration (R_g). Remarkably, the impact of these extremely thin layers [12] propagates up to distances on the order of 5 R_g's.

Vanroy et al. [13] showed that the crystallization rate of films of poly(ethylene terephthalate) capped between aluminum layers increases upon confinement and that samples totally composed by adsorbed chains do not crystallize within extremely long experimental times ($>10^5$ folds the bulk crystallization time). In these extreme conditions, the entropic penalty required for the formation of stems is excessively high, indicating that the rate of transition from the amorphous to the crystalline state drops to extremely low values.

Nguyen et al. noticed that the formation of an adsorbed layer of poly(vinyl acetate) on aluminum, is accompanied by a reduction in the maximum water uptake, [14] see Chap. 7. This interesting switch in the hydrophobic/hydrophilic character of thin polymer layers was achieved because, upon adsorption, the increase in interfacial monomer density reduces the free volume where water can be trapped. Same as in the previous cases, this structural transition was possible by simple thermal annealing protocols that modify the adsorption degree. It is noteworthy noticing that these modifications occur without affecting the interfacial chemistry.

With these considerations in mind, the development of fabrication methods permitting to finely tune materials properties, based on the control of the adsorption kinetics of polymer chains onto a supporting substrate (thin films, nanocomposites, nanotubes, nanospheres,) could be explored. Noteworthy, this type of processing does not require a modification of the interfacial chemistry. The previous examples, in fact, show the feasibility of modifying the properties of a thin polymer layer without changing its thickness or its supporting substrate.

The achievement of these goals is, however, limited by the scarce information available on the kinetics of adsorption in polymer melts. At the state of the art, in fact, the knowledge on the mechanisms of adsorption is mostly limited to equilibrium conditions and to dilute solutions, while the development of new materials would require processing of melts (the limit of very concentrated polymer solution). Moreover, the formation of a stable polymer/solid interface does not occur immediately after the melt gets in contact with the substrate. In the case of weakly polar systems, as for example PS, adsorption can require timescales exceeding by even more than 10 orders of magnitude the segmental relaxation time [15]. Information on the kinetics of this phenomenon is thus strongly required.

To overcome this gap, together with the investigation of structure and dynamics of the adsorbed layers, respectively in Chaps. 6 and 7, here we investigated the kinetics of adsorption of polystyrene on silicon wafers covered by silicon oxide, the most commonly investigated system for studies of the deviation from bulk behavior under 1D confinement. In the next sessions, after reviewing current theoretical models on adsorption of polymer chains (Sect. 5.2), we will present recent experimental results (Sect. 5.3) and the outcome of molecular dynamics simulations on a similar model system (Sect. 5.4).

5.2 Kinetics of Irreversible Chain Adsorption

5.2.1 Theoretical Background

Consider a polymer melt in proximity of a solid non-repulsive wall. At thermodynamic equilibrium the interface will be covered by a number of monomers fixed by the polymer/wall surface tension. Differently than small molecules, long chains

are stabilized against desorption already when the enthalpy gain upon adsorption of one repeating unit is smaller than $k_B T$. Because more monomers of the same molecule can adsorb at the same time, desorption of the whole chain, requiring cooperative detachment of the whole set of adsorbed segments, is unlikely on the experimental time scale of the experiment. This mechanism of adsorption is thus considered irreversible [16].

Differently than in the case of dilute solutions, due to experimental difficulties related to the characterization of buried interfaces and extremely thin (<10 nm) layers, the literature on the kinetics of adsorption of polymer melts is rather limited. In a pioneering work, Durning et al. monitored the adsorption of melts of poly (methyl methacrylate) onto quartz using neutron reflection [17]. The kinetics of thickening of the adsorbed layer was followed employing a saturating exponential function of the type

$$h_{ads}(t) = h_{t=0} + \Delta h[1 - \exp(-t/\tau)] \qquad (5.1)$$

where, τ is a characteristic time, $h_{t=0}$ the value of the thickness of the adsorbed layer at very short annealing times (virtually for t = 0) and Δh the increment in thickness at $t/\tau \gg 1$; for $t \ll \tau$, the growth rate $\partial h_{ads}/\partial t = \Delta h/\tau$. While this equation could also be used for different experimental data sets, such as those of Napolitano et al. for PS on Al, [5] Vanroy et al. PET on Al [13] and Gin et al. PS on SiO_2, [18] a weak point of this approach is related to the observation that no information on the macromolecular nature are included. Moreover Eq. 5.1 assumes that the mechanism of adsorption and the conformation of interfacial chains do not dependent on surface coverage. Large experimental evidence, on the contrary, confutes these assumptions. For example, Schneider et al. [19] showed that the first chains arriving on the substrate assume flat conformations (the parallel component of the gyration radius exceeds the perpendicular one), and get anchored to the substrate via a large number of contacts per chain. Instead, those arriving at a later stage adsorb onto the limited portion of the substrate not occupied by other chains; this restriction, elegantly pictured by Granick with the idea of "lesser footprint", [20] yields a neat reduction in number of contacts per chain.

We searched for models taking into consideration these findings. Ligoure and Leibler [21] proposed a mechanism of adsorption for solutions of block copolymers where the number of chains anchored in the early stages of adsorption increases linearly with time (first order reaction mechanism, see below). Chains adsorbed in this first regime are treated as a barrier opposing further increase in surface coverage, and the corresponding loss in configurational entropy imposes the onset of a slower growth rate, logarithmic in time. The larger the enthalpic gain upon pinning of one monomer onto the substrate, the denser the first layer of chains adsorbed in the linear regime, and, in turn, the slower the completion of whole interfacial layer. A later model by O'Shaughnessey and Vavylonis [16] for ultra-dilute polymer solutions proposes a time evolution of the adsorbed amount complying with this latter scenario. This model is based on the adsorption of single chains, but we

anticipate that its predictions in the late stage of adsorption are valid also for polymer melts.

In the early stages of adsorption, we assume a first order reaction mechanism with monomer reaction rate q, so that, the number of monomers directly adsorbing in the unit of time on a unit of surface, $\partial \Gamma_{dir}/\partial t$, is given by $q\rho_{surf}$, where ρ_{surf} is the equilibrium monomer density at the surface. In case of weakly adsorbing systems (monomer/wall energy gain $< k_B T$), the adsorption of one chain is possible upon independent pinning of a minimum number of monomers, n_{min}. In the following treatment, for a simple approach, we will fix $n_{min} = 1$. Furthermore, we will neglect the entropic costs due to the reduction in the number of configurations in the adsorbed layer with comparison to an unconfined melt [22]. At first approximation, the role of these effects can be treated as a perturbation in the value of q. Under these assumptions, the adsorbed amount Γ, corresponding to the sum of the directly and indirectly adsorbed monomers, increases in time as

$$\Gamma(t) = q\rho_{surf}Nt \tag{5.2}$$

where N is the polymerization degree, and we considered the monomer size equal to 1. Indicating the bulk monomer density with ρ, we evaluate the ratio ρ_{surf}/ρ considering that a chain of N monomers makes $N^{1/2}$ contacts with a surface. We can thus replace ρ_{surf} with $\rho N^{-1/2}$ in Eq. (5.2), obtaining

$$\Gamma(t) = q\rho N^{1/2}t \tag{5.3}$$

Experimental determination of the adsorbed amount is possible via the conversion the thickness of the adsorbed layer into the total number of adsorbed monomers in the approximation that the investigated volume has bulk density. We get

$$\Gamma(t) \approx h_{ads}(t) = qN^{1/2}t \equiv vt \tag{5.4}$$

with v the linear growth rate of the thickness of the adsorbed layer.

Once the number of monomers per unit of surface reaches a critical value Γ_{crit}, surface crowding inhibits the first reaction mechanism. We thus expect a reduction in adsorption rate, in correspondence of a crossover thickness h_{cross} and a crossover time t_{cross}. Assuming n_{min} constant implies that the condition Γ_{crit} occurs at constant number of adsorbed chains, thus h_{cross} scales as $N^{1/2}$ and t_{cross} is independent on the polymerization degree. Alternatively, one can recover the latter condition considering, via comaparison of Eqs. (5.3) and (5.4), that $t_{cross} = v/h_{cross} \sim N^{1/2}/N^{1/2} = const$.

O'Shaughnessey and Valylonis proposed that the morphology of adsorbed layer at $\Gamma_{dir} \gg \Gamma_{crit}$ can be described with a dense film containing a limited number of free sites (holes), where the addition of new coming chains into the adsorbed amount is possible. In this regime, adsorption proceeds via the formation of loops among the
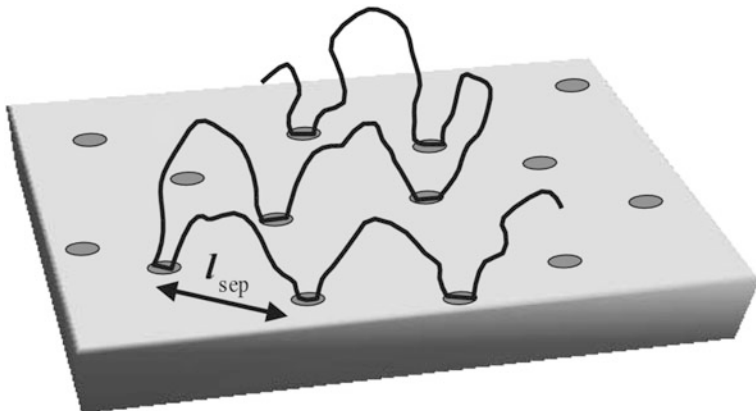
Fig. 5.2 Sketch of the typical configuration of an adsorbed chain in the late stage of adsorption, readapted from produced and modified with permission from Ref. [16]

free sites, see Fig. 5.2. This mechanism implies that the linear correlation between the number of monomers directly adsorbed and the corresponding number of adsorbed chains, found in the first linear regime, see Eq. (5.3), can no longer hold.

At homogenous density of holes, ϕ_{holes}, assuming that the size of the loops corresponds to the separation between two neighboring holes, l_{sep}, for chains in a θ solvent (e.g. polymer melt), we get:

$$N_{\text{loop}}^{1/2} \sim l_{\text{sep}} \sim \phi_{\text{holes}}^{-1/2} \tag{5.5}$$

where $N_{\text{loop}}(\ll N)$ is the number of monomers involved in a loop. Assuming that each hole contains n_{hol} monomers, we get

$$d\Gamma_{\text{dir}} = n_{\text{hol}}/N_{\text{loop}}d\Gamma \tag{5.6}$$

Upon further adsorption, the density of holes decreases, implying that adsorption of new chains is possible only upon formation of larger and larger loops (increase in N_{loop}), which yields to a reduction of $\partial\Gamma_{\text{dir}}(t)/\partial\Gamma(t)$. We remark that the increase in N_{loop} implies larger entropic penalties [22] but, aiming at identifying the form of the kinetics, we neglect this energetic contribution in our simple treatment.

Considering an upper limit for the number of totally adsorbed monomers monomers, Γ^{∞}, and an upper limit for the number of directly adsorbed monomers, $\Gamma_{\text{dir}}^{\infty}$, and that at each time t the adsorption of new chains is possible only in the free sites, we get upon integration of Eq. (5.6)

$$\frac{\partial \Gamma}{\partial t} = q\rho N^{1/2}\Delta\Gamma_{dir} = q\rho N^{1/2}[exp(-\Gamma(t)) - exp(-\Gamma^{\infty})] \tag{5.7}$$

which, by further integration leads to

$$\Gamma(t) = \Gamma^\infty + \ln[1 - A\exp(-t/\tau)] \tag{5.8}$$

where $A = 1 - \exp(-\Delta\Gamma(0)) \approx 1$ and $\tau = [\exp(-\Gamma^\infty)q\rho N^{1/2}]^{-1}$.

Comparing experimental trends to Eq. (5.8) would permit testing the validity of this model, but before introducing the next section, we discuss on the limitation of this approach. Here, in the regime $t > t_{cross}$ we considered only increases in the adsorbed amount due to the incorporation of chains forming loops of well-defined size. Other mechanisms of adsorption are, however, possible. We could consider, for example, the formation of loops of different length within the same chain, which implies increases in Γ_{dir} not contributing to Γ as expected via Eq. (5.6), e.g. if the new loops come from a previously adsorbed chain. Moreover, we anticipate that sample degradation and the uncertainty in the determination of the adsorbed amount do not permit to clearly identify the onset of the regime where $\Gamma^\infty - \Gamma(t)$ is smaller than the standard deviation. With these considerations in mind, we focused on the condition $\Gamma << \Gamma^\infty$, that in regime $t > t_{cross}$, provides an approximation of Eq. (5.8) in $\Gamma(t) \sim \log(t\text{-const})$. We thus propose an analytical form of the kinetics of adsorption of the type

$$h_{ads}(t) = \begin{cases} h_{t=0} + vt & t \ll t_{cross} \\ h_{cross} + \Pi\log(t - t_{cross}) & t \gg t_{cross} \end{cases} \tag{5.9}$$

where Π is the adsorption rate in the logarithmic regime, and we considered the thickness of the adsorbed layer as experimentally measurable quantity. We will us this expression to fit our experimental data in the next section, and we will consider Eq. (5.8) for the analysis of the data obtained via molecular dynamics simulations in Sect. 5.4.

5.3 Kinetics of Irreversible Adsorption of the Model System PS on SiO$_2$

To test the ideas discussed in the previous section, we considered the model system most widely used for the investigation of the effects of confinement in thin polymer films – polystyrene on wafers of silicon covered by a native oxide layer [23].

To reduce the systematic errors in the determination of the adsorption rate, we studied a large number of samples (>1300), as a function of the annealing time ($300 < t(s) < 259200$), the temperature of annealing ($393 < T(K) < 443$), the molecular weight ($49.4 < M_w(kg/mol) < 1460$, thus above entanglement length). To effectively reduce the impact of structural relaxation, we pre-annealed our films (thickness > 8 R_g) for 10 min, after which we fixed the onset of our annealing experiments at the same temperature ($t_{preANN} = 10$ min $\rightarrow t = 0$). The melts were thus isothermally annealed at the temperature T, for a time t. Soon after annealing,
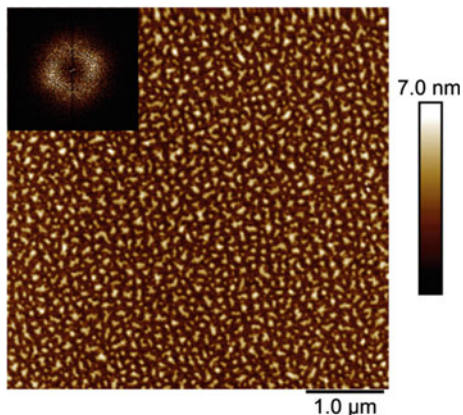
Fig. 5.3 Typical AFM topography image of surface a film of PS spincoated on SiO₂, annealed for a short time, after washing in a good solvent. In the *inset* 2D Fourier transformation of the image confirmed the occurrence of spinodal dewetting

the non-adsorbed chains were removed by soaking for 30 min the films into the same solvent used for spin-coating (Guiselin's experiment [24]). At short annealing times, Atomic Force Microscopy (AFM) images of well-dried samples revealed a pattern typical of the spinodal decomposition: the characteristic size of the pattern was revealed by the 2D Fourier transformation of the images, as see Fig. 5.3. Because of the excessively high surface roughness, we could not assign a thickness and we did not include these samples in the analysis of the kinetics of the adsorption. Upon further annealing (the minimum annealing time varied with M_w and T) we reached roughness values not exceeding 4 Å, in line with previous reports [25]. These extremely flat surfaces permitted us to model our system as continuous films and measured their thickness via ellipsometry considering a simple multilayer model, air/PS/SiO₂/Si (substrate).

We used a spectroscopic ellipsometer (MM-16, Horiba) with a wavelength range $\lambda = 430–850$ nm, and we fitted the measured spectroscopic angles Ψ and Δ using a Cauchy model with bulk values. To reduce the number of free parameters, the thickness of the oxide layer was determined before deposition of the organic layer and then fixed to the measured value during the fitting process of the PS adsorbed layer. Considering a global change in density not exceeding 5 % in comparison to bulk value, the perturbation in refractive index should not be larger than the same threshold and that thus the absolute error on the determination of the thickness should be smaller than the surface roughness.

As a further proof of the validity of our model, we compared the results of our ellipsometric fit with those obtained via AFM, where the film thickness was considered as the height of steps produced by removing the organic layer with a soft pen. For a selection of samples covering the whole investigated range of h_{ads} we found an excellent agreement between the two approaches, which strongly supports the validity of our ellipsometric model.

Fig. 5.4 Comparison of fitting of a kinetics of adsorption to Eq. (5.1), *red dotted line*, and Eq. (5.2), *green dashed line* on experimentally determined thickness of the adsorbed layer, for a film of PS deposited on SiO$_2$. The residuals, *red squares* for Eq. (5.1) and *green triangles* for Eq. (5.9), are given in the lower panel
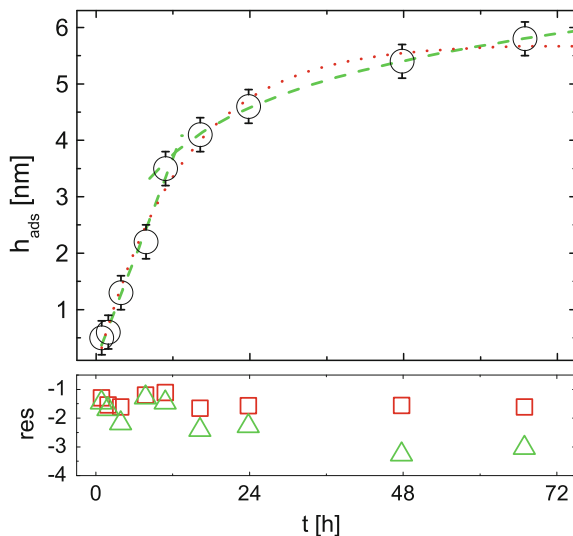
Due to the large experimental uncertainties, in many published data sets it is not possible to distinguish between a saturating exponential kinetics, Eq. (5.1) and a linear regime followed by a slower logarithmic growth at a later stage, as in Eq. (5.9). Thanks to the latest improvement in experimental instrumentation and to the larger number of data we could acquire, we are now capable to distinguish between the different models. An example is given in Fig. 5.4, where we compared the quality of the fitting functions for the kinetics of adsorption of PS on silicon oxide. At any annealing time the residuals (res = log[|h$_{ads}$ − h$_{fit}$|/h$_{ads}$]) are smaller in the case of Eq. (5.9), which proves the better accuracy of the modeling we propose. The same trend was found for all the kinetics investigated. Further advantages of Eq. (5.9) are given by the possibility to discriminate between the linear regime at short times and its deviation upon increase of the adsorbed amount. In the next paragraphs, we present a physical picture based on the temperature and molecular weight dependence of the parameters on Eq. (5.9).

The left panel of Fig. 5.5 provides an example of the time evolution of h$_{ads}$ for melts of PS of the same M$_w$ at different temperatures. Equation (5.9) successfully fitted the trends in h$_{ads}$(t) for all the kinetics (M$_w$, T) investigated. At short annealing times, the thickness of the adsorbed layer grows linearly and after a crossover time t$_{cross}$, the kinetics slows down becoming logarithmic in time. Following previous work [5, 7, 13, 18], differences between the different stages of adsorption can be analyzed introducing a dimensionless parameter t* = t/t$_{cross}$. In the following discussion, we looked to the formation of a polymer/solid interface in the three regimes described by Eq. (5.1), to which we will refer as *linear* (t* ≪1), *crossover* (t* ∼ 1) and *logarithmic* (t* ≫1).

We evaluated the value of the adsorption rate v both as ∂h$_{ads}$/∂t(t* ≪1) and as Δh/τ via fits of Eq. (5.1), obtaining results independent on the fitting procedure used. The rate of adsorption at t* ≪1 increased as M$_w^{0.50\pm0.04}$, in line with the
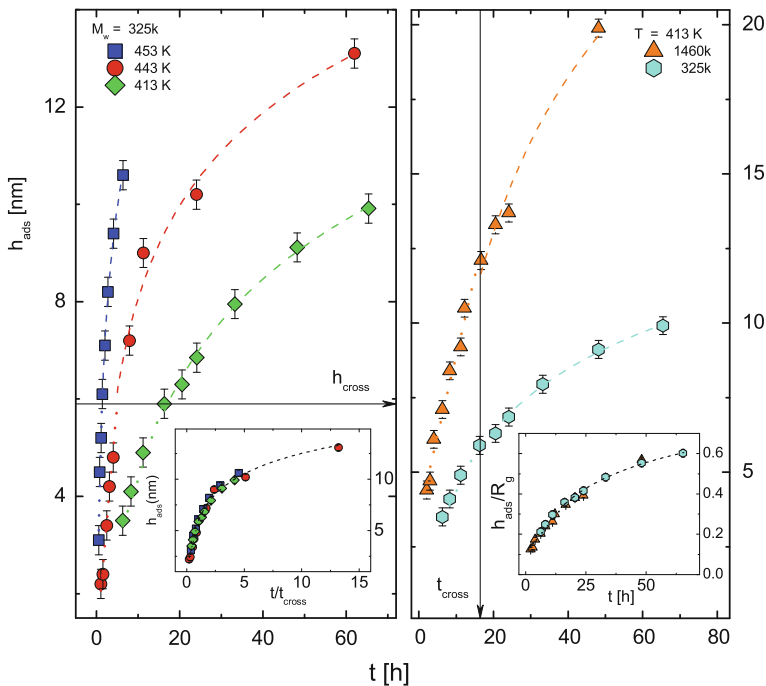
Fig. 5.5 Kinetics of irreversible adsorption of melts of PS of constant molecular weight and different temperatures (*left panel*) and at constant temperature and different molecular weight (*right panel*). In the *inset* in the *right panel*, data were plotted as a function of the time normalized to the crossover time; in the *inset* in *right panel*, the thickness of the adsorbed layer was normalized to the gyration radius. Reproduced with permission of the American Chemical Society from Ref. [23]

scaling law $v \sim N^{1/2}$, see Fig. 5.6a and the right panel of Fig. 5.5. This trend verifies Eq. (5.4). Consequently thickening proceeds via a simple pinning mechanism: every time a monomer (or a small group of consecutive monomers) irreversible adsorbs onto the substrate, the whole chain get stuck in the adsorbed films and the layer increases by a quantity proportional to the molecular size.

To complete the analysis on the mechanisms of adsorption at t* <<1, we analyzed the temperature dependence of v, see panel 6d. The linear adsorption rate follows a thermally activated law, $v \sim \exp(-E/k_B T)$, with an activation energy $E = 66 \pm 11$ kJ/mol, comparable to that reported for local non-cooperative rearrangements in PS. Lupascu et al., for example, determined an activation energy of ~ 80 kJ/mol for the helix inversion in sindiotactic regions intrinsically present in atactic samples [26]. Remarkably such a process is a possible mechanism for the kink propagation described in the sliding model of de Gennes for the transport of free volume within a thin polymer film [27]. A similar value (70 ± 6 kJ/mol) was reported by Chowdhury et al. for the relaxation of non-equilibrium conformations not coupled to the structural relaxation [28]. Such evidence furthermore strengthens
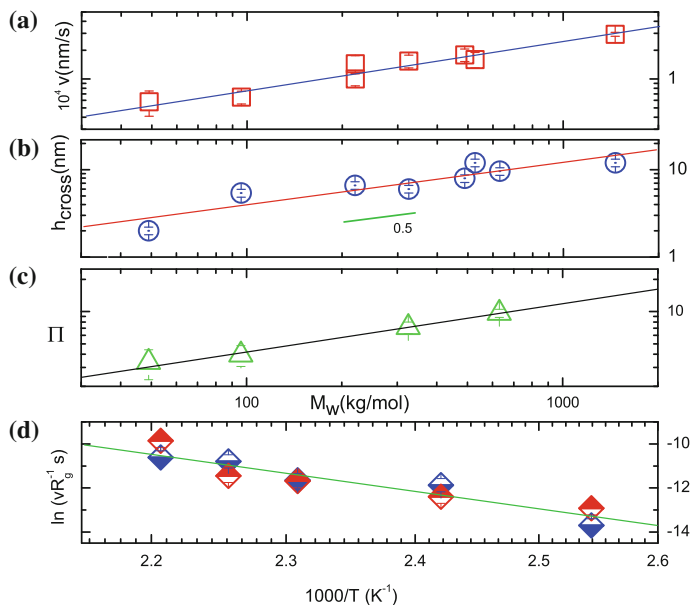
Fig. 5.6 *Top panels* molecular weight dependence of (**a**) the linear growth rate at 433 K, **b** the crossover thickness, and **c** the logarithmic growth rate. *Bottom panel* **d** temperature dependence of the linear growth rate normalized to the gyration radius for chains of molecular weight 325 kg/mol (*blue diamonds*) and 1460 kg/mol (*red diamonds*). Each point is the average of the results of at least 6 independent data sets. Reproduced with permission of the American Chemical Society from Ref. [23]

the idea that adsorption could be exploited in the equilibration in polymers confined at the nanoscale level.

The just mentioned mechanisms are not merely associated to surface processes or to the liquid state, but they are active also below T_g and in bulk. In particular, Lupașcu et al. showed that the helix inversion process does not change activation energy when crossing the structural relaxation. This observation implies that the two molecular processes are decoupled. Consequently, we associate the rearrangement permitting adsorption to spontaneous fluctuations taking place at length scales smaller than those responsible for the glass transition (typically 3–5 monomers). The value we found for PS on SiO_2 is much smaller than what is found in the case of irreversible adsorption of neat PS and PS decorated with polar moieties on thermally evaporated aluminum [5, 15]. In these systems v increased upon cooling following the glassy dynamics (superArrhenius behavior with a T dependent activation energy >>100 kJ/mol) and it had a much stronger M_w dependence, decreasing at larger polymerization degrees. We speculate that these deviations arise from the disparity in the roughness of the adsorbents, <2 Å (same as local processes) for the wafers of SiO_2 used in this work, and >20 Å (in line with the cooperative length scale of the glass transition) for Al, yielding a coupling to molecular processes of similar characteristic size.

The temperature and molecular weight dependence of the growth rate in the regime t* >> 1 followed the same trends as v, implying that Π/v is a constant. This observation is in line with the discussion in the previous section, compare, for example, Eqs. (5.2) and (5.6). Thus the mechanism of adsorption for monomers at short distances from a rigid wall is identical in both logarithmic and linear regimes, but due to topological constrictions (less available space for pinning) the overall probability of adsorption in the latest stages of adsorption is reduced, resulting in a neat reduction of $\partial h_{ads}/\partial t$ at t* >> 1. The absolute value of Π (= $\partial h_{ads}/\partial \log(t)$) has a different meaning in the model proposed by Ligoure and Leibler and in that by O'Shaughnessy and Valylonis. While in the former, Π is related to the barrier that opposes the thickening, so that, larger barrier corresponds to slower kinetics and, in turn, smaller values of Π correspond to larger barriers, in the latter model Π is limited by Γ_{mon}^{∞}. We can reconcile the two models assuming that the number of monomers directly adsorbed onto the surface at thermodynamic equilibrium is limited by the reduction of free energy upon adsorption, once we consider the entropic penalty for the formation of the adsorbed layer.

Figure 5.6c and Fig. 5.5 provide also details on the crossover region, t* ~ 1. In line with the model discussed in the previous section, we found that t_{cross} is molecular weight independent while h_{cross} scales as $N^{1/2}$ ($h_{ads} \sim M_w^{0.48\pm0.08}$). These two observations indicate that 1) it is possible to obtain a master curve of kinetics of different M_w taken in isothermal conditions, rescaling the thickness of the adsorbed layer by a quantity proportional to $N^{1/2}$, e.g. R_g 2) for any annealing time, the number of chains adsorbed is independent on M_w.

Furthermore, we considered the role of temperature on the kinetics, and observed that it is possible to obtain a master curve rescaling the absolute time by t_{cross}, as see in the inset in the right panel of Fig. 5.5. This procedure is possible since t_{cross} (T) $\sim v^{-1}$ (T), which further verifies the hypothesis in Eq. (5.4), v(T) $\sim q$(T).

To verify the universality of our claims, in the next section we compare the results of our experimental investigation to the outcome of molecular dynamics simulations.

5.4 Simulations

In our Molecular Dynamics simulations we adopted a coarse-grained polymer melt + substrate system [29]. Here N-beads chains interact via a sum of bead-bead Lennard-Jones (LJ) interactions truncated and shifted at r_{cutoff} = 2.3σ, combining repulsive (short range) and attractive (medium range) interactions.

The bead mass m, the LJ hard core size σ and the LJ well depth ε are used as basic units for mass, length and energy, while the unit of time it $\tau_0 = \sigma (m/\varepsilon)^{1/2}$. The bonding potential between two successive beads of the same chain harmonic with equilibrium distance $l_0 = 0.967\sigma$ and force constant $k_s = 1111 \, \varepsilon/\sigma^2$. The remaining intra-chain interactions are LJ, taken identical to intermolecular ones. The adsorbing potential is given as a sum of monomer-wall interactions, function of the

normal distance x of the monomer to the wall, using the usual x^{-9}(repulsive) $-x^{-3}$(attractive) potential. This potential presents a minimum of value $-\varepsilon_w$ at $z = 3^{1/6} \sigma_w$, where the suffix $_w$ indicates properties of the wall. We have adopted $\sigma_w = \sigma$ and considered different values of the ratio $e = \varepsilon_w/\varepsilon$ to model various substrate attraction intensities.

The system, studied at temperature $k_BT/\varepsilon = 1$ consists of a film of M chains of N beads with fixed transverse square surface A. Along the normal direction, the phenomenon of adsorption takes place at $x = 0$, while the film/vacuum interface is characterized by a zero normal pressure. The film thickness L, a function of the thermodynamic conditions L = L(N, M, A, T, p), is $\approx$ N M/(A ρ(T, p)). Zero normal pressure is established throughout the film, as mechanical equilibrium is established. Parallel to the interfaces, the system is subject to 2D periodic boundary conditions. A weak coupling with a Langevin thermostat (friction and random forces connected through fluctuation-dissipation theorem) with imposed bath temperature T) is added to Newton's equations of motion of all monomers. These stochastic equations are numerically integrated in time with the Paterlini-Ferguson algorithm [30].

The adsorption at equilibrium is defined on the basis of the equilibrium monomer density $\rho(x)$ profile along the normal direction x, with wall geometrical position defining $x = 0$. At $p = 0$, $kT/\varepsilon = 1$ and for a particular value of the wall attraction intensity e described above, we define the equilibrium adsorption (keeping the thermodynamic state (p, T, M) implicit) as

$$\Gamma^\infty(e) = \int_0^\infty \rho_{ads}(x; e)dx \qquad (5.10)$$

where $\rho_{ads}(x; e)$ is the adsorbed monomer density regrouping in the averaging procedure all monomers of adsorbed chains. A chain is considered adsorbed when at least one of its monomers is located within the first peak region of the global equilibrium monomer density $\rho(x; e)$ at the thermodynamic state considered (supposing the existence of a well resolved peak against the wall). We also define the directly-adsorbed equilibrium amount as

$$\Gamma_{dir}^\infty(e) = \int_0^{x_{min(e)}} \rho(x; e)dx \qquad (5.11)$$

where $x_{min}(e)$ is the normal distance corresponding to the position of the minimum between the first and second peaks of $\rho(x; e)$ (supposing they exist) at the considered thermodynamic state.

Figure 5.7 provides the equilibrium densities $\rho(x; e)$ and $\rho_{ads}(x; e)$ for a system of M = 98 chains of size N = 20 over a substrate of area $156.25\sigma^2$. The thickness of the film (h $\approx$ 15σ) is definitely larger than the height of the adsorbed layer and the polymer/wall and the polymer/air interfaces are thus independent.
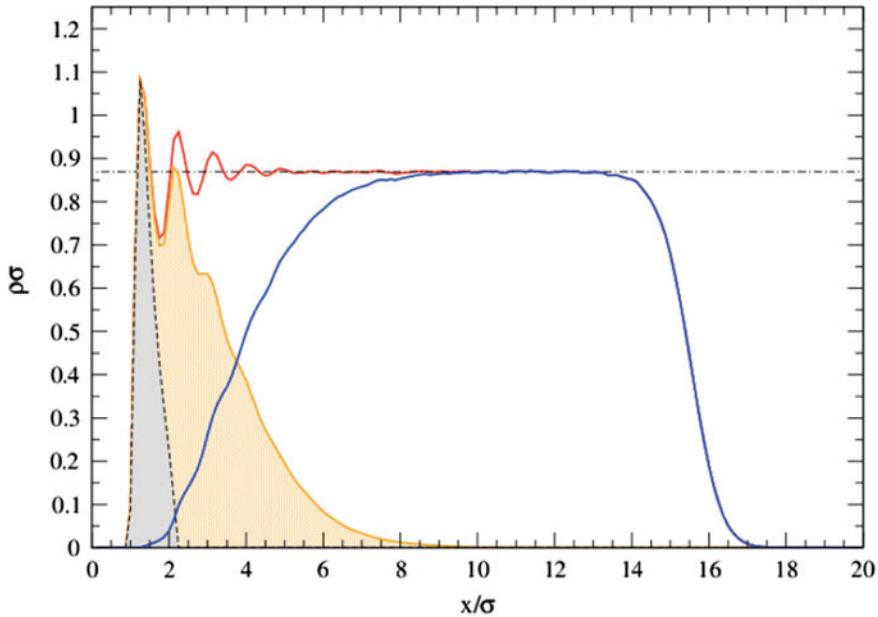
Fig. 5.7 Monomer number density profiles in a polymer film of chains of length $N = 20$ at $p = 0$ and $k_{BT}/\varepsilon = 1$ for wall attraction parameter $e = \varepsilon_w/\varepsilon = 1.0$. The density of directly attached monomers (area shaded in *grey*) gives $\Gamma_{dir}^{\infty}(e)$ while area in *orange* provides the density of indirectly attached monomers. The density of unadsorbed monomers (*blue line*) is also separately shown; the *red curve* is the total monomer density. Note that averages are based on four successive runs of $T_{max} = 6000\tau_0$

To reproduce the experimental conditions discussed in the previous section, we set up a dynamical non-equilibrium adsorption experiment, via different steps:

(a) equilibration of a given film at preset conditions (M, T, p) against the substrate with $e = e_0 = 0.3$. We verified that this monomer/wall interaction parameter corresponds, at the investigated thermodynamic state point, to a "partial dewetting" situation. We obtained uniform films stabilized by periodic boundary conditions and pressed against the flat substrate by the weak attractive component of the wall-monomer interactions. This system at equilibrium is characterized by $\Gamma_{dir}^{\infty}(e_0)$ and $\Gamma^{\infty}(e_0)$.

(b) a very long equilibrium run, in which microscopic configurations (positions and velocities of all monomers) of this film are saved at sufficiently large time intervals to be considered as independent.

(c) a kinetic run starting at time $t = 0$ from any microscopic configuration and with the wall parameter e set to a larger value $e = e_1 > e_0$. During the dynamics, the relevant quantities are averaged at given times over all independent trajectories. The densities $\rho^{neq}(x, t; e_1)$ and $\rho_{ads}^{neq}(x, t; e_1)$ and their integrals $\Gamma_{dir}(t; e_1)$ and $\Gamma(t; e_1)$, defined similarly to Eq. (5.10) and Eq. (5.11), are followed over a

time sufficient to observe the plateau corresponding to the new equilibrium situation characterized by $\rho(x; e_1)$ and $\Gamma^\infty_{dir}(e_1)$, or by $\rho_{ads}(x; e_1)$ and $\Gamma^\infty(e_1)$

In Fig. 5.8 we plotted the time evolution of the adsorbed amount during a kinetic experiment where a film previously equilibrated at $e_0 = 0.3$ was suddenly placed in contact with a more attractive wall, $e_1 = 1.0$. $\Gamma(t)$ starts from the equilibrium value $\Gamma^\infty_{dir}(e_0) \approx 2$ and increases in time along three successive regimes, until reaching $\Gamma^\infty_{dir}(e_1) \approx 2.5$. In line with our experimental evidence at very short times the adsorbed amount increases linearly with time $(t < t^*)$ and we observed a reduction in $\partial\Gamma/\partial t$ at a crossover time $(t^* \sim 1)$ after which the growth rate become logarithmic in time $(t^* > 1)$. At very long times, in a regime not explored in our experiments due to the occurrence of degradation $(t^* > 5)$, $\Gamma(t)$ follows a final exponential regime, see the limit of Eq. (5.9) for $t/\tau \gg 1$, characterized by a ultraslow equilibrium path where the number of single monomer attachments and detachments converges to the same order de magnitude.
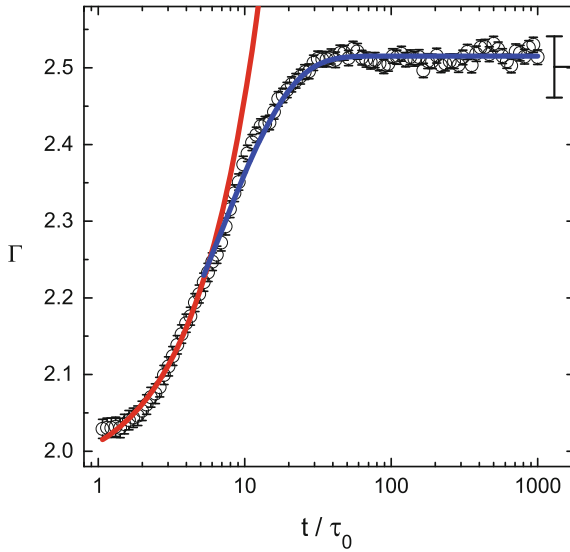
Fig. 5.8 Evolution of $\Gamma(t; e_1)$ averaged over 600 independent initial configurations (taken from equilibrium sampling at $e_0 = \varepsilon_w/\varepsilon = 0.3$) for chains of size $N = 20$ at $p = 0$ and $k_BT/\varepsilon = 1$ after setting the wall attraction parameter to $e_1 = \varepsilon_w/\varepsilon = 1.0$ at $t = 0$. The discrete times t_n ($n = 1, 100$) at which $\Gamma(t; e_1)$ is reported are built as $t_n/\tau_0 = (T_{max}/\tau_0)^{n/100}$ where $T_{max}/\tau_0 = 1000$. The *red line* indicates a fit to a linear increase in adsorbed amount, as in Eq. (5.4), the *blue line* is a fit of Eq. (5.9). The *dashed horizontal line* indicates the $\Gamma^\infty(e_1)$ at $e_1 = 1.0$ estimated from the average of four successive runs of length $T_{max} = 6000\ \tau_0$ each

5.5 Conclusions

We discussed on a model for the adsorption of polymer melts considering two regimes, linear at short times and logarithmic at longer times. The former is related to a first order mechanism, where the adsorbed amount scales as the chain length at the exponent 1/2. At later stages of annealing, when surface crowding inhibits this simple mechanism, adsorption of new chains requires the formation of loops. In this regime the rate of incorporation of new chains becomes gets logarithmic in time. We verified the validity of our model considering the large experimental evidence collected on melts of polystyrene on silicon oxide over very broad temperature and chain length ranges. Our claims are further confirmed by the outcome of molecular dynamics simulation on a coarse-grained polymer melt/substrate system.

References

1. Ediger, M.D., Forrest, J.A.: Macromolecules **47**, 471 (2013)
2. Glynos, E., Frieberg, B., Oh, H., Liu, M., Gidley, D.W., Green, P.F.: Phys. Rev. Lett. **106** (2011)
3. Glynos, E., Frieberg, B., Chremos, A., Sakellariou, G., Gidley, D.W., Green, P.F.: Macromolecules **48**, 2305 (2015)
4. Napolitano, S., Capponi, S., Vanroy, B.: Eur. Phys. J. E **36**, 61 (2013)
5. Napolitano, S., Wubbenhorst, M.: Nat. Commun. **2**, 260 (2011)
6. de Gennes, P.G.: J. Chem. Phys. **55**, 572 (1971)
7. Napolitano, S., Rotella, C., Wubbenhorst, M.: Acs Macro Lett. **1**, 1189 (2012)
8. Napolitano, S., Cangialosi, D.: Macromolecules **46**, 8051 (2013)
9. Yang, Z.H., Fujii, Y., Lee, F.K., Lam, C.H., Tsui, O.K.C.: Science **328**, 1676 (2010)
10. Koga, T., Li, C., Endoh, M.K., Koo, J., Rafailovich, M., Narayanan, S., Lee, D.R., Lurio, L. B., Sinha, S.K.: Phys. Rev. Lett. **104** (2010)
11. Chai, Y., Salez, T., McGraw, J.D., Benzaquen, M., Dalnoki-Veress, K., Raphaël, E., Forrest, J. A.: Science **343**, 994 (2014)
12. Koga, T., Jiang, N., Gin, P., Endoh, M.K., Narayanan, S., Lurio, L.B., Sinha, S.K.: Phys. Rev. Lett. **107** (2011)
13. Vanroy, B., Wubbenhorst, M., Napolitano, S.: Acs Macro Lett. **2**, 168 (2013)
14. Nguyen, H.K., Labardi, M., Lucchesi, M., Rolla, P., Prevosto, D.: Macromolecules **46**, 555 (2013)
15. Rotella, C., Napolitano, S., Vandendriessche, S., Valev, V.K., Verbiest, T., Larkowska, M., Kucharski, S., Wubbenhorst, M.: Langmuir **27**, 13533 (2011)
16. O'Shaughnessy, B., Vavylonis, D.: Eur. Phys. J. E **11**, 213 (2003)
17. Durning, C.J., O'Shaughnessy, B., Sawhney, U., Nguyen, D., Majewski, J., Smith, G.S.: Macromolecules **32**, 6772 (1999)
18. Gin, P., Jiang, N., Liang, C., Taniguchi, T., Akgun, B., Satija, S.K., Endoh, M.K., Koga, T.: Phys. Rev. Lett. **109** (2012)
19. Schneider, H.M., Frantz, P., Granick, S.: Langmuir **12**, 994 (1996)
20. Granick, S.: Eur. Phys. J. E **9**, 421 (2002)
21. Ligoure, C., Leibler, L.: J. Phys. **51**, 1313 (1990)
22. De Gernier, R., Curk, T., Dubacheva, G.V., Richter, R.P., Mognetti, M.M.: J. Chem. Phys. **141**, 244909 (2014)
23. Housmans, C., Sferrazza, M., Napolitano, S.: Macromolecules **47**, 3390 (2014)

24. Guiselin, O.: Europh. Lett. **17**, 225 (1991)
25. Fujii, Y., Yang, Z., Leach, J., Atarashi, H., Tanaka, K., Tsui, O.K.C.: Macromolecules **42**, 7418 (2009)
26. Lupascu, V., Picken, S.J., Wübbenhorst, M.: Macromolecules **39**, 5152 (2006)
27. de Gennes, P.G.: Eur. Phys. J. E **2**, 201 (2000)
28. Chowdhury, M., Freyberg, P., Ziebert, F., Yang, A.C.M., Steiner, U., Reiter, G.: Phys. Rev. Lett. **109** (2012)
29. Peter, S., Napolitano, S., Meyer, H., Wubbenhorst, M., Baschnagel, J.: Macromolecules **41**, 7729 (2008)
30. Paterlini, G.M., Ferguson, D.M.: Chem. Phys. **236**, 243 (1998)

Chapter 6
Structures and Dynamics of Adsorbed Polymer Nanolayers on Planar Solids

Naisheng Jiang, Maya K. Endoh and Tadanori Koga

Abstract Solid-polymer interfaces play crucial roles in the multidisciplinary field of nanotechnology and are the confluence of physics, chemistry, biology, and engineering. There is now growing evidence that polymer chains irreversibly adsorb even onto weakly attractive solid surfaces, forming a nanometer-thick adsorbed polymer layer ("adsorbed polymer nanolayers"). In this Chapter, we review our recent experimental results on the structures and dynamics of the adsorbed polymer chains. Furthermore, we shed light on the mechanism giving rise to the extraordinary properties of the adsorbed nanolayers and on how these properties can propagate into the film interior over distances of several tens of nanometers, resulting in heterogeneities of local crystalline structures, viscosity, interdiffusive motions (in the melts and a solvent) of supported polymer thin films.

6.1 Introduction

Owing to strong demands for new nanotechnologies, many sophisticated devices are now moving towards nanometer scales while maintaining their exceptional performance properties. Ultrathin polymer films (thickness of less than 100 nm) have been studied intensively during the last few decades, especially for the development of newly emerging applications such as nanostructured templates,

N. Jiang · M.K. Endoh · T. Koga (✉)
Department of Materials Science and Engineering, Stony Brook University,
Stony Brook, NY 11794-2275, USA
e-mail: tadanori.koga@stonybrook.edu

M.K. Endoh · T. Koga
Department of Chemistry, Stony Brook University, Stony Brook, NY 11794-3400, USA

T. Koga
Chemical and Molecular Engineering Program, Stony Brook University,
Stony Brook, NY 11794-2275, USA

photovoltaic cells, semiconductor chips, and biosensors [1]. At the same time, the anomalous features of ultrathin polymer films which include glass transition [2–8], viscoelastic properties [9–15], chain diffusion [16, 17], and physical aging [18, 19] have generated many fundamental and relevant questions in the field of polymer physics.

In many industrial applications, ultrathin polymer films are deposited onto inorganic supporting substrates via various coating methods. A spin-coating process via quick solvent evaporation is the most commonly used to prepare smooth and uniform homogeneous ultrathin polymer films on planar solids such as silicon, carbon, mica, glass, metals or steels. Between the polymer-solid interface and polymer-air interface, within distances comparable to the size of an unperturbed polymer coil, the polymer chains are confined and frozen in a non-equilibrium state. A post-thermal annealing process is then mandatory to remove residual stress via solvent evaporation and equilibrate the polymer chains [20]. However, since the equilibration time required for ultrathin polymer films may be $\sim 10^5$ times longer than that of its bulk counterparts, particular care must be taken during the post annealing process for these ultrathin films [21]. In contrast to the enhanced dynamics at the polymer-air interface [8, 15, 22], recent studies have shown that such an extremely slow equilibration process is attributed to irreversible adsorption (physisorption) of polymer chains at the polymer-solid interface [23–25].

When a single polymer chain is in contact with an impenetrable solid surface, adsorption occurs if the total enthalpic gain due to an increase in a number of surface-segmental contacts overcomes a loss in the conformational entropy of the chain during the transition from a randomly coiled state to an adsorbed state [26, 27]. Depending on specific interaction forces involved, polymer adsorption can be classified into two categories [28]: one is chemisorption, where a polymer chain is attached to a substrate due to covalent or chemical bonding forces between the substrate and the chain; the other is physisorption, where no significant chemical reactions are involved, and the polymer chains are attached via dispersion, dipolar forces or van der Waals interactions. The monomer sticking free energy in physisorption, which is on the order of $k_B T$ (k_B is the Boltzmann constant and T is the absolute temperature), is generally one or two orders of magnitude less than those in chemisorption. Although the interaction energy is weak, irreversible physisorption is still widely observed in polymer solutions (from dilute solutions to melts) due to the fact that the overall desorption kinetics is often much slower than the kinetics of adsorption [28–32]. Especially when multiple surface-segment contacts of a single chain are formed, the energy required to desorb the chain is not simply the sum of the bonding energy per each contact, but requires all the contacts to detach from the surface simultaneously. Since we mainly focus on the physisorption of polymer chains on solid surfaces, the term adsorption in this Chapter refers to physisorption, unless otherwise stated.

The early theoretical picture given by Simah and co-workers [33] showed that the equilibrium adsorbed polymer chain on a solid surface consists of three types of segment sequences: "trains" (adsorbed segments), "loops" (sequences of free segments connecting successive trains), and "tails" (non-adsorbed chain ends). Later

studies based on mean-field [27, 34, 35], scaling theories [36, 37], Monte Carlo [38, 39], and Brownian dynamic simulations [40–44] considered other parameters such as intramolecular architectures, intermolecular interactions, surface-segment interactions, polymer concentrations, and surface coverages to understand the nature of both equilibrium and non-equilibrium polymer adsorption processes. However, most of these studies dealt with the adsorption of polymer chains from dilute solutions. Substantial experimental studies on the polymer adsorption from the melts on the basis of the Guiselin's approach [37] have been just realized within the past few years [23–25, 45–55] and the topic has been recently paid a great attention in the field of polymer thin films. The purpose of this chapter therefore aims to review our recent experimental findings in the structures and dynamics of the "adsorbed nanolayers" on solid surfaces and their roles in the unusual physical and mechanical properties of polymeric materials confined at the nanometer scale.

This chapter is organized as follows: In the next section, we introduce the well-established experimental approach used for our studies on the adsorbed polymer nanolayers formed at the polymer melt-solid interface. In Sect. 6.3, we describe the novel chain conformations of the adsorbed nanolayers composed of amorphous and semicrystalline homopolymers. In addition, the molecular scale descriptions of the formation mechanism are presented. In Sect. 6.4, we focus on the unusual features of the adsorbed nanolayers and their profound impacts on various properties of supported polymer melt films and swollen films. New perspectives are followed by a brief conclusion.

6.2 Experimental Approach to Unveil Adsorbed Polymer Layers

Guiselin [37] proposed the experimental procedure (known as Guiselin's approach) to unveil an irreversiblely adsorbed polymer layer buried under the polymer melts: One has to equilibrate the melts or dense solution against a solid surface. The unadsorbed chains can be effectively removed by a good solvent, while the adsorbed chains are assumed to maintain the same conformations due to the irreversible freezing through many physical solid-segment contacts. Despite the experimental difficulties, several research groups have proved that Guiselin's approach is practical for various homopolymers, as will be discussed below.

Durning and co-workers studied the adsorption of poly(methyl methacrylate) (PMMA) on planar hydroxylated quartz substrates using neutron reflectivity [45]. Note that PMMA has a strong surface-segment interaction with hydroxylated quartz due to the formation of strong hydrogen bonding. They reported that a very thin PMMA adsorbed layer was formed upon thermal annealing of the as-cast films at a high temperature ($165\ °C \gg T_g$) and subsequently quenched below T_g rapidly. The adsorbed layers were extracted with solvent leaching using benzene. It was found that a gradual increase in the thickness of the adsorbed layer occurred with

increasing annealing time. They also showed that the final thickness (h_{ads}) of the adsorbed layer after prolonged thermal annealing can be scaled as $h_{\mathrm{ads}} \sim N^{0.5}$, where N is the degree of polymerization. Similar scaling was reported by Housmans and co-workers in polystyrene (PS) on silicon (Si) substrates [54]. This scaling implies that a polymer chain with N segments still maintains the reflected random walk statistics near the impenetrable wall, indicating that the approach enables the achievement of equilibrium melts against the surface and effectively preserves the adsorbed layer.

Fujii and co-workers later studied the adsorption of PS on Si substrates by using X-ray photoelectron spectroscopic (XPS) and ellipsometry [23]. In contrast to the strongly attractive interaction between PMMA and hydroxylated quartz, the interaction between PS and Si substrates is considerably weaker. Interestingly, thin PS adsorbed layers were formed on both hydrogen fluoride (HF)-etched Si substrates (more hydrophobic nature) and native hydrophilic Si substrates (i.e., without HF etching). This finding implies that the formation of the irreversible adsorbed layer takes place even when polymer-solid attractive interactions are weak. Strong dependence of the adsorbed layer thickness on molecular weight (M_{w}) was also reported, which is consistent with the aforementioned work [45].

Napolitano and coworkers used dielectric relaxation spectroscopy and second-harmonic generation to investigate the formation of the adsorbed PS layers on aluminum substrates [24, 47]. The interfacial energy (5.6 mJ/m^2) is higher than the threshold value for PS (2 mJ/m^2), proving an attractive polymer/metal interaction [24]. Upon annealing, the adsorption process was extremely slow. They explained the situation by adopting the idea of a "lesser footprint" [29]: the growth of the adsorbed layer is a self-retarded process inhibited by the continuous reduction of adsorption sites for the long polymer chains. They also pointed out that the adsorbed chains reach only a metastable (or quasiequilibrium [39]) state with an extremely long relaxation time [24].

Despite these stimulating experimental findings, there are still some discrepancies with theoretical predictions. For example, the strong dependence of the thickness of the quasiequilibrium adsorbed layers on M_{w} reported by Durning [45], Fujii [23] and Housmans [54] is in sharp contrast to lattice mean-field model studies reported by Schuetjens and Fleer [27, 34, 35]. The latter model predicts that the conformational features of homopolymer melts at the polymer-solid interface are independent of chain intramolecular architectures, molecular weights, and strength of surface-segment interactions. Unfortunately, experimental studies to gain the chain statistics of the adsorbed polymer chains separately from those of unadsorbed chains remain challenging so far. In order to overcome this difficulty, we utilize the established Guiselin's protocol to extract the quasiequilibrium adsorbed layer and characterize them by using a variety of nano-sensitive real-space and reciprocal space tools to bridge the gap between the theoretical and experimental viewpoints.

6.3 Quasiequilibrium Chain Conformations of the Adsorbed Polymer Chains

6.3.1 Coexistence of Two Different Nano-Architectures at the Solid-Polymer Interface

For polymer adsorption from dilute solutions, several studies have shown that the structures and formation mechanism of the adsorbed layers are governed by a non-equilibrium growth process, i.e., piecemeal deposition with differential spreading or "parking problem" [28–32, 56–60] instead of the conformational equilibrium to minimize the free energy. During the early stage adsorption, early arriving chains to a solid surface adsorb with a more flattened configuration to maximize the surface-segment contacts. On the other hand, later arriving polymer chains adsorb more loosely with fewer adsorbed sites since available sites become limited [29–32]. Granick and coworkers also found that the relaxation process of these adsorbed chains is so sluggish that different kinetically trapped conformations of adsorbed chains were present at the solid surface [29, 30].

Motivated by these results, we aimed to reveal the detailed structures of the adsorbed layers developed at the polymer melt-solid interface. We used a PS as a model system and prepared the nanometer-thick adsorbed layers ("adsorbed nanolayers") on HF-etched Si substrates using the established approach: spin-cast PS films ($\approx$ 50 nm in thickness) prepared on cleaned HF-etched Si substrates were first annealed at $T = 150$ °C for a long period of time (t_{an} up to 100 h) and then solvent leached with toluene at room temperature. The adsorbed nanolayers were further dried under vacuum at $T = 150$ °C to remove any excess solvent trapped in the films. Synchrotron X-ray reflectivity (XR) in conjunction with a Fourier transformation (FT) method, a powerful tool was used to obtain detailed structures for low X-ray contrast polymer multilayers [61, 62].

Figure 6.1 shows the XR profile (red symbols) of the quasiequilibrium PS ($M_w = 290$ kDa) adsorbed nanolayer after thermal annealing at 150 °C for 100 h and subsequent solvent leaching with toluene. The solid line in the figure corresponds to the best-fit to the data based on the dispersion (δ) profile shown in the inset (the red line). From the fitting results, we can see that the adsorbed PS nanolayer is composed of two distinct regions of different density: the inner higher-density region ($\sim$ 10 % higher than the bulk with about 2 nm in thickness) and the outer bulk-like density region (as schematically shown in Fig. 6.2) [48, 52]. In fact, all the PS adsorbed layers with $M_w \geq 123$ kDa show similar architectures composed of a nearly identical inner higher density region regardless of M_w and the outer bulk-like density region whose thickness increases with increasing M_w. The two-layer formation within the adsorbed nanolayer is similar to the one formed via polymer adsorption from dilute solutions [29–32]. Hence, polymer adsorption from the melts is also governed by piecemeal deposition with differential spreading dictated by the still-uncovered surface area. Furthermore, solvent leaching with chloroform (a better solvent than toluene for PS) allows the unveiling of the lone inner
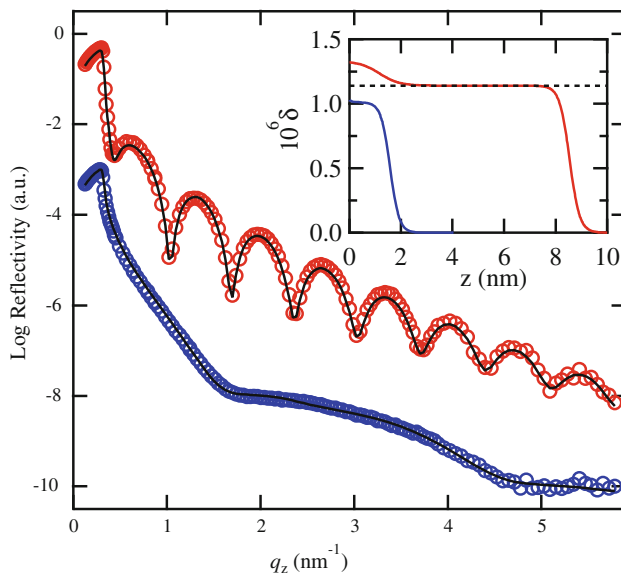
Fig. 6.1 XR curves of the quasiequilibrium PS (M_w = 290 kDa) interfacial sublayer (*red circles*) and flattened layer (*blue circles*) at t_{an} = 100 h. The *solid lines* correspond to the best-fits to the data based on the dispersion (δ) profiles against the distance (z) from the surface of SiO$_2$ layer (1.3 nm in thickness) shown in the inset: *red line*: the interfacial sublayer; *blue line*: the flattened layer. The *dotted line* in the inset corresponds to the δ value of bulk PS. Figure reproduced from Ref. [52] with permission from American Chemical Society

high-density region [52]. As shown in Fig. 6.1 (blue symbols), the XR result shows that the thickness of the lone flattened layer after the chloroform leaching is in good agreement with that of the inner high-density region of the adsorbed nanolayer extracted with toluene. Hence, the results validate that we have successfully extracted the lone flattened layer via the chloroform rinsing. Note that the δ value of the lone flattened layer is smaller than that within the interfacial sublayer due to the empty (air) spaces of the film, as will be discussed below. As schematically depicted in Fig. 6.2, this selective extraction of the two adsorbed layers is possible owing to the large difference in the desorption energy between the outer loosely adsorbed chains and the inner flattened chains, which is proportional to the number of segment-surface contacts [31, 32]. We hereafter assign the inner high-density layer as the "flattened layer", while the entire adsorbed layer composed of the inner flattened chains and outer loosely adsorbed chains is designated as the "interfacial sublayer" [63]. It should be emphasized that the M_w dependent PS adsorbed layers reported by Fujii and co-workers [23] and Napolitano and co-workers [24, 54] should correspond to the interfacial sublayer, while the existence of the M_w independent flattened layers has been overlooked.

Figure 6.3 shows the surface morphologies of the quasiequilibrium (a) PS flattened layer and (b) PS interfacial sublayer after solvent leaching and dried under

Outer loosely adsorbed chains

(Bulk-like density)

(higher density)

Si

Inner flattened chains

Enhanced desorption energy

Si
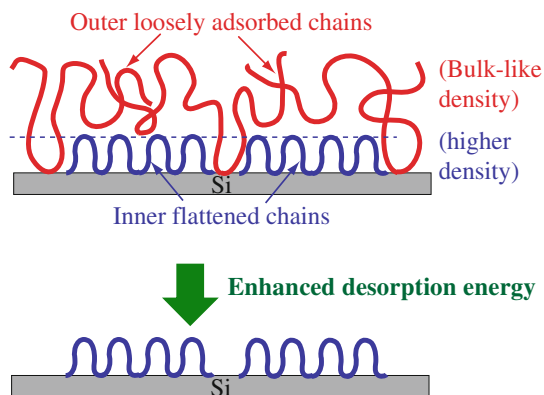
Fig. 6.2 Schematic view of the interfacial sublayer composed of the two different chain conformations and the extraction of the lone flattened layer by enhancing the desorption energy of a solvent
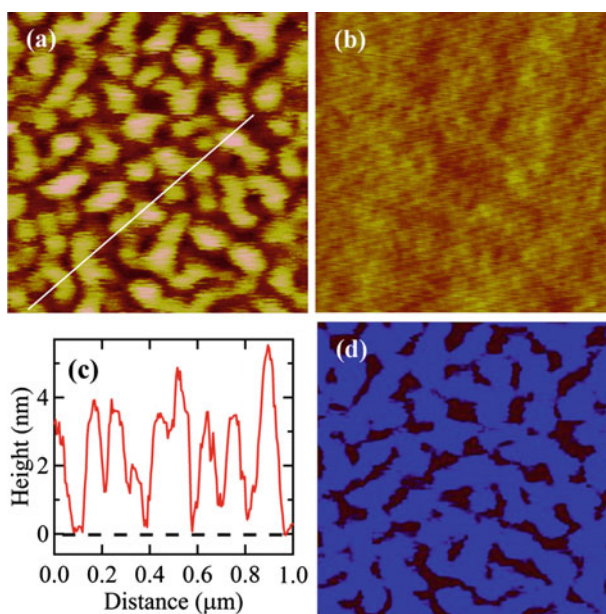
Fig. 6.3 AFM height images of **a** the PS (M_w = 290 kDa) flattened layer surface and **b** interfacial sublayer surface at t_{an} = 100 h. The scan sizes and height scales of the images are 1 μm × 1 μm and 0–6 nm, respectively. The corresponding height profile along the *white line* in (**a**) is plotted in (**c**). The dotted line corresponds to the SiO_2 surface. **d** Corresponding bearing area analysis result for the AFM image shown in (**a**). The areas occupied by the polymer (bearing areas) are colored in *blue*. Figure reproduced from Ref. [52] with permission from American Chemical Society

vacuum. It is evident that the flattened layer has microscopic "textures" with a characteristic length of about 100 nm, while the surface of the interfacial sublayer is homogeneous. Based on the image analysis (Fig. 6.3c, d), we estimated the surface coverage (ϕ_p) of the flattened layer to be ≈ 75 % [52], which is in good agreement with the observed δ value of the lone flattened layer assuming the empty region of ∼ 25 % (Fig. 6.1). Since the loosely adsorbed chains cover the substrate homogeneously at the quasiequilibrium state (Fig. 6.3b), it is reasonable to suppose that the empty regions of the flattened layer correspond to the sites where the loosely adsorbed chains grew and were then removed by the chloroform leaching. These results are consistent with a set of polymer adsorption experiments from dilute solutions reported by Granick and coworkers [30, 64] who proved that the flattened chain conformations have much higher fractions than the loosely adsorbed chains at the solid surface. The present surface coverage of 75 % is much larger than the "jamming limit" (54.7 % of surface sites) predicted for rigid disks [65], suggesting that flexible polymer chains can adsorb more effectively and compactly by taking advantage of their flexibility to accommodate the limited surface sites.

6.3.2 Formation Mechanism of the Two Different Chain Conformations

Figure 6.4a shows the time evolution of the thicknesses of the PS flattened layer and interfacial sublayer on the HF-etched Si substrates during the thermal annealing process measured by XR. We can see from this figure that, at the early stage, both the flattened layer and interfacial sublayer grow with time. After reaching the identical crossover time (t_c) at around 4 h, the flattened layer reached the quasi-equilibrium conformation with the thickness of 2.1 nm, while the interfacial sub-layer gives a way to a slower logarithmic growth followed by a plateau region at $t_{an} > 96$ h. Hence, the important conclusion is the two different chain architectures emerge and grow independently on the solid surface. It should be noted that the lateral correlation length of the textures seen in the flattened layer is less than the coherent length ($\xi_{surface}$, or coherently illuminated length) of X-ray beams at the sample position ($\xi_{surface} \sim 20$ μm in the present case). Therefore, X-rays are sensitive to the textures and would interfere with them, possibly causing a drastic change in the "amplitude" of Kiessig oscillation fringes. This would make the accuracy of the data fitting (for the density and roughness of the flattened layer) somewhat ambiguous, while the thickness can be independently and still accurately determined from the "period" of the oscillation fringes. Hence, it is likely that the height scale of the AFM result shown in Fig. 6.3c is somehow overestimated. Further experiments to clarify this concern are currently in progress.

The question arises: When is the formation of the flattened chains initiated on the substrate surface? According to previous simulation results, the time scale for early arriving polymer chains to lie flat on solids is only a few hundred nanoseconds [40–44], which is far beyond our experimental time scale. In fact, we found the
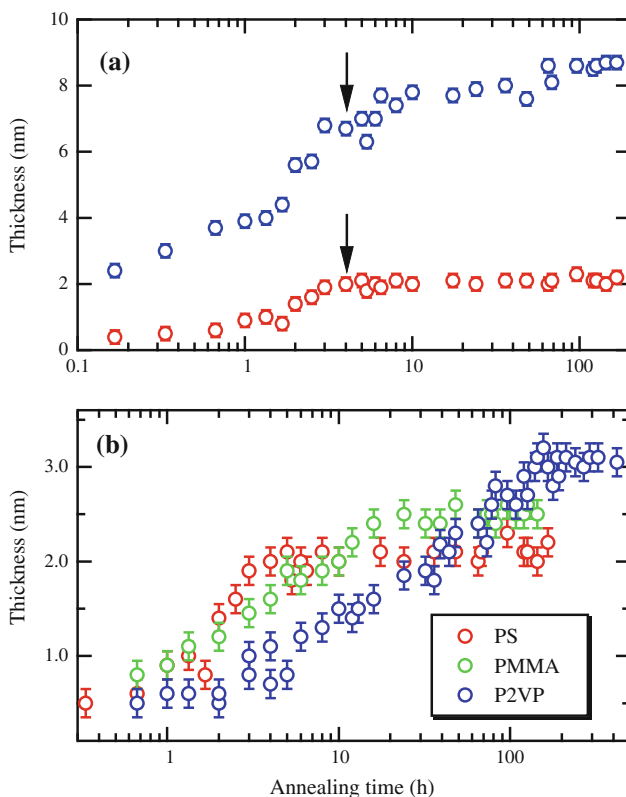
Fig. 6.4 **a** Growth of the PS ($M_w = 290$ kDa) interfacial sublayer (*blue circles*) and flattened layer (*red circles*) against t_{an} during thermal annealing at 150 °C under vacuum. The dotted lines correspond to the best-fits of the power-law growth described in the text. The crossover times from the power-law growth to logarithmic growth for the interfacial sublayer and from the power-law growth to the quasiequilibrium state for the flatten layer are indicated in the *arrows*. **b** Growth of the PS ($M_w = 290$ kDa) (*red circles*), PMMA ($M_w = 97$ kDa) (*green circles*), and P2VP ($M_w = 200$ kDa) (*blue circles*) flattened layers against t_{an}. Figure reproduced from Ref. [52] with permission from American Chemical Society

formation of a very thin PS adsorbed layer (less than 1 nm in thickness) resulted from spin-casting alone without subsequent thermal annealing, as previously reported [23–25, 47]. Hence, we expect that the initial (non-equilibrium) flattened chains emerge under solution conditions rather than under melt conditions [45]. The adsorption kinetics of the flattened layer at $t < t_c$ thus corresponds to a "collapse and zipping-down" process onto the solid surfaces [31, 32] and the proceeding relaxation and re-arrangement of the flattened conformations take place toward their quasiequilibrium states in the melt.

On the other hand, as shown in Fig. 6.4a, the adsorption of the late arriving chains (i.e., the origin of the loosely adsorbed polymer chains) also occurs at $t < t_c$, but it is somewhat retarded due to screening caused by the flattened chains already

present on the surface. As a result, the late arriving chains form bridges jointing up nearby empty sites [31]. The competition between the zipping down of the flattened chains and the adsorption of the late coming chains continues until $t = t_c$ when the substrate surface is fully covered. At $t > t_c$, the zipping down of the flattened layer formation is over and a "reeling-in" process of the partially adsorbed (late arriving) chains governs [39]. This reeling-in process in the melt is more sluggish due to excluded-volume repulsion of the already existing adsorbed chains and chain entanglements with unadsorbed chains, resulting in a very slow logarithmic growth of the film thickness before reaching the final state (Fig. 6.4a). This is the reason why the resultant two chain architectures composed of the interfacial sublayer is analogous to those formed via polymer adsorption from a dilute solution [29–32, 58–60, 66–69]. It should be mentioned that the overall adsorption kinetics of the interfacial sublayer shown in Fig. 6.4a is in good agreement with the adsorption of PS on Al substrates [25, 47] as well as on Si substrates [54].

6.3.3   Effects of Polymer-Substrate Interactions on the Formation of the Adsorbed Nanolayers

It is expected that an increase in the surface-segment interaction can reduce the segmental mobility of polymer chains at the solid-polymer interface. In order to investigate the effects of the interactions, poly(methyl methacrylate) (PMMA) and poly(2-vinylpyridine) (P2VP), which have similar chain stiffness and bulk T_g compared to PS, but have much stronger interactions with Si due to the presence of hydrogen bonding and polar forces [6, 70, 71], were used. The PMMA and P2VP flattened layers on the non-HF etched Si substrates were prepared via Guiselin approach along with the use of toluene for PMMA and DMF for P2VP. A comparison of the adsorption kinetics among the PS, PMMA and P2VP flattened layers is shown in Fig. 6.4b. It was found that the final thickness and the t_c values increased with increasing magnitude of the solid-segment interactions: P2VP > PMMA > PS. Based on an independent experiment, we also proved that the effect of the viscosity alone cannot explain the large difference (more than two orders of magnitude) in the t_c values between the PS ($M_w = 290$ kDa) and P2VP ($M_w = 200$ kDa). Hence, it is reasonable to conclude that the magnitude of the interactions controls not only the final thickness but also the kinetics of the flattened layer formation. This trend can be qualitatively explained by simulation results showing that the number of adsorbed polymer chains increases with increasing solid-segment interactions [41]. In addition, AFM experiments revealed that the surface coverage of the quasiequilibrium flattened layer also increases with increasing the magnitude of the solid-segment interactions: the average ϕ_p follows P2VP > PMMA ≈ PS. Interestingly, the quasiequilibrium P2VP flattened layer (∼ 3 nm in thickness layer) surface was reasonably uniform ($\phi_p \sim 90$ %) [52].

6.3.4 Adsorbed Semicrystalline Polymer Nanolayers

The adsorption of semicrystalline polymers at the polymer melt-solid interface is another interesting question to be answered. When a monolayer of semicrystalline polymer molecules is prepared on a solid surface, nucleation and crystal growth can be very different from that found in the bulk due to confinement effects [72–78]. Polymer chains in the vicinity of the solid surface tend to crystallize into lamellar crystals with either flat-on or edge-on orientations, depending on specific interactions with solids [79–81]. Among a variety of morphologies reported in the literature, the formation of dendrites or seaweed structures via the so-called diffusion-limited aggregation (DLA) process was the most commonly observed in semicrystalline polymer monolayers [76, 82].

According to the picture given by Reiter and Sommer [76, 78], a strongly adsorbed amorphous chain in the vicinity of a crystal front has to partially detach from the solid and subsequently stretch in the direction normal to the solid, in order to fold itself. Such a movement of the adsorbed chain towards a new crystal front would leave behind unoccupied surface areas on a solid (i.e., a depletion zone); the crystallization of the adsorbed chains could continue until the depletion zone becomes so large that other amorphous adsorbed chains could not further diffuse towards the crystal fronts. However, compared to the crystallization of non-adsorbed polymer chains, the existence of many surface-segment contacts generates an additional energy barrier that the adsorbed chains arriving the nearest crystal front must overcome before they crystallize [50]. As a consequence, the crystal growth rate of the adsorbed chains is often much smaller than that of the non-adsorbed chains [55, 74, 77, 83–86]. In some cases, the formation of long range ordered structures was not observed within the experimental time scales [50, 53, 87].

In our recent study [55], 50 nm-thick PEO films ($M_w = 20$ kDa) were spin-coated onto HF-etched Si substrates and pre-annealed at $T = 85\ °C > T_m$ (64 °C) for 2 h to induce the irreversible adsorption of the PEO chains on the substrate. To investigate the adsorbed nanolayers in detail, the annealed samples were solvent-leached with fresh chlorobenzene repeatedly. The adsorbed nanolayers were then post-annealed at 85 °C for 1 h to remove any excess solvent trapped in the films. Figure 6.5 shows representative AFM height images of the PEO adsorbed nanolayers after a series of leaching experiments. As seen from the figure, finger-like seaweed lamellar structures produced via the DLA process are seen in the 6.5 nm-thick interfacial sublayer, while the surface of the 2.5 nm-thick flattened layer is featureless (i.e., no crystalline structures were observed). Grazing incidence X-ray diffraction (GID) measurements with a high brilliant synchrotron X-ray beams at SPring-8 (Japan) also confirmed that there are no crystalline structures formed in the 2.5 nm-thick flattened layer (Fig. 6.5c). Hence, it is reasonable to conclude that the PEO flattened chains are strongly bound to the solid such that they are not able to crystallize, while the loosely adsorbed PEO polymer chains can fold and grow via the DLA process. We also found that in the case of PEO chains on the HF-etched Si
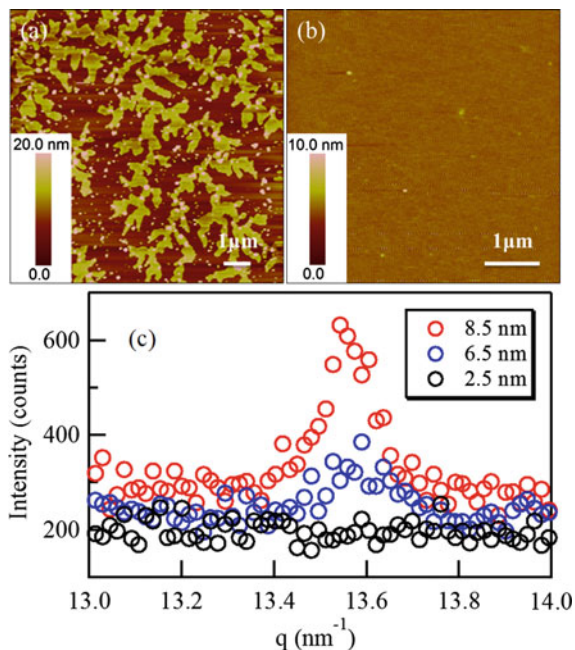
Fig. 6.5 AFM topographic images of the PEO **a** interfacial sublayers and **b** flattened layer. The samples were annealed at 85 °C for 1 h and rapidly quenched to 25 °C to induce the recrystallization. The corresponding one-dimensional GID results are shown in (**c**). The presence of the 120 diffraction peak at $q = 13.6$ nm^{-1} was used to determine the existence of the crystalline structure. Figure reproduced from Ref. [55] with permission from The Royal Society of Chemistry

(a strongly attractive interaction), the chains adopt a flat-on orientation on the substrate [55]. On the other hand, polyethylene (PE) chains prefer to have an edge-on orientation on the HF-etched Si [49] (i.e., a weak interaction). These results are in good agreement with previous Monte Carlo simulations [79] and experimental results [80, 81].

Napolitano and coworkers studied the cold crystallization of poly(ethylene terephthalate) (PET) and poly(L-lactide) (PLLA) films confined between two Al layers (i.e., sandwiched films) [50, 53]. They reported that, after thermal annealing at a temperature where the maximum crystallization rate in the bulk was achieved, crystallization was inhibited when the thickness of the films was less than ~ 20 nm for PET or less than ~ 10 nm for PLLA. Such a threshold corresponds to the thickness of the adsorbed layers (i.e., a great reduction in the molecular mobility compared to the bulk) formed between the two solid substrates. Judging from the ratio between the thicknesses of the adsorbed layers and corresponding R_g of the polymers, their adsorbed layers are considered as the interfacial sublayer in our classifications. Hence, the discrepancy is noticed between the "uncapped" PE and PEO interfacial sublayers, where we can clearly see the seaweed structures (Fig. 6.5a), and the "sandwiched" PET and PLLA interfacial sublayer. This contrast

suggests that the effect of the free surface (the polymer/air interface) enhances the local segmental mobility of the loosely adsorbed chains. Future investigation is needed to clarify this point.

6.4 Unique Properties of the Adsorbed Nanolayers

In this Section, we highlight the unique physical properties of the adsorbed nanolayers and their long-range perturbations on the local structures and properties of supported polymer thin films.

6.4.1 Are the Adsorbed Nanolayers Mobile or Immobile?

Figure 6.6 shows the temperature stability of the adsorbed nanolayers composed of three different homopolymers measured by in situ X-ray reflectivity. Hence, it is clear that both the flattened layers and interfacial sublayers exhibit nearly zero thermal expansion within the temperature range up to 200 °C [48, 52]. If we use the same definition of T_g as for bulk melts (i.e., a change in the thermal expansion coefficient when crossing the glass transition [88]), the XR data indicates that there is no glass transition of these adsorbed nanolayers up to 200 °C, while the bulk T_gs of these polymers are about 100 °C. These findings may be consistent with
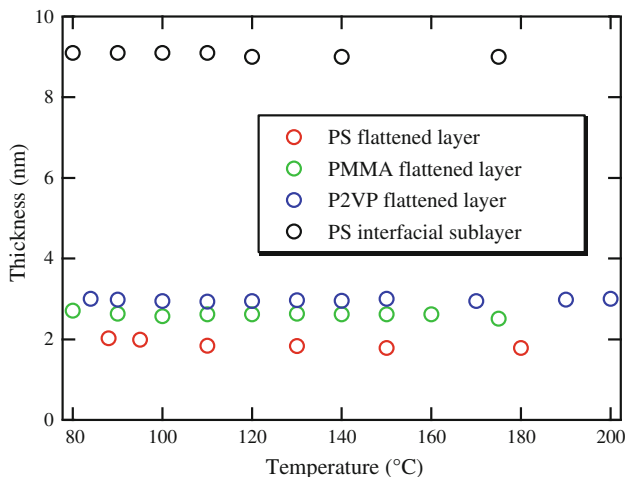
Fig. 6.6 Film thicknesses of the three polymer flattened layers and the PS interfacial sublayers against temperature determined by the in-situ XR measurements [52]. The XR data was collected during the cooling process and heating processes, and we confirmed that all the temperature dependences of the film thicknesses are independent of the thermal processes

previous differential scanning calorimetry experiments which showed no evidence of T_g of intercalated PS chains confined between clay particles within the domain spacing of 3 nm [89]. Furthermore, using neutron reflectivity, we found no inter-diffusion between hydrogenated PS (h-PS, $M_w = 123 \times 10^3$) interfacial sublayer and deuterated PS (d-PS $M_w = 334 \times 10^3$, $M_w/M_n = 1.05$, Polymer Source, 51 nm in thick) overlayers floated onto the interfacial sublayer after severe annealing for at least 3 days at 170 °C ($\gg T_g$) [46]. These results indicate that the dynamics of the adsorbed polymer chains in the direction normal to the film surface is strongly hindered even at $T \gg T_g$, possibly due to the presence of the large number of the segment-solid contacts. It should be noted that as mentioned in the previous section and described elsewhere [52, 55], the flattened chains and loosely adsorbed chains are able to move or slide in the lateral direction.

On the other hand, Napolitano and co-workers indicated that the segmental relaxation of the adsorbed PS chains capped between two solid surfaces is slightly enhanced in comparison to the bulk [24]. In another study, by means of capacitive dilatometry, an increase in T_g was observed when the thickness of polycarbonate (PC) films was less than 20 nm [90], suggesting that the adsorbed PC chains would also exhibit an increased dynamic T_g relative to the bulk. Kremer and co-workers [91] measured the segmental dynamics of chains of P2VP chains supported on an attractive solid substrate (nanostructured electrode). They reported that for semi-isolate and isolate chains in contact with a strongly attractive solid substrate, only 12 % of the segments showed the slower relaxation dynamics compared to the bulk, while the rest still exhibited a bulk-like dynamic T_g. This suggests that for a single chain adsorbed on a solid, the free tail ends are still mobile and only the adsorbed segments or the segments neighboring to the adsorbed ones are immobile or less mobile. Hence, the local segmental mobility and chain dynamics strongly depend on the conformations of the adsorbed chains at the polymer-solid interface.

6.4.2 Heterogeneous Viscosity Distributions Caused by the Adsorbed Nanolayers

In the past 20 years, our understanding of polymer melt dynamics near a solid surface has been greatly established based on the anomalous T_g changes in thin polymer films [2–8]. In a bulk system, a shift in T_g is accompanied with a change in the molecular mobility of a glass former, hence resulting in deviations in temperature dependent physical and mechanical properties. However, in the case of polymer thin films, several authors have proposed that the correlation between T_g and various properties may not be valid [92–96]; the T_g value of a confined polymer film depends on the time and length scales of dynamics which experimental techniques are sensitive to. Therefore, measurements of other physical and mechanical properties of supported polymer thin films (such as modulus, viscosity and diffusion/interdiffusion behavior) are of great importance in improving our

understanding of the correlations in thin polymer films. In the following, we highlight our recent local viscosity measurements [46, 97] of supported PS thin films using the state of the art technique, a "marker grazing-incidence X-ray photon correlation spectroscopy" (marker GIXPCS) [98], and discuss the heterogeneous viscosity distributions associated with the interplay between the two interfaces.

During the past years, investigations regarding in situ rheological properties of polymer thin films have involved two major techniques: atomic force microscopy (AFM) and grazing-incidence X-ray photon correlation spectroscopy (GIXPCS). AFM has mainly been used for surface viscosity measurements by probing (i) a change in surface modulus or friction forces based on the interaction between a sample and AFM tip, or (ii) time evolution of surface morphologies, such as surface roughness [99–101], nanodeformation [15, 102], capillary leveling [103–105] or nanoparticle embedding [106–109], of the film. As expected, this technique is not sensitive enough to distinguish the inner properties of the film from those of the entire film or surface. On the other hand, Sinha and co-workers have demonstrated that the GIXPCS technique is the most direct and unambiguous way to study the lateral dynamics of polymer thin films prepared on solid substrates based on the surface capillary wave fluctuations [110–117]. Using normal hydrodynamic theory for capillary wave fluctuations on viscous liquid films, they have shown that the viscosity of single PS films that are several tens of nanometers thick is similar to that of the bulk [110]. However, it should be emphasized that, because of the propagation of the capillary fluctuations into the film interior, the viscosity obtained by this methodology also corresponds to the value "averaged" over the entire thickness. Thus, another strategy is required to determine the local rheological properties of polymer thin films as a function of the distance from the interfaces and to clarify to what extent the two interfacial effects propagate into the film interior. This question, which has not yet been answered *theoretically or experimentally,* motivated our study.

To solve this problem, we have established the marker GIXPCS technique to determine local viscosity of thin polymer films by monitoring the Brownian motion of embedded gold nanoparticles in the PS films [46, 97, 98]. The schematic view of the marker GIXPCS setup is shown in Fig. 6.7. The marker GIXPCS experiments were performed at the 8-ID beam line at the Advanced Photon Source (APS) in Argonne National Laboratory with the X-ray energy of 7.5 keV. This type of strategy is the so-called tracer diffusion approach by taking advantage of inherently strong X-ray contrasts of gold nanoparticles, which act as "markers" in the polymer matrix. To apply this strategy to a given system, the concentration of the markers should be sufficiently low enough, and the markers should be neutral to the surrounding materials; otherwise, the effects of particle-fluid interactions and the interference among the markers would make the XPCS analysis complicated.

Six different molecular weights (M_w) of PS (M_w = 30, 65, 123, 200, 290, and 400 kDa) having narrow polydispersities (M_w/M_n = 1.02-1.05) were used. Thiol-functionalized (octadecanethiol ($C_{18}H_{37}SH$)) Au nanoparticles were prepared as markers using the one-phase synthesis method [118]. The average radius of the
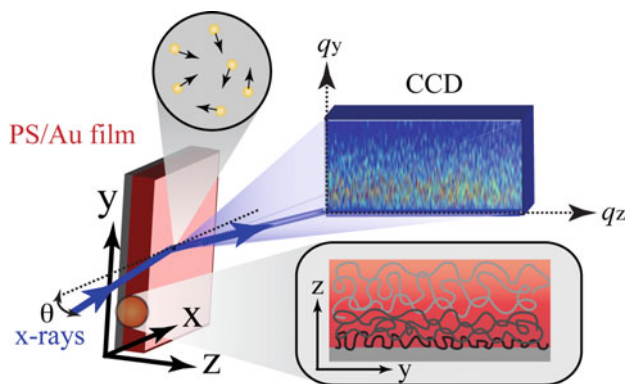
Fig. 6.7 Schematic configuration of the marker GIXPCS experiments. The use of resonance enhanced X-ray scattering for GIXPCS enables one to intensify, by more than one order of magnitude, the probing electrical field in the regions of interest within single nanometer polymer films. Figure reproduced from Ref. [98] with permission from Nature Publishing Group

core Au particles was 1.5 ± 0.2 nm, and the thickness of the $C_{18}H_{37}SH$ shell layer was approximately 1.3 nm. Solutions of PS were first prepared in toluene. The Au nanoparticles (the volume fraction was fixed to 0.2 %) were then added to the PS solutions, which were further sonicated for 30 min. The PS/Au thin films were prepared by spin-casting the solutions onto HF-etched Si substrates and annealed for up to 4 days in a vacuum of 10^{-3} Torr at $T = 170$ °C. Four different film thicknesses (32, 57, 128, and 235 nm) were prepared. We confirmed that the Au particles were well dispersed in all of the films and no surface segregation of the Au nanoparticles occurred at the two interfaces before or after the marker GIXPCS experiments. The in-plane dynamics of the Au nanoparticles were monitored by recording time series of speckled scattering intensity using a CCD camera.

In addition, two illuminating modes with different incident angles (θ_i) were used for the GIXPCS measurements to explore the marker dynamics at the topmost surface ("surface-mode") and at the near-center region of the film ("center-mode") independently [46, 97]. In the surface-mode, an incident angle of $\theta_i = 0.15°$, which is just below the critical angle of the total external reflection of the PS films with the X-ray energy ($\theta_c = 0.16°$), was used. According to previous calculations of the electric field intensity (EFI) based on Parratt's exact recursive method [119], the EFI in the surface-mode is 3–4 times higher than that of the incident beam within the topmost surface region (approximately 9 nm in thickness), and it then decays exponentially into the film interior. Hence, the scattering intensity in the surface-mode is dominated by a surface region of thickness of approximately 9 nm. For the center-mode, we utilized the "first resonance mode" ($\theta_i > \theta_c$) [120] in which resonance enhancement of the EFI in a polymer film takes place and resonance-enhanced X-rays (REX) are significantly intensified at a position close to the center of the film. Use of this mode also allowed us to reduce the scattering signals from both interfacial regions drastically. The viscosity (η) of the surrounding PS at the

topmost surface and the near-center region of the film can be independently extracted via the well-known Stoke-Einstein (SE) relation:

$$D = \frac{k_B T}{6\pi\eta R}, \tag{6.1}$$

where D is the diffusion constant of the markers, R is the radius of the markers, k_B is the Boltzmann constant, T is the absolute temperature. It should be noted that all the marker GIXPCS measurements on the PS films were performed at high temperatures (156 °C ≤ T ≤ 186 °C) under vacuum to avoid the hyperdiffusive dynamic behavior observed near T_g [121, 122]. The readers are referred to a recent review [98] for more details of the marker GIXPCS technique.

Table 6.1 summarizes the local viscosity of PS films (M_w = 123 kDa) in the surface mode (η_{sur}) and the center mode (η_{cen}) calculated from the D values using the Stoke-Einstein relation (Eq. 6.1). It is clear that for h (the thickness of the PS film) ≥ 128 nm, the viscosity values at the surface probed region are identical and approximately 30 % lower than those at the center region of the films. These results provide direct evidence of the reduced viscosity layer at the surface region of the single entangled PS melt films at temperatures far above T_g. Although the similar surface reduced viscosity layer is also found in the PS film with h = 57 nm, a slight increase in the η_{sur} value is observed. As the film thickness further decreases to 32 nm, the surface viscosity η_{sur} gets almost 2 orders of magnitude larger than that of the thicker films, indicating a significant slowing down of the polymer dynamics even at the surface region. In addition, the nanoparticle motion in the center region of the 32 nm thick films exhibited extremely slow dynamics, which could not be determined quantitatively within the time resolution of the technique. These results indicate that the η_{sur} value is perturbed by the substrate effect.

We further explored whether the change in the local η value is associated with the change in local T_g. Figure 6.8 shows the temperature dependence of the local viscosity for the 128 nm film (M_w = 123 kDa). The data was fit with the Williams-Landel-Ferry (WLF) equation,

$$\log\left(\frac{\eta(T)}{\eta(T_0)}\right) = -c\left(\frac{T - T_0}{T - T_\infty}\right), \tag{6.2}$$

Table 6.1 Measured diffusion coefficients of the Au nanoparticles and calculated viscosities of PS (M_w = 123 kDa) based on the SE law at the surface and the near-center of the films at 186 °C

h (nm)	D_{sur} (nm²/s)	D_{cen} (nm²/s)	η_{sur} (Ns/m²)	η_{cen} (Ns/m²)
32	0.016	–[a]	7.7×10^6	–[a]
57	6.58	0.76	1.8×10^4	1.6×10^5
128	7.80	5.30	1.5×10^4	2.2×10^4
235	7.84	5.42	1.5×10^4	2.2×10^4

[a]Ultraslow dynamics (the very weak $q_{//}$ dependence of the relaxation time)
Table reproduced from Ref. [46] with permission from American Physical Society
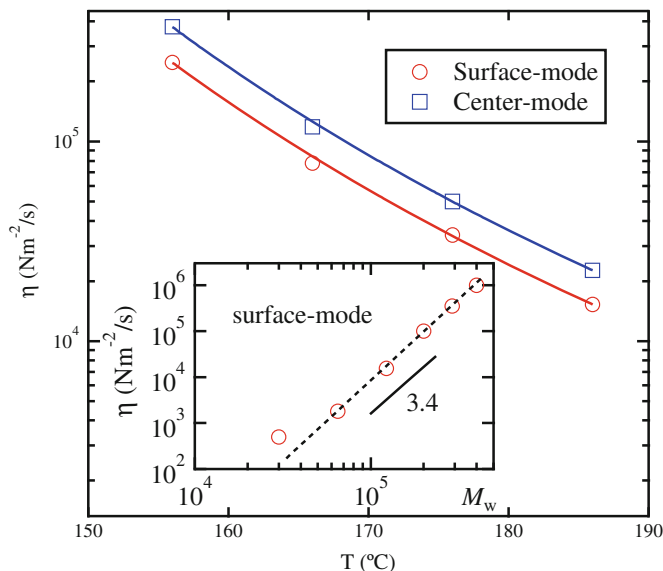
Fig. 6.8 Temperature dependences of the viscosity of the 128 nm-thick PS (M_w = 123 kDa)/Au film (*open symbols*). The *solid lines* correspond to the best-fits of the WLF equation (Eq. 6.2) to the data with c = 4.0 ± 0.5 and T_∞ = 42 ± 2 °C for the surface-mode and c = 4.0 ± 0.5 and T_∞ = 47 ± 2 °C for the center-mode, respectively. In the *inset*, a log-log plot of the viscosity of the PS/Au film against M_w of PS at T = 186 °C is shown. Figure reproduced from Ref. [97] with permission from American Physical Society

where T_0 is the chosen reference temperature, c is a numerical constant, and T_∞ is the fixed temperature at which log $(\eta(T)/\eta(T_0))$ diverges regardless of the arbitrary choice of T_0. Hence, the local T_g value at the surface and near the center region of the film can be estimated via the temperature scaling of viscosity with the WLF equation (i.e. the solid lines in Fig. 6.8). Interestingly, for the 128 nm thick film, the values of T_g (50 °C above T_∞ [123]) at the surface and near the center region of the 128 nm film were almost bulk-like ($\approx$ 100 °C). By using the temperature scaling of viscosity with the WLF equation (Eq. 6.2), the local T_g values at the surface and near the center of the 57 nm film were estimated to be 100 and 115 °C, respectively. However, the estimated local T_g values are inconsistent with the one reported by Ellison and Torkelson [4] who showed large decreases in T_g (32 °C below the bulk value) at the free surface of supported PS films with comparable thickness. Such discrepancy, as mentioned early by several authors [14, 99, 108, 124, 125], is possibly due to the fact that the well-established dynamic correlation between viscosity and T_g in bulk polymers (the value of T_g is strongly correlated with the time scale for segmental dynamics and the temperature dependences of the viscosity) may no longer be valid in nanoconfined systems [92, 95, 96]. Another explanation of such discrepancy is that the difference in the sample annealing protocol, which is one of the key factors that determines the irreversible adsorption of polymer chains at the solid interface, may possibly result in different values of

T_g [24]. In fact, the estimated bulk-like T_g or slightly increased T_g is somewhat in line with several other T_g studies in which the PS films were thermally annealed at $T \gg T_g$ for a long period of time [24, 25, 51, 93]. This again highlights the importance of the irreversible chain adsorption in the polymer dynamics near the solid interface that should be considered in future dynamical studies.

We now show how the formation of the adsorbed nanolayer plays a vital role in determining the local viscosity of PS thin films. To ensure the existence of the adsorbed nanolayer, all the PS/Au films were thoroughly rinsed with toluene, a good solvent for PS, after the marker GIXPCS experiments. Using XR, we found that an adsorbed PS nanolayer with a thickness of approximately 7 nm was formed on the HF etched Si substrates regardless of the original film thickness and M_w [46]. Note that this adsorbed nanolayer corresponds to the interfacial sublayer composed of both flattened chains and loosely adsorbed chains (Fig. 6.2). Since the thickness of the adsorbed nanolayer is only 7 nm, the ultraslow dynamics of the markers at the center of the 32 nm thick film is not directly linked to this "immobile" adsorbed nanolayer. This reminds us the presence of the so-called "reduced mobility interface (RMI) layer" [70, 126, 127] in between the unadsorbed chains in a matrix and the adsorbed layer via chain entanglements [128], which acts as a "transition zone" to ensure continuity in the mobility profile from the adsorbed nanolayer to the bulk. Hence, the effect of the adsorbed nanolayer propagates into the film interior via the RMI layer, leading to the long-range perturbations of the local viscosity. From the thickness dependence of the η_{sur} values, it is clear that the effect of the PS adsorbed nanolayer can propagate up to 60 nm from the substrate surface through the RMI layer, overwhelming the effect of the surface reduced viscosity layer.

6.4.3 Heterogeneous Crystalline Structures Induced by the Adsorbed Nanolayers

In Sect. 6.3.4, we showed that the loosely adsorbed chains were able to fold, forming the finger-like seaweed lamellar structures. The question then arises: what are the effects of the adsorbed chains on inner crystalline structures of supported thin polymer films. It is known that lamellar orientations near solid surfaces are controlled by several parameters, including chain mobility, crystallization temperature, film thickness, and interactions between polymers and substrates. A recent experimental study showed coexistence of different lamellar orientations (i.e., flat-on and edge-on) in a single poly(bisphenol A hexane ether) film under a fixed crystallization temperature [81]. Wang and co-workers explained the anomalous behavior by using a multi-layered T_g model considering different nucleation rates at the polymer-air and the polymer-solid interfaces. Hence, the key to control crystalline structures and lamellar orientations of supported ultrathin polymer films is the interplay between the top surface induced nucleation and bottom surface induced nucleation. However, the details still remain unclear.

By combining in situ grazing incidence small-angle X-ray scattering (GISAXS) and X-ray diffraction (GID), we aimed to clarify the interplay between these interfacial effects on local recrystallized structures of polymer thin films. Linear low-density polyethylene (LLDPE, bulk melting temperature (T_m) = 117 °C) films were prepared on HF-etched Si substrates (25, 50 and 100 nm in thickness) as a model system [49]. The two different incident angles below and above the critical angle of LLDPE were used for the measurements such that the crystalline structures at the topmost surface region ($\sim$ 9 nm in thickness, "surface mode") and the rest of the film ("film mode") are probed independently. Figure 6.9 shows the GISAXS
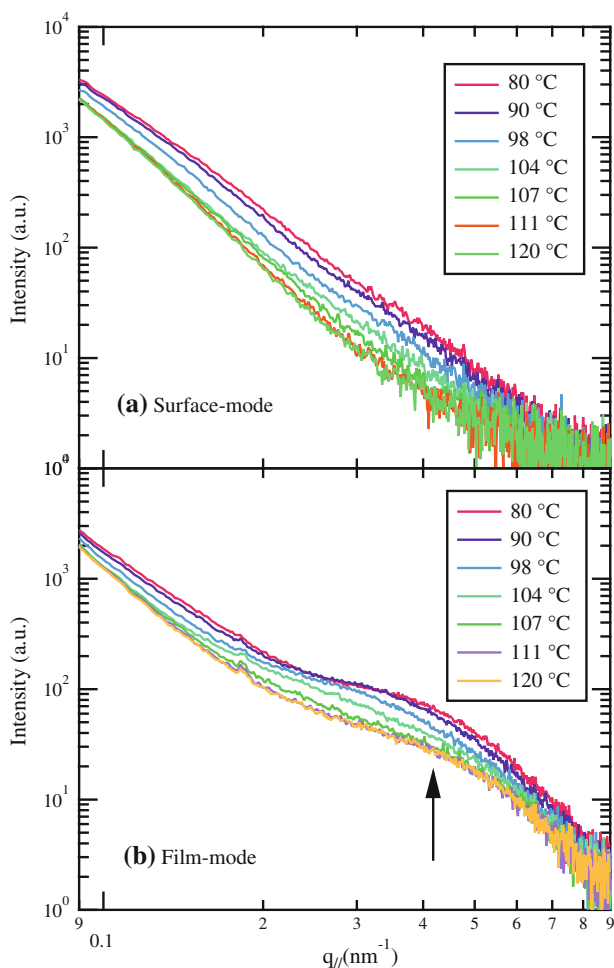
Fig. 6.9 GISAXS profiles for the 25 nm thick film with elevating temperature: **a** the surface-mode; **b** the film-mode. Figure reproduced from Ref. [49] with permission from American Chemical Society

profiles in the surface mode and film mode for the 25 nm thick LLDPE film. Note that before the GISAXS measurements, the presence of edge-on lamellar structures was confirmed at the surface of the film by using AFM. The GISAXS profiles in the film mode clearly show the broad scattering maximum corresponding to the interlamellar spacing, the so-called "long period" of the edge-on lamellae at around the lateral scattering vector ($q_{//}$) of 0.4 nm^{-1}, while no scattering peak is seen in the surface-mode. As the temperature increases, the peak position in the film mode shifts to the lower q-region at $T \leq T_{m}$. At the same time, the weak broad shoulder (indicated by the arrow) is observed in the film-mode even at $T > T_{m}$. This broad shoulder implies the persistence of an edge-on lamellar structure within the film even at $T > T_{m}$. The crystalline structures within the film are thus quite heterogeneous in the direction normal to the film surface. After the GISAXS experiments, we utilized Guiselin's approach to study the interfacial structure near the substrate. AFM measurements showed string-like structures [49] which resemble typical edge-on lamellar structures formed in ultrathin polymer films [81]. Hence, we conclude that the adsorbed nanolayer, which was not dissolved during the intensive washing process, is associated with the substrate-bound lamellar layer observed in the GISAXS profiles.

Although this preferential edge-on lamellar orientation at the Si substrate can be explained by the concept of minimization of the free energy during the primary nucleation step [73, 80], its formation mechanism has not been clarified. We propose that the substrate-bound lamellae are formed during the spin-coating of the hot polymer/toluene solutions onto heated Si substrates at around 150 °C. Spin-coating at high temperature was necessary to prevent immediate crystallization of the chains while forming films on the substrates. The spin-cast films were then rapidly quenched to room temperature, inducing crystallization of the polymer chains within the entire film. Although we pre-annealed the films at 150 °C for 24 h to erase the memory of the sample preparation before melt crystallization, the GISAXS results proved that this heating step is not sufficient to completely melt the bound lamellae formed near the substrate interface. Instead, the long high temperature pre-annealing would accelerate the growth of the adsorbed nanolayer and induce reorganization of the chain conformations deformed during the spin-coating process [21]. Since the structural relaxation of the polymer chains adsorbed onto solid substrates is typically very slow [20], the structures/properties of the adsorbed nanolayer are considered as metastable states with extremely long lifetime [24]. Hence, we suppose that the substrate-bound lamellar structure is also attributed to the metastable conformations associated with the reduced chain mobility.

These results provide insight into the formation process of the heterogeneous structures within supported ultrathin semicrystalline films. According to previous results where polymer chains were quenched from the melt to a low crystallization temperature [81], the nucleation is triggered at the polymer/air interface due to the surface mobile layer. However, it is not conclusive yet whether the surface mobile layer is present within a few tens of nanometer thick films prepared on the solid surfaces [46]. Instead, the present results indicate that the polymer/substrate interface plays a vital role in inducing the heterogeneous structures. As mentioned above, there

exists the RMI layer that acts as a transition zone ensuring continuity in the mobility profile from the substrate to the bulk through chain entanglements [70, 126, 127]. Napolitano et al. reported that the RMI layer of poly(ethylene terephthalate) thin films prepared on Al substrates is about 20 nm in thickness [129]. Noting that the extent of the RMI layer should depend on the strength of the substrate interactions and the flexibility of the polymer chains, it is reasonable to suppose that part or even the whole of the interior region of the 25 nm thick LLDPE film corresponds to the transition zone. We therefore postulate that the recrystallization is initiated from the substrate-bound lamellar layer as seeds, independently of the primary nucleation at the polymer/air interface. The polymer chains in the transition zone would then form the edge-on lamellae with the same orientation as for the substrate-bound lamellar layer in order to maximize the contacts, thereby stabilizing the interface [130]. Consequently, the surface disordering observed in the 25 nm thick film is attributed to the substrate effect induced by the substrate-bound lamellar layer. In fact, we found that the recrystallized structures and melting behavior at the surfaces of the 50 and 100 nm thick films recover to bulk (thick film)-like characteristics due to the effect of the surface mobile layer, while the substrate-bound lamellar layer is found to be formed regardless of the film thickness [49]. Hence, we conclude that this substrate effect is limited to the region within 50 nm from the solid interface.

The formation of the heterogeneous crystalline structures induced by the adsorbed nanolayer is more evident in ultrathin PEO thin films on Si [55]. As shown in the previous section, the loosely adsorbed PEO chains prefer the flat-on orientation on Si substrates due to the strong polymer-solid interaction. Figure 6.10 shows representative AFM height images and GID results for the thermally annealed PEO thin films (20 and 50 nm thick) recrystallized at 25 °C. From the AFM images, the surface of the 20 nm thick film crystallized into flat-on lamellar structures, while a sheaf-like morphology is observed for the 50 nm thick film. The latter indicates the formation of edge-on lamellae at the surface. The presence of the flat-on lamellae within the 20 nm thick-film was further confirmed by the GID results, where we can see the position of the (120) diffraction peak located along the q_{xy} axis. However, the (120) diffraction peak from the 50 nm-thick film shifts to the off-axis position and is rather azimuthally smeared. Combining the AFM results with the GID patterns, it is reasonable to conclude that the flat-on lamellae dominate the entire 20 nm thick film, while two lamellar geometries (i.e., the edge-on lamellae at the top surface and flat-on lamellae near the solid interface) coexist within the 50 nm thick film. Since the adsorbed PEO layer at the solid interface has a flat-on lamellar orientation [55], this adsorbed layer could also act as the seeds to initiate further growth of crystals with the same lamellar orientation into the film interior, as mentioned in the PE/Si system. It should also be noted that the melt crystallization process along with the adsorbed nanolayer is analogous to the "self-seeding" process for replicating polymer single crystals on Si substrates [131]. Based on the experimental results, the critical threshold above which the bulk behavior is recovered is estimated to be less than 50 nm. Further experiments are currently in progress to elucidate the correlation between the critical thickness and the strength of the interactions, the flexibility of the polymer chains, or the size of polymer chains.
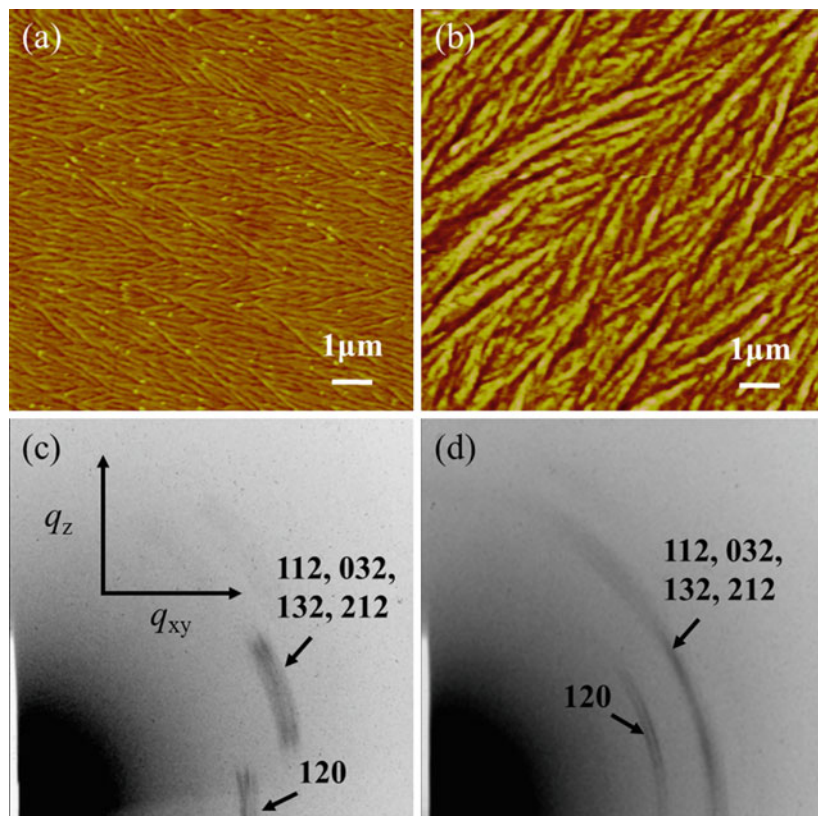
Fig. 6.10 AFM topographic images of the thermally annealed PEO thin films recrystallized at $T_{cr} = 25$ °C: **a** 20 nm; **b** 50 nm thick film. The corresponding two-dimensional GID results are shown in **c** for the 20 nm thick and **d** for the 50 nm thick, respectively. Figure reproduced from Ref. [55] with permission from The Royal Society of Chemistry

6.4.4 Are the Long Range Perturbations Modified in the Presence of a Solvent?

In parallel with thermal annealing, solvent annealing has been widely used as an alternative to process supported thin polymer films. Especially, the use of solvent vapor annealing has been shown to have a great advantage in controlling orientations of block copolymer thin films on solid surfaces [132]. However, an unsolved question arises: Are the long-range perturbations associated with the adsorbed layer facilitated or diluted in the presence of solvent molecules? To answer this question, using a high-pressure neutron reflectivity (NR) technique [133], we investigated the effect of CO_2 solvent annealing on the interdiffusive motion at the chemically identical polymer/polymer interface as a function of the distance from the substrate interface [134]. We used PS because (i) a wide variety of monodisperse

hydrogenated and deuterated PS are commercially available; (ii) the long-range perturbations on Si substrates have been characterized in melts [16, 17, 46]; (iii) the protocol to prepare the adsorbed layer has been established [48, 52]; (iv) the swelling [133, 135–138] and interdiffusion [139, 140] behavior of polymer thin films in CO_2 has been reported. It is known that sorption of CO_2 molecules into polymers plays a role as a diluent or plasticizer for glassy polymers by significantly lowering the glass transition temperature (T_g) and hence enhancing chain mobility [141–144]. At the same time, our previous studies have shown that the excess sorption of CO_2 molecules is induced within the narrow temperature and pressure regimes near the critical point of CO_2, known as the "density fluctuation ridge" [145], which results in the anomalous swelling of polymer films [133] and enhanced interdiffusion at the hydrogenated PS (h-PS)/deuterated PS (d-PS) interface even at temperatures below the bulk T_g [140].

Figure 6.11 summarizes the effective segment diffusion constant D_{eff} values for the h-PS (M_w = 650 kDa)/d-PS (M_w = 334 kDa) bilayers as a function of the initial film thickness of the bottom h-PS spin-cast films scaled by R_g (R_g is the radius of polymer gyration of the h-PS), while the thickness of the d-PS overlayers was fixed to $3R_g$. We chose the ridge condition of T = 36 °C and P = 8.2 MPa (i.e., the density fluctuation ridge condition) for all the interdiffusion experiments to maximize the plasticization effect of CO_2 [140]. The details of high-pressure NR experiments performed on the NG-7 horizontal reflectometer at the National Institute of Standards and Technology, Center for Neutron Research have been described elsewhere [133]. Based on the root-mean-square (RMS) roughness (σ) between the two layers, D_{eff} values were calculated. The diffusive motion gets extremely slow when the distance of the h-PS/d-PS interface is less than $1R_g$ from the substrate. This is due to the formation of an adsorbed PS nanolayer with $0.6R_g$ thick on the HF-etched Si substrate during the CO_2 annealing [134]. Hence, the adsorbed segments do interdiffuse with the free chains in CO_2, but the dynamics remains hindered due to the presence of the segment-solid contacts. The D_{eff} value was roughly doubled when the distance from the substrate increased from $1R_g$ to $2R_g$. At the
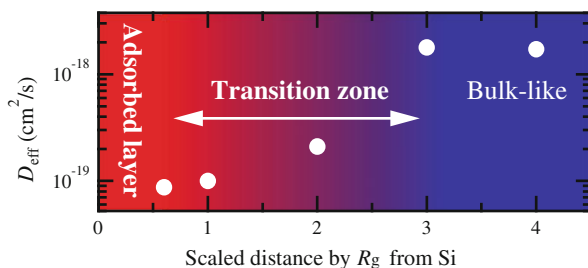
Fig. 6.11 D_{eff} values for the bilayers composed of the $3R_g$ thick d-PS (M_w = 334 kDa) overlayers on top of the h-PS (M_w = 650 kDa) spin cast films with the different scaled film thicknesses by R_g of the h-PS polymer. Figure reproduced from Ref. [134] with permission from American Chemical Society

distances beyond $3R_g$, the hindered chain dynamics at the polymer/polymer interface recovers the bulk diffusion, resulting in a sharp increase in D_{eff}. This finding indicates that the long-range perturbations far beyond the characteristic size of the unperturbed chain reported in the melts [17, 146] vanish in CO_2. Since the distance of $0.6R_g$ from the substrate corresponds to the thickness of the adsorbed layer, the effective transition zone in the mobility profile from the adsorbed nanolayer to the bulk is estimated to be about $2R_g$ thick in the density fluctuating CO_2 medium. Therefore, it is reasonable to suppose that the neighboring unadsorbed chains directly interacting with the adsorbed chains are the origin of the transition zone formed in CO_2. The present results thus reveal that the robust entanglements between the irreversibly adsorbed polymer chains and neighboring unadsorbed chains induce a critical threshold even in the presence of the effective plasticizer, while the polymer chains located at the distance of at least $3R_g$ from the substrate are freely entangled/disentangled with the neighboring unadsorbed chains in CO_2. Such unusual cohesion strength is possibly attributed to the formation of loops in the adsorbed chains, which would provide a structure with which unadsorbed polymer chains can entangle effectively [147, 148]. Further studies on the adhesive properties of multiply bound adsorbed chains compared to those of traditional singly bound polymer structures (i.e., polymer brushes) deserve future work.

6.5 Conclusions and Outlook

Recent research efforts have demonstrated that the formation of the adsorbed polymer nanolayers on solid substrates shows profound impact on the physical and mechanical properties of supported ultrathin polymer films. Since irreversible chain adsorption from the melts is a universal feature regardless of the magnitude of attractive segment/solid interactions, the formation of the adsorbed nanolayers is almost unavoidable when annealing a thin polymer film at $T \gg T_g$. This thermal annealing process is crucial for various fabrication processes of polymer based nanodevices and plays an essential role in controlling the morphologies and properties of the confined systems. We have also shown that similar irreversible polymer adsorption is induced by supercritical carbon dioxide as a plasticizer for glassy polymer thin films. Hence, it is of great importance to take into account the long-range effects in order to understand the emerging structures and properties of ultrathin polymer thin films. However, it should be emphasized that the existence of the free surface effects indicates that the topmost mobile (or reduced viscosity) layer serves to control many of the properties of polymer thin films. In addition, the free surface effect and substrate effect associated with the adsorbed nanolayer are often coupled together and difficult to distinguish from one another. Hence, new experimental strategies or techniques that enable us to directly and independently obtain structures/dynamics and properties at a region of interest in polymer thin films would be a key advancement for the development of new polymer nanostructures and nanoscale devices.

References

1. Geoghegan, M., Krausch, G.: Wetting at polymer surfaces and interfaces. Prog. Polym. Sci. **28**(2), 261–302 (2003)
2. Keddie, J.L., Jones, R.A.L., Cory, R.A.: Interface and surface effects on the glass-transition temperature in thin polymer-films. Faraday Discuss. **98**, 219–230 (1994)
3. Keddie, J.L., Jones, R.A.L., Cory, R.A.: Size-dependent depression of the glass-transition temperature in polymer-films. Europhys. Lett. **27**(1), 59–64 (1994)
4. Ellison, C.J., Torkelson, J.M.: The distribution of glass-transition temperatures in nanoscopically confined glass formers. Nat. Mater. **2**, 695–700 (2003)
5. Fakhraai, Z., Forrest, J.A.: Probing slow dynamics in supported thin polymer films. Phys. Rev. Lett. **95**, 025701 (2005)
6. Roth, C.B., McNerny, K.L., Jager, W.F., Torkelson, J.M.: Eliminating the enhanced mobility at the free surface of polystyrene: Fluorescence studies of the glass transition temperature in thin bilayer films of immiscible polymers. Macromolecules **40**(7), 2568–2574 (2007)
7. Tsui, O.K.C., Russell, T.P.: Polymer thin films. World Scientific, Singapore (2008)
8. Ediger, M.D., Forrest, J.A.: Dynamics near free surfaces and the glass transition in thin polymer films: a view to the future. Macromolecules **47**(2), 471–478 (2014)
9. Hu, H.W., Granick, S.: Viscoelastic dynamics of confined polymer melts. Science **258**, 1339–1342 (1992)
10. Masson, J.L., Green, P.F.: Viscosity of entangled polystyrene thin film melts: film thickness dependence. Phys. Rev. E. **65**(3) (2002)
11. O'Connell, P.A., McKenna, G.B.: Rheological measurements of the thermoviscoelastic response of ultrathin polymer films. Science **307**(5716), 1760–1763 (2005)
12. Bodiguel, H., Fretigny, C.: Reduced viscosity in thin polymer films. Phys. Rev. Lett. **97**, 266105 (2006)
13. Li, C.H., Kim, H.J., Jiang, J., Li, C., Koga, T., Lurio, L., Schwarz, S., Narayanan, S., Lee, H. J., Lee, Y.J., Jiang, Z., Sinha, S., Rafailovich, M.H., Sokolov, J.C.: The effect of surface interactions on the viscosity of polymer thin films. Europhys. Lett. **73**(6), 899–905 (2006)
14. Bodiguel, H., Fretigny, C.: Viscoelastic properties of ultrathin polystyrene films. Macromolecules **40**(20), 7291–7298 (2007)
15. Fakhraai, Z., Forrest, J.A.: Measuring the surface dynamics of glassy polymers. Science **319** (5863), 600–604 (2008)
16. Zheng, X., Sauer, B.B., Vanalsten, J.G., Schwarz, S.A., Rafailovich, M.H., Sokolov, J., Rubinstein, M.: Reptation dynamics of a polymer melt near an attractive solid interface. Phys. Rev. Lett. **74**(3), 407–410 (1995)
17. Zheng, X., Rafailovich, M.H., Sokolov, J., Strzhemechny, Y., Schwarz, S.A., Sauer, B., B., Rubinstein, M.: Long-range effects on polymer diffusion induced by a bounding interface. Phys. Rev. Lett. **79**, 241–244 (1997)
18. Priestley, R.D., Ellison, C., Broadbelt, L.J., Torkelson, J.M.: Structural relaxation of polymer glasses at surfaces, interfaces, and in between. Science **309**, 456–459 (2005)
19. Tang, Q., Hu, W., Napolitano, S.: Slowing down of accelerated structural relaxation in ultrathin polymer films. Phys. Rev. Lett. **112**(14), 148306 (2014)
20. Barbero, D.R., Steiner, U.: Nonequilibrium Polymer Rheology in Spin-Cast Films. Phys. Rev. Lett. 102(24) (2009)
21. Thomas, K.R., Chenneviere, A., Reiter, G., Steiner, U.: Nonequilibrium behavior of thin polymer films. Phys. Rev. E **83**(2), 021804 (2011)

22. Paeng, K., Swallen, S.F., Ediger, M.D.: Direct measurement of molecular motion in freestanding polystyrene thin films. J. Am. Chem. Soc. **133**(22), 8444–8447 (2011)
23. Fujii, Y., Yang, Z.H., Leach, J., Atarashi, H., Tanaka, K., Tsui, O.K.C.: Affinity of polystyrene films to hydrogen-passivated silicon and its relevance to the T-g of the films. Macromolecules **42**(19), 7418–7422 (2009)
24. Napolitano, S., Wübbenhorst, M.: The lifetime of the deviations from bulk behaviour in polymers confined at the nanoscale. Nat. Commun. **2**, 260 (2011)
25. Napolitano, S., Rotella, C., Wübbenhorst, M.: Can thickness and interfacial interactions univocally determine the behavior of polymers confined at the nanoscale? ACS Macro Lett. **1** (10), 1189–1193 (2012)
26. Fleer, G.J.: Polymers at Interfaces. Springer, New York (1993)
27. Scheutjens, J.M.H.M., Fleer, G.J.: Statistical theory of the adsorption of interacting chain molecules. 2. Train, loop, and tail size distribution. J. Phys. Chem. **84**(2), 178–190 (1980)
28. O'Shaughnessy, B., Vavylonis, D.: Non-equilibrium in adsorbed polymer layers. J. Phys. Condens. Mat. **17**(2), R63–R99 (2005)
29. Schneider, H.M., Frantz, P., Granick, S.: The bimodal energy landscape when polymers adsorb. Langmuir **12**(4), 994–996 (1996)
30. Douglas, J.F., Schneider, H.M., Frantz, P., Lipman, R., Granick, S.: The origin and characterization of conformational heterogeneity in adsorbed polymer layers. J. Phys. Condens. Mat. **9**(37), 7699–7718 (1997)
31. O'Shaughnessy, B., Vavylonis, D.: Irreversible adsorption from dilute polymer solutions. Eur. Phys. J. E **11**(3), 213–230 (2003)
32. O'Shaughnessy, B., Vavylonis, D.: Irreversibility and polymer adsorption. Phys. Rev. Lett. **90**(5), 056103 (2003)
33. Simha, R., Frisch, H.L., Eirich, F.R.: The adsorption of flexible macromolecules. J. Phys. Chem. **57**(6), 584–589 (1953)
34. Scheutjens, J.M.H.M., Fleer, G.J.: Statistical theory of the adsorption of interacting chain molecules. 1. Partition function, segment density distribution, and adsorption isotherms. J. Phys. Chem. **83**(12), 1619–1635 (1979)
35. Scheutjens, J.M.H.M., Fleer, G.J.: Interaction between two adsorbed polymer layers. Macromolecules **18**(10), 1882–1900 (1985)
36. Aubouy, M., Guiselin, O., Raphaël, E.: Scaling description of polymer interfaces: flat layers. Macromolecules **29**(22), 7261–7268 (1996)
37. Guiselin, O.: Irreversible adsorption of a concentrated polymer solution. Europhys. Lett. **17** (3), 225–230 (1992)
38. Bitsanis, I., Hadziioannou, G.: Molecular-dynamics simulations of the structure and dynamics of confined polymer melts. J. Chem. Phys. **92**(6), 3827–3847 (1990)
39. Zajac, R., Chakrabarti, A.: Irreversible polymer adsorption from semidilute and moderately dense solutions. Phys. Rev. E **52**(6), 6536–6549 (1995)
40. Linse, P.: Effect of solvent quality on the polymer adsorption from bulk solution onto planar surfaces. Soft Matter **8**(19), 5140–5150 (2012)
41. Linse, P., Källrot, N.: Polymer adsorption from bulk solution onto planar surfaces: effect of polymer flexibility and surface Attraction in good solvent. Macromolecules **43**(4), 2054–2068 (2010)
42. Källrot, N., Linse, P.: Dynamics of Competitive polymer adsorption onto planar surfaces in good solvent. J. Phys. Chem. B **114**(11), 3741–3753 (2010)
43. Källrot, N., Dahlqvist, M., Linse, P.: Dynamics of polymer adsorption from Bulk solution onto planar surfaces. Macromolecules **42**(10), 3641–3649 (2009)
44. Källrot, N., Linse, P.: Dynamic Study of single-chain adsorption and desorption. Macromolecules **40**(13), 4669–4679 (2007)
45. Durning, C.J., O'Shaughness, B., Sawhney, U., Nguyen, D., Majewski, J., Smith, G.S.: Adsorption of poly(methyl methacrylate) melts on quartz. Macromolecules **32**(20), 6772–6781 (1999)

46. Koga, T., Jiang, N., Gin, P., Endoh, M.K., Narayanan, S., Lurio, L.B., Sinha, S.K.: Impact of an irreversibly adsorbed layer on local viscosity of nanoconfined polymer melts. Phys. Rev. Lett. **107**(22), 225901 (2011)

47. Rotella, C., Napolitano, S., Vandendriessche, S., Valev, V.K., Verbiest, T., Larkowska, M., Kucharski, S., Wübbenhorst, M.: Adsorption kinetics of ultrathin polymer films in the melt probed by dielectric spectroscopy and second-harmonic generation. Langmuir **27**(22), 13533–13538 (2011)

48. Gin, P., Jiang, N., Liang, C., Taniguchi, T., Akgun, B., Satija, S.K., Endoh, M.K., Koga, T.: Revealed architectures of adsorbed Polymer chains at solid-polymer melt interfaces. Phys. Rev. Lett. **109**(26), 265501 (2012)

49. Asada, M., Jiang, N., Sendogdular, L., Gin, P., Wang, Y., Endoh, M.K., Koga, T., Fukuto, M., Schultz, D., Lee, M., Li, X., Wang, J., Kikuchi, M., Takahara, A.: Heterogeneous lamellar structures near the polymer/substrate interface. Macromolecules **45**(17), 7098–7106 (2012)

50. Vanroy, B., Wübbenhorst, M., Napolitano, S.: Crystallization of thin polymer layers confined between two adsorbing walls. ACS Macro Lett. **2**(2), 168–172 (2013)

51. Napolitano, S., Capponi, S., Vanroy, B.: Glassy dynamics of soft matter under 1D confinement: How irreversible adsorption affects molecular packing, mobility gradients and orientational polarization in thin films. Eur. Phys. J. E **36**(6), 1–37 (2013)

52. Jiang, N., Shang, J., Di, X., Endoh, M.K., Koga, T.: Formation mechanism of high-density, flattened polymer nanolayers adsorbed on planar solids. Macromolecules **47**(8), 2682–2689 (2014)

53. Martínez-Tong, D.E., Vanroy, B., Wübbenhorst, M., Nogales, A., Napolitano, S.: Crystallization of poly(l-lactide) confined in ultrathin films: competition between finite size effects and irreversible chain adsorption. Macromolecules **47**(7), 2354–2360 (2014)

54. Housmans, C., Sferrazza, M., Napolitano, S.: Kinetics of irreversible chain adsorption. Macromolecules **47**(10), 3390–3393 (2014)

55. Asada, M., Jiang, N., Sendogdular, L., Sokolov, J., Endoh, M.K., Koga, T., Fukuto, M., Yang, L., Akgun, B., Dimitriou, M., Satija, S.: Melt crystallization/dewetting of ultrathin PEO films via carbon dioxide annealing: the effects of polymer adsorbed layers. Soft Matter **10**(34), 6392–6403 (2014)

56. Pefferkorn, E., Haouam, A., Varoqui, R.: Thermodynamic and kinetic factors in adsorption of polymers on a plane lattice. Macromolecules **21**(7), 2111–2116 (1988)

57. Pefferkorn, E., Haouam, A., Varoqui, R.: Kinetics of exchange between adsorbed and free polymers at a solid liquid interface. Macromolecules **22**(6), 2677–2682 (1989)

58. Fu, Z., Santore, M.: Effect of layer age and interfacial relaxations on the self-exchange kinetics of poly(ethylene oxide) adsorbed on silica. Macromolecules **32**(6), 1939–1948 (1999)

59. Frantz, P., Granick, S.: Infrared dichroism, chain flattening, and the bound fraction histogram in adsorbed poly(methyl methacrylate) layers. Macromolecules **28**(20), 6915–6925 (1995)

60. Granick, S.: Perspective: kinetic and mechanical properties of adsorbed polymer layers. Eur. Phys. J. E **9**(1), 421–424 (2002)

61. Seeck, O.H., Kaendler, I.D., Tolan, M., Shin, K., Rafailovich, M.H., Sokolov, J.C., Kolb, R.: Appl. Phys. Lett. **76**, 2713 (2000)

62. Koga, T., Seo, Y.S., Jerome, J., Ge, S., Rafailovich, M.H., Sokolov, J.C., Chu, B., Seeck, O. H., Tolan, M., Kolb, R.: Appl. Phys. Lett. **83**, 4309 (2003)

63. Buenviaje, C., Ge, S., Rafailovich, M., Sokolov, J., Drake, J.M., Overney, R.M.: Confined flow in polymer films at interfaces. Langmuir **15**(19), 6446–6450 (1999)

64. Schneider, H.M., Granick, S.: Kinetic traps in polymer adsorption: exchange of polystyrene between the adsorbed state and a good solvent. Macromolecules **25**(19), 5054–5059 (1992)

65. Feder, J., Giaever, I.: Adsorption of ferritin. J. Colloid. Interf. Sci. **78**(1), 144–154 (1980)

66. Fu, Z., Santore, M.M.: Evolution of layer density and thickness during poly (ethylene oxide) adsorption onto silica. Langmuir **13**(21), 5779–5781 (1997)

67. Johnson, H.E., Granick, S.: New mechanism of nonequilibrium polymer adsorption. Science **255**(5047), 966–968 (1992)
68. Soga, I., Granick, S.: Flow-induced deformation and desorption of adsorbed polymers. Langmuir **14**(15), 4266–4271 (1998)
69. Douglas, J.F., Johnson, H.E., Granick, S.: A simple kinetic-model of polymer adsorption and desorption. Science **262**(5142), 2010–2012 (1993)
70. vanZanten, J.H., Wallace, W.E., Wu, W.L.: Effect of strongly favorable substrate interactions on the thermal properties of ultrathin polymer films. Phys. Rev. E **53**(3), R2053–R2056 (1996)
71. Priestley, R.D., Ellison, C.J., Broadbelt, L.J., Torkelson, J.M.: Structural relaxation of polymer glasses at surfaces, interfaces and in between. Science **309**(5733), 456–459 (2005)
72. Massa, M.V., Carvalho, J.L., Dalnoki-Veress, K.: Confinement effects in polymer crystal nucleation from the bulk to few-chain systems. Phys. Rev. Lett. **97**(24), 247802 (2006)
73. Wang, Y., Ge, S., Rafailovich, M., Sokolov, J., Zou, Y., Ade, H., Lüning, J., Lustiger, A., Maron, G.: Crystallization in the thin and ultrathin films of poly(ethylene–vinyl acetate) and linear low-density polyethylene. Macromolecules **37**(9), 3319–3327 (2004)
74. Schönherr, H., Frank, C.W.: Ultrathin films of poly(ethylene oxides) on oxidized silicon. 1. Spectroscopic characterization of film structure and crystallization kinetics. Macromolecules **36**(4), 1188–1198 (2003)
75. Schönherr, H., Frank, C.W.: Ultrathin films of poly(ethylene oxides) on oxidized silicon. 2. In situ study of crystallization and melting by hot stage AFM. Macromolecules **36**(4), 1199–1208 (2003)
76. Reiter, G., Sommer, J.-U.: Crystallization of adsorbed polymer monolayers. Phys. Rev. Lett. **80**(17), 3771–3774 (1998)
77. Massa, M.V., Dalnoki-Veress, K., Forrest, J.A.: Crystallization kinetics and crystal morphology in thin poly(ethylene oxide) films. Eur. Phys. J. E **11**(2), 191–198 (2003)
78. Sommer, J.-U., Reiter, G.: The formation of ordered polymer structures at interfaces: a few intriguing aspects. In: Vancso, G.J. (ed.) Ordered Polymeric Nanostructures at Surfaces. Advances in Polymer Science, vol. 200, pp. 1–36. Springer, Berlin Heidelberg (2006)
79. Ma, Y., Hu, W., Reiter, G.: Lamellar crystal orientations biased by crystallization kinetics in polymer thin films. Macromolecules **39**(15), 5159–5164 (2006)
80. Yang, J.P., Liao, Q., Zhou, J.J., Jiang, X., Wang, X.H., Zhang, Y., Jiang, S.D., Yan, S.K., Li, L.: What determines the lamellar orientation on substrates? Macromolecules **44**(9), 3511–3516 (2011)
81. Wang, Y., Chan, C.M., Ng, K.M., Li, L.: What controls the lamellar orientation at the surface of polymer films during crystallization? Macromolecules **41**(7), 2548–2553 (2008)
82. Zhu, D.-S., Liu, Y.-X., Chen, E.-Q., Li, M., Chen, C., Sun, Y.-H., Shi, A.-C., Van Horn, R. M., Cheng, S.Z.D.: Crystal Growth mechanism changes in pseudo-dewetted poly(ethylene oxide) thin layers. Macromolecules **40**(5), 1570–1578 (2007)
83. Despotopoulou, M., Frank, C., Miller, R., Rabolt, J.: Kinetics of chain organization in ultrathin poly (di-n-hexylsilane) films. Macromolecules **29**(18), 5797–5804 (1996)
84. Napolitano, S., Wübbenhorst, M.: Slowing down of the crystallization kinetics in ultrathin polymer films: a size or an interface effect? Macromolecules **39**(18), 5967–5970 (2006)
85. Napolitano, S., Prevosto, D., Lucchesi, M., Pingue, P., D'Acunto, M., Rolla, P.: Influence of a reduced mobility layer on the structural relaxation dynamics of aluminum capped ultrathin films of poly(ethylene terephthalate). Langmuir **23**, 2103–2109 (2007)
86. Napolitano, S., Wübbenhorst, M.: Effect of a reduced mobility layer on the interplay between molecular relaxations and diffusion-limited crystallization rate in ultrathin polymer films. J. Phys. Chem. B **111**(21), 5775–5780 (2007)
87. Capitán, M.J., Rueda, D.R., Ezquerra, T.A.: Inhibition of the crystallization in nanofilms of poly(3-hydroxybutyrate). Macromolecules **37**(15), 5653–5659 (2004)
88. Kovacs, A.J.: Glass transition in amorphous polymer: phenomenological study. Adv. Polym. Sci. **3**, 394–508 (1964)

89. Li, Y., Ishida, H.: A study of morphology and intercalation kinetics of polystyrene–organoclay nanocomposites. Macromolecules **38**(15), 6513–6519 (2005)
90. Yin, H.J., Napolitano, S., Schonhals, A.: Molecular mobility and glass transition of thin films of poly(bisphenol a carbonate). Macromolecules **45**(3), 1652–1662 (2012)
91. Tress, M., Mapesa, E.U., Kossack, W., Kipnusu, W.K., Reiche, M., Kremer, F.: Glassy dynamics in condensed isolated polymer chains. Science **341**(6152), 1371–1374 (2013)
92. Fukao, K., Miyamoto, Y.: Glass transitions and dynamics in thin polymer films: dielectric relaxation of thin films of polystyrene. Phys. Rev. E **61**(2), 1743–1754 (2000)
93. Tress, M., Erber, M., Mapesa, E.U., Huth, H., Müller, J., Serghei, A., Schick, C., Eichhorn, K.-J., Voit, B., Kremer, F.: Glassy Dynamics and glass transition in nanometric thin layers of polystyrene. Macromolecules **43**(23), 9937–9944 (2010)
94. Boucher, V.M., Cangialosi, D., Yin, H., Schonhals, A., Alegria, A., Colmenero, J.: T g depression and invariant segmental dynamics in polystyrene thin films. Soft Matter **8**(19), 5119–5122 (2012)
95. Priestley, R.D., Cangialosi, D., Napolitano, S.: On the equivalence between the thermodynamic and dynamic measurements of the glass transition in confined polymers. J. Non-Cryst. Solids **407**, 288–295 (2015)
96. Kremer, F., Tress, M., Mapesa, E.U.: Glassy dynamics and glass transition in nanometric layers and films: a silver lining on the horizon. J. Non-Cryst. Solids **407**, 277–283 (2015)
97. Koga, T., Li, C., Endoh, M.K., Koo, J., Rafailovich, M., Narayanan, S., Lee, D.R., Lurio, L. B., Sinha, S.K.: Reduced viscosity of the free surface in entangled polymer melt films. Phys. Rev. Lett. **104**(6) (2010)
98. Jiang, N., Endoh, M.K., Koga, T.: 'Marker' grazing-incidence X-ray photon correlation spectroscopy: a new tool to peer into the interfaces of nanoconfined polymer thin films. Polymer J **45**(1) (2013)
99. Yang, Z.H., Clough, A., Lam, C.H., Tsui, O.K.C.: Glass transition dynamics and surface mobility of entangled polystyrene films at equilibrium. Macromolecules **44**(20), 8294–8300 (2011)
100. Yang, Z.H., Fujii, Y., Lee, F.K., Lam, C.H., Tsui, O.K.C.: Glass transition dynamics and surface layer mobility in unentangled polystyrene films. Science **328**(5986), 1676–1679 (2010)
101. Yang, Z.H., Lam, C.H., DiMasi, E., Bouet, N., Jordan-Sweet, J., Tsui, O.K.C.: Method to measure the viscosity of nanometer liquid films from the surface fluctuations. Appl. Phys. Lett. **94**(25) (2009)
102. Qi, D., Fakhraai, Z., Forrest, J.A.: Substrate and chain size dependence of near surface dynamics of glassy polymers. Phys. Rev. Lett. **101**(9) (2008)
103. Chai, Y., Salez, T., McGraw, J.D., Benzaquen, M., Dalnoki-Veress, K., Raphaël, E., Forrest, J.A.: A direct quantitative measure of surface mobility in a glassy polymer. Science **343** (6174), 994–999 (2014)
104. McGraw, J.D., Salez, T., Bäumchen, O., Raphaël, E., Dalnoki-Veress, K.: Self-similarity and energy dissipation in stepped polymer films. Phys. Rev. Lett. **109**(12), 128303 (2012)
105. Salez, T., McGraw, J., Cormier, S., Bäumchen, O., Dalnoki-Veress, K., Raphaël, E.: Numerical solutions of thin-film equations for polymer flows. Eur. Phys. J. E **35**(11), 1–9 (2012)
106. Ilton, M., Qi, D., Forrest, J.A.: Using nanoparticle embedding to probe surface rheology and the length scale of surface mobility in glassy polymers. Macromolecules **42**(18), 6851–6854 (2009)
107. Daley, C.R., Fakhraai, Z., Ediger, M.D., Forrest, J.A.: Comparing surface and bulk flow of a molecular glass former. Soft Matter **8**(7), 2206–2212 (2012)
108. Qi, D., Ilton, M., Forrest, J.A.: Measuring surface and bulk relaxation in glassy polymers. Eur. Phys. J. E **34**(6) (2011)
109. Teichroeb, J.H., Forrest, J.A.: Direct imaging of nanoparticle embedding to probe viscoelasticity of polymer surfaces. Phys. Rev. Lett. **91**(1) (2003)

110. Kim, H., Ruhm, A., Lurio, L.B., Basu, J.K., Lal, J., Lumma, D., Mochrie, S.G.J., Sinha, S. K.: Surface dynamics of polymer films. Phys. Rev. Lett. **90**(6) (2003)
111. Kim, H., Ruhm, A., Lurio, L.B., Basu, J.K., Lal, J., Mochrie, S.G.J., Sinha, S.K.: X-ray photon correlation spectroscopy on polymer films with molecular weight dependence. Phys. B **336**(1–2), 211–215 (2003)
112. Mochrie, S.G.J., Lurio, L.B., Ruhm, A., Lumma, D., Borthwick, M., Falus, P., Kim, H.J., Basu, J.K., Lal, J., Sinha, S.K.: X-ray photon correlation spectroscopy studies of colloidal diffusion and the capillary modes of polymer films. Phys. B **336**(1–2), 173–180 (2003)
113. Kim, H., Ruhm, A., Lurio, L.B., Basu, J.K., Lal, J., Mochrie, S.G.J., Sinha, S.K.: Synchrotron radiation studies of the dynamics of polymer films. J. Phys. Condens. Mat. **16** (33), S3491–S3497 (2004)
114. Jiang, Z., Kim, H., Jiao, X., Lee, H., Lee, Y.J., Byun, Y., Song, S., Eom, D., Li, C., Rafailovich, M.H., Lurio, L.B.: Sinha, S.K.: Evidence for viscoelastic effects in surface capillary waves of molten polymer films. Phys. Rev. Lett. **98**(22) (2007)
115. Kim, H., Jiang, Z., Lee, H., Lee, Y.J., Jiao, X.S., Li, C.H., Lurio, L., Rafailovich, M., Sinha, S.K.: Hydrodynamic surface fluctuations of polymer films by coherent X-ray scattering. Thin Solid Films **515**(14), 5536–5540 (2007)
116. Jiang, Z., Mukhopadhyay, M.K., Song, S., Narayanan, S., Lurio, L.B., Kim, H., Sinha, S.K.: Entanglement effects in capillary waves on liquid polymer films. Phys. Rev. Lett. **101**(24) (2008)
117. Li, C.H., Koga, T., Jiang, J., Sharma, S., Narayanan, S., Lurio, L.B., Hu, Y., Jiao, X., Sinha, S.K., Billet, S., Sosnowik, D., Kim, H., Sokolov, J.C., Rafailovich, M.H.: Viscosity measurements of very thin polymer films. Macromolecules **38**(12), 5144–5151 (2005)
118. Yee, C.K., R., J., A., U., H., W., A., K., M., R., J., S.: Novel one-phase synthesis of thiol-fuctionalized gold, palladium, and iridium nanoparticles using superhydride. Langmuir **15**, 3486–3491 (1999)
119. Jiang, Z.: X-ray scattering studies of structure and dynamics of surfaces and interfaces of polymeric liquids. In: Ph.D. dissertation, vol. b5455306. University of California, San Diego (2007)
120. Wang, J., Bedzyk, M.J., Caffrey, M.: Resonance-enhanced X-rays in thin-films—a structure probe for membranes and surface-layers. Science **258**(5083), 775–778 (1992)
121. Guo, H.Y., Bourret, G., Corbierre, M.K., Rucareanu, S., Lennox, R.B., Laaziri, K., Piche, L., Sutton, M., Harden, J.L., Leheny, R.L.: Nanoparticle motion within glassy polymer melts. Phys. Rev. Lett. **102**(7) (2009)
122. Narayanan, S., Lee, D.R., Hagman, A., Li, X.F., Wang, J.: Particle dynamics in polymer-metal nanocomposite thin films on nanometer-length scales. Phys. Rev. Lett. **98** (18) (2007)
123. Ferry, J.D.: Viscoelastic properties of polymers. Wiley, New York (1980)
124. Bodiguel, H., Fretigny, C.: Reduced viscosity in thin polymer films. Phys. Rev. Lett. **97**(26) (2006)
125. Rathfon, J.M., Cohn, R.W., Crosby, A.J., Rothstein, J.P., Tew, G.N.: Confinement effects on chain entanglement in free-standing polystyrene ultrathin films. Macromolecules **44**(13), 5436–5442 (2011)
126. Wallace, W.E., Vanzanten, J.H., Wu, W.L.: Influence of an impenetrable interface on a polymer glass-transition temperature. Phys. Rev. E **52**(4), R3329–R3332 (1995)
127. Napolitano, S., Wübbenhorst, M.: Dielectric signature of a dead layer in ultrathin films of a nonpolar polymer. J. Phys. Chem. B **111**(31), 9197–9199 (2007)
128. Bruinsma, R.: Slow spreading of polymer melts. Macromolecules **23**(1), 276–280 (1990)
129. Napolitano, S., Prevosto, D., Lucchesi, M., Pingue, P., D'Acunto, M., Rolla, P.: Influence of a reduced mobility layer on the structural relaxation dynamics of aluminum capped ultrathin films of poly(ethylene terephthalate). Langmuir **23**(4), 2103–2109 (2007)
130. Zhang, F., Baralia, G.G., Nysten, B., Jonas, A.M.: Melting and van der Waals stabilization of PE single crystals grown from ultrathin films. Macromolecules **44**(19), 7752–7757 (2011)

131. Xu, J., Ma, Y., Hu, W., Rehahn, M., Reiter, G.: Cloning polymer single crystals through self-seeding. Nat. Mater. **8**(4), 348–353 (2009)
132. Sinturel, C., Vayer, M., Morris, M., Hillmyer, M.A.: Solvent vapor annealing of block polymer thin films. Macromolecules **46**(14), 5399–5415 (2013)
133. Koga, T., Seo, Y.S., Shin, K., Zhang, Y., Rafailovich, M.H., Sokolov, J.C., Chu, B., Peiffeer, D., Satija, S.K.: The role of elasticity in the anomalous swelling of polymer thin films in density fluctuating supercritical fluids. Macromolecules **36**, 5236–5343 (2003)
134. Jiang, N., Sendogdular, L., Di, X., Sen, M., Gin, P., Endoh, M.K., Koga, T., Akgun, B., Dimitriou, M., Satija, S.: Effect of CO2 on a mobility gradient of polymer chains near an impenetrable solid. Macromolecules **48**(6), 1795–1803 (2015)
135. Koga, T., Seo, Y.S., Zhang, Y., Sin, K., Kusano, K., Nishikawa, K., Rafailovich, M.H., Sokolov, J.C., Chu, B., Peiffer, D., Occhiogrosso, R., Satija, S.K.: Phys. Rev. Lett. **89**, 125506 (2002)
136. Koga, T., Ji, Y., Seo, Y.S., Rafailovich, M.H., Sokolov, J.C., Satija, S.K. J. Polym. Sci., Part B: Polym. Phys. **42**, 3282 (2004)
137. Li, Y., park, E., Lim, K., Johnston, K.P., Green, P.F.: Role of interfacial interactions on the anomalous swelling of polymer thin films in supercritical carbon dioxide. J. Polym. Sci., Part B: Polym. Phys. **45**, 1313–1324 (2007)
138. Chebil, M.S., Vignaud, G., Grohens, Y., Konovalov, O., Sanyal, M.K., Beuvier, T., Gibaud, A.: In situ X-ray reflectivity study of polystyrene ultrathin films swollen in carbon dioxide. Macromolecules **45**(16), 6611–6617 (2012)
139. Gupta, R.R., Lavery, K.A., Francis, T.J., Webster, J.R.P., Smith, G.S., Russell, T.P., Watkins, J.J.: Self-diffusion of polystyrene in a CO_2-swollen polystyrene matrix: a real time study using neutron reflectivity. Macromolecules **36**(2), 346–352 (2002)
140. Koga, T., Seo, Y.S., Hu, X., Kwanwoo, S., Zhang, Y., Rafailovich, M.H., Sokolov, J.C., Chu, B., Satija, S.K.: Dynamics of polymer thin films in supercritical carbon dioxide. Europhys. Lett. **60**, 559–565 (2002)
141. Wissinger, R.G., Paulaitis, M.E.: Swelling and sorption in polymer-CO_2 mixtures at elevated pressures. J. Poly. Sci. Polym. Phys. Ed. **25**, 2497–2510 (1987)
142. Goel, S.K., Beckman, E.J.: Plasticization of poly(methyl methacrylate) networks by supercritical carbon dioxide. Polymer **34**, 1410–1417 (1993)
143. McHugh, M.A., Krukonis, V.: Supercritical fluids extraction principles and practice. Woburn, MA (1994)
144. Condo, P.D., Paul, D.R., Johnston, K.P.: Glass transitions of polymers with compressed fluid diluents: Type II and III behavior. Macromolecules **27**, 365–371 (1994)
145. Nishikawa, K., Tanaka, I., Amemiya, Y.: Small-angle X-ray scattering study of supercritical carbon dioxide. J. Phys. Chem. **100**, 418–421 (1996)
146. Frank, B., Gast, A.P., Russell, T.P., Brown, H.R., Hawker, C.J.: Polymer mobility in thin films. Macromolecules **29**(20), 6531–6534 (1996)
147. Huang, Z.Y., Ji, H.N., Mays, J.W., Dadmun, M.D.: Understanding the grafting of telechelic polymers on a solid substrate to form loops. Macromolecules **41**(3), 1009–1018 (2008)
148. Patton, D., Knoll, W., Advincula, R.C.: Polymer loops vs. brushes on surfaces: adsorption, kinetics, and viscoelastic behavior of alpha, omega-thiol telechelics on gold. Macromol. Chem. Phys. **212**(5), 485–497 (2011)

Chapter 7
Irreversibly Adsorbed Layer in Supported Ultrathin Polymer Film Investigated by Local Dielectric Spectroscopy

Hung Kim Nguyen, Daniele Prevosto, Massimiliano Labardi, Simone Capaccioli and Mauro Lucchesi

Abstract Polymer chains can adsorb onto a solid substrate without the formation of chemical bonds. Because this mechanism of adsorption is driven by the weak dipolar interactions and requires simultaneous pinning of many repeating units of the chain, its kinetics can be extremely slow, especially for polymer melt. As a consequence, polymer chains at the interface with a substrate can reside for very long times in non-equilibrium states, before reaching the equilibrium configuration. Remarkably, recent works verified that the deviations from the bulk behavior in the dynamics of nanoconfined polymers are strongly affected by those non-equilibrium configurations assumed in adsorbed layers. In this Chapter, we report experimental evidences on the existence of an irreversibly adsorbed layer in poly(vinyl acetate) (PVAc) films in contact with different substrates. The presence of such a layer is proved through atomic force microscopy imaging of the residual layer remaining on the substrate after washing the polymer film in a good solvent. Moreover, we demonstrate that the evolution of the irreversibly adsorbed layer is unambiguously related to the change in relaxation dynamics of polymer films under annealing at a high temperature ($\sim T_g + 60$ K). Finally, we demonstrate the direct effect of this adsorbed layer on the maximum moisture uptake of supported ultrathin PVAc films, hence providing a simple approach for controlling the moisture absorption of the nanosized polymer films.

H.K. Nguyen
WPI-Advanced Institute for Materials Research, Tohoku University, 2-1-1 Katahira, Aoba, Sendai 980-8577, Japan

D. Prevosto (✉) · M. Labardi · S. Capaccioli
Institute for Chemical and Physical Processes, CNR-IPCF, Largo B. Pontecorvo 3, Pisa 56127, Italy
e-mail: prevosto@df.unipi.it

S. Capaccioli · M. Lucchesi
Department of Physics, University of Pisa, Largo B. Pontecorvo 3, Pisa 56127, Italy

7.1 Introduction

Glass-forming materials are intrinsically in a thermodynamically non-equilibrium state. Because of their structural disorder, this condition persists even below the melting temperature, T_m, where the crystalline state is the one minimizing free energy [1]. When heated above the glass transition temperature, T_g ($<T_m$), a lower energy metastable state (supercooled liquid) is reached in a short time, typically <100 s. Unless the material undergoes cold crystallization, this disordered state can survive for infinitely long time [1]. In the glassy state, below T_g, different non-equilibrium thermodynamic states can be reached depending on the thermo-dynamic history of the material. In this regime, the system evolves through different metastable configurations towards lower and lower energy states, within timescales that can be of few minutes, hours or reach years [2]. The evolution toward the lowest energy state, usually named physical aging, is accompanied by structural rearrangements of molecules and changes in physical properties affecting the performance of glassy materials.

When considering nanostructured polymers, such as ultrathin films or interfacial polymer layers, the picture gets more complicated. For example, chain conformations at the interface with a metal evolve in time because of local reconfigurations upon adsorption. Large experimental evidence demonstrated that adsorption of melts and solutions takes place at timescales like those for molecular relaxation [3–16]. As a consequence, the presence of non-equilibrium metastable states evolving over time scales of hours has been evidenced both in the case of adsorption from solution and from melt [14, 15, 17–20]. Moreover, chain config-urations can be altered during the preparation of the films, for example by spin coating; in case of confinement in regions smaller or comparable to the equilibrium chain dimension, finite size effects perturbing chain organization induce the sta-bilization of new configurations, not observed in bulk melts; similarly, chains at the free surface or at the interface with another material can assume different equilib-rium conformations with respect to the bulk, due to the presence of specific interfacial interactions. Whether some peculiar properties of confined polymers are intrinsic in the physics of these systems or they are determined simply by prepa-ration procedure is strongly debated in literature (see for example [21–32]).

When studying spin-coated ultrathin polymer films, an annealing procedure is usually needed to remove solvent and residual stresses. However, in the second half of the last decade, it has been observed that, during annealing at $T > T_g$, some physical properties of ultrathin (few tens on nm thick) films keep on changing over long time scales (days) [21]. Apparently ultrathin films behave as annealing over days at at $T >$ bulk T_g is not sufficient to reach equilibrium configurations. This behavior was unexpected since, on the basis of the knowledge of bulk materials, it is well known that characteristic times of molecular mobility, and hence timescale of diffusion, drop easily in the range of ms when temperature is raised few tens of degrees above T_g. Moreover, in many cases T_g of ultrathin film is smaller than the bulk. Instead, Serghei et al. reported that in PVAc Al-capped 13 nm thick films the

(negative) shift of the dynamic glass transition, T_α, was reduced from 6 to 2.5 K after 63 h at $\sim T_g + 60$ K (see details in Ref. [21]). In another experiment Barbero et al. observed recovery of bulk-like viscosity of PS films after annealing at $T_g + 55$ K for 145 h [20]. It is noteworthy that in both cases annealing times are much longer than any conventional time scale used to determine physical processes of polymers such as the structural relaxation or reptation times at the annealing temperatures.

Napolitano and coworkers in 2011 reported a detailed investigation of the evolution of confinement-induced variations of T_g for ultrathin PS films with annealing and they explained the observed behavior in terms of formation of irreversibly adsorbed polymer layers, i.e. Guiselin brushes [5], at the interface with the substrate [33].

In the case of ultrathin films, irreversibly adsorbed layers can develop during the annealing at $T > T_g$ at the polymer substrate interface. Although the presence of such a phenomenon was well known, its relevance on physical properties of ultrathin film has been investigated only recently [30, 33–41]. Moreover, irreversible adsorption occurs also in nanocomposite materials, at the polymer/inorganic nanoparticle interface, possibly affecting reinforcement, gas barrier and other material properties [7, 13, 42–44]. Studying the effects of the irreversibly adsorbed layer on polymer properties is thus important not only to achieve a better understanding on nanoconfinement effects on dynamics, but also to provide some opportunities in tuning physical properties of ultrathin polymer films in various nanotechnology applications.

In this contribution, we employ local dielectric spectroscopy (LDS), a method recently used to characterize relaxation dynamics of ultrathin polymer films at nanometer scale [45–47], to study the evolution of irreversibly adsorbed layers in poly(vinyl acetate) films deposited on different solid substrates, i.e. aluminum, gold and silicon, under annealing above the T_g [30, 41, 48]. After describing the setup and sample preparation in Sect. 7.2, we present, in Sect. 7.3, our results on the growth of the layer as a function of the interfacial interaction. The influence of the adsorbed layer on the relaxation dynamics of nano-confined PVAc films and their capacity to absorb moisture in various degrees of relative humidity is studied in details.

7.2 Experiment Setup

7.2.1 LDS

Dielectric relaxation behavior of materials is commonly addressed by Broadband Dielectric Spectroscopy (BDS), where a parallel plate capacitor is filled with the material under study, and sinusoidal (ac) currents are measured after application of a sinusoidal potential, yielding the electrical impedance in a frequency range that

can extend from 10^{-3} to 10^7 Hz. In such a geometry, where the sample is subjected to a uniform electric field, the complex capacitance $C^*(\omega)$ is related to the dielectric function $\varepsilon(\omega)$ as $C^*(\omega) = \varepsilon(\omega)C_0$, where C_0 is the void capacitance. This technique provides the average response of an extended slab of material. To address the response of a nanoscopic volume or to study interfacial regions, a smaller electrode is necessary. In the last years, our laboratory developed a powerful setup to achieve this goal. We use as electrode the force sensor of an atomic force microscope (AFM), which is is usually a cantilever spring (spring constant k) with a pyramidal or conical tip attached to it. The apex radius R of the tip can be as small as a few nanometers. If the probe is coated by a conductive layer, it can be used as a nanoscopic electrode. In AFM the tip can be controlled in contact or at a distance z from the sample surface. Local impedance measurements are possible in this configuration [49]; however, the capacitance of this system might be too small to provide measurable currents. LDS was introduced and first applied to detect local fluctuations of dynamical polarization on a PVAc surface [45]. In this setup an electric force is measured instead of a current, exploiting the very high sensitivity of AFM in force detection. The charge driven on the tip by the applied potential induces polarization of the sample in a small interaction volume, whose extension is of the order of the tip apex radius. The situation is depicted in Fig. 7.1.

The electrostatic force, F_z, in z (normal) direction is given by:

$$F_z = \frac{1}{2}\frac{\partial C}{\partial z}(V_{CPD} - V)^2 \tag{7.1}$$

where C is the system capacitance, and V and V_{CPD} are the applied potential and the contact potential difference between tip and sample surface. The capacitance depends on the tip position as well as on the sample dielectric properties in the vicinity of the tip. If a sinusoidal electric potential $V(t) = V_{\mathrm{dc}} + V_0\cos(\omega t)$ at frequency ω is applied, the resulting force has the form

$$F_{el} = F_{dc} + F_\omega \cos(\omega t) + F_{2\omega}\cos(2\omega t) \tag{7.2}$$
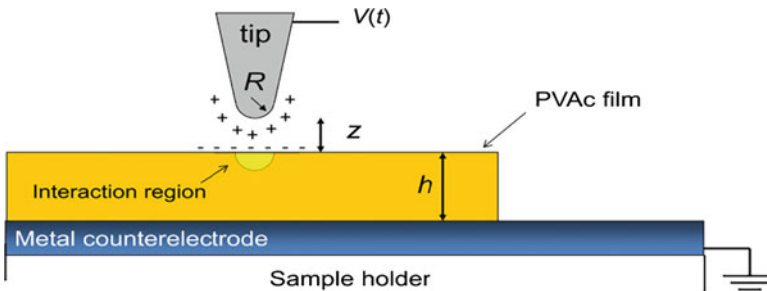
Fig. 7.1 Sketch of the LDS measurement configuration

where

$$F_{dc} = \frac{1}{2}\frac{\partial C}{\partial z}\left[(V_{CPD} - V_{dc})^2 + \frac{1}{2}V_0^2\right]$$

$$F_\omega = -\frac{\partial C}{\partial z}(V_{CPD} - V_{dc})V_0$$

$$F_{2\omega} = \frac{1}{4}\frac{\partial C}{\partial z}V_0^2$$

Measurement of components at the fundamental (ω) and second-harmonic (2ω) modulation frequency can be carried out by phase-sensitive detectors, such as lock-in amplifiers. The second-harmonic component does not depend on V_{CPD}, while the fundamental component can be nulled by application of a $V_{dc} = V_{CPD}$. Therefore, both local capacitance gradient and contact potential difference can be determined.

By sweeping the frequency of the applied ac voltage, dielectric spectra can be obtained similarly to BDS, although LDS has a more limited frequency range (10^{-1}-10^5 Hz) because of the mechanical nature of the measurement involved. Nevertheless, two main features motivate LDS employment: (1) nanometer lateral resolution can be achieved, enabling us to select regions of the surface with different characteristics as well as to detect heterogeneous properties due to the material spatial inhomogeneity or to the presence of interfaces in blended or nanocomposite systems [47, 50]; (2) dielectric relaxation of ultrathin films (down to a few nanometers) can be studied without concerns of possible short circuits between the polarizing electrodes, that could instead happen in BDS with the extended metal plates delimiting the ultrathin film.

Besides such advantages, the interpretation of LDS data is not as straightforward as in BDS, since here the capacitance does not depend linearly on the dielectric function. In fact, the asymmetry of tip shape causes the applied field to be highly asymmetric, concentrated near the tip and departing in radial direction from it. Therefore, a suitable model correlating the system capacitance to the dielectric function must be assumed. Computer simulation validates the following simple model for tip/sample distance much smaller than the tip radius, $z \ll R$ [51]

$$F_{el} = F_{macro} - \pi\varepsilon_0 V^2 \frac{R}{z + \frac{h}{\varepsilon}}$$

where F_{macro} indicates all the contributions from different parts of the probe to the electrostatic force, except for the tip apex. Indeed, the long range of the electrostatic force can lead to large backgrounds in dielectric measurements, which may prevent resolution enhancement. Improved models for the tip/sample capacitance have been also proposed to extend the validity to larger distance [52].

An effective strategy to increase the resolution of LDS measurements is the measurement of force z-gradients [53], reducing the probed volume because of the

smaller decay range. Additionally, if the AFM sensor is resonantly oscillated along z, force gradients induce a shift of its resonance frequency f_0, that can be conveniently measured e.g. by lock-in techniques. Such a frequency shift, provided that oscillation amplitude is much smaller than the force gradient decay range, amounts to

$$\Delta f_0 = -\frac{f_0}{2k}\frac{\partial F_{el}}{\partial z} \tag{7.3}$$

A convenient quantity measured by LDS is the loss tangent $\tan\delta_v$, defined as

$$\tan\delta_v = \frac{\mathrm{Im}[\Delta f_0^{2\omega}]}{\mathrm{Re}[\Delta f_0^{2\omega}]} \tag{7.4}$$

where

$$\Delta f_0^{2\omega} = -\frac{f_0}{2k}\frac{\partial F_{2\omega}}{\partial z} = -\frac{f_0}{8k}\frac{\partial^2 C}{\partial z^2}V_0^2 \tag{7.5}$$

implying that δ_v only depends on the capacitance $C(z)$. In the application to characterize relaxation dynamics of polymers, the Havriliak-Negami, HN, function [54]

$$\varepsilon_{HN}(\omega) = \varepsilon_\infty + \frac{\Delta\varepsilon}{(1 + (i\omega\tau)^\alpha)^\beta} \tag{7.6}$$

gives a well-accepted phenomenological description of experimental spectra related to a relaxation process in terms of a relaxation time τ, a dielectric strength $\Delta\varepsilon$, and two shape parameters α and β, where ε_∞ is the dielectric constant at high frequency. Each relaxation process shows up as a peak in dielectric loss spectra $\tan\delta = \mathrm{Im}[\varepsilon]/\mathrm{Re}[\varepsilon]$ obtained by BDS. Loss tangent spectra obtained by LDS have a similar meaning, but their shape, and in particular their peak maximum frequency v_{max}, will generally be different. However, fitting of Havriliak-Negami function to the LDS experimental data, by application of the proper tip/sample capacitance model, is used to provide dielectric parameters that have the same meaning, and therefore can be compared, to the macroscopic ones.

7.2.2 Sample Preparation

Poly(vinyl acetate) (PVAc) with molecular weight $M_w = 350$ kg/mol, polydispersity index PDI = 2.80 was purchased from Scientific Polymer Products, Inc, whereas the sample with $M_w = 167$ kg/mol was purchased from Sigma-Aldrich. The estimated values of the gyration radius for these two polymers are $R_g \sim 17$ nm and ~ 12 nm, respectively [55]. Ultrathin PVAc films were prepared by spin-coating toluene

solutions of PVAc onto three different substrates: gold, silicon and aluminium. 30 nm thick gold layers were obtained by thermal evaporation on glass disks previously evaporated with a $\sim$5 nm adhesion layer of chromium, whereas 50 nm thick aluminium layers were directly evaporated onto glass disks. Silicon substrates were obtained from standard monocrystalline, doped Si(100) wafers for micro-electronics use. The roughness of substrate surfaces was measured by atomic force microscopy (AFM) in tapping mode, resulting 0.3, 0.45, and 1.5 nm RMS on Si, gold and aluminium, respectively. PVAc films with thickness ranging from 8 to 233 nm were obtained by properly changing the concentration of polymer solutions as well as the spinning speed. Prior to spin-coating, contact angles of water on each substrate were measured at room temperature using a KSV CAM 200 optical contact angle meter.

After spin-coating and before LDS measurement, each polymer film was annealed at 323 K ($\sim T_g$ + 15 K) under vacuum ($<10^{-1}$ mbar) for about 3 days. Such annealing procedure was performed for a time period much longer than any characteristic time scale of bulk polymer dynamics at the treatment temperature and it is sufficient to reach negligible values of solvent and absorbed moisture concentration. In fact, we verified that films with thickness of 233 nm have the same T_g as bulk samples after such annealing [41].

Long times non-equilibrium states due to the evolution of irreversibly adsorbed layers at the substrate interface were studied by further annealing the samples at 366 K ($\sim T_g$ + 60 K) under vacuum at different time steps, up to about ten days.

The influence of irreversibly adsorbed layers on plasticization due to moisture adsorption was investigated in PVAc ultrathin films with different contents of moisture. In order to obtain an equilibrium value of absorbed moisture, PVAc films were kept at fixed conditions of ambient humidity and temperature for at least 4 h before each measurement. This time was considered sufficient to reach the equilibrium of the moisture absorption process. In fact, we have verified that the time needed to reach the equilibrium state in bulk PVAc upon humidity exposure is about 4 h for grains with average diameter of about 1 mm. It is expected that this time should be much shorter for ultrathin PVAc films due to a larger fraction of surface area to volume in an ultrathin film compared to the bulk sample, and to its smaller thickness.

7.2.3 Sample Characterization

Dielectric relaxation of supported polymer films was measured for dry as well as wet samples by using the LDS method. A Veeco Multimode AFM (Nanoscope IIIa with ADC5 extension) was adapted to a frequency-modulated electrostatic force microscope (FM-EFM) and operated in lift mode (details are reported in Refs. [41, 47]) FM-EFM with improved bandwidth was here implemented through a RHK Technology PLLProII phase-locked-loop (PLL) frequency detector, having a nominal response bandwidth of 4 kHz that could be extended to about 10 kHz by

appropriate setting of internal filters and DAC sampling rates. In essence, such bandwidth indicates the limit frequency at which the PLL detector is able to follow a rapid change of the resonant frequency of the AFM cantilever. The latter frequency is made to shift by the effect of the electric force gradient induced by biasing of the tip. Such gradient is proportional to the term $\mathrm{d}^2C/\mathrm{d}z^2$, where C is the tip/sample capacitance, as reported in Sect. 7.2.1. For electric excitation and acquisition of dielectric spectra, an external dual-phase lock-in amplifier (SRS SR830DSP) was used, controlled through a GPIB interface by a home-made LabView routine. Oscillation amplitude of the cantilever was calibrated as customary by AFM tapping mode amplitude/distance curves. By this way, the distance between the AFM tip and the sample surface during the electric measurements was calculated by summing the average tip-sample distance on tapping mode with the set-lift height. For all dielectric measurements, the tip/sample distance was estimated around 20 nm.

LDS was operated in controlled humidity within a homemade enclosure that allows one to obtain a relative humidity as low as 3 % by using desiccants and flowing nitrogen gas through the enclosure, and as high as 80 % by placing a dish full of distilled water inside the enclosure and discontinuing the nitrogen flow. The temperature of the ambient around the sample was stable for all our measurements within a range ± 3 K around 300 K. This introduces an uncertainty on the amount of absorbed water much smaller than the variation due to the imposed change of RH and can consequently be neglected. On the basis of ambient temperature bulk data, in this RH interval, the PVAc sample is expected to absorb up to a maximum of 3 % w/w of water. The sample temperature was controlled using a thermal application controller (TAC, Veeco Instruments, Inc.). The actual temperature on the sample surface was measured using a PT100 sensor.

The presence and the thickness of irreversibly adsorbed layer were studied according to a procedure defined by Guiselin [5]. A spin coated polymer film is washed for several minutes in the same solvent used for the initial solution so that the non-adsorbed chains are removed and only those irreversibly adsorbed remain on the substrate. The thickness of the residual layer was measured via the analysis of AFM tapping mode images performed with the same instrument as for LDS measurements.

7.3 Experimental Results

7.3.1 Interface Effects on Relaxation Dynamics in PVAc

Using LDS we measured dielectric response of polymer films with thickness ranging from a few to hundreds of nanometers, over four orders of magnitude in frequency. Despite the early claims for a sensitivity of the technique to the surface only [45, 56], it is now clear that the technique is sensitive also to the sample in
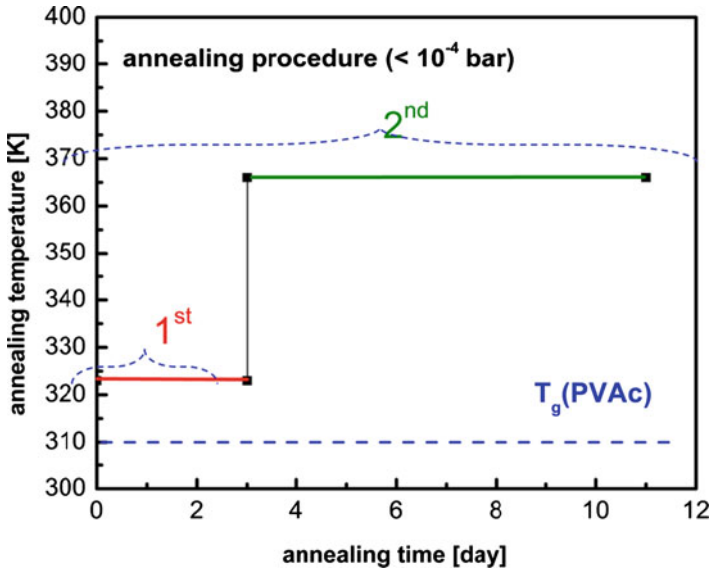
Fig. 7.2 Thermal histories used to anneal PVAc ultrathin films

depth, at least to thickness of about 100 nm when AFM probes with apical radius of 30 nm or larger are used [57]. This sensitivity guarantees that the effect on the relaxation dynamics of the evolution of metastable states in the proximity of interfaces with the substrate due to annealing can be detected in ultrathin polymer films with thickness smaller than 100 nm. Before going into the details, we recall the main results of our investigation about the thickness and substrate effects on relaxation dynamics in PVAc ultrathin films. Measurements herein reported are made on samples annealed in vacuum at $T_g + 15$ K for about 3 days (first annealing, Fig. 7.2). As previously pointed out, LDS spectra qualitatively resemble standard dielectric loss spectra, showing the presence of a peak whose characteristic frequency decreases on decreasing temperature (Fig. 7.3). In Fig. 7.3 the tangent of electric phase shift angle δ_v is presented for a rather thick film. Although the tan δ_v spectra presented in Fig. 7.3 look similar to those commonly measured by standard BDS, the two quantities differ because tan δ_v in LDS contains information on the geometry of the capacitor formed by the tip-sample-substrate system.

In Fig. 7.4 some simulated LDS spectra are reported. The curves are calculated using Eqs. (7.4), (7.5) and (7.6) and for the capacitance the equation proposed by L. Fumagalli and co-workers [52]. tanδ_v curves are calculated for different values of tip-sample distance and sample thickness, but the same dielectric function $\varepsilon(\omega)$, described by a HN(Eq. 7.6) with parameters values $\alpha = 0.7$, $\beta = 0.3$, $\varepsilon_\infty = 3.5$ $\Delta\varepsilon = 6$, $\tau = 0.43$ s, resembling those of bulk PVAc. The simulation is performed with a symmetric tip having aperture angle of $\pi/6$ rad. Although the relaxation properties of the material are always the same, it can be noted that the peak
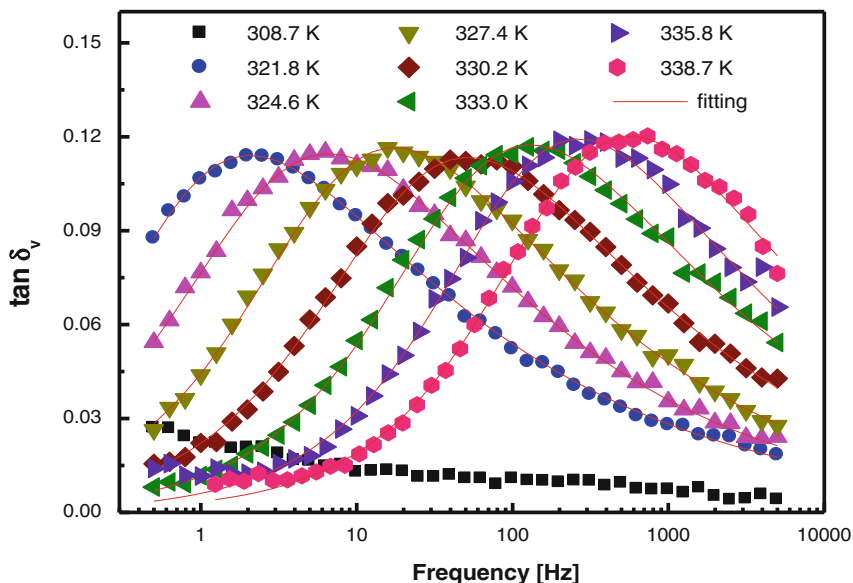
Fig. 7.3 LDS frequency spectra for different values of temperatures on a 233 nm thick PVAc film. Continuous lines are fitting obtained with the procedure described in the text. Reproduced from Ref. [41] with permission from American Chemical Society

frequency (and intensity) changes by varying tip-sample distance z from $R/5$ to $2R$, where R (= 25 nm) is the radius of the tip (Fig. 7.4a). On the other hand, the peak frequency is unaffected when the film thickness h is varied within the range $R/5 < h < 7R/5$ (Fig. 7.4b). Simulations on more extended interval of values of thicknesses by Miccio et al. [58] showed an effect on the peak frequency, not observed in our studies [41]. These results evidence two facts: if LDS spectra are fitted with a superposition of HN functions, as usually done for standard dielectric spectra, an erroneous interpretation of the results can emerge especially when comparison of relaxation frequency is performed with the bulk; in the region where usually confinement effects appear (less than 50 nm), the variation of tip-sample-substrate capacitance with sample thickness does not affect the peak frequency of LDS spectra.

In order to consider geometry effects and extract the parameters characterizing the dielectric function, $\varepsilon(\omega)$, we developed a fitting program with an optimization algorithm in Matlab. Details are reported elsewhere [41]. As a confirmation of the reliability of this procedure, we verified that values of maximum frequency, v_{max}, estimated with this procedure in 137 nm thick films are the same as those obtained from standard dielectric spectroscopy (Fig. 7.5).
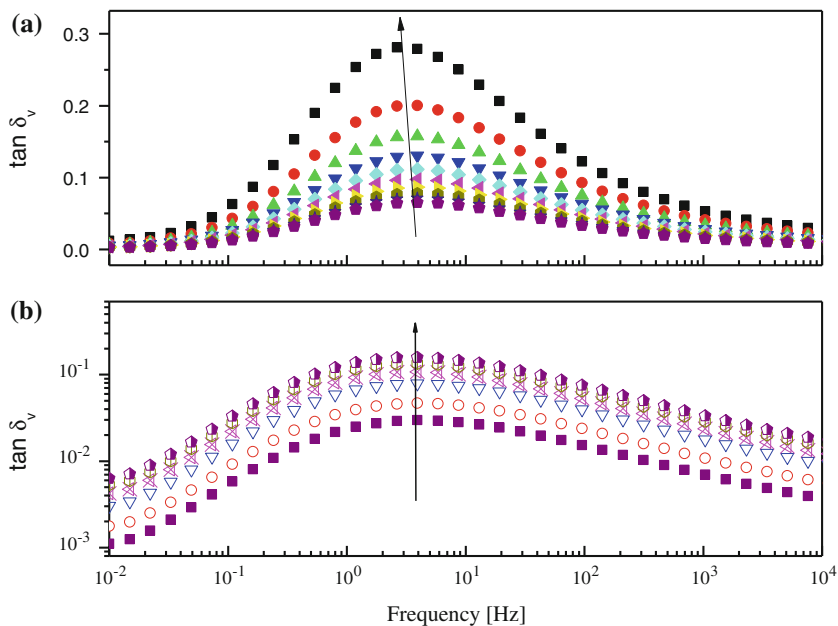
Fig. 7.4 Simulation of LDS spectra for a polymeric film **a** with constant thickness and different values of tip-surface distance, z, ranging from $R/5$ to $2R$ from higher to lower intensity peak, see text for details; **b** same value of z and different values of thickness, h, ranging from $R/5$ to $7R/5$ from lower to higher intensity peaks, see text for details. Arrows indicate the peak frequency

By decreasing the film thickness, we observed a small but systematic increase of v_{max} for film prepared on Au and Al substrates (Fig. 7.5c, d), whereas no deviation from the bulk was observed on Si-supported films with thicknesses as small as 12 nm (Fig. 7.5b). Comparing the values obtained for films prepared on different substrates we have evidenced that relaxation dynamics of samples thinner than 30 nm slow down with the increase of the interfacial energy between the polymer and supporting substrate. The variation of relaxation dynamics can be related to a decrease of the glass transition temperature, that usually is estimated as the temperature where $v_{max} = 1/(200\pi)$. Since LDS spectra do not allow estimation of such a long characteristic time, in order to avoid extrapolation of the temperature dependence of $v_{\max}$ over many decades, we used the characteristic temperature of the dynamic glass transition at 1 s, T_α, the value such that $v_{\max}(T_\alpha) = 1/(2\pi)$. In this aspect, we observed that T_α changes with respect to the bulk for about 2 K at most (Fig. 7.6). This value is small if compared with the variations observed in ultrathin film of polystyrene, but it is comparable to that found in other polymers [59–61]. The difference of about a factor two in the shift of T_α herein reported and that reported in Refs. [59, 60] could be explained by the presence of only one metal/polymer interface in LDS experiment instead of the two interfaces of the others. At this level of information, a tight connection among interfacial energy, γ,
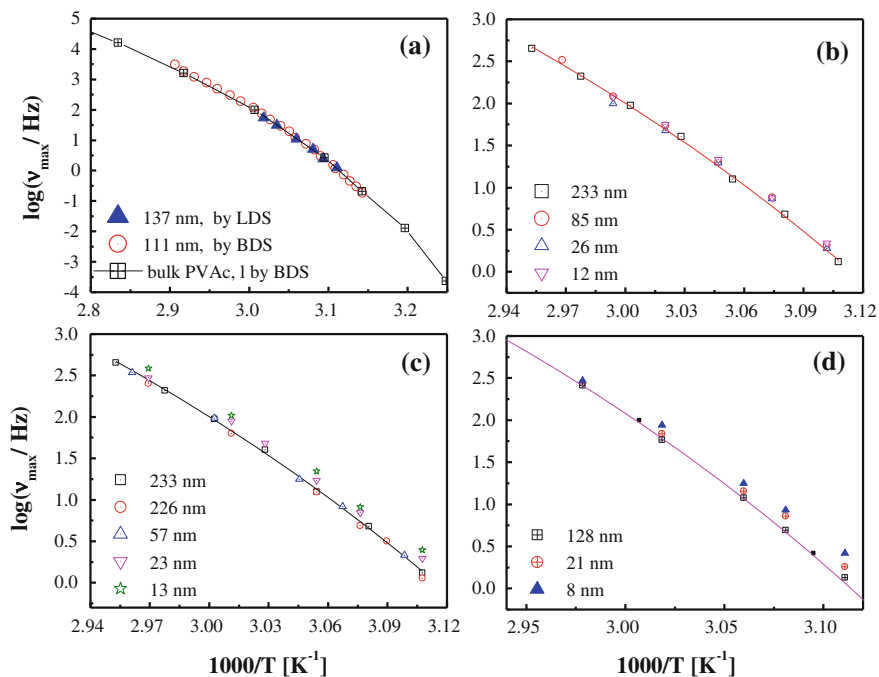
Fig. 7.5 Arrhenius map reporting the logarithm of maximum frequency of the dielectric relaxation as a function of inverse temperature for **a** PVAc bulk (from Ref 59) and 111 nm thick (from Ref. 46) film measured by conventional dielectric spectroscopy, 137 nm thick film measured by LDS (this work); ultrathin films of different thicknesses (see legend) on **b** Si, **c** Al, **d** Au substrates. Readapted from Ref. [41] with permission from American Chemical Society

and deviation of dynamics could be suggested, in agreement with some literature on other materials [62]. In fact, several data confirm that dynamics become faster on decreasing film thickness for γ smaller than a threshold value, whereas above such threshold the dynamics becomes slower (inset Fig. 7.6).

7.3.2 Evolution of Polymer Metastable States at Polymer/Solid Interface

Here we discuss the results of the investigation of the formation of an irreversibly adsorbed layer in PVAc films supported on the three substrates, i.e. Al, Au and Si under the two steps of annealing reported in Fig. 7.2. We prepared, on each of the three substrates, several PVAc films with similar thickness. Each of them was subjected to a first annealing at 323 K for 3 days (first annealing Fig. 7.2), and then one film for each substrate was taken as reference. After that, the other samples were further annealed at 366 K ($\sim T_g + 60$ K) for several periods up to a maximum
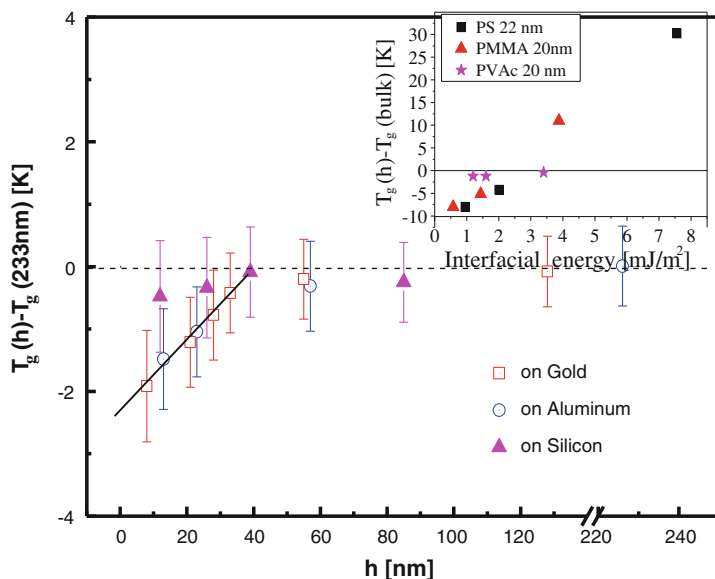
Fig. 7.6 Thickness dependence of the characteristic temperature T_α for PVAc film with $M_w = 350$ kg/mol. Reproduced from Ref. [41] with permission from American Chemical Society

of 10 days. To examine the presence of an irreversibly adsorbed layer after these annealing steps, we rinsed and soaked the polymer films in the toluene (a good solvent of PVAc) for ∼10 min. Finally, we gently scratched the surface with a blade to remove a part of the adsorbed polymer and expose some of the substrate. The residual layer was characterized by AFM topographic image, imaging the region at the border between the exposed substrate and the film.

When imaging the sample rinsed after the first annealing, it was impossible to find out the ridge of the scratch (Fig. 7.7a). Just to exclude the possibility that the scratch was not formed, the topographic image was analyzed in terms of roughness compared with that of the substrate as produced. For example, the roughness, r_{RMS}, of the as-produced Au substrate is about 0.45 nm, and 0.4 nm after rinsing the sample. For the Al substrate we found a roughness $r_{RMS} = 1.5$ nm, and $r_{RMS} = 0.89$ nm for the rinsed sample after the first annealing. Such reduction could be possibly due to the presence of chains adsorbed on the substrate, smoothing out its asperities, but not easily distinguishable from the metal in our AFM images. Finally, for Si we found that $r_{RMS} = 0.3$ nm for the bare substrate remained unchanged after the rinsing procesure.

For the film subjected to the second annealing, a residual layer was observed on Al and Au substrates after rinsing. After a sufficiently long settling time, the layer appeared as a continuous film. The thickness of the irreversibly adsorbed layers was observed to continuously increase with the duration of the second step of annealing. As an example in Fig. 7.7b we show a topographic image of the region next to the
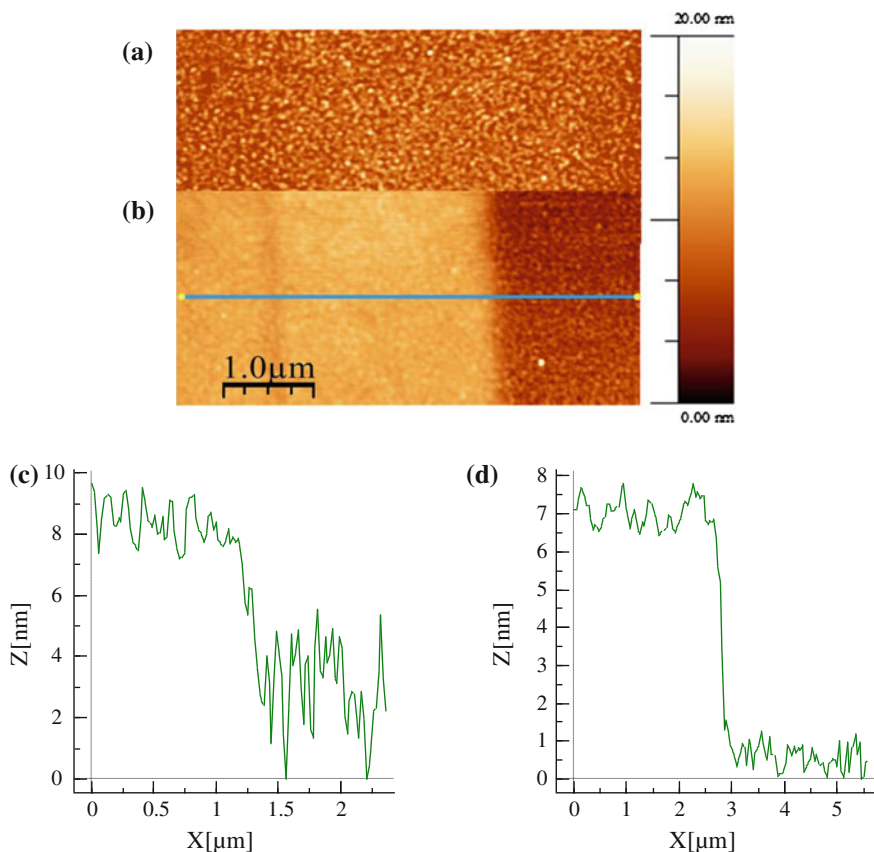
Fig. 7.7 AFM height images of the rinsed Al- supported PVAc films (M_w = 167 kg/mol) **a** after the first annealing and **b** a further annealing for 6 days at 366 K. The profile of the surface showing **c** a 5.5 nm thick irreversibly adsorbed layer as obtained from analysis of panel (**b**), and **d** a 7 nm thick irreversibly adsorbed PVAc layer developed on Au after 7 days at 366 K. Readapted with permission from Ref. [30] with permission from American Chemical Society

scratch for a PVAc film on Al substrate, after rinsing the sample with toluene. Two regions with different heights can be easily observed: the surface of the residual polymer film and the bare substrate exposed after scratching. The roughness analysis revealed r_{RMS} = 0.4 nm for the surface of the polymer in both cases, thus confirming that we are observing the PVAc film surface. The measured roughness is much smaller that the bare Al substrate as expected, and practically the same on the Au substrate. For this reason, the residual layer on Au could not be distinguished by roughness analysis. However the Tapping Mode phase image (Fig. 7.8) clearly revealed the difference in mechanical response of the two materials, thus ruling out the possibility that the two regions are two parts of substrate with different height.
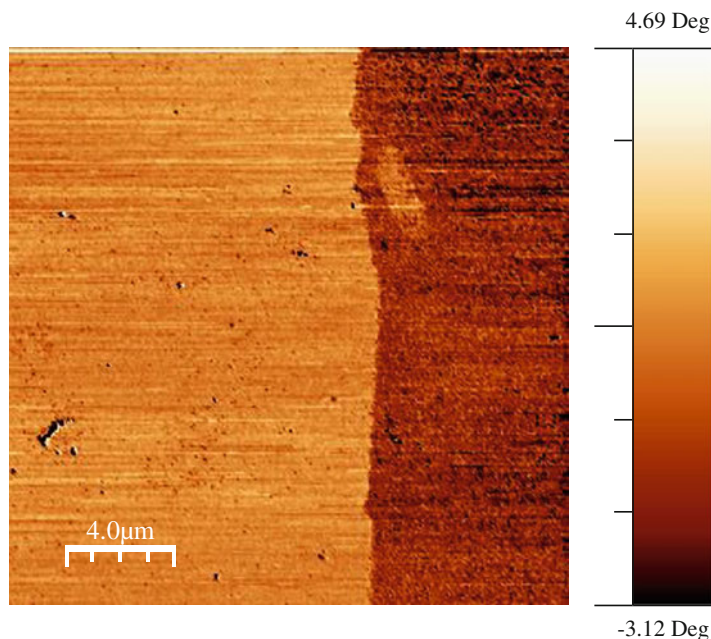
Fig. 7.8 TM phase image of the region of the scratch for a film of PVAc deposited on Au substrate. The brighter region reflects the residual PVAc layer remaining after the rinsing, the darker color reflects the metallic substrate exposed with the scratching

The thickness of the residual layer was evaluated by measuring the step height between the polymer surface and the exposed metallic substrate. Two examples of profiles of residual layers investigated after annealing PVAc film for 7 days on Al and Au are reported in Fig. 7.7c, d respectively. At this annealing stage a similar thickness was observed for the residual layers on both substrates, about 5 nm for the one on Al and 7 nm for the one on gold, as estimated with an uncertainty of about 1 nm. It is to be noted that the residual layer of irreversibly adsorbed chains was obtained from a film whose original thickness, before rinsing, was 22 nm for the case of Al and 27 nm for Au. The interfacial energy between PVAc and Al (1.6 ± 0.2 mJ/m^2) or Au (1.2 ± 0.2 mJ/m^2) are very similar in values, but the roughness of the substrate differs for about a factor 3–4. Which is the role of these properties on the development of the irreversibly adsorbed layer has still to be clarified.

Here, we found that the thickness of the residual layer is about 0.5 R_g for the used molecular weight of PVAc ($R_g = 12$ nm), but there is evidence that these values refer to adsorbed layers that are not yet at the equilibrium state. The presence of irreversibly adsorbed layer on hard surfaces was already observed for polystyrene films supported on Si and hydrogen-passivated Si substrates after a long annealing time at $\sim T_g + 50$ K [63]. In these two cases the thickness of the residual layer after long annealing was 0.5 R_g and 0.8 R_g, where the latter value was

obtained for the less hydrogen-passivated Si substrate. Thickness values herein reported for PVAc are in the same range.

Moreover, an investigation of the molecular weight dependence of the equilibrium thickness of the residual layer was performed, and a scaling was found with R_g [63]. Moreover, a recent work confirmed that the thickness of the residual layer scales as R_g [39] not only at the equilibrium but at any annealing time.

The presence of an irreversibly adsorbed layer on a flat surface was also found in poly(methyl methacrylate) on quartz scaling with R_g [64]. In the latter case it is suggested that the layer is formed due to the presence of hydrogen bonds between polymer and substrate, which is not the case for PS and unlikely for PVAc. Similarly, irreversible adsorption occurs also on surface of nanoparticles dispersed in a polymer matrix, and also in this case it is found that the amount of adsorbed polymer scales as the molecular weight, i.e. R_g [13].

A different situation is observed in case of PVAc films prepared on Si substrate. In fact, in this case we did not observe the development of a continuum residual layer, but the appearance of island of polymeric material onto the substrate (Fig. 7.9). Comparing topographic AFM images of the residual layer after annealing for 1 day at 366 K, a different formation of residual layer is evident for the three substrates. On Au, the kinetics of growth of the layer seems faster than in the others, and in fact already after 1 day a uniform layer is present with thickness of about 4 nm. For Al some islands of polymer are present: their height is less than 1 nm, and they probably reflect the presence of polymer chains adsorbed on the surface in a flat-on configuration. On the contrary, after a further day of annealing a uniform layer is developed on Al (image not reported). Finally, on Si the kinetics is really slowed down. Up to 3 days of annealing at 366 K were not sufficient to produce a uniform film, but only islands of polymer with a height of about 1–2 nm were present. On the fourth day of annealing the organic material appears more spread over the substrate producing a quite uniform coverage, with a thickness that is comparable to the normal roughness (<0.5 nm).

7.3.3 Influence of the Irreversibly Adsorbed Layer on the Structural Dynamics of PVAc Films

In order to clarify the influence of the adsorbed layer on the average relaxation dynamics of PVAc films the loss-tangent spectra of thick ($\sim$ 226 nm) and thin ($\sim$ 23 nm) films supported on the three different substrates were measured for different annealing times. Some representative results are reported in Fig. 7.10.

For the 226-nm thick film, the structural relaxation appears independent of the annealing condition, indicating that the formation of the adsorbed layer, if any, does not affect appreciably the average relaxation behavior of this film—in Fig. 7.10, spectra of films deposited on Al substrate are reported. This result was expected for two reasons. As shown above, after 6 days of annealing at 366 K a $\sim$5-nm thick
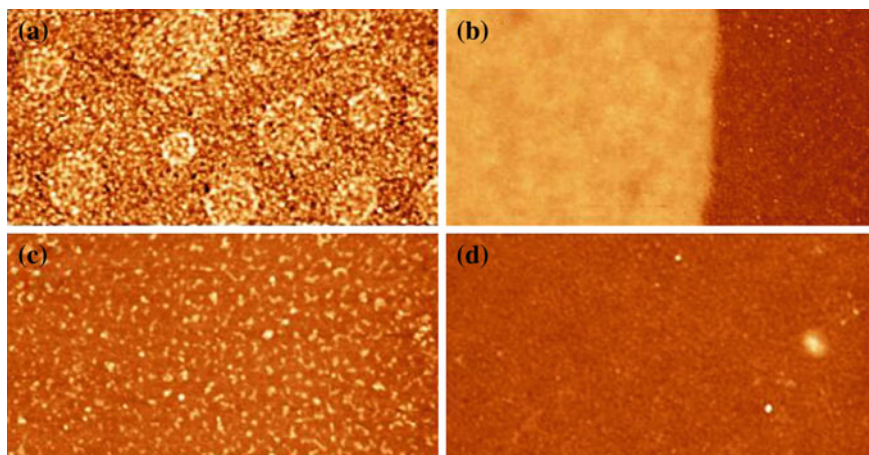
Fig. 7.9 TM topographic image of a sample of PVAc rinsed after 1 day of annealing at the second step prepared on **a** Al, **b** Au, **c** Si. Figure **d** represent the residue of rinsed PVAc sample on Si after 5 days of second step annealing. z scale is 10 nm for images (**a**), (**c**) and 16 nm for image (**c**). The lateral size of the image is 5 μm × 2.5 μm

adsorbed layer is formed on Al, but this thickness is much smaller than the total thickness of the films. The contribution of this tiny layer to the average dynamics is very small and probably difficult to be detected. Moreover, due to the greater sensitivity of the LDS technique to the upper surface region of the film, the slowing down of the adsorbed layer dynamics has insignificant influence on the average dynamics of the 226-nm thick film.

In contrast, the relaxation behavior of the 23-nm thick film shows an evident dependence on the annealing time (Fig. 7.10a for a film deposited on Al). As already discussed in Sect. 7.3.1, after the first annealing step ultrathin films with thickness smaller than 30 nm have larger relaxation frequencies than the bulk (Fig. 7.5). When the second step of annealing is applied, the characteristic frequency of structural dynamics changes with time. After 6 days of annealing at 366 K the peak position in tan δ_v recovers the same position than in the bulk. This result was found also for films on gold substrate. In the previous section we reported that in 6 days a 5–7 nm thick irreversibly adsorbed layer is formed for these two kinds of samples. This observation imples that about 25 % of the total thickness of the film is occupied by irreversibly adsorbed chains. On the other hand when the experiment has been repeated on the 26-nm thick film deposited on silicon, where no continuous adsorbed layer was detected within the same annealing time, we observe no difference in the peak position of loss-tangent spectra obtained for different annealing times (Fig. 7.10b).

This result evidences a correlation between the growth of the irreversibly adsorbed layer at the polymer/solid interface and a slowing down of structural dynamics of thin samples. In fact, the time dependence of shift in relaxation
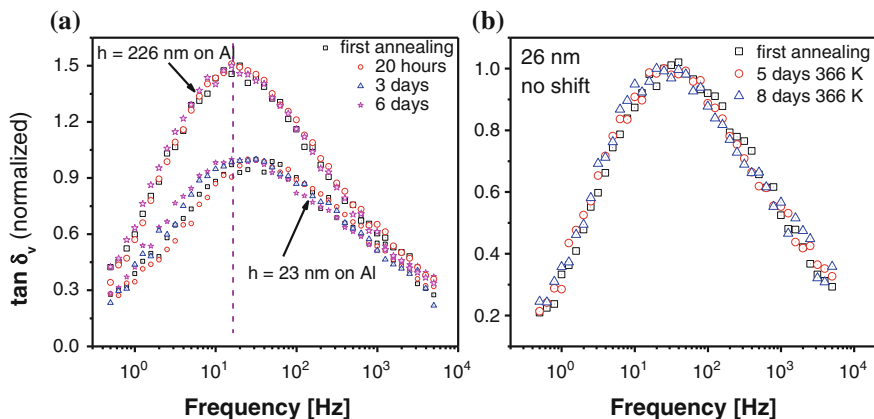
Fig. 7.10 The time evolution of loss-tangent spectra of ultrathin PVAc film supported on (**a**) Al and (**b**) Si with annealing. Reproduced from Ref. [41] with permission from American Chemical Society

frequency is observed only for those samples where the irreversibly adsorbed layer was present. Of course this result does not exclude that on longer times an irreversibly adsorbed layer can develop also on Si influencing average dynamics. The interfacial energy between PVAc and Si is about three times larger than that with the two other substrates.

Besides the influence on the dynamics of ultrathin polymer films, the presence of an adsorbed layer at the interface with the substrate might lead to a modification of some other properties of the films. However, investigation of these modifications has to be performed yet in details since the range of propagation of such perturbation far from the interface is unknown, as well as the extent of alteration of materials' average properties.

In the following, an indirect test of the prediction of higher density of the irreversibly adsorbed layer is proposed, and some consequences of that are shown.

7.3.4 Impact of Interfacial Densification on the Maximum Water Uptake of PVAc Films

Monitoring moisture absorption in ultrathin polymer films is crucial in various applications of these films as coatings, sensors, and microelectronics [65–67]. When considering bulk samples, moisture absorption is only determined by the properties of the materials themselves. However, in ultrathin films the situation can be much different. In fact, when ultrathin films are considered, i.e. with thickness of a few tens of nm, the polymer region at the interface is a relevant portion of the sample. Moreover, the nature of the substrate can also affect moisture absorption

possibly inducing a gradient of water molecule concentration in case of highly hydrophobic or hydrophilic substrates [65, 67–69]. Because the moisture absorption into ultrathin polymer films can be strongly related to the hydrophilicity of the substrate material, one of the common ways to reduce the amount of absorbed moisture is to chemically modify the substrate surface. For example, hydrophobic materials such as n-octyltrichlorosilane (OTS) [67] or hexamethyldisilizane (HMDS) [68] have been used to cover the surface of hydrophilic substrates before the deposition of polymer films. Since packing of interfacial polymer chains increases during adsorption, the presence of irreversibly adsorbed layers can contrast the effect of hydrophilic interactions of the substrate, and lead to a change in the maximum moisture uptake.

To test this idea, we prepared 21 nm thick Au supported and 23 nm thick, Al supported, PVAc films. LDS spectra of the Au supported film measured at various degrees of absorbed humidity after the first annealing are reported in Fig. 7.11. The equilibrium value of absorbed moisture was obtained by keeping the PVAc film at fixed conditions of ambient humidity for at least 4 h before each measurement [30]. This time was verified to be sufficient to reach the equilibrium condition, so that different values of RH correspond to different amounts of adsorbed water into the film. At higher RH the relaxation peak moves towards higher frequencies, evidencing an increase of the structural relaxation rate due to plastification. This observation is consistent with previous investigation of bulk PVAc [70] showing a reduction of the T_g with increasing RH. The normalized loss-tangent spectrum at 332.1 K and RH of 3 % is also presented for a comparison with the spectrum at 327.4 K and RH of 75 %. The spectra measured in such two cases show a similarity in both the shape and peak position of the relaxation. This result suggests that the absorption of moisture mainly increases the rate of the structural relaxation. In addition, the effect on the relaxation dynamics of the PVAc film by increasing the RH from 3 to 75 % corresponds to that of increasing the temperature of about 5 K at 327.4 K.

In Fig. 7.12a we report the Arrhenius plot for the above mentioned Au and Al supported ultrathin films as measured in dry (RH equal or less than 3 %) and wet (RH = 40 %) conditions. We observe that in dry conditions the relaxation frequencies of dielectric peakes coincide, in agreement with what reported in Sect. 3.1. In wet conditions the enhancement of relaxation dynamics can be observed for both films. This condition occurs because the amount of moisture absorbed into the film is expected to increase at higher RH degree, causing stronger plasticization effect. However, we note a larger plasticization of Al supported film. This result is a consequence of the different affinity to water of the two substrates. In fact, the aluminum surface is more hydrophilic than the gold one as evidenced by the smaller measured contact angle with water: $\sim 28°$ for Al in comparison to 89° for Au. After dielectric measurements, Al supported films were subjected to the second annealing, and then measured at different values of RH following the same procedure as above reported. The second annealing has an evident impact on such an enhancement at all values of RH (Fig. 7.12b) reducing the plasticization effect.
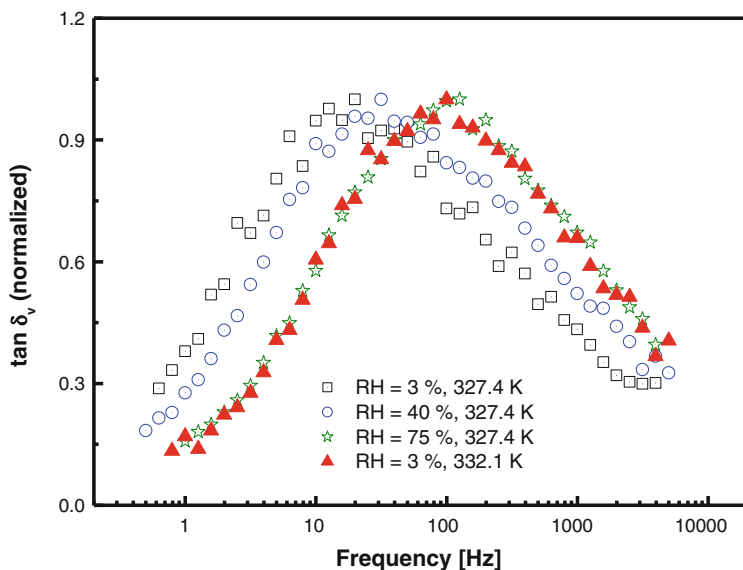
Fig. 7.11 Normalized loss-tangent spectra on the 21 nm thick Au supported film at 327.4 K equilibrated at different values of RH (*open symbols*) and in dry condition at 332.1 K (*red full symbols*). Reproduced from Ref. [41] with permission from American Chemical Society
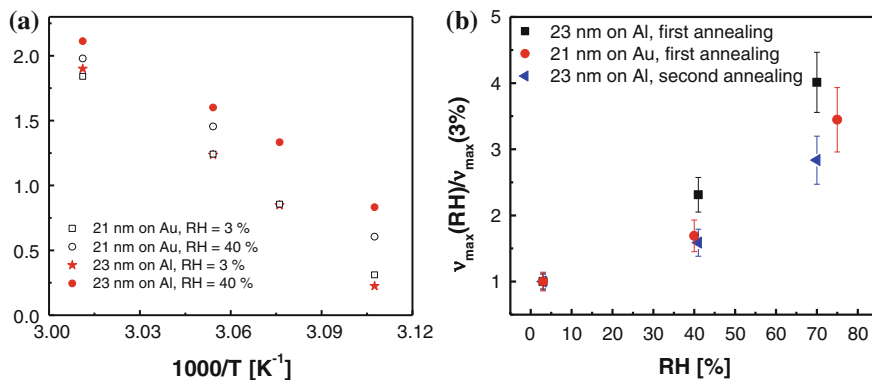
Fig. 7.12 a Logarithm of maximum frequency of structural relaxation vs inverse temperature in the 21 nm thick Au-supported and 23 nm thick Al-supported films at two different values of RH. **b** Effect of annealing on the RH-induced plasticization of dynamics in Al-supported 23 nm thick film at T = 327.4 K. The data measured on Au-supported 21 nm thick film are also presented for a comparison. Reproduced from Ref. [41] with permission from American Chemical Society

Considering that during the second annealing the irreversibly adsorbed layer develops, we can infer that the amount of absorbed moisture is reduced by the higher density of this. The higher density of the irreversibly adsorbed layer has been also verified in several cases such as PS [3, 36, 71] and poly(dimethylsiloxane) [3, 64, 72], poly(methyl methacrylate) [64, 71], poly(2-vinylpyridine) [71] showing a reduction of free volume at the interface during the development of the adsorbed layer. In particular, Koga and coworkers reported an increase in the density of directly adsorbed PS chains on Si by 20 % [73]. A further proof that the observed effect is related to the interface only can be obtained by comparing the plasticization effect of Au supported films after the first annealing (i.e. without the irreversibly adsorbed layer) and that of Al supported after the second annealing (Fig. 7.12b). In fact, we observe that after the second annealing, in presence of the irreversibly adsorbed layer, the plasticization effect in Al supported films is similar to that of Au supported ones. The higher density polymer layer screens out the hydrophilicity of the substrate, leading to the decrease of the moisture absorption capacity of the ultrathin film. This effect somehow is similar to that of the above mentioned HMDS layer covering SiO_x substrates or the OTS layer covering Al_2O_3 substrates to reduce the amounts of absorbed humidity [67, 68]. However, the physical mechanism leading to such a reduction is different. HMDS or OTS layers have hydrophobic nature due to unfavorable electrostatic interaction with water molecules, whereas the irreversibly adsorbed layer is characterized by a higher density that reduces the solubility of water molecules. The phenomenon here described suggests the feasibility of tuning the moisture absorption capacity of ultrathin polymer films supported on hydrophilic substrates using moderate annealing without the need of using chemical modification of the surface. The use of a simple thermal treatment is applicable after the deposition of the film onto the desired adsorbing substrate. In the case of a coating, it is possible to envisage a protective coating changing its behavior under the application of an external stimulus. It should be noted that there are suggestions that such densification process can be at least partially reversible [73], which should be a fundamental property for the realization of a smart coating.

7.4 Final Remarks

The physics of ultrathin films is still a hot topic presenting several unresolved issues. In the recent years, it has been definitively shown that the development of irreversibly adsorbed layer affects many physical properties of ultrathin films, and likely can be at the origin of some of the not yet resolved problems. In this Chapter we reported clear evidences on the impact of the irreversibly adsorbed layer on the average relaxation dynamics of ultrathin film. This result, in agreement with several others in literature, can shed light in the observed evolution of relaxation time of ultrathin film with annealing above T_g.

Moreover, we evidenced how the irreversibly adsorbed layer can affect the moisture uptake of PVAc films. The observed reduction of water into these films is

readily connected with the higher density of the adsorbed layer with respect to the bulk, as observed in other polymers.

Despite the interesting and new results obtained in the recent years, it appears evident that further experimental investigation is needed to achieve a complete knowledge of the phenomenon. It is important to note that irreversibly adsorbed layers still lack a definitive characterization in terms of kinetics of growth, role of substrate roughness, interaction energy between polymer and substrate, and polymer molecular architecture. In addition to larger sensitivity required to investigate these extremely thin layers, a further difficulty in the investigation of adsorbed layers resides in the current limitation in characterizing order in amorphous systems.

References

1. Debenedetti, P.G., Stillinger, F.H.: Supercooled liquids and the glass transition. Nature **410**, 259 (2001)
2. Struik, L.C.E.: Physical aging in amorphous glassy polymers, Annals of the New York Academy of Sciences, **279**, 78 (1976)
3. Guiselin, O., Lee, L.T., Farnoux, B., Lapp, A.: Adsorbed polymers—neutron reflectivity and concentration profiles. J. Chem. Phys. **95**, 4632 (1991)
4. De Gennes, P.G.: Polymer solutions near an interface: adsorption and depletion layers. Macromolecules **14**, 1637 (1981)
5. Guiselin, O.: Irreversible adsorption of a concentrated polymer solution. Europhys. Lett. **17**, 225 (1992)
6. Auvray, L., Cruz, M., Auroy, P.: Irreversible adsorption from concentrated polymer solutions. J. Phys. II France **2**, 1133 (1992)
7. Aubouy, M., di Meglio, J.-M., Raphaël, E.: Irreversible adsorption of a polymer melt on a colloidal particle. Europhys. Lett. **24**, 87 (1993)
8. Sawhney, U., Durning, C.J., O'Shaughnessy, B., Smith, G.S., Majewski, J.: Irreversible adsorption of polymer melts. MRS Online Proc. Libr. **464**, e1997 (1996)
9. O'Shaughnessy, B., Vavylonis, D.: Irreversible adsorption from dilute polymer solutions. Eur. Phys. J. E. Soft Matter **11**, 213 (2003)
10. Zajac, R., Chakrabarti, A.: Irreversible polymer adsorption from semidilute and moderately dense solutions. Phys. Rev. E **52**, 6536 (1995)
11. Douglasy, J.F., Schneider, H.M., Frantzz, P., Lipmanx, R., Granickz, S.: The origin and characterization of conformational heterogeneity in adsorbed polymer layers. J. Phys. Condens. Matter **9**, 7699 (1997)
12. Addad, J.P.C., Dujourdy, L.: Silica concentration dependence of the kinetics of polydimethylsiloxane adsorption on aggregates. Polym. Bull. **41**, 253 (1998)
13. Cohen-Addad, J.P.: Silica-siloxane mixtures. Structure of the adsorbed layer: chain length dependence. Polymer **30**, 1820 (1989)
14. Pefferkorn, E., Haouam, A., Varoqui, R.: Thermodynamic and kinetic factors in adsorption of polymers on a plane lattice. Macromolecules **21**, 2111 (1988)
15. Pefferkorn, E., Haouam, A., Varoqui, R.: Kinetics of exchange between adsorbed and free polymers at a solid liquid interface. Macromolecules **22**, 2677 (1989)
16. Vanalsten, J.G., Sauer, B.B., Walsh, D.J.: Polymer dynamics at the melt solid interface—experimental-evidence of reduced center of mass mobility. Macromolecules **25**, 4046 (1992)
17. Frantz, P., Granick, S.: Kinetics of polymer adsorption and desorption. Phys. Rev. Lett. **66**, 899 (1991)

18. Schneider, H.M., Granick, S.: Kinetic traps in polymer adsorption—exchange of polystyrene between the adsorbed state and a good solvent. Macromolecules **25**, 5054 (1992)
19. Fu, Z.L., Santore, M.: Effect of layer age and interfacial relaxations on the self-exchange kinetics of poly(ethylene oxide) adsorbed on silica. Macromolecules **32**, 1939 (1999)
20. Barbero, D.R., Steiner, U.: Nonequilibrium polymer rheology in spin-cast films. Phys. Rev. Lett. **102**, 248303 (2009)
21. Serghei, A., Kremer, F.: Metastable states of glassy dynamics, possibly mimicking confinement-effects in thin polymer films. Macromol. Chem. Phys. **209**, 810 (2008)
22. Boucher, V.M., Cangialosi, D., Yin, H., Schönhals, A., Alegría, A., Colmenero, J.: Tg depression and invariant segmental dynamics in polystyrene thin films. Soft Matter **8**, 5119 (2012)
23. Fakhraai, Z., Sharp, J.S., Forrest, J.A.: Effect of sample preparation on the glass-transition of thin polystyrene films. J. Polym. Sci. Part B Polym. Phys. **42**, 4503 (2004)
24. Kim, S., Mundra, M.K., Roth, C.B., Torkelson, J.M.: Suppression of theTg-nanoconfinement effect in thin poly(vinyl acetate) films by sorbed water. Macromolecules **43**, 5158 (2010)
25. McKenna, G.B.: Ten (or more) years of dynamics in confinement: perspectives for 2010. Eur. Phys. J. Spec. Top. **189**, 285 (2010)
26. O'Connell, P.A., Hutcheson, S.A., McKenna, G.B.: Creep behavior of ultra-thin polymer films. J. Polym. Sci. Part B Polym. Phys. **46**, 1952 (2008)
27. O'Connell, P.A., McKenna, G.B.: Rheological measurements of the thermoviscoelastic response of ultrathin polymer films. Science **307**, 1760 (2005)
28. Pye, J.E., Roth, C.B.: Two simultaneous mechanisms causing glass transition temperature reductions in high molecular weight freestanding polymer films as measured by transmission ellipsometry. Phys. Rev. Lett. **107**, 235701 (2011)
29. Ngai, K.L., Prevosto, D., Grassia, L.: Viscoelasticity of nanobubble-inflated ultrathin polymer films: justification by the coupling model. J. Polym. Sci. Polym. Phys. **51**, 214 (2013)
30. Nguyen, H.K., Labardi, M., Lucchesi, M., Rolla, P., Prevosto, D.: Plasticization in ultrathin polymer films: the role of supporting substrate and annealing. Macromolecules **46**, 555 (2013)
31. Ngai, K.L.: Interpreting the dynamics of nano-confined glass-formers and thin polymer films: importance of starting from a viable theory for the bulk. J. Polym. Sci. Part B Polym. Phys. **44**, 2980 (2006)
32. Prevosto, D., Capaccioli, S., Ngai, K.L.: Origins of the two simultaneous mechanisms causing glass transition temperature reductions in high molecular weight freestanding polymer films. J Chem. Phys. **140**, 074903 (2014)
33. Napolitano, S., Wübbenhorst, M.: The lifetime of the deviations from bulk behaviour in polymers confined at the nanoscale. Nat. Commun. **2**, 260 (2011)
34. Rotella, C., Napolitano, S., Vandendriessche, S., Valev, V.K., Verbiest, T., Larkowska, M., Kucharski, S., Wubbenhorst, M.: Adsorption kinetics of ultrathin polymer films in the melt probed by dielectric spectroscopy and second-harmonic generation. Langmuir ACS J. Surf. Colloids **27**, 13533 (2011)
35. Rotella, C., Wübbenhorst, M., Napolitano, S.: Probing interfacial mobility profiles via the impact of nanoscopic confinement on the strength of the dynamic glass transition. Soft Matter **7**, 5260 (2011)
36. Napolitano, S., Rotella, C., Wübbenhorst, M.: Can thickness and interfacial interactions univocally determine the behavior of polymers confined at the nanoscale? ACS Macro Lett. **1**, 1189–1193 (2012)
37. Napolitano, S., Capponi, S., Vanroy, B.: Glassy dynamics of soft matter under 1D confinement: how irreversible adsorption affects molecular packing, mobility gradients and orientational polarization in thin films. Eur. Phys. J. E. Soft Matter **36**, 61 (2013)
38. Vanroy, B., Wubbenhorst, M., Napolitano, S.: Crystallization of thin polymer layers confined between two adsorbing walls. ACS Macro Lett. **2**, 168 (2013)
39. Housmans, C., Sferrazza, M., Napolitano, S.: Kinetics of irreversible chain adsorption. Macromolecules **47**, 3390 (2014)

40. Tang, Q., Hu, W., Napolitano, S.: Slowing down of accelerated structural relaxation in ultrathin polymer films. Phys. Rev. Lett. **112**, 148306 (2014)
41. Nguyen, H.K., Labardi, M., Capaccioli, S., Lucchesi, M., Rolla, P., Prevosto, D.: Interfacial and annealing effects on primary α-relaxation of ultrathin polymer films investigated at nanoscale. Macromolecules **45**, 2138 (2012)
42. Levresse, P., Feke, D.L., Manas-Zloczower, I.: Analysis of the formation of bound poly (dimethylsiloxane) on silica. Polymer **39**, 3919 (1998)
43. Passaglia, E., Bertoldo, M., Ciardelli, F., Prevosto, D., Lucchesi, M.: Evidences of macromolecular chains confinement of ethylene–propylene copolymer in organophilic montmorillonite nanocomposites. Eur. Polym. J. **44**, 1296 (2008)
44. Coiai, S., Prevosto, D., Bertoldo, M., Conzatti, L., Causin, V., Pinzino, C., Passaglia, E.: Chemistry of interfacial interactions in a LDPE-based nanocomposite and their effect on the nanoscale hybrid assembling. Macromolecules **46**, 1563 (2013)
45. Crider, P.S., Majewski, M.R., Zhang, J., Oukris, H., Israeloff, N.E.: Local dielectric spectroscopy of polymer films. Appl. Phys. Lett. **91**, 013102 (2007)
46. Riedel, C., Arinero, R., Tordjeman, P., Ramonda, M., Leveque, G., Schwartz, G.A., de Oteyza, D.G., Alegria, A., Colmenero, J.: Determination of the nanoscale dielectric constant by means of a double pass method using electrostatic force microscopy. J. Appl. Phys. **106**, 024315 (2009)
47. Labardi, M., Prevosto, D., Nguyen, K.H., Capaccioli, S., Lucchesi, M., Rolla, P.: Local dielectric spectroscopy of nanocomposite materials interfaces. J. Vac. Sci. Technol. B **28**, C4D11 (2010)
48. Nguyen, H.K., Ito, M., Fujinami, S., Nakajima, K.: Viscoelasticity of inhomogeneous polymers characterized by loss tangent measurements using atomic force microscopy. Macromolecules **47**, 7971 (2014)
49. Fumagalli, L., Ferrari, G., Sampietro, M., Casuso, I., Martinez, E., Samitier, J., Gomila, G.: Nanoscale capacitance imaging with attofarad resolution using ac current sensing atomic force microscopy. Nanotechnology **17**, 4581 (2006)
50. Riedel, C., Arinero, R., Tordjeman, P., Leveque, G., Schwartz, G.A., Alegria, A., Colmenero, J.: Nanodielectric mapping of a model polystyrene-poly(vinyl acetate) blend by electrostatic force microscopy. Phys. Rev. E **81**, 010801 (2010)
51. Sacha, G.M., Sahagún, E., Sáenz, J.J.: A method for calculating capacitances and electrostatic forces in atomic force microscopy. J. Appl. Phys. **101**, 024310 (2007)
52. Fumagalli, L., Ferrari, G., Sampietro, M., Gomila, G.: Dielectric-constant measurement of thin insulating films at low frequency by nanoscale capacitance microscopy. Appl. Phys. Lett. **91**, 243110 (2007)
53. Colchero, J., Gil, A., Baró, A.: Resolution enhancement and improved data interpretation in electrostatic force microscopy. Phys. Rev. B **64**, 245403 (2001)
54. Kremer, F., Schönhals, A. (Eds). Broadband Dielectric Spectroscopy. Springer, Berlin (2003)
55. Casuso, I., Fumagalli, L., Samitier, J., Padrós, E., Reggiani, L., Akimov, V., Gomila, G.: Nanoscale electrical conductivity of the purple membrane monolayer. Phys. Rev. E **76**, 041919 (2007)
56. Crider, P.S., Majewski, M.R., Zhang, J., Oukris, H., Israeloff, N.E.: Local dielectric spectroscopy of near-surface glassy polymer dynamics. J. Chem. Phys. **128**, 044908 (2008)
57. Fumagalli, L., Gramse, G., Esteban-Ferrer, D., Edwards, M.A., Gomila, G.: Quantifying the dielectric constant of thick insulators using electrostatic force microscopy. Appl. Phys. Lett. **96**, 183107 (2010)
58. Miccio, L.A., Kummali, M.M., Schwartz, G.A., Alegria, A., Colmenero, J.: Dielectric spectroscopy at the nanoscale by atomic force microscopy: a simple model linking materials properties and experimental response. J. Appl. Phys. **115**, 184305 (2014)
59. Serghei, A., Tress, M., Kremer, F.: Confinement effects on the relaxation time distribution of the dynamic glass transition in ultrathin polymer films. Macromolecules **39**, 9385 (2006)

60. Fukao, K., Uno, S., Miyamoto, Y., Hoshino, A., Miyaji, H.: Dynamics of α and β processes in thin polymer films: poly(vinyl acetate) and poly(methyl methacrylate). Phys. Rev. E **64**, 051807 (2001)
61. O'connell, P.A., Hutcheson, S.A., Mckenna, G.B.: Creep behavior of ultra-thin polymer films. J. Polym. Sci. Part B Polym. Phys. **46**, 1952 (2008)
62. Fryer, D.S., Peters, R.D., Kim, E.J., Tomaszewski, J.E., de Pablo, J.J., Neale, P.F., White, C. C., Wu, W.-L.: Dependence of the glass transition temperature of polymer films on interfacial energy and thickness. Macromolecules **34**, 5627 (2001)
63. Fujii, Y., Yang, Z., Leach, J., Atarashi, H., Tanaka, K., Tsui, O.K.C.: Affinity of polystyrene films to hydrogen-passivated silicon and its relevance to the Tg of the films. Macromolecules **42**, 7418 (2009)
64. Durning, C.J., O'Shaughnessy, B., Sawhney, U., Nguyen, D., Majewski, J., Smith, G.S.: Adsorption of poly(methyl methacrylate) melts on quartz. Macromolecules **32**, 6772 (1999)
65. Vogt, Bryan D., Soles, Christopher L., Jones, Ronald L., Wang, Chia-Ying, Lin, Eric K., Wen-li, Wu, Satija, Sushil K.: Interfacial effects on moisture absorption in thin polymer films. Langmuir **20**, 5285 (2004)
66. Sharp, J.S., Jones, R.A.L.: Micro-buckling as a route towards surface patterning. Adv. Mater. **14**, 799 (2002)
67. Vogt, Bryan D., Prabhu, Vivek M., Soles, Christopher L., Satija, Sushil K., Lin, Eric K., Wen-li, Wu: Control of moisture at buried polymer/alumina interfaces through substrate surface modification. Langmuir **21**, 2460 (2005)
68. Vogt, B.D., Soles, C.L., Lee, H.-J., Lin, E.K., Wu, W.-L.: Moisture absorption into ultrathin hydrophilic polymer films on different substrate surfaces. Polymer **46**, 1635 (2005)
69. Vogt, Bryan D., Soles, Christopher L., Lee, Hae-Jeong, Lin, Eric K., Wen-li, Wu: Moisture absorption and absorption kinetics in polyelectrolyte films: influence of film thickness. Langmuir **20**, 1453 (2004)
70. Miyagi, K.T.Z.: Sorption of water vapor by poly(vinyl acetate). Colloid Polym. Sci. **257**, 259 (1979)
71. Jiang, N., Shang, J., Di, X., Endoh, M.K., Koga, T.: Formation mechanism of high-density, flattened polymer nanolayers adsorbed on planar solids. Macromolecules **47**, 2682 (2014)
72. Marzolin, C., Auroy, P., Deruelle, M., Folkers, J.P., Léger, L., Menelle, A.: Neutron reflectometry study of the segment-density profiles in end-grafted and irreversibly adsorbed layers of polymer in good solvents. Macromolecules **34**, 8694 (2001)
73. Gin, P., Jiang, N., Liang, C., Taniguchi, T., Akgun, B., Satija, S.K., Endoh, M.K., Koga, T.: Revealed architectures of adsorbed polymer chains at solid-polymer melt interfaces. Phys. Rev. Lett. **109**, 265501 (2012)

Part III
Glass Transition and Material Properties

Chapter 8
Non-equilibrium Structure Affects Ferroelectric Behavior of Confined Polymers

Daniel E. Martínez-Tong, Alejandro Sanz, Jaime Martín, Tiberio A. Ezquerra and Aurora Nogales

Abstract The effect of interfacial interactions and finite size effects in polymer ferroelectric structures is discussed. The comparison of results on confinement in different geometries demonstrates that the presence of interfaces with a solid wall can stabilize a ferroelectric phase not otherwise spontaneously formed under normal bulk processing conditions.

8.1 Introduction

Polymers are hierarchical systems, with structure organized at different length scales. Most macroscopic properties of polymers have their origin in physical phenomena associated with length scales of the order of nanometers. Hence, confining polymers to the nanoscale level may end up in a material with different physical properties. This fact is remarkably important nowadays with the development of polymer applications in devices with smaller and smaller sizes. From the fundamental viewpoint, for several decades, experiments have been designed to evaluate the role of limitation of space in several physical processes, like the glass transition of polymers [1], changes in the dynamics, either local or segmental [2], among others. However, in those experiments, besides the pure finite size effects, another issue has to be inevitably considered, and that is the presence of interphases, that become extremely important in confinement experiments, when the

D.E. Martínez-Tong · T.A. Ezquerra · A. Nogales (✉)
Instituto de Estructura de la Materia IEM-CSIC, C/Serrano 121, Madrid 28006, Spain
e-mail: aurora.nogales@csic.es

A. Sanz
DNRF Centre "Glass and Time", IMFUFA, Department of Sciences, Roskilde University, Postbox 260, 4000 Roskilde, Denmark

J. Martín
Department of Materials and Centre of Plastic Electronics, Imperial College London, London SW7 2AZ, UK

characteristic size is in the length scale of the interaction between system and substrate. This aspect has drawn the attention of many researchers recently, and the presence of adsorption layers, and how this layer can be modified and tuned to lead to different polymer properties is an area of intense research nowadays [3–6].

The presence of interfaces, either with solid substrates or free surfaces, modifies parameters such as number of entanglements, chain orientation, chain packing, local chain mobility and glass transition temperature (T_g), mechanical properties, crystallization kinetics or crystals orientation [7–12], from their bulk counterpart.

Semicrystalline polymeric materials exhibit a rich variety of morphologies [13] which are responsible, to a high extent, for the macroscopic properties of the manufactured polymer product. For example, depending on the morphology, chemically equivalent polymers can generate materials with very different macro-scopical moduli [14]. Therefore, the resultant morphology is as discriminating as to the attainment of specific properties as the chemical composition. The presence of interfaces is one of those aspects that modify extensively the morphology in semicrystalline polymers. In some particular cases, when the polymer exhibits more than one crystalline form, the presence of interfaces can favor the development of high energy crystalline forms, otherwise not stable [15, 16]. This effect has been used by the industry to design additives that nucleate a particular crystalline form, like the β nucleants in isotactic polypropylene [17–19]. In other cases, confined at the nanoscale level, polymers crystallize much slower than in bulk, and sometimes, the formation of ordered structures results inhibited for extremely long experimental time scales [7, 12, 20].

One of the bulk properties that is directly related to the polymer crystalline morphology and crystal form is ferroelectricity in poly(vinylidene fluoride) (PVDF) and its copolymers with trifluoroethylene (P(VDF-TrFE)). In general, ferroelectrics are polar substances of either solids (inorganic or polymeric) or liquid crystals, in which spontaneously generated electric polarization can be reversed by inverting the external electric field [21]. The critical electric field for reversing the polari-zation is called the coercive field. The electric displacement (D) as a function of field strength (E) consequently draws a hysteretic curve (D–E loop) between opposite polarities, and this electric bistability can be used, for example, for non-volatile memory elements [22–24]. The ferroelectric compounds usually have a Curie temperature (T_C) for a ferroelectric-to-paraelectric phase transition. As the temperature approaches T_C, the dielectric constant (ε), obeying the Curie–Weiss law, is amplified to large values. Such a tremendous increase in dielectric constant can be exploited for a high-ε condenser. Specifically, P(VDF-TrFE) copolymers with TrFE content higher than ≈ 10 % crystallize in a ferroelectric phase [24, 25], monoclinic or orthorhombic, which is similar to the β-crystalline and ferroelectric phase of PVDF [26]. This ferroelectric phase is stable at room temperature and suffers a phase transition to a paraelectric form, hexagonal, as temperature increases [22, 27].

Confinement and interfaces are particularly important issues for these systems, since arrays of polymeric nanostructures showing ferroelectric and piezoelectric behavior, have a well-recognized potential for the fabrication of miniaturized and

novel organic electronic devices, such as high density nonvolatile memories, [28, 29] low voltage operation polymer capacitors [30], nanopressure sensors [31], among other applications [32]. However, the use of ferroelectric materials in microelectronics is still not very wide. The continuous downscaling of electronics requires, in fact, overcoming the technological drawback, arising from the difficulty on stabilizing ferroelectricity at the nanoscale.

It has been reported how, by imposing confinement and interaction with the walls of an alumina template, a PVDF homopolymer is able to crystallize in the polar γ crystalline form, when the system is processed by solution wetting. In this case, the interaction between polymer chains and the porous membrane's walls imposes a flat-on lamella growth along the nanorrods long axis, while improving crystal orientation [33].

The presence of interfaces on the dynamics of PVDF confined in alumina nanopores has been also investigated by dielectric spectroscopy [34]. A strong deviation of the relaxation behavior of PVDF embedded within the nanopores is observed as compared to that of the bulk. When the restriction in size is larger, that is, when the pore diameter is comparable with the size of the adsorbed layer, the existence of a highly constrained relaxation associated with the polymer-alumina interfacial layer is observed [34].

In the above mentioned work, the presence of interfaces induces the crystallization of PVDF in a polar phase. P(VDF-TrFE) copolymers however, spontaneously crystallize in the β polar phase, and they present ferroelectric properties at room temperature under normal processing conditions. The question is whether confinement and interfaces modify this intrinsically ferroelectric phase.

To shed some light into that question, we discuss here on the behavior of ferroelectric copolymers P(VDF-TrFE) under different confinement conditions, where the dimensionality of the confinement has been modified, from 1D confined (thin films), 2D confined (nanorods) or 3D confined (nanospheres).

8.2 Short Review on the Crystalline Structure, Thermal Properties and Morphology of Bulk Ferroelectric Polymers

Copolymers of PVDF with trifluoroethylene are semicrystalline systems in which the crystalline part exhibits ferroelectricity. For TrFE molar fractions below 85 %, this crystalline phase suffers a phase transition below the melting point. TrFE units are included in the unit cell of PVDF and enlarge it since they are bulkier. This enlargement weakens the intermolecular interactions among chains, and destabilizes the ferroelectric phase with the all-trans conformation. The more TrFE segments in the chain, the more unstable the ferroelectric phase becomes. As a direct consequence, the ferroelectric-to-paraelectric Curie transition temperature decreases with the increase of TrFE units [24]. This change in the crystalline structure, from

the pseudohexagonal phase where parallel chains are in all-trans planar conformations to the hexagonal paraelectric phase can be easily observed by differential scanning calorimetry (DSC) where an endothermic peak before the melting temperature is observed. Figure 8.1a shows the DSC traces of PVDF-TrFE with different molar content. Two main endothermic peaks appear. The one at lower temperature corresponds to the ferro-para phase transition (F-P transition). The position of this peak is the Curie temperature. As observed, T_C is higher for the smaller TrFE content. The endothermic peak appearing at higher temperature is associated to the melting of the paraelectric phase.

At room temperature, Wide Angle X Ray Scattering (WAXS, CuKα) patterns of bulk P(VDF-TrFE) show a sharp maximum in the region around $2\theta \approx 20°$, characteristic of the *200*, *110* reflections of the orthorhombic ferroelectric crystalline phase of P(VDF-TrFE). The exact position of these reflections depends slightly on the molar content of TrFE [26]. As an example, Fig. 8.1b shows the WAXS pattern corresponding to the 56:44 PVDF-TrFE copolymer at room temperature. However, at temperatures above T_C, the WAXS pattern exhibits also an intense and sharp
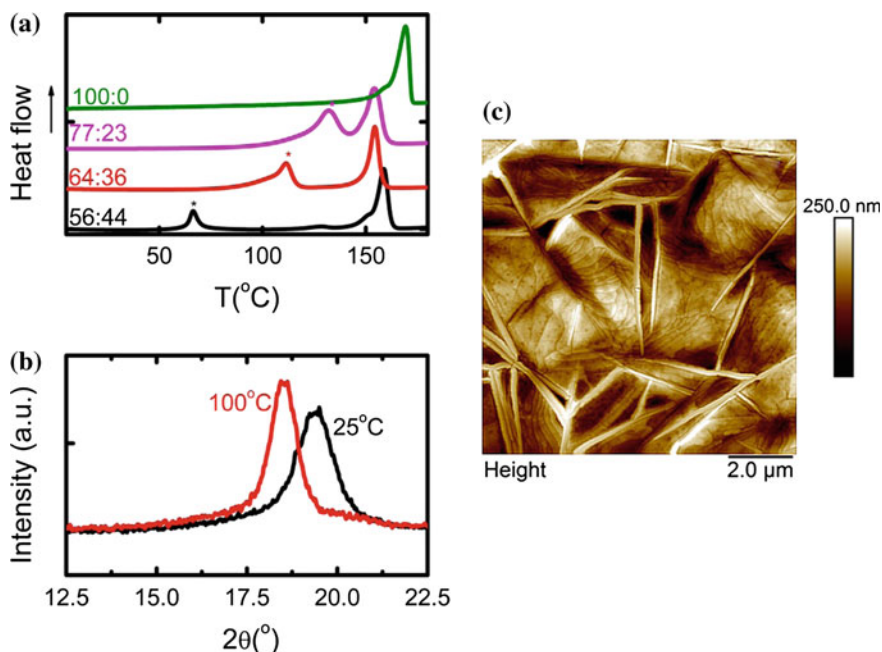
Fig. 8.1 **a** Differential Scanning Calorimetry traces obtained at 20°/min, for different TrFE molar contents, as indicated in the label. The *star* indicates the Curie temperature. For comparison, the DSC trace showing the melting of the non ferroelectric α phase of the PVDF homopolymer (labelled as 100:0) has been included. **b** WAXS measurements at 25 °C (*black*) and 100 °C (*red*) for P(VDF-TrFE) 56:44 copolymer. Both temperatures are below and above the Curie temperature respectively. **c** AFM topography image of a P(VDF-TrFE) 56:44 film of thickness ≈200 nm

maximum, but at a different position, particularly at $2\theta \approx 18.5^\circ$ for the 56:44 P (VDF-TrFE) copolymer.

From the morphological viewpoint, P(VDF-TrFE) copolymers are characterized by random large needlelike crystals [35]. This morphology has been associated to edge-on lamellae, that also coexist with flat-on crystals appearing as irregular flakes on the AFM image, Fig. 8.1c.

In the vicinity of T_C, the dielectric constant shows a strong increase. This increase can be observed by broadband dielectric spectroscopy, which also provides an excellent method for investigating the molecular dynamics in ferroelectric copolymers below and above the T_C. Figure 8.2a, b show the dielectric permittivity and dielectric loss values respectively as a function of temperature for particular frequencies. At low temperatures, around $-40\ ^\circ$C, a maximum in $\varepsilon''(T)$ is observed. This can be attributed to the segmental relaxation associated to the glass transition in agreement with previous reports [25, 36, 37]. In this type of polymers the segmental relaxation has been labeled as β-relaxation since dynamical mechanical analysis shows another relaxation, labeled originally as α, associated to the crystalline phase appearing at higher temperatures in isochronal conditions [25, 37]. In order to comply with the literature we adopt here a similar criterion.

Figure 8.2c shows isothermal dielectric loss, ε'', data as a function frequency for bulk PVDF-TrFE 56:44 copolymer. In isothermal plots, the β relaxation appears as
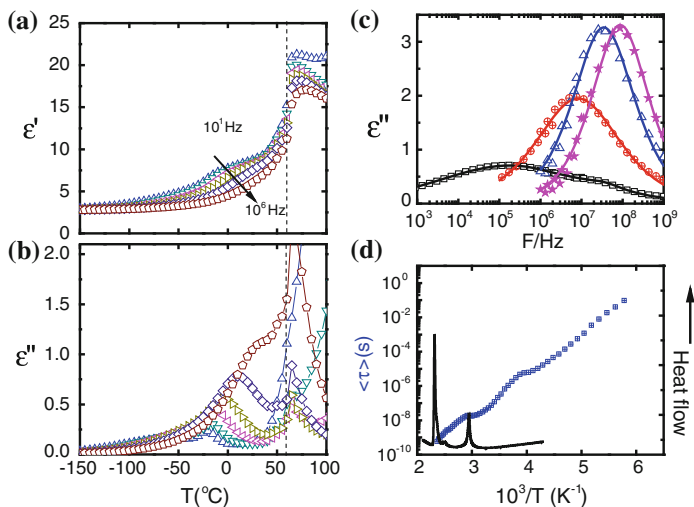
Fig. 8.2 Dielectric spectroscopy of bulk 56:44 P(VDF-TrFE). **a**, dielectric constant ε' and **b**, dielectric losses ε'' at various frequencies: 10^1, 10^2, 10^3, 10^4, 10^5 and 10^6 Hz. The discontinuous line indicates the T_C. **c** ε'' as a function of frequency for various temperatures: 0 °C (□), 50 °C (⊗), 100 °C (△) and 125 °C (★). **d** Relaxation map for the 56:44 PVDF-TrFE copolymer, with the average relaxation time obtained from the position of the maximum loss as $<\tau> = (2\pi F)^{-1}$ (□) and the DSC trace (continuous) line

a peak that at T = 0 °C is centered at 10^5 Hz, and whose position shifts toward higher frequencies as temperature is increased. A dramatic increase of the intensity of the relaxation is observed as the F-P transition is approached (>60 °C for the 56:44 copolymer). It has been proposed that for these type of copolymers the intense relaxation peak centered around 10^7–10^8 Hz is a consequence of the onset of rotational motion of the molecules within the paraelectric crystalline phase [25, 36]. This process coexists with the segmental relaxation, β, occurring in the amorphous phase. The relaxation map of this system is presented in Fig. 8.2d, together with the DSC trace for the 56:44 P(VDF-TrFE) copolymer. As observed, at low temperatures (10^3/T> 4.5) the mean relaxation time <τ> shows an Arrhenius behavior. In this region, local motions are responsible for the maximum observed in the dielectric loss as a function of temperature. Following this peak, at higher temperatures, the relaxation time follows the Vogel Fulcher Tamman law, in correspondence of the region where the segmental relaxation becomes relevant. Around 10^3/T = 3 K^{-1}, (T ∼ 60 °C) a clear kink is observed in <τ>, which corresponds to the crystalline transition from the ferroelectric to the paraelectric phase. At higher temperatures, the most important contribution to the dielectric losses is the relaxation associated to the rotational dynamics in the paraelectric crystalline phase. As observed in Fig. 8.2d, the relaxation time here follows an Arrhenius behavior. This trend is reproduced for other copolymer molar fractions, where, as a universal feature, the kink in <τ> occurs at T_C [25].

8.3 Non-equilibrium Effects in Ferroelectric Polymers Confined in 1, 2 and 3 Dimensions

Experiments in confined geometries, particularly in the case of polymers, require several considerations. Besides the existence or absence of interfaces, the geometry itself plays an important role. 1D confinement geometry (thin films) and 2D confinement (nanotubes and nanorods) implies that the polymer chain has to accommodate in an anisotropic fashion, whereas in 3D (nanospheres) the confinement is isotropic. In each of the above mentioned experiments, interfaces play a fundamental role. In the particular case of 1D confinement, as for supported thin films, it has been demonstrated that there is a strong impact of interfaces on the static and dynamical properties of the polymer [38]. These interfaces also appear in the case of polymers confined in cylindrical pores. Tanaka and coworkers demonstrated that the slower dynamics near a substrate is related to a wall-induced enhancement of 'glassy structural order', which is a manifestation of strong interparticle correlations [39]. The presence of the solid interface favours the presence of clusters with a preferential bond orientational order. When the polymer system under these circumstances is semicrystalline, the crystallization process is modified in two different ways. On one hand, the slower dynamics due to the polymer-chain interactions delays the crystallization process [12, 20]. On the other

hand, the development of clusters with preferential orientation templates the crystallization in particular directions [8, 9, 40]. In the following subsections, non-equilibrium effects in the ferroelectric character of P(VDF-TrFE) copolymers, due to confinement and to the presence of interfaces will be discussed. The case of 1D confinement on supported thin films, 2D confinement on alumina cilindrical nanopores and 3D confinement in free standing nanospheres will be considered.

8.4   1D Confinement. P(VDF-TrFE) Thin Films

The interaction with an external surface in any material may induce a discontinuity and anisotropy in the energetic balance of the system, imposing effects different from those observed in bulk. In ferroelectric materials, it has been observed that finite size effects may also appear. However, it was verified that ultrathin films of P (VDF-TrFE) copolymers prepared via the Langmuir-Blodgett (LB) technique exhibit a F-P transition with a T_C nearly equal to the bulk value, but, in addition, another transition appears at a lower temperature, associated with the surface layers only [41]. LB films are highly crystalline, therefore, interfacial layers in this particular case do not present a large number of defects. Nevertheless, dielectric experiments have reported the presence of a dielectric segmental relaxation in P (VDF-TrFE) LB films, attributed to the motion of amorphous chains [42].

Polar interfacial phases are also reported in PVDF homopolymer LB films [43]. It was found that by LB deposition direct formation of ferroelectric β phase in PVDF is possible, with the molecular chains parallel to the substrates and the dipoles aligned perpendicular to the substrates. These experiments are clear evidence on how the presence of an interface favors a different crystallographic phase, which in bulk represents a higher energy structure, here stabilized via interactions with the surface.

The dielectric properties of ferroelectric P(VDF-TrFE) thin films prepared by spin coating have not been widely studied. It has been reported [44] that the dielectric behavior of P(VDF-TrFE) spin coated thin films is similar to that of the bulk system. P(VDF-TrFE) polymers prepared in the same polar β form, show a relaxation behavior characteristic of the bulk [45, 46]. The preferential orientation of the crystal depends highly on the interaction with the substrate [45–47], and because of that, in thin films prepared in this way, the control of the polarization is difficult due to the strong heterogeneity of the crystalline morphology leading to non-uniform local fields and non-uniform spreading of the ferroelectric domains. To overcome this effect, several methods were successful in stopping the spreading of the ferroelectric domains, e.g. by confining the crystallization to limited space [29, 40, 48–50].

8.4.1 PVDF and Ferroelectric P(VDF-TrFE) Confined into Tubes and Rods (2D Confinement)

Several types of nanostructures have been employed to study the confined crystallization of polymers. The system, composed of polymers confined into anodic aluminum oxide (AAO) nanopore arrays, has been widely used because of its high tunability on the degree of confinement in terms of the pore diameter, a mechanical rigidity of the hard pore walls, and a well-defined confining geometry [51]. Moroever, high surface energy solids such as metal oxides are wettable by almost all low surface energy systems like polymer melts. When a polymer melt is deposited on top of a porous anodic aluminum oxide (AAO) template, the polymer wets the pores. Depending on the size of the pore, the annealing temperature, and the spreading coefficient for the given polymer/alumina system, two wetting regimes (partial and total wetting) are observed, giving rise to two different polymeric nanostructures inside the pores (nanorods or nanotubes) [52].

For the preparation of polymer nanorods or nanotubes confined into alumina templates, several polymer pellets were placed onto the AAO templates in order to carry out the infiltration by melt wetting. Figure 8.3a shows Atomic Force
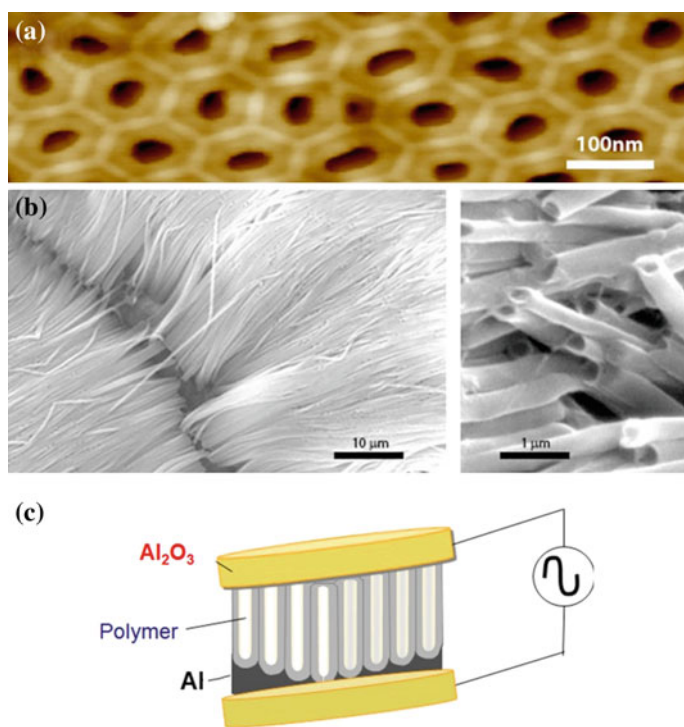
Fig. 8.3 a AFM image of an AAO template surface. **b** SEM image of PVDF nanotubes at different magnifications after being removed from the AAO template. **c** Schematic drawing of the capacitor ensemble employed for dielectric characterization

Microscopy (AFM) images of an AAO template. The molten polymer wets the surface of the AAO template by forming a precursor film. Depending on whether the radius of the pore is larger or smaller than the thickness of that precursor film, either a complete filling is obtained (polymer nanorods) or a partial filling (polymer nanotubes). The AAO with the polymer pellets were then annealed at 240 °C under a nitrogen atmosphere for 45 min. After the infiltration process, the samples were quenched in iced water. In order to force the separated crystallization of each individual nanorod, the residual polymer film located on the AAO surface, which would interconnect the nanostructures, was removed with a blade. Finally, the nanorods not connected by the residual film, were again molten at 240 °C and quenched in iced water.

Figure 8.3b shows Scanning Electron Microscopy pictures obtained at two different magnifications of the nanostructures of PVDF, removed from the template.

Dielectric measurements were performed at selected frequencies and temperatures. Figure 8.3c presents a sketch of the measuring set-up used. With this measuring set-up, the dielectric signal recorded has a contribution from the polymer nanostructures and from the alumina. However, the contribution from alumina is independent of temperature, as it was proved by performing the dielectric experiment on an empty template. Therefore, the changes in the dielectric signal observed as a function of temperature can be attributed solely to the polymer nanostructures.

Figure 8.4 presents the dielectric loss (left) and the dielectric permittivity (right) as a function of temperature for bulk PVDF and PVDF nanostructures, precisely,

Fig. 8.4 Dielectric Loss (ε'') (**a**, **c** and **e**) and Dielectric Permitivitty (**b**, **d** and **f**) (ε') for the different studied PVDF nanostructures and comparison with the bulk behavior at different frequencies. (O) $10°$Hz, (□) 10^2 Hz, (▽) 10^4 Hz and (☆) 10^6Hz
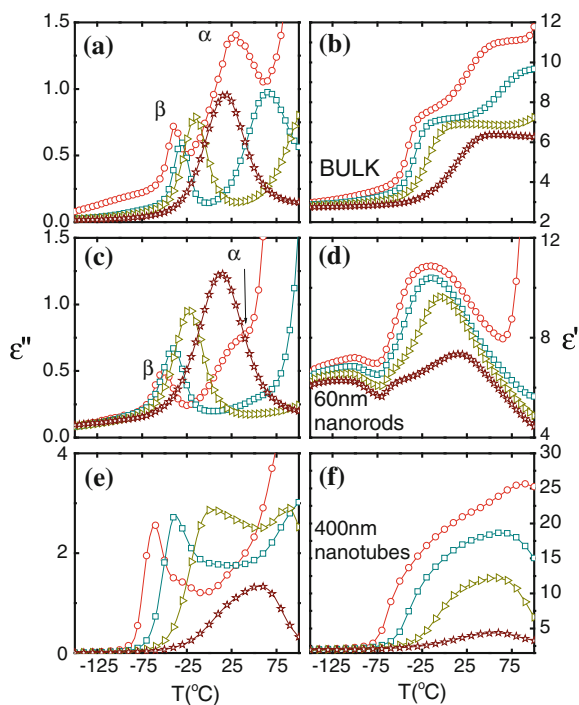
nanorods of 60 nm in diameter and nanotubes of 400 nm in diameter. The dielectric loss for bulk PVDF exhibits two main relaxation processes in the studied frequency-temperature window. The one appearing at lower temperatures (β relaxation) can be attributed to the segmental motions of amorphous PVDF chains above the glass transition temperature. The peak in dielectric loss at higher temperatures, that we have labeled as α, consistently with the literature, is attributed to local motions in the crystalline phase of PVDF. The β and α relaxation processes are also present in the dielectric loss spectra of the 60 nm rods. Previous results show that this behavior persists even in smaller nanorods down to 35 nm in diameter [34]. For smaller rod diameters, the dielectric loss spectra change dramatically, due to the existence of a highly constrained relaxation associated with the polymer-alumina interfacial layer [34]. This sort of highly constrained behavior is also present in the PVDF nanotubes of 400 nm in diameter. Despite the higher diameter of these nanostructures, the results can be understood considering that the wall thickness of the nanotubes is also of the order of 20 nm (see Fig. 8.3), and therefore, the entire dielectric signal is associated with interfacial PVDF. This interfacial phase of PVDF must be also present in nanorods with higher diameter (60 nm), although its detection based on ε" only is rather difficult. However, dielectric permittivity (ε′) values show strong changes compared to those of the bulk for all the nanostructures studied. Rods of 60 nm diameter present a sudden increase of ε′ around −75 °C, which corresponds to the increase observed in bulk PVDF and can be associated, in a first attempt, to the segmental β relaxation. Remarkably instead of the typical step like behavior, in the 60 nm nanostructures ε′ exhibits a very broad maximum. This temperature dependence of ε′ does not resemble that of a F-P transition, since here the maximum in ε′ shifts progressively toward higher temperature with frequency. This is feature has been commonly observed in relaxor ferroelectrics [53] and in PVDF based ferroelectric polymers being chemically modified or irradiated [54]. As mentioned before, recently, X ray micro diffraction studies have proved that it is possible to obtain arrays of isolated polar nanorods of PVDF by solution wetting nanoporous alumina templates, and that the polymer crystallized into the polar γ-phase. This peculiar crystallization is attributed to confinement effects and interaction of the polymer solution with the alumina walls during wetting [33]. The dielectric results presented in Fig. 8.4 indicate that these polar structures are also present in PVDF nanorods prepared by melt wetting the alumina template, and therefore, it is the interaction with the alumina wall to be responsible for the stabilization of a polar phase in PVDF. This interpretation is also in line with recent reports where the [55] arrangement of the first layers in the homopolymer PVDF in LB films crystallize in the polar phase.

Modifications of the bulk ferroelectric character are also observed in nanostructures of P(VDF-TrFE) copolymers. Figure 8.5 shows ε′ and ε″ values obtained for nanorods of P(VDF-TrFE) 56:44 molar fraction with two different diameters, 60 nm and 35 nm and the dielectric response of the same system in the bulk for comparison. There is a strong increase of ε′ in the nanorods at temperatures around −50 °C. This temperature region corresponds to that of the segmental relaxation region of the bulk polymer, and therefore, can be attributed to the β relaxation.

To highlight further differences between the nanorods and the bulk dynamics, Fig. 8.6a, b show ε' and ε'' for P(VDF-TrFE) copolymer confined in 60 nm and 35 nm diameter pores, together with the values corresponding to the bulk, normalized to the value at the maximum located around T = −40 °C. As observed, the β relaxation, associated to the segmental motion above T_g, is clearly visible in the confined systems. However this process appears slightly shifted towards lower temperatures, which is compatible with a lower crystalline content upon confinement [56]. The main difference in the behavior of the bulk and nanopore confined system appears in the proximity of the bulk T_C. As mentioned before, a strong increase in ε' in the bulk ferroelectric copolymer is associated to the Curie transition. However, this increase is not observed in polymers confined into alumina templates (Fig. 8.5). Instead, ε' exhibits a relaxation like behavior, where ε' decreases when increasing the temperature.

At temperatures around T_C, the confined system shows different features, like a maximum in both ε' and ε'' and the absence of the strong increase associated to the F-P transition. These results may indicate an inhibition of the F-P transition in the
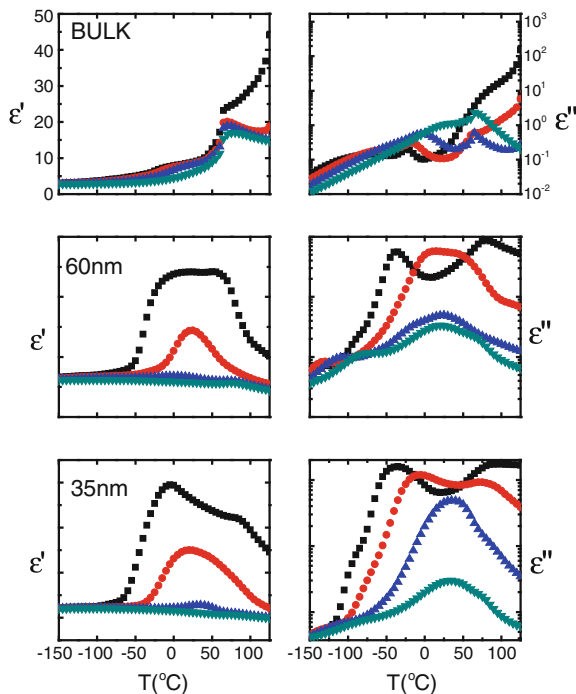
Fig. 8.5 *Left* Dielectric Permitivitty (ε') and (*Right*) Dielectric Losss (ε'') values as a function of temperature for different diameter PVDF-TrFE nanorods, as indicated by the label and comparison with the bulk behavior at different frequencies. (■) 10^0 Hz, (●) 10^2 Hz, (▲) 10^4 Hz and (◆) 10^6 Hz. Values for the 60 nm and 35 nanorods should be considered as relative, since the geometric factor cannot be calculated in this measuring geometry
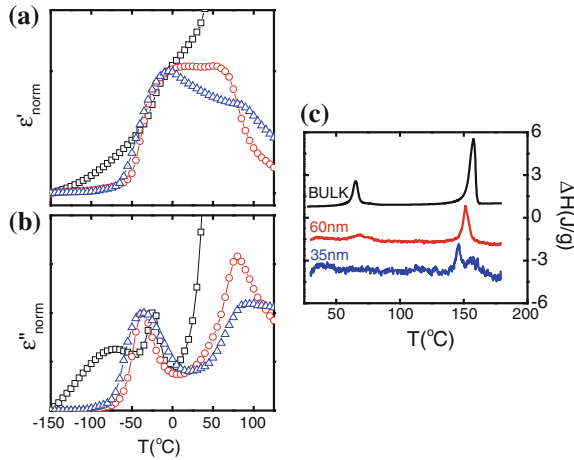
Fig. 8.6 **a** Dielectric Permittivity and **b** Dielectric Loss as a function of frequency for the bulk 56:44 P(VDF-TrFE) (□) and different diameter nanorods confined in alumina templates (○)60 nm rods and (△) 35 nm rods at F = 10^4 Hz. Values are normalized to the value of ε′ and ε″ at the maximum of the β relaxation (T around −50 °C). **c** Differential scanning calorimetry of the bulk 56:44 PVDF-TrFE polymer and for the nanorods of 60 and 35 nm respectively

ferroelectric polymer confined into alumina nanopores. DSC results also support this idea. In Fig. 8.6c the DSC traces for P(VDF-TrFE) confined into pores with 60 nm and 35 nm in diameter is presented, and compared with that of the bulk. As observed, in the 60 nm confined sample, a very weak and broad endothermic F-P peak appears at higher temperatures. In the 35 nm confined system, this peak is not observed.

Previous experiments performed on ferroelectric copolymers in confined geometries [41] have shown that ferroelectricity is preserved, but the F-P transition is broadened and, in particular cases, an interfacial F-P transition is observed. In particular, highly ordered Langmuir-Blodgett multilayers of PVDF-TrFE (70:30) exhibit an interfacial ferroelectric transition around 20 °C [57]

The results described here indicate that confining PVDF and P(VDF-TrFE) copolymers in cylindrical nanopores formed in alumina templates induces severe changes in the ferroelectric behavior of the polymer. In the case of the PVDF homopolymer, confinement into alumina templates induces an enhancement of ferroelectric-like features that might indicate the formation of an interfacial ferro-electric phase. In the case of the P(VDF-TrFE) copolymers, confinement into alumina templates yields inhibition of the ferro-para transition. In order to check whether this inhibition is due to purely spatial confinement or to the interaction with the confining walls, we confined P(VDF-TrFE) in nanospheres, where no interac-tion with walls is present. The results are discussed in the following section.

8.4.2   Ferroelectric P(VDF-TrFE) Confined in the Form of Nanospheres (3D Confinement)

8.4.2.1   Preparation of the nanospheres

P(VDF-TrFE) nanoparticles were prepared by the dialysis nanoprecipitation method [58]. The polymer was dissolved in *N,N*-dimethyl acetamide (DMA) at room temperature under continuous stirring. A dialysis membrane, with molecular weight cutoff 10–12 kg/mol (Visking), was carefully washed in water, soaked in DMA and left inside a glass container with the solvent for 30 min. This procedure ensures the complete rinse of the membrane on the solvent eliminating water and avoiding macroscopic precipitation. Afterwards, the polymer solution was poured into the membrane and subsequently, the membrane was submerged and dialyzed against 2 L of distilled water under mild stirring. This step allows the exchange of solvent/water molecules giving rise to the nanoprecipitation. During the first 2 h, the dialysis solution was replaced with fresh distilled water every 30 min. Subsequently, for the next 4 h, the water was replaced every hour. Dialysis nanoprecipitation was allowed to take place overnight, resulting in a total exchange

Fig. 8.7 AFM image and histogram for P(VDF-TrFE) nanoparticles. Histogram represents the diameter distribution of the nanoparticles
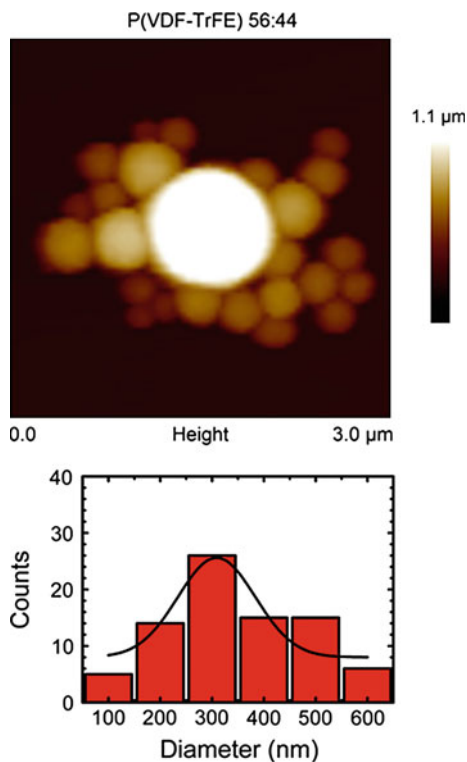
time of about 20 h. The final result is a white aqueous emulsion of surfactant free nanoparticles inside the membrane, where no DMA solvent is left. The nanoparticles were deposited onto a silicon wafer by spin coating, in order to evaluate their size distribution by AFM (Fig. 8.7).

The dielectric loss values, measured as a function of frequency for the nanoparticles, show similar features as those characteristics of the bulk. In Fig. 8.8, ε' and ε'' are presented as a function of temperature for different frequencies.

Comparison of Figs. 8.2 and 8.8 revealed that the only difference between bulk and spheres is the appearance of a relaxation peak in ε'' centered at -125 °C for 1 Hz. Although this peak has not been reported before, and it is not visible in other confining geometries, we may speculate that this relaxation peak is actually a local relaxation that can be better observed here than in the bulky system since in the present case, the crystallinity is lower and therefore, relaxations in the amorphous chain become more obvious. As temperature increases, the maximum of this relaxation process shifts towards higher frequencies and the relaxation peak becomes sharper. Similar with what it has been observed in the dielectric
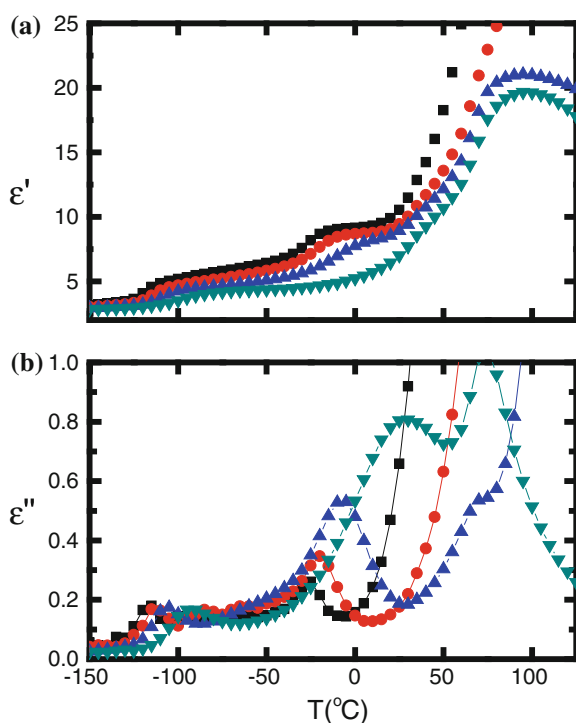
Fig. 8.8 a Dielectric permittivity and **b** dielectric loss as a function of temperature for various frequencies obtained from 56:44 P(VDF-TrFE) nanospheres. (■)10^0 Hz, (●)10^2 Hz, (▲)10^4 Hz(▼) 10^6 Hz

experiments for the bulk system, a dramatic increase of the intensity of the relaxation is observed as the ferroelectric-paraelectric transition is approached (T_C approx. 50 °C for the 56:44 copolymer). This process coexists with the segmental relaxation, β, occurring in the amorphous phase.

The dielectric behavior in the ferroelectric polymer nanoparticles is therefore, very similar to that of the bulk and considerably different from what was observed in the case of the ferroelectric polymer nanorods confined into alumina cylindrical pores, particularly in the small diameter case. For the nanospheres, there is no indication supporting the presence of interfacial relaxations.

In order to evidence these differences, Fig. 8.9 shows ε″ for the bulk, the 60 nm and 35 in diameter rods in alumina template samples and the nanospheres measured at high frequency. As observed, the relaxation associated to the paraelectric phase is clearly visible in the nanospheres and also in the case of the 60 nm in diameter rods. However, the relaxation is absent in the case of the 35 nm in diameter nanorods, which supports the interpretation of inhibition of the F-P transition in these highly constrained structures.

These features can be further observed in the relaxation map presented in Fig. 8.10. The different confined systems, in the region of the segmental relaxation ($10^3/T > 3.5$ K^{-1} in the relaxation map) exhibit subtle differences with respect to the bulk relaxation time, which can be associated with differences in the crystallinity. However, the main differences are observed in the paraelectric relaxation region ($10^3/T < 3.5$ K^{-1}). The Arrhenius behavior in this temperature region, that should correspond to the relaxation time of the paraelectric relaxation, is observed for the nanospheres and the nanorods with larger diameter. However, this Arrhenius tendency is not observed for the nanorods of smaller diameter, and this fact is in agreement with the observation that no relaxation is observed at high frequencies
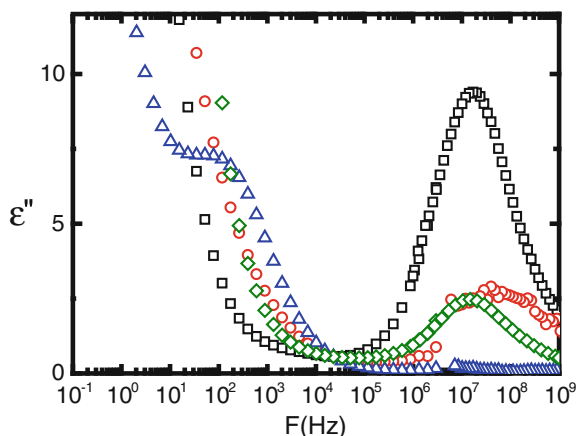
Fig. 8.9 ε″ as a function of frequency for the confined system studied in this work: nanorods in alumina pores of 60 and 35 nm diameter respectively (O, △); nanospheres (◇). Bulk values are also presented for comparison (□)

Fig. 8.10 Relaxation map in the region of the segmental motion and the paraelectric relaxation for the confined system studied in this work: nanorods in alumina pores of 60 and 35 nm diameter respectively (O, △); nanospheres (◇). Bulk values are also presented for comparison (□)
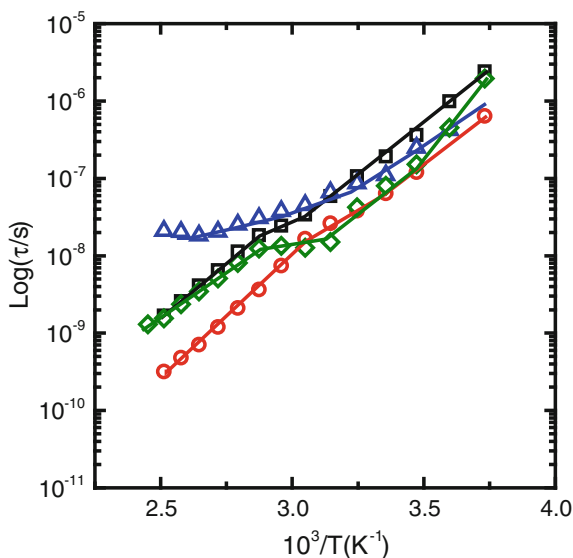
for this system. In the smaller diameter rods, the ferroelectric polymer is highly constrained, and the F-P transition is inhibited.

8.5 Conclusions

Ferroelectric properties in PVDF and P(VDF-TrFE) copolymers are directly associated with their crystalline phase. Confinement may alter the structure of the crystalline phase. We remark that the changes in the ferroelectric behaviour cannot be solely attributed to spatial confinement (finite size effects). The occurrence of peculiar ferroelectric behavior is dictated by the presence of interfaces with solid walls, with whom the polymer chains interacts. To name some of the features discussed in this chapter: when PVDF is confined into alumina cylindrical templates, an interfacial layer showing ferroelectric like behavior appears, whereas the bulk phase of this homopolymer is paraelectric under normal processing conditions. However, in P(VDF-TrFE) copolymers confined in alumina templates, due to the the severe confinement conditions, the transition from ferroelectric to paraelectric is inhibited, indicating that the interaction with the confining wall stabilizes de ferroelectric phase. Confinement without interfaces, like in the case of 3D confined nanospheres, does not affect the ferroelectric character of the polymer. The confinement in nanoparticles may decrease the crystallinity of the system, but the crystals, responsible for the ferroelectric character of the polymer, have essentially the same properties as in the bulk.

References

1. Alcoutlabi, M., Mckenna, G.B.: J. Phys.: Condens. Matter **17**, R461–R524 (2005)
2. Priestley, R.D., Cangialosi, D., Napolitano, S.: J. Non-Cryst. Solids **407**, 288–295 (2015)
3. Jiang, N., Shang, J., Di, X., Endoh, M.K., Koga, T.: Macromolecules **47**, 2682–2689 (2014)
4. Napolitano, S., Rotella, C., Wubbenhorst, M.: Acs Macro Lett. **1**, 1189–1193 (2012)
5. Napolitano, S., Wubbenhorst, M.: Nat. Commun. **2**, 260 (2011)
6. Xu, J., Ding, L., Chen, J., Gao, S., Li, L., Zhou, D., Li, X., Xue, G.: Macromolecules **47**, 6365–6372 (2014)
7. Capitan, M.J., Rueda, D.R., Ezquerra, T.A.: Macromolecules **37**, 5653–5659 (2004)
8. Martín, J., Campoy-Quiles, M., Nogales, A., Garriga, M., Alonso, M.I., Goni, A.R., Martin-Gonzalez, M.: Soft Matter **10**, 3335–3346 (2014)
9. Martín, J., Nogales, A., Mijangos, C.: Macromolecules **46**, 7415–7422 (2013)
10. Napolitano, S., Wubbenhorst, M.: Macromolecules **39**, 5967–5970 (2006)
11. Sun, X., Chen, Z., Wang, F., Yan, S., Takahashi, I.: Macromolecules **46**, 1573–1581 (2013)
12. Vanroy, B., Wübbenhorst, M., Napolitano, S.: ACS Macro Lett. **2**, 168–172 (2013)
13. Bassett, D.C.: Principles of Polymer Morphology. Cambridge University Press, Cambridge (1981)
14. Wilkinson, A.N., Ryan, A.J.: Polymer Processing and Structure Development. Dordrecht, Kluwer (1999)
15. Balik, C., Hopfinger, A.: Macromolecules **13**, 999–1001 (1980)
16. Hua, T.-T., Itoh, T., Hou, J.-A., Fujiwara, S., Hashimoto, M.: Jpn. J. Appl. Phys. **46**, L1170 (2007)
17. Gahleitner, M., Grein, C., Bernreitner, K.: Eur. Polymer J. **48**, 49–59 (2012)
18. Gahleitner, M., Grein, C., Kheirandish, S., Wolfschwenger, J.: Int. Polym. Proc. **26**, 2–20 (2011)
19. Mollova, A., Androsch, R., Mileva, D., Gahleitner, M., Funari, S.S.: Eur. Polymer J. **49**, 1057–1065 (2013)
20. Martínez-Tong, D.E., Vanroy, B., Wübbenhorst, M., Nogales, A., Napolitano, S.: Macromolecules **47**, 2354–2360 (2014)
21. Horiuchi, S., Tokura, Y.: Nat. Mater. **7**, 357–366 (2008)
22. Yang, L., Li, X., Allahyarov, E., Taylor, P.L., Zhang, Q.M., Zhu, L.: Polymer **54**, 1709–1728 (2013)
23. Youn Jung, P., In-Sung, B., Seok Ju, K., Jiyoun, C., Cheolmin, P.: IEEE Trans. Dielectr. Electr. Insul. **17**, 1135–1163 (2010)
24. Zhu, L., Wang, Q.: Macromolecules **45**, 2937–2954 (2012)
25. Yagi, T., Tatemoto, M., Sako, J.: Polym. J. **12**, 209–223 (1980)
26. Lovinger, A.J.: Science **220**, 1115–1121 (1983)
27. Baltá-Calleja, F.J., Arche, A.G., Ezquerra, T.A., Cruz, C.S., Batallan, F., Frick, B., Cabarcos, E.L.: Adv. Polym. Sci. **108**, 1–48 (1993)
28. Chuanqi, Z., Maotian, G., Yingying, L., Qing, W.: Macromol. Symp. **279**, 52–58 (2009)
29. Martínez-Tong, D.E., Soccio, M., García-Gutiérrez, M.C., Nogales, A., Rueda, D.R., Alayo, N., Perez-Murano, F., Ezquerra, T.A.: Appl. Phys. Lett. **102**, 191601–191605 (2013)
30. Jung, S.W., Yoon, S.M., Kang, S.Y., Choi, K.J., Shin, W.C., Yu, B.G.: Electrochem. Solid State Lett. **12**, H325–H328 (2009)
31. Mandal, D., Yoon, S., Kim, K.J.: Macromol. Rapid Commun. **32**, 831–837 (2011)
32. Cauda, V., Canavese, G., Stassi, S.: J. Appl. Polym. Sci. **132,** n/a-n/a (2015)
33. García-Gutiérrez, M.-C., Linares, A., Hernández, J.J., Rueda, D.R., Ezquerra, T.A., Poza, P., Davies, R.J.: Nano Lett. **10**, 1472–1476 (2010)
34. Martín, J., Mijangos, C., Sanz, A., Ezquerra, T.A., Nogales, A.: Macromolecules **42**, 5395–5401 (2009)
35. Jung, H.J., Chang, J., Park, Y.J., Kang, S.J., Lotz, B., Huh, J., Park, C.: Macromolecules **42**, 4148–4154 (2009)

36. Ezquerra, T.A., Kremer, F., Baltá-Calleja, F.J., Lopez, E.: Cabarcos. J. Polym. Sci., Part B: Polym. Phys. **32**, 1449–1455 (1994)
37. Ngoma, J.B., Cavaille, J.Y., Paletto, J., Perez, J.: Polymer **32**, 1044–1048 (1991)
38. Napolitano, S., Capponi, S., Vanroy, B.: Eur. Phys. J. E **36**, 1–37 (2013)
39. Watanabe, K., Kawasaki, T., Tanaka, H.: Nat. Mater. **10**, 512–520 (2011)
40. Garcia-Gutierrez, M.-C., Linares, A., Martin-Fabiani, I., Hernandez, J.J., Soccio, M., Rueda, D.R., Ezquerra, T.A., Reynolds, M.: Nanoscale **5**, 6006–6012 (2013)
41. Bune, A.V., Fridkin, V.M., Ducharme, S., Blinov, L.M., Palto, S.P., Sorokin, A.V., Yudin, S.G., Zlatkin, A.: Nature **391**, 874–877 (1998)
42. Meng, X.J., Kliem, H., Lin, T., Chu, J.H.: J. Appl. Phys. **103**, 034110 (2008)
43. Chen, S., Li, X., Yao, K., Tay, F.E.H., Kumar, A., Zeng, K.: Polymer **53**, 1404–1408 (2012)
44. Martin, B., Mai, M.F., Kliem, H.: Phys. B-Condens. Matter **407**, 4398–4404 (2012)
45. Park, Y.J., Kang, S.J., Lotz, B., Brinkmann, M., Thierry, A., Kim, K.J., Park, C.: Macromolecules **41**, 8648–8654 (2008)
46. Park, Y.J., Kang, S.J., Park, C., Lotz, B., Thierry, A., Kim, K.J., Huh, J.: Macromolecules **41**, 109–119 (2008)
47. Lee, J.S., Prabu, A.A., Kim, K.J.: Polymer **51**, 6319–6333 (2010)
48. Hu, Z.J., Jonas, A.M.: Soft Matter **6**, 21–28 (2010)
49. Nougaret, L., Kassa, H.G., Cai, R., Patois, T., Nysten, B., Van Breemen, A.J.J.M., Gelinck, G.H., De Leeuw, D.M., Marrani, A., Hu, Z., Jonas, A.M.: ACS Nano **8**, 3498–3505 (2014)
50. Piraux, L., Hamoir, G., Lee, M.-W., Ferain, E., Jonas, A.M., Huynen, I., Medina, J.D.L.: Torre. Appl. Phys. Exp. **4**, 115001 (2011)
51. Martin, J., Maiz, J., Sacristan, J., Mijangos, C.: Polymer **53**, 1149–1166 (2012)
52. Steinhart, M.W., Greiner, A., Wherspohn, R.B., Nielsch, K., Schilling, J., Choi, J., Gösele, U.: Science **296** (2002)
53. Yuan, F., Peng, Z., Liu, J.M.: Mater. Sci. Eng. B **117**, 265–270 (2005)
54. Bobnar, P.V., Vodopivec, B., Levstik, A., Kosec, M., Hilczer, B., Zhang, Q.M.: Macromolecules **36**, 4436–4442 (2003)
55. Zhu, H., Yamamoto, S., Matsui, J., Miyashita, T., Mitsuishi, M.: J. Mater. Chem. C **2**, 6727–6731 (2014)
56. Nogales, A., Denchev, Z., Ezquerra, T.A.: Macromolecules **33**, 9367–9375 (2000)
57. Palto, S., Blinov, L., Dubovik, E., Fridkin, V., Petukhova, N., Sorokin, A., Verkhovskaya, K., Yudin, S., Zlatkin, A.: EPL (Europhys. Lett.) **34**, 465 (1996)
58. Zhang, C., Chung, J.W., Priestley, R.D.: Macromol. Rapid Commun. **33**, 1798–1803 (2012)

Chapter 9
Interfacial Role in the Increase of Structural Order of a Discotic Liquid Crystal

Gabin Gbabode and Basab Chattopadhyay

Abstract In this chapter, we investigate the unusual phase behavior of a thermotropic discotic liquid crystal (DLC), processed as thin and ultrathin films. The physical confinement imposed by the reduced size is responsible for the stabilization, at reduced film thickness i.e. less than 30 nm, of a new structural arrangement different from the bulk stable columnar rectangular phase. The presence of this new singular non-equilibrium form is unambiguously revealed by microscopy and X-ray diffraction techniques. Grazing incidence X-ray diffraction clearly put forward a net increase in packing order between the non-equilibrium phase and the thermodynamically stable structure. In particular, the latter presents a conventional two-dimensional molecular packing typical for columnar phases of DLCs, while the former is characterized by full three-dimensional packing. Surprisingly, extensive optical and scanning probe microscopy observations carried out as a function of time demonstrate that this new crystal form is favored by interfaces and is effectively able to nucleate at the substrate/film as well as at the film/air interface, independently of film thickness.

G. Gbabode (✉)
Sciences et Méthodes Séparatives, SMS EA 3233, Normandie Université, IRCOF Building,
1 Rue Lucien Tesnière, 76821 Mont-Saint-Aignan Cedex, France
e-mail: gabin.gbabode@univ-rouen.fr

B. Chattopadhyay
Department of Solid State Physics, Indian Association for the Cultivation of Science, Kolkata
700032, India
e-mail: basab.chattopadhyay@ulb.ac.be

B. Chattopadhyay
Laboratory of Polymer Chemistry, Université Libre de Bruxelles (ULB), C.P. 206/01,
Boulevard Du Triomphe, 1050 Brussels, Belgium

9.1 Introduction

Discotic liquid crystals (DLC) are a particular class of mesogenic compounds, often composed of a rigid disk-like conjugated core surrounded by long aliphatic chains grafted on it [1]. DLCs typically self-assemble into columns which pack into two-dimensional crystal lattices (hexagonal, square, rectangular or oblique), characterized by a long range crystalline order in the directions perpendicular to the columnar axis. A liquid-like order prevails in the direction parallel to the columnar axis [2, 3].

Since a few decades, a growing interest has emerged on applications of DLCs in the field of organic electronics, where these materials are used as active layers in electronic devices such as field-effect transistors [4–6] or, given their high optical properties, also in organic light-emitting diodes and photovoltaic cells [7, 8]. In particular, the ability to orient the columns on large scales (µm to mm) brought the idea that these assemblies could act as independent molecular wires, capable of transmitting current by charge hopping from one conjugated core to the other, along the columnar direction [9–12].

However, to achieve a good understanding of the semiconducting properties of DLCs, their phase behavior has to be carefully characterized in bulk samples but also, and more importantly, in thin films. Indeed, charge transport properties are directly related to the structural packing adopted by the molecules on a few molecular layers on top of the underlying substrate [13, 14]. In thin (>100 nm) and ultrathin (≤100 nm) film geometry, because the role of interfacial interactions cannot be neglected [15], further constraints are imposed on the structural packing of molecules. Hence, non-equilibrium structural arrangements of molecules in bulk samples, e.g. metastable phases, can be stabilized upon confinement. Such thin film phases have been aptly rechristened as substrate-induced phases (SIP) [16, 17].

In the case of π-conjugated crystalline compounds, several examples of SIP have been reported among the past 20 years [18–24]. The impact of these non-equilibrium structures on organic electronic devices performance has recently been unambiguously proven [25]. In the case of liquid crystals, few cases have been revealed for rod-like molecules [26, 27] but, to the best of our knowledge, prior to our works no SIP was reported for DLCs [16, 17]. In this chapter, we focus on a phthalocyanine derivative, hereafter called **Pc**, for which we demonstrate the presence of a SIP with significantly enhanced packing order compared to the bulk columnar phase. Based on X-ray diffraction and microscopy measurements, structural, thermodynamic and kinetic aspects of the SIP will be considered. The comparison of these results permitted us to get a better understanding of stabilization of the SIP in thin film geometry.

9.2 Identification and Structural Characterization of the Substrate-Induced Phase

Figure 9.1a shows the molecular structure of **Pc**, the phthalocyanine derivative considered herein. It is composed of a phthalocyanine conjugated core tetra-substituted by long branched alkyl chains, which are well known to induce mesophases [28, 29]. The bulk thermotropic properties of **Pc** are well characterized and are indicated at the bottom of Fig. 9.1a: **Pc** exhibits a columnar rectangular phase **Col$_r$** at room temperature, transforming into a columnar hexagonal phase **Col$_h$** at *ca* 58 °C and subsequently melting upon further heating at *ca* 182 °C. A typical specular X-ray diffraction (sXRD) pattern of **Col$_r$** measured for thick **Pc** samples (tens of µm-thick typically i.e. bulk samples) is reproduced in Fig. 9.2b. Characteristic peaks of the rectangular lattice are well distinguished at low q values, notably the intense 11 and 20 reflections at $q_z = 0.23$ Å^{-1} and $q_z = 0.25$ Å^{-1} respectively, and much less intense higher order reflections in the [0.35–0.55 Å^{-1}] q_z range. Note that Miller indices are noted hk as they are related to a 2D crystal lattice described by lattice constants *a* and *b*. No additional reflections are revealed at higher q values, except a broad diffuse halo centered at $q_z = 1.34$ Å^{-1} (not shown), representative of the liquid-like arrangement of the disk-like molecule along the columnar axis.

Pc thin films have been realized by spin-coating of toluene solutions with various concentrations onto Si/SiO$_x$ silicon wafers (800 µm-thick wafers with a native oxide top layer of around 2 nm). Keeping the same spin-coating conditions, film thickness varied linearly with solution concentration, as verified by ellipsometry and X-ray reflectivity (Fig. 9.2a), thus allowing a precise control of film thickness ranging from *ca* 3 to *ca* 100 nm (Table 9.1). All these films have been analyzed by sXRD at room temperature and the results are gathered in Fig. 9.2b. To be noticed,
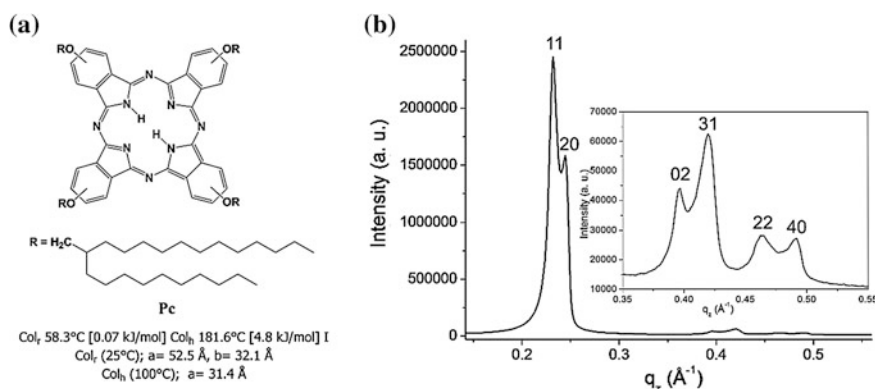
Fig. 9.1 **a** Molecular structure and bulk thermotropic properties of **Pc** (cell parameters determined for **Col$_r$** and **Col$_h$** are also indicated). **b** sXRD pattern of **Col$_r$** represented in the [0.14–0.56 Å^{-1}] q_z range. Inset is a zoom of the [0.35–0.55 Å^{-1}] q_z range showing higher order reflections
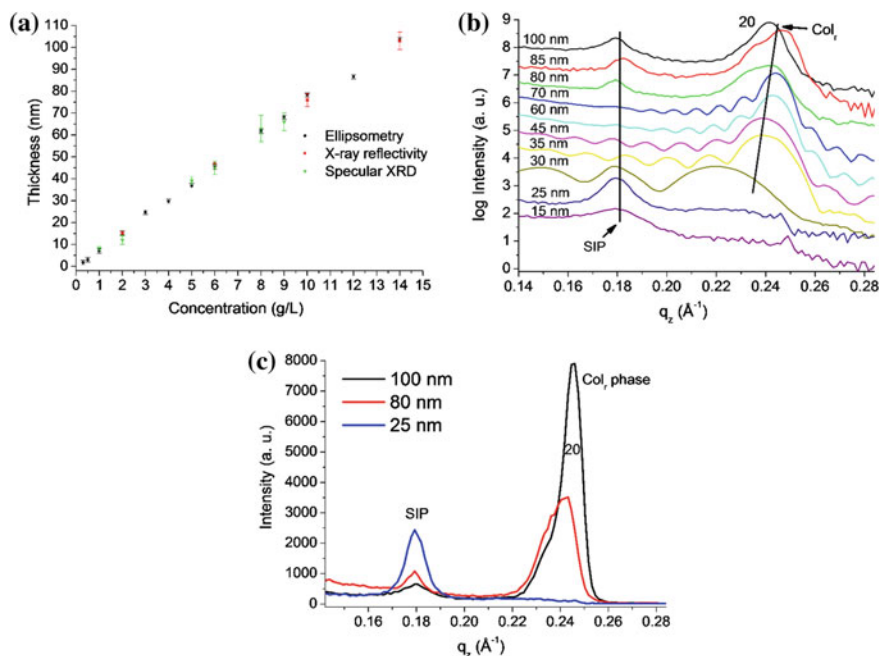
Fig. 9.2 a Chart representing the linear relationship between film thickness (values given in Table 9.1) and solution concentration. **b** sXRD patterns of thin films with film thickness ranging from 15 to 100 nm measured at room temperature and represented in the [0.14–0.28 Å^{-1}] q_z range. **c** Selected sXRD patterns of (**b**) showing the evolution of the relative amount of **Col$_r$** and the **SIP** when film thickness decreases

sXRD patterns of 3 and 7 nm-thick films are not represented as hardly no signal was visible due to the lack of unit cell repetition in the film out-of-plane direction (equivalent to one or two crystalline layers considering cell parameters of **Col$_r$**). Several important peculiarities are put forward when comparing sXRD patterns measured for thick and thin films. First, in several cases Kiessig fringes (characteristic undulated peaks) are visible and mask the low q_z part below the intense 20 reflection. Observation of Kiessig fringes denotes the presence of sharp interfaces (**Pc** film/air and substrate/**Pc** film) then suggesting very uniform films. Interestingly, this effect was principally put forward for **Pc** films of intermediate thickness namely from 30 to 70 nm approximately. Alternatively, the positions of Kiessig fringes allow us to determine film thickness and confirm results from ellipsometry and X-ray reflectivity (Table 9.1).

Second, only 20 reflection and its corresponding higher order reflections (see Figs. 9.3a, b) of **Col$_r$** are visible in thin films, while several different hk reflections are observed for thick films (see Fig. 9.1). These results indicate a high preferential orientation of the rectangular unit cell in thin films so that (20) planes are parallel to the substrate surface. This unit cell orientation is consistent with a planar alignment

Table 9.1 Relation between solution concentration and film thickness as determined by ellipsometry, X-ray reflectivity and specular X-ray diffraction (see text)

Concentration (g /L)	Film thickness (nm)		
	Ellipsometry	X-ray reflectivity	sXRD
0.5	3 ±	–	–
1	7 ± 1	–	8 ± 1
2	15 ± 1	15 ± 1	12 ± 2
3	25 ± 1	–	–
4	30 ± 1	–	–
5	37 ± 1	–	39 ± 2
6	45 ± 1	47 ± 1	45 ± 3
7	52 ± 1	–	–
8	62 ± 1	–	63 ± 6
9	68 ± 1	–	66 ± 4
10	78 ± 1	76 ± 3	–
12	87 ± 1	–	–
14	103 ± 1	103 ± 4	–

of **Pc** columns (columnar axis parallel to the substrate surface) as depicted in the inset of Fig. 9.3a. Markedly, the position of 20 reflection is constantly shifted to lower q_z values with decreasing film thickness. This trend demonstrates a constant increase of intercolumnar distances when film thickness is reduced. Last, but not least, a new reflection at $q_z = 0.18$ Å^{-1} is revealed for all thin films (at least when not hidden by the presence of Kiessig fringes). Corresponding second and third order reflections can be seen at higher q_z values as shown in Fig. 9.3. Observation of these reflections unambiguously proves the presence of a new structural arrangement in thin films together with the known **Col$_r$**. As described in the next section, appearance of this new phase is related to the aging of the films. In this section, we concentrate on understanding the structural features of this phase. Noticeably, this new phase was also present in thin films deposited onto glass substrates (Marienfeld cover glasses Cat. No. 0101040, around 160 μm-thick) as shown in Fig. 9.3b. Furthermore and very interestingly, the relative amount of the two phases (qualitatively evaluated from the relative intensity of 20 reflection and the peak at $q_z = 0.18$ Å^{-1}) evolves constantly from 100 nm-thick films, for which **Col$_r$** is largely predominant, to 25 nm-thick films, where **Col$_r$** is nearly absent while the new phase prevails (Fig. 9.2c).

These results strongly suggest that this new structural arrangement is stabilized in the vicinity of the substrate surface (less than 30 nm distance), and co-exists with the bulk phase. Accordingly, the new phase will hereafter be referred to as the substrate-induced phase, **SIP**.

Additional evidences of the existence of the **SIP** for **Pc** are brought by investigation of the surface of the films by Tapping Mode Atomic Force Microscopy (TM-AFM). For films of thickness well above 30 nm (Fig. 9.4), irregularly-shaped mosaic-like structures are revealed on top of the surface with reduced lateral
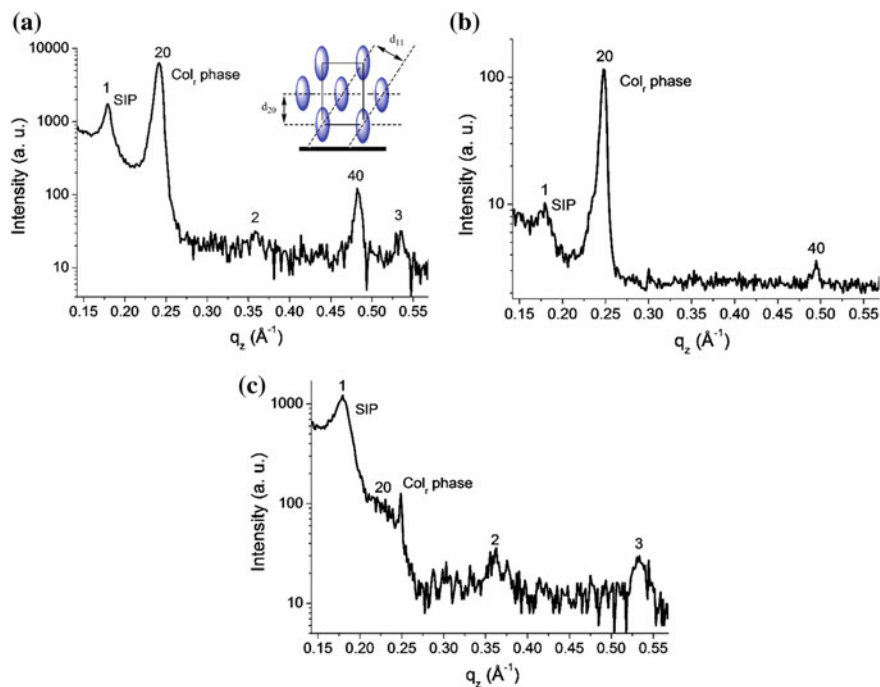
Fig. 9.3 sXRD patterns represented in the [0.14–0.57 Å^{-1}] q$_z$ range and measured at room temperature for **a** a 100 nm-thick **Pc** film deposited onto a Si/SiO$_x$ substrate **b** a 150 nm-thick **Pc** film deposited onto a glass substrate and **c** a 15 nm-thick **Pc** film deposited onto a Si/SiO$_x$ substrate. *Inset* in (**a**) is a schematic description of the preferential orientation of the unit cell of **Col$_r$** (columnar axis is perpendicular to the plane of the drawing)

dimensions (few hundreds of nm). These features are even more evident in the phase image (Fig. 9.4 right).

To the contrary, for films with thickness smaller than 30 nm (Fig. 9.5) large homogeneous domains of several µm span the entire surface. Moreover, large scale images (Fig. 9.5b) show that these domains organize into rather well defined terraces whose height is 3 ± 0.2 nm, in good agreement with the reticular distance

Fig. 9.4 Large scale (5 × 5 µm^2) TM-AFM height (*left*) and phase (*right*) images of a 100 nm-thick **Pc** film
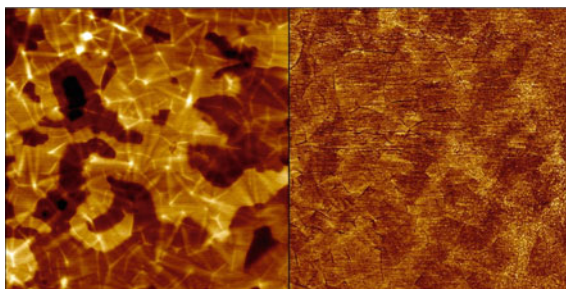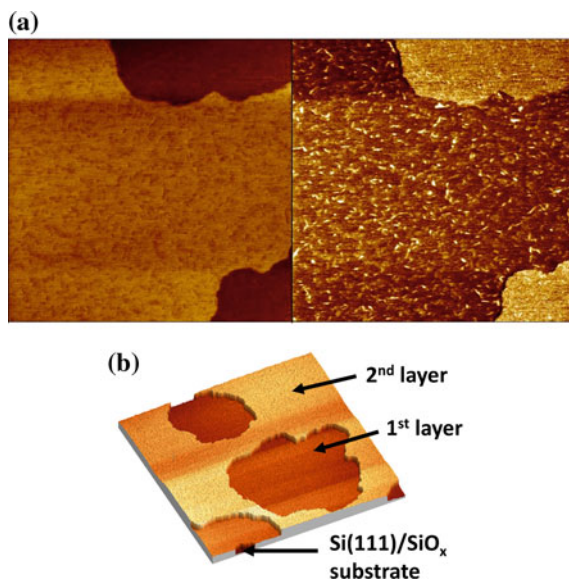
Fig. 9.5 a Large scale (5×5 μm^2) TM-AFM height (*left*) and phase (*right*) images of a 7 nm-thick **Pc** film. **b** Larger scale (12×12 μm^2) TM-AFM height images of the same film showing a fine terrace-like organization with two molecular layers on top of the silicon wafer

corresponding to the first order reflection of the **SIP** revealed by sXRD (3.5 nm). In particular, two molecular layers are clearly distinguished in Fig. 9.5b, the topmost of which being not completely covered, in good agreement with film thickness of around 7 nm, determined by ellipsometry and sXRD (Table 9.1 and Fig. 9.2a).

Lastly, a combination of both surface features is pointed out for films with thickness close to 30 nm (Fig. 9.6). Indeed, rather homogeneous islands with lateral size of several hundreds of nm are observed on top of an also homogeneous smooth surface extending over much larger length scales (several microns wide).
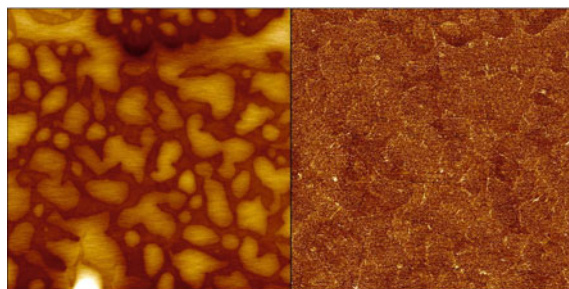
Fig. 9.6 Large scale (5×5 μm^2) TM-AFM height (*left*) and phase (*right*) images of a 30 nm-thick **Pc** film
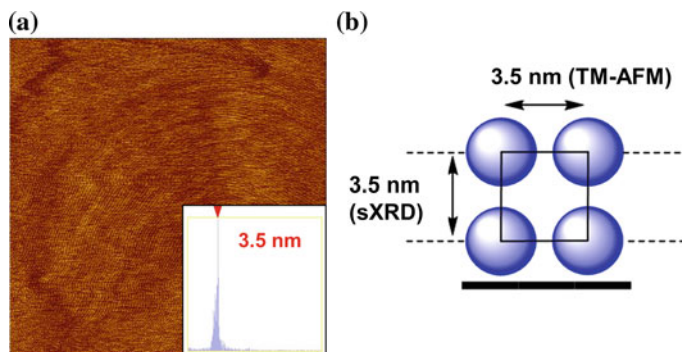
Fig. 9.7 a Higher resolution (400 × 400 nm^2) TM-AFM phase image of a 30 nm-thick **Pc** film. *Inset* is the histogram of distances obtained from a 2D Fourier analysis performed on the image and showing a maximum at 3.5 nm. **b** Schematic representation of the square lattice inferred from both sXRD and TM-AFM measurements. Reproduced from [16] with permission from WILEY-VCH Verlag GmbH & Co. KGaA, Weinheim

The existence of these three distinct regimes strengthens our hypothesis: the **SIP** grows directly on the substrate surface up to a critical thickness above which the organization in **Col$_r$** dominates. According to sXRD and AFM results this critical thickness amounts to around 30 nm.

Higher resolution TM-AFM images taken for films thinner than 30 nm (Fig. 9.7a) allowed resolving individual columns lying flat on the surface (planar alignment). Rather than being straight, the columns are bent and form concentric stripes as already observed for **Pc** in previous studies [30]. A columnar width of 3.5 nm has been determined from a 2D Fourier analysis performed on a 100 nm × 200 nm^2 area of the image shown in Fig. 9.7a which shows a quite sharp distribution of distances around the mean value (inset in Fig. 9.7a). Combining sXRD and TM-AFM results, an identical intercolumnar distance of 3.5 nm is obtained in the directions perpendicular and parallel to the film surface, suggesting a square lattice for the **SIP**, as schematically represented in Fig. 9.7b.

To gain more insight on the structural arrangement of **Pc** molecules in the **SIP**, we performed grazing incidence X-ray diffraction (GIXD) measurements (beamline 1D10B of ESRF, Grenoble, France) on 25 and 30 nm-thick films deposited on Si/SiO$_x$ substrates, that is, the thickness range presenting majorly the **SIP**. The experimental set-up used is represented in Fig. 9.8a. Briefly, a monochromatic X-ray beam (8 keV, 1.55 Å) illuminated the sample at a grazing incident angle α of typically 0.18° (less than the critical angle for total external reflection of the substrate), so that X-ray photons effectively probe the film due to their reduced penetration depth at this incident angle. The diffracted rays were collected on a linear position sensitive detector (PSD) that can be moved in directions parallel (γ angle) and perpendicular (δ angle) to the coplanar scattering plane. A 2D (δ, γ) image of the diffracted intensities is then obtained and subsequently converted into reciprocal coordinates (q_{xy}, q_z) using the PyGid software [16, 23, 31], q_{xy} and q_z being the
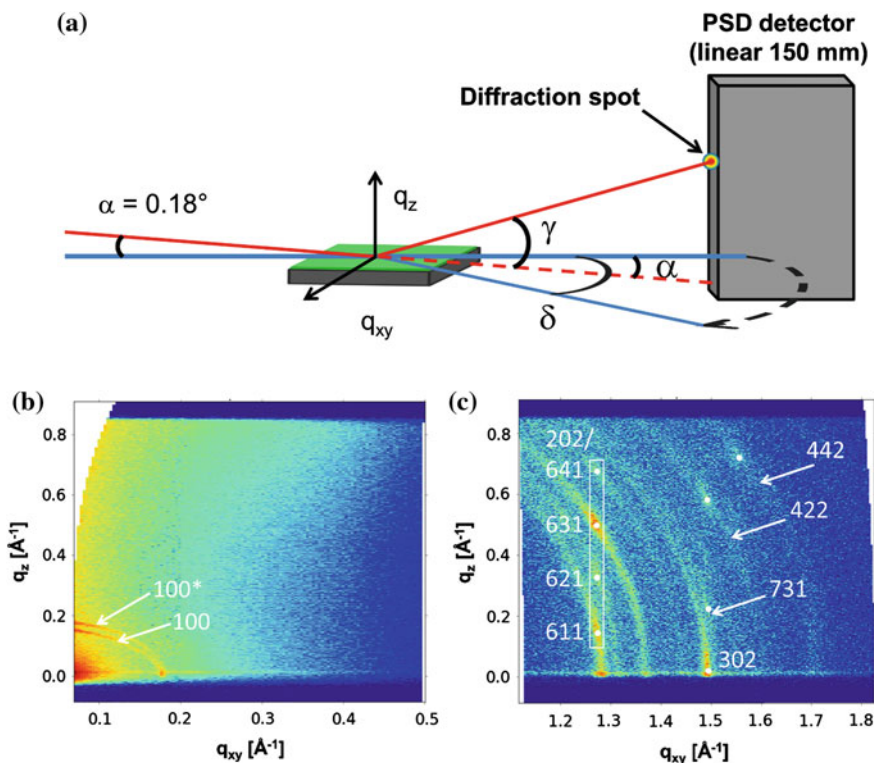
Fig. 9.8 **a** Schematic representation of the experimental set-up used for the GIXD measurements performed at 1D10B of ESRF. **b** Low *q* and **c** high *q* GIXD images obtained for a 25 nm-thick **Pc** film deposited on a Si/SiO$_x$ substrate. For each image, the intensity of all reflections is scaled to the most intensive reflection. Indexations of the observed reflections are given. Diffraction rings are indicated by *white arrows* and the observed maximum intensity in each ring by *white dots*. The *white rectangle* in **c** is put to emphasize the 6k1 family of reflections. Reproduced from [16] with permission from WILEY-VCH Verlag GmbH & Co. KGaA, Weinheim

components of the scattering vector in directions parallel and perpendicular to the film surface, respectively. Figures 9.8b,c display the results of GIXD measurements obtained for 25 nm-thick samples, equivalent results were obtained for 30 nm-thick films.

At low q values (Fig. 9.8b), two diffraction rings are visible at close positions. The position of the inner ring along q_z (indexed as 100 in Fig. 9.8b) is at $q_z = 0.18$ Å^{-1} so exactly at the same position as the first order reflection of the **SIP** revealed by sXRD (see Figs. 9.2 and 9.3). The outer distorted ring (indexed as 100* in Fig. 9.8b) originates, in fact, from the diffraction by the same 100 reciprocal plane of the X-ray beam, after one reflection on the Si/SO$_x$ substrate. Hence, it is shifted upwards from the position of the inner ring of a value Δq which is related to 2α, the angular difference between the incident X-ray beam and the one reflected by

the silicon substrate surface (α is the X-ray beam incident angle, see Fig. 9.8a). The low q GIXD image is therefore consistent with a square lattice ($a = b = 3.5$ nm) with the presence of a unique ring (the outer ring being excluded) extending from ($q_{xy} = 0$, $q_z = 0.18$ Å^{-1}) to ($q_{xy} = 0.18$ Å^{-1}, $q_z = 0$). At high q values, several diffraction rings are revealed, indicating an overall enhanced columnar order compared to the bulk phase. In particular, a family of reflections can be distinguished at $q_{xy} = 1.3$ Å^{-1} (intensity maxima of the rings are equally spaced on a vertical line, see Fig. 9.8c). These reflections could only be indexed with hkl indices with $l \neq 0$, suggesting an enhanced intracolumnar order with the center of mass of the molecules located on a regular lattice. In other words, the **SIP** exhibits a 3D crystal packing of molecules (both inter and intracolumnar long range order), while only 2D packing order prevails for the stable bulk **Col_r** (intercolumnar long range order only). All reflections of the GIXD images, could be indexed using a tetragonal unit cell with the following cell parameters: $a = b = 3.56$ nm, $c = 0.9$ nm, containing 4 molecules and with a density of 1.125 g/cm^3. From packing and symmetry considerations, we propose a structural model for the **SIP** (see Figs. 9.9a, b), consisting of a tetragonal lattice, where the aromatic cores of neighboring **Pc** molecules are rotated by an angle of 45° along the columnar axis. This structural model is consistent with the P4/mcc space group (No 124) with two independent molecules in the asymmetric unit (one at the corner and the other at the center of the unit cell) but too few reflections are available to confirm this assumption. However, taking into account the steric hindrance created by the bulky side chains, this proposition is definitely reasonable [32]. This phase is designated as a *columnar tetragonal crystal plastic phase* [33], since no regular position of atoms can be deduced from GIXD images or sXRD patterns although the center of mass of molecules are located on a regular lattice.
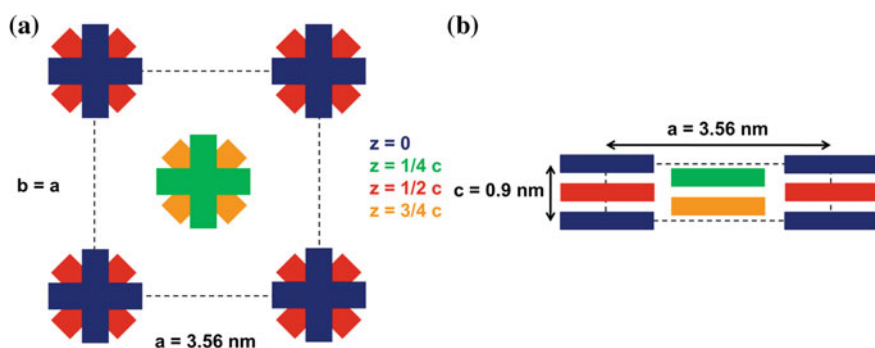
Fig. 9.9 **a** Top view and **b** side view of the proposed molecular packing (at scale) for the **SIP**. In (**a**) crosses represent **Pc** cores and their different colors indicate their respective position along the columnar axis ("z" direction perpendicular to the plane of the drawing) as depicted in (**b**) (*blue*: molecules in the plane of the drawing, *green*: molecules translated of *c/4* from this plane along the columnar axis, *red*: molecules translated of *c/2* and *orange*: molecules translated of *3c/4*). Reproduced from [16] with permission from WILEY-VCH Verlag GmbH & Co. KGaA, Weinheim

9.3 Evolution of the SIP with Time and Temperature

To investigate the non-equilibrium character of this phase, the evolution of the **SIP** was monitored as a function of time and temperature, using polarized optical microscopy (POM) and sXRD. The POM study reveals distinct changes in the morphology of the **Pc** films. Pristine 74 nm-thick **Pc** films show high birefringence, due to the edge-on columnar orientation parallel to the substrate surface (Fig. 9.10a). However with the evolution of time, dendritic growth occurs on the surface (Fig. 9.10b, c). The appearance of dendritic structures in 74 nm film coincides with the appearance of the peak in the sXRD pattern at $q_z = 0.18$ Å^{-1}. Figure 9.10c shows the evolution of sXRD pattern of a 74 nm-thick film as a function of time. As evident from Fig. 9.10, the **SIP** appears to be stable over a longer time scale and exists along with the bulk LC- phase. For films thicker than 150 nm the changes in the morphology upon appearance of the dendrites is not detectable by optical microscopy, but the characteristic diffraction peaks of the **SIP**
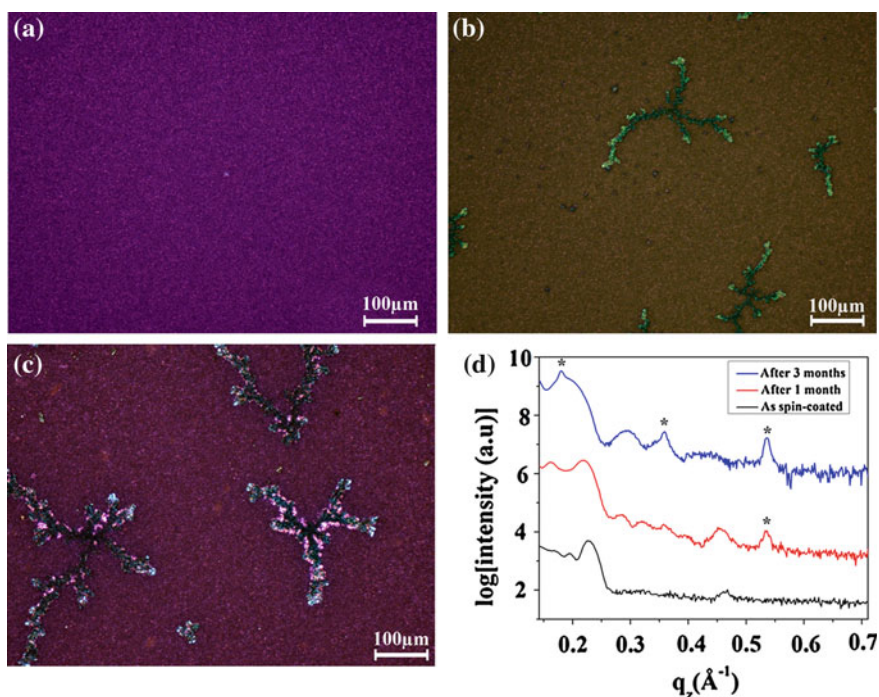
Fig. 9.10 Polarized optical microscopy images of a 74 nm deposited on Si/SiO$_x$ substrates captured for **a** as spin-coated film, and films aged for **b** 1 month and **c** 3 months, showing the changes in morphology. sXRD patterns collected at various times of a 74 nm-thick film deposited on Si/SiO$_x$ substrates; the plots are vertically shifted for clarity. Reflections from the **SIP** (100, 200 and 300) are marked with *star* (*)
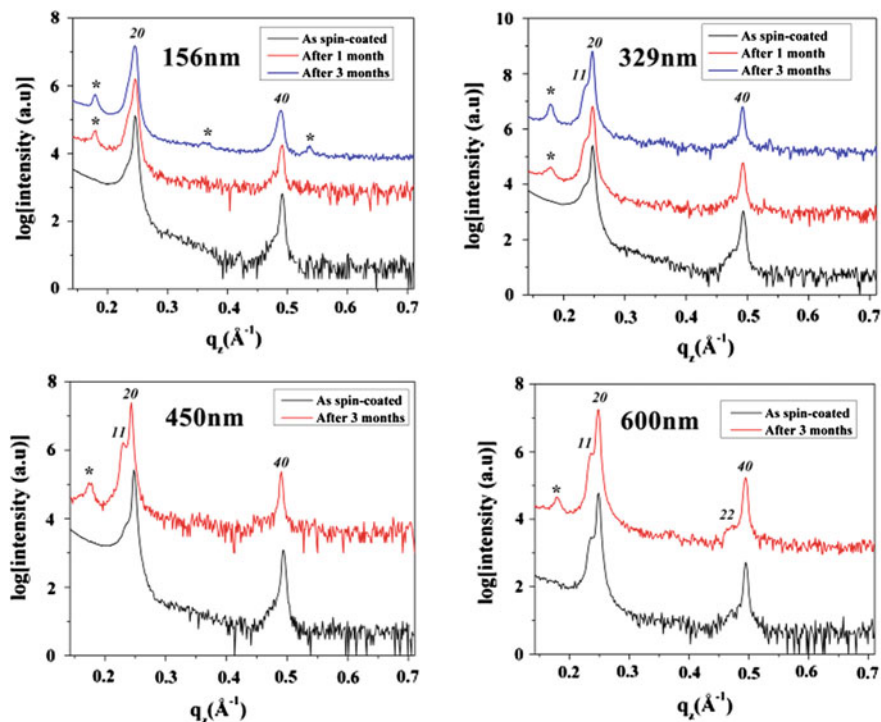
Fig. 9.11 sXRD patterns for as spin-coated films and after 3 months of aging. The *20*, *11* and *40* reflections of the bulk phase are marked and the reflection from the **SIP** are marked with *star* (*)

are distinctly observed at low angle, even for films as thick as 600 nm. The evolution of the sXRD patterns thick films (>150 nm) are illustrated in Fig. 9.11. It must be noted that in the bulk, the sXRD pattern remains unchanged even if the material is studied after storage of 6 months (Fig. 9.12). This behavior is also evident from AFM images (Fig. 9.13) in which the **SIP** is imaged for aged films of 74 nm deposited on a Si/SiO$_x$ substrate. This is quite a unique observation of nucleation and growth initiated by the substrate. Previously a limited number of studies on LCs showed a similar trend, although the main goal of those investigations was the stabilization of a particular orientation in liquid crystal films [34, 35].

In order to determine the temperature window in which the **SIP** exists, variable temperature POM and sXRD studies were performed on a 74 nm-thick **Pc** film deposited on Si/SiO$_x$ substrate (Fig. 9.14). As seen from the POM images (Fig. 9.14a–e), at around 85 °C the dendritic features of the **SIP** start to progressively disappear upon heating, going through different stages of dewetting, finally ending in the formation of isolated droplets at 90 °C. Dewetting is restricted to the regions covered by the dendritic structure, characteristic of the **SIP**. The plastic crystalline **SIP** is found to be stable up to *ca* 85 °C. This phenomenon can be
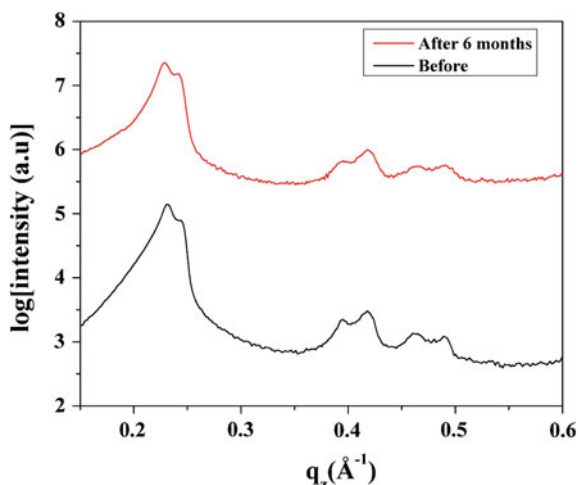
Fig. 9.12 sXRD patterns of bulk **Pc** collected before and after 6 months
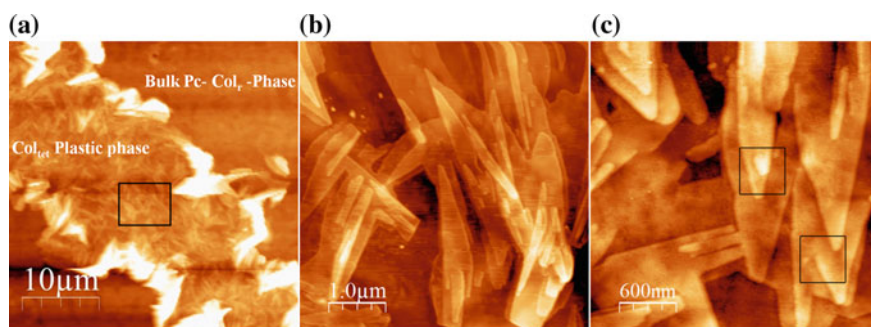
Fig. 9.13 (**a–c**) TM-AFM phase image of a 74-nm-thick **Pc** film deposited on a Si/SiO$_x$ substrate that has been aged for 6 months. The region magnified in (**a**) is shown with a *black square*. In (**c**), the *black squares* highlight the screw dislocations

considered as a transformation of the plastic crystalline **Col$_{tet}$** phase to the high temperature **Col$_h$** mesophase characteristic of **Pc** in bulk and thin films [36–38]. The thermal characteristic of the **SIP** is independent of the nature of the substrate, as well as the time of aging of the film. The **SIP** does not reappear when an aged sample is cooled to room temperature, on the contrary, the dendritic structures are replaced by pseudo focal conical domains (Fig. 9.14e) characteristic of columnar mesophases [37]. This observation is corroborated by sXRD data (Fig. 9.14f) where it is observed that the diffraction peak corresponding to the **SIP** completely disappears at 90 °C. The decrease in intensity of the higher order peaks of the **SIP** from 84 °C (Fig. 9.14f) indicate gradual disappearance of the **SIP**.
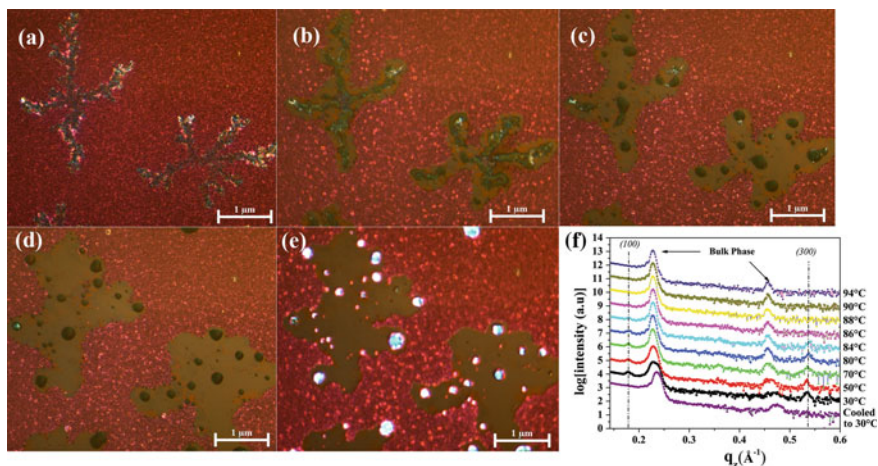
Fig. 9.14 POM images collected at **a** 30 °C, **b** 83.5 °C, **c** 85 °C and **d** 90 °C for a 74 nm-thick **Pc** film deposited on a Si/SiO$_x$ substrate that has been aged for 6 months. **e** POM image of the film as it was cooled to 30 °C. Images were acquired as the films are heated from 30 to 94 °C at 1 °C/min. **f** Variable temperature sXRD patterns of a 74 nm-thick **Pc** film deposited on a Si/SiO$_x$ substrate that has been aged for 6 months; the plots are vertically shifted for clarity. Data were collected at various temperature as the film is heated at a rate of 0.02 °C/s. Reflections from the **SIP** (100 and 300) are marked. The data collected after the film was cooled to 30 °C is shown at the *bottom*

9.4 Nature of Interface and SIP

After having determined the structure of the **SIP** and the morphological changes associated with its appearance, we sought to decipher the reasons responsible for the formation of the substrate-induced phase. To gain some insights into these intriguing questions we modified the interfaces and studied its effect on the **SIP** (Fig. 9.15).

Fig. 9.15 Different film stacks that have been used in our study, the **Pc**-substrate interface is modified in each case
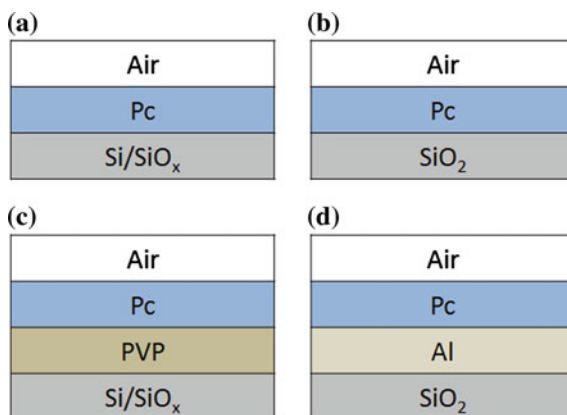
   The formation of the **SIP** was also observed on glass (SiO$_2$) which has a low dielectric constant of ε = 3.9, as already shown in the first section (Fig. 9.3b). We tested the impact of the nature of the substrate by coated Si/SiO$_x$ and SiO$_2$ substrates respectively with PVP and aluminum. Successively, we spin-coated a layer of the **Pc** on the above mentioned multilayers. The sXRD pattern and POM images of 3 months aged **Pc**-films grown on PVP and Al surfaces are illustrated in Fig. 9.16. Aging of the **Pc** films in both the cases result in the appearance of **Col$_{tet}$** plastic phase with the characteristic dendritic morphology. TM-AFM done on a 74 nm-thick **Pc** film deposited on 100 nm layer of PVP reveals that the morphology of the **SIP** is similar to that of the film deposited on Si/SiO$_x$ substrates, i.e. lamellar stacks growing via screw dislocations (Fig. 9.17). Other stacks of **Pc** films were also studied viz. where the **Pc**-air interface was modified. In another experiment, a layer of PVP was deposited on top of **Pc** films. Also in this case, the appearance of
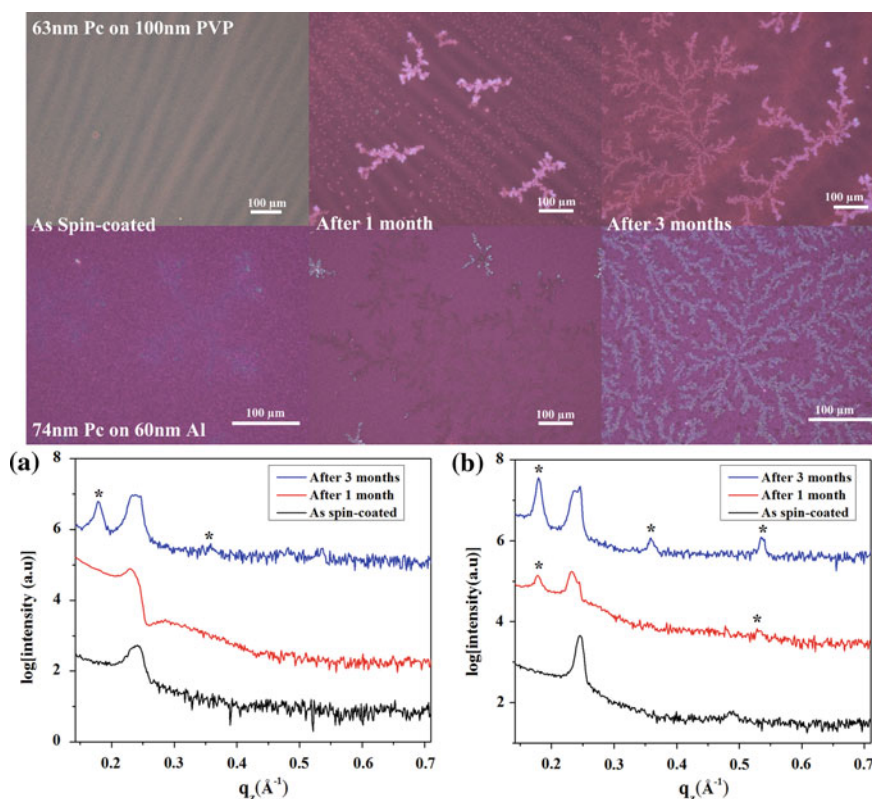
Fig. 9.16 POM images (*top panels*) and sXRD patterns (*bottom panels*) collected for **Pc**-films deposited on **a** layer of 100 nm-thick PVP and **b** 60 nm-thick Aluminum; all the films are aged for 3 months. The sXRD plots are *vertically* shifted for clarity. Reflections from the **SIP** (100, 200 and 300) are marked with *star* (*)
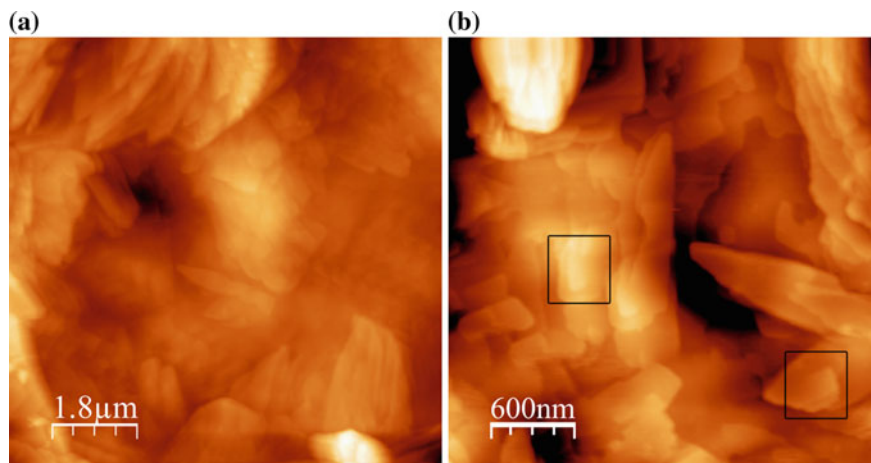
Fig. 9.17 TM-AFM phase image of a 74-nm-thick **Pc** film deposited on **a** 100 nm-thick PVP layer that has been aged for 6 months. In **b**, the *black squares* highlight the screw dislocations

the **SIP** was not altered. Thus, we conclude that the overall nature of the **SIP** is not affected by the nature of the interfaces.

Previous studies demonstrated that the molecular alignment of **Pc** can be controlled by a introduction of a sacrificial layer [30], inducing a conversion of the initial molecular orientation from planar to homeotropic. Like the substrate modification, PVP was the preferred material for the fabrication of the sacrificial layer. Figure 9.18 shows the AFM image of **Pc** films where the initial molecular orientation was successively tuned to homeotropic. The appearance of small crystallites, as seen from the image proves that the formation of the **SIP**, is independent of the starting LC-orientation.

Fig. 9.18 AFM image of a **Pc** film fabricated with the starting orientation as homeotropic which has been aged > 6 months
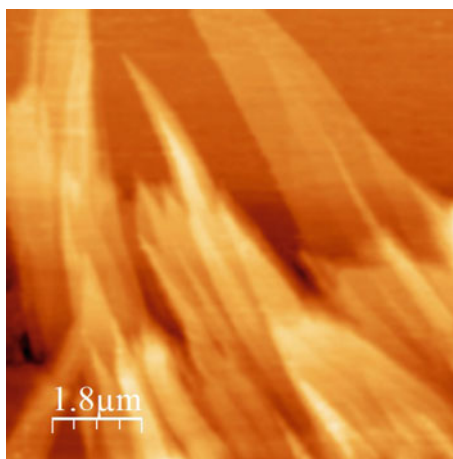
9.5 Discussion on the Origin of the SIP

The thickness of the **SIP** is expected to be a function of the dielectric constant of the substrate. This fact is established by studies done on thin films of pentacene and polystyrene [15, 39, 40]. In our scenario, this theory does not apply, as the **SIP** is observed on Si/SiO$_x$ substrates (composed of a thin SiO$_x$ layer of 2 nm on top of silicon) having a dielectric constant of $\varepsilon = 11.9$ as also on glass (SiO$_2$), PVP and AlO$_x$ with a dielectric constant of $\varepsilon = 3.9$, 5.0 and 9.9, respectively. On the top, the substrate-induced phase exists in contact with air or a sacrificial layer, and the bulk phase. The rectangular lattice of the bulk DLC-phase is incommensurable with the tetragonal phase of the **SIP**. The substrate-induced phase thus forms regardless of the thickness and the structure of the bulk phase as a function of time due to nucleation events initiated by the solid substrate.

In conclusions, the bulk **Col$_r$** phase can thus be considered as intrinsically metastable with respect to the **Col$_{tet}$** phase, and the growth of the latter being kinetically slow with a nucleation process promoted by the presence of solid interfaces. A schematic representation of the phase transition observed here is given in Fig. 9.19. The **SIP** can be viewed as a kinetically hindered phase, whose appearance and growth is a consequence of the geometrical effect imposed by the rigid and impenetrable flat substrate. The **Col$_r$** $\rightarrow$ **Col$_{tet}$** can, hence, be considered a kinetically hindered phase transition stimulated by the substrate. It is an intrinsic material property and no amount of surface engineering can affect its formation.

Fig. 9.19 A schematic overview of the phase transitions in **Pc**
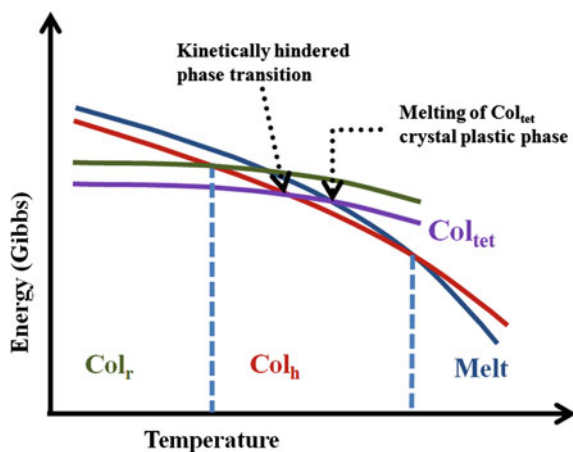
9.6   Conclusions

The implication of such substrate-induced transitions is huge in the field of organic electronics especially in organic transistors where charge transport occurs at the interface between the organic semiconductors and the dielectric. Furthermore, recently developed processing conditions of OSC thin films effectively enhancing device performance, conversely involve far from equilibrium conditions [20, 41–43]. Thus, the knowledge of such non-equilibrium phenomenon is crucial to understand and establish the structure-property relationship in materials. The **SIP** dealt with herein is a perfect example of the drastic modification of the phase behavior of an organic compound at non equilibrium conditions.

References

1. Chandrasekhar, S., Sadashiva, B.K., Suresh, K.A.: Mol. Cryst. Liq. Cryst. **397**, 295 (2003)
2. Levelut, A.M.: J. Chim. Phys. **80**, 149 (1983)
3. Guillon, D.: Struct. Bonding **95**, 41 (1999)
4. Bao, Z., Lovinger, A.J., Dodabalapur, A.: Adv. Mater. **9**, 42 (1997)
5. Bao, Z., Lovinger, A.J., Brown, J.: J. Am. Chem. Soc. **120**, 207 (1998)
6. Liu, X., Usui, T., Hanna, J.: Chem. Mater. **26**, 5437 (2014)
7. Schmidt-Mende, L., Fechtenkötter, A., Müllen, K., Moons, E., Friend, R.H., MacKenzie, J.D.: Science **293**, 1119 (2001)
8. Levitsky, I.A., Euler, W.B., Tokranova, N., Xu, B., Castracane, J.: Appl. Phys. Lett. **85**, 6245 (2004)
9. Ohta, K., Hatsusaka, K., Sugibayashi, M., Ariyoshi, M., Ban, K., Maeda, F., Naito, R., Nishizawa, K., van de Craats, A.M., Warman, J.M.: Mol. Cryst. Liq. Cryst. **397**, 25 (2003)
10. Laschat, S., Baro, A., Steinke, N., Giesselmann, F., Hägele, C., Scalia, G., Judele, R., Kapatsina, E., Sauer, S., Schreivogel, A., Tosoni, M.: Angew. Chem. Int. Ed. **46**, 4832 (2007)
11. Sergeyev, S., Pisula, W., Geerts, Y.H.: Chem. Soc. Rev. **36**, 1902 (2007)
12. Bisoyi, H., Li, Q.: Nanoscience with Liquid Crystals, p. 209. Q. Li (ed.) Springer International Publishing, Dordrecht (2014)
13. Brédas, J.L., Calbert, J.P., da Silva Filho, D.A., Cornil, J.: Proc. Natl. Acad. Sci. U.S.A. **99**, 5804 (2002)
14. Dinelli, F., Murgia, M., Levy, P., Cavallini, M., Biscarini, F., de Leeuw, D.M.: Phys. Rev. Lett. **92**, 116802 (2004)
15. Drummy, L.F., Martin, D.C.: Adv. Mater. **17**, 903 (2005)
16. Gbabode, G., Dumont, N., Quist, F., Schweicher, G., Moser, A., Viville, P., Lazzaroni, R., Geerts, Y.H.: Adv. Mater. **24**, 658 (2012)
17. Chattopadhyay, B., Ruzié, C., Resel, R., Geerts, Y.H.: Liq. Cryst. **41**, 302 (2014)
18. Bouchoms, I.P.M., Schoonveld, W.A., Vrijmoeth, J., Klapwijk, T.M.: Synth. Met. **104**, 175 (1999)
19. Mattheus, C.C., Dros, A.B., Baas, J., Oostergetel, G.T., Meetsma, A., de Boer, J.L., Palstra, T. T.M.: Synth. Met. **138**, 475 (2003)

20. Giri, G., Verploegen, E., Mannsfeld, S.C.B., Atahan-Evrenk, S., Kim, D.H., Lee, S.Y., Becerril, H.A., Aspuru-Guzik, A., Toney, M.F., Bao, Z.: Nature **480**, 504 (2011)
21. Giri, G., Li, R., Smilgies, D.-M., Li, E.Q., Diao, Y., Lenn, K.M., Chiu, M., Lin, D.W., Allen, R., Reinspach, J., Mannsfeld, S.C.B., Thoroddsen, S.T., Clancy, P., Bao, Z., Amassian, A.: Nat Commun **5** (2014)
22. Salzmann, I., Nabok, D., Oehzelt, M., Duhm, S., Moser, A., Heimel, G., Puschnig, P., Ambrosch-Draxl, C., Rabe, J.P., Koch, N.: Cryst. Growth Des. **11**, 600 (2011)
23. Wedl, B., Resel, R., Leising, G., Kunert, B., Salzmann, I., Oehzelt, M., Koch, N., Vollmer, A., Duhm, S., Werzer, O., Gbabode, G., Sferrazza, M., Geerts, Y.: RSC Adv. **2**, 4404 (2012)
24. Jones, A.O.F., Geerts, Y.H., Karpinska, J., Kennedy, A.R., Resel, R., Röthel, C., Ruzié, C., Werzer, O., Sferrazza, M.: ACS Appl. Mater. Interfaces **7**, 1868 (2015)
25. Diao, Y., Lenn, K.M., Lee, W.-Y., Blood-Forsythe, M.A., Xu, J., Mao, Y., Kim, Y., Reinspach, J.A., Park, S., Aspuru-Guzik, A., Xue, G., Clancy, P., Bao, Z., Mannsfeld, S.C.B.: J. Am. Chem. Soc. **136**, 17046 (2014)
26. Werzer, O., Boucher, N., de Silva, J.P., Gbabode, G., Geerts, Y.H., Konovalov, O., Moser, A., Novak, J., Resel, R., Sferrazza, M.: Langmuir **28**, 8530 (2012)
27. Lercher, C., Resel, R., Balandier, J.-Y., Niebel, C., Geerts, Y.H., Sferrazza, M., Gbabode, G.: J. Cryst. Growth **386**, 128 (2014)
28. Collard, D.M., Lillya, C.P.: J. Am. Chem. Soc. **113**, 8577 (1991)
29. Tylleman, B., Gbabode, G., Amato, C., Buess-Herman, C., Lemaur, V., Cornil, J., Gómez Aspe, R., Geerts, Y.H., Sergeyev, S.: Chem. Mater. **21**, 2789 (2009)
30. Pouzet, E., Cupere, V.D., Heintz, C., Andreasen, J.W., Breiby, D.W., Nielsen, M.M., Viville, P., Lazzaroni, R., Gbabode, G., Geerts, Y.H.: J. Phys. Chem. C **113**, 14398 (2009)
31. Moser, A.: PhD, Graz University of Technology, 2012
32. Tant, J., Geerts, Y.H., Lehmann, M., De Cupere, V., Zucchi, G., Laursen, B.W., Bjørnholm, T., Lemaur, V., Marcq, V., Burquel, A., Hennebicq, E., Gardebien, F., Viville, P., Beljonne, D., Lazzaroni, R., Cornil, J.: J. Phys. Chem. B **109**, 20315 (2005)
33. Simmerer, J., Glüsen, B., Paulus, W., Kettner, A., Schuhmacher, P., Adam, D., Etzbach, K.-H., Siemensmeyer, K., Wendorff, J.H., Ringsdorf, H., Haarer, D.: Adv. Mater. **8**, 815 (1996)
34. Grelet, E., Dardel, S., Bock, H., Goldmann, M., Lacaze, E., Nallet, F.: Eur. Phys. J. E **31**, 343 (2010)
35. Cour, I., Pan, Z., Lebruin, L.T., Case, M.A., Furis, M., Headrick, R.L.: Org. Electron. **13**, 419 (2012)
36. Mouthuy, P.-O., Melinte, S., Geerts, Y.H., Jonas, A.M.: Nano Lett. **7**, 2627 (2007)
37. De Cupere, V., Tant, J., Viville, P., Lazzaroni, R., Osikowicz, W., Salaneck, W.R., Geerts, Y.H.: Langmuir **22**, 7798 (2006)
38. Calo, A., Stoliar, P., Cavallini, M., Sergeyev, S., Geerts, Y.H., Biscarini, F.: J. Am. Chem. Soc. **130**, 11953 (2008)
39. Herminghaus, S., Jacobs, K., Mecke, K., Bischof, J., Fery, A., Ibn-Elhaj, M., Schlagowski, S.: Science **282**, 916 (1998)
40. Jacobs, K., Seemann, R., Herminghaus, S.: Polym. thin films **243** (2008)
41. Amassian, A., Pozdin, V.A., Li, R., Smilgies, D.-M., Malliaras, G.G.: J. Mater. Chem. **20**, 2623 (2010)
42. Tracz, A., Makowski, T., Masirek, S., Pisula, W., Geerts, Y.H.: Nanotechnology **18**, 485303 (2007)
43. Schweicher, G., Paquay, N., Amato, C., Resel, R., Koini, M., Talvy, S., Lemaur, V., Cornil, J. R.M., Geerts, Y., Gbabode, G.: Cryst. Growth Des. **11**, 3663 (2011)

Chapter 10
1D Confinement Stabilizes Non-equilibrium Liquid Phase with Enhanced Orientational Order

Simona Capponi, Simone Napolitano and Michael Wübbenhorst

Abstract Recent models of the glass transition rationalize the relevant features of vitrification by introducing the concept of medium range order in supercooled liquids. In particular, a crucial role is assigned to the orientational order induced by intermolecular bonding (bond orientational order, BOO). Although this idea is very appealing, severe difficulties limit the experimental determination of the BOO in molecular liquids: because of the small difference in entropy and in form factor between the isotropic liquid and the phase rich in orientational order, calorimetry and scattering techniques cannot be used to assess the BOO. In this chapter we describe an innovative model to investigate BOO via broadband dielectric spectroscopy. We verified that ultrathin films of polyols deposited by physical vapor deposition below their glass transition temperature show an extraordinary enhancement in bond orientational, indicated by a huge enhancement of the dielectric strength with respect to the bulk values. Hint of an underlying phase transition was found from a liquid phase enriched in bond orientational order, with a metastable character, towards an ordinary liquid phase. The kinetic stability of the metastable phase could be tuned by varying the deposition conditions and the molecular size. The impact of film thickness and of the presence of a solid substrate on the persistence of enhanced BOO were also investigated. We demonstrate that confinement stabilizes the non-equilibrium character of our supercooled liquids with enhanced orientational order.

S. Capponi (✉)
School of Physics, University College Dublin, Belfield D4 Dublin, Ireland
e-mail: simona.capponi@ucd.ie

S. Napolitano
Laboratory of Polymer and Soft Matter Dynamics, Faculté Des Sciences, Université Libre de Bruxelles (ULB), Boulevard Du Triomphe, Brussels 1050, Belgium

M. Wübbenhorst (✉)
Laboratory of Acoustics and Thermal Physics, Department of Physics and Astronomy, Katholieke Universiteit Leuven, Celestijnenlaan 200D, Leuven 3001, Belgium
e-mail: michael.wubbenhorst@fys.kuleuven.be

Symbols

$\Delta\varepsilon_N^{max}$	Maximum value of $\Delta\varepsilon_N$
g_6^{3D}	Spatial correlation function of g_6
LFSs	Locally favoured structures
μ	Dielectric dipole moment
m	Fragility index
MROL	Medium Range Order Liquid
OL	Ordinary Liquid
S	Concentration of locally favoured structures
τ	Structural relaxation time
T_g	Glass transition temperature
TOP	Two Order Parameters (Model)
v	MROL to OL transformation velocity

10.1   Introduction

The glass transition is one of the most fascinating unsolved problems of condensed matter. One of the largest difficulties in understanding the mechanisms governing the conversion of a supercooled liquid into a glass is the apparent absence of any order at length scales larger than the short range (first shell of neighbors). In particular, when crossing the glass transition temperature, T_g, from high to low temperatures, minor variations in density (<5 %) are accompanied by a tremendous increase in viscosity (by more than 10 decades).

Recent models rationalize these crucial features of vitrification with the presence of medium-range ordered regions coexisting with the isotropic liquid. In this framework, the Two Order Parameter (TOP) model, proposed by Tanaka, offers a promising advance in the field towards a self-consistent theory of glass transition.

By introducing an anisotropic contribution to the intermolecular interaction potential, the isotropic liquid gets enriched in structures abundant in bond orientational order (BOO) at temperatures below the melting point. Unfortunately, direct observation of BOO in supercooled liquids by classic diffraction techniques, like X-rays, electron or neutron diffraction, has so far failed.

In this chapter we illustrate an experimental study of the BOO in ultrathin films of supercooled polyols, grown by physical vapor deposition and investigated by broadband dielectric spectroscopy.

We observed an extraordinary enhancement in bond orientational order, in ultrathin films deposited below their glass transition temperature, as revealed by extraordinary high values of the dielectric strength with respect to the bulk [1]. By varying the deposition conditions and the molecular size, we could tune the kinetic stability of the liquid phase enriched in bond orientational order (MROL) towards conversion into the ordinary liquid phase.

Monitoring the recovery of bulk values of the dielectric strength upon heating revealed very high kinetic stability of our systems (very slow conversion), suggesting the existence of a metastable liquid phase with improved orientational correlations. Remarkably the MROL non-equilibrium phase is stabilized upon confinement by the presence of solid supporting substrates. This chapter is organized as follows. In Sect. 2 we revise recent theories of the glass transition predicting the presence of medium range order, in Sect. 3 we present our experimental evidences supporting these new models.

10.2 Medium Range Order and Glass Transition

The presence of clusters with short or medium range order in the liquid phase has been predicted, on the basis of free energy considerations, since 1983 by Steinhardt and co-workers [2]. Considering Lennard-Jones liquids below the equilibrium melting temperature, T_m, the formation of particle clusters is characterised by short-range translational order with extended orientation correlations. The average mutual molecular orientation between two neighbour molecules was defined as bond-orientational order (BOO). In the following decades the role of BOO as a driver for vitrification upon cooling has been extensively discussed [3–6].

A class of theoretical models, named frustration models, considers the glass transition as the consequence of an avoided phase transition of a liquid into its crystalline state, due to presence of molecular clusters whose organisation is incompatible with the long range positional order, required for crystallization. Despite this apparent shortcoming, such clusters are stabilized by their ability to minimize local free energy by a higher degree of specific energetic interactions, like directional bonds (e.g. hydrogen bonds). Hence they are indicated as locally favoured structures (LFSs).

The most stable type of cluster is composed of a central atom and a shell of twelve neighbours, forming an icosahedron, whose spatial structure does not fit to any known crystalline phase. Regardless of these topological details, the molecular arrangement in a LFS can be described by a local order parameter, ψ (r,t). In the case of icosahedra the most commonly used parameter is given by the hexatic order and it has the form [7]:

$$\psi_6(r, t) = \sum_{ij} \left| \vec{u}_i(t) - \vec{u}_j(t) \right| \tag{1}$$

where $\vec{u}_i(t)$ is the orientation of the i-th molecule.

Upon cooling below T_m, the orientational order of the LFSs can occasionally grow towards medium range order, forming regions with increasing size upon temperature reduction. This scenario is confirmed by the two order parameters model (TOP), developed by Tanaka [5, 6]. Differently from the aforementioned theories, the TOP model does not rationalise the frustration of crystallization solely on the basis of geometrical considerations, but it accounts as well for the energetic contribution of LFSs to the energy potential of the system. In this framework, vitrification is described as the result from two competing processes occurring during the liquid to solid transition: the density ordering, controlled by the molecular density ρ, which drives the system to crystallization, and the bond ordering controlled by ψ_6, maximising the intermolecular bonds and promoting the formation of LFSs, which in turn frustrates crystallization.

The molecular bond energy that derives from intermolecular interactions inside the LFSs gives an anisotropic contribution $\delta V(r,\Omega)$ to the overall potential of the system $V(r,\Omega)$, which is thus given by:

$$V(r, \Omega) = V(r) + \delta V(r, \Omega) \tag{2}$$

where r is the distance from the centre of mass of a given molecule, and Ω expresses its orientation. Both the concentration of LFSs and the depth of the minima they occupy in the energy landscape are determined exclusively by $\delta V(r,\Omega)$. Similarly, the energy barrier ΔE separating the LFSs from the isotropic liquid is determined only by $\delta V(r,\Omega)$, while their concentration is given by [3]:

$$S = S_0 \exp\left(\frac{\Delta E - P\Delta V}{k_B T}\right) \tag{3}$$

where P and ΔV are respectively the pressure and the change in volume induced by the formation of LFSs, $\Delta E = n\delta V(r,\Omega)$, being n the number of LFSs.

Upon cooling, the molecules in proximity of the LFSs assume a correlated orientation, forming regions characterized by medium range order. These regions, called medium range crystalline ordered regions (MCRO), are surrounded by amorphous liquid. The extent of molecular orientation within the MRCOs is quantified by the bond orientational order parameter, for which the hexatic form described by Eq (1) is assumed.

Applying the thermodynamic treatment proposed by [8] for critical phenomena, the TOP model is able to predict both the correlation length $\xi(T)$, i.e. the spatial extent of the intermolecular orientational correlation and the structural relaxation time inside the MRCO, τ_{MRCO}. The thermodynamic fluctuations of $\psi_6(r,t)$ are described by the equation:

$$\frac{d\psi_6}{dt} = -L_0 \frac{\delta F(\psi_6)}{d\psi_6^*} \tag{4}$$

where F is a functional for the free energy, and L_0 is a microscopic transport coefficient. The solutions of Eq. (4) are the hydrodynamic modes of the system, characterized by a wave vector k and a relaxation rate Γ_k, which represents the extinction rate of the correlation function of the hexatic order parameter:

$$C(k, t) = \langle \psi_k(t) - \psi_{-k}(t) \rangle = C(k, 0) \exp\left(-\Gamma_k(t)\right) \tag{5}$$

Thus, the lifetime of a MRCO region, τ_{MRCO}, is naturally defined as the inverse of Γ_k, $\tau_{MRCO} = 1/\Gamma_k$. The characteristic size of a MRCO is instead identified with the correlation length of $\psi_6(r,t)$ defined as $\xi \equiv k^{-1}$ and related to the critical temperature T_0 by the relation:

$$\xi = \xi_0 \left(\frac{T - T_0}{T_0}\right)^{\upsilon} \tag{6}$$

where ξ_0 and υ are respectively the bare correlation length (corresponding to the molecular size) and a critical exponent. Γ_k and ξ are related according to:

$$\Gamma_k \propto [1 + (k\xi)] \tag{7}$$

Numerical values for the structural relaxation time of the whole liquid, τ_α, can be computed by numerical simulations via Eq. (4). The results revealed a Vogel-Fulcher-Tammann like temperature dependence for τ_α:

$$\tau_\alpha = \tau_0 \exp\left(\frac{DT_0}{T - T_0}\right) \tag{8}$$

where D is the fragility parameter, dependent on the anisotropic contribution to the potential energy, δV. This implies that materials with higher anisotropic potential (higher frustration against crystallization) possesses a higher dynamic fragility [6].

The TOP model also explains the origin of the increase in the dynamic heterogeneity in supercooled liquids upon cooling, as a natural consequence of the increase of the spatial extent of orientation correlation at lower temperatures. The extent of heterogeneity is quantified by the spatial correlation function of ψ_6, given by [9, 10]:

$$g_6^{3D}(r) \propto r^{-1} \exp\left(\frac{r}{\xi_6}\right) \tag{9}$$

where ξ_6 is the correlation length of the hexatic order parameter. Numerical simulations reveal that g_6^{3D} decreases upon cooling, implying an increase in the correlation length ξ_6, i.e. a larger spatial extent of the bond orientational correlation between molecules. The volume of the MRCOs increases against the isotropic liquid, hence the system becomes more heterogeneous.

10.3 Experimental Evidence of the MRCOs

Despite the interest raised by medium ordered structures in the last decades, direct experimental evidence of their presence in supercooled liquids has not been achieved so far by means of diffraction techniques like X-rays, electron or neutron diffraction. In 2010, Zeng and co-workers obtained indirect evidence of large ordered crystalline structures in metallic glasses, [11] whose presence was deduced by the pressure induced crystallization of the entire system. However the detection of the incipient, local cluster was not possible. This was explained by the fact, proved by classical molecular simulations [11], that the structure factor of the glass with or without crystalline structures is virtually undistinguishable. Such result would also explain the previous failures.

To overcome these experimental issues, we successfully developed an experimental approach permitting to investigate bond orientational order in supercooled liquids. This approach combines physical vapor deposition (PVD) in the glassy state, leading to an enhancement of the BOO, with in situ dielectric spectroscopy to monitor orientation correlations after recovery of the super-cooled liquid state. PVD of organic glass formers below T_g allows the production of ultra-dense glasses, characterized by an unprecedented low excess enthalpy, high glass density and thermodynamic and kinetic stability, hence the name "ultrastable glasses" [12]. Vapor deposition in the glassy state takes advantage of the enhanced molecular mobility at the free surface, where evaporated molecules can rapidly sample the energetic landscape and reach deeper minima before being buried by the upcoming molecular layers. The improved sampling of the energy landscape can also be exploited to obtain a liquid phase enriched in regions with medium-range order. To verify this idea, we considered highly polar materials with low molecular weight like glycerol, threitol and xylitol, where enhanced BOO is expected, due to the presence, already in the liquid state, of temporary H-bonded networks that rely on highly directional, i.e., anisotropic, intermolecular interactions [13, 14].

Figure 10.1 shows a scheme of the experimental set up we used for our studies.

In our experiment organic thin layers are grown directly on the surface of an interdigitated comb electrode (IDE), which senses the dielectric properties of the layer. This specific sensor is employed because its open-electrode configuration allows performing in situ dielectric spectroscopy while permitting a continuous evaporation of material on the target substrate. IDEs were produced by UV lithography, and are composed of 100 gold fingers (height $\sim$ 200 nm; length $\sim$ 15 mm) deposited on a quartz substrate. Each pair of fingers is spaced 1.25 mm apart, resulting in a total capacitance of 5 pF. Silver wires were glued on the connectors of the IDE via a thermally and electrically conductive epoxy resin filled with silver nanoparticles (Ecolit E 325) and soldered to a high-vacuum feedthrough, which allowed connection to an impedance analyzer (ALPHA, Novocontrol). The intensity of the applied electric field E was below 10^6 Vm^{-1}, a regime in which the polarization response is linearly proportional to E.
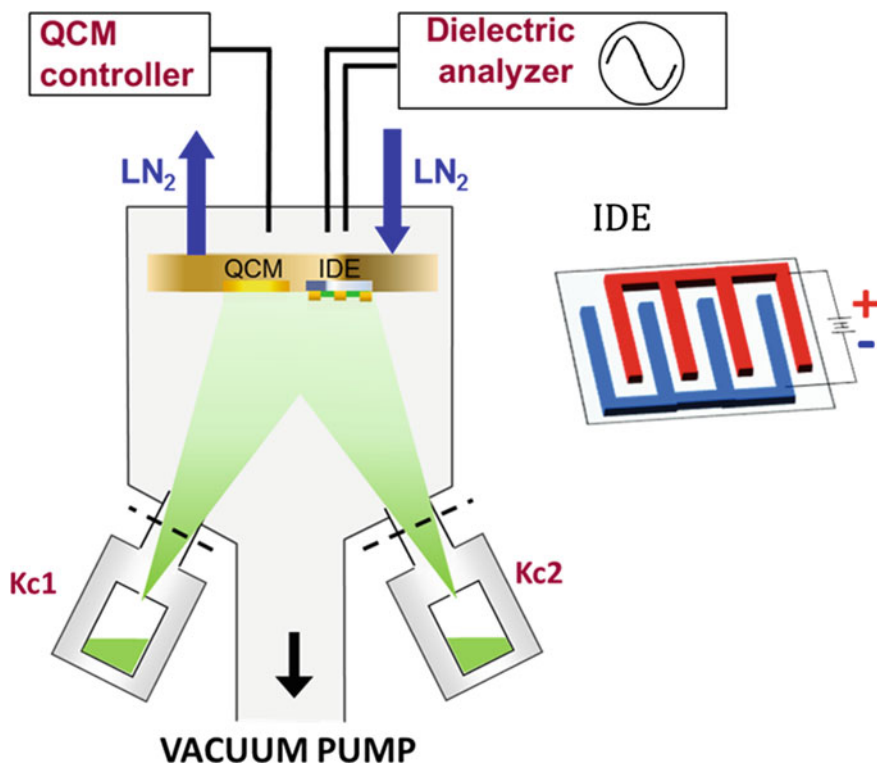
Fig. 10.1 Sketch of the experimental set up. The starting bulk material is heated above its melting temperature in a crucible connected, to a vacuum chamber via a pneumatic valve. The films are deposited directly on interdigitated comb electrode (IDE) used to perform dielectric measurements. The thickness is monitored via a quartz crystal microbalance (QCM). The temperature of the substrate, T_{sub}, is controlled by the combined action of a resistance heating and a cooling flux of gaseous nitrogen

Evaporation is performed in ultra-high vacuum at a pressure $p \sim 10^{-8}$ mbar. A quartz crystal microbalance (QCM) monitors the growth rate and the absolute layer thickness with monolayer sensitivity. Both the IDE and the QCM are located inside the vacuum chamber, and mounted on a metallic plate, serving as stage for the temperature control of the two sensors. The temperature control is achieved by the combined action of a resistance heating and a cooling flux of gaseous nitrogen. A Pt100 sensor is glued to the substrate of the IDE with Elecolit E 325 to monitor the temperature as close as possible to the IDE structures, T_{sub}. The organic material to be evaporated is stored in two Knudsen cells, which can be independently attached/detached to the vacuum, by electro-pneumatic valves, interposed between the cells and the fits that connect them to the chamber. The deposition rate can be tuned by varying the temperature and aperture's size of the Knudsen cells.

Investigation of the BOO of our systems is performed analyzing the dielectric permittivity. In particular, the strength of the structural relaxation $\Delta\varepsilon$ is directly

correlated to the BOO, because $\Delta\varepsilon$ depends on the average orientation of the molecular dipole moment μ [15]. Indeed relationship between $\Delta\varepsilon$ and μ is given by:

$$\Delta\varepsilon = \frac{1}{3\varepsilon_0} F \cdot g \frac{\mu^2}{k_B T} \frac{N}{V} \tag{10}$$

with F the Fröhlich parameter, N the number of dipole moments in the volume V and g the Kirkwood correlation factor. This last quantity is given by

$$g = \frac{\left\langle \sum_{i=1}^{N} \vec{\mu}_i \sum_j \vec{\mu}_j \right\rangle}{N\mu^2} \approx 1 + z\langle \cos\psi \rangle \tag{11}$$

where $\vec{\mu}_i$ is the dipole moment of the ith molecule; z is the number of correlated molecules around a given central molecule, and <cos(ψ)> is a statistically averaged cosine of the angle ψ between two neighboring dipoles. Thus, if the dipole moments have a tendency for parallel orientation, then g > 1, whereas 0 < g < 1 implies an antiparallel orientation. A random orientation of the dipoles, instead, corresponds with the absence of orientational correlation expressed by g = 1. Accordingly, enrichment in MRO regions would lead to a variation in g, due to locally enhanced orientational correlation: g might increase or a decrease depending on the spatial organization of the molecules in the local clusters [15].

Dielectric spectroscopy also allows monitoring the structural relaxation time and, eventually, its slowdown as expected in the case of higher fractions of MROs. Furthermore, investigation of the form of the relaxation peaks in the frequency domain permitted us to characterize the dynamic heterogeneity of our films. For this purpose, a quantitative analysis was achieved via fits of the experimental data to the Havrialiak-Negami equation

$$\varepsilon * (\omega) = \varepsilon_\infty - \frac{\Delta\varepsilon}{\left[1 + (i\omega\tau_{HN})^\alpha\right]^\beta} \tag{12}$$

where ε_∞ is the dielectric constant in the limit of very high frequencies, τ_{HN} is the structural relaxation time, while α and β are shape parameters, respectively related to symmetric and asymmetric broadening.

For our measurements, we used interdigitated comb electrodes (also shown in Fig. 10.1), where the electric field is applied parallel to the surface. Consequently, the contribution of each layer to the dielectric strength is purely additive:

$$\Delta\varepsilon = \sum_j \Delta\varepsilon_j h_j \tag{13}$$

where h_j is the thickness of the j-th layer.

Glycerol films with thickness in the range between 10 and 130 nm showed a tremendous enhancement in the dielectric strength, over three times higher than the value measured for bulk glycerol films deposited well above the glass transition temperature T_g [16]. This behavior is indeed consistent with the concept of a liquid state having enhanced medium range order (MRO) and enhanced BOO, with respect to the ordinary liquid phase (OL). Hereafter, this particular liquid phase will be denoted as medium-range order enriched liquid (MROL).

Figure 10.2a, b below show the dielectric response of an 11 nm thick glycerol film, deposited at 166 K (T_g − 22 K), while Fig. 10.3 shows the temperature evolution of $\Delta\varepsilon_N = \Delta\varepsilon_{MROL}/\Delta\varepsilon_{OL}$ upon heating, just after deposition, and upon subsequent cooling down to the previous temperatures.

The parameter $\Delta\varepsilon_N$ quantitatively expresses the perturbation in the molecular orientation in the MROL, and its temperature dependence is a measure of the kinetic stability of the system against transformation into OL. A progressive reduction of $\Delta\varepsilon_N$ is observed upon heating, until a value of 1.7 is reached.

To better understand this trend, we calculated the value of $\Delta\varepsilon$ assuming the scenario of a system composed by two phases, MROL and OL, where the MROL transforms continuously into the ordered liquid state. Owing to the linear

Fig. 10.2 a Temperature dependence of C"(f, T), the imaginary part of the capacitance, showing a strong, gradual reduction in the intensity of the structural peak, at T > 203 K (*black arrow* in both panels).
b Correspondent temperature dependence of the frequency f_{max}, (*solid line*), compared to the values obtained for bulk glycerol (*dashed line*)
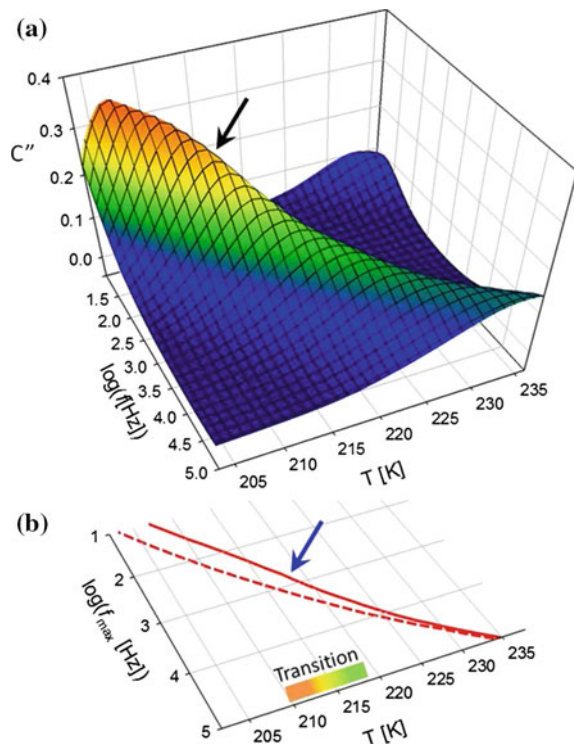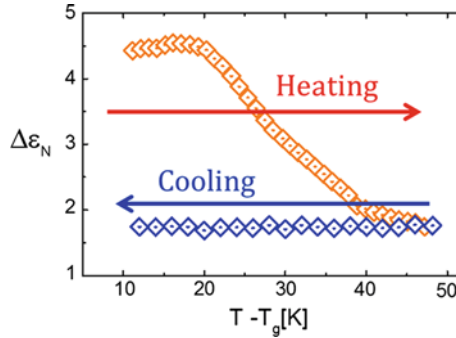
Fig. 10.3 Temperature evolution of dielectric strength normalized to the values in the ordinary supercooled liquid ($\Delta\varepsilon_N/\Delta\varepsilon_{OL}$) for the same film, as measured during heating after deposition (*orange diamonds*) and during subsequent cooling (*blue diamonds*)

deconvolution of the signal arising from the different layers composing the film ensured by Eq. 13, we computed the total dielectric response of the system as:

$$\varepsilon_{TOT} = x_{OL} \cdot R\varepsilon_{OL} + x_{MROL} \cdot \varepsilon_{OL} = R\varepsilon_{OL}(L - \Delta l)/L + \varepsilon_{OL} \cdot \Delta l/L \qquad (14)$$

where x_{OL} and x_{MROL} are the volume fractions of the two phases, and $R = \Delta\varepsilon_N^{max}/\Delta\varepsilon_{OL}$. The results are summarized in Fig. 10.4. In panel B we observe a broadening of the dielectric loss, indicating an increase in the dynamic heterogeneity of the system, resulting from the simultaneous presence of the two different liquid phases. We verified that our experimental evidence confirms this prediction. In Fig. 10.5, we compared the values of the shape parameters obtained in our simulated scenario with the measured dielectric spectra. In particular, an increase in spatial heterogeneity is given by an asymmetric broadening of the peaks, thus a reduction of both α and β, (see Eq. 12).

Films in the MROL phase also showed slower dynamics, as indicated by values of the structural relaxation time τ_{MROL} 4–5 times longer than the OL phase, corresponding to a shift in T_g of $\sim$ 4 K (Fig. 10.2d). This finding is in line with the quantitative predictions proposed both for Lennard–Jones liquids [6], and for model polymeric systems [17]. However, τ_{MROL} decreases continuously upon cooling, until the bulk value is fully recovered, and it remains unchanged upon following cooling.

However, while both $\Delta\varepsilon_N$ and τ_{MROL} manifest the presence of an underlying phase transition, the second one shows much lower sensitivity to variation in the BOO with respect to $\Delta\varepsilon_N$ and lower kinetic stability against transformation (Figure 10.6).

By fitting simulated dielectric curves with Eq. 12 we could calculate the dependence of both parameters on the volume fraction of converted liquid (Fig. 10.7). Here, $\Delta\varepsilon_N$ shows the expected linear dependence on the OL volume fraction (i.e. on the conversion), while τ remains almost constant up to a conversion
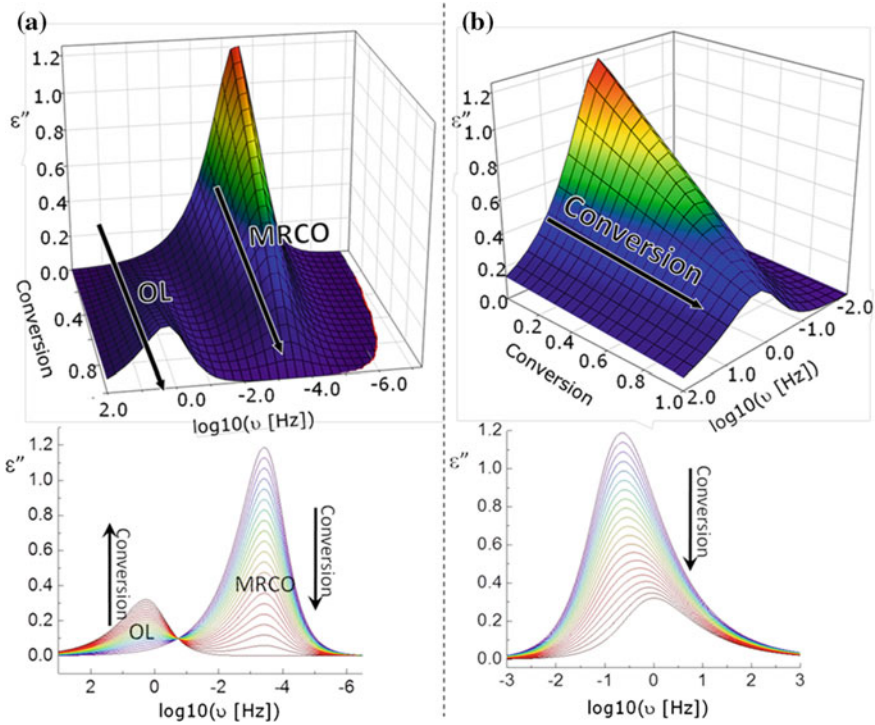
Fig. 10.4 Simulated dielectric spectra during the conversion from MRCO to OL. The impact of the separation in the timescale of the relaxation processes in the two liquids was studied by varying the ratio A = τ_{MRCO}/τ_{OL}; A = 5000 (*left panel*) and A = 5 (*right panel*, reproducing the experimental value). In both cases the maximum enhancement of the dielectric strength, $\Delta\varepsilon^{N}_{max}$ reached 3.7

fraction x $\sim$ 0.3. The yellow area marks the conversion range within which τ appears constant, within numerical error, while $\Delta\varepsilon_N$ steadily decreases. The green area, on the other hand, marks the conversion range where the relaxation time does not any longer differs from τ_{OL} significantly while $\Delta\varepsilon_N$ can still be as large as $\sim$1.7.

Such a striking difference is due to the intrinsically different impact of the contribution coming from MROL phase on the dielectric response, expressed by (Eq. 12).

Indeed, while the overall dielectric strength, $\Delta\varepsilon_{TOT}$, is given by the sum of the contributions coming from the two phases, this simple linear convolution relation does not apply for the relaxation time, which instead depends also on the shape, position and relative intensity of the peaks related to relaxation processes of the two phases [18, 19]. For this reason we investigated the kinetics of MROL to OL transformation by analyzing $\Delta\varepsilon_N$ as displayed in Fig. 10.7.

Fig. 10.5 Shape parameters α and β, as obtained from fits of the dielectric spectra to the Havriliak Negami (HN) equation, and from simulations of the spectra via Eq. 14. To ease comparison, data are normalized to the values measured in the ordinary liquid
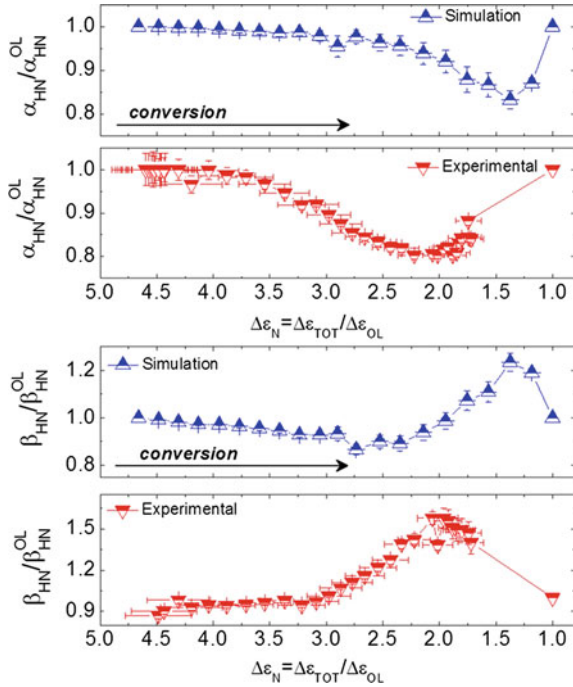
We observed that the increase in $\Delta\varepsilon_N$ exceeds 5.0 at 9 nm, while its maximum value in the scanned temperature range, $\Delta\varepsilon_N^{max}$, decays progressively before settling to a constant value of 3.7, in films thicker than 15–20 nm.

Furthermore, we compared the temperature dependence of $\Delta\varepsilon_N$ for films of glycerol with thicknesses between 11 and 126 nm with that of films of other molecules from the homologous glycerol series like xylitol (65 nm) and threitol (65 nm). For glycerol films the onset temperature increases with the thickness of the films. Already at 27 nm, annealing at 238 K (T_g + 50 K) for 23 h was necessary in order to fully recover the bulk value of $\Delta\varepsilon$. On the contrary, this transformation is much faster in xylitol and threitol films (65 nm), for which $\Delta\varepsilon_N$ reaches unity at T_g + 20 K and T_g + 33 K respectively. Because the fragility indexes of glycerol, threitol and xylitol are in progressive order ($m_{xylitol} < m_{threitol} < m_{glycerol}$) [20], this finding is in agreement with another prediction of the TOP model, according to which more fragile glass formers are characterized by lower frustration, thus by a lower concentration of (locally) ordered structures [6]. This behavior rationalizes the decreasing dielectric "excess" strength with increasing molecular size.
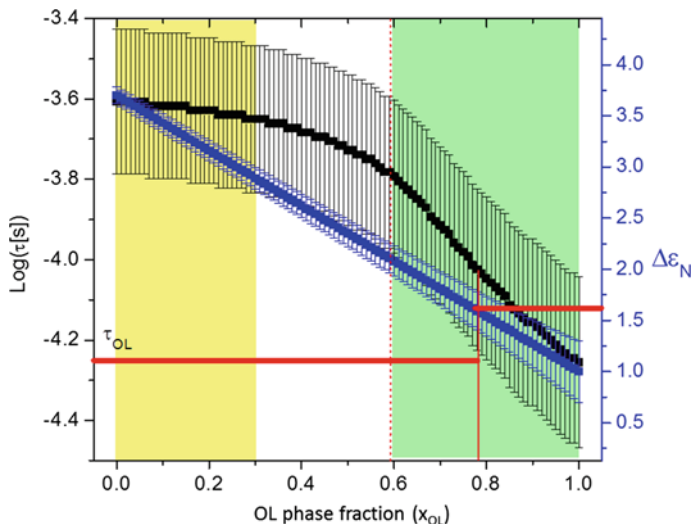
Fig. 10.6 Simulated values of the normalized dielectric strength (*blue squares*) and of the structural relaxation time (*black squares*), as a function of conversion. The dielectric function was obtained assuming a linear convolution of the contributions of the two liquid phases, averaged over their volume fraction, $\Delta\varepsilon_{TOT} = x_{OL}\Delta\varepsilon_{OL} + x_{MROL}\Delta\varepsilon_{MROL}$
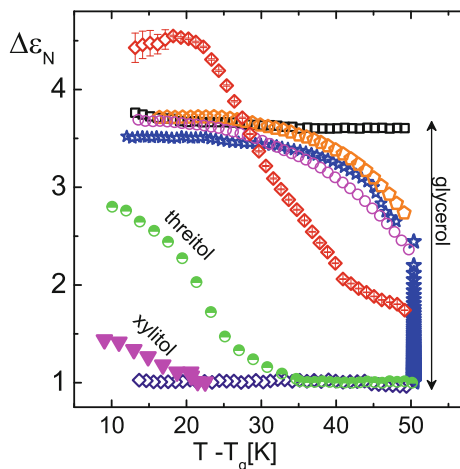
Fig. 10.7 Temperature evolution of $\Delta\varepsilon_N$ at different thicknesses and for different polyols. Changes in $\Delta\varepsilon N$ for glycerol films (*open symbols*) of different thicknesses, evaporated at 0.88 T_g, compared to xylitol and threitol films, both 65 nm thick, deposited at the same temperature. The *open blue stars* represent the values of $\Delta\varepsilon_N$ of an 89-nm-thick glycerol film deposited at 0.97 T_g, during isothermal transformation at 238 K for 23 h. *Open navy diamonds* are the literature data for a 27 nm film deposited above T_g [16]. Where not visible, error bars are smaller than the symbol size

10.4   Kinetics of the MRCOL to OL Transformation

The thickness dependence of $\Delta\varepsilon_N$ and of $\Delta\varepsilon_N^{max}$ is compatible with the scenario, predicted by the TOP model [21], of a higher BOO in proximity to the interfaces that is expected to decay over a length of a few nanometers. A rough estimation of the actual propagation length of the extra BOO from the substrate through the upper layers can be obtained from the analysis of the excess in $\Delta\varepsilon_N$ with respect to the threshold value 3.7 for films of different thicknesses. Such a value, plotted in Fig. 10.8, can be fitted with a single exponential, having a characteristic decay length of 5.9 ± 1.0 nm. This value can be considered as an upper bound for the actual propagation length.

To discern the impact of the interface-induced ordering caused by steric effects from the possible impact of molecular interactions with the substrate, we investigated MROL glycerol films grown on OL layers of the same material, previously deposited well above T_g (see green symbols in Fig. 10.8). The quantitative agreement with the values measured in the single-layer films of comparable thickness proves that the MROL phase is not affected by the interactions between the polyols and the substrate of the dielectric sensor.

Measurements of $\Delta\varepsilon_N$ during isothermal transformation revealed a constant transformation rate, is in line with the scenario of a growth front-like transformation process, where the liquid–liquid interface between the two phases propagates
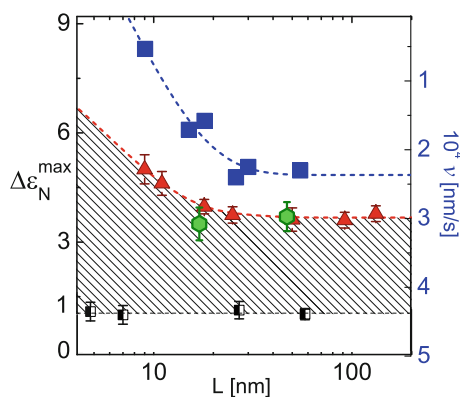
Fig. 10.8 Thickness dependence of the maximum enhancement in dielectric strength, $\Delta\varepsilon_N^{max}$, determined at $T_g + 20$ K, before the onset of the conversion into the ordinary liquid phase (*red triangles*). *Green squares* refer glycerol films grown on top of a layer previously deposited above T_g. The *semi-open black squares* represent the literature data on glycerol films deposited above T_g [16]. The *blue squares* indicate the transformation rate v at $T_g + 45$ K (right y-axis goes from the top to the bottom). The *dotted red* and the *blue lines* represent the exponential fits of the thickness dependence of $\Delta\varepsilon_N^{max}$ and of v; characteristic decay lengths of (5.9 ± 1.0) nm and (7.2 ± 2.0) nm were obtained, respectively

Fig. 10.9 Time evolution of $\Delta\varepsilon_N$ during step isothermal annealing of glycerol films. Data reported here refer to a 20 nm thick film
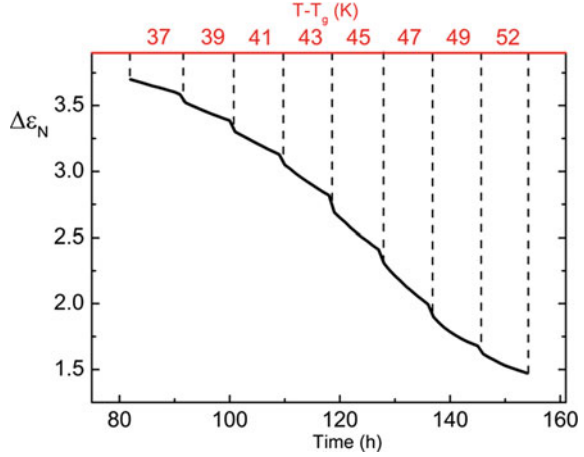
through the film at a constant velocity [22]. Such assumption allows measuring the velocity of the transformation from MROL to OL, by analyzing the time evolution of $\Delta\varepsilon_N$ (Fig. 10.9).

Because the conversion is linear in time, the velocity v is given by $v = \Delta l(t-t_0)/(t-t_0)$, where t_0 is the onset time, and Δl the thickness of the layer transformed into the OL phase at time t. The value of Δl is obtained assuming that $\Delta\varepsilon$ is the sum of the contribution of the two liquid phases averaged over their volume fractions, x_{OL} and x_{MROL} respectively (cf. Eq. 13). This assumption is justified in case of by front-like conversion scenario, in which case Eq. 14 holds also for $\Delta\varepsilon_{TOT}$:

$$\Delta\varepsilon_{TOT} = R\Delta\varepsilon_{OL}(L-\Delta l)/L + \Delta\varepsilon_{OL}\Delta l/L \qquad (15)$$

The time evolution of the parameter $\Delta\varepsilon_N$ during an isothermal conversion is then given by:

$$\Delta\varepsilon_N(t - t_0) = \Delta\varepsilon_{TOT}(t - t_0)/(\Delta\varepsilon_{OL}L) = R - (R - 1)\Delta l/L, \qquad (16)$$

which leads to:

$$v = \Delta l(t - t_0)/(t - t_0) = L/(t - t_0)[\Delta\varepsilon_N(t_0) - \Delta\varepsilon_N(t - t_0)]/(\Delta\varepsilon_N^{max} - 1) \qquad (17)$$

By investigating glycerol films with different thicknesses, we observed continuously decreasing velocities upon thickness reduction. In particular, films thicker than 15 nm presented conversion rates on the order of 10^{-4} ms^{-1} 50 K above T_g, while below this threshold, v increases exponentially, with a characteristic length of (7.2 ± 2.0) nm (Fig. 10.8).

These findings are ascribable to the fact that the volume fraction of the interfacial layer with enhanced BOO is higher for the thinnest films, thus $\Delta\varepsilon_N^{max}$ increases upon confinement and, again according to Eq. 17, the transformation rate decreases with L, i.e. the conversion into the ordinary liquid is slower for thinner films, see Eq 17. There is no contradiction with the temperature evolution shown in Fig. 10.7, where the onset temperature seems to be lower for thinnest films. In this case indeed, for thicker films the onset of the transformation into the OL phase is less evident. This effect is caused by the different time necessary to reach the conversion of the same volume fraction in samples of different thickness. For example, a reduction in $\Delta\varepsilon$ by 5 % in a film thick 50 nm requires the double of time necessary to achieve the same drop in a film by 25 nm, as v in this regime is thickness independent. The same reasoning can be easily extrapolated in the case of T scans, provided that $\partial v(T)/\partial h = 0$ (the velocity is constant along the thickness of the film).

The thickness dependence of v is given in Fig. 10.9. Remarkably, this quantity presents an exponential trend similarly to $\Delta\varepsilon_N^{max}$, with a characteristic decay length of 7 nm. Interestingly, such strong correlation to $\Delta\varepsilon_N^{max}$ is also found for the conversion time, defined as $t_c = 1/v$, as revealed by the close similarity between the temperature dependence of the two parameters, see Fig. 10.7.

The excellent match between the trends plotted in Figs. 10.8 and 10.9 proves that an enhancement in the orientational order of the system, as revealed by an increased dielectric strength, is correlated with a greater kinetic stability of the MROL phase.

The evidence that the conversion rate of the MROL phase drops upon reduction of the thickness is a further example of non-equilibrium structures stabilized upon confinement, in line with the other examples provided in this book.

10.5 Conclusions

In this chapter we have described a novel experimental approach to reveal the presence of medium range orientational order in supercooled liquids by dielectric spectroscopy, performed on thin films prepared by physical vapour deposition below the glass transition temperature. We have argued that PVD of glassy films provides a unique route to enhance the number and the stability of long-lived locally favoured structures (LPS), resulting in enhanced stability of the MRO after liquid recovery from the glassy state. This effect is ascribed to enhanced molecular mobility at the free surface of the growing glassy film, which enables the system to reach more efficiently lower states in the potential energy landscape accompanied by a lower overall enthalpy and enriched bond orientation order.

By monitoring films of different thickness we found that orientational order is even more enhanced in the thinnest films, indicating that the BOO is higher in proximity of the substrate. Consistently, we found that the transformation velocity into the ordinary liquid is slower at lower thicknesses, which indicates a correlation between the degree of orientational order and the kinetic stability of the MROL phase.

Furthermore, an analysis of the isothermal MROL to OL transition supports the scenario of a front like transformation. We propose a top down transformation mechanism, where the upper layers convert to OL first, and the front between the two phases propagates towards the substrate, reaching more stable layers, where its velocity decreases. All experimental findings were discussed in the framework of the TOP model and are in both qualitative and quantitative agreement with various model predictions.

However, further investigations are still necessary to unveil the molecular origin of the transformation process and the origin of such high kinetic stability. Such investigations would require determining the lifetime of the LPSs and their stability against annealing, also by computer simulation. If successful, we believe this investigation would be of capital importance for the understanding of the nature of the glass transition.

References

1. Capponi, S., Napolitano, S., Wübbenhorst, M.: Nat. Commun. **3**, 1233 (2012)
2. Steinhardt, P.J., Nelson, D.R., Ronchetti, M.: Phys. Rev. B **28**, 784 (1983)
3. Tanaka, H.: J. Chem. Physics **111**, 3163 (1999)
4. Tanaka, H.: J. Phys. Condens. Matter **23**, 17 (2011)
5. Shintani, H., Tanaka, H.: Nat. Phys. **2**, 200 (2006)
6. Tanaka, H., Kawasaki, T., Shintani, H., Watanabe, K.: Nat. Mater. **9**, 324 (2010)
7. Tarjus, G., Kivelson, S.A., Nussinov, Z., Viot, P.: J. Phys. Condens. Matter **17**, R1143 (2005)
8. Hohenberg, P. C., Halperin, B. I.: Rev. Mod. Phys. **49**, 435 (1977)
9. See supplementary information of Ref. [5] http://www.nature.com/nphys/journal/v2/n3/extref/nphys235-s1.pdf. Accessed 23 April 2015
10. The definition the definition of the hexatic order parameter in a 3D system, is given by $g_6^{3D}(r) = \frac{4\pi}{13} \left\langle \sum_{m=-6}^{6} Q_{6m}(r) Q^*_{6m}(0) \right\rangle \Big/ g(r)$ where Q_{6m} is the complex bond order parameter in 3D, g(r) is the normalized to the radial distribution. Numerical simulations reported in ref 8 proved that g_6^{3D} is well fitted by eq.7
11. Oh, S.H., Kauffmann, Y., Scheu, C., Kaplan, W.D., Rühle, M.: Science **310**, 661 (2005)
12. Swallen, S.F., Kearns, K.L., Mapes, M.K., Kim, Y.S., McMahon, R.J., Ediger, M.D., Wu, T., Yu, L., Satija, S.: Science **315**, 353 (2007)
13. Pauling, L.: The Nature of the Chemical Bond. Cornell University Press (1939)
14. Note: EOH•••O = 8-11 kBT/ bond, Douglas, B.E., McDaniel, D.H., Alexander, J.J.: Concepts and Models of Inorganic Chemistry. Wiley, New York City (1994)
15. The reader should note that, in case of centrosymmetric structures the term z<cosy>=0, and the Kirkwood factor is 1. In this case Δε provides no information about the average orientational order. However, that does not occur for our samples, because poliols ar linear chains and very unlikely they can form centrosymmetric structures via hydrogen intermolecular bondings
16. Capponi, S., Napolitano, S., Behrnd, N.R., Couderc, G., Hulliger, J., Wübbenhorst, M.: J. Phys. Chem. C **114**, 16696 (2010)
17. Asai, M., Shibayama, M., Koike, Y.: Macromolecules **44**, 6615 (2011)
18. Napolitano, S., Wübbenhorst, M.: Macromolecules **39**, 5967 (2006)
19. Rotella, C., Wübbenhorst, M., Napolitano, S.: Soft Matter **7**, 5260 (2011)

20. Paluch, M., Grzybowska, K., Grzybowski, A.: J. Phys. Condens. Matter **19**, 12 (2007)
21. Watanabe, K., Kawasaki, T., Tanaka, H.: Nat. Mater. **10**, 512 (2011)
22. Swallen, S.F., Traynor, K., McMahon, R.J., Ediger, M.D., Mates, T.E.: Phys. Rev. Lett. **102**, 065503 (2009)

Chapter 11
Dynamics of Confined Glass-Forming Liquids Near Equilibrium Conditions

Sindee L. Simon

Abstract The influence of nanopore confinement on the glass transition and dynamics of glass-forming liquids is reviewed. Recent calorimetric measurements are discussed for small molecules, oligomers, and polymers confined to pores, including those having specific interactions with the pores walls, and results are placed in the context of previous work. The ability to extract information on the dynamics of nanopore-confined chains from changes in the polymerization kinetics and thermodynamics is also discussed. Of particular interest are changes in the dynamics for glass-forming liquids in nanconfined but near-equilibrium conformations.

11.1 Introduction

Since the seminal work of Jackson and McKenna [1, 2] in the early 1990s showing that melting and vitrification occur at lower temperatures in nanopores, it has been established that the glass transition and properties of materials, in general, are impacted when they are confined to nanometer dimensions, i.e., to length scales less than approximately 100 nm [3–7]. An understanding of the impact of nanoconfinement on T_g is important at the fundamental level since such changes are not readily explained in the framework of our current understanding of the glass transition [8]. For example, one expects that entropy may decrease upon confinement, and this is indeed consistent with the reduction in the absolute heat capacity observed in work on stacked polystyrene ultrathin films [9]—however, according to configurational entropy theory [10], a reduction in entropy would be expected to lead to an increase not a decrease in T_g [8]. Hence, the observation of a T_g reduction at the nanometer size scale is not only surprising, but its full understanding may

S.L. Simon (✉)
Department of Chemical Engineering, Texas Tech University,
Lubbock, TX 79409-3121, USA
e-mail: sindee.simon@ttu.edu

lead to a better understanding of the glass transition phenomenon itself. Of particular interest in this debate is the import of surfaces and interfaces, as well as the role of nonequilibrium configurations, on observed changes. Since confinement of liquids in nanopores is thermodyamically favorable [11], unlike confinement of liquids to ultrathin films which spontaneously dewet except in the case of strong interactions between the substrate and liquid, the influence of nanopore confinement on T_g and the associated dynamics of glass-forming liquids is the focus of this chapter.

The chapter is organized in two principal parts. The first part deals with the glass transition of nanopore-confined glass-formers, with discussion of non-hydrogen-bonding low-molecular weight, oligomeric, and polymeric materials followed by that of hydrogen-bonding materials where interfacial effects play a larger role. The second part of the chapter deals with the influence of nanopore confinement on, first, the polymerization kinetics in free radical polymerizations and, then, on the thermodynamics of the same reactions. The chapter ends with brief conclusions.

11.2 T_g Changes for Glass-Formers in Nanopores

In Jackson and McKenna's early work [1, 2], small organic molecules were imbibed into the pores of controlled pore glass (CPG) and differential scanning calorimetry was used to study the melting and glass transition behavior. Although crystallization was suppressed in the pores, the melting point linearly decreased with reciprocal pore size as expected based on the Gibbs' Thompson equation [12–15]:

$$\Delta T_m = \frac{2\sigma T_m}{r \Delta H_f \rho_s} \tag{11.1}$$

where ΔT_m is the change in melting point, T_m is bulk melting point, σ is the surface energy of the solid-liquid interface, r is the pore radius, ΔH_f is the bulk enthalpy of fusion and ρ_s is the solid density. For benzyl alcohol, the melting point depression was found to be 26 K in 8.5 nm-diameter pores. As Jackson and McKenna note, based on the relationship between T_g and T_m, i.e., $T_g/T_m \approx 2/3$, one might expect that the percent changes in T_g and T_m to be similar. This simple idea, however, turns out not to be the case. For example, benzyl alcohol's T_g was depressed only 3 K (1.8 %) in 8.5 nm-diameter pores compared to a depression of 11 % for the melting transition [1]. The implication, then, is that the physics governing the depression of the glass transition differ from those governing the depression of the melting point, the latter of which can be associated with the decrease in the chemical potential due to curvature of the liquid surface in the nanopore in an analogy to the boiling point depression in capillary condensation [13].

Jackson and McKenna also investigated o-terphenyl (oTP) in CPG pores and observed T_g depressions of 8.8 and 18.2 K in 8.5 and 4.0 nm-diameter pores, respectively [1, 2]. Subsequent work by Novrotskya and coworkers [16] using DSC and by Koppensteiner and Schranz [17] using a linear mechanical technique

corroborated the magnitude of the T_g depression for oTP. Shortly after Jackson and McKenna's seminal work [1], Zhang, Liu, and Jonas [18] published similar results on different glass-formers, namely isopropylbenzene, glycerol, di-n-buyl phthalate, tert-butylbenzene, and n-butyl acetate in CPG, reporting calorimetric T_g depressions ranging from 2.2 K for glycerol in 7.2 nm-diameter pores to as much as 8.8 K for di-n-butyl phthalate in 3.8 nm-diameter pores. For non-hydrogen-bonding glass-formers in pores, T_g does not always decrease with decreasing pore size, but in fact, can behave non-monotonically. Alba-Simionesco and coworkers [19] investigated toluene in MCM-41 and SBA-15 nanopores using adiabatic calorimetry and found that T_g initially decreased as pore size decreased and then T_g increased for even smaller pores showing a maximum T_g depression of 6 K in 4.7 nm-diameter pores. These results, corroborated by Koppensteiner and coworkers [17] using a linear dynamic mechanical technique, were interpretted as arising from a competition between confinement effects which dominate at larger pore sizes and interfacial effects dominating at the smallest pore sizes. Interestingly, benzene in similar pores only showed an elevation of T_g presumably due to strong interactions with the pore surface [20].

With respect to the debate over whether or not the T_g depression in nanopores is an artifact, it is important to recognize that small molecules imbied in pores do so without the use of any solvents—hence, plasticization by residual solvent and inadequate annealing procedures suggested by Kremer and coworkers [21, 22] as potential problems for polymeric ultrathin film work are not problematic for small molecules in nanopores. McKenna and coworkers also ruled out artifacts related to plasticization by species adsorbed to the surface of the pores by examining the relative strength of depressions for oTP and benzyl alcohol in hydrophobic and hydrophilic pores [2]. In the same work, they discussed negative pressure effects [2], and later Simon, Park, and McKennna [23] used the fact that negative pressure influences the equilibrium line reached after structural recovery to model this effect. The modeling work [23], in particular, concludes that the nanoconfined liquid is at equilibrium and at ambient pressure above its glass transition temperature, whereas upon vitrification, an isochoric condition is imposed resulting in an increasing negative pressure building up during cooling; the finding that the isochoric conditions are imposed at the depressed T_g not at the bulk T_g indicates that the isochoric condition cannot be the cause of the observed T_g depression. The recent argument that T_g changes may be related to the use of nonlinear temperature scanning measurements as opposed to linear measurements [24] is also inconsistent with the fact that Koppensteiner and coworkers [17] have reproduced the results for several glass-formers using a mechanical linear dynamic susceptibility measurement. For the case of ultrathin films, McKenna and coworkers have also reported T_g depressions of the same order of magnitude as those observed in ellipsometry using linear viscoelastic measurements [25–28].

The T_g depression for organic non-hydrogen bonding small molecules in nanopores is generally small and less than 10–20 K even at the smallest pore sizes, although there are exceptions, such as benzene showing a 50 K elevation in 2.4 nm-diameter pores relative to the T_g of a 20 nm-diameter emulsion [20].

However, in general, larger confinement effects can be expected for higher molecular weight glass-formers. Park and McKenna observed that a 14 % solution of polystyrene in oTP showed a calorimetric depression of 12 K in 11.6 nm-diameter pores [29]. In our own work, we wanted to explore the effect of 2-D cylindrical confinement on neat glass-formers of high molecular weights that are difficult to imbibe into pores in reasonable time scales. To that end, we imbibed reactive species, including monomers, in pores and then reacted the systems to obtain nanoconfined materials of higher molecular weights. One particular system that we studied is that of mono- and di-cyanate esters which homopolymerize via trimerization, thereby avoiding issues associated with inhomogeneities that could arise in two-component systems. The T_g depression in the resulting cyanurates, shown in Fig. 11.1, is impressively over 50 K for the crosslinked polycyanurate [30, 31] network, over 30 K for the low-molecular-weight trimer [32], and intermediate in the polycyanurate oligomer [33]. The depression increases with increasing molecular weight, crosslink density, and the value of the bulk T_g, and thus, inversely with the configurational entropy or free volume of the material [34]. A similar result was found upon changing conversion in the dicyanate ester system, with increasing conversion resulting in a decrease in entropy, an increase in chain stiffness, an increase in T_g, and larger T_g depressions [34].

Important for the debate concerning the origin of the T_g depression is the fact that glass-formers in pores often display the presence of two relaxations or T_gs, one associated with the surface or interface and the other associated with material in the center of the pore [29, 35, 36]. Although the presence of strongly absorbed layers have been identified in supported polymer thin films and related to non-universal behavior of T_g under nanoconfinement [37, 38], the signature of two relaxations in ultrathin films, one associated with such an absorbed layer, has not been reported in

Cyanurate Trimer
M_n = 712 g/mol
Bulk T_g = 47 °C
ΔT_g = -31 K at 8 nm
T_{g2}-T_{g1} = 23 K at 8 nm

Polycyanurate Oligomer
M_n = 5240 g/mol
Bulk T_g = 82 °C
ΔT_g = -44 K at 8 nm
T_{g2}-T_{g1} = 40 K at 8 nm

Polycyanurate Network
M_n = ∞
Bulk T_g = 198 °C
ΔT_g = -52 K at 11.5 nm
T_{g2}-T_{g1} = 23 K at 11.5 nm
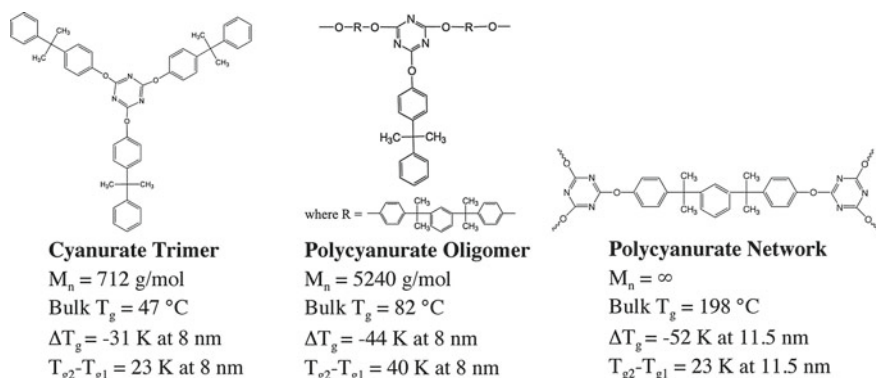
Fig. 11.1 Structures of fully reacted cyanurates along with their molecular weights, bulk T_g, T_g depression, and difference T_{g2}–T_{g1}, including a cyanurate trimer synthesized from a monofunctional cyanate ester, a polycyanurate from a mixture of mono- and di-functional cyanate esters, and a polycyanurate network from a dicyanate ester. After Refs. [30, 32–34]

calorimetric or ellipsometric experiments to the best of the author's knowledge – presumably because annealing has been insufficient to grow such layers and because the signal is too weak being related to the ratio of interfacial volume to the total; for example, a 1-nm thick interface at the substrate of a 10 nm-thick supported film is only 10 % of the sample, whereas in a 10 nm-diameter pore, a 1 nm-thick interfacial layer comprises 36 % of the sample volume and will, thus, give a much stronger relative signal. Park and McKenna were the first to report two calorimetric T_gs in their work on oTP /polystyrene solutions [29], one depressed relative to the bulk and associated with material in the core, and the second elevated relative to the bulk and associated with material at the pore wall; the difference in the two T_g values ranged from 32 to 40 °C and increased weakly with decreasing pore size. Alba-Simionesco demonstrated two associated relaxations for oTP in a similarly confined system using neutron spin echo measurements with the relaxation time of the interfacial material depending on pore surface chemistry [39]. The polycyanurates that we studied also show similar behavior, as depicted in Fig. 11.2 for the polycyanurate oligomer, with the inset showing the two distinct transitions observed in the calorimetric traces. Interestingly, for the polycyanurates, $T_{g2}-T_{g1}$ does not depend strongly on pore surface treatment although the reaction kinetics in the pores does [34].

The leading explanation in the polymer community for the T_g depression in ultrathin films invokes an increase in mobility arising from that at the free surface. Glass-formers in pores do not have a free surface, and consequently in this case, mobility has been invoked as arising from the interface. However, the interfacial layer is obviously less mobile than the core given its higher glass transition temperature, and furthermore, the two transitions appear to be intimately related with $T_{g2}-T_{g1}$ being only a weak function of pore diameter [34]. Moreover, T_{g2} can be
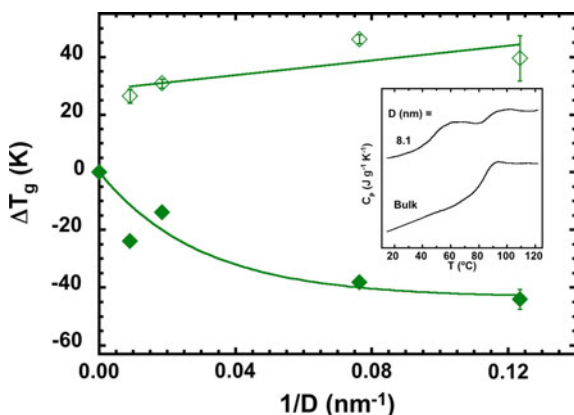
Fig. 11.2 T_g depression (*filled diamonds*) and difference $T_{g2}-T_{g1}$ (open diamonds) for the polycyanurate oligomer versus reciprocal pore diameter. The *inset* shows the heat capacity traces depicting two transitions in the pores. The structure of the polycyanurate is shown in Fig. 11.1. After ref. [33]

either depressed, elevated, or unchanged relative to the bulk depending on the magnitude of the primary T_g depression. Hence, although substrate interactions are obviously important, it is not clear how the T_g depression in nanopores can simply be attributed to the mobility gained at the interface.

The thickness of the interfacial layer ξ associated with T_{g2} can be determined assuming that the step changes in the heat capacity at the two glass transitions are proportional to the volume fraction of material associated with each transition [29]:

$$\xi = r \left[1 - \left(1 - \frac{\Delta C_{p2}}{\Delta C_{pT}} \right)^{1/2} \right] \tag{11.2}$$

where r is the nanopore radius, ΔC_{p2} is the heat capacity change at the glass transition associated with the secondary T_g, and ΔC_{pT} is the total heat capacity change at the glass transition associated with both transitions. The length scale associated with the secondary T_g appears to decrease with decreasing pore diameter. For oTP, for example, the length scale is between 2 and 2.5 nm for pores of 25–50 nm in diameter and approximately 1 nm for the 11 nm-diameter pores [29]. For the various polycyanurates, the length scale ranges from 6 to 9 nm for the material in pores of 111–120 nm to less than 1 nm for the smallest 8 nm-diameter pores [33]. Such a dependence of interfacial length scale on pore size, however, has yet to be explained, but may be related to the assumption of constant density in the pore and the influence of pore size on packing at the pore walls.

Thus far, we have not discussed hydrogen-bonding glass-formers which can strongly interact with silanol moieties at silica and alumina silicate surfaces. Perhaps not surprisingly, for such liquids, there seem to more disparate results in the literature. These differences may be due, in part, to differences in pore surface chemistries, experimental protocols, and associated interaction strengths. Differences in the literature may also arise from a larger variety of techniques used to study hydrogen-bonding liquids in nanopores since, unlike simple hydrocarbons, they can be studied using solvation dynamics and dielectric spectroscopy. The relatively small changes in T_g observed may also contribute to the seeming discrepancies. An example is shown in Fig. 11.3 for nanoconfined glycerol. For confinement in native (hydrophilic) GelSil or Vycor glasses, Richert and coworkers observed an increase in T_g with decreasing pore size using solvation dynamics [40], whereas dielectric spectroscopy work from Kremer's laboratory [41] shows no change within the error of the experiments, and our calorimetric work [42] shows a 5 K depression at 2.5 nm. On the other hand, the calorimetry by Navrotsky and coworkers [16] for glycerol confined to native SBA-15 and MCM-41 show substantive T_g elevations, whereas DSC studies by Jonas and coworkers [18] for glycerol in native CPG showed the opposite trend. The data clearly show the importance of interfacial interactions in such systems, as well as differences between measurement techniques. In addition, pore fullness can affect the measured change in T_g for liquids having strong interactions with the pore walls—in our own calorimetric work [42], a T_g depression is observed for glycerol in completely filled
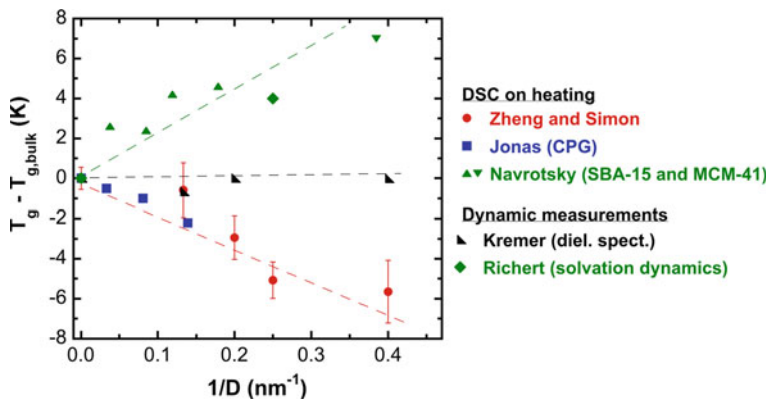
Fig. 11.3 The change in T_g from the bulk value for glycerol confined in native (hydrophilic) nanopores plotted as a function of the inverse of nominal pore diameter. Results from Zheng and Simon [42], Jonas [18], Navrotsky [16], Kremer [43], and Richert [41] are compared. Confinement matrices are native GelSil and Vycor except as noted

native pores, whereas no change is observed for partially filled native pores. In silanized hydrophobic pores, on the other hand, the degree of pore fullness does not seem to affect the measured T_g depression for either hydrogen-bonding and non-hydrogen-bonding glass-formers [34, 42], presumably because the material fills as a "plug" rather than wetting the wall.

Similarly discrepant results are observed for propylene glycol in native nanopores, as shown in Fig. 11.4, with T_g depressions as large as 12 K observed, as well
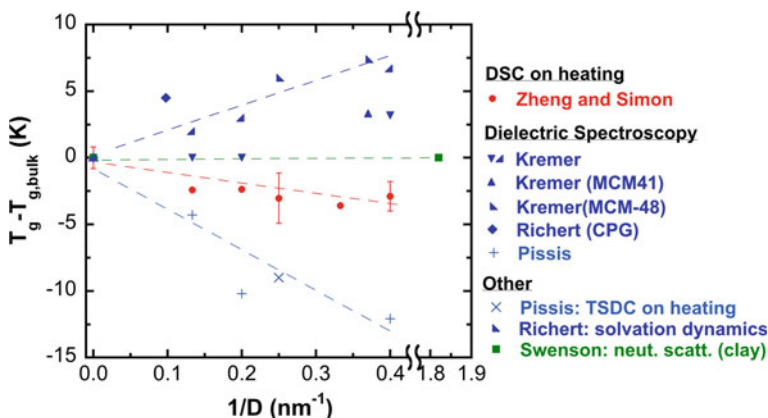
Fig. 11.4 The change in T_g from the bulk value for propylene glycol confined in native (hydrophilic) nanopores plotted as a function of the inverse of nominal pore diameter. Results from Zheng and Simon [42], Kremer [44–46], Richert [35, 40, 43], Pissis [47, 48], and Swenson [49] are included. *Open symbols* represent results for the second T_g. Confinement matrices are native GelSil and Vycor except as noted

as T_g elevations of up to 9 K. Richert and coworkers [35, 40, 43] observed increases in T_g with decreasing pore size based on solvation dynamics and dielectric spectroscopy studies, as did Kremer and coworkers [44–46]. Pissis, on the other hand reported T_g decreasing and broadening with decreasing pore size, using both dielectric spectroscopy and a thermally stimulated depolarization current technique (TSDC) [47, 48], and Swenson's neutron scattering work using a clay as the confinement media shows no change even at 0.6 nm [49]. Calorimetry work from the author's laboratory show small depressions of approximately 3 K at 2.5 nm [42]. Related work by Schönhals and coworkers [50] reported a nonmonotonic change in T_g for oligomeric poly(propylene glycol) by dielectric spectroscopy in native pores, with decreases as pore size decreased to 3 nm and increases at smaller pore sizes.

The glass transition temperature is found to increase for poly(methyl methacrylate) (PMMA) synthesized in 5 nm-diameter sol-gel-derived SiO_2 pore glasses [51] and in 3 nm zeolite mesopores [52] and in PMMA nanocomposites [53, 54]. Strong specific interactions, such as hydrogen bonding, between PMMA and the substrate[55] presumably account for the increase in T_g. We similarly find an increase in the T_g of PMMA after its synthesis at 80 °C in 13-nm diameter CPG, using both native hydrophilic and silanized hydrophobic pores [56]. Calorimetric traces are shown in Fig. 11.5 with solid lines depicting the DSC scans for fully converted PMMA samples after residual MMA removal (i.e., using a pinhole in the lid of hermetic DSC pan), and dashed lines showing the results for samples after extraction from the CPG after the synthesis in the nanopores. The results clearly show that T_g and the breadth of the transition both increase under nanoconfinement with samples synthesized in hydrophilic pores showing a more pronounced effect. Comparing the T_g of the fully converted samples in the CPG to that of the extracted samples (solid vs. dashed lines), we attribute the 8 K increase in T_g in the

Fig. 11.5 DSC traces for PMMA synthesized at 80 °C in bulk and in 13-nm diameter hydrophobic and native pores. Also shown as dashed lines are the scans for the PMMA after extraction from the pores. After Ref. [56]
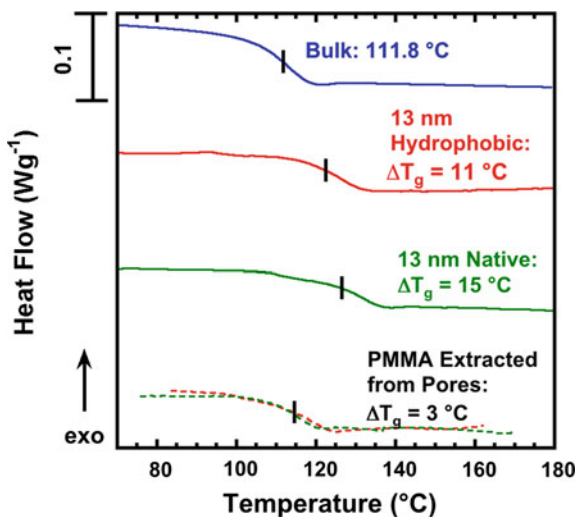
hydrophobic pores solely to the effect of nanoconfinement. The 12 K increase between the samples in and out of the native hydrophilic CPG can be explained by the confinement effect (8 K) and an additional 4 K elevation due to the interaction between PMMA and the silanol surface group—such an interaction was observed by Keddie, Jones, and Cory [55] for atactic PMMA ultrathin films supported on native silicone substrates. It is noted that although the tacticity of the polymer synthesized in the nanopores changes, as discussed later, the PMMA is still atactic and T_g of the material extracted from the pores is only 3 K higher than that synthesized in bulk; hence, the influence of tacticity on the T_g depression, which has been reported for ultrathin PMMA films [57], is not expected to be important.

Recently, Xue and coworkers [58, 59] have been reported that a PMMA oligomer confined in 80 nm anodic aluminum oxide (AAO) templates shows one T_g after being hyperquenched at cooling rates of 120 K/s and shows two or more T_gs after slow cooling or after annealing above $T_{g,bulk}$ for several hours. Development of an interfacial layer of nearly 60 nm or 25 oligomeric chains is claimed [59]. We have been unable to reproduce such an effect; rather we always observe a broadened single T_g with no indication of mulitple relaxations even after 24 h of annealing at temperatures ranging from 130 to 150 °C. One possible explanation for the seeming discrepancy between our work and Xue's is our much smalller pores, which may not be able to support a large gradient in mobility, consistent with the work of Ellison and Torkelson [60]; another explanation may be our much higher molecular weights which do not facilitate growth of an interfacial layer in reasonable time scales, consistent with the work of Napolitano and Wübbenhorst [37].

11.3 Free Radical Polymerizations in Nanopores: Reaction Kinetics and Thermodynamics

Until recent work by Simon and coworkers [61–64], little attention had been given to the influence of nanoconstraints on polymerization—in spite of the relevance to nanocomposite, nanolithography, and nanoelectronic applications in which nano-scale constraints are imposed by the distances between nanoparticles in the case of nanocomposites or by the size scale of the features in the case of nanolithography and nanoelectronics. Perhaps more interestingly, the influence of nanconfinement on polymerization can provide insight into the dynamics of nanoconfined liquids because, for example, changes in reaction kinetics can be directly related to changes in the mobility of diffusing species.

For the free radical polymerization of methyl methacrylate (MMA) with 0.5 wt% 2,2′-azo-bis-isobutyronitrile (AIBN) initiator, the reaction is accelerated in nanopores, as shown in Fig. 11.6, where conversion × versus time is shown for the reaction in the bulk, as well as in native hydrophilic and silanized hydrophobic 13-nm diameter pores of controlled pore glass (CPG); [63, 64] experimental results are symbols and the solid lines are the model calculations. The free radical

Fig. 11.6 Conversion versus
time for MMA
polymerization at 80 °C with
0.5 wt% of AIBN initiator in
bulk and in native hydrophilic
and silanized hydrophobic
13 nm-diameter CPG pores.
Symbols are experimental data
from three separate
polymerizations. *Solid lines*
are model calculations. After
Refs. [63, 64]
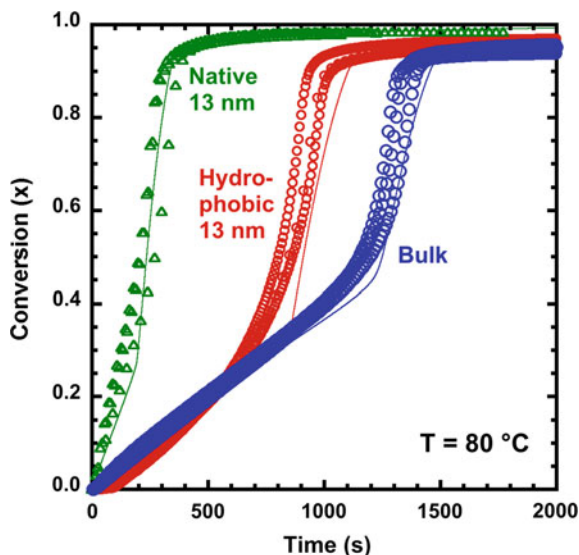
polymerization reaction is first order in MMA concentration such that the con-
version increases approximately linearly with time at low conversions. As con-
version increases, polymer yield and viscosity increase. At approximately 45 %
conversion in the bulk system, and at lower conversions in the nanoconfined sys-
tems, an upturn in the conversion versus time curve is observed. This phenomenon,
known as autoacceleration, occurs as viscosity increases, chain diffusivity decrea-
ses, and the rate of termination decreases relative to the rate of propagation. For
confinement in hydrophobic 13 nm-diameter pores, the initial reaction rate is
essentially unchanged but autoacceleration occurs much earlier indicating that chain
diffusivity is reduced in nanoconfinement [62, 63]. For confinement in hydrophilic
native 13 nm-diameter pores, on the other hand, autoacceleration occurs even
earlier and the initial reaction rate is higher [62, 64], as shown in Fig. 11.7, where
the effective rate constant is plotted as a function of reciprocal temperature.
Although in hydrophobic pores the rate constant and activation energy are
unchanged from the bulk, in native hydrophilic pores, the rate constant is higher
and the activation energy lower—consistent with catalysis of the reaction by the
silanol groups on the surface of the native pores. Catalysis of an amidation reaction
by surface hydroxyl groups was similarly suggested by Lutkenhaus and coworkers
[65] to explain an increase in the reaction rate and a concomitant decrease in the
activation energy with decreasing film thickness for reactive layer-by-layer polymer
assemblies on both alumina and native silicon substrates. Catalysis by the surface in
our system would appear to require the end of the growing free radical chain to be
in the vicinity of the wall stabilized by silanol groups and to preferentially react
with MMA monomer in a particular orientation—interestingly, this preference to a
particular reaction orientaion also leads to a significant increase in isotacticity (with

Fig. 11.7 Temperature
dependence of the effective
rate constant k at low
conversions (<20 %) for
MMA polymerization with
0.5 wt% AIBN initiator in
bulk (*blue circles*) and in
native hydrophilic (*green
triangles*) and silanized
hydrophobic (*red squares*)
13 nm-diameter CPG pores.
After Ref. [62]
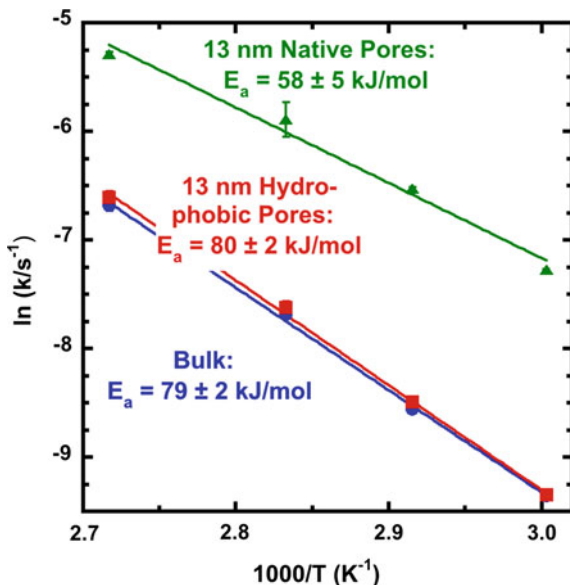
more than 50 % of triads being isotactic for polymerization at 95 °C in 13-nm
diameter native pores compared to only 11 % in the bulk reaction) [56].

In order to extract information concerning the dynamics of the nanoconfined
liquid from the reaction kinetics data, it is necessary to model the reaction. We
employ an extension of the kinetic model of Verros et al. [66] for chain poly-
merization which uses 2×10^5 differential equations to describe the time evolution
of the concentrations of all species in the mixture: initiator, monomer, and all
lengths of free radicals (active chains) and polymers; to decrease computation time,
free radical and polymeric species are binned in groups of 20, reducing the equa-
tions to 1×10^4 [63, 64]. The model captures the autoacceleration effect in the bulk
system, as shown in Fig. 11.6, by accounting for the changes in diffusivity with
increasing conversion and molecular weight. Under nanoconfinement, diffusivity
decreases even further—at least in the direction perpendicular to cylindrical pore
walls [67] and near rough walls [68, 69]. In fact, Monte Carlo studies suggest that
chain diffusivity under confinement, $\overline{D}_{p,conf}$, will scale inversely with molecular
weight M to the third power and confinement diameter D to the 4/3 power, the latter
for the case of good solvent conditions [70, 71]:

$$\overline{D}_{p,conf} \propto \frac{D^{1.3}}{M^3} \tag{11.3}$$

Hence, chain diffusion is slowed dramatically upon nanoconfinement, whereas
monomer diffusion is not; the result is that autoacceleration occurs much earlier in
nanoconfined free radical polymerization. Good agreement is obtained between the
experimental data and the model, as shown for the data in Fig. 11.6. Only one

adjustable parameter, the proportionality constant in Eq. (11.3), is used to describe the nanoconfined results for four reaction temperatures and three pore sizes in hydrophobic pores; all other parameters were taken from those used to model the bulk system [63]. In the case of the native hydrophilic pores, the situation is more complicated due to the catalysis by the pore surface; this is accounted for by assuming that the propagation rate constant scales inversely with pore diameter [64]. In addition, the absolute value of the apparent diffusivity of chains appears to be higher in the hydrophilic pores perhaps due to the flux of diffusing species associated with a concentration gradient if the reaction occurs preferentially at the pore surface.

The changes in the reaction kinetics of nanoconfined free radical methyl methacrylate polymerization can be explained simply by macroscopic physics coupled with the dependence of the diffusion constant of confined chains on molecular weight and pore size. For the 13 nm hydrophobic pores, chain diffusivity is reduced to 20–50 % of the bulk value, depending on the reaction temperature, with larger reductions observed at higher reaction temperatures. Although increases in chain diffusivity might be expected given the increases in T_g shown in Fig. 11.5, the relatively modest magnitude of the increases are inconsistent with the 8–12 K increase observed in T_g. This seeming discrepancy may be related to the difference in the temperature dependences of relaxation times in bulk and nanoconfined systems, with the apparent activation energy for the α-relaxation being lower in nanoconfinement for systems with a T_g depression [72–74] resulting in behavior becoming more bulk-like the higher the temperature is above the nominal T_g. Since our reactions are performed in the liquid, equilibrium state (until very high conversions are reached), we are in a regime where changes in T_g and associated glass dynamics will not influence the reaction until high conversion. Another intriguing possibility, of course, is that the effects of nanopore confinement on chain diffusion is decoupled from that of the segmental diffusion associated with the glass transition.

In addition to explaining the earlier onset of autoacceleration, the model for nanoconfined free radical polymerization also qualitatively predicts without any adjustable parameters the changes in molecular weight and decreases in polydispersity (PDI) that are observed for polymer synthesized under nanoconfinement. In our work, the number-average molecular weight of PMMA near full conversion increases from 1.7×10^5 g/mol for the bulk sample to 2.4×10^5 for the material synthesized in 13-nm diameter hydrophobic pores to 5.0×10^5 for 13-nm diameter native hydrophilic pores [56]. Concomitantly, PDI near full conversion decreases from 2.5 to 2.3 to 1.5 for these three cases [56]. Even larger changes in molecular weights have been observed by other researchers for polymerization in smaller pores. For example, polymerization of methyl methacrylate in the 2.7 nm pores of zeolite MCM-41 was found to increase M_n by one order of magnitude and to decrease PDI from 2.8 to 1.7, [75] and similar results were obtained for poly(methyl methacrylate) synthesized in gel silica glass having 4.4 nm pores and for various vinyl polymers formed in the nanochannels of porous coordination polymers (PCP) [76, 77], Increases in the degree of isotacticity have also been observed

in our polymerization of PMMA [56], as well as for styrene, methyl methacrylate, and vinyl acetate for polymerizations in the nanochannels of PCPs [77]. An increase in the number of linear chains were also observed for poly(vinyl acetate) formed in PCP [77]. The latter result is consistent with the arguments set forth by Sakaue and Raphaël [78] that branched chains experience stronger confinement effects than linear chains under cylindrical confinement.

Beyond reaction kinetics and the properties of the resulting polymers, nano-confinement also influences monomer/polymer equilibrium. Dimerization of bio-molecules has been studied both theoretically and by experiment [79–81]. Using molecular simulations, the stability of protein dimers is found to depend on both confinement size and molecular concentration with maximal dimer stabilization observed at concentration levels near those observed in vivo, and this effect, which occurs only when a nanoscale volume is completely isolated has been attributed to a decrease in the entropy of mixing: for example, in the limiting case of two reactant molecules in a volume, the entropy of mixing vanishes, resulting in a shift of the equilibrium completely to the right (i.e., to the dimer product) for an exothermic reaction [81].

Changes in monomer/polymer equililbrium may also arise from the decrease in entropy associated with confining long chains to nanoscale environments. Such an effect has been observed for sulfur by Andrikopoulus, Yannopoulos, and coworkers [82, 83]. As shown in Fig. 11.8, the transition between the eight-membered cyclic sulfur monomer and sulfur chains is experimentally found to be shifted to higher temperatures on confinement to nanopores, and the transition becomes weaker and broader as confinement increases. The shift of the sulfur monomer/polymer floor temperature to higher temperatures indicates that the change in entropy on propagation decreases under nanoconfinement, i.e., that ΔS_p is a smaller positive number, such that a higher temperature must be reached before ΔG_p becomes negative. In order to try to quantify this effect, the data can be modeled [84], but to do so, assumptions must be made concerning how the entropy of a confined chain depends on chain length and confinement size.

The entropy that is lost upon confinement of a polymer chain to nanoscale dimensions depends on both chain size and confinement size. deGennes argued that this confinement entropy scales with the length of the chain and inversely with the confinement size [85]:

$$\Delta S_{\text{confchain}} \propto N^{-m}\left(\frac{a}{D}\right)^{1/\upsilon} \tag{11.4}$$

where N is the number of segments of length a that comprises the chain, D is the confinement tube diameter, and the scaling exponent for chain length is m = 1.0. The Flory exponent υ is 0.5 for the ideal chain in θ solvent and 3/5 for a good solvent. This scaling has been confirmed by simulation for dilute linear chains confined in cylindrical pores, as well as in slits [86–88], regimes referred to as the weak confinement regime [78]. In this regime, if the above scaling holds, one would anticipate no effect on the thermodynamics of equilibrium polymerizations because
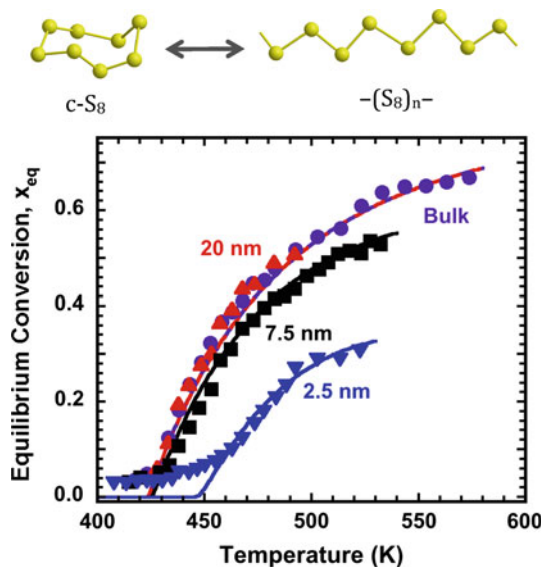
Fig. 11.8 The extent of polymerization or conversion × as a function of temperature for polymerization of cyclic sulfur (c-S$_8$) to form linear chains, shown at top. The reaction is shown at the *top*. Data for the bulk reaction (*purple circles*) and in 20, 7.5, and 2.5 nm pores (*red triangles*, *black squares*, and *blue triangles*, respectively) are from Ref. [83]. Model fits (*lines*) are from reference 84. View in color for best clarity

the entropy loss on confinement of the product M_{N+1} of a given propagation step is the same as the entropy loss on confining the reactants ($M_N + M_1$) such that no net change in ΔS_p occurs, i.e.,

$$\Delta S_{confchain} = \Delta S_{p\infty} + c[(N+1) - N - 1]\left(\frac{a}{D}\right)^{1/\upsilon} = \Delta S_{p\infty} \qquad (11.5)$$

where $\Delta S_{p\infty}$ is the entropy change of the bulk reaction, $\Delta S_{conf\ reaction}$ is that under confinement, and c is the scaling prefactor.

However, in the strong confinement regime, chains are highly compressed, and due to excluded volume effects, confinement entropy does not scale with N to the first power (i.e., m in Eq. 11.4 is greater than 1.0). The strong confinement regime occurs for linear chains confined to spherical geometries at sufficiently high concentrations, for example, above a monomer volume fraction of approximately 0.2 in the molecular simulation work of Cacciuto and Luijten [89]. The strong confinement regime has also been shown to occur for branched chains in the cylindrical geometry [78]. In this regime for good solvents, the mean field result [90] yields a scaling of the confinement entropy with N^2 and Monte Carlo simulations [78] give a scaling with $N^{9/4}$, whereas for θ-solvents, the scaling goes as N to the third power [78, 89]. The latter scaling with N^3 is also consistent with experiments for poly (ethylene glycol) in nanochannels created by α-toxin [91]. Thus, in the strong

confinement regime, the Gibbs free energy of the propagation reaction should be modified by confinement such that the equilibrium constant K will decrease from the bulk value by an amount that depends on chain length to the m-1 power:

$$ln\left(\frac{K_{N+1}}{K_\infty}\right) = -\frac{cN^{m-1}}{R}\left(\frac{a}{D}\right)^{1/\upsilon} \tag{11.6}$$

where c is again a constant prefactor, K_{N+1} is the equilibrium constant for the nanoconfined reaction form a chain of length N + 1, and K_∞ is the bulk equilibrium constant which is assumed to independent of chain length for mean field calculations [92]. For nanoconfined sulfur polymerization, the model quantitatively captures the literature data from Yannopoulos and coworkers assuming that the change of entropy of nanoconfined chains scales with molecular size to the second power and with nanopore diameter to the −3.8 power, as shown in Fig. 11.8.

In contrast to the shift of the sulfur monomer/polymer floor temperature to higher temperatures, recent work from our laboratory shows that nanoconfinement shifts equilibrium in free radical methyl methacrylate (MMA) polymerization towards monomer [93]. Results are shown in Fig. 11.9 again for MMA polymerized by 0.5 wt% AIBN, where the equilibrium conversion is plotted versus temperature. Conversions at low reaction temperatures are less than 100 % due to the effect of vitrification (i.e., the reaction cannot reach equilibrium because the reaction mixture turns to a glass and the reaction stops prior to 100 % conversion being reached). As the reaction temperature approaches and rises above the glass transition of the neat polymer ($T_{g,p} \approx 110$ °C), vitrification effects disappear and the conversion reaches the maximum value of 1.0. At higher temperatures, conversion again decreases,

Fig. 11.9 Temperature dependence of equilibrium conversion for MMA polymerization with 0.5 wt% AIBN initiator in bulk (*blue circles*) and in native hydrophilic (*green triangles*) and silanized hydrophobic (*red squares*) 13 nm-diameter CPG pores. After Ref. [93]
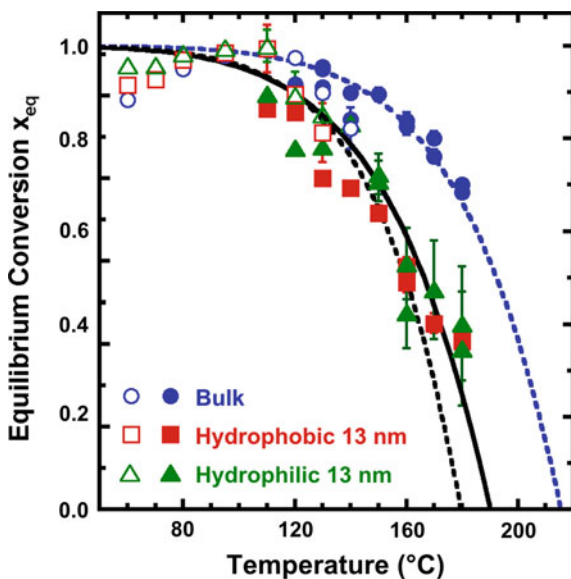
now because depolymerization becomes dominant and the reaction equilibrium shifts towards monomer. Data for the bulk unconfined reaction are shown as blue circles and can be described by the relationship between the equilibrium conversion x_{eq} and the equilibrium constant K:

$$K = 1/(1 - x_{eq}) \tag{11.7}$$

where $K = \exp(-\Delta H_p/RT + \Delta S_p/R)$ and the enthalpy and entropy of propagation needed to fit the bulk data agree with literature values: $\Delta H_p = 56$ kJ/mol [62] and $\Delta S_p = -115 \pm 1$ J mol^{-1} K^{-1}, the latter is consistent with values in the literature [92]. In addition, T_c is calculated to be 216 ± 2 °C, which is also consistent with the value reported in the literature [92].

For polymerization in 13-nm diameter pores having either hydrophobic or hydrophilic surface chemistries, shown as red squares and green triangles, respectively, the equilibrium conversion are smaller than bulk samples for a given reaction temperature indicating that the monomer/polymer equilibrium is shifted towards the monomer under nanoconfinement [93]. Applying the same Eq. 11.7 to the nanoconfined cases and assuming the bulk value of ΔH_p, which has been experimentally verified [62], the model (shown as black dashed line) only qualitatively describes the trend with a more negative change in entropy of propagation for the confined reaction, $\Delta S_{conf\ reaction} = -124 \pm 1$ J mol^{-1} K^{-1}. The solid line, on the other hand, assumes that the entropy of propagation for the confined reaction depends on temperature, becoming more bulk-like as temperature increases, presumably because chain lengths are decreasing and confinement effects are becoming less prominent [93]. Quantitative testing of the scaling laws for the entropy of a confined chain with respect to chain length and confinement size are anticipated in future work, and these scaling laws will also be used to further examine the relationships between thermodynamics and dynamics.

11.4 Conclusions

Confinement of small molecules to nanopores provides a thermodynamically favorable confinement regime for studying the influence of finite size and interfacial/surface effects on the glass transition temperature and related dynamics. Furthermore, polymerization of reactive small molecules under these conditions results in stress-free reaction products, which can range from low molecular weight species to oligomers to polymers to crosslinked network materials. Modeling of the kinetics and thermodynamics of these polymerizations is capable of providing insights into how nanopore confinement influences chain diffusivity and entropy under equilibrium conditions, and it is anticipated that such measurements and modeling will facilitate our future understanding of the relationship between thermodynamics and dynamics, including the glass transition at the nanoscale.

References

1. Jackson, C.L., McKenna, G.B.: J. Non-Cryst. Solids **131–133**, 221–224 (1991)
2. Jackson, C.L., McKenna, G.B.: Chem. Mater. **8**, 2128–2137 (1996)
3. Forrest, J.A., Jones, R.A.L.: The glass transition and relaxation dynamics in thin polymer films. In: Karim, A., Kumar S. (eds.) Polymer Surface Interfaces and Thin Films. World Scientific, Singapore (2000)
4. Forrest, J.A., Dalnoki-Veress, K.: Adv. Coll. Interface Sci. **94**(1–3), 167–196 (2001)
5. Alcoutlabi, M., McKenna, G.B.: J. Phys.: Condens. Matter **17**, R461–R524 (2005)
6. Alba-Simionesco, C., Coasne, B., Dosseh, G., Dudzidak, G., Gubbins, K.E., Randhakrishnan, R., Silininska-Bartkowiak, M.: J. Phys.: Condens. Matter **18**, R15–R68 (2006)
7. Roth, C.B., Dutcher, J.R.: J. Electroanal. Chem. **584**, 13–22 (2005)
8. McKenna, G.B.: J. Phys. IV France **10**(Pr7), 53–57 (2000)
9. Koh, Y.P., McKenna, G.B., Simon, S.L.: J. Polym. Sci. Part B: Polym. Phys. **44**, 3518–3527 (2006)
10. Gibbs, J.H., DiMarzio, E.A.: J. Chem. Phys. **28**(3), 373–383 (1958)
11. Huber, P., Grüner, S., Schäfer, C., Knorr, K., Kityk, A.V.: Eur. Phys. J. Spec. Topics **141**, 101–105 (2007)
12. Gibbs, J.W.: The Collected Works of J. Willard Gibbs. Yale University Press, New Haven (1948)
13. Defay, R., Prigogine, I., Bellemans, A., Everett, D.H.: Surface Tension and Adsorption. Wiley Inc, New York (1967)
14. Makkonen, L.: Langmuir **16**, 7669–7672 (2000)
15. Wunderlich, B.: Macromolecular Physics, vol. 3. Academic Press, New York (1980)
16. Trofymluk, O., Levchenko, A.A., Navrotsky, A.: J. Chem. Phys. **123**, 194509 (2005)
17. Koppensteiner, J., Schranz, W.: Phase Transit. **83**(9), 744–757 (2010)
18. Zhang, J., Liu, G., Jonas, J.: J. Phys. Chem. **96**, 3478–3480 (1992)
19. Morineau, D., Xia, Y.D., Alba-Simionesco, C.: J. Chem. Phys. **117**(19), 8966–8972 (2002)
20. Xia, Y.D., Dosseh, G., Morineau, D., Alba-Simionesco, C.: J. Phys. Chem. B **110**, 19735–19744 (2006)
21. Serghei, A., Kremer, F.: Prog. Colloid Polym. Sci. **132**, 33–40 (2006)
22. Tress, M., Erber, M., Mapesa, E.U., Huth, H., Muller, J., Serghei, A., Schick, C., Eichhorn, K., Voit, B., Kremer, F.: Macromolecules **43**, 9937–9944 (2010)
23. Simon, S.L., Park, J.-Y., McKenna, G.B.: Eur. Phys. J. E **8**, 209–216 (2002)
24. Priestley, R.D., Cangialosi, D., Napolitano, S., Non-Cryst, J.: Solids **407**, 288–295 (2015)
25. O'Connell, P.A., McKenna, G.B.: Science **307**(5716), 1760–1763 (2005)
26. O'Connell, P.A., McKenna, G.B.: Rev. Sci. Inst. **78**, 013901 (2007)
27. Wang, J.H., McKenna, G.B.: Macromolecules **46**(6), 2485–2495 (2013)
28. Wang, J.H., McKenna, G.B.: J. Polym. Sci. Part B—Polym. Phys. **51**(18), 1343–1349 (2013)
29. Park, J.Y., McKenna, G.B.: Phys. Rev. B **61**(10), 6667–6676 (2000)
30. Li, Q.X., Simon, S.L.: Macromolecules **41**(4), 1310–1317 (2008)
31. Li, Q.X., Simon, S.L.: Macromolecules **42**(10), 3573–3579 (2009)
32. Koh, Y.P., Simon, S.L.: J. Phys. Chem. B **116**, 7754–7761 (2012)
33. Lopez, E., Simon, S.L.: Macromolecules **48**(13), 4692–4701 (2015)
34. Koh, Y.P., Li, Q.X., Simon, S.L.: Thermochim. Acta **492**(1–2), 45–50 (2009)
35. Mel'nichenko, B.Yu, Schüller, J., Richert, R., Ewen, B., Loong, C.-K.: J. Chem. Phys. **103**, 2016–2024 (1995)
36. Stannarius, R., Kremer, F., Arndt, M.: Phys. Rev. Lett. **75**(25), 4698–4701 (1995)

37. Napolitano, S., Wübbenhorst, M.: Nat. Commun. **2**, 260 (2011)
38. Napolitano, S., Capponi, S., Vanroy, B.: Eur. Phys. J. E **36**(6), 61 (2013)
39. Dosseh, G., Le Quellec, C., Brodie-linder, N., Alba-simionesco, C., Haeussler, W., Levitz, P., Non-Crystal, J.: Solids **352**, 4964–4968 (2006)
40. He, F., Wang, L.-M., Richert, R.: Phys. Rev. B **71**, 144205 (2005)
41. Arndt, M., Stannarius, R., Gorbatschow, W., Kremer, F.: Phys. Rev. E **54**, 5377 (1996)
42. Zheng, W., Simon, S.L.: J. Chem. Phys. **127**, 194501 (2007)
43. Schüller, J., Mel'nichenko, Yu B., Richert, R., Fischer, E.W.: Phys. Rev. Lett. **73**, 2224 (1994)
44. Gorbatschow, W., Arndt, M., Stannarius, R., Kremer, F.: Europhys. Lett. **35**, 719 (1996)
45. Huwe, A., Arndt, M., Kremer, F., Haggenmüller, C., Behrens, P.: J. Chem. Phys. **107**, 9699–9701 (1997)
46. Kremer, F., Huwe, A., Arndt, M., Behrens, P., Schwieger, W.: J. Phys.: Condens. Matter **11**, A175 (1999)
47. Pissis, P., Kyritsis, A., Barut, G., Pelster, R., Nimtz, G., Non-Cryst, J.: Solids **235–237**, 444–449 (1998)
48. Pissis, P., Kyritsis, A., Daoukaki, D., Barut, G., Pelster, R., Nimtz, G.: J. Phys.: Condens. Matter **10**, 6205–6227 (1998)
49. Swenson, J., Engberg, D., Howells, W.S., Seydel, T., Juranyì, F.: J. Chem. Phys. **122**, 244702 (2005)
50. Schönhals, A., Goering, H., Schick, Ch., Non-Cryst, J.: Solids **305**, 140–149 (2002)
51. Kalogeras, I.M., Neagu, E.R.: Eur. Phys. J. E **14**(2), 193–204 (2004)
52. Moller, K., Bein, T., Fischer, R.X.: Chem. Mater. **10**(7), 1841–1852 (1998)
53. Zanotto, A., Spinella, A., Nasillo, G., Caponetti, E., Luyt, A.S.: eXPRESS Polym. Lett. **6**(5), 410–416 (2012)
54. Ouaad, K., Djadoun, S., Ferfera-Harrar, H., Sbirrazzuoli, N., Vincent, L.: J. Appl. Polym. Sci. **119**(6), 3227–3233 (2011)
55. Keddie, J.L., Jones, R.A.L., Cory, R.A.: Faraday Discuss. **98**, 219–230 (1994)
56. Zhao, H.Y., Yu, Z.N., Begum, F., Hedden, R.C., Simon, S.L.: Polymer **55**, 4959–4965 (2015)
57. Grohens, Y., Hamon, L., Reiter, G., Soldera, A., Holl, Y.: Eur. Phys. J. E **8**(2), 217–224 (2002)
58. Li, L.L., Zhou, D.S., Huang, D.H., Xue, G.: Macromolecules **47**(1), 297–303 (2014)
59. Li, L.L., Chen, J., Deng, W.J., Zhang, C., Sha, Y., Cheng, Z., Xue, G., Zhan, D.S.: J. Phys. Chem. B **119**, 5057–5064 (2015)
60. Ellison, C.J., Torkelson, J.M.: Nat. Mater. **2**(10), 695–700 (2003)
61. Begum, F., Simon, S.L.: Polymer **52**, 1539–1545 (2011)
62. Zhao, H.Y., Simon, S.L.: Polymer **52**, 4093–4098 (2011)
63. Begum, F., Zhao, H.Y., Simon, S.L.: Polymer **53**, 3261–3266 (2012)
64. Begum, F., Zhao, H.Y., Simon, S.L.: Polymer **53**, 3238–3244 (2012)
65. Jang, W.S., Jensen, A.T., Lutkenhaus, J.L.: Macromolecules **43**(22), 9473–9479 (2010)
66. Verros, G.D., Latsos, T., Achilias, D.S.: Polymer **46**, 539–552 (2005)
67. Baschnagel, J., Binder, K.: J. Phys. I **6**(10), 1271–1294 (1996)
68. Scheidler, P., Kob, W., Binder, K.: Eur. Phys. J. E **12**, 5–9 (2003)
69. Tebouland, V., Alba Simionesco, C.: J. Phys.: Condens. Matter **14**, 5699–5709 (2002)
70. Avramova, K., Milchev, A.: J. Chem. Phys. **124**, 024909 (2006)
71. Cui, T., Ding, J.D., Chen, J.Z.Y.: Phys. Rev. E **78**, 061802 (2008)
72. Fakhraai, Z., Forrest, J.A.: Phys. Rev. Lett. **95**, 025701 (2005)
73. Koh, Y.P., Simon, S.L.: J. Polym. Sci. Part B: Polym. Phys. **46**, 2741–2753 (2008)
74. Gao, S.Y., Koh, Y.P., Simon, S.L.: Macromolecules **46**, 562–570 (2013)
75. Ng, S.M., Ogino, S.-I., Aida, T., Koyana, K.A., Tatsumi, T.: Macromol. Rapid Commun. **18**, 991–996 (1997)
76. Li, X., King, T.A., Pallikari-Viras, F., Non-Cryst, J.: Solids **170**, 243–249 (1994)
77. Uemura, T., Ono, Y., Kitagawa, K., Kitagawa, S.: Macromolecules **41**, 87–94 (2008)
78. Sakaue, T., Raphaël, E.: Macromolecules **39**(7), 2621–2628 (2006)

79. Wang, W., Xu, W.-X., Levy, Y., Trizac, E., Wolynes, P.G.: Proc. Natl. Acad. Sci. **106**(14), 5517–5522 (2009)
80. Shon, M.J., Cohen, A.E.: J. Am. Chem. Soc. **134**, 14618–14623 (2012)
81. Rubinovich, L., Polak, M.: Nano Lett. **13**, 2247–2251 (2013)
82. Kalampounias, A.G., Andrikopoulos, K.S., Yannopoulos, S.N.: J. Chem. Phys. **119**(14), 7543–7553 (2003)
83. Andrikopoulos, K.S., Kalampounias, A.G., Yannopoulos, S.N.: Soft Matter **7**, 3404–3411 (2011)
84. Begum, F., Sarker, R.H., Simon, S.L.: J. Phys. Chem. B **117**, 3911–3916 (2013)
85. de Gennes, P.-G.: Scaling Concepts in Polymer Physics. Cornell University Press, Ithaca (1979)
86. Ishinabe, T.: J. Chem. Phys. **83**(1), 423–427 (1985)
87. Van Vliet, J.H., Luyten, M.C., Ten Brinke, G.: Macromolecules **25**(14), 3802–3806 (1992)
88. van Giessen, A.E., Szleifer, I.: J. Chem. Phys. **102**(22), 9069–9076 (1995)
89. Cacciuto, A., Luijten, E.: Nano Lett. **6**(5), 901–905 (2006)
90. Kong, C.Y., Muthukumar, M.: J. Chem. Phys. **120**, 3460–3466 (2004)
91. Bezrukov, S.M., Vodyanoy, I., Brutyan, R.A., Kasianowicz, J.J.: Macromolecules **29**, 8517–8522 (1996)
92. Odian, G.: Principles of Polymerization, 3rd edn. Wiley, New York (2004)
93. Zhao, H.Y., Simon, S.L.: Polymer **6**(1), 173–178 (2015)

Chapter 12
Effect of Confinement Geometry on Out-of-Equilibrium Glassy Dynamics

Daniele Cangialosi

Abstract Glassy dynamics under nanoscale confinement have been subject of under intense debate in soft matter physics in the last 20 years. Scientific impetus in the field was provided by the increasing employment of glasses confined at the nanoscale. Furthermore, investigation of confined glasses may deliver information of the still unsolved problem of the glass transition. Within this context, the present chapter critically discusses the experimental findings in the field. Special attention is devoted to literature dealing with polymers under 1-D confinement, that is, thin polymer film. Results on different confinement geometries, such as polymer nanocomposites and nanospheres, are discussed as well. In discussing these results, we emphasize how the out-of-equilibrium dynamics, that is, the glass transition temperature (T_g) and the spontaneous evolution towards equilibrium in the so-called physical aging regime, is in numerous cases decoupled from the equilibrium dynamics, namely the rate of spontaneous fluctuations in the glass former. In particular, arguments based exclusively on the modification of the rate of spontaneous fluctuations in confinement are not able to provide a comprehensive description of the deviation of the T_g and the rate of physical aging. In the search for the factors affecting the out-of-equilibrium dynamics in confinement, we show solid experimental evidence that this is mainly determined by the amount of free interface. In this sense the crucial role of irreversible chain adsorption is highlighted. Finally a framework, based on free volume holes diffusion (FVHD), to describe the entire phenomenology of glassy dynamics in confinement is reviewed. This is able to catch the enhancement of the out-of-equilibrium dynamics, that is, the T_g depression and the speed-up of physical aging in confinement, with no need to invoke any acceleration of the rate of spontaneous fluctuations of the polymer.

D. Cangialosi (✉)
Centro de Física de Materiales (CSIC-UPV/EHU), Paseo Manuel de Lardizabal 5, 20018 San Sebastián, Spain
e-mail: swxcacad@sw.ehu.es

12.1   Introduction

Polymers confined at the nanoscale are assuming increasing importance in a wide range of applications where miniaturization is required [31, 121, 127, 186, 187]. The technological interest on polymer confined at the nanoscale has generated intense research in an attempt of understanding how properties are modified by the presence of the polymer/external world interface. Due to the large area of such interface to volume of polymer ratio, these can dramatically deviate from those of the corresponding bulk system. Among the aspects that have recently received considerable attention, the study of glassy dynamics in nanoscale confinement is certainly one of the most important. Apart from the specificity of glassy dynamics in confinement, this attention is due to the intrinsic interest on the glass transition, a phenomenon that has attracted the scientific curiosity since many decades and is yet an unsolved problem in condensed matter physics. Among glass forming systems in confinement, polymers are an important class. This is due to the mentioned relevance in application and to the facility of supercooling their amorphous state below their melting temperature. Among the possible confinement configurations that of thin polymer films is by far the most investigated. However, in recent years other kind of confinement received considerable attention, in particular polymer nano-composites and nanospheres.

   In this chapter, we first summarize the main aspects of glassy dynamics, in particular those that will be employed in discussing the topic in confined polymer glasses. In doing so, we split the treatment of glassy dynamics in the equilibrium and out-of-dynamics aspects. This distinction, conceptual in nature, assumes special importance in the second part of the chapter where the experimental activity in glassy dynamics in confinement is reviewed. First we summarize the most recent results on the equilibrium dynamics, probed by techniques where linear perturbations are imposed to the confined sample. Secondly, it is shown how the out-of-equilibrium dynamics, that is the glass transition temperature (T_g) and the recovery of equilibrium in the glassy state, may be drastically modified in confinement. The relation with equilibrium (linear) dynamics is discussed. Within this context, it is emphasized how it is not possible to predict the overall phenomenology of the out-of-equilibrium dynamics in confinement according to arguments solely based on the equilibrium dynamics. Hence, a significant part of the chapter is devoted to rationalize the factors playing a role in the modification of the out-of-equilibrium dynamics. Among them, special attention is dedicated to the effect of irreversible chain adsorption on the out-of-equilibrium dynamics. Within this context, it is shown how, differently from bulk glass-forming polymers, confined systems exhibit non-equilibrium features also above their T_g. These have a dramatic impact in determining the magnitude of T_g and rate of physical aging deviation from bulk behaviour. This means that in principle such deviations can be tuned simply subjecting the confined polymer melt to different thermo-mechanical histories. An important aspect is that the amount of interfacial free interface essentially determines the magnitude of such deviations. In the final part of the

chapter, the recent activity in the application of the free volume hole diffusion (FHVD) model is presented. In particular, it is demonstrated how such model can describe the out-of-equilibrium dynamics accounting for the amount of free interface as the crucial parameter.

12.2 Glassy Dynamics: Established Facts

From a structural point of view and in contrast with crystalline solids, liquids are characterized by the absence of long range order. Apart from this, the main signature of liquid-like behaviour is the ability to flow. This can only occur if thermodynamic properties spontaneously fluctuate in space and time. The typical time scale at which such fluctuations occur determines the liquid viscosity. A class of liquids can be driven below the melting temperature (T_m), thus avoiding crystallization. In those cases where crystallization does not occur over large time scales, one can classify the system as metastable [36, 154]. A considerable number of polymers belongs to the category of glass formers, that is, systems that can be easily maintained amorphous below their T_m. This is due to the presence of chain connectivity and, in some cases, conformational irregularities, which often make crystallization unfavourable.

Normal liquids exhibit Arrhenius temperature dependence of the typical time scale of spontaneous fluctuations. However, once below their T_m, a steep super-Arrhenius temperature dependence of such time scale is observed. This, in a more or less wide temperature range, is often described by the so-called Vogel Vogel-Fulcher-Tammann (VFT) equation [62, 166, 178]: $\tau = \tau_0 \exp (B/(T - T_0))$. Here τ is the relaxation time relevant for spontaneous fluctuations, τ_0 a pre-exponential factor, and B and T_0 the Vogel activation energy and temperature, respectively.

In the experimental practice, the presence of the time scale for spontaneous fluctuations implies that, if the observation time is smaller than such time scale, an out-of-equilibrium system is probed. This is what happens when thermodynamic (or related to) magnitudes are monitored as a function of temperature at a given cooling rate. There exists a temperature below which spontaneous fluctuations are frozen in the time scale of the experiment dictated by the applied cooling rate. This is the glass transition temperature. Its signature is a relatively sudden jump in second order thermodynamic properties (specific heat, coefficient of thermal expansion, compressibility etc.). Evidently, the T_g will depend on the applied cooling rate and, therefore, is not a true thermodynamic transition. Conversely the glass transition is a kinetic transition intimately related to the temperature dependence of the typical time scale of spontaneous fluctuations.

The one-to-one connection between the cooling rate dependent T_g and the rate of spontaneous fluctuations has been shown by several studies in the past [41, 153, 180]. In particular it has been shown that, if the cooling rate is plotted as a function of T_g^{-1}, its temperature dependence can be fitted by the VFT equation, in ways analogous to the description of the time scale of spontaneous fluctuations τ.

Similar arguments can be employed if one considers the evolution toward the metastable equilibrium of a glass below its T_g. This phenomenon is known as physical aging or structural recovery [86, 162] and is the obvious consequence of the out-of-equilibrium nature of glasses. In bulk systems, the recovery of equilibrium occurs with kinetics that can be fully described considering the instantaneous rate of spontaneous fluctuations [74, 86]. Nevertheless, it is worth remarking that, from a conceptual point of view, the rate of spontaneous fluctuations, on the one hand, and the cooling rate dependent T_g and the recovery of equilibrium, on the other, are two distinct aspects of the glass transition. In particular, in the former case an intrinsic property of the glass former is considered, that is, its unperturbed molecular mobility. This can only be probed applying a perturbation in the linear regime. In this case the fluctuation-dissipation theorem [17, 122] is fulfilled. Conversely, measuring the T_g under a given applied cooling rate or following the equilibrium recovery in the physical aging regime are based on application of non-linear perturbations. In this case we can address the dynamics that is probed as out-of-equilibrium glassy dynamics. In the same way, the determination of the rate of spontaneous fluctuations can be addressed as the equilibrium dynamics of the glass. The mentioned conceptual difference indicates that there is no reason why the equilibrium and the out-of-equilibrium glassy dynamics should be one-to-one related in *any* condition. As we will show in a subsequent section of the chapter, this is *not* the case for glasses under certain conditions of confinement.

Apart from the intrinsic interest of studying the glass transition in confinement, significant impulse to this kind of investigation has been provided by the search for the typical length associated to the fluctuations in glass-forming liquids. This was long ago put forward by Adam and Gibbs (AG) [1]. They developed a theory of the glass transition where the decrease of the configurational entropy (S_c) with decreasing temperature implies a concomitant increase of the length scale of the glass transition (z^*).

Since the AG theory, numerous approaches have been presented in the search for the relevant length scale of the α relaxation. As the AG theory, some of them, such as that proposed by Donth [40, 75] and the random first order theory (RFOT) [101], rely on thermodynamics. Conversely others, such as that based on string-like motion [39] and the four point dynamic susceptibility [8], are based on the estimation of dynamically correlated structural units. Among the different approaches seeking for the relevant length scale of the α process, within the context of the present chapter, it is worth considering that based on the self-concentration [97]. Such concept was introduced to explain the presence of two glass transitions in miscible polymer blends. It relies on the fact, that due to the limited size of CRR(s), the effective concentration within the cooperative volume differs from the macroscopic one [18, 19, 24]. In particular, it is richer in the component of the target unit at the center of the CRR. As such the self-concentration approach provides information on how far the dynamics of a given structural unit is affected by its surrounding. This is especially relevant once the effect of an interface in nanoscale confinement is considered. In all approaches providing an estimation of the relevant length of the α relaxation, this is generally found to be in the order of several

nanometers or, for some polymers and within some approaches, even smaller than 1 nm [5, 18, 19].

12.3 Equilibrium Dynamics Under Nanoscale Confinement

Reports on the rate of spontaneous fluctuations in confinement are relatively recent. With regards to thin polymer films, pioneering studies in this sense have been performed by broadband dielectric spectroscopy (BDS) on Al-capped thin PS films more than one decade ago by Fukao and Miyamoto [60]. This technique probes the reorientation of dipoles under the application of electric fields in the linear regime [88], and therefore is ideal to characterize the intrinsic molecular mobility in glass formers. Fukao and Miyamoto found that the typical relaxation time remains bulk-like down to thicknesses of 20 nm. For smaller thicknesses, acceleration of the rate of spontaneous fluctuations was observed. Similar results were later reported by others [73, 165].

Subsequent studies have emphasized important aspects on the sample preparation and experimental conditions. In particular, Kremer and co-workers [157] showed that upon annealing above T_g the dielectric response of thin films was gradually shifting towards lower frequencies. This is interpreted considering that films after spin-coating exhibit significant amount of solvent. As a result, the plasticizing effect of the solvent would be responsible for the fast segmental dynamics. Once this is removed by annealing above T_g the dynamics appears to be slowed down. The presence of solvent in spin-coated samples and the difficulty of removing it was later revealed by Perlich et al. [130]. The work of Kremer and co-workers [157] also evidenced the importance of performing experiments in inert atmosphere rather than in air. The most important outcome of that study was that, once annealed for sufficiently long time and measured in inert atmosphere, thin polymer films essentially exhibited bulk-like dynamics. This was later confirmed in numerous works in capped, supported and freestanding films by techniques ranging from BDS [16, 91, 104, 118, 119, 156, 174, 175, 188, 191], specific heat spectroscopy [77, 104, 174], shear modulation force microscopy (SMFM) [65], near-edge X-ray absorption line structure (NEXAFS) [95] and optical photobleaching [125]. Recently bulk-like segmental dynamics have been found for (semi)isolated polymer chains, that is the smallest achievable size when polymers are considered [175]. Morevoer, Paeng and co-worker [125] showed that pronounced bulk like-dynamics exist for freestanding polymer films with thickness ~ 10 nm. As will be seen in the subsequent sections of chapter, in view of the large deviations of the out-of-equilibrium dynamics found in freestanding systems, this result appears to be especially interesting. A summary of results on the equilibrium dynamics in thin films is shown in Fig. 12.1, taken from ref. [89]. As can be observed, all summarized results indicate that there exists a prominent component with bulk-like dynamics.
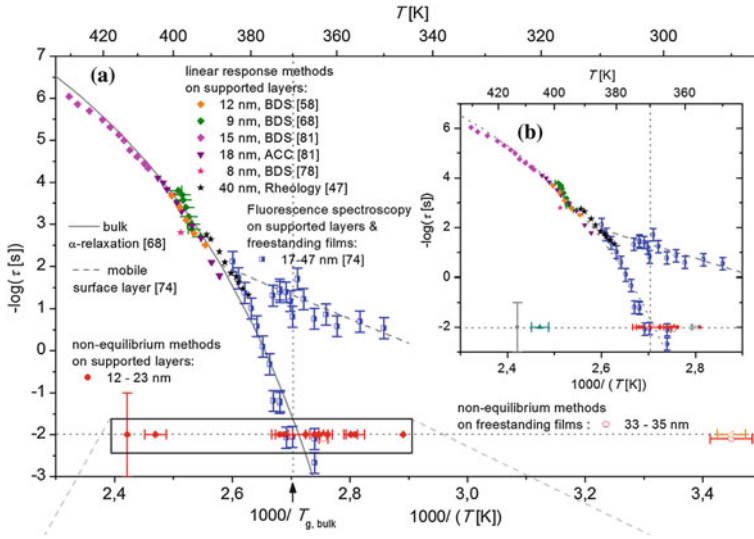
Fig. 12.1 Relaxation time of spontaneous fluctuations and equilibration time corresponding to the thermal T_g as a function of the inverse temperature measured by different techniques. The inset is an enlargement of the main panel in the neighbourhood of the bulk thermal T_g (reprinted with permission from ref. [89])

Dominant bulk-like dynamics was also found for freestanding PS nanospheres [193]. This was measured by BDS for a wide range of spheres diameters down to 90 nm. In terms of surface/volume ratio, this corresponds to a 30 nm thick films. This is evident from the observation of Fig. 12.2 where the loss part of the dielectric permittivity (ε''), taken from ref. [193], is shown as a function of temperature for freestanding PS nanospheres and bulk PS. The main relaxation peak in BDS was also employed to characterize the rate of spontaneous fluctuations in polymer nanocomposites with weak interaction polymer/filler [9, 12, 14, 15, 22, 164]. In all case no influence of the presence of nanofillers was found, which means that the segmental dynamics remained bulk-like.

In view of the previous discussion, the presence of a dominant component exhibiting bulk-like dynamics in a wide variety of confined polymer glasses is nowadays a well established fact [43, 89, 136]. However it has to be remarked that confined systems exhibits complex relaxational behaviour. With regards to freestanding films [125] and nanospheres [193], there exists a relatively fast component with Arrhenius-like behaviour. This is shown in Figs. 12.1 and 12.2 [89]. In the latter case, this component appears as a broad relaxation at relatively low temperatures. This has been interpreted as associated to the polymer layer in proximity of the free surface. The presence of faster than bulk dynamics in freestanding PS films or on the free surface of supported films was also reported by other authors [27, 49, 120, 123, 165]. The thickness of the layer with fast dynamics is estimated to be of the order of nanometers [125]. Intriguingly, a relaxational process
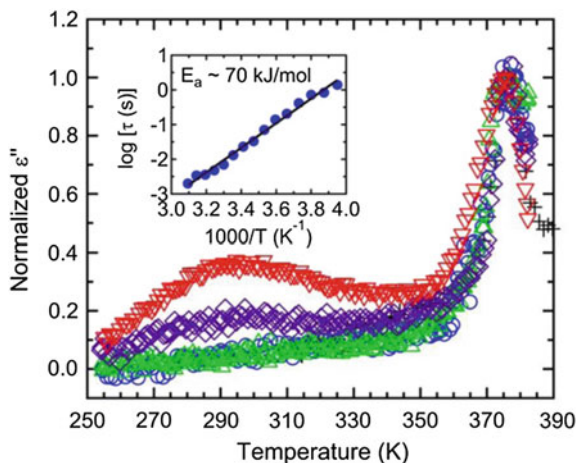
Fig. 12.2 Loss part of the dielectric permittivity normalized to its maximum value, as a function of temperature for PS nanospheres obtained by BDS at 0.5 Hz and a heating rate of 3 K.min^{-1} with the following diameters: 379 nm (*blue circles*), 286 nm (*green up-triangles*), 200 nm (*violet diamonds*), 130 nm (*red down-triangles*); and for bulk PS (*black crosses*). The inset shows the typical relaxation time of the relatively fast component of the dynamics as a function of the inverse temperature for the nanospheres with diameter of 130 nm. (reprinted with permission from ref. [193])

exhibiting Arrhenius temperature dependence was observed also in capped PS films [60, 103, 135]. Hence, the interpretation based on enhanced mobility in proximity of a free surface needs to be inspected in more details. As will be shown in a subsequent section of the chapter, adsorption of the polymer on the substrate is in numerous cases and in some experimental conditions incomplete. This implies that there exists a portion of the interface that is free [32, 117]. This might be responsible for the Arrhenius-like process observed even in capped films. Whether such process is actually associated to the polymer segments in proximity of a free surface is currently matter of open debate [43, 89].

To close this section, it is worth mentioning that, for confined polymers strongly interacting with the supporting substrate, a slowing down of the segmental dynamics is generally observed. This is seen in numerous polymers. Among them we recall Al-capped polycarbonate (PC) [189], poly(ethylene terephthalate) (PET) [116] and poly(L-lactice) [107]. Several polymer nanocomposites in certain conditions also exhibit slowing down of the segmental dynamics [22, 90, 92, 138].

12.4   Out-of-Equilibrium Dynamics

The previous section has emphasized how glass forming polymers under confinement generally exhibit pronounced bulk-like equilibrium dynamics. This is true in the vast majority of cases, except for those polymers where strong interactions with

the interface result in slowing down of the equilibrium dynamics. In this section, we will revise results on the out-of-equilibrium dynamics of glass forming polymers under confinement, in terms of their thermal glass transition and the physical aging behaviour, that is, where a non-linear perturbation is applied, with the aim of answering the following question: does the presence of a component exhibiting bulk-like behaviour in the equilibrium dynamics imply that such behaviour exists in the out-of-equilibrium dynamics too? To do so, this section is divided in two parts: (i) the first part deals with the critical review of the thermal glass transition in different confining configurations; (ii) the second part aims to review recent results on the way physical aging of glassy polymers is affected by confinement.

12.4.1 Thermal Glass Transition

The first study reporting on the thermal glass transition of polymers under confinement is that of Keddie et al. [82]. They studied the temperature dependent thickness of thin PS films supported on silicon wafers by means of ellipsometry. They found negative deviations in the T_g for PS bulk for thicknesses below 30–40 nm. The study of Keddie et al. [82] represented an important impulse for the study of the thermal glass transition in confinement and, since then, a huge number of works have been presented in the topic.

The presence of negative deviations in the T_g in supported thin polymer films was later proved by several research group by means of different techniques [4, 37, 44, 46, 48, 54, 59, 63, 68, 70, 148, 155, 167, 176, 179]. Similarly, the T_g of thin polymer films capped between two interfaces was investigated [16, 60, 102, 135]. In both supported films, that is, systems with one free surface, and capped films moderate T_g deviations were observed. These appear at thicknesses of the order of 40 nm and were as large as 30–40 K for films thinner than 10 nm. These results were later summarized in a review [55] and are shown in Fig. 12.3. An update of results reporting T_g deviations from bulk behaviour in thin PS films is shown in Fig. 12.1. From the observation of these figures, it is realized that—although data point toward the same trend of T_g reduction with decreasing film thickness—large scattering of data exists. This suggests that, apart from the thickness of the films, other factors must play a role in determining the magnitude of T_g deviations. One important factor is certainly the cooling rate employed to the determine the T_g. If cooling rates as large as several thousands K min^{-1} are employed, as was done by Efremov et al. [44], no detectable T_g depression was observed for thin PS films as thin as several nanometers supported on platinum. Subsequent studies on the same polymer supported on a similar support [48] and on silicon wafers [67] showed how the magnitude of T_g depression decreased with the cooling rate increase. This is shown in Fig. 12.4, where data taken from ref. [48] and re-elaborated in ref. [13] are reported.

However, arguments based on the cooling rate cannot explain alone the large scattering observed in the determination of the T_g of thin PS films. Several works systematically studied how the interaction between the polymer and substrate

Fig. 12.3 Thickness dependence of the T_g measured by several techniques (reprinted with permission from ref. [55])
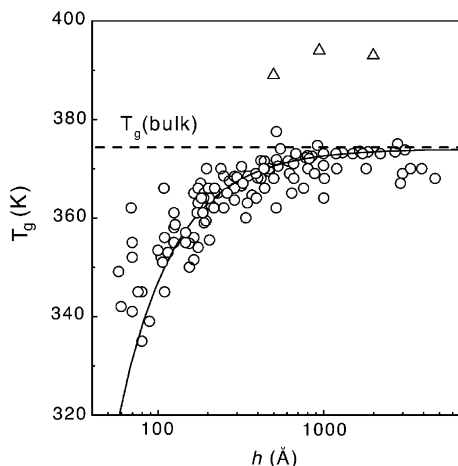
Fig. 12.4 Cooling rate dependent T_g of thin PS films for different thicknesses (reprinted with permission from ref. [13])
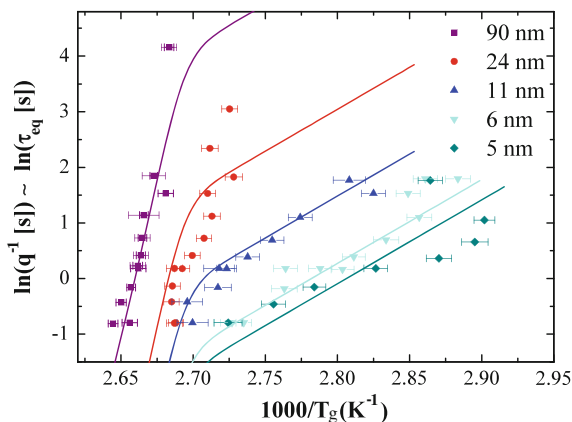
affects the magnitude of T_g deviation from bulk behaviour. This was first shown by Keddie et al. [81]. By mean of ellipsometry, they showed that, depending on whether thin poly(methyl methacrylate) (PMMA) films were supported on gold or native silicone oxide wafers, depression or enhancement of T_g was observed respectively. In the latter case, the obvious explanation for the T_g increase was the hydrogen bonding formation at the PMMA/silicon oxide interface. The importance of the interaction at the interface was later emphasized by Wallace et al. [192]. Once thin PS films were supported on hydrogen terminated silicon substrates, an increase of T_g with decreasing film thickness was observed, differently from the vast majority of experiments showing T_g depression in thin PS films. More recently the effect of interfacial interaction was studied in several experiments [47, 70, 115, 126, 139, 149, 167, 185] and simulations [173, 184]. This was done by systematically altering the interfacial energy polymer/substrate.

Beyond the role of the cooling rate and that of the polymer/substrate interaction, the polymer chain architecture [30, 68] and the stress induced to the film when measuring the T_g on a cooling ramp or during solvent evaporation in spin coated samples were considered [144, 168]. In the former case it was shown how different architectures in star-shaped PS induced more or less pronounced T_g deviations [68]. These deviations were found to be both positive or negative. Thin films of PS dendrimers and oligomers exhibited larger negative T_g deviations than high molecular weight linear PS [30]. Regarding the role of applied stress it is well established how this has an effect on glassy dynamics of thin polymer films [168]. The effect on the T_g needs to be investigated in details in the future [144].

In the case of freestanding films, the absence of a solid interface implies that the interfacial interaction is not a variable. As such, results on the T_g deviations of thin films in this configuration exhibit more limited scattering in comparison to supported and capped films. A general outcome is that the T_g freestanding thin polymer films is found to be strongly depressed in comparison to the bulk counterpart [4, 11, 16, 57, 83, 84, 111, 141, 181]. Such depression is much larger than that of capped and supported films and can be as large as 70 K for thin PS films thinner than 30 nm. In addition, deviations from bulk behaviour were observed for films larger than 100 nm [11, 16]. Similarly to supported films [48, 67], it has been shown that the applied cooling rate is a factor of importance in determining T_g deviations from bulk behaviour [11]. In particular, larger deviations were observed at lower cooling rates. This is shown in Fig. 12.5, where the T_g is reported as a function of the film thickness for thin PS films at two cooling rates.

Apart from thin polymer films, considerable scientific activity has been devoted to the study of polymer under other kind of confinement. Polymer nanocomposites are among them and, similarly to thin films and in those cases where weak interactions at the polymer/nanofiller interface exist, T_g depression is observed [7, 12, 15, 22, 28, 29, 145]. However in the case of polymer nanocomposites deviations of the T_g from bulk behaviour are generally milder than those observed in supported

Fig. 12.5 T_g as a function of film thickness for stacked thin PS films at two cooling rates (reprinted with permission from ref. [11])
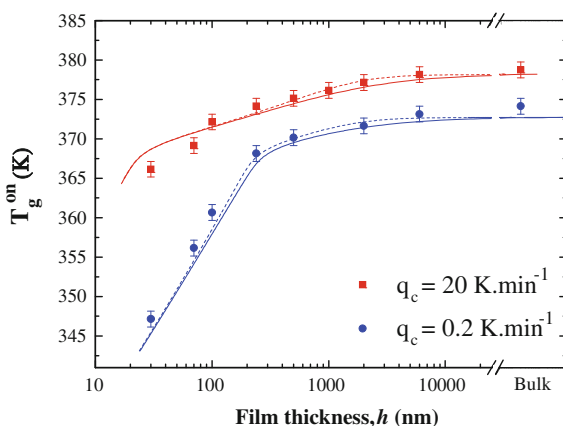
and capped thin polymer films (maximum ~ 10–15 K). This—apart from the different dimensionality of confinement, whose effect on the T_g is a priori non trivial –, is certainly caused by the difficulty in dispersing uniformly the nanofiller in the polymer. Hence, the effective surface/volume ratio is such that it corresponds to (capped) thin films thicker than 30–40 nm [7]. Analogy with polymer thin films exists also for what concerns the existence of nanocomposites exhibiting increase in T_g. This has been found for systems with strong interactions at the interface, for instance hydrogen bonding [99, 138, 145, 183]. Finally, it is worth recalling that a number of polymer nanocomposites exhibit no experimentally detectable deviations from bulk T_g. This was found for PMMA/silica nanocomposites where silica nanoparticles were previously silanized to avoid strong hydrogen bonding with the polymer [10, 14]. This was the case for low silica contents in the polymer. However once such content is increased, T_g depression was observed [22]. Nanocomposites exhibiting no evidence of deviation from bulk T_g are those of PVAc with neat silica [3] and poly(ether imide) (PEI) with carbon fiber [35].

Several works have been devoted to the study of the glass transition in polymer nanospheres. Similarly to polymer nanocomposites the radius of curvature of the spheres may play a role in determining the magnitude of T_g deviations. The first study on polymer nanospheres was performed by Gaur and Wunderlich [64]. They investigated the T_g of PS nanospheres with diameter as low as 85 nm. Though they found no significant modification of the T_g in comparison to the bulk, the specific heat versus temperature traces showed considerably broader glass transition intervals and decreased jumps, that is, the difference between melt and glass heat capacities. More recently, similar results were found also in PS nanospheres in acqeous suspension by DSC [172]. More recently, a number of works showed negative T_g deviations in PS [38, 51, 193, 194] and PMMA [50] nanospheres. This can be as large as 70 K for PS nanospheres with diameter ~ 20 nm [51]. In the works of Feng et al. [50, 51], it was demonstrated how the presence of a surfactant on the surface of the nanosphere and its nature (ionic or nonionic) has a crucial effect on the magnitude (if any) of deviations from bulk T_g. In particular, surfactant free PS nanospheres and, to a minor extent, those recovered by an ionic surfactant exhibit negative deviations of the T_g [51]. Conversely no detectable change of T_g with the diameter was present in nanosphere recovered by a nonionic surfactant. The opposite was shown for nanospheres made of a polar polymer, PMMA [50]. In this case, the T_g was found to be depressed in comparison to its bulk value for freestanding nanospheres and those recovered with a nonionic surfactant, whereas no deviations were observed in nanospheres presenting a ionic surfactant on the surface. The nature of the interface was revealed to be an issue by Zhang et al. [194]. They showed that, once recovered by silica, PS nanospheres exhibit bulk-like T_g, where the same nanospheres when freestanding show considerable depression.

Beside studies showing negative or no T_g deviations from bulk behaviour, it is worth mentioning that there exist several studies where T_g increase was found. This was the case of freestanding poly(ethyl methacrylate) (PEMA) [105, 106]. In the same works, it was hypothesised that the T_g increase was due to loss of configurational entropy caused by the limited number of monomers present in each

nanosphere. However, the fact that other studies observed different results in freestanding nanospheres [38, 50, 51, 193, 194] appears to be in contradiction with those on PEMA. At present there exists no explanation for the discrepancy among these results and future work is needed to clarify.

12.4.2 Physical Aging

In this subsection, we critically review another aspect of the out-of-equilibrium dynamics of confined polymer glasses, that is, their physical aging behaviour. This aspect of the out-of-equilibrium dynamics in confinement has received increasing attention in the last years, and several reviews can be consulted for details [23, 133]. A glass former can be brought out-of-equilibrium through several routes. However, cooling down a melt from its equilibrium state into the glass by crossing the T_g is by far the most common route. Hence, when studying the kinetics of equilibrium recovery in the aging regime, the knowledge of the T_g at the cooling rate employed to obtain the out-of-equilibrium glass is essential. In other words if effect on the glass transition, that is on the T_g, the breadth of the transition and/or the specific heat jump at the T_g, exist, one should expect effects on the physical aging behaviour too.

Concerning thin polymer films, several works demonstrated that alteration of the kinetics of equilibrium recovery during physical aging is actually associated to a decrease of T_g [11, 85]. In these works, it was found that recovery of equilibrium at a given temperature was faster in thin films than in bulk and increasingly faster with decreasing thickness. Though a characterization of the T_g is not provided, it is worth mentioning that faster rapidity of equilibrium achievement is a well documented fact for several thin films made of polymer membranes [42, 76, 108, 131, 150, 151]. Interestingly, these studies and that of Boucher et al. in thin PS films [11] indicate that the acceleration of physical aging is already visible at thickness as large as several microns. This is shown in Fig. 12.6, where the recovered enthalpy, shown in terms of the distance from equilibrium, is presented as a function of the aging time for several thicknesses (and bulk PS) at 358 K. Indications for accelerated recovery of equilibrium in micrometer thick films are provided by Cangialosi et al. [25, 26]. They followed the evolution with aging time of the dielectric permittivity in micrometer thick PC films and showed how the evolution toward equilibrium proceeds faster than in bulk PC.

Other studies focus on the so-called rate of physical aging, that is, the slope of the equilibrium recovery function in a given aging time interval. This was done by means of several techniques including ellipsometry [6, 58, 140, 142, 143], fluorescent spectroscopy [134, 137, 138] and dielectric methods [61]. In such a case, it is not always possible to draw conclusions regarding the rapidity of equilibrium achievement. Nevertheless this kind of studies provides interesting information on the modification of the kinetics of physical aging in confinement. In several cases, the aging rate is found to be reduced in comparison to bulk samples. In thin films where a concomitant reduction of the T_g exists [6, 58, 134, 137, 140, 142, 143], the

Fig. 12.6 Amount of recovered enthalpy, shown as the distance from equilibrium, as a function of the aging time at 358 K for freestanding thin PS films and the corresponding bulk polymer (reprinted with permission from ref. [11])
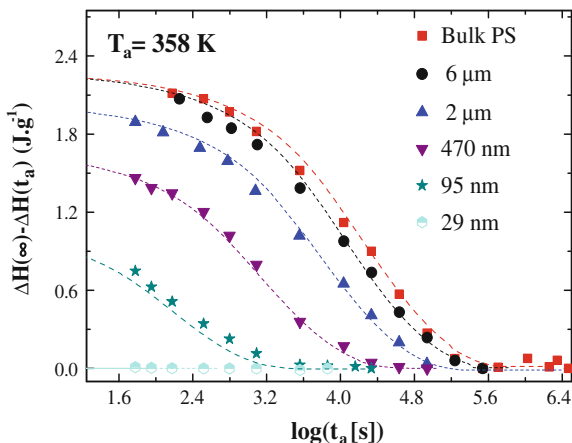
obvious explanation is that the amount of recovery is smaller in thin films due to the vicinity to their T_g. However when no reduction or T_g increase is observed, that is, in supported or capped films with strong interactions at the interface, a reduced aging rate is generally interpreted as being due to reduced mobility [134, 137].

Indications that thin polymer films exibiting T_g reduction age faster than the corresponding bulk systems are provided by the study of Kawana and Jones [80]. They studied how the overshoot in the coefficient of thermal expansion, as measured by ellipsometry, changes with aging time and thickness on thin PS films supported on silica wafers. In doing so, they found that the thinnest films employed, ~10 and 18 nm thick, hardly exhibited any overshoot in the linear coefficient of thermal expansion. Furthermore, for these films the coefficient of thermal expansion in the glassy state was only marginally reduced in comparison to the melt value. Altogether, these results indicate that thin films are able to maintain equilibrium or recover it when drawn in the glassy state more efficiently than bulk. Concerning the value of the coefficient of thermal expansion in the glassy state, similar results showing that its value in the glassy state is larger in thin films than in bulk were found in several studies [79, 112, 160, 177]. Furthermore, by means of ellipsometry and x-ray reflectivity Vignaud et al. [177] showed that the larger coefficient in the glassy state results in thin films exhibiting larger densities than bulk.

As for the T_g, polymer nanocomposites generally exhibit physical aging behaviour analogous to that of thin films [23, 133]. Polymer nanocomposites exhibiting negative deviations of the T_g generally exhibit faster recovery of equilibrium, as expected. This was found for nanocomposites with silanized silica of PMMA [10, 14, 22], PS [22] and PVAc [3, 12]; those of gold with PS [15]; and those of carbon-fiber with poly(ether imide)(PEI) [35]. Concerning polymer nanocomposites with T_g lower than the bulk value, there exist several studies where the slope of the recovery function, that is, the aging rate, is characterized in a given aging time interval. In ways analogous to polymer thin films, in several

nanocomposites exhibiting negative deviations from bulk T_g, reduced aging rates are measured as a consequence of the reduced driving force of equilibration [146]. This is directly related to $T_g - T_a$, where T_a is the aging temperature.

Reduced aging rates were also found for nanocomposites exhibiting T_g increase. However, as previously discussed, in this case this is an obvious consequence of the reduced segmental mobility. Hence, in these studies the recovery function is only monitored at the very beginning of the aging process.[1] The reduced aging rate with T_g increase was found for epoxy in nancomposites with POSS [92] and MMT [100]; poly(2-vinyl pirolidine) P2VP in nanocomposites with alumina and silica [146]; and PMMA in nancomposites with non-silanized silica [138, 145]. Reduced aging rates are also encountered for nanocomposites based on SWCNT [53, 69, 96].

In recent years, the recovery of equilibrium after cooling down through the T_g has been reported for polymer nanospheres. However, for this confinement configuration studies are considerably less scarce and, to our knowledge, the study of Guo et al. [72] on PS nanospheres is the only one where this topic is investigated systematically. In that work, it was found that freestanding nanospheres age faster than bulk PS, whereas in spheres capped by silica the rate of equilibrium achievement assumes bulk value, regardless of the sample diameter. These results generally agree with the presence of negative deviations from bulk-like T_g in the former case and the absence of diameter dependent effects on the T_g in the latter [193, 194]. Accelerated equilibrium recovery was found for a non-polymeric glass-former confined in spherical nanopores [159]. In this case, an additional factor, that is, the presence of negative pressure effects inside the nanopores during polymer densification, was put forward to explain accelerated aging.

12.5 Factors Determining the Out-of-Equilibrium Dinamics in Confinement

The previous sections of the chapter provided a panoramic view on how confinement affects the equilibrium (linear) dynamics, that is the rate of spontaneous fluctuations, on the one hand, and the out-of-equilibrium (non-linear) dynamics on the other. The main conclusion that can be drawn from the summary of these results are: (i) There exists a wide variety of polymer glass formers exhibiting a dominant component with bulk-like equilibrium dynamics; (ii) Beside such dominant component, other relaxational processes have been detected in some cases, in particular a fast component in confined glasses; (iii) A class of polymers strongly interacting with the interface displays slowing down of the equilibrium dynamics as compared

---

[1]The recovery function generally exhibits a sigmoid shape when plotted as a function of the logarithm of the aging time. This is due to the fact that small aging rates are present at the beginning and the end of the aging process, whereas at intermediate aging times the most rapid evolution is observed.

to the bulk; (iv) Negative T_g deviations and acceleration of equilibrium recovery in the physical aging regime are found for those polymers where dominant bulk-like equilibrium dynamics exists; (v) Confined polymers exhibiting slowing down of the equilibrium dynamics also present increased T_g and reduced kinetics of physical aging.

Concerning confined polymers exhibiting slowing-down of both the equilibrium and the out-of-equilibrium dynamics, the obvious conclusion is that there exists full interdependence between the two aspects of glassy dynamics in confinement. This agrees with findings on bulk glass former, which, as shown by several studies, display the same interdependence [20, 41, 74, 87, 153, 163, 180].

For confined polymers with enhanced out-of-equilibrium dynamics, the following important question needs to be answered: can such enhancement be fully described on the base of the equilibrium dynamics of the glass? To answer this question a fair comparison between results on the two kind of aspects of glassy dynamics must be performed. One way to do this is having studies providing the equilibrium and out-of-equilibrium dynamics in the same experiment. The first study in this sense, where simultaneous measurements of these two aspects of glassy dynamics were performed, was that of Fukao et al. [60], followed by that of Lupascu et al. [103]. In these studies, the authors measured the equilibrium dynamics of Al-capped thin PS films by BDS, that is, they determined the rate of spontaneous fluctuations of the polarization. At the same time they exploited the capability of BDS to measure the thermal glass transition, given by the kink of the temperature dependent real part of the permittivity at frequencies larger than those where relaxational processes are located. The main outcome of the study was that the equilibrium dynamics was weakly dependent on the film thickness, whereas significant T_g decrease exists.

More recently, Boucher et al. [16] employed BDS and specific heat spectroscopy to systematically study the equilibrium dynamics and the T_g of thin PS films in various configurations of confinement. They used specimens prepared in identical conditions. In doing so they tested the possibility that deviations from bulk behaviour could be due to improper sample preparation [130, 157]. Furthermore, as for the study of Lupascu et al. [103], BDS offered the possibility to study the two aspects of the glass transition in the same experiment. In doing so, Boucher et al. [16] found thickness independent bulk-like equilibrium dynamics. Conversely, in all samples configurations including Al-capped, supported and freestanding negative deviations from bulk T_g were observed. Similar observations were made by other authors [33, 78, 158, 161, 193]. Altogether these studies indicate that T_g depression is observed in confined polymers where bulk-like equilibrium dynamics exist.

The important consequence of the previous observations is that in confinement the equilibrium dynamics, in terms of rate of spontaneous fluctuations, and out-of-equilibrium one, that is, the T_g and the kinetics of equilibrium recovery in the glassy state, are decoupled. Apart from experiments where the two aspects of glassy dynamics are probed in samples prepared under identical preparation conditions [16, 33, 78, 103, 158, 161, 193] and, in some cases, in the same experiment

[16, 103, 193], there are striking indications that the mentioned decoupling really exists. The first is that, as mentioned in a previous section, dominant bulk-like dynamics is found even in the most extreme confinement configurations. This is the case of freestanding films as thin as ∼10 nm [125] and (semi)isolated polymer coils, that is, the smallest achievable size in polymers, supported on native silica [175]. Conversely, deviations of the out-of-equilibrium dynamics from bulk behaviour are observed for freestanding films [16, 42, 76, 108, 150, 151] and nanocomposites [12, 15, 22, 93] with typical confinement length scale as large as several microns.

It is worth noticing that, in some works, the interpretation on glassy dynamics in confinement was objected in view of the temperature/time scale range normally accessed in the case of equilibrium and out-of-equilibrium dynamics respectively. In the majority of cases, the equilibrium dynamics is probed in a temperature range higher than that where the T_g, obtained at relatively low cooling rates, is located and the equilibrium recovery followed. It has been therefore put forward the scenario that, on probing the equilibrium dynamics at lower temperatures, acceleration in comparison to bulk-like dynamics would be observed [67]. This acceleration would, within this framework, explain the enhancement of out-of-equilibrium dynamics in terms of negative T_g deviations and acceleration of physical aging. Furthermore, this scenario would be in accordance with the fact that—once measured at high cooling rates, that is those providing T_g(s) in the range where equilibrium dynamics is normally observed—the T_g exhibits no detectable deviations from bulk behaviour [45, 48, 67]. However, there exists one important report where the equilibrium dynamics of thin PS films is probed in a temperature range in proximity of the (bulk) T_g [125]. In Fig. 12.7, we show data of the relaxation time of freestanding PS films from equilibrium measurements (in this case, based on probe reorientation) from Ref. [125] with thickness as low as ∼10 nm (upper panel); the specific heat *vs* temperature taken from Ref. [16][2] (middle panel); and the thickness versus temperature, measured by ellipsometry, taken from Ref. [141] (bottom panel). From the observation of the three panels of the figure, the following conclusion can be drawn: in the temperature range where the glass transition of bulk PS is located, the equilibrium dynamics exhibits bulk-like behaviour for freestanding thin PS films as thin as 14 nm. However, the presence of bulk-like dynamics in films with similar thicknesses is *not* accompanied by *any* signature of thermal glass transition. This is evidenced by the absence of any hint of decrease in the specific heat and coefficient of thermal expansion in proximity of the bulk T_g [16, 141].

The critical analysis of recently published experimental results allows concluding that, differently from bulk glass formers [41, 74, 86, 180], the equilibrium and out-of-equilibrium dynamics are decoupled in confinement [16, 23]. In other words, it is not possible to describe the T_g and the kinetics of equilibrium recovery

---

[2]In ref. [16] stacked films are actually investigated. However, these behave similar to a single freestanding film, provided that very high molecular weight polymers are employed.
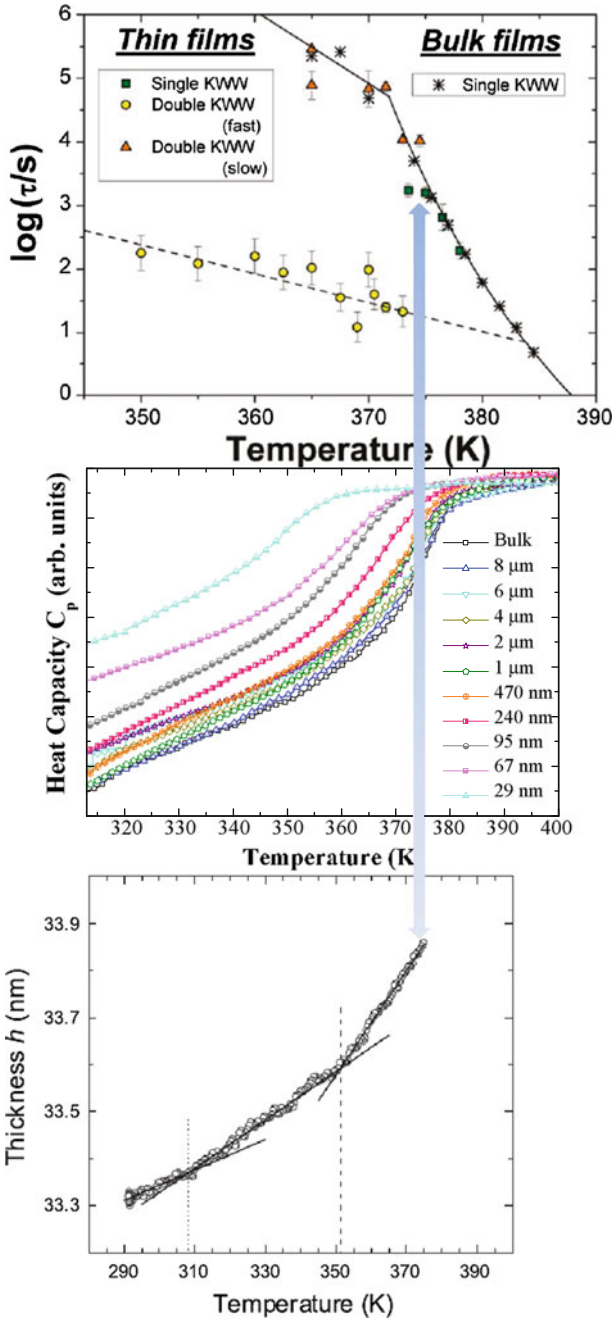
Fig. 12.7 Typical relaxation time of spontaneous fluctuations (*upper panel*); specific heat (*middle panel*); and thickness (*lower panel*) as a function of temperature for freestanding thin PS films. The arrow indicates the location of PS bulk T_g (Reprinted with permission from refs. [16, 125, 141])

in the physical aging regime according to arguments exclusively based on the rate of spontaneous fluctuations. The next part of the manuscript will show which factors, beyond the molecular mobility, are responsible for the deviation of the out-of-equilibrium dynamics in confinement.

12.6 Free Interface and Out-of-Equilibrium Dynamics in Confined Polymers

The diversity of results reporting deviations of the out-of-equilibrium dynamics from bulk constitutes a challenge in an attempt of unveiling the factors affecting such behaviour. For instance, it has been shown how films with the same thickness can exhibit more or less pronounced decrease and, in some cases, even increase of T_g (see e.g. Fig. 12.3). One of the possible reasons for the scattering of results, that is the applied cooling rate, has been already emphasized in a previous section in light of recent experimental findings [45, 48, 67]. Here we show how the interaction with the interface plays a dominant role in determining the direction and magnitude of T_g deviations. Obviously, due to the close relation between T_g and the recovery of equilibrium, these argument can be applied to physical aging data. However, in this case data are much more scarce and, therefore, we focus our attention on T_g data.

A glance on the effect of interfacial energy on T_g deviations from bulk behaviour is provided by Napolitano et al. [115]. These data are shown in Fig. 12.8. As can be observed there exist a positive correlation between the magnitude and sign of T_g deviations and the interfacial energy between the confined polymer and the substrate. A further step forward in the comprehension of factors affecting T_g deviations was provided by Napolitano et al. [119]. They showed that for a given polymer/substrate couple, in the case of ref. [119] PS on Al, prolonged annealing well above the polymer T_g induces a reduction of negative T_g deviations. Other studies point in the direction of reduced confinement effects once annealing well above T_g for polymers exhibiting T_g reduction [117, 119, 147, 157, 190]. In some cases, it was shown that T_g deviations could be even removed and bulk-like behaviour recovered. An important outcome of this research activity was that the annealing time needed to recover the bulk T_g was depending on the polymer molecular weight [119]. These results suggest a close relation between the magnitude of T_g deviations and adsorption at the interface, whose kinetics is regulated by the polymer chain dynamics. It is in fact well-known that—under certain conditions of interfacial tension, that is, attractive or mildly repulsive—irreversible adsorption at the interface occurs [52]. The presence of so-called Guiselin brushes [71], that is, a layer of polymer that cannot be removed from the substrate even under extreme conditions (for instance in good solvents), constitutes a proof of the connection between chain adsorption and magnitude of T_g deviations.

In a subsequent study, Napolitano et al. [117] showed that the essential parameter in the process of adsorption regulating the magnitude of T_g deviations
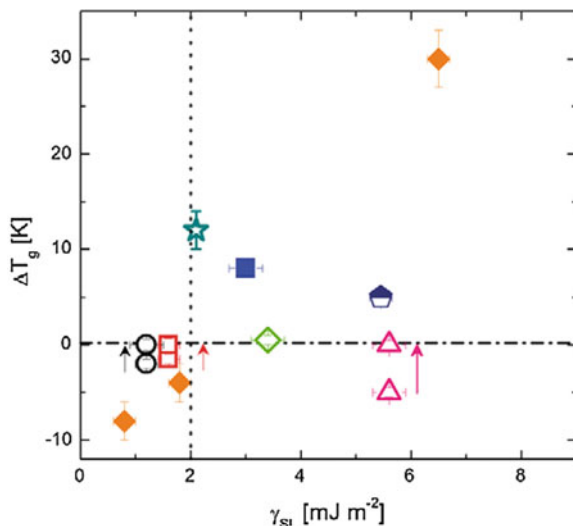
Fig. 12.8 T_g as a function of the nominal interfacial energy for the following confined polymers: 22 nm thick PS supported on OTS (*orange diamonds*); 20 nm thick PS capped in Al (*pink triangles*); 22 nm PVAc supported on silicon oxide (*green open diamonds*); 22 nm PVAc supported on Al (*red open squares*); 22 nm PVAc supported on gold (*black open circles*); 13 nm PET capped in Al (*blue squares*); 10 nm polysulfone (PSF) capped in Al (*blue pentagon*); 22 nm PC capped in Al (*dark cyan stars*). The arrows indicate the shift of T_g occurring after prolonged annealing in the melt state (reprinted with permission from ref. [115])

from bulk behaviour is the amount of free interface, that is, the portion of interface exhibiting no adsorbed polymer chains. As will be seen in a subsequent section of the chapter, the free volume holes diffusion model nicely rationalizes the connection between the magnitude of T_g deviations and the amount of free interface. In the work of Napolitano et al. [117], such magnitude was characterized measuring the dielectric strength of labelled PS. This is shown in Fig. 12.9, where the T_g of a 20 nm thick PS film is shown as a function of a magnitude directly related to the amount of interface. As can be observed, such film appears to have the largest T_g deviation when the amount of free interface is at its maximum, that is before annealing at T_g bulk plus 60 K. However, once the free interface is eliminated after prolonged annealing, the T_g assumes the bulk value.

Altogether results on the characterization of adsorption phenomena at the interface of the confined polymer at the interface suggest the following scenarios for the T_g behaviour: (i) There exist large interfacial energy between the polymer and the substrate. In such a case, polymer adsorption is thermodynamically favoured and, during sample preparation, no free interface is left out. Furthermore, linear dynamics is slowed down. As a consequence of these phenomena, positive T_g deviations from bulk behaviour are observed. (ii) The interfacial energy between polymer and substrate is weakly repulsive or attractive. Negative T_g deviations are observed and these are associated to incomplete adsorption of the polymer on the
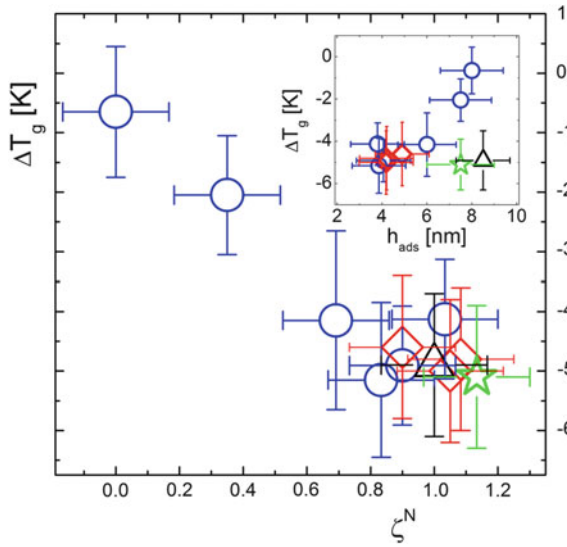
Fig. 12.9 (Negative) T_g deviation from bulk behaviour as a function of a parameter directly related to the amount of free interface for: for PS97 (*blue circles*), PS160 (*red diamond*), PS640 (*green star*), and PS932 (*black triangle*). The inset shows the dependence of the (negative) T_g deviation with the thickness of irreversibly adsorbed layer (reprinted with permission from ref. [117])

substrate. In this way, a significant portion of free interface is left out. However, depending on the molecular weight and the annealing time well above the bulk T_g, such free interface can be filled by additional polymer chains with the result of increasing the film T_g, in some cases recovering the bulk behaviour; (iii) The polymer and the substrate exhibit strong repulsive interaction. In such a case the film easily dewets and any characterization of glassy dynamics on a given film thickness is infeasible.

12.7   Theoretical Frameworks

The previous section of the manuscript has highlighted how arguments exclusively based the effect of confinement on the equilibrium dynamics are unable to provide a full description to deviations of the out-of-equilibrium dynamics in terms of T_g and rate of equilibrium recovery in the aging regime. The out-of-equilibrium dynamics can be described by an equilibration time τ_{eq}, that is, the time to recover equilibrium or the inverse of the cooling rate corresponding to a given T_g. The critical review of recent scientific activity indicates that, differently from bulk glass formers [20, 41, 74, 87, 153, 163, 180], the τ_{eq} of confined polymers cannot be related *exclusively* to the rate of spontaneous fluctuations, described by a typical relaxation time τ. In such a case, the connection between the two time scales must be mediated by a function

$g(h)$ solely depending on the geometry of the confined polymer: $\tau_{eq} = g(h)\tau$. Here h is the *confinement length scale*, whose meaning will be rationalized in the remaining part of this section within available theoretical frameworks. In doing so, the problem of the connection of out-of-equilibrium dynamics to the rate of spontaneous fluctuations via geometrical arguments is set in its most general form. Furthermore, the function $g(h)$ must include the amount of free interface, since this has been shown to be a crucial parameter in determining the magnitude of T_g deviations from bulk behaviour [117]. Hence, the challenge is now to unveil what physics stands behind the function $g(h)$.

Approaches based on the modification of the equilibrium dynamics are certainly of interest [56, 110]. However, in view of the previous arguments, it must be remarked that these approaches, rather than describing the thermal T_g, are suitable to describe the so-called "dynamic" T_g, that is, the temperature corresponding to a given time scale of spontaneous fluctuations (e.g. 100 s). Hence, in view of the presence of predominant bulk like dynamics even under extreme conditions of confinement—for instance freestanding polymer films as thin as ~ 10 nm [124, 125] and (semi)isolated polymer chains [175] –, these approaches predict a dynamic T_g showing up at temperatures as large as the bulk T_g. This is experimentally not observed for the thermal T_g as shown in Fig. 12.7. Hence, these approaches fail to provide a comprehensive description of glassy dynamics in confinement, specifically out-of-equilibrium phenomena.

In recent years, percolation arguments have been employed to describe T_g deviations (both negative and positive) [94, 98]. Though, in their original formulation, approaches based on such arguments rely on the effect of altered equilibrium dynamics on the thermal T_g, it is worth remarking that, since they are based on geometrical arguments, they can in principle be adapted to describe deviations in the out-of-dynamics (partially) decoupled from those of the equilibrium dynamics.

In the next part of this section, we show how the free volume hole diffusion (FVHD) model is potentially an appropriate framework to describe the entire phenomenology of the out-of-equilibrium dynamics. The model does not claim to provide a description of molecular motion in glass forming liquids. It rather describes how a glass leaves or recover equilibrium under given thermo-mechanical histories. The idea that equilibrium in glasses is maintained via diffusion through the interface with the external world was long ago proposed by Alfrey et al. [2]. Such idea was neglected during several decades once Braun and Kovacs [86] showed that there existed no size dependent of the equilibrium recovery in powdered glassy PS. Since the typical size of such powdered PS fibers was of the order of microns, Simha and co-workers [34], in an attempt to revitalize the idea of free volume holes diffusion, proposed that there exists some ill-defined *internal length scale*. The presence of such length scale would overcome the absence of size effects in powdered PS with dimensions of several microns. Though the so-developed model was able to describe volume recovery data of another archetype polymer, PVAc, the *ad hoc* assumption of an internal length scale was a major limitation on further exploring the ideas based on free volume holes diffusion. Nonetheless,

similar arguments were later developed by Perez [128, 129]. He developed a defect diffusion model and was also able to describe volume recovery of glassy PVAc.

New impulse to the model [21, 26, 109, 169, 171] was provided by the finding of accelerated physical aging in numerous polymer glasses with typical confinement length scale of the order of microns or shorter [10–12, 14, 15, 22, 108, 113, 132, 150]. The basic equations of the model are: (i) the second equation of Fick:

$$\frac{\partial f_v(\mathbf{r}, t)}{\partial t} = \nabla(D\nabla f_v(\mathbf{r}, t)) \tag{12.1}$$

In Eq. 12.1, f_v is the fractional free volume and D is the diffusion coefficient of free volume holes; and (ii) and the equation relating the mean square displacement (MSD) ($\langle x^2 \rangle$) to the time. This, for one-dimensional linear diffusion[3] reads:

$$\langle x^2 \rangle = 2Dt \tag{12.2}$$

Equation 12.1 can be employed to fit the evolution of thermodynamic (or related to) magnitudes related to the free volume holes fraction during physical aging. In the relatively small range of variation typical of equilibrium recovery experiments, proportionality between the change of free volume and that of other properties such as the enthalpy or the volume has been established [66]. The description of the T_g depression can be performed employing Eq. (12.2). According to the FVHD model, the system looses equilibrium, and therefore undergoes the glass transition, once $\langle x^2 \rangle$ in the observation time $t \sim q^{-1}$, where q is the applied cooling rate, is equal to the square of half the confinement length scale: $(h/2)^2 = \langle x^2 \rangle = 2Dq^{-1}$. An important aspect of the model is that it is possible to have negative T_g deviations and acceleration of equilibrium recovery without significant alteration of the equilibrium dynamics, that is the free volume diffusion coefficient D. If one assumes confinement length scale independent D, from Eq. 12.2, for a given observation time, shorter confinement length scales imply smaller D. Considering that D decreases with decreasing temperature, decreasing the confinement length scale naturally results in smaller T_g(s). In all cases where the FVHD model was applied, confinement length scale independent D was assumed. This is a reasonable assumption given the presence of predominant bulk-like equilibrium dynamics, even in the most extreme case of nanostructuring [125, 175], in confined glasses exhibiting enhanced out-of-equilibrium dynamics. Obviously, the model can be refined accounting for the presence of other relaxational components in the confined polymer, for instance fast dynamics in proximity of a free interface [43].

A concern in the application of the model originates from the fact that, above a confinement length scale of the order of microns, the out-of-equilibrium dynamics exhibit no dependence on such length scale. Hence, on increasing the confinement

---

[3]The assumption of one-dimensional confinement is obviously true is thin films. For polymer nanocompsites and nanospheres it is approximately valid if the radius of curvature of nanoparticles and nanospheres, respectively, is considerably larger than the size of free volume holes.

length scale, the "bulk" mechanism of equilibration, whatever its description, gradually replaces that based on free volume holes diffusion. This can be either approached employing the FVHD model, assuming the presence of an internal length scale, as in the original work of Simha and co-workers [34]; or employing the most general framework for equilibrium recovery in bulk [11].

Another crucial point for the application of the FVHD model is the definition of the confinement length scale h. This depends on the amount of free interface available for volume holes diffusion. In the case of freestanding films, since *all* the interface is free, the confinement length scale is trivially the thickness of the films. In Figs. 12.5 and 12.6 (lines), it can be seen how, when applied to the description of the T_g and enthalpy recovery of freestanding thin PS films, the FVHD provides accurate fit of data [11]. Other examples of application of the FVHD model concern freestanding polymer membranes [109, 170].

Concerning supported and capped confined systems, in order to define the relevant confinement length scale, the free interface must be considered. In particular, only such interface would be available to interchange of free volume holes with the external world. Conversely, the portion of interface with adsorbed polymer chains represents an infinitely high energetic barrier for diffusion and, therefore, must be disregarded. This agrees, at least qualitatively, with the dependence of T_g deviations with the amount of free interface [117]. According to these arguments, for partially adsorbed polymers, it is possible to define the confinement length scale as: $h_{eff} = V/A_{free}$, where A_{free} is the amount of free interface. In other words, h_{eff} is the thickness of the freestanding films exhibiting the same T_g depression as the capped or supported confined system under consideration. Having clarified what the confinement length scale is for supported and capped systems, the FVHD model can be applied to sets of data where the preparation conditions are identical and, therefore, also the fraction of free interface. For instance this applies to supported films [13] and polymer nanocomposites [14, 15, 21, 22]. For these systems, successful fits of the FVHD model were pursued, as shown by the continuous lines in Fig. 12.4, on T_g data at different cooling rates for thin PS films supported on platinum coated silicon nitride [13, 48]. Furthermore, the amount of free interface in capped films can be deduced from T_g depression data within the FVHD model. This was done for data on Al-capped thin PS films for which the amount of free interface and the T_g depression were determined experimentally (see Fig. 12.9) [117]. The comparison between the experimentally determined amount of free interface and that determined within the FVHD model shows that the two magnitudes are directly related [114]. This constitutes a further proof of the suitability of the FVHD to describe the out-of-equilibrium dynamics of variously confined glasses.

Finally, further indications of the compatibility of the FVHD model with experimental data on out-of-equilibrium dynamics of confined glasses come from results on the depth profile evolution of a given magnitude during the physical aging of thin polymer films. This was done by Priestley et al. [137], monitoring the aging rate via fluorescent probes located in different positions in the film; and by Rowe et al. [152], following the evolution with aging time of the free volume by means variable energy positron annihilation lifetime spectroscopy (PALS). In both

cases in line with the prediction of the FVHD model (in particular Eq. 12.1), a parabolic profile in the space of the magnitude under consideration, indicating faster densification closer to the free interface, was found.

12.8   Conclusions and Perspectives

In this chapter, we have reviewed experimental activity pursued over the last two decades aiming to clarify glassy dynamics in confinement. Special attention has been dedicated to the effect of reducing the typical length scale of confinement on the out-of-equilibrium dynamics, that is, the T_g and the equilibrium recovery in the physical aging regime. In doing so, it is shown how the out-of-equilibrium dynamics can exhibit both acceleration or slowing down depending on the confinement geometry. The latter, in terms of T_g increase and deceleration of approach towards equilibrium, is straightforwardly explained in terms of decreased rate of spontaneous fluctuations. However, importantly, T_g decrease and acceleration of equilibrium recovery *cannot* be described according to arguments *exclusively* based on a change in the equilibrium dynamics of the confined glass formers. This marks a crucial difference with bulk glass formers where a change of the out-of-equilibrium dynamics is directly connected to an analogous change of the rate of spontaneous fluctuations.

   In recognizing that arguments based on the rate of spontaneous fluctuations fail to describe the out-of-equilibrium dynamics and in view of recent activity on the influence of adsorption on the glassy dynamics in confinement, we identify the free interfacial surface as the main parameter determining the magnitude of negative deviations from bulk behaviour. In doing so, we emphasize how a suitable model for the description of the out-of-equilibrium dynamics in confinement must account for the presence of dominant bulk linear dynamics and the amount of free interface. We show how there exists solid indications that the FVHD model nicely fits in the idea that the free interface is the key parameter to describe the out-of-equilibrium dynamics in confinement.

   The main aspect highlighted in this chapter, that is, the ability of certain confined polymer glasses to maintain equilibrium, opens important lines of research in an attempt of understanding glassy dynamics in general. This is due to the fact that polymer glasses confined under certain conditions are able to explore the energy landscape down to considerable low values. This without significant modifications of the rate of spontaneous fluctuations, which remains mainly bulk. Furthermore, recent theoretical activity has shown that neither the thermodynamics is significantly affected in freestanding thin PS films with thickness as low as 30 nm [182]. The main consequence of these observations is that it is possible to investigate the dynamics and thermodynamics of polymer glasses down in the landscape. This allows achieving information on the alleged divergence of the relaxation time and the vanishing of the configurational entropy at a finite temperature, that is, the Vogel and the Kauzmann temperatures respectively. Furthermore, insight on the

presence of multiple relaxations at temperature well below the nominal bulk T_g, recently shown in bulk polymers subjected to aging times as long as one year or more [20], can be obtained with observation times not longer than several days. A recent study on freestanding PS films by means of ellipsometry actually shows the presence of two discontinuities in the linear coefficient of thermal expansion at cooling rates of the order of some kelvin per minute [141]. These findings opens new perspective in the understanding of fundamental properties of glasses down in the energy landscape and should provide new impetus for further investigations.

References

1. Adam, G., Gibbs, J.H.: On temperature dependence of cooperative relaxation properties in glass-forming liquids. J. Chem. Phys. **43**(1), 139–146 (1965)
2. Alfrey, T., Goldfinger, G., Mark, H.: The apparent second-order transition point of polystyrene. J. Appl. Phys. **14**(12), 700–705 (1943)
3. Amanuel, S., Gaudette, A.N., Sternstein, S.S.: Enthalpic relaxation of silicapolyvinyl acetate nanocomposites. J. Polym. Sci. Pol. Phys. **46**(24), 2733–2740 (2008)
4. Baeumchen, O., McGraw, J.D., Forrest, J.A., Dalnoki-Veress, K.: Reduced glass transition temperatures in thin polymer films: surface effect or artifact? Phys. Rev. Lett. **109**(5), 055–701 (2012)
5. Bahar, I., Erman, B., Kremer, F., Fischer, E.: Segmental motions of cis-polyisoprene in the bulk state—interpretation of dielectric-relaxation data. Macromolecules **25**(2), 816–825 (1992)
6. Baker, E.A., Rittigstein, P., Torkelson, J.M., Roth, C.B.: Streamlined ellipsometry procedure for characterizing physical aging rates of thin polymer films. J. Polym. Sci. Pt. B-Polym. Phys. **47**(24SI), 2509–2519 (2009)
7. Bansal, A., Yang, H., Li, C., Cho, K., Benicewicz, B., Kumar, S., Schadler, L.: Quantitative equivalence between polymer nanocomposites and thin polymer films. Nat. Mater. **4**(9), 693–698 (2005)
8. Berthier, L., Biroli, G., Bouchaud, J.P., Cipelletti, L., Masri, D.E., L'Hôte, D., Ladieu, F., Pierno, M.: Direct experimental evidence of a growing length scale accompanying the glass transition. Science **310**(5755), 1797–1800 (2005)
9. Bogoslovov, R.B., Roland, C.M., Ellis, A.R., Randall, A.M., Robertson, C.G.: Effect of silica nanoparticles on the local segmental dynamics in poly(vinyl acetate). Macromolecules **41**(4), 1289–1296 (2008)
10. Boucher, V.M., Cangialosi, D., Alegría, A., Colmenero, J.: Enthalpy recovery of pmma/silica nanocomposites. Macromolecules **43**(18), 7594–7603 (2010)
11. Boucher, V.M., Cangialosi, D., Alegría, A., Colmenero, J.: Enthalpy recovery in nanometer to micrometer thick ps films. Macromolecules **45**(12), 5296–5306 (2012)
12. Boucher, V.M., Cangialosi, D., Alegría, A., Colmenero, J.: Time dependence of the segmental relaxation time of poly(vinyl acetate)-silica nanocomposites. Phys. Rev. E **86**(4 Part 1), 041501 (2012)
13. Boucher, V.M., Cangialosi, D., Alegria, A., Colmenero, J.: Accounting for the thickness dependence of the {T}g in supported {PS} films via the volume holes diffusion model. Thermochim. Acta **575**, 233–237 (2014)

14. Boucher, V.M., Cangialosi, D., Alegría, A., Colmenero, J., Gonzalez-Irun, J., Liz-Marzan, L. M.: Accelerated physical aging in pmma/silica nanocomposites. Soft Matter **6**(14), 3306–3317 (2010)

15. Boucher, V.M., Cangialosi, D., Alegría, A., Colmenero, J., Pastoriza-Santos, I., Liz-Marzan, L.M.: Physical aging of polystyrene/gold nanocomposites and its relation to the calorimetric t (g) depression. Soft Matter **7**(7), 3607–3620 (2011)

16. Boucher, V.M., Cangialosi, D., Yin, H., Schoenhals, A., Alegría, A., Colmenero, J.: T-g depression and invariant segmental dynamics in polystyrene thin films. Soft Matter **8**(19), 5119–5122 (2012)

17. Callen, H., Greene, R.: On a theorem of irreversible thermodynamics. Phys. Rev. **86**(5), 702–710 (1952)

18. Cangialosi, D., Alegría, A., Colmenero, J.: Route to calculate the length scale for the glass transition in polymers. Phys. Rev. E **76**(11), 011, 514 (2007)

19. Cangialosi, D., Alegría, A., Colmenero, J.: "self-concentration" effects on the dynamics of a polychlorinated biphenyl diluted in 1,4-polybutadiene. J. Chem. Phys. **126**(20), 204904 (2007)

20. Cangialosi, D., Boucher, V., Alegría, A., Colmenero, J.: Direct evidence of two equilibration mechanisms in glassy polymers. Phys. Rev. Lett. **111**, 095701 (2013)

21. Cangialosi, D., Boucher, V.M., Alegría, A., Colmenero, J.: Free volume holes diffusion to describe physical aging in poly(mehtyl methacrylate)/silica nanocomposites. J. Chem. Phys. **135**(1), 014901 (2011)

22. Cangialosi, D., Boucher, V.M., Alegría, A., Colmenero, J.: Enhanced physical aging of polymer nanocomposites: The key role of the area to volume ratio. Polymer **53**(6), 1362–1372 (2012)

23. Cangialosi, D., Boucher, V.M., Alegría, A., Colmenero, J.: Physical aging in polymers and polymer nanocomposites: recent results and open questions. Soft Matter **9**(36), 8619–8630 (2013)

24. Cangialosi, D., Schwartz, G., Alegria, A., Colmenero, J.: Combining configurational entropy and self-concentration to describe the component dynamics in miscible polymer blends. J. Chem. Phys. **123**(14), 144908 (2005)

25. Cangialosi, D., Wubbenhorst, M., Groenewold, J., Mendes, E., Picken, S.: Diffusion mechanism for physical aging of polycarbonate far below the glass transition temperature studied by means of dielectric spectroscopy. J. Non-Cryst. Solids **351**(33–36), 2605–2610 (2005)

26. Cangialosi, D., Wübbenhorst, M., Groenewold, J., Mendes, E., Schut, H., van Veen, A., Picken, S.J.: Physical aging of polycarbonate far below the glass transition temperature: evidence for the diffusion mechanism. Phys. Rev. B **70**, 224213 (2004)

27. Chai, Y., Salez, T., McGraw, J.D., Benzaquen, M., Raphal, E., Forrest, J.A., Dalnoki-Veress, K.: A direct quantitative measure of surface mobility in a glassy polymer. Science **343**(6174), 994–999 (2014)

28. Chandran, S., Basu, J.: Effect of nanoparticle dispersion on glass transition in thin films of polymer nanocomposites. Eur. Phys. J. E **34**(9), 99 (2011)

29. Chandran, S., Basu, J.K., Mukhopadhyay, M.K.: Variation in glass transition temperature of polymer nanocomposite films driven by morphological transitions. J. Chem. Phys. **138**(1), 014902 (2013)

30. Chen, J., Li, L., Zhou, D., Xu, J., Xue, G.: Effect of molecular chain architecture on dynamics of polymer thin films measured by the ac-chip calorimeter. Macromolecules **47**(10), 3497–3501 (2014)

31. Cho, W.K., Kong, B., Choi, I.S.: Highly efficient non-biofouling coating of zwitterionic polymers: Poly((3-(methacryloylamino)propyl)-dimethyl(3-sulfopropyl)ammonium hydroxide). Langmuir **23**(10), 5678–5682 (2007)

32. Chowdhury, M., Freyberg, P., Ziebert, F., Yang, A.C.M., Steiner, U., Reiter, G.: Segmental Relaxations have macroscopic consequences in glassy polymer films. Phys. Rev. Lett. **109** (13), 136102 (2012)

33. Clough, A., Peng, D., Yang, Z., Tsui, O.K.C.: Glass transition temperature of polymer films that slip. Macromolecules **44**(6), 1649–1653 (2011)
34. Curro, J.G., Lagasse, R.R., Simha, R.: Diffusion model for volume recovery in glasses. Macromolecules **15**(6), 1621–1626 (1982)
35. D'Amore, A., Caprino, G., Nicolais, L., Marino, G.: Long-term behaviour of pei and pei-based composites subjected to physical aging. Compos. Sci. Technol. **59**(13), 1993–2003 (1999)
36. Debenedetti, P.G.: Metastable Liquids: Concepts and Principles. Princeton University Press, Princeton (1996)
37. DeMaggio, G.B., Frieze, W.E., Gidley, D.W., Zhu, M., Hristov, H.A., Yee, A.F.: Interface and surface effects on the glass transition in thin polystyrene films. Phys. Rev. Lett. **78**, 1524–1527 (1997)
38. Ding, J., Xue, G., Dai, Q., Cheng, R.: Glass-transition temperature of polystyrene microparticles. Polymer **34**(15), 3325–3327 (1993)
39. Donati, C., Douglas, J., Kob, W., Plimpton, S., Poole, P., Glotzer, S.: Stringlike cooperative motion in a supercooled liquid. Phys. Rev. Lett. **80**(11), 2338–2341 (1998)
40. Donth, E.: The size of cooperatively rearranging regions at the glass-transition. J. Non. Cryst. Sol. **53**(3), 325–330 (1982)
41. Donth, E., Korus, J., Hempel, E., Beiner, M.: Comparison of dsc heating rate and hcs frequency at the glass transition. Thermochim. Acta **305**(6), 239–249 (1997)
42. Dorkenoo, K.D., Pfromm, P.H.: Experimental evidence and theoretical analysis of physical aging in thin and thick amorphous glassy polymer films. J. Polym. Sci. Pt. B-Polym. Phys. **37**(16), 2239–2251 (1999)
43. Ediger, M.D., Forrest, J.A.: Dynamics near free surfaces and the glass transition in thin polymer films: a view to the future. Macromolecules **47**(2), 471–478 (2014)
44. Efremov, M., Olson, E., Zhang, M., Zhang, Z., Allen, L.: Glass transition in ultrathin polymer films: calorimetric study. Phys. Rev. Lett. **91**(8), 085703 (2003)
45. Efremov, M.Y., Olson, E.A., Zhang, M., Zhang, Z.S., Allen, L.H.: Probing glass transition of ultrathin polymer films at a time scale of seconds using fast differential scanning calorimetry. Macromolecules **37**(12), 4607–4616 (2004)
46. Ellison, C.J., Torkelson, J.M.: The distribution of glass-transition temperatures in nanoscopically confined glass formers. Nat. Mater. **2**(10), 695–700 (2003)
47. Evans, C.M., Torkelson, J.M.: Dramatic tunability of polystyrene tg via neighboring domains: Equivalence of multilayer films and binary blends. Abs. Pap. Am. Chem. Soc. **244**, 469 (2012)
48. Fakhraai, Z., Forrest, J.A.: Probing slow dynamics in supported thin polymer films. Phys. Rev. Lett. **95**(2), 025701 (2005)
49. Fakhraai, Z., Forrest, J.A.: Measuring the surface dynamics of glassy polymers. Science **319**(5863), 600–604 (2008)
50. Feng, S., Chen, Y., Mai, B., Wei, W., Zheng, C., Wu, Q., Liang, G., Gao, H., Zhu, F.: Glass transition of poly(methyl methacrylate) nanospheres in aqueous dispersion. Phys. Chem. Chem. Phys. **16**, 15941–15947 (2014)
51. Feng, S., Li, Z., Liu, R., Mai, B., Wu, Q., Liang, G., Gao, H., Zhu, F.: Glass transition of polystyrene nanospheres under different confined environments in aqueous dispersions. Soft Matter **9**(18), 4614–4620 (2013)
52. Fleer, G.J., Stuart, M.A.C., Scheutjens, J.M.H.M., Cosgrove, T., Vincent, B. (eds.): Polymers at Interfaces. Chapman and Hall, London (1993)
53. Flory, A.L., Ramanathan, T., Brinson, L.C.: Physical aging of single wall carbon nanotube polymer nanocomposites: effect of functionalization of the nanotube on the enthalpy relaxation. Macromolecules **43**(9), 4247–4252 (2010)
54. Forrest, J., DalnokiVeress, K., Dutcher, J.: Interface and chain confinement effects on the glass transition temperature of thin polymer films. Phys. Rev. E **56**(5B), 5705–5716 (1997)
55. Forrest, J.A., Dalnoki-Veress, K.: The glass transition in thin polymer films. Adv. Colloid Interface Sci. **94**(1-3SI), 167–196 (2001)

56. Forrest, J.A., Dalnoki-Veress, K.: When does a glass transition temperature not signify a glass transition? ACS Macro Lett. **3**(4), 310–314 (2014)

57. Forrest, J.A., Dalnoki-Veress, K., Stevens, J.R., Dutcher, J.R.: Effect of free surfaces on the glass transition temperature of thin polymer films. Phys. Rev. Lett. **77**(10), 2002–2005 (1996)

58. Frieberg, B., Glynos, E., Sakellariou, G., Green, P.F.: Physical aging of star-shaped macromolecules. ACS Macro Lett. **1**(5), 636–640 (2012)

59. Fryer, D., Peters, R., Kim, E., Tomaszewski, J., de Pablo, J., Nealey, P., White, C., Wu, W.: Dependence of the glass transition temperature of polymer films on interfacial energy and thickness. Macromolecules **34**(16), 5627–5634 (2001)

60. Fukao, K., Miyamoto, Y.: Glass transitions and dynamics in thin polymer films: dielectric relaxation of thin films of polystyrene. Phys. Rev. E **61**(2), 1743–1754 (2000)

61. Fukao, K., Tahara, D.: Aging dynamics in the polymer glass of poly(2-chlorostyrene): dielectric susceptibility and volume. Phys. Rev. E **80**(5), 051802 (2009)

62. Fulcher, G.S.: Analysis of recent measurements of the viscosity of glasses. J. Am. Ceram. Soc. **8**(6), 339–355 (1925)

63. Gao, S., Koh, Y.P., Simon, S.L.: Calorimetric glass transition of single polystyrene ultrathin films. Macromolecules **46**(2), 562–570 (2013)

64. Gaur, U., Wunderlich, B.: Study of microphase separation in block co-polymers of styrene and alpha-methylstyrene in the glass-transition region using quantitative thermal-analysis. Macromolecules **13**(6), 1618–1625 (1980)

65. Ge, S., Pu, Y., Zhang, W., Rafailovich, M., Sokolov, J., Buenviaje, C., Buckmaster, R., Overney, R.: Shear modulation force microscopy study of near surface glass transition temperatures. Phys. Rev. Lett. **85**(11), 2340–2343 (2000)

66. Gitsas, A., Floudas, G., White, R.P., Lipson, J.E.G.: Effect of pressure on the phase behavior and segmental dynamics in blends of polystyrene with poly(methylphenyl siloxane). Macromolecules **42**(15), 5709–5716 (2009)

67. Glor, E.C., Fakhraai, Z.: Facilitation of interfacial dynamics in entangled polymer films. J. Chem. Phys. **141**(19), 194505 (2014)

68. Glynos, E., Frieberg, B., Oh, H., Liu, M., Gidley, D.W., Green, P.F.: Role of molecular architecture on the vitrification of polymer thin films. Phys. Rev. Lett. **106**(12), 128301 (2011)

69. Grady, B.P., Paul, A., Peters, J.E., Ford, W.T.: Glass transition behavior of single-walled carbon nanotube-polystyrene composites. Macromolecules **42**(16), 6152–6158 (2009)

70. Grohens, Y., Brogly, M., Labbe, C., David, M.O., Schultz, J.: Glass transition of stereoregular poly(methyl methacrylate) at interfaces. Langmuir **14**(11), 2929–2932 (1998)

71. Guiselin, O.: Irreversible adsorption of a concentrated polymer solution. EPL (Europhysics Letters) **17**(3), 225 (1992)

72. Guo, Y., Zhang, C., Lai, C., Priestley, R.D., D'Acunzi, M., Fytas, G.: Structural relaxation of polymer nanospheres under soft and hard confinement: isobaric versus isochoric conditions. ACS Nano **5**(7), 5365–5373 (2011)

73. Hartmann, L., Gorbatschow, W., Hauwede, J., Kremer, F.: Molecular dynamics in thin films of isotactic poly(methyl methacrylate). Eur. Phys. J. E **8**(2), 145–154 (2002)

74. Hecksher, T., Olsen, N.B., Niss, K., Dyre, J.C.: Physical aging of molecular glasses studied by a device allowing for rapid thermal equilibration. J. Chem. Phys. **133**(17), 174514 (2010)

75. Hempel, E., Hempel, G., Hensel, A., Schick, C., Donth, E.: Characteristic length of dynamic glass transition near t-g for a wide assortment of glass-forming substances. J. Phys. Chem. B **104**(11), 2460–2466 (2000)

76. Huang, Y., Paul, D.R.: Physical aging of thin glassy polymer films monitored by gas permeability. Polymer **45**(25), 8377–8393 (2004)

77. Huth, H., Minakov, A.A., Schick, C.: Differential ac-chip calorimeter for glass transition measurements in ultrathin films. J. Polym. Sci. Pt. B-Polym. Phys. **44**(20), 2996–3005 (2006)

78. Inoue, R., Kanaya, T., Nishida, K., Tsukushi, I., Telling, M.T.F., Gabrys, B.J., Tyagi, M., Soles, C., Wu, W.I.: Glass transition and molecular mobility in polymer thin films. Phys. Rev. E **80**(3), 031802 (2009)
79. Kawana, S., Jones, R.A.L.: Character of the glass transition in thin supported polymer films. Phys. Rev. E **63**, 021501 (2001)
80. Kawana, S., Jones, R.A.L.: Effect of physical ageing in thin glassy polymer films. Eur. Phys. J. E **10**(3), 223–230 (2003)
81. Keddie, J.L., Jones, R.A.L., Cory, R.A.: Interface and surface effects on the glass-transition temperature in thin polymer films. Faraday Discuss. **98**, 219–230 (1994)
82. Keddie, J.L., Jones, R.A.L., Cory, R.A.: Size-dependent depression of the glass-transition temperature in polymer-films. Europhys. Lett. **27**(1), 59–64 (1994)
83. Kim, J.H., Jang, J., Zin, W.C.: Estimation of the thickness dependence of the glass transition temperature in various thin polymer films. Langmuir **16**(9), 4064–4067 (2000)
84. Koh, Y.P., McKenna, G.B., Simon, S.L.: Calorimetric glass transition temperature and absolute heat capacity of polystyrene ultrathin films. J. Polym. Sci. Pt. B-Polym. Phys. **44**(24), 3518–3527 (2006)
85. Koh, Y.P., Simon, S.L.: Structural relaxation of stacked ultrathin polystyrene films. J. Polym. Sci. Pt. B-Polym. Phys. **46**(24), 2741–2753 (2008)
86. Kovacs, A., Braun, G.: Glass transition in powdered polystyrene. Phys. Chem. Glas. **4**(4), 152–160 (1963)
87. Kovacs, A.J.: Glass transition in amorphous polymers: a phenomenological study. Fortsch. Hochpolym. Fo. **3**(1/2), 394–508 (1963)
88. Kremer, F., Schonhals, A. (eds.): Broadband Dielectric Spectroscopy. Springer, Berlin (2003)
89. Kremer, F., Tress, M., Mapesa, E.U.: Glassy dynamics and glass transition in nanometric layers and films: a silver lining on the horizon. J. Non-Cryst. Solids **407**, 277–283 (2015)
90. Kyriakos, K., Raftopoulos, K.N., Pissis, P., Kyritsis, A., Naether, F., Haeussler, L., Fischer, D., Vyalikh, A., Scheler, U., Reuter, U., Pospiech, D.: Dielectric and thermal studies of the segmental dynamics of poly(methyl methacrylate)/silica nanocomposites prepared by the solgel method. J. Appl. Pol. Sci. **128**(6), 3771–3781 (2013)
91. Labahn, D., Mix, R., Schoenhals, A.: Dielectric relaxation of ultrathin films of supported polysulfone. Phys. Rev. E **79**(1 Part 1), 011801 (2009)
92. Lee, A., Lichtenhan, J.D.: Viscoelastic responses of polyhedral oligosilsesquioxane reinforced epoxy systems. Macromolecules **31**(15), 4970–4974 (1998)
93. Lin, Y., Liu, L., Cheng, J., Shangguan, Y., Yu, W., Qiu, B., Zheng, Q.: Segmental dynamics and physical aging of polystyrene/silver nanocomposites. RSC Adv. **4**, 20086–20093 (2014)
94. Lipson, J.E.G., Milner, S.T.: Percolation model of interfacial effects in polymeric glasses. Eur. Phys. J. B **72**(1), 133–137 (2009)
95. Liu, Y., Russell, T., Samant, M., Stohr, J., Brown, H., Cossy-Favre, A., Diaz, J.: Surface relaxations in polymers. Macromolecules **30**(25), 7768–7771 (1997)
96. Lizundia, E., Oleaga, A., Salazar, A., Sarsua, J.R.: Nano- and microstructural effects on thermal properties of poly (l-lactide)/multi-wall carbon nanotube composites. Polymer **53**(12), 2412–2421 (2012)
97. Lodge, T., McLeish, T.: Self-concentrations and effective glass transition temperatures in polymer blends. Macromolecules **33**(14), 5278–5284 (2000)
98. Long, D., Lequeux, F.: Heterogeneous dynamics at the glass transition in van der waals liquids, in the bulk and in thin films. Eur. Phys. J. E **4**(3), 371–387 (2001)
99. Lu, H., Nutt, S.: Restricted relaxation in polymer nanocomposites near the glass transition. Macromolecules **36**(11), 4010–4016 (2003)
100. Lu, H.B., Nutt, S.: Enthalpy relaxation of layered silicate-epoxy nanocomposites. Macromol. Chem. Phys. **204**(15), 1832–1841 (2003)
101. Lubchenko, V., Wolynes, P.G.: Theory of structural glasses and supercooled liquids. Annu. Rev. Phys. Chem. **58**, 235–266 (2007)

102. Lupascu, V., Huth, H., Schick, C., Wubbenhorst, M.: Specific heat and dielectric relaxations in ultra-thin polystyrene layers. Thermochim. Acta **432**(2), 222–228 (2005)

103. Lupascu, V., Picken, S.J., Wubbenhorst, M.: Cooperative and non-cooperative dynamics in ultra-thin films of polystyrene studied by dielectric spectroscopy and capacitive dilatometry. J. Non-Cryst. Solids **352**(52–54), 5594–5600 (2006)

104. Mapesa, E.U., Tress, M., Schulz, G., Huth, H., Schick, C., Reiche, M., Kremer, F.: Segmental and chain dynamics in nanometric layers of poly(cis-1,4-isoprene) as studied by broadband dielectric spectroscopy and temperature-modulated calorimetry. Soft Matter **9**(44), 10592–10598 (2013)

105. Martinez-Tong, D.E., Soccio, M., Sanz, A., Garcia, C., Ezquerra, T.A., Nogales, A.: Chain arrangement and glass transition temperature variations in polymer nanoparticles under 3d-confinement. Macromolecules **46**(11), 4698–4705 (2013)

106. Martnez-Tong, D.E., Cui, J., Soccio, M., Garca, C., Ezquerra, T.A., Nogales, A.: Does the glass transition of polymers change upon 3d confinement? Macromol. Chem. Phys. **215**(17), 1620–1624 (2014)

107. Martí-nez-Tong, D.E., Vanroy, B., Wübbenhorst, M., Nogales, A., Napolitano, S.: Crystallization of poly(l-lactide) confined in ultrathin films: competition between finite size effects and irreversible chain adsorption. Macromolecules **47**(7), 2354–2360 (2014)

108. McCaig, M.S., Paul, D.R.: Effect of film thickness on the changes in gas permeability of a glassy polyarylate due to physical aging part i. experimental observations. Polymer **41**(2), 629–637 (2000)

109. McCaig, M.S., Paul, D.R., Barlow, J.W.: Effect of film thickness on the changes in gas permeability of a glassy polyarylate due to physical aging part i. experimental observations. Polymer **41**(2), 639–648 (2000)

110. Mirigian, S., Schweizer, K.S.: Communication: slow relaxation, spatial mobility gradients, and vitrification in confined films. The Journal of Chemical Physics **141**(16), 161103 (2014)

111. Miyazaki, T., Inoue, R., Nishida, K., Kanaya, T.: X-ray reflectivity studies on glass transition of free standing polystyrene thin films. Eur. Phys. J. Spec. Top. **141**, 203–206 (2007)

112. Miyazaki, T., Nishida, K., Kanaya, T.: Contraction and reexpansion of polymer thin films. Phys. Rev. E **69**, 022801 (2004)

113. Murphy, T.M., Langhe, D.S., Ponting, M., Baer, E., Freeman, B.D., Paul, D.R.: Physical aging of layered glassy polymer films via gas permeability tracking. Polymer **52**(26), 6117–6125 (2011)

114. Napolitano, S., Cangialosi, D.: Macromolecules **46**(19), 8051–8053 (2013)

115. Napolitano, S., Capponi, S., Vanroy, B.: Glassy dynamics of soft matter under 1d confinement: How irreversible adsorption affects molecular packing, mobility gradients and orientational polarization in thin films. Eur. Phys. J. E **36**(6), 61 (2013)

116. Napolitano, S., Prevosto, D., Lucchesi, M., Pingue, P., D'Acunto, M., Rolla, P.: Influence of a reduced mobility layer on the structural relaxation dynamics of aluminum capped ultrathin films of poly(ethylene terephthalate). Langmuir **23**(4), 2103–2109 (2007)

117. Napolitano, S., Rotella, C., Wübbenhorst, M.: Can thickness and interfacial interactions univocally determine the behavior of polymers confined at the nanoscale? ACS Macro Lett **1**(10), 1189–1193 (2012)

118. Napolitano, S., Rotella, C., Wuebbenhorst, M.: Is the reduction in tracer diffusivity under nanoscopic confinement related to a frustrated segmental mobility? Macromol. Rapid Commun. **32**(11), 844–848 (2011)

119. Napolitano, S., Wübbenhorst, M.: The lifetime of the deviations from bulk behaviour in polymers confined at the nanoscale. Nat. Commun. **2**, 260 (2011)

120. Napolitano, S., Wuebbenhorst, M.: Structural relaxation and dynamic fragility of freely standing polymer films. Polymer **51**(23), 5309–5312 (2010)

121. Noh, Y.Y., Zhao, N., Caironi, M., Sirringhaus, H.: Downscaling of self-aligned, all-printed polymer thin-film transistors. Nat. Nanotech. **2**(12), 784–789 (2007)

122. Nyquist, H.: Thermal agitation of electric charge in conductors. Phys. Rev. **32**(1), 110–113 (1928)

123. O'Connell, P., McKenna, G.: Rheological measurements of the thermoviscoelastic response of ultrathin polymer films. Science **307**(5716), 1760–1763 (2005)

124. Paeng, K., Richert, R., Ediger, M.D.: Molecular mobility in supported thin films of polystyrene, poly(methyl methacrylate), and poly(2-vinyl pyridine) probed by dye reorientation. Soft Matter **8**, 819–826 (2012)

125. Paeng, K., Swallen, S.F., Ediger, M.D.: Direct measurement of molecular motion in freestanding polystyrene thin films. J. Am. Chem. Soc. **133**(22), 8444–8447 (2011)

126. Park, C.H., Kim, J.H., Ree, M., Sohn, B.H., Jung, J.C., Zin, W.C.: Thickness and composition dependence of the glass transition temperature in thin random copolymer films. Polymer **45**(13), 4507–4513 (2004)

127. Paul, D.R., Robeson, L.M.: Polymer nanotechnology: nanocomposites. Polymer **49**(15), 3187–3204 (2008)

128. Perez, J.: Defect diffusion model for volume and enthalpy recovery in amorphous polymers. Polymer **29**(3), 483–489 (1988)

129. Perez, J.: Physics and mechanics of amorphous polymers. A.A. Balkema, Rotterdam (1998)

130. Perlich, J., Koerstgens, V., Metwalli, E., Schulz, L., Georgii, R., Mueller-Buschbaum, P.: Solvent content in thin spin-coated polystyrene homopolymer films. Macromolecules **42**(1), 337–344 (2009)

131. Pfromm, P.H., Koros, W.J.: Accelerated physical aging of thin glassy polymer-films—evidence from gas-transport measurements. Polymer **36**(12), 2379–2387 (1995)

132. Pfromm, P.H., Koros, W.J.: Accelerated physical aging of thin glassy polymer-films - evidence from gas-transport measurements. Polymer **36**(12), 2379–2387 (1995)

133. Priestley, R.D.: Physical aging of confined glasses. Soft Matter **5**(5), 919–926 (2009)

134. Priestley, R.D., Broadbelt, L.J., Torkelson, J.M.: Physical aging of ultrathin polymer films above and below the bulk glass transition temperature: effects of attractive vs neutral polymer-substrate interactions measured by fluorescence. Macromolecules **38**(3), 654–657 (2005)

135. Priestley, R.D., Broadbelt, L.J., Torkelson, J.M., Fukao, K.: Glass transition and alpha-relaxation dynamics of thin films of labeled polystyrene. Phys. Rev. E **75**(6, 1), 061806 (2007)

136. Priestley, R.D., Cangialosi, D., Napolitano, S.: On the equivalence between the thermodynamic and dynamic measurements of the glass transition in confined polymers. J. Non-Cryst. Solids **407**, 288–295 (2015)

137. Priestley, R.D., Ellison, C.J., Broadbelt, L.J., Torkelson, J.M.: Structural relaxation of polymer glasses at surfaces, interfaces and in between. Science **309**(5733), 456–459 (2005)

138. Priestley, R.D., Rittigstein, P., Broadbelt, L.J., Fukao, K., Torkelson, J.M.: Evidence for the molecular-scale origin of the suppression of physical ageing in confined polymer: fluorescence and dielectric spectroscopy studies of polymer-silica nanocomposites. J. Phys. Condens. Matt. **19**(20), 2996–3005 (2007)

139. Pryamitsyn, V., Ganesan, V.: A comparison of the dynamical relaxations in a model for glass transition in polymer nanocomposites and polymer thin films. Macromolecules **43**(13), 5851–5862 (2010)

140. Pye, J.E., Rohald, K.A., Baker, E.A., Roth, C.B.: Physical aging in ultrathin polystyrene films: evidence of a gradient in dynamics at the free surface and its connection to the glass transition temperature reductions. Macromolecules **43**(19), 8296–8303 (2010)

141. Pye, J.E., Roth, C.B.: Two simultaneous mechanisms causing glass transition temperature reductions in high molecular weight freestanding polymer films as measured by transmission ellipsometry. Phys. Rev. Lett. **107**(23), 235701 (2011)

142. Pye, J.E., Roth, C.B.: Physical aging of polymer films quenched and measured free-standing via ellipsometry: controlling stress imparted by thermal expansion mismatch between film and support. Macromolecules **46**(23), 9455–9463 (2013)

143. Rauscher, P.M., Pye, J.E., Baglay, R.R., Roth, C.B.: Effect of adjacent rubbery layers on the physical aging of glassy polymers. Macromolecules **46**(24), 9896–9817 (2013)

144. Reiter, G., Napolitano, S.: Possible origin of thickness-dependent deviations from bulk properties of thin polymer films. J. Polym. Sci. Part B Polym. Phys. **48**(24), 2544–2547 (2010)

145. Rittigstein, P., Priestley, R.D., Broadbelt, L.J., Torkelson, J.M.: Model polymer nanocomposites provide an understanding of confinement effects in real nanocomposites. Nat. Mater. **6**(4), 278–282 (2007)

146. Rittigstein, P., Torkelson, J.M.: Polymer-nanoparticle interfacial interactions in polymer nanocomposites: confinement effects on glass transition temperature and suppression of physical aging. J. Polym. Sci. Pol. Phys. **44**(20), 2935–2943 (2006)

147. Rotella, C., Wubbenhorst, M., Napolitano, S.: Probing interfacial mobility profiles via the impact of nanoscopic confinement on the strength of the dynamic glass transition. Soft Matter **7**(11), 5260–5266 (2011)

148. Roth, C., Dutcher, J.: Glass transition temperature of freely-standing films of atactic poly (methyl methacrylate). Eur. Phys. J. E **12**(1), S103–S107 (2003)

149. Roth, C.B., McNerny, K.L., Jager, W.F., Torkelson, J.M.: Eliminating the enhanced mobility at the free surface of polystyrene: fluorescence studies of the glass transition temperature in thin bilayer films of immiscible polymers. Macromolecules **40**(7), 2568–2574 (2007)

150. Rowe, B.W., Freeman, B.D., Paul, D.R.: Physical aging of ultrathin glassy polymer films tracked by gas permeability. Polymer **50**(23), 5565–5575 (2009)

151. Rowe, B.W., Freeman, B.D., Paul, D.R.: Influence of previous history on physical aging in thin glassy polymer films as gas separation membranes. Polymer **51**(16), 3784–3792 (2010)

152. Rowe, B.W., Pas, S.J., Hill, A.J., Suzuki, R., Freeman, B.D., Paul, D.R.: A variable energy positron annihilation lifetime spectroscopy study of physical aging in thin glassy polymer films. Polymer **50**(25), 6149–6156 (2009)

153. Schawe, J.E.K.: Vitrification in a wide cooling rate range: the relations between cooling rate, relaxation time, transition width, and fragility. J. Chem. Phys. **141**(18), 184905 (2014)

154. Schmelzer, J.W.P., Gutzow, I.S., Mazurin, O.V., Priven, A.I., Todorova, S.V., Petrov, B.P.: Glasses and the Glass Transition. Wiley-VCH Verlag GmbH and Co. KGaA, Weinheim (2011)

155. See, Y., Cha, J., Chang, T., Ree, M.: Glass transition temperature of poly(tert-butyl methacrylate) langmuir-blodgett film and spin-coated film by x-ray reflectivity and ellipsometry. Langmuir **16**(5), 2351–2355 (2000)

156. Serghei, A., Huth, H., Schick, C., Kremer, F.: Glassy dynamics in thin polymer layers having a free upper interface. Macromolecules **41**(10), 3636–3639 (2008)

157. Serghei, A., Kremer, F.: Metastable states of glassy dynamics, possibly mimicking confinement-effects in thin polymer films. Macromol. Chem. Phys. **209**(8), 810–817 (2008)

158. Sharp, J.S., Forrest, J.A.: Free surfaces cause reductions in the glass transition temperature of thin polystyrene films. Phys. Rev. Lett. **91**, 235701 (2003)

159. Simon, S.L., Park, J.Y., McKenna, G.B.: Enthalpy recovery of a glass-forming liquid constrained in a nanoporous matrix: negative pressure effects. Eur. Phys. J. E **8**, 209–216 (2002)

160. Singh, L., Ludovice, P.J., Henderson, C.L.: Influence of molecular weight and film thickness on the glass transition temperature and coefficient of thermal expansion of supported ultrathin polymer films. Thin Solid Films **449**(12), 231–241 (2004)

161. Soles, C., Douglas, J., Wu, W., Peng, H., Gidley, D.: Comparative specular x-ray reflectivity, positron annihilation lifetime spectroscopy, and incoherent neutron scattering measurements of the dynamics in thin polycarbonate films. Macromolecules **37**(8), 2890–2900 (2004)

162. Struik, L.C.E.: Physical aging in amorphous polymers and other materials. Technische Hogeschool Delft. (1977)

163. Struik, L.C.E.: Physical Aging in Amorphous Glassy Polymers and Other Materials, 1st edn. Elsevier Science, Amsterdam (1978)

164. Sulym, I., Klonos, P., Borysenko, M., Pissis, P., Gun'ko, V.M.: Dielectric and thermal studies of segmental dynamics in silica/pdms and silica/titania/pdms nanocomposites. J. Appl. Pol. Sci. **131**(23), 41154 (2014)

165. Svanberg, C.: Glass transition relaxations in thin suspended polymer films. Macromolecules **40**(2), 312–315 (2007)
166. Tammann, G., Hesse, W.: The dependancy of viscosity on temperature in hypothermic liquids. Z. Anorg. Allg. Chem. **156**, 245–257 (1926)
167. Tanaka, Y., Yamamoto, T.: Enthalpy relaxation of comb-like polymer analysed by combining activation energy spectrum and tnm models. J. Non-Cryst. Solids **358**(14), 1687–1698 (2012)
168. Thomas, K.R., Chenneviere, A., Reiter, G., Steiner, U.: Nonequilibrium behavior of thin polymer films. Phys. Rev. E **83**, 021804 (2011)
169. Thornton, A.W., Hill, A.J.: Vacancy diffusion with time-dependent length scale: An insightful new model for physical aging in polymers. Ind. Eng. Chem. Res. **49**(23), 12119–12124 (2010)
170. Thornton, A.W., Hill, A.J.: Vacancy diffusion with time-dependent length scale: An insightful new model for physical aging in polymers. Ind. Eng. Chem. Res. **49**(23), 12119–12124 (2010)
171. Thornton, A.W., Nairn, K.M., Hill, A.J., Hill, J.M., Huang, Y.: New relation between diffusion and free volume: Ii. predicting vacancy diffusion. J. Membr. Sci. **338**(1–2), 38–42 (2009)
172. Thurau, C.T., Ediger, M.D.: Change in the temperature dependence of segmental dynamics in deeply supercooled polycarbonate. J. Chem. Phys. **118**(4), 1996–2004 (2003)
173. Torres, J.A., Nealey, P.F., de Pablo, J.J.: Molecular simulation of ultrathin polymeric films near the glass transition. Phys. Rev. Lett. **85**(15), 3221–3224 (2000)
174. Tress, M., Erber, M., Mapesa, E.U., Huth, H., Mueller, J., Serghei, A., Schick, C., Eichhorn, K.J., Volt, B., Kremer, F.: Glassy dynamics and glass transition in nanometric thin layers of polystyrene. Macromolecules **43**(23), 9937–9944 (2010)
175. Tress, M., Mapesa, E.U., Kossack, W., Kipnusu, W.K., Reiche, M., Kremer, F.: Glassy dynamics in condensed isolated polymer chains. Science **341**(6152), 1371–1374 (2013)
176. Tsui, O., Russell, T., Hawker, C.: Effect of interfacial interactions on the glass transition of polymer thin films. Macromolecules **34**(16), 5535–5539 (2001)
177. Vignaud, G.S., Chebil, M., Bal, J.K., Delorme, N., Beuvier, T., Grohens, Y., Gibaud, A.: Densification and depression in glass transition temperature in polystyrene thin films. Langmuir **30**(39), 11599–11608 (2014)
178. Vogel, H.: The temperature dependence law of the viscosity of fluids. Phys. Z. **22**, 645–646 (1921)
179. Wallace, W., Vanzanten, J., Wu, W.: Influence of an impenetrable interface on a polymer glass-transition temperature. Phys. Rev. E **52**(4), 3329–3332 (1995)
180. Wang, L., Velikov, V., Angell, C.: Direct determination of kinetic fragility indices of glassforming liquids by differential scanning calorimetry: kinetic versus thermodynamic fragilities. J. Chem. Phys. **117**(22), 10184–11019 (2002)
181. Wang, X., Zhou, W.: Glass transition of microtome-sliced thin films. Macromolecules **35**(18), 6747–6750 (2002)
182. White, R.P., Lipson, J.E.G.: Thermodynamic treatment of polymer thin-film glasses. Phs. Rev. E **84**(4,1), 041801 (2011)
183. Wong, M., Tsuji, R., Nutt, S., Sue, H.J.: Glass transition temperature changes of melt-blended polymer nanocomposites containing finely dispersed zno quantum dots. Soft Matter **6**, 4482–4490 (2010)
184. Xia, W., Mishra, S., Keten, S.: Substrate vs. free surface: competing effects on the glass transition of polymer thin films. Polymer **54**(21), 5942–5951 (2013)
185. Xu, J., Ding, L., Chen, J., Gao, S., Li, L., Zhou, D., Li, X., Xue, G.: Sensitive characterization of the influence of substrate interfaces on supported thin films. Macromolecules **47**(18), 6365–6372 (2014)
186. Yang, X.N., Loos, J., Veenstra, S.C., Verhees, W.J.H., Wienk, M.M., Kroon, J.M., Michels, M.A.J., Janssen, R.A.J.: Nanoscale morphology of high-performance polymer solar cells. Nano Lett. **5**(4), 579–583 (2005)

187. Yave, W., Car, A., Wind, J., Peinemann, K.V.: Nanometric thin film membranes manufactured on square meter scale: ultra-thin films for CO_2 capture. Nanotechnology **21**, 395301 (2010)

188. Yin, H., Cangialosi, D., Schoenhals, A.: Glass transition and segmental dynamics in thin supported polystyrene films: the role of molecular weight and annealing. Thermochim. Acta **566**, 186–192 (2013)

189. Yin, H., Napolitano, S., Schoenhals, A.: Molecular mobility and glass transition of thin films of poly(bisphenol a carbonate). Macromolecules **45**(3), 1652–1662 (2012)

190. Yin, H., Napolitano, S., Schoenhals, A.: Molecular mobility and glass transition of thin films of poly(bisphenol a carbonate). Macromolecules **45**(3), 1652–1662 (2012)

191. Yin, H., Schoenhals, A.: Calorimetric glass transition of ultrathin poly(vinyl methyl ether) films. Polymer **54**(8SI), 2067–2070 (2013)

192. van Zanten, J.H., Wallace, W.E., Wu, Wl: Effect of strongly favorable substrate interactions on the thermal properties of ultrathin polymer films. Phys. Rev. E **53**, R2053–R2056 (1996)

193. Zhang, C., Boucher, V.M., Cangialosi, D., Priestley, R.D.: Mobility and glass transition temperature of polymer nanospheres. Polymer **54**(1), 230–235 (2013)

194. Zhang, C., Guo, Y., Priestley, R.D.: Glass transition temperature of polymer nanoparticles under soft and hard confinement. Macromolecules **44**(10), 4001–4006 (2011)

Index